# Quantum corrections to anti-de Sitter space-times: back-reaction from the stress-energy tensor

**Jacob C. Thompson**

**Submitted in partial fulfilment for the degree of Doctor of Philosophy**

**School of Mathematical and Physical Sciences**

**March 2026**

**Supervisor: Elizabeth Winstanley**

*"Un hombre con ideas nuevas es un loco hasta que sus ideas triunfan."*

*"A man with new ideas is a madman, until his ideas triumph."*

*—Marcelo Bielsa*

## Acknowledgements

It would be remiss of me not to thank my gorgeous partner, Grace. Without all of her constant love and support, this thesis would not exist. To Grace: thank you and I love you.

I also want to thank my wonderful mother, who has supported and nurtured me through many ups and downs, and without whom, I wouldn't be the person I am today. Thank you, Mum.

To Dad: thank you for all of your supportive visits to Sheffield, and for letting me 'borrow' your Leeds United season ticket!

I would also like to thank Judy and Gary for welcoming me into their family with open arms and being wonderful parents to Grace. Thank you also to Ian, who has supported my mum through thick and thin.

I also want to thank my sister, Alex, and my closest childhood friends: Devon and Eddie - it doesn't matter how long it has been, it never feels like its been more than a day.

I would also like to thank my PhD brother, Ethan, without whom I am sure I would've gone crazy long before! Thanks for all of your help on the coding side of things (lord knows I didn't have a scooby!), and thanks to both you and Amin for the constant distractions at lunch playing all of those geography games (TimeGuessr is still the MVP).

I need to also pay particular thanks to my amazing supervisor, Elizabeth. Without her, this PhD would not have happened. Thank you for your constant encouragement and support throughout, especially when it came to giving talks. I also have a massive amount of gratitude for you reading through this mammoth thesis! I would also like to thank my supervisor at York, Chris, who taught me so much and instilled a great deal of interest

into me. Thank you both.

Last but certainly not least, I must acknowledge the most important pooches in my life: Bessie (the toods), Remi and Elsie.

I would also like to take this opportunity to reflect on all of the amazing and exotic places I have been able to travel to as part of this PhD, 'working' (and definitely not drinking) at various conferences, including: Granada, Leipzig (twice), Tours, Lisbon, Malta, Paris, London, Birmingham, Southampton, York and Lancaster.

I have had an amazing time over these past four years, and as hard as it has been at times, I wouldn't want to do anything else.

"Time is an illusion. . . lunchtime doubly so."

Douglas Adams

## Abstract

In this thesis we consider a massless and conformally-coupled scalar field propagating, according to quantum field theory on curved space-time, on three- and four-dimensional anti-de Sitter space. The scalar field is taken to either be static or rigidly-rotating about the polar axis, and is subject to Dirichlet, Neumann or transparent boundary conditions on the anti-de Sitter boundary. Using the framework of Hadamard renormalisation, renormalised stress-energy tensors (QFT-RSETs) are constructed in a thermal state. We also model the quantum scalar field as a classical, thermal gas of noninteracting bosonic particles in the framework of relativistic kinetic theory, constructing macroscopic stress-energy tensors (RKT-SETs). We investigate how well these RKT-SETs approximate the QFT-RSETs by expressing them in terms of four physical quantities: energy density, isotropic pressure, anisotropic pressure and heat flux. The dependence of these on the inverse temperature of the quantum state, the angular speed of rigid rotation and the boundary conditions applied to the field is investigated. We find that at high temperatures, modelling the scalar as a gas of bosonic particles provides a good approximation, but at low temperatures, quantum effects dominate. Within the framework of semi-classical gravity, we then study the back-reaction of the quantum scalar field on anti-de Sitter space-time, using the stress-energy tensors previously constructed. We find that the quantum-corrected geometry is that of massive solitons sourced by the quantum scalar field. The mass of these solitons is investigated, in particular its dependence on the inverse temperature, angular speed and the boundary conditions applied to the field. For linear corrections in three dimensions, the mass is ever-increasing with increasing temperature; for nonlinear corrections in four dimensions, the mass exhibits a limiting value at some temperature, above which the mass decreases. We speculate that this is a manifestation of the breakdown of the semi-classical regime.

# Preface

Five publications (three published, two in draft form) have arisen from the work in this thesis. The content of chapter 5 (in particular sections 5.1.2-5.3.4) is contained within [355] and one of the unpublished papers. The content of chapter 7 is contained within [354] and the other unpublished paper. The content of chapter 8 is original work that is not yet published or in draft form. The content of chapter 9 and sections 6.2.2, 6.3, 6.4 can be found in [353]. The remaining chapters contain literature reviews (chapters 1, 2 and 3) or presentations of well established results in the literature (chapter 4 and the remainder of chapter 6). The algebraic and numerical calculations performed throughout work in this thesis were all done in `Mathematica`, making extensive use of the `GeneralRelativityTensors` package from the `BlackHolePerturbationToolkit` repository [198]. For numerical calculations too computationally intensive for a mere laptop, the HPC facilities at the University of Sheffield were utilised. We therefore acknowledge IT Services at The University of Sheffield for the provision of services for High Performance Computing.

## Declaration of Authorship

I hereby confirm that, except where clear reference is made to the work of others, this thesis is my own work. I am aware of the University's Guidance on the Use of Unfair Means (www.sheffield.ac.uk/ssid/unfair-means). This work has not previously been presented for an award at this, or any other, university. The following publications have arisen from work in this thesis:

- [353] J. C. Thompson and E. Winstanley. Quantum-corrected anti–de Sitter spacetime. *Phys. Rev. D*, 110:125003, 2024.
- [355] J. C. Thompson and E. Winstanley. Quantum effects in rotating thermal states on anti-de Sitter space-time. *Phys. Lett. B*, 868:139780, 2025.
- [354] J. C. Thompson and E. Winstanley. Quantum-corrected three-dimensional AdS space-time. In *24th International Conference on General Relativity and Gravitation (GR24) and 16th Edoardo Amaldi Conference on Gravitational Waves (Amaldi16)*, 2025.
- J. C. Thompson and E. Winstanley. Quantum-corrected rotating $AdS_3$. In preparation, 2026.
- J. C. Thompson and E. Winstanley. As yet untitled. In preparation, 2026.

# Contents

**List of Figures** **xv**

**I Introduction and background** **1**

**1 Introduction** **2**

1.1 Quantum gravity or quanta and gravity? . . . . . 3

1.2 Overview of the thesis . . . . . 17

**2 Classical and quantum fields on curved space-times** **22**

2.1 Preliminaries and conventions . . . . . 23

2.2 Classical field theory and general relativity . . . . . 31

2.2.1 Classical field theory: the basics . . . . . 31

2.2.2 The Einstein field equations . . . . . 33

2.2.3 The stress-energy tensor and scalar fields . . . . . 37

2.2.3.1 Energy conditions . . . . . 39

2.2.3.2 Scalar field theory . . . . . 42

2.2.3.3 Fluid stress-energy tensors . . . . . 46

2.3 Relativistic kinetic theory and orthonormal frames in general relativity . . . 46

2.3.1 RKT-stress-energy tensor in three-dimensional space-times . . . . . 52

2.3.2 RKT-stress-energy tensor in four-dimensional space-times . . . . . 54

2.3.3 Rigidly rotating distributions in Minkowski space-time . . . . . 56

2.4 Quantum field theory on flat space-time . . . . . 61

2.4.1 Canonical quantisation . . . . . 62

2.5 Flat space-time expectation values and Green functions . . . . . 68

2.6 Quantum field theory on curved space-times . . . . . 82

2.6.1 Canonical quantisation . . . . . 83

2.7 Curved space-time expectation values and Hadamard renormalisation . . . 88

2.7.1 Renormalisation by state subtraction . . . . . 104

2.8 Summary . . . . . 105

**3 Towards quantum gravity 109**

3.1 Different approaches . . . . . 110

3.2 The semi-classical regime . . . . . 113

3.3 Analytical approximations to the renormalised stress-energy tensor . . . . . 123

3.4 Perturbative approaches . . . . . 125

3.5 Quantum corrections . . . . . 127

3.6 Semi-classical gravity and quantum-corrected geometry on maximally symmetric spaces . . . . . 128

3.7 Summary . . . . . 134

**II Quantum field theory on anti-de Sitter space-time 135**

**4 Anti-de Sitter space-time 136**

4.1 Geometry . . . . . 138

4.2 Conformal structure . . . . . 143

4.3 Maximal symmetry and the geodesic interval . . . . . 147

4.4 Anti-de Sitter space in rotating coordinates and vielbeins . . . . . 151

4.5 Boundary conditions . . . . . 157

4.6 Quantisation . . . . . 159

4.7 Quantum states on anti-de Sitter space . . . . . 167

4.8 Summary . . . . . 169

**5 Stress-energy tensor renormalisation 171**

5.1 Four-dimensional anti-de Sitter space-time . . . . . 172

5.1.1 Static fields . . . . . 172

5.1.2 Rigidly-rotating fields . . . . . 183

5.2 Three-dimensional anti-de Sitter space-time . . . . . 204

5.2.1 Static fields . . . . . 204

5.2.2 Rigidly-rotating fields . . . . . 214

5.3 A brief interlude: QFT vs RKT . . . . . 224

5.3.1 RKT in four-dimensional anti-de Sitter space . . . . . 224

5.3.1.1 Static distributions . . . . . 225

5.3.1.2 Rigidly-rotating distributions . . . . . 226

5.3.2 RKT in three-dimensional anti-de Sitter space . . . . . 231

5.3.2.1 Static distributions . . . . . 232

5.3.2.2 Rigidly-rotating distributions . . . . . 234

5.3.3 QFT in the frame: three- and four-dimensional anti-de Sitter space . 238

5.3.3.1 Static fields in four dimensions . . . . . 239

5.3.3.2 Rigidly-rotating fields in four dimensions . . . . . 240

5.3.3.3 Static fields in three dimensions . . . . . 242

5.3.3.4 Rigidly-rotating fields in three dimensions . . . . . 242

5.3.4 Stress-energy tensor comparisons between RKT and QFT . . . . . 243

5.3.4.1 Four-dimensional anti-de Sitter space-time . . . . . 245

5.3.4.2 Three-dimensional anti-de Sitter space-time . . . . . 285

5.4 Is RKT a suitable approximation to QFT? Summary of the chapter . . . . 305

**III Quantum-corrected anti-de Sitter space-time 309**

**6 Quantum-corrected maximally symmetric space-times 310**

6.1 Minkowski space-time . . . . . 311

6.1.1 RSET on Minkowski space-time . . . . . 311

6.1.2 Quantum-corrected Einstein equations . . . . . 314

6.2 De Sitter space-time . . . . . 315

6.2.1 RSET on de Sitter . . . . . 316

6.2.2 Quantum-corrected Einstein equations . . . . . 319

6.3 Vacuum anti-de Sitter space-time . . . . . 320

6.4 The Einstein static universe . . . . . 321

6.4.1 RSET on the ESU . . . . . 322

6.4.2 Quantum-corrected Einstein equations . . . . . 324

6.5 The BTZ black hole . . . . . 325

6.5.1 RSET on BTZ . . . . . 327

6.5.2 Quantum-corrected Einstein equations . . . . . 329

6.6 Summary . . . . . 334

**7 Linear corrections in three dimensions 337**

7.1 Prelude . . . . . 338

7.2 Coordinate transformed (renormalised) stress-energy tensors . . . . . 340

7.2.1 RSET for static fields . . . . . 340

7.2.2 RSET for rigidly-rotating fields . . . . . 342

7.2.3 RKT-SET . . . . . 343

7.3 Linearised quantum-corrected Einstein equations . . . . . 344

7.4 Solving the LQCEE . . . . . 350

7.5 RKT-corrected metric perturbations . . . . . 356

7.6 Quantum-corrected metric perturbations . . . . . 359

7.7 Solitons . . . . . 363

7.7.1 RKT sourced solitons . . . . . 367

7.7.2 QFT sourced solitons . . . . . 376

7.7.3 Comparison of the RKT and QFT sourced solitons . . . . . 383

7.8 Summary . . . . . 390

**8 Linear corrections in four dimensions 394**

8.1 Prelude and a word of warning . . . . . 395

8.2 Coordinate transformed stress-energy tensors . . . . . 396

8.2.1 RSET for static fields . . . . . 396

8.2.2 RSET for rigidly-rotating fields . . . . . 398

8.2.3 RKT-SET . . . . . 402

8.3 Linearised quantum-corrected Einstein equations . . . . . 403

8.4 Summary . . . . . 408

**9 Nonlinear corrections in four dimensions 410**

9.1 Prelude . . . . . 411

9.2 Quantum-corrected Einstein equations . . . . . 411

9.3 Solving the QCEE . . . . . 414

9.3.1 Taylor series expansions of the QFT-RSET components . . . . . 415

9.3.2 Taylor series expansions of the quantum-corrected metric functions . 418

9.3.3 Numerical method for finding the QC metric functions . . . . . 421

9.4 Quantum-corrected adS metric . . . . . 422

9.4.1 Dirichlet and Neumann boundary conditions . . . . . 422

9.4.2 Transparent boundary conditions, the ESU and RKT . . . . . 434

9.5 Quantum-corrected adS solitons . . . . . 445

9.5.1 Spherically symmetric quantum-corrected Einstein equations . . . . 445

9.5.2 Solving the solitonic QCEE . . . . . 448

9.5.3 Quantum-corrected adS soliton masses . . . . . 459

9.6 Summary . . . . . 470

**IV Conclusions, appendices and the bibliography 474**

**10 Conclusions and outlook 475**

**Appendices 485**

**A Checks and balances on the numerics 486**

**B Taylor series coefficients for the nonlinear, four-dimensional QCEE 490**

B.1 QFT-RSET components . . . . . 491

B.2 Metric function $A(\rho)$ . . . . . 492

B.3 Metric function $C(\rho)$ . . . . . 494

**Bibliography 498**

# List of Figures

1.1 The standard model of particle physics. This shows the elementary particles, grouping each into which type of field theory describes them. The yellow particle (Higgs boson) is described by scalar field theories; the purple and green particles are described by fermionic field theories (the difference between the green and purple particles being which symmetry group represents them); and the red particles are described by vector field theories. Figure taken from [88]. . . . . 7

1.2 The Penrose energy extraction process for a rotating black hole. The black region in the middle is the black hole, whilst the grey region is the ergosphere. The body (red circle) starts outside the ergosphere and drops in. The body splits into its positive and negative energy parts (white circle). The negative energy part falls into the black hole, whilst the positive energy part (yellow circle) escapes the ergosphere with a greater total energy than the body entered with. . . . . 11

1.3 Schematic of Hawking radiation. Spontaneous creation of particle/anti-particle ($e^-/e^+$) pairs occurs due to vacuum fluctuations outside the event horizon $\mathcal{H}$ (red line) of the black hole (shaded grey region). Most particle/anti-particle pairs usually recombine and annihilate each other (top right of the diagram). Hawking radiation occurs when the anti-particle falls into the black hole but the particle escapes to infinity with positive energy. The spectrum of positive energy particles spontaneously emitted (whilst their anti-particle counterpart falls into the black hole) is the Hawking radiation. Figure adapted from [75, 273]. . . . . 13

2.1 The classical, four-dimensional, contravariant stress-energy tensor pictorially depicted by identifying each component with its physical meaning. Since the stress-energy tensor is symmetric under interchange of its indices, the energy flux and momentum density, and the momentum flux and shear stress, are generally interchangeable. Figure adapted from the "stress-energy tensor" Wikipedia page. . . . . 40

2.2 Examples of the possible deformed contours in the complex $\omega$ plane for the integral (2.5.39). Each is associated with a different Green function; the top gives the Wightman functions; the second gives the Pauli-Jordan (blue) and Hadamard (red) Green functions; the third gives the retarded (blue) and advanced (red) Green functions; and the bottom gives the Feynman Green function. The poles, represented by the crosses, are at the points $\omega = \pm\sqrt{|\mathbf{k}|^2 + m^2}$, and are located on the real line. Figures adapted from [45]. . . . . 77

2.3 Schematic flowchart for the Hadamard renormalisation procedure for a scalar operator $\widehat{Q}(x)$ in a general Hadamard state $|\psi\rangle$. The operator $\mathcal{Q}_{\mu\nu}$ is some general differential operator that depends on the two space- or time-like separated points $x$ and $x'$. . . . . 97

2.4 Schematic flowchart for the Hadamard renormalisation procedure for a rank-2 operator $\widehat{Q}_{\mu\nu}(x)$ in a general Hadamard state $|\psi\rangle$. The differential operator $\mathcal{Q}_{\mu\nu}(x, x')$ depends, in general, on the two space- or time-like separated points $x$ and $x'$. The addition of the state-independent tensor $\Theta_{\mu\nu}$ is *not* required for a meaningful expectation value, but is necessary for a well-defined renormalised stress-energy tensor according to Wald's axioms [369, 370, 371]. See the text for more detail. . . . . 101

4.1 Anti-de Sitter space-time visualised as a single-sheeted hyperboloid, embedded in three-dimensional Minkowski space-time with $n-2$ angular coordinates suppressed. Figure adapted from [13]. . . . . 142

4.2 Carter-Penrose diagram of pure anti-de Sitter space-time (left) and its universal covering space (right). The time periodicity of pure-adS is shown by virtue of the horizontal lines with arrows being identified. The blue lines represent null rays, whilst the red curve is a space-like hypersurface $\Sigma$ within its domain of dependence $\mathcal{D}(\Sigma)$, which is denoted by the shaded pink region. For $\Sigma$ to be a Cauchy surface, boundary data must be specified on $\mathscr{I}$ to allow it to uniquely propagate into the future (and from the past). Figures adapted from [31]. . . . . 145

4.3 The two-dimensional ESU cylinder shown embedded in three dimensional Minkowski space, with the angular dimensions suppressed (left) and the Carter-Penrose diagram of the ESU (right). The ESU is a globally hyperbolic space-time [190], and as such, there exists a Cauchy surface $\Sigma$ that can be uniquely evolved through the ESU space-time. The Carter-Penrose diagram demonstrates the conformal mapping between the ESU and anti-de Sitter space (purple region) and the universal covering space of adS (red region). The blue lines are null rays, and the arrows on the time-like boundary $\mathscr{I}$ indicate that $\rho = \pi$ is identified. Diagrams adapted from [13]. . . . . 148

4.4 Carter-Penrose diagrams of the transparent (left) and reflective (right) boundary conditions applied to anti-de Sitter space, mapped onto the ESU. The green and blue lines are null geodesics, whilst the red lines are time-like geodesics. (C)adS is the region contained within the dashed lines at $\rho = \pi/2$, and the vertical lines with arrows are identified. Figures adapted from [13]. 160

4.5 Flowchart for the conformal mapping procedure between anti-de Sitter space and the ESU, in order to construct the Hadamard Green function of a quantum scalar field on anti-de Sitter space with suitable boundary conditions applied. There are two possible paths: red and green. The red path relies on mapping the field in anti-de Sitter space to the ESU, applying boundary conditions to the field in the ESU and constructing the Hadamard Green function of the ESU from the field. The other path, the green path, is a more common procedure. One starts by constructing the Hadamard Green function of anti-de Sitter space (exploiting maximal symmetry), before mapping this to the Hadamard Green function of the ESU, applying suitable boundary conditions to the ESU Hadamard Green function before mapping back to the Hadamard Green function of anti-de Sitter space (which now has correct boundary behaviour). . . . . 164

5.1 Plots for the components of the thermal expectation value of the stress-energy tensor, keeping the adS length scale $a = 1$ while varying the inverse temperature within the range $\beta \in [\pi/3, 5\pi/6]$. These plots are for the case of Dirichlet boundary conditions. . . . . 179

5.2 Plots for the components of the thermal expectation value of the stress-energy tensor, keeping the adS length scale $a = 1$ while varying the inverse temperature within the range $\beta \in [\pi/3, 5\pi/6]$. These plots are for the case of Neumann boundary conditions. . . . . 180

5.3 Plots for the components of the thermal expectation value of the stress-energy tensor, keeping the adS length scale $a = 1$ while varying the inverse temperature within the range $\beta \in [\pi/3, 5\pi/6]$. These plots are for the case of transparent boundary conditions. . . . . 181

5.4 Plots for the components of the thermal expectation value of the stress-energy tensor, keeping the adS length scale $a = 1$ and inverse temperature $\beta = 5\pi/6$ fixed. These plots show the differences in each component between the three cases of boundary conditions. For each, Dirichlet boundary conditions are represented by a solid line; Neumann boundary conditions by a dashed line; and transparent by a dotted line. . . . . 182

5.5 The $\tau\tau$-component of the renormalised stress-energy tensor. The inverse adS length scale $a = 1$ is kept fixed, as is the inverse temperature $\beta = \pi/6$. The angular rotation speed $\Omega$ is varied. Dirichlet boundary conditions are applied to the field. . . . . 197

5.6 Minus the $\tau\phi$-component of the renormalised stress-energy tensor. The inverse adS length scale $a = 1$ is kept fixed, as is the inverse temperature $\beta = \pi/6$. The angular rotation speed $\Omega$ is varied. Dirichlet boundary conditions are applied to the field. . . . . 198

5.7 The $\rho\rho$-component of the renormalised stress-energy tensor. The inverse adS length scale $a = 1$ is kept fixed, as is the inverse temperature $\beta = \pi/6$. The angular rotation speed $\Omega$ is varied. Dirichlet boundary conditions are applied to the field. . . . . 199

5.8 The $\rho\theta$-component of the renormalised stress-energy tensor. The inverse adS length scale $a = 1$ is kept fixed, as is the inverse temperature $\beta = \pi/6$. The angular rotation speed $\Omega$ is varied. Dirichlet boundary conditions are applied to the field. . . . . 200

5.9 The $\theta\theta$-component of the renormalised stress-energy tensor. The inverse adS length scale $a = 1$ is kept fixed, as is the inverse temperature $\beta = \pi/6$. The angular rotation speed $\Omega$ is varied. Dirichlet boundary conditions are applied to the field. . . . . 200

5.10 The $\phi\phi$-component of the renormalised stress-energy tensor. The inverse adS length scale $a = 1$ is kept fixed, as is the inverse temperature $\beta = \pi/6$. The angular rotation speed $\Omega$ is varied. Dirichlet boundary conditions are applied to the field. . . . . 201

5.11 The renormalised stress-energy tensor components at angular rotation speed $\Omega = 0.96$ either on the equatorial plane, $\theta = \pi/2$, or at $\theta = 6\pi/25$ (for the $\rho\theta$-component). The inverse adS length scale $a = 1$ is kept fixed, as is the inverse temperature $\beta = 5\pi/6$. The boundary conditions applied to the field are varied. . . . . 203

5.12 The components of the renormalised stress-energy tensor. The inverse adS length scale is kept fixed at $a = 1$. The inverse temperature is varied within the range $\beta \in [\pi/3, 5\pi/6]$. Dirichlet boundary conditions are applied to the field. . . . . 212

5.13 Plots for the components of the renormalised stress-energy tensor. The inverse adS length scale is kept fixed at $a = 1$, as is the inverse temperature at $\beta = 5\pi/6$. The boundary conditions applied to the field are varied, with the solid line corresponding to Dirichlet boundary conditions; the dashed line to Neumann boundary conditions; and the dotted line to transparent boundary conditions. . . . . 213

5.14 The $\tau\tau$-component of the renormalised stress-energy tensor at two different angular speeds $\Omega$. The inverse adS length scale is kept fixed at $a = 1$. The inverse temperature is varied within the range $\beta \in [\pi/3, 5\pi/6]$. Dirichlet boundary conditions are applied to the field. . . . . 221

5.15 The $\rho\rho$-component of the renormalised stress-energy tensor at two different angular speeds $\Omega$. The inverse adS length scale is kept fixed at $a = 1$. The inverse temperature is varied within the range $\beta \in [\pi/3, 5\pi/6]$. Dirichlet boundary conditions are applied to the field. . . . . 222

5.16 The negative $\tau\phi$-component of the renormalised stress-energy tensor at two different angular speeds $\Omega$. The inverse adS length scale is kept fixed at $a = 1$. The inverse temperature is varied within the range $\beta \in [\pi/3, 5\pi/6]$. Dirichlet boundary conditions are applied to the field. . . . . 223

5.17 The $\phi\phi$-component of the renormalised stress-energy tensor at two different angular speeds $\Omega$. The inverse adS length scale is kept fixed at $a = 1$. The inverse temperature is varied within the range $\beta \in [\pi/3, 5\pi/6]$. Dirichlet boundary conditions are applied to the field. . . . . 223

5.18 Surface plots of the rotating four-dimensional adS RKT-SET prefactor (5.3.15). The adS length scale is fixed, $a = 1$, as well as the global inverse temperature $\beta = \pi/6$. The angular speed is varied. . . . . 227

5.19 Surface plots of the $\tau\tau$-component of the rotating four-dimensional adS RKT-SET. The adS length scale is fixed, $a = 1$, as well as the global inverse temperature $\beta = \pi/6$. The angular speed is varied. . . . . 229

5.20 Minus the $\tau\phi$-component of the rotating four-dimensional adS RKT-SET. The adS length scale is fixed, $a = 1$, as well as the global inverse temperature $\beta = \pi/6$. The angular speed is varied. . . . . 230

5.21 Surface plots of the $\rho\rho$-component of the rotating four-dimensional adS RKT-SET. The adS length scale is fixed, $a = 1$, as well as the global inverse temperature $\beta = \pi/6$. The angular speed is varied. . . . . 231

5.22 Surface plots of the $\theta\theta$-component of the rotating four-dimensional adS RKT-SET. The adS length scale is fixed, $a = 1$, as well as the global inverse temperature $\beta = \pi/6$. The angular speed is varied. . . . . 232

5.23 Surface plots of the $\phi\phi$-component of the rotating four-dimensional adS RKT-SET. The adS length scale is fixed, $a = 1$, as well as the global inverse temperature $\beta = \pi/6$. The angular speed is varied. . . . . 233

5.24 Surface plot of the rotating three-dimensional adS RKT-SET prefactor. The adS length scale is fixed, $a = 1$, as well as the global inverse temperature $\beta = \pi/6$. The angular speed is varied. . . . . 235

5.25 The $\tau\tau$-component of the RKT-SET. The angular speed and inverse temperature are varied, while the inverse adS length scale is fixed at $a = 1$. The inverse temperature range is $\beta \in [\pi/3, 5\pi/6]$. . . . . 236

5.26 Minus the $\tau\phi$-component of the RKT-SET, plotted for two values of the angular speed, and with inverse temperature varied in the range $\beta \in [\pi/3, 5\pi/6]$. The inverse adS length scale is fixed at $a = 1$. . . . . 237

5.27 The $\rho\rho$-component of the RKT-SET, for two values of the angular speed, and with inverse temperature varied in the range $\beta \in [\pi/3, 5\pi/6]$. The inverse adS length scale is fixed at $a = 1$. . . . . 238

5.28 The $\phi\phi$-component of the RKT-SET, plotted for two values of the angular speed, and with inverse temperature varied in the range $\beta \in [\pi/3, 5\pi/6]$. The inverse adS length scale is fixed at $a = 1$. . . . . 239

5.29 Energy density of the QFT-RSET (solid) and RKT-SET (dashed) on the equatorial plane $\theta = \pi/2$. The angular speed is varied, whilst the inverse temperature is in the range $\beta \in [\pi/6, 5\pi/12] \cup [3\pi/4, \pi]$ for the right and left plots respectively. The inverse adS length scale is fixed at $a = 1$, whilst Dirichlet boundary conditions are applied to the field. . . . . 247

5.30 Energy density of the QFT-RSET (solid) and RKT-SET (dashed) on the equatorial plane $\theta = \pi/2$. The angular speed is varied, whilst the inverse temperature is in the range $\beta \in [\pi/6, 5\pi/12] \cup [3\pi/4, \pi]$ for the right and left plots respectively. The inverse adS length scale is fixed at $a = 1$, whilst Neumann boundary conditions are applied to the field. . . . . 249

5.31 Energy density of the QFT-RSET (solid) and RKT-SET (dashed) on the equatorial plane $\theta = \pi/2$. The angular speed is varied, whilst the inverse temperature is in the range $\beta \in [\pi/6, 5\pi/12] \cup [3\pi/4, \pi]$ for the right and left plots respectively. The inverse adS length scale $a = 1$ is fixed, whilst transparent boundary conditions are applied to the field. . . . . 250

5.32 Energy density of the QFT-RSET and RKT-SET on the equatorial plane. The angular speed is varied, whilst the inverse temperature is fixed at either $\beta = \pi$ (left) or $\beta = \pi/4$ (right). The inverse adS length scale $a = 1$ is fixed, and the boundary conditions are varied. . . . . 253

5.33 The difference in energy densities between the QFT-RSETs and RKT-SET on the equatorial plane. The angular speed is varied, whilst the inverse temperature is fixed at either $\beta = \pi$ (left) or $\beta = \pi/4$ (right). The inverse adS length scale $a = 1$ is fixed, and the boundary conditions are varied. . . 254

5.34 Surface plot of the energy density of the QFT-RSET. The inverse temperature is held fixed at $\beta = \pi/4$ as is the inverse adS length scale $a = 1$. The angular speed is varied, while Dirichlet boundary conditions are applied to the field. . . . . 255

5.35 Surface plot of the difference in energy densities of the QFT-RSET and RKT-SET. The inverse temperature is held fixed at $\beta = \pi/4$ as is the inverse adS length scale $a = 1$. The angular speed and boundary conditions varied. . . . 255

5.36 Minus the heat flux on the equatorial plane $\theta = \pi/2$. The angular speed is varied, whilst the inverse temperature is in the range $\beta \in [\pi/6, 5\pi/12] \cup [3\pi/4, \pi]$ for the right and left plots respectively. The inverse adS length scale is fixed at $a = 1$, whilst Dirichlet boundary conditions are applied to the field. The solid lines correspond to the QFT-RSET, and the dashed lines correspond to the RKT-SET (which is identically zero). . . . . 258

5.37 Minus the heat flux on the equatorial plane $\theta = \pi/2$. The angular speed is varied, whilst the inverse temperature is in the range $\beta \in [\pi/6, 5\pi/12] \cup [3\pi/4, \pi]$ for the right and left plots respectively. The inverse adS length scale is fixed at $a = 1$, whilst Neumann boundary conditions are applied to the field. The solid lines correspond to the QFT-RSET, and the dashed lines correspond to the RKT-SET (which is identically zero). . . . . 259

5.38 Minus the heat flux on the equatorial plane $\theta = \pi/2$. The angular speed is varied, whilst the inverse temperature is in the range $\beta \in [\pi/6, 5\pi/12] \cup [3\pi/4, \pi]$ for the right and left plots respectively. The inverse adS length scale is fixed at $a = 1$, whilst transparent boundary conditions are applied to the field. The solid lines correspond to the QFT-RSET, and the dashed lines correspond to the RKT-SET (which is identically zero). . . . . 260

5.39 Minus the heat flux plots on the equatorial plane. The angular speed is varied, whilst the inverse temperature is fixed at either $\beta = \pi$ (left) or $\beta = \pi/4$ (right). The inverse adS length scale $a = 1$ is fixed, and the boundary conditions are varied. . . . . 261

5.40 Surface plot of minus the heat flux. The inverse temperature is held fixed at $\beta = \pi/4$ as is the inverse adS length scale $a = 1$. The angular speed is varied and boundary conditions are Dirichlet. . . . . 262

5.41 Difference in heat fluxes for the differing boundary conditions. The inverse temperature is held fixed at $\beta = \pi/4$ as is the inverse adS length scale $a = 1$, while the angular speed is varied. . . . . 262

5.42 The $\rho\rho$-component of the pressure deviator, plotted on the equatorial plane $\theta = \pi/2$. The angular speed is varied, whilst the inverse temperature is in the range $\beta \in [\pi/6, 5\pi/12] \cup [3\pi/4, \pi]$ for the right and left plots respectively. The inverse adS length scale is fixed at $a = 1$, whilst Dirichlet boundary conditions are applied to the field. The solid lines correspond to the QFT-RSET, and the dashed lines correspond to the RKT-SET (which is identically zero). . . . . 265

5.43 Plots of the pressure deviator $\rho\rho$-component, on the equatorial plane $\theta = \pi/2$. The angular speed is varied, whilst the inverse temperature is in the range $\beta \in [\pi/6, 5\pi/12] \cup [3\pi/4, \pi]$ for the right and left plots respectively. The inverse adS length scale is fixed at $a = 1$, whilst Neumann boundary conditions are applied to the field. For the angular speed of $\Omega = 0$, minus the pressure deviator is instead plotted. The solid lines correspond to the QFT-RSET, and the dashed lines correspond to the RKT-SET (which is identically zero). . . . . 266

5.44 The $\rho\rho$-component of the pressure deviator on the equatorial plane $\theta = \pi/2$. The angular speed is varied, whilst the inverse temperature is in the range $\beta \in [\pi/6, 5\pi/12] \cup [3\pi/4, \pi]$ for the right and left plots respectively. The inverse adS length scale is fixed at $a = 1$, whilst transparent boundary conditions are applied to the field. The pressure deviator is identically zero for an angular speed of $\Omega = 0$, hence its exclusion in this figure. The solid lines correspond to the QFT-RSET, and the dashed lines correspond to the RKT-SET (which is identically zero). . . . . 267

5.45 Pressure deviator $\rho\rho$-component plots on the equatorial plane. The angular speed is varied, whilst the inverse temperature is fixed at either $\beta = \pi$ (left) or $\beta = \pi/4$ (right). The inverse adS length scale $a = 1$ is fixed, and the boundary conditions are varied. For $\Omega = 0$, we show the absolute value of the pressure deviator component. . . . . 268

5.46 The $\rho\rho$-component of the pressure deviator, plotted at a fixed inverse temperature $\beta = \pi/4$. The inverse adS length scale is fixed $a = 1$, whilst both the angular speed and boundary conditions are varied. . . . . 269

5.47 The $\phi\phi$-component of the pressure deviator, plotted on the equatorial plane $\theta = \pi/2$. The angular speed is varied, whilst the inverse temperature is in the range $\beta \in [\pi/6, 5\pi/12] \cup [3\pi/4, \pi]$ for the right and left plots respectively. The inverse adS length scale is fixed at $a = 1$, whilst Dirichlet boundary conditions are applied to the field. For $\Omega = 0$, minus the pressure deviator component is plotted since it is everywhere negative. The solid lines correspond to the QFT-RSET, and the dashed lines correspond to the RKT-SET (which is identically zero). . . . . 272

5.48 The pressure deviator $\phi\phi$-component, on the equatorial plane $\theta = \pi/2$. The angular speed is varied, whilst the inverse temperature is in the range $\beta \in [\pi/6, 5\pi/12] \cup [3\pi/4, \pi]$ for the right and left plots respectively. The inverse adS length scale is fixed at $a = 1$, whilst Neumann boundary conditions are applied to the field. The solid lines correspond to the QFT-RSET, and the dashed lines correspond to the RKT-SET (which is identically zero). . . . . 273

5.49 The $\phi\phi$-component of the pressure deviator on the equatorial plane $\theta = \pi/2$. The angular speed is varied, whilst the inverse temperature is in the range $\beta \in [\pi/6, 5\pi/12] \cup [3\pi/4, \pi]$ for the right and left plots respectively. The inverse adS length scale is fixed at $a = 1$, whilst transparent boundary conditions are applied to the field. When there is no rotation ($\Omega = 0$), the pressure deviator vanishes for transparent boundary conditions, hence the exclusion of plots corresponding to $\Omega = 0$ here. The solid lines correspond to the QFT-RSET, and the dashed lines correspond to the RKT-SET (which is identically zero). . . . . 274

5.50 Pressure deviator $\phi\phi$-component plots on the equatorial plane. The angular speed is varied, whilst the inverse temperature is fixed at either $\beta = \pi$ (left) or $\beta = \pi/4$ (right). The inverse adS length scale $a = 1$ is fixed, and the boundary conditions are varied. When $\Omega = 0$, the absolute value of the pressure deviator component is plotted. . . . . 275

5.51 Surface plot of the pressure deviator component $\Pi^{(\phi)(\phi)}$. The inverse temperature $\beta = \pi/4$ and inverse adS length scale $a = 1$ are fixed. Both the angular speed and boundary conditions are varied. . . . . 276

5.52 Surface plot of the pressure deviator component $\Pi^{(\theta)(\theta)}$. The inverse temperature $\beta = \pi/4$ and inverse adS length scale $a = 1$ are fixed. Both the angular speed and boundary conditions are varied. . . . . 278

5.53 The difference between the $\phi\phi$- and $\theta\theta$-components of the pressure deviator on the equatorial plane $\theta = \pi/2$. The angular speed is varied, whilst the inverse temperature is fixed at either $\beta = \pi$ (left plots) or $\beta = \pi/4$ (right plots). The inverse adS length scale is fixed at $a = 1$, whilst the boundary conditions are varied. . . . . 279

5.54 The difference in pressure deviator components $\Pi^{(\phi)(\phi)}$ and $\Pi^{(\theta)(\theta)}$. The inverse temperature $\beta = \pi/4$ and inverse adS length scale $a = 1$ are fixed. The angular speed is varied and Dirichlet boundary conditions are applied to the field. . . . . 280

5.55 Differences in pressure deviator components $\Pi^{(\phi)(\phi)}$ and $\Pi^{(\theta)(\theta)}$, between the differing boundary conditions. The inverse temperature $\beta = \pi/4$ and inverse adS length scale $a = 1$ are fixed. The angular speed is varied. . . . . 281

5.56 The pressure deviator component $\Pi^{(\rho)(\theta)}$. The inverse temperature $\beta = \pi/4$ and inverse adS length scale $a = 1$ are fixed. The angular speed is varied, whilst Dirichlet boundary conditions are applied to the field. . . . . 283

5.57 Differences in pressure deviator component $\Pi^{(\rho)(\theta)}$ between the differing boundary conditions. The inverse temperature $\beta = \pi/4$ and inverse adS length scale $a = 1$ are fixed. The angular speed is varied. . . . . 284

5.58 Energy density of the QFT-RSET (solid) and RKT-SET (dashed) in three-dimensional anti-de Sitter space-time. The inverse temperature is in the range $\beta \in [\pi/6, 5\pi/12] \cup [3\pi/4, \pi]$ for the right and left plots respectively. The angular speed is varied and Dirichlet boundary conditions are applied to the field. The inverse adS length scale is fixed $a = 1$. . . . . 287

5.59 Energy density of the QFT-RSET (solid) and RKT-SET (dashed) in three-dimensional anti-de Sitter space-time. The inverse temperature is in the range $\beta \in [\pi/6, 5\pi/12] \cup [3\pi/4, \pi]$ for the right and left plots respectively. The angular speed is varied and Neumann boundary conditions are applied to the field. The inverse adS length scale is fixed $a = 1$. . . . . 288

5.60 Energy density of the QFT-RSET (solid) and RKT-SET (dashed) in three-dimensional anti-de Sitter space-time. The inverse temperature is in the range $\beta \in [\pi/6, 5\pi/12] \cup [3\pi/4, \pi]$ for the right and left plots respectively. The angular speed is varied and transparent boundary conditions are applied to the field. The inverse adS length scale is fixed $a = 1$. . . . . 289

5.61 Energy density of the QFT-RSETs (dashed lines) and RKT-SET (solid line) at two fixed inverse temperatures, $\beta = \pi$ (left column) or $\beta = \pi/4$ (right column). The angular speed and boundary conditions applied to the field are varied, whilst the inverse adS length scale is kept fixed $a = 1$. . . . . 290

5.62 Magnitude of the differences in the energy densities of the QFT-RSETs and RKT-SET at two fixed inverse temperatures, $\beta = \pi$ (left column) or $\beta = \pi/4$ (right column). The angular speed and boundary conditions applied to the field are varied, whilst the inverse adS length scale is kept fixed $a = 1$. . . . 291

5.63 Heat fluxes of the QFT-RSET (solid) and RKT-SET (dashed - identically zero). The inverse temperature is varied in the range $\beta \in [\pi/6, 5\pi/12] \cup [3\pi/4, \pi]$ for the right and left plots respectively. The angular speed is varied and the inverse adS length scale is fixed $a = 1$. Dirichlet boundary conditions are applied to the field. . . . . 294

5.64 Heat fluxes of the QFT-RSET (solid) and RKT-SET (dashed - identically zero). The inverse temperature is varied in the range $\beta \in [\pi/6, 5\pi/12] \cup [3\pi/4, \pi]$ for the right and left plots respectively. The angular speed is varied and the inverse adS length scale is fixed $a = 1$. Neumann boundary conditions are applied to the field. . . . . 295

5.65 Heat fluxes of the QFT-RSET (solid) and RKT-SET (dashed - identically zero). The inverse temperature is varied in the range $\beta \in [\pi/6, 5\pi/12] \cup [3\pi/4, \pi]$ for the right and left plots respectively. The angular speed is varied and the inverse adS length scale is fixed $a = 1$. Transparent boundary conditions are applied to the field. . . . . 296

5.66 Heat fluxes of the QFT-RSET for the three different cases of boundary conditions. The inverse temperature is either $\beta = \pi$ (left column) or $\beta = \pi/4$ (right column). The angular speed is varied whilst the inverse adS length scale is kept fixed $a = 1$. . . . . 297

5.67 The nonzero components of the anisotropic pressure of the QFT-RSET (solid lines) - it is identically zero for the RKT-SET (dashed lines). Dirichlet boundary conditions are applied to the field and the inverse adS length scale is kept fixed $a = 1$. The angular speed and inverse temperature are varied, with the latter in the range $\beta \in [\pi/6, 5\pi/12] \cup [3\pi/4, \pi]$, for the right and left plots respectively. . . . . 301

5.68 The nonzero components of the anisotropic pressure of the QFT-RSET - it is identically zero for the RKT-SET. Neumann boundary conditions are applied to the field and the inverse adS length scale is kept fixed $a = 1$. The angular speed and inverse temperature are varied, with the latter in the range $\beta \in [\pi/6, 5\pi/12] \cup [3\pi/4, \pi]$, for the right and left plots respectively. 302

5.69 The nonzero components of the anisotropic pressure of the QFT-RSET - it is identically zero for the RKT-SET. Transparent boundary conditions are applied to the field and the inverse adS length scale is kept fixed $a = 1$. The angular speed and inverse temperature are varied, with the latter in the range $\beta \in [\pi/6, 5\pi/12] \cup [3\pi/4, \pi]$, for the right and left plots respectively. 303

5.70 The absolute value of the nonzero anisotropic pressure components of the QFT-RSETs, for the three different boundary conditions of interest. The inverse temperature is either $\beta = \pi$ (left column) or $\beta = \pi/4$ (right column). The inverse adS length scale is kept fixed, whilst the angular speed is varied. 304

7.1 The ratio $(1 + r^2 - \widetilde{\Gamma}^{-1}_{(3)})/(1 - r^2 + \widetilde{\Gamma}^{-1}_{(3)})$, for $r, \Omega \in [0, 1)$. This ratio is always nonnegative. . . . . 357

7.2 The perturbed mass $\delta M$ and angular momentum $\delta J$ against inverse temperature $\beta$. For the BTZ bound (6.5.2) to hold, the perturbed mass must always be greater than the perturbed angular momentum. As the angular speed is increased, the difference between the perturbed mass and angular momentum decreases, and verification of the BTZ bound is less obvious. The inverse adS length scale is fixed $a = 1$, and the inverse temperature is varied in the range $\beta \in [\pi/12, 59\pi/120]$. . . . . 375

7.3 Plots of the perturbed mass $\delta M$ (solid line) and angular momentum $\delta J$ (dashed line) against inverse temperature $\beta$. The BTZ bound (6.5.2) requires the perturbed mass to always be greater than the perturbed angular momentum. As the angular speed is increased, the difference between the perturbed mass and angular momentum decreases, and, whilst the BTZ bound is still satisfied, this is less obvious. The left column of plots is for an angular speed of $\Omega = 0.5$ and the right column is for an angular speed of $\Omega = 0.96$. The different rows correspond to different boundary conditions applied to the quantum scalar field, with Dirichlet (top), Neumann (middle) and transparent (bottom) boundary conditions considered. The inverse temperature is varied in the range $\beta \in [\pi/12, 59\pi/120]$, and the inverse adS length scale is fixed $a = 1$. . . . . 384

7.4 The perturbed mass $\delta M$ plotted against inverse temperature $\beta$. The solid line denotes the QFT mass with Dirichlet boundary conditions applied to the field; the long dashed line is for Neumann boundary conditions; the dotted line corresponds to transparent boundary conditions; and the short dashed line denotes the RKT mass. The inverse adS length scale is set to unity, $a = 1$, whilst the inverse temperature is varied in the range $\beta \in [\pi/12, 59\pi/120]$. The angular speed $\Omega$ is $\Omega = 0$ (top row), $\Omega = 0.5$ (middle row) or $\Omega = 0.96$ (top row). . . . . 386

7.5 The perturbed angular momentum $\delta J$ plotted against inverse temperature $\beta$. The solid line denotes the QFT angular momentum with Dirichlet boundary conditions applied to the field; the long dashed line is for Neumann boundary conditions; the dotted line corresponds to transparent boundary conditions; and the short dashed line denotes the RKT angular momentum. The inverse adS length scale is set to unity, $a = 1$, whilst the inverse temperature is varied in the range $\beta \in [\pi/12, 59\pi/120]$. The angular speed $\Omega$ is $\Omega = 0.5$ or $\Omega = 0.96$ (top row); the angular momentum is identically zero when the angular speed is zero. . . . . 387

7.6 Ratios of the perturbed mass $\delta M$, between the three boundary conditions and the RKT case for an angular speed of $\Omega = 0$ (top plots), $\Omega = 0.5$ (middle plots) and $\Omega = 0.96$ (bottom plots). The solid lines correspond to the ratio of (the perturbed mass in the case of) Dirichlet boundary conditions and the RKT; the long dashed lines correspond to the ratio of Neumann boundary conditions and the RKT; the dotted lines correspond to the ratio of transparent boundary conditions with the RKT case; the short dashed lines correspond to the ratio of the RKT case with itself and is thus identically unity. On the left plots, all four ratios are shown, whilst the right plots only show the ratio of transparent boundary conditions with the RKT. The inverse adS length scale is fixed $a = 1$, and the inverse temperature is considered in the range $\beta \in [\pi/12, 59\pi/120]$. . . . . 389

7.7 Ratios of the perturbed angular momentum $\delta J$, between the three boundary conditions and the RKT case for an angular speed of $\Omega = 0.5$ (top plots) and $\Omega = 0.96$ (bottom plots). The solid lines correspond to the ratio of (the perturbed angular momentum in the case of) Dirichlet boundary conditions and the RKT; the long dashed lines correspond to the ratio of Neumann boundary conditions and the RKT; the dotted lines correspond to the ratio of transparent boundary conditions with the RKT case; the short dashed lines correspond to the ratio of the RKT case with itself and is thus identically unity. On the left plots, all four ratios are shown, whilst the right plots only show the ratio of transparent boundary conditions with the RKT. The inverse adS length scale is fixed $a = 1$, and the inverse temperature is varied in the range $\beta \in [\pi/12, 59\pi/120]$. . . . . 391

9.1 The three QC metric functions as ratios with their pure adS counterparts. In the top row, Dirichlet boundary conditions are applied to the field; in the bottom row, Neumann boundary conditions are applied. The left column shows the functions when the local inverse temperature is fixed at $\beta = \pi/4$, whilst in the right column, the local inverse temperature is fixed at $\beta = \pi$. The original inverse adS length scale is fixed at $a = 1$. . . . . 424

9.2 Ratios of the three QC metric functions when Neumann and Dirichlet boundary conditions are applied to the field. The left column shows the functions when the local inverse temperature is fixed at $\beta = \pi/4$, whilst in the right column, the local inverse temperature is fixed at $\beta = \pi$. The original inverse adS length scale is fixed at $a = 1$. . . . . 424

9.3 The three quantum-corrected metric functions as ratios with their pure adS counterparts. The local inverse temperature is varied in the range $\beta \in [\pi/12, 11\pi/24] \cup [5\pi/8, \pi]$ for the left and right plots respectively. The unrenormalised inverse adS length scale is fixed $a = 1$, whilst Dirichlet boundary conditions are applied to the quantum scalar field. . . . . 427

9.4 The three quantum-corrected metric functions as ratios with their pure adS counterparts. The local inverse temperature is varied in the range $\beta \in [\pi/12, 11\pi/24] \cup [5\pi/8, \pi]$ for the left and right plots respectively. The unrenormalised inverse adS length scale is fixed $a = 1$, whilst Neumann boundary conditions are applied to the quantum scalar field. . . . . 429

9.5 Ratios of the three quantum-corrected metric functions between the cases when Neumann and Dirichlet boundary conditions are applied to the field. The local inverse temperature is varied in the range $\beta \in [\pi/12, 11\pi/24] \cup [5\pi/8, \pi]$ for the left and right plots respectively, and the unrenormalised inverse adS length scale is fixed $a = 1$. . . . . 431

9.6 The ratio of the metric functions $A(\rho)$ and $B(\rho)$ for both Dirichlet (top row) and Neumann (bottom row) boundary conditions. The local inverse temperature is varied in the range $\beta \in [\pi/12, 11\pi/24] \cup [5\pi/8, \pi]$ for the left and right plots respectively, and the unrenormalised inverse adS length scale is fixed to be $a = 1$. . . . . 433

9.7 Ratio of the prefactors of the mixed indices RKT-SET and QFT-RSET when transparent boundary conditions are applied to the field. The left shows the inverse temperature over a domain of $\beta \in (0, 20]$ and the right over the reduced domain $\beta \in [\pi/12, \pi]$. The unrenormalised inverse adS length scale is set to unity. . . . . 435

9.8 The three QC metric functions as ratios with their pure adS counterparts (although $A^{(\mathrm{T})}(\rho)/\sec^2(\rho)$ is exactly unity). Transparent boundary conditions are applied to the field. In the left plot, the local inverse temperature is fixed at $\beta = \pi/4$, while in the right it is fixed at $\beta = \pi$. The unrenormalised inverse adS length scale is fixed at $a = 1$. . . . . 438

9.9 The QC metric functions $B^{(\mathrm{T})}(\rho)$ and $C^{(\mathrm{T})}(\rho)$ as ratios with their pure adS counterparts. The inverse temperature is varied in the range $\beta \in [\pi/12, 11\pi/24] \cup [5\pi/8, \pi]$ for the left and right plots respectively. Transparent boundary conditions are applied to the field, and the original inverse adS length scale is fixed at $a = 1$. . . . . 440

9.10 Ratios of the QC metric function $B(\rho)$ when transparent and Dirichlet boundary conditions (top row) are applied, and when transparent and Neumann boundary conditions are applied (bottom row). The local inverse temperature is varied in the range $\beta \in [\pi/12, 11\pi/24] \cup [5\pi/8, \pi]$ for the left and right columns respectively, and the original inverse adS length scale is fixed at $a = 1$. . . . . 441

9.11 Ratios of the QC metric function $C(\rho)$ when transparent and Dirichlet boundary conditions (top row) are applied, and when transparent and Neumann boundary conditions are applied (bottom row). The local inverse temperature is varied in the range $\beta \in [\pi/12, 11\pi/24] \cup [5\pi/8, \pi]$ for the left and right columns respectively, and the original inverse adS length scale is fixed at $a = 1$. . . . . 443

9.12 The derivative $\frac{\mathrm{d}m}{\mathrm{d}\rho}$ for Dirichlet (top row), Neumann (middle row) or transparent (bottom row) boundary conditions. The inverse temperature lies in the range $\beta \in [\pi/12, 11\pi/24] \cup [5\pi/8, \pi]$ for the left and right columns respectively. The unrenormalised adS length scale is $a = 1$. . . . . 450

9.13 The derivative $\frac{\mathrm{d}m}{\mathrm{d}r}$ for Dirichlet (top row), Neumann (middle row) or transparent (bottom row) boundary conditions. The inverse temperature lies in the range $\beta \in [\pi/12, 11\pi/24] \cup [5\pi/8, \pi]$ for the left and right columns respectively. The unrenormalised adS length scale is $a = 1$. . . . . 452

9.14 The derivative $\frac{\mathrm{d}\psi}{\mathrm{d}\rho}$ for Dirichlet (top row), Neumann (middle row) or transparent (bottom row) boundary conditions. The inverse temperature lies in the range $\beta \in [\pi/12, 11\pi/24] \cup [5\pi/8, \pi]$ for the left and right columns respectively. The unrenormalised adS length scale is $a = 1$. . . . . 453

9.15 The derivative $\frac{\mathrm{d}\psi}{\mathrm{d}r}$ for Dirichlet (top row), Neumann (middle row) or transparent (bottom row) boundary conditions. The inverse temperature lies in the range $\beta \in [\pi/12, 11\pi/24] \cup [5\pi/8, \pi]$ for the left and right columns respectively. The unrenormalised adS length scale is $a = 1$. . . . . 454

9.16 All four derivatives $\frac{\mathrm{d}m}{\mathrm{d}\rho}$ (top left), $\frac{\mathrm{d}m}{\mathrm{d}r}$ (top right), $\frac{\mathrm{d}\psi}{\mathrm{d}\rho}$ (bottom left) and $\frac{\mathrm{d}\psi}{\mathrm{d}r}$ (bottom right). Dirichlet boundary conditions are represented by a solid line, Neumann boundary conditions by a dashed line and transparent boundary conditions by a dotted line. The inverse temperature is fixed at $\beta = \pi/4$ and the original inverse adS length scale is $a = 1$. . . . . 456

9.17 The quantum-corrected metric function $\psi(r)$ as a function of the new radial coordinate $r$. The quantum scalar field satisfies either Dirichlet (top row), Neumann (middle row) or transparent (bottom row) boundary conditions. The inverse temperature is in the range $\beta \in [\pi/12, 11\pi/24] \cup [5\pi/8, \pi]$ for the left and right columns respectively. The original inverse adS length scale is fixed $a = 1$. . . . . 461

9.18 Ratios between the QC metric function $\psi(r)$ when the boundary conditions are altered. The original inverse adS length scale $a = 1$ is fixed, whilst the inverse temperature is varied in the range $\beta \in [\pi/12, 11\pi/24] \cup [5\pi/8, \pi]$ for the left and right columns respectively. . . . . 463

9.19 The quantum-corrected mass function $m(r)$ as a function of the new radial coordinate $r$. The quantum scalar field satisfies either Dirichlet (top row), Neumann (middle row) or transparent (bottom row) boundary conditions. The inverse temperature is in the range $\beta \in [\pi/12, 11\pi/24] \cup [5\pi/8, \pi]$ for the left and right columns respectively. The original inverse adS length scale is fixed $a = 1$. . . . . 465

9.20 Ratios between the QC mass function $m(r)$ when the boundary conditions are altered. The original inverse adS length scale $a = 1$ is fixed, whilst the inverse temperature is varied in the range $\beta \in [\pi/12, 11\pi/24] \cup [5\pi/8, \pi]$ for the left and right columns respectively. . . . . 466

9.21 The quantum-corrected soliton mass $M = \lim_{r\to\infty} m(r)$ as a function of the inverse temperature $\beta$. The quantum scalar field satisfies either Dirichlet (solid line), Neumann (dashed line) or transparent (dotted line) boundary conditions. The inverse adS length scale is fixed to be $a = 1$. . . . . 468

A.1 `NSumTerms` required against inverse temperature $\beta$ such that the relative error in the infinite sums (5.1.18) is less than $10^{-8}$. The inverse adS length scale is fixed at $a = 1$. . . . . 488

A.2 The relative error in the metric functions $A(\rho)$ (top), $B(\rho)$ (middle) and $C(\rho)$ (bottom). The blue curves represent the relative error between $\epsilon = 10^{-3}$ and $\epsilon = 10^{-2}$, whilst the orange curves represent the relative error between $\epsilon = 10^{-3}$ and $\epsilon = 10^{-4}$. Dirichlet boundary conditions are applied to the field, and the adS length scale is fixed $a = 1$. The temperature is chosen to be the highest in the range we consider, that is $\beta = \pi/12$, since this is where the highest relative error occurs. . . . . 489

# Part I

# Introduction and background

# Chapter 1

# Introduction

"See first, think later, then test. But always see first. Otherwise, you only see what you were expecting. Most scientists forget that."

*Douglas Adams*

## § 1.1 Quantum gravity or quanta and gravity?

One of the biggest open questions currently in theoretical physics is how one might postulate a *theory of everything*; that is, a theory that unifies *all* fundamental forces under one framework. There are four fundamental forces: the *strong interaction*, the *weak interaction*, the *electromagnetic* and *gravitational* force. The early twentieth century was a hotbed of discovery for theories describing the four fundamental forces. On the one hand, Einstein's theory of *general relativity* revolutionalised the way we thought about gravity. On the other hand, the *standard model of particle physics* incorporates the remaining three fundamental forces, describing each by *quantum field theories*. General relativity and quantum field theory are perhaps two of the most successful physical theories to date. How one might bridge the gap between the two has been the subject of intense discussion for nigh-on a century.

By the mid nineteenth century, it was widely accepted that gravity was an attractive force, described by Newtonian gravity [278]. Under the framework of Newtonian gravity, masses attract each other and the strength of the attraction weakens with increasing distance. However, nearing the end of the nineteenth century, two observations were made forcing the abandonment[1] of Newtonian gravity: the precession of Mercury's perihelion deviated from the Newtonian prediction [237]; and the speed of light is constant and independent of the observer's motion [261]. In order to describe the latter observation, Einstein (incorporating earlier work by Maxwell, Lorentz and Poincaré) developed what he later named the *theory of special relativity* [123]. However it was not until ten years later, when Einstein developed what is known as the *theory of general relativity* [124, 125] that the anomalous precession of Mercury's perihelion was fully predicted [126]. General relativity is still the most successful

[1] This is not to say that Newtonian gravity is a bad theory; there are many regimes in which Newtonian gravity is still a very good model. For example, in weak gravitational fields or for objects undergoing motion at speeds much less than the speed of light.

theory of gravity to date.

The theory of general relativity differs in its description of gravity from Newtonian gravity by one major concept: gravity is not an attractive force between two masses, but rather the manifestation of the warping (or curving) of space-time by those masses. The theory of general relativity is described by *Einstein's field equations*[2], which relate the curvature of space-time to (the energy density of) matter. They are perhaps encapsulated best by Wheeler's now iconic phrase that [380]

"*Space-time tells matter how to move; matter tells space-time how to curve.*"

On the left-hand-side of the Einstein field equations are geometric objects such as the Riemann tensor and Ricci scalar, along with the metric tensor and cosmological constant. These geometric objects (the metric tensor, Riemann tensor and Ricci scalar) govern how space-time should curve. The cosmological constant affects the expansion rate of the universe, although Einstein initially added this to counterbalance the effect of gravity, seeking field equations that described a static universe, as was the consensus of our own universe at the time. After Hubble's discovery that our universe was in fact expanding [202], Einstein abandoned the cosmological constant altogether, claiming it was his life's "grösste Eselei", or "greatest blunder" [128, 161, 162, 244, 282]. After discovering that the rate of the expansion of the universe is accelerating [298, 313], physicists sought to reincorporate the cosmological constant into the Einstein field equations, using it to describe the exponential expansion rate of the universe. On the right-hand-side of the Einstein field equations lies the stress-energy tensor, which encodes the matter content of space-time, which is anything that can carry energy (including light).

At the turn of the twentieth century, great strides were being made into describing physics at the atomic scale. Planck introduced the first concept of *quanta* in order to explain the full spectrum of thermal radiation emitted by a thermal body [304]. In particular,

[2]The field equations will be derived in earnest in chapter 2.

classical physics predicted that, at short wavelengths, energy would be emitted by a hot body at an infinite rate; this is known as the *ultraviolet catastrophe*. In order to resolve the ultraviolet catastrophe, Planck proposed that thermal radiation should be modelled by a set of harmonic oscillators, each emitting an integer number of units of energy, rather than a continuous and arbitrary amount of energy. He postulated that the quantum of energy of a light quantum is proportional to its frequency, with the constant of proportionality now known as *Planck's constant*

$$h = 6.62607015 \times 10^{-34} \mathrm{kg} \cdot \mathrm{m}^2 \cdot \mathrm{s}^{-1}.$$

This was the first notion of energy being *quantised*. Concurrently with his work on special relativity, in 1905 Einstein extended this concept by proposing that light behaves as particles [122], which we now know as *photons*. Then, in 1924, de Broglie proposed that matter particles must also exhibit wave-like properties, leading to the *wave-particle* duality phenomenon [98]. A year later, Heisenberg, Born and Jordan [49, 51, 192][3] developed the mathematical theory of matrix mechanics to describe this, followed by Schrödinger who developed wave mechanics [329], and showed that wave and matrix mechanics made the same predictions about the properties of the electron. In the late 1920s, Dirac attempted to use Schrödinger's framework to quantise the electromagnetic field [110, 111]; since special relativity was borne of classical electromagnetism, it was believed that the quantised electromagnetic field must include relativistic effects. Dirac's work culminated in the *Dirac equation*, which established that particles are quanta of underlying fields and successfully combined quantum mechanics with special relativity. This marked the birth of *quantum electrodynamics*. Initially, the Dirac equation was interpreted as a single particle equation like the Schrödinger equation, but this was later abandoned in favour of the true field interpretation [112, 193]. Simultaneously, Schrödinger was able to find the relativistic generalisation of the Schrödinger equation, known as the Klein-Gordon equation. And thus, quantum field theory was born.

[3] See [50, 52, 194, 364] for English translations.

Quantum field theory has successfully unified three of the four fundamental forces into one framework: quantum electrodynamics for the electromagnetic force; *quantum chromodynamics* for the strong interaction; and *quantum flavourdynamics* for the weak interaction (though the electromagnetic and weak forces are usually referred to together as *electroweak theory*). They come under the umbrella term of *the standard model of particle physics*. The standard model utilises quantum field theory to express *every* fundamental particle by a suitable quantum field theory: either a *scalar* field theory, a *fermion* field theory, or a *vector* field theory. All three play an important part in describing particle physics; undoubtedly, however, scalar field theory is a simpler mathematical object and proves a useful playground for understanding particle physics. The different types of field theory considered correspond to a different set of particles. For example, scalar fields describe spin-0 particles, such as the Higgs boson; spinor fields describe spin-1/2 particles, which are known as fermions, and include, for example, electrons, protons and neutrons; and vector fields describe spin-1 particles, such as photons and W/Z bosons. We can be more specific, by specifying whether a field theory is real or complex; a field being real or complex denotes that the corresponding field theory describes uncharged and charged particles, respectively. Of the fields and corresponding particles mentioned above, real scalar fields model the uncharged Higgs boson; complex scalar fields model the charged Higgs boson and charged pions; real spinor fields describe neutrinos, whilst complex spinor fields model, amongst others, electrons and protons; real vector fields describe all gauge bosons (such as the photon or gluon); and finally, complex vector fields model, for example, the $W^+$ and $W^-$ bosons. These lists are far from exhaustive; there are many other particles described by all three field theories. See, for example, standard particle physics textbooks such as [68, 330, 356]. Figure 1.1 shows the standard model of elementary particles, grouping the elementary particles by which field theory describes them (bosonic or fermionic).

Despite their individual successes, it has thus far proved difficult to unify the two competing theories. A year after Einstein published his theory of general relativity, he noted that

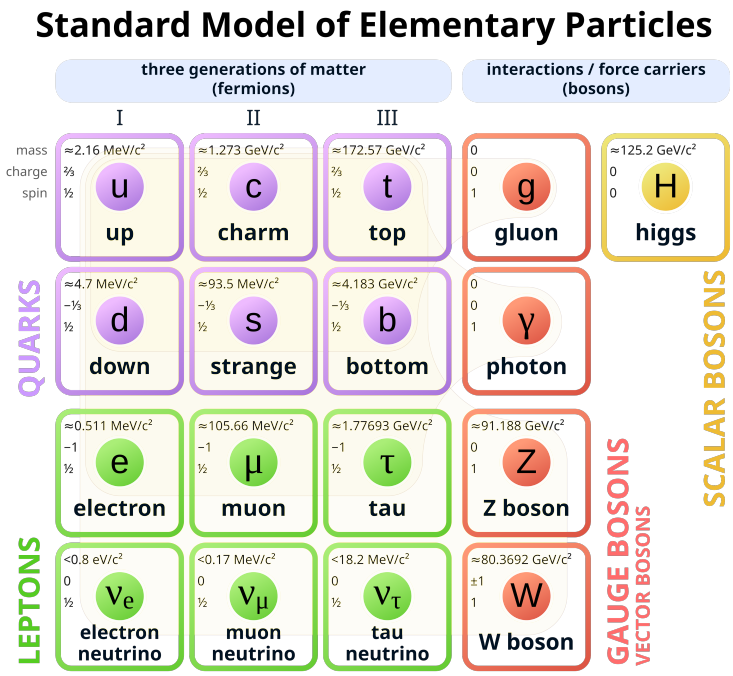


Figure 1.1: The standard model of particle physics. This shows the elementary particles, grouping each into which type of field theory describes them. The yellow particle (Higgs boson) is described by scalar field theories; the purple and green particles are described by fermionic field theories (the difference between the green and purple particles being which symmetry group represents them); and the red particles are described by vector field theories. Figure taken from [88].

quantum effects must eventually modify his theory of general relativity [127]. However, it was not until the mid 1930s that it was understood that there were fundamental differences between general relativity and quantum mechanics. In 1935 Bronstein deduced, via a simple Gedankenexperiment, that general relativity will break down at scales below the Planck scale [56]. Part of the issue of incompatibility between the two theories stems from how they perceive motion: in general relativity, the movement of massive bodies is a result of the curvature of space; whereas in quantum theory (described by the standard model), the motion of massive (and massless) bodies is interpreted as the propagation of energy via excitations of particles, and forces are mediated by the exchange of virtual particles.

By the late 1940s and early 1950s, three main directions emerged in the search for a theory of quantum gravity: the *sum over histories* approach; the *canonical* approach; and the *covariant* approach [321]. The sum over histories approach has not received the same attention as the canonical and covariant approaches in the literature, but has produced some interesting approaches to quantum gravity; in particular, most of the discrete approaches - such as causal sets and casual dynamical triangulations (see section 3.1) - were born of the sum over histories paradigm. The canonical approach to quantum gravity entails quantising the space-time itself (following the quantisation procedure for fields initiated by Dirac [114]), rather than treating gravity as a field on the background. Its major advantage is that the ensuing theory of quantum gravity is background independent; on the other hand, its biggest disadvantage is that it is plagued by the so-called 'problem of time' [203]. The first major breakthrough of the canonical approach came in 1967, when the *Wheeler-DeWitt equation* was derived [107], which described quantum gravity by the wave equation for the universe, though it was found to be ill-defined in general. It was not until the late 1980s that a well-defined version of the Wheeler-DeWitt equation was found, sparking the birth of *loop quantum gravity* (see section 3.1) [30, 323, 324]. The final strand of the three directions, the covariant approach, is where the work of this thesis lies.

The covariant approach takes essentially the opposite view to the canonical approach.

Whilst the canonical approach attempts to quantise space-time, the covariant approach instead treats space-time as a fixed background and attempts to treat gravity as a quantum field. The general method of the covariant approach is to treat the metric as a small perturbation away from a fixed background, performing the quantisation procedure on this background. Usually, the background is taken to be flat space, since quantum field theory on flat space is well understood. The most successful approach to (covariant) quantum gravity is perhaps *string theory*, which treats the fundamental building blocks of matter not as particles, but vibrating strings in higher space-time dimensions, where individual particles are represented by different excitations of these strings (see section 3.1 for more detail). String theory[4] has predicted the existence of the *graviton*, which is postulated to be the fundamental interaction particle of gravity. Despite its theoretical prediction, the existence of the graviton has yet to be experimentally validated, with a consensus among a large number of physicists that *direct* detection is practically impossible [119, 320].

By the late 1950s and early 1960s, research into quantum gravity was stalling. Nevertheless, there were many groups still devoted to the task. Much of the focus surrounded the approaches of DeWitt, Dirac, Feynman, Schwinger amongst many others, following either the canonical, covariant or sum-over-histories schema. It was not until the mid 1960s that there was a resurgence in interest surrounding quantum gravity. This was sparked by Parker's seminal work [289], where he took a different and somewhat solitary approach compared to the consensus at the time. Under the supervision of Coleman, Parker "*...wanted to find new consequences of the quantum field theory of elementary particles in the context of Einstein's theory of general relativity.*" [291], by "[*studying*] *quantised elementary particle fields in the curved space-times that were solutions of the nonlinear Einstein gravitational field equations*" [291]. In essence, Parker's approach was to treat the background gravitational field as a fixed classical object, and quantise the matter fields (i.e. elementary particles); this is known as a *semi-classical approach*. Parker found that, in an expand-

[4]Other theories have also predicted the existence of the graviton.

ing universe modelled by the Friedmann-Lemaître-Robertson-Walker (FLRW) geometry [153, 154, 238, 239, 316, 317, 318, 375], particle production occurred, stimulated by the gravitational field. This is one of four groundbreaking phenomena in the subject that Parker unknowingly initiated, now known as *quantum field theory in curved space-times*. However, it was not until the 1980s that quantum field theory in curved space-times reached maturity, culminating in the highly influential monograph by Birrell and Davies [45]. Since then, work on quantum field theory in curved space-times has been both vast and varied, and the area of quantum field theory in curved space-times is still a highly active area of research. See, for example, recent textbooks such as [271, 293]. It is important to stress that quantum field theory on curved space-times is not a *full* theory of quantum gravity, but rather a semi-classical approximation of one.

One of the key ideas in quantum field theory in curved space-time is that the concept of particles and vacua are both highly ambiguous (this is discussed in more detail in section 2.6.1) in a general curved space. This issue is highly exacerbated in regions with large curvature, such as close to, and moments after, the 'big bang' singularity, and near black holes (where, by definition, classically, nothing can escape). One might consider, therefore, that black hole space-times may well be the least promising of places to seek effects of particle creation. However, Parker's results demonstrated quantum particle creation in an expanding universe containing a big bang singularity. It is therefore perhaps not so unnatural to think that one may also find evidence of quantum particle creation in black hole space-times.

If one were to consider a rotating black hole, then there is a region outside of its event horizon called the *ergosphere*, where a stationary observer at infinity views an observer in the ergosphere as rotating in the same direction as the black hole, and whose total energy relative to infinity is negative. Penrose [297] realised that this process could be exploited to extract energy from the black hole, by having a body break up into two fragments in the ergosphere, one with positive energy and one with negative energy. The negative energy

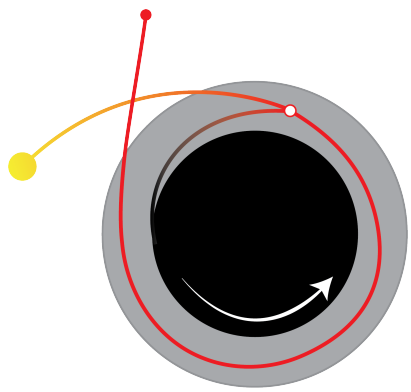

Figure 1.2: The Penrose energy extraction process for a rotating black hole. The black region in the middle is the black hole, whilst the grey region is the ergosphere. The body (red circle) starts outside the ergosphere and drops in. The body splits into its positive and negative energy parts (white circle). The negative energy part falls into the black hole, whilst the positive energy part (yellow circle) escapes the ergosphere with a greater total energy than the body entered with.

fragment falls into the black hole, reducing its mass, whilst the positive energy fragment escapes to infinity, carrying a greater total energy than the body initially sent into the ergosphere. This is called the *Penrose (energy extraction) process*. Figure 1.2 shows a schematic of this procedure.

Only a few years after Penrose's discovery, it was found that there exists a wave analogue of the Penrose process [339, 392]. Instead of sending a body (read: classical particle) into the ergosphere, one could have a classical wave impinge upon a rotating black hole, such that part of the wave will be absorbed by the black hole and part of it emitted to infinity. If arranged correctly, the absorbed part of the wave will have negative energy relative to an observer at infinity, and the emitted part of the wave will have a greater energy than the initial wave. This process is known as *superradiant scattering*. Starobinskii noted that superradiant scattering appeared to be the classical analogue of stimulated emission in quantum theory [339]. However, in instances where stimulated emission occurs,

spontaneous emission must also occur; this seemingly suggested that spontaneous emission (i.e. spontaneous particle creation from the vacuum) should occur for a rotating black hole. Around a year after Starobinskii postulated this, Unruh [360] confirmed this process for a rotating (Kerr [223]) black hole [360]. And thus, the second great result of quantum field theory in curved space-times was discovered: *Starobinskii-Unruh radiation.*

In Unruh's calculation [360] of particle creation by a rotating black hole, an idealised space-time model was utilised. In this model, there was a natural, but not necessarily physically correct, choice of vacuum state. In the same year as Unruh's calculation [360], Hawking [188] managed to circumvent this issue by considering a space-time describing gravitational collapse to a black hole. What followed was one of the most remarkable results in modern theoretical physics. Hawking found that, even for nonrotating black holes, particle creation occurs at late times and produces a nonzero flux of particles to infinity [188]. In particular, Hawking found that for a nonrotating black hole, the spectrum of particles emitted at late times is thermal in nature, with a temperature given by the surface gravity of the black hole divided by a factor of $2\pi$ [188]. This remarkably simple result is known as *Hawking radiation*, and is arguably the greatest result in quantum field theory on curved space-times. Figure 1.3 shows a schematic of this procedure.

However, as beautiful as Hawking's result was, it featured a rather disturbing issue: using a seemingly natural notion of 'particles' near the event horizon of the black hole there appeared to be a divergent number and energy density of ultra-high-frequency particles present (due to the gravitational blue-shift). In order to understand this issue, Unruh reconsidered the notion of 'particles' altogether; instead of thinking of 'particles' in the usual sense, he considered a 'particle' to be a state of the field that makes a particle detector register [361]. Unruh showed that, in Minkowski space, when a quantum field is in its default configuration (i.e. the 'vacuum' state), a particle detector carried by an accelerating observer will click, i.e. the detector will detect a 'particle' [361]. In particular, Unruh showed that a uniformly accelerating observer will 'see' a thermal bath (i.e. spectrum)

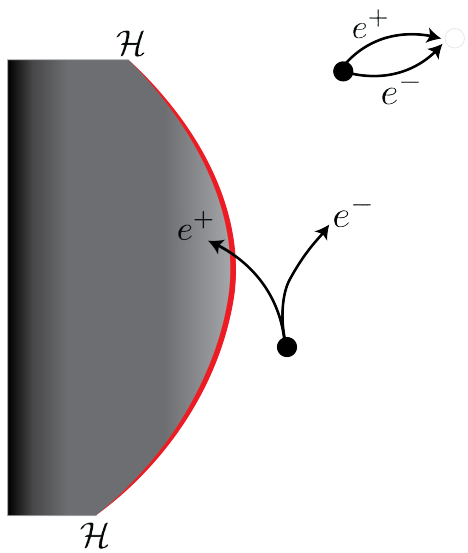


Figure 1.3: Schematic of Hawking radiation. Spontaneous creation of particle/anti-particle ($e^-/e^+$) pairs occurs due to vacuum fluctuations outside the event horizon $\mathcal{H}$ (red line) of the black hole (shaded grey region). Most particle/anti-particle pairs usually recombine and annihilate each other (top right of the diagram). Hawking radiation occurs when the anti-particle falls into the black hole but the particle escapes to infinity with positive energy. The spectrum of positive energy particles spontaneously emitted (whilst their anti-particle counterpart falls into the black hole) is the Hawking radiation. Figure adapted from [75, 273].

of particles at a temperature directly proportional to the acceleration of the observer, divided by a factor of $2\pi$ [361]. This is known as the *Unruh effect*. The Unruh effect explained the issue of gravitational blue-shift near the horizon of a black hole; particles undergoing gravitational blue-shift are 'seen' by a stationary observer relative to the black hole, but in order for this observer to remain stationary relative to infinity, they must undergo an enormous amount of acceleration. Therefore, what this observer 'sees' near the black hole horizon is actually the manifestation of the Unruh effect. Correspondingly, a freely-falling (into the black hole) observer will not see any gravitationally blue-shifted 'particles', just as an inertial observer in Minkowski space does not see any 'particles' in the Minkowski vacuum. The Unruh effect was the third great result of quantum field theory in curved space-times in as many years, between 1974 and 1976. Clearly, the notion of 'particles' in quantum field theory in curved space-times is plagued with ambiguities; one cannot consider 'particles' as the fundamental object in quantum field theory, but one must

instead consider fields as the fundamental object.

In an effort to circumvent the inherent ambiguities, a popular approach to quantum field theory in curved space-times began to emerge by the 1980s: *algebraic quantum field theory*. The framework of algebraic quantum field theory was laid in the 1960s by the formulation of the *Haag-Kastler axioms* [181], which arose in an attempt to make quantum field theories both mathematically rigorous and precise. However, it was not until later that it was used as a framework with which to describe quantum field theory in curved space-times, with key early work due to Araki [22], Haag [180], Kay [217, 218] and others. The idea behind algebraic quantum field theory is to replace the notion of 'particles' with the notion of local observables, some of which *will* correspond to particles and others will correspond to fields. The advantage of the algebraic approach is that one does not need to specify a vacuum state, nor is one forced to make a particular choice of representation at the outset, unlike the 'usual' approach (following the Wightman axioms [343, 384, 385]). Algebraic quantum field theory is one of the most fruitful approaches to quantum field theory in curved space-times to date, spawning a plethora of literature and new research areas, such as *perturbative algebraic quantum field theory* [64, 117, 152, 311] amongst others. There are many recent review papers focussed on algebraic quantum field theory, such as [63, 143].

Algebraic quantum field theory spawned out of a desire to make quantum field theory mathematically precise. However, algebraic quantum field theory is not the only approach at making quantum field theory precise; another approach which followed the Haag-Kastler axioms in the 1960s [181] was the more general *axiomatic quantum field theory* (in particular the *Wightman axioms* [343, 385]), which is generally referred to as the 'usual' approach to rigorous quantum field theory, and encapsulated by the term *the Wightman programme*. The Wightman programme lays out a set of axioms that any mathematically rigorous quantum field theory should obey. The general idea is to specify a 'vacuum' state and construct a Fock space as the Hilbert space of all states, defining operators on the Fock

space such as the *creation* and *annihilation* operators[5]. Though the Wightman programme does not have the advantage of not requiring a specific choice of representation and 'vacuum' state from the outset, it nevertheless proves a useful framework with which to perform calculations and construct *noninteracting* theories.

Using the Wightman programme, there are two ways one can proceed to construct and entirely specify a quantum field theory: one can either employ the usual *canonical quantisation procedure*[6], whereby one constructs fields by decomposing them into positive and negative frequency modes; or one can utilise the *Wightman reconstruction theorem* [343, 384, 385], which states that for a quantum field theory, one can entirely reconstruct a quantum field from the full set of $n$-point correlation functions. In particular, one can entirely specify a noninteracting (i.e. free) quantum field theory from a single two-point correlation function. In the literature, two-point correlation functions are frequently referred to as *Green functions* or *propagators*. Green functions/$n$-point correlation functions/propagators play a key role in quantum field theory on curved space-times.

Quantum field theory on curved space-times is a semi-classical approximation to quantum gravity. The semi-classical approximation is described by the *semi-classical Einstein equations*, which are almost identical to the classical Einstein equations except for one major detail: on the right-hand-side of the classical Einstein equations lies the classical stress-energy tensor, which describes the matter content of the universe; in the semi-classical regime, this is replaced by a *renormalised stress-energy tensor* which describes the quantum matter content of the universe. The renormalised stress-energy tensor is constructed out of Green functions and is actually an *expectation value* of a stress-energy tensor opera-

[5]This is the approach we take in this thesis, though we omit the groundwork and start by defining a 'vacuum' state.

[6]For a time in the literature, this was known by the incorrect nomenclature *second quantisation*. This is a misnomer, since one is not quantising again, and comes from the fact that at one time, it was thought that the Dirac equation described a relativistic wave-function. It is now understood that the Dirac equation describes a classical spinor field, which, when quantised, yields a fermionic quantum field theory.

tor on the Fock space in some quantum state, whether that be the 'vacuum' state or some excited state such as a state at some thermodynamical temperature. The left-hand-side of the semi-classical Einstein equations (the classical aspect) is still governed by Einstein's theory of general relativity, whilst the right-hand-side (the quantum aspect) is governed by the framework of quantum field theory on curved space-times. In particular, general relativity governs the curvature of space-time, whilst quantum field theory on curved space-times governs the propagation of matter through the space-time. However, it is understood that the semi-classical regime is only a valid approximation when the quantum effects of gravity are negligible; furthermore, if the fluctuations arising from the quantum matter are sufficiently large (i.e. above the Planck scale) then it is expected that the semi-classical approximation will break down.

There is one further key ingredient of the semi-classical approximation that we have thus far neglected to mention: *back-reaction*. In general relativity, the motion of bodies affects the curvature and thus underlying geometry of space-time. Should a similar effect also be expected for quantum matter? This is the key idea behind back-reaction. Quantum field theory on curved space-times is a highly successful approximation that governs the propagation of quantum matter on classical backgrounds. But it does not tell us anything about how this quantum matter affects the very space-time on which it propagates. Whilst it is expected that in most scenarios, the effect of back-reaction will be negligible, there are scenarios in which it is expected to play a key role. For example, consider the first key result of quantum field theory on curved space-times: particle creation by a gravitational field in an expanding universe. It is now understood that initial quantum fluctuations drove the early expansion of the universe [179, 272], especially close to the Planck time [147, 185, 186, 199, 200, 287, 288, 332, 391, 393]; this itself is back-reaction. Another example arises when considering (arguably) the greatest result of quantum field theory on curved space-times: Hawking radiation. As Hawking radiation is emitted from a black hole, energy is emitted towards infinity, increasing the overall entropy of the system. Without

back-reaction, the black hole would maintain a constant energy and mass, meaning its entropy would stay the same. This means the overall entropy of the system would increase without bound, violating the second law of thermodynamics. Including back-reaction forces the black hole to lose mass, thereby decreasing its entropy, ensuring the second law of thermodynamics is satisfied [38, 188, 201, 374].

To summarise: Ought a full theory of quantum gravity be expected to include quantum effects on the space-time? By extension, should any self-respecting approximation of quantum gravity aim to include such effects? This is why understanding the mechanism of back-reaction, even in the semi-classical approximation, is vital. It is the back-reaction of quantum matter on classical space-time backgrounds where the scope of this thesis lies.

## § 1.2 Overview of the thesis

In this section, the layout of the thesis will be outlined. This thesis is grouped into four parts:

- **Part I** introduces the theoretical background material required in this thesis. In particular, the framework for the 'construction' of quantum matter is laid out.
- **Part II** moves onto the 'quantum matter' aspect of the back-reaction process, constructing a suitable quantum field theory and calculating the 'quantum matter' of the semi-classical Einstein equations (i.e. the renormalised stress-energy tensor on the right-hand-side).
- **Part III** deals with the final piece in the puzzle of back-reaction: the back-reaction itself. Using the quantum matter constructed in part II, we analyse the effect of back-reaction on two different space-times, in the form of *quantum corrections* to the classical geometry.
- **Part IV** concludes the thesis and includes appendices and the bibliography.

Each part is further split into chapters as follows:

- **Chapter 1:** The background theory that underpins the work in this thesis is heuristically introduced. In particular, a brief historical account is given of the theory in order to provide a suitable motivation for the work in this thesis.

- **Chapter 2:** Here, the background theory required is more fully introduced, with technical details. This chapter is split roughly into two parts: sections 2.1-2.3 deal with classical scalar fields, whilst sections 2.4-2.7 treat quantum scalar fields. In particular, a 'ground up' treatment is given for the classical Einstein equations from Lagrangian mechanics, with a particular focus on scalar fields when deriving the classical stress-energy tensor. In addition, we introduce relativistic kinetic theory and derive the macroscopic stress-energy tensor. In the 'quantum part' of this chapter, we discuss quantum field theory on flat and curved space-times, heuristically describing the canonical quantisation procedure for both, and discussing in detail the Wightman programme (i.e. the Green function approach). In particular, we describe the Hadamard renormalisation scheme for quantum scalar fields.

- **Chapter 3:** We discuss in earnest some different approaches to quantum gravity. We pay particular attention to the semi-classical regime, since this is the focus of this thesis. In addition, we discuss different methods of solving the semi-classical Einstein equations, including analytical approximations to the stress-energy tensor, perturbative approaches and the quantum-corrected regime. Furthermore, we show how the semi-classical regime (and the different methods of solving the semi-classical Einstein equations) simplifies when considering a maximally-symmetric background space-time. This chapter marks the end of part I.

- **Chapter 4:** This chapter is the first of two in part II. The choice of background space-time is fixed: anti-de Sitter space-time. Its basic geometry is discussed, as well as its conformal structure and its properties of maximal symmetry. Additionally,

rigid-rotation is introduced and discussed, including speed-of-light surfaces and orthonormal frames (i.e. vielbeins) for three- and four-dimensional anti-de Sitter space. Finally, the quantum field theory for a conformally-coupled scalar field on anti-de Sitter space is studied, by explicitly constructing the Hadamard Green function; a small discussion of quantum states is also presented.

- **Chapter 5:** The latter chapter of two in this part, it is devoted to constructing expectation values of the stress-energy tensor, i.e. renormalised stress-energy tensors. Four are constructed: the renormalised stress-energy tensors corresponding to static and rigidly-rotating, massless and conformally-coupled scalar fields in three- and four-dimensional anti-de Sitter space. Additionally, by using the vielbeins constructed in the previous chapter, macroscopic stress-energy tensors from relativistic kinetic theory are also derived. Much of the chapter is devoted to comparing the renormalised and macroscopic stress-energy tensors, by decomposing into a thermometer frame, in order to see how well the macroscopic stress-energy tensors approximate the renormalised stress-energy tensors.

- **Chapter 6:** The first of the chapters in part III, this chapter represents the first foray into back-reaction calculations. The background space-time in the semi-classical Einstein equations is taken to be a maximally-symmetric space-time, with the exception of both the Einstein static universe and the BTZ black hole geometry; their inclusion is nevertheless justified. These space-times provide simple examples of the types of back-reaction problem one must solve, with the majority of the quantum corrections in this chapter corresponding to renormalisations of characteristic parameters of the theory, such as the cosmological constant.

- **Chapter 7:** This is the first of two chapters dedicated to solving the linearised, quantum-corrected Einstein equations. In particular, the background space-time is taken to be three-dimensional anti-de Sitter space, and the renormalised stress-energy

tensor corresponds to both a static and rigidly-rotating, massless and conformally-coupled quantum scalar field; the case where the linearised, quantum-corrected Einstein equations are sourced by the macroscopic stress-energy tensor of relativistic kinetic theory is also investigated. In order to find the explicit forms of the linearised, quantum-corrected Einstein equations, an ansatz for the quantum-corrected metric must be made; two different ansätze are made, the first corresponding to an isotropic and static geometry, with the second corresponding to a solitonic metric, inspired, in part, by the quantum-corrected BTZ geometry discussed in the previous chapter. Primarily of interest is the solitonic interpretation, whereby it is found that the quantum-corrected geometry is that of solitons sourced by the renormalised stress-energy tensor or the macroscopic stress-energy tensor, with a characteristic mass. The dependence of this mass on the temperature of the quantum state, the boundary conditions imposed on the quantum scalar field and the angular speed of the rigid rotation is investigated.

- **Chapter 8:** This chapter is the second devoted to finding solutions to the linearised, quantum-corrected Einstein equations. This time, the background space-time is taken to be *four*-dimensional anti-de Sitter space. However, the work of this chapter remains unfinished, and instead preliminary calculations are shown, such as the explicit forms of the linearised, quantum-corrected Einstein equations.

- **Chapter 9:** Finally, to conclude part III, a full *nonlinear* treatment of the back-reaction problem is undertaken. Like the previous chapter, the background space-time is taken to be four-dimensional anti-de Sitter space. The renormalised stress-energy tensor used as a source in the full, quantum-corrected Einstein equations corresponds to a massless and conformally-coupled quantum scalar field. Just as in chapter 7, two ansätze are made for the quantum-corrected metric. The first corresponds to a simple static and spherically-symmetric geometry, whilst the second follows the solitonic interpretation. In a similar fashion to chapter 7, the primary

interest lies in the solitonic interpretation, and it is found, somewhat unexpectedly, that the mass of the solitons is *not* ever increasing with the temperature of the quantum state.

- **Chapter 10:** The thesis is summarised and concluded, and thoughts regarding future directions of work are shared.
- **Appendix A:** This appendix contains supplementary material regarding numerical consistency checks for solutions to nonlinear, quantum-corrected Einstein equations of chapter 9.
- **Appendix B:** Supplementary material regarding coefficients of the Taylor series expansions in chapter 9 can be found in this appendix.

# Chapter 2

# Classical and quantum fields on curved space-times

"Schau ganz tief in die Natur, und dann verstehst Du alles besser."
"Look deep into nature and then you will understand everything better."

*Albert Einstein*

## § 2.1 Preliminaries and conventions

This thesis is not intended to be a textbook or reference material (in spite of its length), so this section exists merely to include the basic concepts required for the remainder of this thesis. For more detailed treatments of all the concepts, one would refer the reader to the deluge of great textbooks available. In particular, some personal favourites of the author are: [75, 246, 262, 314, 373] for general relativity; [45, 138, 146, 157, 207, 271, 299, 338, 377, 390] for quantum field theory; and [164, 176, 225, 234, 327, 333, 342] for more general concepts such as differential equations and special functions, classical field theory and basic quantum physics.

Before we review the basic material required in this thesis, we state the conventions and nomenclature used.

- We work in the Landau-Lifshitz space-like convention à la Misner, Thorne and Wheeler [234, 262]. That is, we use metric signature $(-1, +1, +1, \ldots, +1)$ and the right-hand-side of the Einstein equations is positive.

- We use the Einstein summation convention, i.e. when indices are 'contracted' (i.e. the same index appears both in the sub- and super-script position), we take this to mean
$$x_\mu z^\mu = \sum_{\mu=0}^{n-1} x_\mu z^\mu = x_0 z^0 + x_1 z^1 + \cdots + x_{n-1} z^{n-1}, \tag{2.1.1}$$
where $n$ is the number of space-time dimensions.

- Unless explicitly reinstated (such as in section 6.4), we work in (modified) Planck units, i.e. we set
$$c = \hbar = 8\pi G_N = 1. \tag{2.1.2}$$
The constants $c, \hbar, G_N$ have dimensions
$$[c] = LT^{-1}, \quad [\hbar] = ML^2T^{-1}, \quad [G_N] = M^{-1}L^{n-1}T^{-2}. \tag{2.1.3}$$

Using (modified) Planck units, each unit $M, L, T$ must also be dimensionless.

- Partial (or coordinate) derivatives are interchangeably denoted by a comma in its indices or using standard derivative notation:

$$X_{,\mu} = \partial_\mu X = \frac{\partial X}{\partial x^\mu}, \quad X_{\mu,\nu} = \partial_\nu X_\mu = \frac{\partial X_\mu}{\partial x^\nu}, \quad X^\mu{}_{,\nu} = \partial_\nu X^\mu = \frac{\partial X^\mu}{\partial x^\nu}. \tag{2.1.4}$$

  In a similar fashion, the covariant derivative is interchangeably denoted by a semi-colon in its indices or by a $\nabla$:

$$X_{;\mu} = \nabla_\mu X, \quad X_{\mu;\nu} = \nabla_\nu X_\mu, \quad X^\mu{}_{;\nu} = \nabla_\mu X^\nu. \tag{2.1.5}$$

- In part of this thesis, the concept of orthonormal frames and *vielbeins* are introduced. Vielbeins are the $n$-dimensional extension of *tetrads*. We refer to four-dimensional vielbeins as *vierbeins*, and three-dimensional vielbeins as *dreibeins*. When distinguishing between frame and space-time coordinates (and thus indices), we adopt Chandrasekhar's notation [81], and denote frame indices by Latin letters inside brackets, e.g. $(a)$. Likewise, we (attempt to) only use Greek letters to refer to space-time indices.

- In the literature, there is considerable discourse surrounding Green('s) functions. In this thesis, we use the nomenclature 'Green functions'[1].

- We interchangeably refer to Green functions as propagators and $n$-point correlators, though we mostly use the term Green function.

Now that the bookkeeping of conventions is dealt with, we can introduce the basic concepts which are required for the work in this thesis.

[1]Reference [388] details the difference between the two. Post millennium, the adjectival form (Green function) is more widely adopted. Additionally, if one were to use the definite form, that would imply the existence of "The Green" when referring to "The Green's functions". Furthermore, in German, due to a wonderfully verbose set of grammatical rules, they are referred to exclusively as "*Greensche Funktions*" - the adjectival form, not the possessive.

We work on a pseudo-Riemannian manifold, which is a manifold that possesses both time- and space-like coordinates in the metric tensor. In particular, space-time is described by a Lorentzian manifold, which is a pseudo-Riemannian manifold with only one time-like direction and coordinate in the metric tensor. A pseudo-Riemannian manifold has a unique affine, curvature connection $\nabla$, known as the *Levi-Civita connection*, the *covariant connection*, or the *covariant derivative* (amongst others). This is defined as an affine connection under which the metric tensor is invariant, i.e.

$$\nabla g \equiv 0, \tag{2.1.6}$$

and is torsion free, i.e. for two vector fields $X$ and $Y$,

$$\nabla_X Y - \nabla_Y X = [X, Y]. \tag{2.1.7}$$

If we specify a coordinate chart, the Levi-Civita connection can be defined by its action on a (co-)vector field $X$ as

$$\nabla_\mu X^\nu = \partial_\mu X^\nu + \Gamma^\nu{}_{\mu\lambda} X^\lambda, \quad \nabla_\mu X_\nu = \partial_\mu X_\nu - \Gamma^\lambda{}_{\nu\mu} X_\lambda, \tag{2.1.8}$$

where the $\partial$ are coordinate derivatives, and the $\Gamma$ are Christoffel symbols (of the connection $\nabla$), defined in the Landau-Lifshitz convention in terms of the metric tensor as

$$\Gamma^\lambda{}_{\mu\nu} = \frac{1}{2} g^{\lambda\gamma} \left( \partial_\mu g_{\gamma\nu} + \partial_\nu g_{\mu\gamma} - \partial_\gamma g_{\mu\nu} \right). \tag{2.1.9}$$

On a pseudo-Riemannian manifold, any connection admits an associated *Riemann tensor*. In particular, the associated Riemann tensor for the Levi-Civita connection can be defined by the action of the Levi-Civita connection on a vector field $u$ as

$$\left( \nabla_\gamma \nabla_\varrho - \nabla_\varrho \nabla_\gamma \right) u^\mu =: R^\mu{}_{\nu\gamma\varrho} u^\nu. \tag{2.1.10}$$

Exploiting the fact that the associated Riemann tensor for the coordinate derivative $\partial$ is zero, we can additionally write the Riemann tensor for the Levi-Civita connection $\nabla$ in terms of Christoffel symbols and the coordinate derivative as

$$R^\mu{}_{\nu\gamma\varrho} = \partial_\gamma \Gamma^\mu{}_{\varrho\nu} - \partial_\varrho \Gamma^\mu{}_{\gamma\nu} + \Gamma^\mu{}_{\gamma\lambda} \Gamma^\lambda{}_{\varrho\nu} - \Gamma^\mu{}_{\varrho\lambda} \Gamma^\lambda{}_{\gamma\nu}. \tag{2.1.11}$$

Each Riemann tensor has an associated *Ricci tensor*, which can be found by contracting the Riemann tensor as

$$R_{\mu\nu} = R^{\lambda}{}_{\mu\lambda\nu} = g^{\gamma\lambda} R_{\gamma\mu\lambda\nu}, \tag{2.1.12}$$

and each Ricci tensor has an associated *Ricci scalar*, which can be found by contracting the Ricci tensor as

$$R = R_{\mu}{}^{\mu} = g^{\mu\nu} R_{\mu\nu}. \tag{2.1.13}$$

Another important curvature tensor is the *Weyl tensor*, defined as

$$C_{\mu\nu\gamma\lambda} = R_{\mu\nu\gamma\lambda} - \frac{2}{n-2}\left(g_{\mu[\gamma}R_{\lambda]\nu} - g_{\nu[\gamma}R_{\lambda]\mu}\right) + \frac{2}{(n-1)(n-2)} R g_{\mu[\gamma} g_{\lambda]\nu}, \tag{2.1.14}$$

where square brackets around indices refer to the antisymmetric part of the (combination of) tensor(s). The Weyl tensor is traceless and is invariant under conformal transformations of the metric. We can also define three second-order *curvature invariants*, the *Kretschmann scalar* $K_1$, the *Chern-Pontryagin scalar* $K_2$ and the *Euler scalar* $K_3$. These are given in terms of the Riemann, Ricci and Weyl tensor and the Ricci scalar as

$$K_1 = R_{\mu\nu\alpha\sigma} R^{\mu\nu\alpha\sigma}, \tag{2.1.15}$$

$$K_2 = \varepsilon^{\mu\nu\alpha\sigma} R^{\delta}{}_{\gamma\mu\nu} R^{\gamma}{}_{\delta\alpha\sigma}, \tag{2.1.16}$$

$$K_3 = -C_{\mu\nu\alpha\sigma} C^{\mu\nu\alpha\sigma} + 2R_{\mu\nu} R^{\mu\nu} - \frac{2}{3} R^2 \tag{2.1.17}$$

where $\varepsilon^{\bullet\bullet\bullet\bullet}$ is the anti-symmetric Levi-Civita tensor.

Much of the scope of this thesis surrounds space-times which are maximally symmetric. Such spaces are defined as being homogeneous (the geometry is the same everywhere) and isotropic (the geometry is the same in every direction), and in particular possess the maximum number of *Killing vectors* which, in $n$-dimensions, is $n(n+1)/2$ [341]. A Killing vector is heuristically defined as a tangent vector field along directions associated with isometries - distance preserving symmetries - of the space-time. Equivalently, if the metric of space-time is invariant in the direction of a coordinate $x^{\mu}$, then the metric possesses an

isometry in the direction of $x^\mu$ and the vector field $\xi = \partial_\mu$ is a Killing vector that generates such an isometry.

This can be defined in a more rigorous way, following Stephani [341]. First, consider the infinitesimal coordinate transformation

$$x^\mu \mapsto \widetilde{x}^\mu = x^\mu + \xi^\mu(x)\,\mathrm{d}\lambda = x^\mu + \delta x^\mu, \tag{2.1.18}$$

where the infinitesimal change is made along the vector field $\xi$ at $x^\mu$, and is given by

$$\delta x^\mu := \xi^\mu(x)\,\mathrm{d}\lambda, \tag{2.1.19}$$

where $\lambda$ is a general parameter along the integral curve of $\xi$ through $x^\mu$. The change in the metric with respect to the coordinate transformation (2.1.18) can be then given as

$$\delta g_{\mu\nu} = \frac{\partial g_{\mu\nu}}{\partial x^\gamma}\xi^\gamma\,\mathrm{d}\lambda. \tag{2.1.20}$$

Since the line element $\mathrm{d}s^2$ must be invariant under coordinate transformations, it must be the case that

$$0 = \delta(\mathrm{d}s^2) = \delta(g_{\mu\nu}\,\mathrm{d}x^\mu\,\mathrm{d}x^\nu) = (g_{\mu\nu,\gamma}\xi^\gamma + g_{\gamma\nu}\xi^\gamma{}_{,\mu} + g_{\mu\gamma}\xi^\gamma{}_{,\nu})\,\mathrm{d}x^\mu\,\mathrm{d}x^\nu\,\mathrm{d}\lambda, \tag{2.1.21}$$

so that any vector field satisfying the condition

$$g_{\mu\nu,\gamma}\xi^\gamma + g_{\gamma\nu}\xi^\gamma{}_{,\mu} + g_{\mu\gamma}\xi^\gamma{}_{,\nu} = 0, \tag{2.1.22}$$

is a generator of an isometry or, equivalently, a symmetry. The condition (2.1.22) is equivalent to requiring that the *Lie derivative* of the metric tensor be zero, i.e. if $\mathcal{L}_\xi$ is the Lie derivative along the vector $\xi$, then

$$\mathcal{L}_\xi g_{\mu\nu} := g_{\mu\nu,\gamma}\xi^\gamma + g_{\gamma\nu}\xi^\gamma{}_{,\mu} + g_{\mu\gamma}\xi^\gamma{}_{,\nu} = 0. \tag{2.1.23}$$

If we further promote the partial derivatives to covariant derivatives, the condition (2.1.22) can be written as

$$\xi_{\mu;\nu} + \xi_{\nu;\mu} = 0, \tag{2.1.24}$$

which is known as *Killing's equation*, and any vector satisfying it (or equation (2.1.22)) is known as a *Killing vector*. By exploiting the symmetries of the Riemann tensor in conjunction with Killing's equation (2.1.24), it can be shown that the maximum number of Killing vectors in an $n$-dimensional space is $n(n+1)/2$ [341].

In maximally symmetric spaces, the Riemann tensor can be given in terms of the number of space-time dimensions (by exploiting its symmetries in conjunction with the Killing equation (2.1.24)) as [341]

$$R_{\mu\nu\gamma\lambda} = \mathscr{K}\left(g_{\mu\gamma}g_{\nu\lambda} - g_{\mu\lambda}g_{\nu\gamma}\right), \tag{2.1.25}$$

where the constant $\mathscr{K}$ is the *radius of curvature*, and is defined in terms of the Ricci scalar and number of space-time dimensions by the relation

$$\mathscr{K} = \frac{R}{n(n-1)}. \tag{2.1.26}$$

Contracting the Riemann tensor (2.1.25) with the metric tensor, we find the Ricci tensor

$$R_{\mu\nu} = \mathscr{K}(n-1)g_{\mu\nu}. \tag{2.1.27}$$

from which, by contracting with the metric tensor once more, we find the Ricci scalar

$$R = \mathscr{K}n(n-1). \tag{2.1.28}$$

In a Lorentzian manifold, there are only three maximally symmetric space-times in any dimension greater than 1. They are classified entirely by the sign of the Ricci scalar (which is constant), with:

$$\begin{aligned} R > 0, &\quad \text{De Sitter space-time,} \\ R = 0, &\quad \text{Minkowski space-time,} \\ R < 0, &\quad \text{Anti-de Sitter space-time.} \end{aligned}$$

When the Ricci scalar is zero, we recover flat (Minkowski) space. In Minkowski space, there is no gravitational curvature nor any vacuum energy (characterised by the cosmological

constant) and so there are no gravitational effects. Conversely, when the Ricci scalar is positive, we have a space-time which is expanding (due to the vacuum energy), and corresponds to de Sitter space-time. Finally, when the Ricci scalar is negative, we have anti-de Sitter space-time; anti-de Sitter space can be thought of as a space-time that is constrained within an infinite 'gravitational box', where the vacuum energy acts to confine the space-time and essentially 'pull everything inwards'. A comprehensive treatment of anti-de Sitter space will be given in chapter 4 of this thesis.

The scope of this thesis (in particular parts II and III) centres around anti-de Sitter space-time. Along with being a space of constant, negative curvature, one of its most interesting (and unhelpful) properties is that it is a *nonglobally hyperbolic* space-time. More details of this can be found in section 4.2, but in order to fully discuss the lack of global hyperbolicity, it is necessary to introduce some theory [373] and define, precisely, what global hyperbolicity means.

We start with two distinct events $\{x, x'\}$ on a space-time $\mathcal{M}$. The two events are said to be *causally related* if one event can be influenced by the other. That is, one event must lie in or on the light-cone of the other event, which is equivalent to requiring that the events be connected either by a null or time-like curve. Suppose further that $x'$ is causally related to $x$, and in particular is in the future of $x'$. Then we can say that $x'$ is in the causal future of $x$, which is denoted by $\mathcal{J}^+(x)$. Similarly, if $x'$ is causally related to and in the past of $x$, then we say that $x'$ is in the causal past of $x$ and denote this by $\mathcal{J}^-(x)$. Now suppose we take an arbitrary hypersurface $\mathcal{H}$ such that $\mathcal{H} \subset \mathcal{M}$. Then the set of all events in the space-time $\mathcal{M}$ that are causally related to events on $\mathcal{H}$ is the union

$$\mathcal{J}(\mathcal{H}) = \mathcal{J}^+(\mathcal{H}) \cup \mathcal{J}^-(\mathcal{H}). \tag{2.1.29}$$

Now let us suppose further that the hypersurface $\mathcal{H}$ is *achronal*, i.e. for events $\{x, x'\} \in \mathcal{H}$, there does not exist a time-like or null curve connecting $x$ and $x'$. Then all possible causal pasts of an event in the causal future of $\mathcal{J}^+(\mathcal{H})$ must intersect $\mathcal{H}$ and all possible causal

futures of an event in the causal past $\mathcal{J}^-(\mathcal{H})$ must intersect $\mathcal{H}$. We call these regions the *future domain of dependence* and the *past domain of dependence* and denote them, respectively, by $\mathcal{D}^+(\mathcal{H})$ and $\mathcal{D}^-(\mathcal{H})$. The future domain of dependence is thus a region in the space-time $\mathcal{M}$ in which events are inevitably causally influenced by events on $\mathcal{H}$. That is to say, any events on $\mathcal{H}$ form a set from which any event in $\mathcal{D}^+(\mathcal{H})$ may always be predicted. Similarly, for the past domain of dependence, any events on $\mathcal{H}$ form a set from which any event in $\mathcal{D}^-(\mathcal{H})$ may always be 'retrodicted'. The *full domain of dependence* is the set of events entirely determined by events on $\mathcal{H}$ and is given by the union of the past and future domains of dependence:

$$\mathcal{D}(\mathcal{H}) = \mathcal{D}^+(\mathcal{H}) \cup \mathcal{D}^-(\mathcal{H}). \tag{2.1.30}$$

If we now assume that the hypersurface $\mathcal{H}$ determines all events on the space-time $\mathcal{M}$, we can write

$$\mathcal{D}(\mathcal{H}) = \mathcal{M}, \tag{2.1.31}$$

and any surface whose domain of dependence is the entire space-time is known as a *Cauchy surface*. Any space-time that admits at least one Cauchy surface is known as *globally hyperbolic*, and the entire future and past of the space-time are (respectively) predictable and retrodictable entirely from the Cauchy surface.

Furthermore, we can think of global hyperbolicity from a field theory perspective (which will be defined in earnest in section 2.2), in which the evolution of 'data' is determined by a wave equation. On globally-hyperbolic space-times, if we were to specify some initial (Cauchy) data on a Cauchy surface, then the entire future of space-time is entirely predictable from this data. Likewise, if we were to specify some final (Cauchy) data on a Cauchy surface, then the entire past of space-time is entirely retrodictable from this data. We thus tend to (also) think of global hyperbolicity as the requirement that any Cauchy data must be uniquely evolvable through space-time. Essentially, then, global hyperbolicity of a space-time is the requirement that the full past and future of the space-time is entirely

determined by data specified on some Cauchy surface (a spatial surface at a particular time).

## § 2.2 Classical field theory and general relativity

In this section the Einstein field equations are derived using classical field theory techniques. In order to facilitate this, in the next subsection, we give an extremely brief overview of the classical field theory and Lagrangian dynamics required.

### 2.2.1 Classical field theory: the basics

The dynamics that underpin classical fields in general relativity are governed by Lagrangian dynamics. To begin, a Lagrangian density $\mathscr{L}[\Phi, \partial\Phi, x]$ is defined which depends (in general) on the field $\Phi$ and its derivatives $\partial\Phi$, and the $n$-dimensional coordinate $x$. An action is then constructed by integrating over the $n$-dimensional volume element $\mathrm{d}^n x$,

$$\mathcal{S}[\Phi, \partial\Phi, x] = \int \mathrm{d}^n x \, \mathscr{L}[\Phi, \partial\Phi, x]. \tag{2.2.1}$$

By varying the action with respect to the field $\Phi$, we have

$$\begin{aligned} \frac{\delta\mathcal{S}}{\delta\Phi} &= \int_\Omega \mathrm{d}^n x \frac{\delta\mathscr{L}}{\delta\Phi} \\ &= \int_\Omega \mathrm{d}^n x \left[ \frac{\partial\mathscr{L}}{\partial\Phi}\frac{\delta\Phi}{\delta\Phi} + \frac{\partial\mathscr{L}}{\partial(\partial_\mu\Phi)}\frac{\delta(\partial_\mu\Phi)}{\delta\Phi} \right], \end{aligned} \tag{2.2.2}$$

where $\Omega$ is some general volume. *Hamilton's principle of least action* [176, 184, 225, 234] states that the 'correct' field configuration is the one that extremises the action with respect to field variations. We therefore rewrite the variational derivative (2.2.2) as

$$\delta\mathcal{S} = \int_\Omega \mathrm{d}^n x \left[ \frac{\partial\mathscr{L}}{\partial\Phi}\delta\Phi + \frac{\partial\mathscr{L}}{\partial(\partial_\mu\Phi)}\partial_\mu(\delta\Phi) \right], \tag{2.2.3}$$

where we have additionally rewritten the second term by using the fact that variational derivatives and partial derivatives commute. To proceed, we note that, by (rearranging)

the product rule, we have

$$\frac{\partial \mathscr{L}}{\partial(\partial_\mu \Phi)}\partial_\mu(\delta\Phi) = \partial_\mu\left(\frac{\partial \mathscr{L}}{\partial(\partial_\mu \Phi)}\delta\Phi\right) - \partial_\mu\left(\frac{\partial \mathscr{L}}{\partial(\partial_\mu \Phi)}\right)\delta\Phi, \tag{2.2.4}$$

and thus the variation of the action (2.2.3) can be written in the form

$$\begin{aligned}\delta\mathcal{S} &= \int_\Omega \mathrm{d}^n x \left[\frac{\partial \mathscr{L}}{\partial \Phi}\delta\Phi + \partial_\mu\left(\frac{\partial \mathscr{L}}{\partial(\partial_\mu \Phi)}\delta\Phi\right) - \partial_\mu\left(\frac{\partial \mathscr{L}}{\partial(\partial_\mu \Phi)}\right)\delta\Phi\right] \\ &= \int_\Omega \mathrm{d}^n x \left[\frac{\partial \mathscr{L}}{\partial \Phi}\delta\Phi - \partial_\mu\left(\frac{\partial \mathscr{L}}{\partial(\partial_\mu \Phi)}\right)\delta\Phi\right] + \int_\Omega \mathrm{d}^n x\, \partial_\mu\left(\frac{\partial \mathscr{L}}{\partial(\partial_\mu \Phi)}\delta\Phi\right).\end{aligned} \tag{2.2.5}$$

Recognising that the second integral on the second line above is the volume integral of a total derivative, we can use Gauss' Law to convert this to a surface integral over the boundary surface $\partial\Omega$ of the volume $\Omega$, i.e.

$$\delta\mathcal{S} = \int_\Omega \mathrm{d}^n x \left[\frac{\partial \mathscr{L}}{\partial \Phi}\delta\Phi - \partial_\mu\left(\frac{\partial \mathscr{L}}{\partial(\partial_\mu \Phi)}\right)\delta\Phi\right] + \oint_{\partial\Omega} \mathrm{d}^{n-1}\boldsymbol{x}\left(\frac{\partial \mathscr{L}}{\partial(\partial_\mu \Phi)}\delta\Phi\right) n_\mu, \tag{2.2.6}$$

where $n_\mu$ is the outward-pointing unit normal vector to the boundary. We henceforth refer to the surface integral as *boundary terms*.

For a space-time that is globally hyperbolic, the spatial boundaries of the space-time are located at spatial infinity; therefore, the volume $\Omega$ extends to infinity and the boundary surface $\partial\Omega$ is located at spatial infinity. For physical (and finite-energy) systems, the fields $\Phi$ (and their variations $\delta\Phi$) must decay to zero as they approach spatial infinity. Therefore, we must have that $\delta\Phi \to 0$ on the spatial boundaries (in particular the boundary surface $\partial\Omega$) and thus the boundary terms in the variation of the action (2.2.6) must vanish identically. However, the situation is not so simple for nonglobally-hyperbolic space-times. For example, take anti-de Sitter space-time (see chapter 4), which has a time-like boundary at spatial infinity. This means that a null ray can reach spatial infinity at finite coordinate time; consequently, the field $\Phi$ and its variation $\delta\Phi$ do not automatically vanish on the boundary surface $\partial\Omega$, and thus the boundary terms in the variation of the action (2.2.6) also do not necessarily vanish. There is a way to circumvent this issue. One can apply *boundary conditions* to the field to ensure that the boundary terms vanish. For the case

of anti-de Sitter space-time, this is mentioned in more detail in chapter 4; in particular, section 4.5. For the remainder of this thesis, we assume that suitable boundary conditions are applied to the field, and that the boundary terms automatically vanish.

With vanishing boundary terms, the variation of the action reduces to

$$\delta\mathcal{S} = \int_\Omega \mathrm{d}^n x \left[\frac{\partial\mathscr{L}}{\partial\Phi}\delta\Phi - \partial_\mu\left(\frac{\partial\mathscr{L}}{\partial(\partial_\mu\Phi)}\right)\delta\Phi\right] = \int_\Omega \mathrm{d}^n x \left[\frac{\partial\mathscr{L}}{\partial\Phi} - \partial_\mu\left(\frac{\partial\mathscr{L}}{\partial(\partial_\mu\Phi)}\right)\right]\delta\Phi, \quad (2.2.7)$$

and by enforcing Hamilton's principle (for *all* field configurations), it must be the case that the term within the square brackets (of the second integral) vanishes; this leads to the much celebrated *Euler-Lagrange equations* [99, 132, 176, 225, 234]:

$$0 = \frac{\partial\mathscr{L}}{\partial\Phi} - \partial_\mu\left(\frac{\partial\mathscr{L}}{\partial(\partial_\mu\Phi)}\right). \quad (2.2.8)$$

These act as the field equations of motion and govern both the field's evolution and dynamics.

Whilst the above analysis has centred around variations with respect to the field, we can also perform variational derivatives with respect to the metric tensor (treating it as the field); it is this method that we use next to derive the *Einstein field equations*. We always assume that any boundary terms vanish, though this requires extra care when considering variations with respect to the metric tensor.

### 2.2.2 The Einstein field equations

In this subsection, we derive the Einstein field equations - the equations of motion governing gravitational fields - using the calculus of variations as outlined in the previous section. Note that the following analysis is for a universe with no matter content; matter fields will be added in section 2.2.3.

We begin by defining a Lagrangian density that depends on the Ricci scalar, defined in terms of the Ricci tensor as

$$R := g^{\mu\nu}R_{\mu\nu}, \quad (2.2.9)$$

and the cosmological constant $\Lambda$. The Lagrangian density, given also in terms of the metric determinant

$$g \equiv \det g_{\mu\nu}, \tag{2.2.10}$$

is then

$$\mathscr{L}_{\mathrm{EH}}[g] = \sqrt{-g}\,(R - 2\Lambda)\,. \tag{2.2.11}$$

Using the arguments set out in section 2.2.1, we can therefore construct the *Einstein-Hilbert action* [190, 262, 373]

$$\mathcal{S}[g] = \frac{1}{2\kappa}\int \mathrm{d}^n x\sqrt{-g}\,(R - 2\Lambda)\,, \tag{2.2.12}$$

where

$$\kappa := \frac{8\pi G_N}{c^4}, \tag{2.2.13}$$

is a constant depending on the speed of light $c$ and gravitational constant $G_N$. If we do not invoke Planck units (2.1.2), this constant has dimensions

$$[\kappa] = \left[\frac{8\pi G_N}{c^4}\right] = M^{-1}L^{n-1}T^{-2}L^{-4}T^4 = M^{-1}L^{n-5}T^2, \tag{2.2.14}$$

using the dimensions of the constants given in equation (2.1.3). If we do in fact impose Planck units, then everything is dimensionless and thus $[\kappa] = 1$; this also means that, in Planck units, the Einstein-Hilbert action is dimensionless.

The action (2.2.12) is then varied with respect to the inverse metric $g^{\mu\nu}$, yielding

$$\frac{\delta\mathcal{S}}{\delta g^{\mu\nu}} = \frac{1}{2\kappa}\int \mathrm{d}^n x\left[\sqrt{-g}\frac{\delta R}{\delta g^{\mu\nu}} + R\frac{\delta\sqrt{-g}}{\delta g^{\mu\nu}} - 2\Lambda\frac{\delta\sqrt{-g}}{\delta g^{\mu\nu}}\right]. \tag{2.2.15}$$

The variations with respect to the inverse metric of the Ricci scalar and $\sqrt{-g}$ can be calculated as

$$\frac{\delta R}{\delta g^{\mu\nu}} = R_{\mu\nu} + g^{\alpha\beta}\frac{\delta R_{\alpha\beta}}{\delta g^{\mu\nu}}, \qquad \frac{1}{\sqrt{-g}}\frac{\delta\sqrt{-g}}{\delta g^{\mu\nu}} = -\frac{1}{2}g_{\mu\nu}. \tag{2.2.16}$$

Substituting these into the variation of the action (2.2.12), we have

$$\frac{\delta\mathcal{S}}{\delta g^{\mu\nu}} = \frac{1}{2\kappa}\int \mathrm{d}^n x\sqrt{-g}\left[R_{\mu\nu} + g^{\alpha\beta}\frac{\delta R_{\alpha\beta}}{\delta g^{\mu\nu}} - \frac{1}{2}Rg_{\mu\nu} + \Lambda g_{\mu\nu}\right]$$

$$= \frac{1}{2\kappa}\int \mathrm{d}^n x\sqrt{-g}\left[R_{\mu\nu} - \frac{1}{2}Rg_{\mu\nu} + \Lambda g_{\mu\nu}\right] + \frac{1}{2\kappa}\int \mathrm{d}^n x\sqrt{-g}\left[g^{\alpha\beta}\frac{\delta R_{\alpha\beta}}{\delta g^{\mu\nu}}\right]. \quad (2.2.17)$$

Using the Palatini identity [284, 285], one can express the variation of the Ricci tensor as covariant derivatives of the Christoffel symbols,

$$\delta R_{\mu\nu} = \nabla_\lambda(\delta\Gamma^\lambda{}_{\mu\nu}) - \nabla_\nu(\delta\Gamma^\lambda{}_{\mu\lambda}), \quad (2.2.18)$$

and by contracting with the contravariant metric tensor (as well as using the definition of the Levi-Civita connection), it can be expressed as a total divergence as

$$g^{\mu\nu}\delta R_{\mu\nu} = \nabla_\mu \mathfrak{r}^\mu, \quad (2.2.19)$$

where

$$\mathfrak{r}^\mu = g_{\alpha\beta}\nabla^\mu(\delta g^{\alpha\beta}) - \nabla_\alpha(\delta g^{\mu\alpha}). \quad (2.2.20)$$

The upshot is that the second integral in the variation of the action (2.2.17) can be written as a boundary integral

$$\frac{1}{2\kappa}\int \mathrm{d}^n x\sqrt{-g}\left[g^{\alpha\beta}\frac{\delta R_{\alpha\beta}}{\delta g^{\mu\nu}}\right] = \frac{1}{2\kappa}\oint \mathrm{d}^{n-1}x\sqrt{|h|}\left[g_{\alpha\beta}\nabla^\lambda\left(\frac{\delta g^{\alpha\beta}}{\delta g^{\mu\nu}}\right) - \nabla_\alpha\left(\frac{\delta g^{\lambda\alpha}}{\delta g^{\mu\nu}}\right)\right]n_\lambda, \quad (2.2.21)$$

where $n_\lambda$ is an outward pointing unit normal vector, and $h$ is the determinant of the metric on the boundary. The variation of the action (2.2.17) therefore reads

$$\begin{aligned}\frac{\delta\mathcal{S}}{\delta g^{\mu\nu}} = &\frac{1}{2\kappa}\int \mathrm{d}^n x\sqrt{-g}\left[R_{\mu\nu} - \frac{1}{2}Rg_{\mu\nu} + \Lambda g_{\mu\nu}\right] \\ &+ \frac{1}{2\kappa}\oint \mathrm{d}^{n-1}x\sqrt{|h|}\left[g_{\alpha\beta}\nabla^\lambda\left(\frac{\delta g^{\alpha\beta}}{\delta g^{\mu\nu}}\right) - \nabla_\alpha\left(\frac{\delta g^{\lambda\alpha}}{\delta g^{\mu\nu}}\right)\right]n_\lambda. \quad (2.2.22)\end{aligned}$$

One needs to be careful in dealing with the boundary terms in this case. Unlike in the scalar field case, where the boundary terms vanished automatically, it is not automatically the case here. Even though the metric variation vanishes on the boundary, the boundary integral includes *derivatives* of the metric variation, which do not automatically vanish. The most common way of dealing with this in the literature is to include a *Gibbons-Hawking-York*

counter term in the action [118], given by [168, 389]

$$\mathcal{S}_{\mathrm{GHY}} = \frac{1}{\kappa} \oint \mathrm{d}^{n-1}x \sqrt{|h|} K, \tag{2.2.23}$$

where $K$ is the trace of the extrinsic curvature on the boundary. When varied with respect to the inverse metric, these terms perfectly cancel out the boundary integral (2.2.21) that arises from the variation of the Ricci tensor[2]. Accounting for this, invoking the action principle simply amounts to considering the case when the integral

$$\frac{1}{2\kappa} \int \mathrm{d}^n x \sqrt{-g} \left[ R_{\mu\nu} - \frac{1}{2} R g_{\mu\nu} + \Lambda g_{\mu\nu} \right] \tag{2.2.24}$$

vanishes. Since this must be true of all metric perturbations, this reduces to requiring that the terms inside the square bracket are zero, i.e.

$$R_{\mu\nu} - \frac{1}{2} R g_{\mu\nu} + \Lambda g_{\mu\nu} = 0, \tag{2.2.25}$$

from which the *Einstein tensor* is defined as [124, 126]

$$G_{\mu\nu} \coloneqq R_{\mu\nu} - \frac{1}{2} R g_{\mu\nu}. \tag{2.2.26}$$

An important property of the Einstein tensor is that it is divergenceless, or conserved, i.e.

$$\nabla^\mu G_{\mu\nu} = 0, \tag{2.2.27}$$

which is shown using the contracted Bianchi identity, as follows. Start with the standard (second) Bianchi identity [44, 190, 262, 368, 373]

$$\nabla_\lambda R_{\alpha\beta\mu\nu} + \nabla_\nu R_{\alpha\beta\lambda\mu} + \nabla_\mu R_{\alpha\beta\nu\lambda} = 0, \tag{2.2.28}$$

and contract with $g^{\alpha\mu}$ to yield

$$\nabla_\lambda R^\mu{}_{\beta\mu\nu} + \nabla_\nu R^\mu{}_{\beta\lambda\mu} + \nabla_\mu R^\mu{}_{\beta\nu\lambda} = 0. \tag{2.2.29}$$

[2]Henceforth, we do not include these steps explicitly, e.g. in section 2.2.3. However, it is assumed to hold, and we justifiably neglect the boundary terms arising from variational principles.

Using the antisymmetry in the indices $\mu$ and $\lambda$, and the definition of the Ricci tensor (2.1.12) in terms of the Riemann tensor, we arrive at the contracted Bianchi identities [190, 262, 373]

$$\nabla_\lambda R_{\beta\nu} - \nabla_\nu R_{\beta\lambda} + \nabla_\mu R^\mu{}_{\beta\nu\lambda} = 0. \tag{2.2.30}$$

Contracting with $g^{\beta\nu}$ and using the definition of the Ricci scalar (2.1.13) in terms of the Ricci tensor, we have

$$\nabla_\lambda R - 2\nabla_\mu R^\mu{}_\lambda = 0, \tag{2.2.31}$$

and by using $\nabla_\lambda R = g^\mu{}_\lambda \nabla_\mu R$ along with lowering the $\mu$ index on the curvature tensors and compensating by raising the index $\mu$ on the covariant derivative, we have

$$\nabla^\mu \left[ R_{\mu\nu} - \frac{1}{2} R g_{\mu\nu} \right] = 0. \tag{2.2.32}$$

Recognising the term inside the brackets as the Einstein tensor[3], we arrive at conservation of the Einstein tensor (2.2.27) [190, 262, 373].

Therefore, combining equations (2.2.25) and (2.2.26), we can write down the Einstein field equations in the absence of matter content as the tensorial equation

$$G_{\mu\nu} + \Lambda g_{\mu\nu} = 0. \tag{2.2.33}$$

There are regimes where the Einstein equations (2.2.33) also include higher-order curvature tensors, such as Gauss-Bonnet [82] and Lovelock [245] gravity. These higher order terms are generally terms such as $R^2$, $R_{\mu\nu}R^{\mu\nu}$ and $R_{\mu\nu\alpha\beta}R^{\mu\nu\alpha\beta}$, and are included by modifying the Einstein-Hilbert action (2.2.12). We mention higher-order curvature corrections to the action in more detail in chapter 3.

### 2.2.3 The stress-energy tensor and scalar fields

The Einstein field equations (2.2.33), whilst being particularly elegant, have one major drawback when used as a model of the universe: there is no description of matter. This

[3] This is in fact how the Einstein tensor was first derived.

is easily remedied, however. If we modify the Einstein-Hilbert Lagrangian density (2.2.11) to include a matter term, as

$$\mathscr{L}[g] = \mathscr{L}_{\mathrm{EH}}[g] + \mathscr{L}_{\mathrm{matter}}[g] = \frac{\sqrt{-g}}{2\kappa}\left(R - 2\Lambda\right) + \sqrt{-g}\,\mathscr{L}_{\mathrm{matter}}[g], \tag{2.2.34}$$

then the action (2.2.12) is modified in the following way:

$$\mathcal{S}[g] = \int \mathrm{d}^n x \sqrt{-g}\left[\frac{1}{2\kappa}\left(R - 2\Lambda\right) + \mathscr{L}_{\mathrm{matter}}\right]. \tag{2.2.35}$$

We must make a small caveat at this stage. If we are using Planck units (2.1.2), we have shown in section 2.2.2 that the constant $\kappa$ is dimensionless and so too is the Einstein-Hilbert Lagrangian density. This means that, in order for units to line up correctly, the matter Lagrangian must also be dimensionless. That is to say, the dimensions of each of the Lagrangian densities in the action must have the same dimensions. This becomes important when we consider *effective actions* in section 3.2.

Following the same methodology as in section 2.2.2, we vary the action with respect to the inverse metric:

$$\frac{\delta\mathcal{S}}{\delta g^{\mu\nu}} = \frac{1}{2\kappa}\int \mathrm{d}^n x\left[\sqrt{-g}\frac{\delta R}{\delta g^{\mu\nu}} + R\frac{\delta\sqrt{-g}}{\delta g^{\mu\nu}} - 2\Lambda\frac{\delta\sqrt{-g}}{\delta g^{\mu\nu}} + 2\kappa\frac{\delta(\sqrt{-g}\mathscr{L}_{\mathrm{matter}})}{\delta g^{\mu\nu}}\right], \tag{2.2.36}$$

and, by using the same justification as before, we have

$$0 = \delta\mathcal{S} \implies 0 = \frac{1}{2\kappa}\frac{\delta R}{\delta g^{\mu\nu}} + \frac{R}{2\kappa\sqrt{-g}}\frac{\delta\sqrt{-g}}{\delta g^{\mu\nu}} - \frac{\Lambda}{\kappa\sqrt{-g}}\frac{\delta\sqrt{-g}}{\delta g^{\mu\nu}} - \frac{1}{\sqrt{-g}}\frac{\delta(\sqrt{-g}\mathscr{L}_{\mathrm{matter}})}{\delta g^{\mu\nu}}. \tag{2.2.37}$$

The first three terms on the right-hand-side of equation (2.2.37) reduce in exactly the same way as before to the Einstein equations (2.2.25), and if we define a new symmetric rank-2 tensor

$$T_{\mu\nu} := \frac{-2}{\sqrt{-g}}\frac{\delta(\sqrt{-g}\mathscr{L}_{\mathrm{matter}})}{\delta g^{\mu\nu}}, \tag{2.2.38}$$

then equation (2.2.37) reduces to

$$R_{\mu\nu} - \frac{1}{2}Rg_{\mu\nu} + \Lambda g_{\mu\nu} = \kappa T_{\mu\nu}, \tag{2.2.39}$$

or, by rewriting in terms of the Einstein tensor (2.2.26),

$$G_{\mu\nu} + \Lambda g_{\mu\nu} = \kappa T_{\mu\nu}. \tag{2.2.40}$$

These are the Einstein field equations incorporating both matter and curvature effects, and we will henceforth refer to these as the *classical Einstein equations* [124, 126].

The rank-2 tensor on the right-hand-side of the classical Einstein equations (2.2.40), defined in terms of the matter Lagrangian as in equation (2.2.38), is called the *stress-energy tensor*, sometimes also the stress-energy-momentum tensor. This encodes the matter content of the theory, and can be fixed by specifying a suitable matter Lagrangian. In particular, the stress-energy tensor describes the density and flux of both the energy and momentum at each point in space-time, and acts as a source for gravitational fields (described by the left-hand-side of the classical Einstein equations) - figure 2.1 shows a common pictorial depiction of this. Crucially, however, the stress-energy tensor *cannot* encode any gravitational stress, energy or momentum, since, by the equivalence principle, gravitational stress, energy or momentum will always locally vanish at any chosen point in some chosen frame [262] (the concept of frames will be outlined in section 2.3).

The classical Einstein equations (2.2.40) therefore relate the matter content of space-time with the curvature of space-time. This relation between the two is perfectly encapsulated by Wheeler's famous quote that "space-time tells matter how to move; matter tells space-time how to curve" [380].

#### 2.2.3.1 Energy conditions

As it stands, the stress-energy tensor (2.2.38) on the right-hand-side of the classical Einstein field equations (2.2.40) has one major drawback: provided the stress-energy tensor is conserved, we can stipulate *any* model of matter and this will satisfy Einstein's field equations. This can include unphysical models such as superluminal travel and wormholes

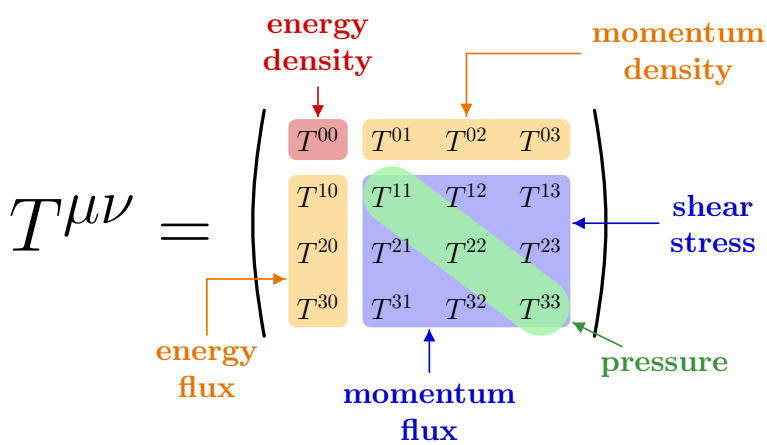


Figure 2.1: The classical, four-dimensional, contravariant stress-energy tensor pictorially depicted by identifying each component with its physical meaning. Since the stress-energy tensor is symmetric under interchange of its indices, the energy flux and momentum density, and the momentum flux and shear stress, are generally interchangeable. Figure adapted from the "stress-energy tensor" Wikipedia page.

[190, 231]. Clearly, if Einstein's field equations are to be deemed a valid physical description of the universe, such exotic behaviour cannot be left untethered. In order to restrict the space of allowable matter models, the *classical energy conditions* were developed. They are summarised as follows [90, 190, 231]:

(WEC) **The weak energy condition:** For any future-directed, time-like vector field $u^\bullet$, we must have $T_{\mu\nu}u^\mu u^\nu \geq 0$. This is the requirement that any observer will *never* see negative energy.

(NEC) **The null energy condition:** For any future-directed, null (light-like) vector field $k^\bullet$, it must be that $T_{\mu\nu}k^\mu k^\nu \geq 0$. This is equivalent to requiring that any particle travelling on a null geodesic always sees non-negative energy density. Equivalently, this is the requirement that gravity is attractive for particles travelling on null geodesics.

(DEC) **The dominant energy condition:** For any future-pointing, causal (non-space-like) vector field $v^\bullet$, the dominant energy condition requires that the vector field given by $-T_\mu{}^\nu v^\mu$ must also be a future-pointing causal vector field. This is often interpreted as the requirement that energy-flux is never faster than light-speed.

(SEC) **The strong energy condition:** For every time-like vector field $u^\bullet$, then the following must hold (in $n$-dimensions)

$$\left(T_{\mu\nu} - \frac{1}{n-2} T_\alpha{}^\alpha g_{\mu\nu}\right) u^\mu u^\nu \geq 0.$$

Physically, this is equivalent to requiring that gravity is always attractive, and matter will gravitate towards matter.

An important point regarding the classical energy conditions is that, whilst they reduce the space of allowable matter models and limit the arbitrariness of the stress-energy tensor, this does *not* mean that they are never violated. Indeed, one may find it surprising that our most successful model of matter to date, quantum field theory, is incompatible with the classical energy conditions. This is because the energy density of a quantum field can be made arbitrarily large and negative at any point in space-time [131]. However, quantum field theory *does* satisfy remnants of the classical energy conditions; these are known as *quantum energy inequalities* (which are a subset of a larger class of *quantum inequalities*). Quantum energy inequalities amount to taking (local) averages of the energy density of a quantum field along worldlines and requiring that they are bounded below by some negative value. These therefore constrain the amount by which the classical energy conditions are violated, by restricting how negative the energy density of the quantum field can become, and for how long negative energy densities can exist. For recent works and more in-depth treatments of quantum energy inequalities, see, for example, [62, 134, 137, 139, 140, 141, 142, 144, 149, 150, 151, 230, 231].

#### 2.2.3.2 Scalar field theory

There are many different choices of stress-energy tensor one could make; these depend largely on what type of theory is considered (i.e. scalar field theory, spinor field theory, vector field theory etc.). In this thesis, we are only interested in (free)[4] scalar field theories, and in particular only free, real scalar fields, which associate a real scalar value to every point in space; they are also invariant under Lorentz transformations. In this case, the Lagrangian density for a free, real scalar field $\Phi$ is given by

$$\mathscr{L}_{\text{matter}}[\Phi, g] = -\frac{1}{2} g^{\mu\nu} \nabla_\mu \Phi \nabla_\nu \Phi - \frac{1}{2} \left( m^2 + \xi R \right) \Phi^2, \tag{2.2.41}$$

where $m$ is the mass of the field and $\xi$ is the coupling constant (that determines the coupling to gravity). There are two key choices of coupling constant in the literature: $\xi = 0$ corresponding to minimal coupling, i.e. the scalar field does not interact with the gravitational fields; and

$$\xi = \xi_c = \frac{(n-2)}{4(n-1)} \tag{2.2.42}$$

which corresponds to conformal coupling (so named as the resulting theory is conformally invariant - see below). The general case $\xi \neq \{0, \xi_c\}$ is referred to as nonminimal coupling. In this thesis, we are primarily interested in massless ($m = 0$) and conformally coupled ($\xi = \xi_c$) scalar fields. By varying the Lagrangian density (2.2.41) with respect to the inverse metric, we can construct the stress-energy tensor for a real, nonminimally coupled scalar field according to the definition (2.2.38). The details of the calculation will be skipped for brevity, but the upshot is the stress-energy tensor[5] is given by [45, 70, 293]

$$\begin{aligned} T_{\mu\nu} = (1 - 2\xi) \nabla_\mu \Phi \nabla_\nu \Phi + \left( 2\xi - \frac{1}{2} \right) g_{\mu\nu} g^{\alpha\beta} \nabla_\alpha \Phi \nabla_\beta \Phi - \frac{1}{2} g_{\mu\nu} m^2 \Phi^2 \\ - 2\xi \Phi \nabla_\mu \nabla_\nu \Phi + 2\xi g_{\mu\nu} \Phi \Box_g \Phi + \xi \left( R_{\mu\nu} - \frac{1}{2} R g_{\mu\nu} \right) \Phi^2, \end{aligned} \tag{2.2.43}$$

[4]'Free' in this case refers to the fact that there is no self interaction by the scalar fields. Adding self-interaction adds higher power terms of the scalar field to the Lagrangian density.

[5]Technically, this is the *new and improved* stress-energy tensor [70].

where $\Box_g = \nabla_\mu \nabla^\mu$ is the curved space-time Laplacian/d'Alembertian operator. In the minimally coupled case, the stress-energy tensor reduces to

$$T_{\mu\nu} = \nabla_\mu \Phi \nabla_\nu \Phi - \frac{1}{2} g_{\mu\nu} g^{\alpha\beta} \nabla_\alpha \Phi \nabla_\beta \Phi - \frac{1}{2} g_{\mu\nu} m^2 \Phi^2, \tag{2.2.44}$$

and one can substitute the conformal coupling constant $\xi_c$ into the stress-energy tensor (2.2.43), and whilst it simplifies somewhat, no extra information is to be gained by our displaying it explicitly. One important aspect of the conformally-coupled stress-energy tensor is that, for massless fields, the theory is conformally invariant iff the stress-energy tensor is traceless. Taking the trace, we have

$$\begin{aligned} g^{\mu\nu} T_{\mu\nu} = & \left(1 - 2\xi_c\right) \nabla_\mu \Phi \nabla^\mu \Phi + \left(2\xi_c - \frac{1}{2}\right) g^{\mu\nu} g_{\mu\nu} \nabla_\alpha \Phi \nabla^\alpha \Phi \\ & \qquad - 2\xi_c \left(1 - g^{\mu\nu} g_{\mu\nu}\right) \Phi \Box_g \Phi + \xi_c R \left(1 - \frac{n}{2}\right) \Phi^2 \\ = & \cancelto{0}{\left[1 - \frac{n}{2} - 2\xi_c (1 - n)\right]} \nabla_\mu \Phi \nabla^\mu \Phi + \xi_c \left[-2 (1 - n) \Box_g \Phi + \left(1 - \frac{n}{2}\right) R \Phi\right] \Phi \\ = & \, 2\xi_c (1 - n) \left[-\Box_g \Phi + \xi_c R \Phi\right] \Phi, \end{aligned} \tag{2.2.45}$$

where in the second line we have used the fact that the conformal coupling constant is given by equation (2.2.42), and that the trace of the metric tensor is the number of dimensions. Since we require that the trace of the stress-energy tensor vanishes in general, clearly $\Phi \neq 0$ and thus

$$\left(-\Box_g + \xi_c R\right) \Phi = 0. \tag{2.2.46}$$

As we will see below, this condition is actually the *Klein-Gordon* equation of motion for a massless and conformally-coupled scalar field, and any field configuration satisfying the Klein-Gordon equation is said to be *on-shell*. Therefore, tracelessness and conformal invariance is only guaranteed for massless, classical field configurations that are on-shell. This will be discussed in further detail below.

Another important property of the stress-energy tensor (for any mass and coupling) is that

it should be conserved, i.e.

$$\nabla^\mu T_{\mu\nu} = 0, \tag{2.2.47}$$

since the left-hand-side of the Einstein equations (2.2.40) is conserved due to the contracted Bianchi identity (which yields equation (2.2.27)) and metric compatibility ($\nabla^\mu g_{\mu\nu} \equiv 0$), and thus it follows that the right-hand-side of the Einstein equations (i.e., the stress-energy tensor) must also be conserved. For the free scalar field stress-energy tensor (2.2.43), we have (after expanding derivatives using the Leibniz rule)

$$\begin{aligned}
\nabla^\mu T_{\mu\nu} = \; & (1-2\xi)\left[\Box_g \Phi \nabla_\nu \Phi + \nabla_\mu \Phi \nabla^\mu \nabla_\nu \Phi\right] \\
& + \left(2\xi - \frac{1}{2}\right) g_{\mu\nu} g^{\alpha\beta}\left[\nabla^\mu \nabla_\alpha \Phi \nabla_\beta \Phi + \nabla_\alpha \Phi \nabla^\mu \nabla_\beta \Phi\right] - g_{\mu\nu} m^2 \Phi \nabla^\mu \Phi \\
& - 2\xi\left[\nabla^\mu \Phi \nabla_\mu \nabla_\nu \Phi + \Phi \Box_g \nabla_\nu \Phi\right] + 2\xi g_{\mu\nu}\left[\nabla^\mu \Box_g \Phi + \Phi \nabla^\mu \Box_g \Phi\right] && (2.2.48) \\
& + 2\xi\left(R_{\mu\nu} - \frac{1}{2} R g_{\mu\nu}\right) \Phi \nabla^\mu \Phi, && (2.2.49)
\end{aligned}$$

and, after much simplification, we arrive at the condition

$$0 = \nabla^\mu T_{\mu\nu} = \left(\Box_g \Phi - m^2 \Phi - \xi R \Phi\right) \nabla_\nu \Phi. \tag{2.2.50}$$

Clearly, $\nabla_\nu \Phi = 0$ corresponds to the trivial case of a constant scalar field that displays no dynamics, and thus we disregard this as a solution. Therefore, for conservation of the stress-energy tensor, we require that

$$0 = \left(\Box_g - m^2 - \xi R\right) \Phi, \tag{2.2.51}$$

which, it transpires, is the Klein-Gordon equation of motion for a (massive and nonminimally coupled) scalar field. This will be derived using variational principles below. This reduces as expected to the Klein-Gordon equation (2.2.46). This therefore means that conservation of the stress-energy tensor is guaranteed only for field configurations that are *on-shell*, i.e. that satisfy the equation of motion - just as was the case for conformal invariance above; see the discussion around equation (2.2.46). The notion of on- and off-shell configurations plays an important part when quantising the field - see section 2.4.1.

To derive the Klein-Gordon equation, recall the Lagrangian density (2.2.41) for the field; we can therefore construct the action

$$\mathcal{S}_{\text{matter}}[\Phi, g] = \int \mathrm{d}^n x \sqrt{-g} \left[ -\frac{1}{2} g^{\mu\nu} \nabla_\mu \Phi \nabla_\nu \Phi - \frac{1}{2} \left( m^2 + \xi R \right) \Phi^2 \right]. \tag{2.2.52}$$

By the principle of least action, the 'correct' field is the one that minimises the variation of the action with respect to the field:

$$\begin{aligned}
\frac{\delta \mathcal{S}_{\text{matter}}[\Phi, g]}{\delta \Phi} &= \int \mathrm{d}^n x \sqrt{-g} \left[ -\frac{1}{2} g^{\mu\nu} \frac{\delta(\nabla_\mu \Phi \nabla_\nu \Phi)}{\delta \Phi} - \frac{1}{2} \left( m^2 + \xi R \right) \frac{\delta(\Phi^2)}{\delta \Phi} \right] \\
&= \int \mathrm{d}^n x \sqrt{-g} \left[ -\frac{1}{2} g^{\mu\nu} \left\{ \frac{\delta(\nabla_\mu \Phi)}{\delta \Phi} \nabla_\nu \Phi + \nabla_\mu \Phi \frac{\delta(\nabla_\nu \Phi)}{\delta \Phi} \right\} - \left( m^2 + \xi R \right) \Phi \frac{\delta \Phi}{\delta \Phi} \right] \\
&= \int \mathrm{d}^n x \sqrt{-g} \left[ -\frac{1}{2} g^{\mu\nu} \left\{ \frac{\nabla_\mu (\delta \Phi)}{\delta \Phi} \nabla_\nu \Phi + \nabla_\mu \Phi \frac{\nabla_\nu (\delta \Phi)}{\delta \Phi} \right\} - \left( m^2 + \xi R \right) \Phi \frac{\delta \Phi}{\delta \Phi} \right] \\
&= \int \mathrm{d}^n x \sqrt{-g} \left[ -g^{\mu\nu} \frac{\delta(\nabla_\mu \Phi)}{\delta \Phi} \nabla_\nu \Phi - \left( m^2 + \xi R \right) \Phi \frac{\delta \Phi}{\delta \Phi} \right],
\end{aligned} \tag{2.2.53}$$

then, by integration by parts (and assuming that the boundary terms vanish[6]), we have

$$\delta \mathcal{S}_{\text{matter}}[\Phi, g] = \int \mathrm{d}^n x \sqrt{-g} \left[ g^{\mu\nu} \nabla_\mu \nabla_\nu \Phi - \left( m^2 + \xi R \right) \Phi \right] \delta \Phi, \tag{2.2.54}$$

and thus, for a general variation $\delta\Phi$, the action is minimised iff

$$0 = g^{\mu\nu} \nabla_\mu \nabla_\nu \Phi - \left( m^2 + \xi R \right) \Phi = \left( \Box_g - m^2 - \xi R \right) \Phi, \tag{2.2.55}$$

which is the Klein-Gordon equation (2.2.51). Throughout this thesis, we are interested in massless and conformally coupled fields, in which case the Klein-Gordon equation reduces to

$$\left( -\Box_g + \xi_c R \right) \Phi = 0, \tag{2.2.56}$$

which matches the Klein-Gordon equation (2.2.46) derived when considering conformal invariance above. We will make extensive use of the Klein-Gordon equation (2.2.56) in further sections.

[6] This is an important point. Whilst we are free to do this in a general curved space-time that exhibits global hyperbolicity, space-times that are nonglobally hyperbolic need extra boundary conditions (which arise from this step) in order to be well-defined. Anti-de Sitter space is one such example, this is covered extensively in chapter 4.

#### 2.2.3.3 Fluid stress-energy tensors

One further, common form for a stress-energy tensor is the *perfect-fluid form*, given in tensorial form as

$$T^{\mu\nu} = (E + P)\, u^{\mu} u^{\nu} + P g^{\mu\nu}, \tag{2.2.57}$$

where $E$ is the energy density of the fluid, $P$ is the isotropic pressure and $u^{\bullet}$ its velocity. This stress-energy tensor is used as an idealised model where matter is modelled by a fluid consisting of noninteracting, isotropically distributed particles; it is used in scenarios such as the interior of a star [75, 262, 281, 358] or an isotropic universe [75, 378]. It transpires that the perfect-fluid stress-energy tensor (2.2.57) is a special case of a more general fluid stress-energy tensor; this will be discussed in section 2.3. The perfect-fluid stress-energy tensor can be easily constructed using the Lagrangian formalism as outlined above, however, there is a second, independent way of constructing it - using *relativistic kinetic theory*. This will be discussed in the next section, section 2.3.

## § 2.3 Relativistic kinetic theory and orthonormal frames in general relativity

In this section, we introduce the concept of orthonormal frames in general relativity and cover, briefly, relativistic kinetic theory and its reason for consideration in this thesis. Neither will be a particular in-depth treatment; instead, we introduce as much as we need in further chapters. We use Chandrasekhar's notation [81] for frame indices, i.e. we enclose frame indices in round brackets, and refer the reader to [81] for a more detailed treatment of frames in general relativity. In a similar fashion, not much detail is provided for the relativistic kinetic approach; instead the reader is referred to the many textbooks on relativistic statistical mechanics that provide a much more detailed treatment, such as, amongst others, [79, 85, 178, 183].

In general relativity, we can introduce a set of pointwise-orthonormal vector fields, that

consist of one time-like vector field and $n-1$ space-like vector fields. Collectively, these are known as *vielbeins*, a German word that literally translates to "many legs". In four dimensions, these are often referred to as tetrads; since we are interested in different dimensions as well as four, for consistency we refer to the four-dimensional case as a *vierbein*, and in three dimensions we refer to the vielbein as a *dreibein*. The vielbein is defined on a Lorentzian manifold and each vielbein has a corresponding dual coframe field. All tensorial quantities can therefore be translated between the space-time and the frame by taking suitable contractions of the vielbeins and their coframes. Since the vielbeins are defined on a Lorentzian manifold, the metric used to raise and lower vielbein indices is the Minkowski metric, $\eta_{(\bullet)(\bullet)} = (-1, 1, \ldots, 1)$. Since the vielbein is constructed to provide a basis for the tangent bundle at every point of the space-time manifold, the metric of space-time and the metric of the vielbein manifold can be related by the vielbein (or coframe) vector fields as

$$g_{\mu\nu} e^{\mu}_{(a)} e^{\nu}_{(b)} = \eta_{(a)(b)} \qquad \Longleftrightarrow \qquad g_{\mu\nu} = w^{(a)}_{\mu} w^{(b)}_{\nu} \eta_{(a)(b)}, \tag{2.3.1}$$

where the vielbein vector fields are denoted by $e^{\bullet}_{(\bullet)}$, the coframe fields are denoted by $w^{(\bullet)}_{\bullet}$, the quantity $g_{\bullet\bullet}$ is the space-time metric, and, as outlined above, indices in round brackets are vielbein indices. The relations (2.3.1) act as conditions on the explicit functional forms of the vielbein fields. The vielbein (and coframe) fields can be used to also transform tensorial quantities. For example, a rank-2 tensor $T^{\mu\nu}$ transforms between the vielbein basis and space-time coordinates as

$$T^{\mu\nu} = e^{\mu}_{(a)} e^{\nu}_{(b)} T^{(a)(b)} \qquad \Longleftrightarrow \qquad T^{(a)(b)} = w^{(a)}_{\mu} w^{(b)}_{\nu} T^{\mu\nu}. \tag{2.3.2}$$

This is a very useful tool, since complicated coordinate expressions can be transformed into vielbein components that may be much simpler and easier to manipulate. Additionally, certain choices of vielbein can correspond to physical systems.

For example, we can define a thermometer frame where the observer is an ideal relativistic thermometer, which is a small (with respect to the system) object that can instantaneously

achieve local thermodynamic equilibrium when in contact with the system, and can exchange both energy and momentum with the system [36]. The system as a whole will describe some non-interacting, relativistic fluid. In a thermometer frame, we can decompose the stress-energy tensor into physical quantities as [19, 36, 363]

$$T^{(a)(b)} = (E + P)\, u^{(a)} u^{(b)} + P\eta^{(a)(b)} + u^{(a)} W^{(b)} + W^{(a)} u^{(b)} + \Pi^{(a)(b)}, \tag{2.3.3}$$

where $E$ is the energy density, $P$ the isotropic pressure, $u$ the fluid velocity, $W$ the heat flux and $\Pi$ the anisotropic pressure. These can be found by contracting the stress-energy tensor with the vielbein vector fields, in particular they are given by [19, 36, 363]

$$E = u^{(a)} u^{(b)} T_{(a)(b)}, \tag{2.3.4a}$$

$$P = \frac{1}{n-1} \Delta^{(a)(b)} T_{(a)(b)}, \tag{2.3.4b}$$

$$W^{(a)} = -\Delta^{(a)(b)} u^{(c)} T_{(b)(c)}, \tag{2.3.4c}$$

$$\Pi^{(a)(b)} = \left[ \Delta^{(a)(c)} \Delta^{(b)(d)} - \frac{1}{n-1} \Delta^{(a)(b)} \Delta^{(c)(d)} \right] T_{(c)(d)}, \tag{2.3.4d}$$

where $\Delta^{(a)(b)} = u^{(a)} u^{(b)} + \eta^{(a)(b)}$ is the projector. The thermometer frame stress-energy tensor can be related to the perfect-fluid stress-energy tensor (2.2.57) introduced in section 2.2.3. The thermometer frame stress-energy tensor (2.3.3) in its current form describes a fluid whose pressure is anisotropically distributed, i.e. different in different directions, and which has a non-static distribution of energy (i.e. there is a nonzero flux of energy and heat). The perfect fluid form, on the other hand, describes a fluid that has zero energy flux and whose pressure is isotropically distributed. Therefore, to describe the perfect fluid form using the thermometer frame decomposition, one would simply discard the anisotropic pressure $\Pi$ and heat flux $W$ terms. This thermometer frame is used extensively in chapter 5, where we compare QFT and RKT stress-energy tensors by writing both in terms of this thermometer frame - see section 5.3.4.

In such a frame, we need to construct the stress-energy tensor; there are two ways of doing this: either construct the space-time stress-energy tensor and move over to the vielbein

manifold using the vielbein vector fields, or construct a stress-energy tensor *in* the vielbein frame. For example, one may construct a stress-energy tensor on space-time in the usual way (or even the expectation value of the stress-energy tensor in a quantum field theory) and then project onto the vielbein manifold using the decomposition (2.3.3, 2.3.4), or find some other theory in which we can construct a stress-energy tensor on flat space (and therefore the vielbein manifold). Finding an alternative theory in which a stress-energy tensor can be constructed (on flat space) will be detailed next.

The choice to study relativistic kinetic theory is motivated, in part, by work done by Ambruş and Winstanley (and following work by Ambruş and collaborators [9, 10, 11, 12, 14, 263, 264, 295]) on rotating frames in Minkowski and anti-de Sitter space for fermionic field theories [13, 16, 17, 18, 19], where they assumed that the system under consideration was comprised solely of noninteracting fermions distributed according to the Fermi-Dirac distribution [19]. This was argued on the basis that rigid rotation can be shown to lead to a state of general thermodynamic equilibrium [19]. Therefore, we work under similar assumptions; i.e., we assume that the matter content (such as a quantum field) under consideration can be modelled by a thermal gas of noninteracting bosons with mass $m$ and momentum $p$. We can use the Boltzmann equation to describe the dynamics and evolution of the gas of particles, given by [79, 85, 178, 183, 319]

$$p^{(a)} e^{\mu}_{(a)} \frac{\partial f}{\partial x^{\mu}} - \Gamma^{(i)}{}_{(a)(b)} p^{(a)} p^{(b)} \frac{\partial f}{\partial p^{(i)}} = C[f], \tag{2.3.5}$$

where $C[f]$ is the collision operator that drives the system towards local thermodynamic equilibrium (and in particular is zero when the system reaches equilibrium), $\Gamma$ are Christoffel symbols of the frame in which the system is modelled (in particular they vanish using a frame embedded in Minkowski space), and $e^{\bullet}_{(\bullet)}$ are vielbein vector fields. The function $f$ is the Bose-Einstein distribution, which gives information about how the particles are distributed. We assume that the matter content (i.e. quantum field) is in local thermodynamic equilibrium and has vanishing chemical potential (which means that the particles

occupy the lowest energy state [227, 235]). Under these assumptions, the Bose-Einstein distribution (in $n$-dimensions) is given by [53, 74, 79, 129, 227, 235, 294, 319]

$$f = \frac{1}{(2\pi)^{n-1}} \frac{1}{e^{\tilde{\beta} u_{(a)} p^{(a)}} - 1}, \tag{2.3.6}$$

where, in addition to the momentum $p$, we have introduced the fluid velocity $u$ (as measured by an observer in the vielbein frame) and local inverse temperature $\widetilde{\beta}$, related to the global inverse temperature $\beta$ (at the coordinate origin) by the Tolman relation [357, 359]

$$\widetilde{\beta} = \beta \sqrt{-g_{\tau\tau}}, \tag{2.3.7}$$

assuming that $\tau$ parameterises the sole time-like coordinate of the space-time manifold, with $g_{\bullet\bullet}$ giving the space-time metric. The Tolman relation (2.3.7) is only valid in stationary space-times; we therefore only consider such space-times for the remainder of this section. It can be shown that using the Bose-Einstein distribution (2.3.6) and assuming local thermodynamical equilibrium, the Boltzmann equation reduces to [9, 79]

$$\frac{1}{2} p^{(a)} p^{(b)} \left[ \nabla_{(b)} (\widetilde{\beta} u_{(a)}) + \nabla_{(a)} (\widetilde{\beta} u_{(b)}) \right] = 0. \tag{2.3.8}$$

Since this must hold for any $p^{(i)}$, this relation reduces to [9, 79]

$$\nabla_{(b)} (\widetilde{\beta} u_{(a)}) + \nabla_{(a)} (\widetilde{\beta} u_{(b)}) = 0, \tag{2.3.9}$$

which is precisely the condition for $\widetilde{\beta} u_{(i)}$ to be a Killing vector field (with respect to the vielbein). Therefore, for the Bose-Einstein distribution (2.3.6) to be valid and for the system to be in local thermodynamical equilibrium, the vector $\widetilde{\beta} u_{(i)}$ must be a Killing vector. In the remainder of this section (and indeed the thesis), we assume that our fluid velocity is at rest, i.e. takes the form

$$u^{(a)} = (1, 0, 0, \dots). \tag{2.3.10}$$

It is easy to see that this choice of fluid velocity automatically satisfies the Killing equation (2.3.9) for any static space-time.

A stress-energy tensor can be constructed using relativistic kinetic theory; this is referred to in the literature as the *macroscopic stress-energy tensor*, although we will refer to it as the RKT-stress-energy tensor (RKT-SET). It is given by the momentum-space integral [9, 74]:

$$\widehat{T}^{(a)(b)} = \int \frac{\mathrm{d}\mathbf{p}}{p^{(0)}} \, f \, p^{(a)} p^{(b)}, \tag{2.3.11}$$

where $p^{(0)}$ is the time-like component of the momentum vector $p$, and can be related to the mass and spatial parts of the momentum vector using the mass-shell condition

$$p^{(0)} = \sqrt{m^2 + |p|^2}, \tag{2.3.12}$$

where $|p|^2$ is the Euclidean norm of the spatial components of the momentum vector, i.e. $|p|^2 = \delta_{(i)(j)} p^{(i)} p^{(j)}$. The RKT-SET (2.3.11) in its current form is defined with respect to some orthonormal frame, characterised by vielbein vector fields $e^{\bullet}_{(\bullet)}$. To then express this in terms of space-time coordinates, we contract with the vielbein vector fields:

$$\widehat{T}^{\mu\nu} = e^{\mu}_{(a)} e^{\nu}_{(b)} \widehat{T}^{(a)(b)}. \tag{2.3.13}$$

The advantage of such an approach is that the RKT-SET only needs to be calculated in Minkowski space; the relation to general curved space-times is contained entirely within the choice of orthonormal frame and local inverse temperature (2.3.7) (which appears in the Bose-Einstein distribution (2.3.6)).

To compute the momentum-space integrals, the dimensions in which one wishes to work need specifying. In this thesis we are interested only in three- and four-dimensional space-times, and, as mentioned previously, fluids at rest with respect to the frame. Both cases will be computed separately below. Note also that, in the remainder of this section, we consider only massless particles, as is the case for parts II and III of this thesis.

### 2.3.1 RKT-stress-energy tensor in three-dimensional space-times

For three-dimensional space-times, the Bose-Einstein distribution function (2.3.6) takes the form [53, 74, 79, 129, 227, 235, 294, 319]

$$f = \frac{1}{(2\pi)^2} \frac{1}{e^{\tilde{\beta} u_{(a)} p^{(a)}} - 1}, \tag{2.3.14}$$

and the integration measure becomes $\mathrm{d}\mathbf{p} = \mathrm{d}p^{(1)}\,\mathrm{d}p^{(2)}$. We choose that the gas of particles be at rest, i.e. we set the fluid velocity to be $u_{(a)} = (1,\,0,\,0)$. This means that the exponent in the distribution function is simply $\tilde{\beta} u_{(a)} p^{(a)} = \tilde{\beta} p^{(0)}$. Recall the mass-shell condition $p^{(0)} = \sqrt{m^2 + |p|^2}$. Since we are only interested in the massless case, this reduces to $p^{(0)} = |p|$. Decomposing the spatial components of the momentum into spherical coordinates yields the following transforms:

$$p^{(1)} = |p| \cos\psi, \quad p^{(2)} = |p| \sin\psi, \tag{2.3.15}$$

for which the Jacobian is $\det\{J(|p|, \psi)\} = |p|$, leading to the new integration measure $\mathrm{d}\mathbf{p} = |p|\,\mathrm{d}|p|\,\mathrm{d}\psi$. The RKT-SET therefore simply becomes

$$\widehat{T}^{(a)(b)} = \int \mathrm{d}|p|\,\mathrm{d}\psi\, f\, p^{(a)} p^{(b)} = \frac{1}{(2\pi)^2} \int_0^{2\pi} \int_0^{\infty} \mathrm{d}|p|\,\mathrm{d}\psi\, \frac{1}{e^{\tilde{\beta}|p|} - 1}\, p^{(a)} p^{(b)}. \tag{2.3.16}$$

Owing to the symmetries of the integration measure and spherical coordinate transform, all off-diagonal terms of the RKT-SET are zero. To see this, consider the following two cases. Firstly,

$$\begin{aligned} \widehat{T}^{(0)(1)} &= \frac{1}{(2\pi)^2} \int_0^{2\pi} \int_0^{\infty} \mathrm{d}|p|\,\mathrm{d}\psi\, \frac{1}{e^{\tilde{\beta}|p|} - 1}\, p^{(0)} p^{(1)} \\ &= \frac{1}{(2\pi)^2} \int_0^{2\pi} \int_0^{\infty} \mathrm{d}|p|\,\mathrm{d}\psi\, \frac{1}{e^{\tilde{\beta}|p|} - 1}\, |p|^2 \cos\psi = 0, \end{aligned} \tag{2.3.17}$$

and secondly

$$\widehat{T}^{(1)(2)} = \frac{1}{(2\pi)^2} \int_0^{2\pi} \int_0^{\infty} \mathrm{d}|p|\,\mathrm{d}\psi\, \frac{1}{e^{\tilde{\beta}|p|} - 1}\, p^{(1)} p^{(2)}$$

$$= \frac{1}{(2\pi)^2} \int_0^{2\pi} \int_0^{\infty} \mathrm{d}|p| \, \mathrm{d}\psi \, \frac{1}{e^{\tilde{\beta}|p|} - 1} \, |p|^2 \cos\psi \sin\psi = 0. \tag{2.3.18}$$

In both instances the fact that the integral of a sine or cosine function over its full period is zero was exploited. To find the non-zero components, there is unfortunately no elegant method to compute all in one go, and we instead compute each one in turn. Starting with the energy density component,

$$\begin{aligned} \widehat{T}^{(0)(0)} &= \frac{1}{(2\pi)^2} \int_0^{2\pi} \int_0^{\infty} \mathrm{d}|p| \, \mathrm{d}\psi \, \frac{1}{e^{\tilde{\beta}|p|} - 1} \, p^{(0)} p^{(0)} \\ &= \frac{1}{(2\pi)^2} \int_0^{2\pi} \int_0^{\infty} \mathrm{d}|p| \, \mathrm{d}\psi \, \frac{1}{e^{\tilde{\beta}|p|} - 1} \, |p|^2 \\ &= \frac{1}{2\pi\tilde{\beta}^3} \int_0^{\infty} \mathrm{d}x \, \frac{x^2}{e^x - 1} = \frac{\zeta(3)\Gamma(3)}{2\pi\tilde{\beta}^3} = \frac{\zeta(3)}{\pi\tilde{\beta}^3} \end{aligned} \tag{2.3.19}$$

using the integral definition of the Riemann-zeta function [280] with $x = \tilde{\beta}|p|$. Next, we consider

$$\begin{aligned} \widehat{T}^{(1)(1)} &= \frac{1}{(2\pi)^2} \int_0^{2\pi} \int_0^{\infty} \mathrm{d}|p| \, \mathrm{d}\psi \, \frac{1}{e^{\tilde{\beta}|p|} - 1} \, p^{(1)} p^{(1)} \\ &= \frac{1}{(2\pi)^2} \int_0^{2\pi} \int_0^{\infty} \mathrm{d}|p| \, \mathrm{d}\psi \, \frac{1}{e^{\tilde{\beta}|p|} - 1} \, |p|^2 \cos^2\psi = \frac{\zeta(3)}{2\pi\tilde{\beta}^3} \end{aligned} \tag{2.3.20}$$

using the results from the previous component case. Computing the final component is trivial, as using the fact that

$$\int_0^{2\pi} \cos^2\psi \, \mathrm{d}\psi = \int_0^{2\pi} \sin^2\psi \, \mathrm{d}\psi \tag{2.3.21}$$

it is clear to see that $\widehat{T}^{(1)(1)} = \widehat{T}^{(2)(2)}$. Therefore, in three-dimensional space-times, the RKT-SET takes the relatively simple form

$$\widehat{T}^{(a)(b)} = \frac{\zeta(3)}{2\pi\tilde{\beta}^3} \mathrm{Diag}\{2,\, 1,\, 1\}. \tag{2.3.22}$$

The quantity

$$\zeta(3) \approx 1.2020569031595942853997381615114499907649862 92\ldots, \tag{2.3.23}$$

is known as Apéry's constant [21, 280].

### 2.3.2 RKT-stress-energy tensor in four-dimensional space-times

The four-dimensional case is somewhat more complicated. Why this is the case becomes apparent when attempting to compute the integrals. Nevertheless, it is possible to compute the integrals in a closed form manner, which will be demonstrated.

The Bose-Einstein distribution function (2.3.6) takes a very similar form to the three-dimensional case, and is given by [53, 74, 79, 129, 227, 235, 294, 319]

$$f = \frac{1}{(2\pi)^3} \frac{1}{e^{\tilde{\beta} u_{(a)} p^{(a)}} - 1}, \tag{2.3.24}$$

with the integration measure, $\mathrm{d}\mathbf{p} = \mathrm{d}p^{(1)}\,\mathrm{d}p^{(2)}\,\mathrm{d}p^{(3)}$, taking a similar form also. We again choose the gas of particles to be at rest, so we set the fluid velocity to be $u_{(a)} = (1,\,0,\,0,\,0)$ in much the same manner as before. This means that the exponent in the distribution function is exactly the same as for the three-dimensional case, i.e. $\tilde{\beta} u_{(a)} p^{(a)} = \tilde{\beta} p^{(0)}$. Again, using the mass-shell condition $p^{(0)} = \sqrt{m^2 + |p|^2}$ and specialising to the massless case yields the useful relation $p^{(0)} = |p|$. Decomposing the spatial components of the momentum into spherical coordinates we have the following transforms:

$$p^{(1)} = |p| \cos\psi, \quad p^{(2)} = |p| \sin\psi \cos\phi, \quad p^{(3)} = |p| \sin\psi \sin\phi, \tag{2.3.25}$$

for which the Jacobian is $\det\{J(|p|, \psi, \phi)\} = |p|^2 \sin\psi$, leading to the new integration measure $\mathrm{d}\mathbf{p} = |p|^2 \sin\psi\,\mathrm{d}|p|\,\mathrm{d}\psi\,\mathrm{d}\phi$. The RKT-SET is therefore

$$\begin{aligned} \widehat{T}^{(a)(b)} &= \int \mathrm{d}|p|\,\mathrm{d}\psi\,\mathrm{d}\phi\,\frac{|p|^2}{p^{(0)}} \sin\psi\, f\, p^{(a)} p^{(b)} \\ &= \frac{1}{(2\pi)^3} \int_0^{2\pi} \int_0^{\pi} \int_0^{\infty} \mathrm{d}|p|\,\mathrm{d}\psi\,\mathrm{d}\phi\, \sin\psi\, \frac{|p|}{e^{\tilde{\beta}|p|} - 1}\, p^{(a)} p^{(b)}. \end{aligned} \tag{2.3.26}$$

In an analogous way to the three-dimensional case, the off-diagonal components are zero; this will be again illustrated using the following three cases. Firstly,

$$\widehat{T}^{(0)(1)} = \frac{1}{(2\pi)^3} \int_0^{2\pi} \int_0^{\pi} \int_0^{\infty} \mathrm{d}|p|\,\mathrm{d}\psi\,\mathrm{d}\phi\, \sin\psi\, \frac{|p|}{e^{\tilde{\beta}|p|} - 1}\, p^{(0)} p^{(1)}$$

$$= \frac{1}{(2\pi)^3}\int_0^{2\pi} \mathrm{d}\phi \underbrace{\int_0^{\pi} \cos\psi \sin\psi \,\mathrm{d}\psi}_{=0} \int_0^{\infty} \mathrm{d}|p| \, \frac{|p|^3}{e^{\tilde{\beta}|p|}-1} = 0, \tag{2.3.27}$$

and similarly,

$$\begin{aligned}\widehat{T}^{(1)(3)} &= \frac{1}{(2\pi)^3}\int_0^{2\pi}\int_0^{\pi}\int_0^{\infty} \mathrm{d}|p|\,\mathrm{d}\psi\,\mathrm{d}\phi\,\sin\psi\,\frac{|p|}{e^{\tilde{\beta}|p|}-1}\,p^{(1)}p^{(3)} \\ &= \frac{1}{(2\pi)^3}\underbrace{\int_0^{2\pi}\sin\phi\,\mathrm{d}\phi}_{=0}\int_0^{\pi}\cos\psi\sin^2\psi\,\mathrm{d}\psi\int_0^{\infty}\mathrm{d}|p|\,\frac{|p|^3}{e^{\tilde{\beta}|p|}-1} = 0,\end{aligned} \tag{2.3.28}$$

and finally,

$$\begin{aligned}\widehat{T}^{(2)(3)} &= \frac{1}{(2\pi)^3}\int_0^{2\pi}\int_0^{\pi}\int_0^{\infty} \mathrm{d}|p|\,\mathrm{d}\psi\,\mathrm{d}\phi\,\sin\psi\,\frac{|p|}{e^{\tilde{\beta}|p|}-1}\,p^{(2)}p^{(3)} \\ &= \frac{1}{(2\pi)^3}\underbrace{\int_0^{2\pi}\cos\phi\sin\phi\,\mathrm{d}\phi\int_0^{\pi}\sin^3\psi\,\mathrm{d}\psi}_{=0}\int_0^{\infty}\mathrm{d}|p|\,\frac{|p|^3}{e^{\tilde{\beta}|p|}-1} = 0.\end{aligned} \tag{2.3.29}$$

All that remains is to find the non-zero components of the RKT-SET. We will consider each in turn: firstly, the energy density component

$$\begin{aligned}\widehat{T}^{(0)(0)} &= \frac{1}{(2\pi)^3}\int_0^{2\pi}\int_0^{\pi}\int_0^{\infty} \mathrm{d}|p|\,\mathrm{d}\psi\,\mathrm{d}\phi\,\sin\psi\,\frac{|p|}{e^{\tilde{\beta}|p|}-1}\,p^{(0)}p^{(0)} \\ &= \frac{1}{(2\pi)^3}\int_0^{2\pi}\mathrm{d}\phi\int_0^{\pi}\sin\psi\,\mathrm{d}\psi\int_0^{\infty}\mathrm{d}|p|\,\frac{|p|^3}{e^{\tilde{\beta}|p|}-1} \\ &= \frac{1}{2\pi^2}\int_0^{\infty}\mathrm{d}|p|\,\frac{|p|^3}{e^{\tilde{\beta}|p|}-1} \\ &= \frac{1}{2\pi^2\tilde{\beta}^4}\int_0^{\infty}\mathrm{d}|p|\,\frac{|p|^3}{e^{|p|}-1} = \frac{\zeta(4)\Gamma(4)}{2\pi^2\tilde{\beta}^4} = \frac{\pi^2}{30\tilde{\beta}^4},\end{aligned} \tag{2.3.30}$$

where again we have used the integral definition of the Riemann-zeta function [280]. For the spatial components, we find similar integrals; the first of which is

$$\begin{aligned}\widehat{T}^{(1)(1)} &= \frac{1}{(2\pi)^3}\int_0^{2\pi}\int_0^{\pi}\int_0^{\infty} \mathrm{d}|p|\,\mathrm{d}\psi\,\mathrm{d}\phi\,\sin\psi\,\frac{|p|}{e^{\tilde{\beta}|p|}-1}\,p^{(1)}p^{(1)} \\ &= \frac{1}{(2\pi)^3}\int_0^{2\pi}\mathrm{d}\phi\int_0^{\pi}\cos^2\psi\sin\psi\,\mathrm{d}\psi\int_0^{\infty}\mathrm{d}|p|\,\frac{|p|^3}{e^{\tilde{\beta}|p|}-1} \\ &= \frac{1}{6\pi^2}\int_0^{\infty}\mathrm{d}|p|\,\frac{|p|^3}{e^{\tilde{\beta}|p|}-1}\end{aligned}$$

$$= \frac{1}{6\pi^2\tilde{\beta}^4}\int_0^\infty \mathrm{d}|p|\,\frac{|p|^3}{e^{|p|}-1} = \frac{\zeta(4)\Gamma(4)}{6\pi^2\tilde{\beta}^4} = \frac{\pi^2}{90\tilde{\beta}^4}, \tag{2.3.31}$$

and similarly,

$$\begin{aligned}
\widehat{T}^{(2)(2)} &= \frac{1}{(2\pi)^3}\int_0^{2\pi}\int_0^{\pi}\int_0^{\infty} \mathrm{d}|p|\,\mathrm{d}\psi\,\mathrm{d}\phi\,\sin\psi\,\frac{|p|}{e^{\tilde{\beta}|p|}-1}\,p^{(2)}p^{(2)} \\
&= \frac{1}{(2\pi)^3}\int_0^{2\pi}\cos^2\phi\,\mathrm{d}\phi\int_0^{\pi}\sin^3\psi\,\mathrm{d}\psi\int_0^{\infty}\mathrm{d}|p|\,\frac{|p|^3}{e^{\tilde{\beta}|p|}-1} \\
&= \frac{1}{6\pi^2\tilde{\beta}^4}\int_0^\infty \mathrm{d}|p|\,\frac{|p|^3}{e^{|p|}-1} = \frac{\zeta(4)\Gamma(4)}{6\pi^2\tilde{\beta}^4} = \frac{\pi^2}{90\tilde{\beta}^4}.
\end{aligned} \tag{2.3.32}$$

Finally,

$$\begin{aligned}
\widehat{T}^{(3)(3)} &= \frac{1}{(2\pi)^3}\int_0^{2\pi}\int_0^{\pi}\int_0^{\infty} \mathrm{d}|p|\,\mathrm{d}\psi\,\mathrm{d}\phi\,\sin\psi\,\frac{|p|}{e^{\tilde{\beta}|p|}-1}\,p^{(3)}p^{(3)} \\
&= \frac{1}{(2\pi)^3}\int_0^{2\pi}\sin^2\phi\,\mathrm{d}\phi\int_0^{\pi}\sin^3\psi\,\mathrm{d}\psi\int_0^{\infty}\mathrm{d}|p|\,\frac{|p|^3}{e^{\tilde{\beta}|p|}-1} \\
&= \frac{1}{6\pi^2\tilde{\beta}^4}\int_0^\infty \mathrm{d}|p|\,\frac{|p|^3}{e^{|p|}-1} = \frac{\zeta(4)\Gamma(4)}{6\pi^2\tilde{\beta}^4} = \frac{\pi^2}{90\tilde{\beta}^4}.
\end{aligned} \tag{2.3.33}$$

Since we now have each of the components, we can simply write down the form of the RKT-SET in four-dimensional space-times as

$$\widehat{T}^{(a)(b)} = \frac{\pi^2}{90\tilde{\beta}^4}\mathrm{Diag}\{3,\,1,\,1,\,1\}. \tag{2.3.34}$$

### 2.3.3 Rigidly rotating distributions in Minkowski space-time

In this section, we provide a simple example of the relativistic kinetic theoretic approach for rigidly rotating distributions in four-dimensional flat space-time. This is to facilitate the comparison with [9, 116], where the authors computed Planckian forms for a rigidly rotating thermal (Bose-Einstein) distribution at temperature $T = \beta^{-1}$. This then extends nicely to section 5.3.4 of this thesis, where we compare relativistic kinetic theory stress-energy tensors with quantum field theory stress-energy tensors on anti-de Sitter space (see section 2.7) to see how well they agree.

We start by specifying the flat space-time metric, in cylindrical coordinates $\{\tau, r, \phi, z\}$, as

$$\mathrm{d}s^2 = -\,\mathrm{d}\tau^2 + \mathrm{d}r^2 + r^2\,\mathrm{d}\phi^2 + \mathrm{d}z^2. \tag{2.3.35}$$

We then make a transformation to coordinates that are rigidly rotating about the $z$ axis at constant angular velocity $\Omega$, by specifying the transformation

$$\tau \mapsto \tilde{\tau} = \tau, \quad \phi \mapsto \tilde{\phi} = \phi - \Omega\tau, \tag{2.3.36}$$

under which the metric becomes[7]

$$\mathrm{d}s^2 = -\Gamma_{\mathbb{M}}^{-2}\,\mathrm{d}\tau^2 + \mathrm{d}r^2 + r^2\,\mathrm{d}\phi^2 + \mathrm{d}z^2 + 2r^2\Omega\,\mathrm{d}\tau\,\mathrm{d}\phi, \tag{2.3.37}$$

where we have defined the Lorentz factor

$$\Gamma_{\mathbb{M}} := \frac{1}{\sqrt{1 - r^2\Omega^2}}. \tag{2.3.38}$$

In order to compute the RKT-SET, we must specify a suitable vierbein basis. This is given by [9, 315]

$$e^{\mu}_{(\tau)}\partial_\mu = \Gamma_{\mathbb{M}}\left[\partial_\tau + \Omega\partial_\phi\right], \quad e^{\mu}_{(r)}\partial_\mu = \partial_r, \quad e^{\mu}_{(\phi)}\partial_\mu = r\Gamma_{\mathbb{M}}\left[\Omega\partial_\tau + r^{-2}\partial_\phi\right], \quad e^{\mu}_{(z)}\partial_\mu = \partial_z, \tag{2.3.39a}$$

which has corresponding covectors

$$w^{(\tau)}_{\mu}\,\mathrm{d}x^\mu = \Gamma_{\mathbb{M}}\left[\mathrm{d}\tau - r^2\Omega\,\mathrm{d}\phi\right], \quad w^{(r)}_{\mu}\,\mathrm{d}x^\mu = \mathrm{d}r,$$
$$w^{(\phi)}_{\mu}\,\mathrm{d}x^\mu = r\Gamma_{\mathbb{M}}\left[\mathrm{d}\phi - \Omega\,\mathrm{d}\tau\right], \quad w^{(z)}_{\mu}\,\mathrm{d}x^\mu = \mathrm{d}z. \tag{2.3.39b}$$

Using the Tolman relation [357, 359], we find the local inverse temperature to be

$$\widetilde{\beta} = \beta\sqrt{-g_{\tau\tau}} = \beta\,\Gamma_{\mathbb{M}}^{-1}. \tag{2.3.40}$$

[7] From this point onwards, the tildes will be dropped for brevity. However, it should be understood that $\phi$ here and henceforth refers to the co-rotating coordinate (similarly for $\tau$).

To find the RKT-SET, we contract the RKT-SET in the frame (2.3.34) with the vierbein basis (2.3.39) as

$$^{\mathrm{RKT}}T^{\mu\nu} = e^{\mu}_{(a)} e^{\nu}_{(b)} T^{(a)(b)}. \tag{2.3.41}$$

Working component by component, we have

$$^{\mathrm{RKT}}T^{\tau\tau} = e^{\tau}_{(\tau)} e^{\tau}_{(\tau)} T^{(\tau)(\tau)} + e^{\tau}_{(\phi)} e^{\tau}_{(\phi)} T^{(\phi)(\phi)} = \frac{\pi^2 \Gamma^6_{\mathbb{M}}}{90\beta^4} \left(3 + r^2\Omega^2\right), \tag{2.3.42a}$$

$$^{\mathrm{RKT}}T^{\tau\phi} = {}^{\mathrm{RKT}}T^{\phi\tau} = e^{\tau}_{(\tau)} e^{\phi}_{(\tau)} T^{(\tau)(\tau)} + e^{\tau}_{(\phi)} e^{\phi}_{(\phi)} T^{(\phi)(\phi)} = \frac{2\pi^2 \Omega \Gamma^6_{\mathbb{M}}}{45\beta^4} \tag{2.3.42b}$$

$$^{\mathrm{RKT}}T^{rr} = e^{r}_{(r)} e^{r}_{(r)} T^{(r)(r)} = \frac{\pi^2 \Gamma^4_{\mathbb{M}}}{90\beta^4}, \tag{2.3.42c}$$

$$^{\mathrm{RKT}}T^{\phi\phi} = e^{\phi}_{(\tau)} e^{\phi}_{(\tau)} T^{(\tau)(\tau)} + e^{\phi}_{(\phi)} e^{\phi}_{(\phi)} T^{(\phi)(\phi)} = \frac{\pi^2 \Gamma^6_{\mathbb{M}}}{90 r^2 \beta^4} \left(1 + 3r^2\Omega^2\right), \tag{2.3.42d}$$

$$^{\mathrm{RKT}}T^{zz} = e^{z}_{(z)} e^{z}_{(z)} T^{(z)(z)} = \frac{\pi^2 \Gamma^4_{\mathbb{M}}}{90\beta^4}, \tag{2.3.42e}$$

with the remaining components (i.e. every other off-diagonal component) vanishing. In section 5.3.1, we compute the RKT-SET in rigidly-rotating, spherical coordinates on anti-de Sitter space-time (see equation (5.3.21)). It can be shown that the anti-de Sitter space RKT-SET will reduce to the Minkowski space RKT-SET (2.3.42) above in an appropriate limit, provided we switch from spherical to cylindrical coordinates. See sections 4.1 and 5.3.1.

In order to facilitate the comparison with the Planckian distribution computed in [116], it is wise to match the index placement between the two stress-energy tensors. That is to say, we consider the mixed indices version of the RKT-SET, by lowering one index using the Minkowski metric (2.3.37). This yields

$$^{\mathrm{RKT}}T_{\tau}{}^{\tau} = -\frac{\pi^2 \Gamma^6_{\mathbb{M}}}{90\beta^4}(3 + r^2\Omega^2), \tag{2.3.43a}$$

$$^{\mathrm{RKT}}T_{\tau}{}^{\phi} = \frac{2\pi^2 r \Omega \Gamma^6_{\mathbb{M}}}{45\beta^4}, \tag{2.3.43b}$$

$$^{\mathrm{RKT}}T_{\phi}{}^{\phi} = \frac{\pi^2 \Gamma^6_{\mathbb{M}}}{90\beta^4}(1 + 3r^2\Omega^2), \tag{2.3.43c}$$

$$^{\text{RKT}}T_r{}^r = \frac{\pi^2\Gamma_{\mathbb{M}}^4}{90\beta^4}, \tag{2.3.43d}$$

$$^{\text{RKT}}T_z{}^z = \frac{\pi^2\Gamma_{\mathbb{M}}^4}{90\beta^4}. \tag{2.3.43e}$$

The Planckian distribution stress-energy tensor, as given by [116],

$$^{\text{Planck}}T_\tau{}^\tau = -\frac{\pi^2\Gamma_{\mathbb{M}}^6}{90\beta^4}(3 + r^2\Omega^2), \tag{2.3.44a}$$

$$^{\text{Planck}}T_\tau{}^\phi = \frac{2\pi^2 r\Omega\Gamma_{\mathbb{M}}^6}{45\beta^4}, \tag{2.3.44b}$$

$$^{\text{Planck}}T_\phi{}^\phi = \frac{\pi^2\Gamma_{\mathbb{M}}^6}{90\beta^4}(1 + 3r^2\Omega^2), \tag{2.3.44c}$$

$$^{\text{Planck}}T_r{}^r = \frac{\pi^2\Gamma_{\mathbb{M}}^4}{90\beta^4}, \tag{2.3.44d}$$

$$^{\text{Planck}}T_z{}^z = \frac{\pi^2\Gamma_{\mathbb{M}}^4}{90\beta^4}. \tag{2.3.44e}$$

Comparing (2.3.43) and (2.3.44), we see that the RKT and Planckian stress-energy tensors match exactly. In fact, this is no coincidence; the Planckian distribution stress-energy tensor is constructed from the Bose-Einstein distribution and thus is itself an RKT-SET [9].

We now briefly discuss an important problem regarding rigidly-rotating distributions in Minkowski space-time. Firstly, in special relativistic scenarios, rigidly-rotating distributions can only exist up to a distance $r = \Omega^{-1}$ from the rotating axis. This is the distance at which co-rotating particles have a linear velocity equal to the speed of light; it is known as the *speed-of-light surface*. To see why rigidly-rotating distributions can only exist up to a distance of $r = \Omega^{-1}$, consider the following. We momentarily reinstate the speed-of-light constant $c$ for clarity. Particles co-rotating with angular speed $\Omega$ will have a linear velocity given by $v = r\Omega$; when $v \geq c$, the particles are travelling at a speed faster than or equal to the speed-of-light. The speed-of-light surface is defined as the point at which the linear velocity and speed of light coincide, i.e $v = r\Omega = c$, therefore the speed-of-light surface is at a radius $r = c\Omega^{-1}$. Reinstating Planck units, i.e. setting $c = 1$, the speed-of-light

surface is therefore at a distance $r = \Omega^{-1}$. Furthermore, if we consider the metric (2.3.37) in co-rotating coordinates, we see that on the speed-of-light surface $r = \Omega^{-1}$, the metric component $g_{tt}$ is zero. When at distances below the speed-of-light surface, the metric component $g_{tt}$ is negative, and any observer travelling with a velocity vector $u^\mu = (1, 0, 0, 0)$ will be travelling on a time-like curve. On the other hand, if we are at distances beyond the speed-of-light surface, i.e. $r > \Omega^{-1}$, then the metric component $g_{tt}$ will be positive, and an observer with velocity vector $u^\mu = (1, 0, 0, 0)$ will be travelling on a space-like curve (i.e. they will be travelling at superluminal speeds). Finally, on the speed-of-light surface, the metric component $g_{tt}$ vanishes, and an observer travelling with velocity vector $u^\mu = (1, 0, 0, 0)$ must be travelling on a null curve, i.e. they are travelling *at* the speed-of-light. By analogy therefore, to find the speed-of-light surface for a space-time, it suffices to consider the surface defined by $g_{tt} = 0$, when the metric is written in (rigidly) co-rotating coordinates. This is discussed for anti-de Sitter space-time in section 4.4.

It was discovered in an investigation of the rotating quantum vacuum, that in order for a vacuum state to be unambiguously defined, an artificial mirror has to be inserted in the space-time at a radius less than the radius at which a speed-of-light surface forms [97]. This is because an observer rotating at the same angular speed as the vacuum fails to remain inert[8] when the space-time is unbounded, or bounded by an artificial mirror that is beyond the speed-of-light surface. In contrast, the observer *will* remain inert when the artificial mirror is located below the speed-of-light surface. It was also discovered that a quantum, thermal distribution will suffer the same pathological issues as the rotating quantum vacuum [116]. It was found that the Planckian distribution (2.3.44) provides a good approximation to the quantum thermal distribution everywhere except for very close to artificial mirror, where there was a Casimir divergence [116].

[8]In this context, by inert, it is meant that the rotating observer will see the rotating vacuum just as an inertial observer sees the nonrotating vacuum. In the context of a particle detector (as in the original paper [97]), this means that the rotating detector will not detect particles or excitations, i.e. it 'sees' the nonrotating vacuum state.

In contrast to the situation on flat space, rigidly-rotating anti-de Sitter space-time does *not* suffer from this pathological behaviour; this is because anti-de Sitter space has a natural boundary. In fact, a vacuum state for rigidly-rotating observers on anti-de Sitter is not only unambiguously defined, but it coincides with the nonrotating vacuum, provided there is no speed-of-light surface [222]. Anti-de Sitter space therefore provides a natural background on which rigidly-rotating quantum states can be studied, since one does not need to artificially insert a mirror. Anti-de Sitter space will be considered in detail in chapter 4, and more attention will be paid towards rigid rotation (section 4.4) and quantum states (section 4.7). In addition, relativistic kinetic theoretic stress-energy tensors for (rigidly-rotating) anti-de Sitter space will be constructed in chapter 5, and compared with the renormalised stress-energy tensor constructed on (rigidly-rotating) anti-de Sitter space; see section 5.3.4.

## § 2.4 Quantum field theory on flat space-time

As mentioned in the introduction (in particular section 1.1) and section 2.2.3, in this thesis we are concerned only with scalar field theories, and not spinor or vector field theories. In the following analysis, therefore, we only treat uncharged, scalar fields. There are a plethora of great works in the literature (too many to list here in entirety), for example, standard textbooks such as [207, 299, 338, 377] treat charged and uncharged quantum spinor and vector field theories in general terms. Additionally outlined in the introduction (see section 1.1), two of the most popular ways of specifying a quantum field theory are via canonical quantisation or using the Wightman reconstruction theorem [343, 384, 385], by constructing all possible $n$-point correlators (i.e. Green functions); for a free scalar field, one only requires one two-point function, in particular the Feynman or Hadamard Green function [343, 384, 385]. On flat space-time, both are well trodden in the literature and comparatively straightforward (compared to curved spaces). For example, see standard textbooks such as [45, 63, 157, 207, 271, 299, 330, 338, 377]. Therefore, the construction of

the quantum field theory by both methods will be detailed briefly for flat space, starting with canonical quantisation in section 2.4.1 and using the method of Green functions in section 2.5.

To quantise fields on Minkowski space-time, we first modify (only slightly) the treatment of the scalar fields in section 2.2.3, since it was performed on a general curved space-time. Beginning with the Lagrangian density for the real scalar field,

$$\mathscr{L}[\Phi, \eta] = -\frac{1}{2}\eta^{\mu\nu}\partial_\mu\Phi\partial_\nu\Phi - m^2\Phi^2, \tag{2.4.1}$$

we see that the main differences between the curved space Lagrangian density (2.2.41) and flat space Lagrangian density (2.4.1) are as follows: we have downgraded the covariant derivatives to coordinate derivatives (since the Christoffel symbols are vanishing on flat space; although for a scalar field the covariant and coordinate derivatives are equal); the general curved space metric $g$ has been replaced by the flat space metric, $\eta$ (which has determinant $\det \eta_{\mu\nu} \equiv -1$); and the coupling term has been removed since (mathematically) the Ricci scalar is zero and (physically) there is no gravitational curvature to couple to on flat space. Following the same methodology as in section 2.2.3, we construct an action

$$\mathcal{S}[\Phi, \eta] = \int \mathrm{d}^n x \left(-\frac{1}{2}\eta^{\mu\nu}\partial_\mu\Phi\partial_\nu\Phi - m^2\Phi^2\right), \tag{2.4.2}$$

and invoking the principle of least action, we arrive at the equation of motion (or mass-shell condition)

$$\left(-\partial_\mu\partial^\mu + m^2\right)\Phi = 0, \tag{2.4.3}$$

which is the flat space Klein-Gordon equation.

### 2.4.1 Canonical quantisation

The starting point in a canonical quantisation procedure is to find mode solutions of the field equation; in our case this is the Klein-Gordon equation (2.4.3). A basic set of solutions

of the flat space Klein-Gordon equation are given by plane-wave solutions of the form

$$\Phi_{\mathbf{k}}(\boldsymbol{x}, t) = \Phi_0\, e^{-i\omega t + i\mathbf{k}\cdot\boldsymbol{x}}, \tag{2.4.4}$$

where $t$ is the single time-like coordinate of our pseudo-Riemannian manifold and $\boldsymbol{x}$ is the remaining spatial coordinates, $\boldsymbol{x} = (x^1, x^2, \ldots, x^{n-1})$. Additionally, $\omega$ is the frequency of the plane waves and $\mathbf{k}$ is the momentum, satisfying the mass-shell condition $\omega^2 = m^2 + |\mathbf{k}|^2$, and $\Phi_0$ is a normalisation constant to be determined. We consider just the positive frequency modes given by $\omega > 0$, since the negative frequency modes can be represented by the complex conjugate $\Phi^*_{\mathbf{k}}$. To determine the normalisation coefficient, we need to first define an inner product

$$\langle \Phi_1, \Phi_2 \rangle = -i \int_{\mathcal{M}} \mathrm{d}^{n-1}\boldsymbol{x}\; \Phi_1 \overleftrightarrow{\partial_t} \Phi_2^*, \tag{2.4.5}$$

where we have defined the operator

$$\Phi_1 \overleftrightarrow{\partial_t} \Phi_2^* \coloneqq \Phi_1 \partial_t \Phi_2^* - \Phi_2^* \partial_t \Phi_1, \tag{2.4.6}$$

and $\mathcal{M}$ is a hypersurface (and in particular a Cauchy surface), with unit normal $n^\mu$; on flat space-time, the unit normal is $n^\mu = -\eta^{\mu t} = 1$ and the hypersurface $\mathcal{M}$ is the Euclidean section of Minkowski space. The inner product (2.4.5) is known as the *Klein-Gordon inner product*[9] on flat space-time. For any field configuration that is on-shell (i.e. satisfying the Klein-Gordon equation (2.4.3)), the inner product is independent of the choice of Cauchy surface $\mathcal{M}$ [45, 75], provided we ignore boundary terms arising when using Stokes' theorem to switch the Klein-Gordon inner product (2.4.5) from an integral over a volume (i.e. the entire flat space manifold) $\mathbb{M}$ to its boundary surface $\partial\mathbb{M} = \mathcal{M}$.

We can use the Klein-Gordon inner product (2.4.5) to determine the normalisation constant $\Phi_0$. We begin by choosing two independent plane-wave solutions

$$\Phi_1(\boldsymbol{x}, t) = \Phi_0 e^{-i\omega_1 t + i\mathbf{k}_1\cdot\boldsymbol{x}}, \qquad \Phi_2(\boldsymbol{x}, t) = \widetilde{\Phi}_0 e^{-i\omega_2 t + i\mathbf{k}_2\cdot\boldsymbol{x}}, \tag{2.4.7}$$

[9] Technically speaking, this is not a well defined inner product since it is not positive definite, though it is sufficient for our use. We elect to leave the finer details such as this to the algebraic quantum theorists.

before taking the Klein-Gordon inner product (on a space-like hyperplane of simultaneity) between the two solutions:

$$\langle \Phi_1, \Phi_2 \rangle = \int_\Sigma \mathrm{d}^{n-1}\boldsymbol{x}\ \Phi_0 \widetilde{\Phi}_0^* \left(\omega_1 + \omega_2\right) e^{-i(\omega_1-\omega_2)t + i(\mathbf{k}_1-\mathbf{k}_2)\cdot\boldsymbol{x}}. \tag{2.4.8}$$

To reduce this, we note that, by using the Fourier transform definition of the $(n-1)$-dimensional Dirac-delta function

$$\delta^{n-1}(\mathbf{k}_1 - \mathbf{k}_2) = (2\pi)^{1-n} \int \mathrm{d}^{n-1}\boldsymbol{x}\ e^{i(\mathbf{k}_1-\mathbf{k}_2)\cdot\boldsymbol{x}}, \tag{2.4.9}$$

we can write the inner product as

$$\langle \Phi_1, \Phi_2 \rangle = \Phi_0 \widetilde{\Phi}_0^* \left(\omega_1 + \omega_2\right) e^{-i(\omega_1-\omega_2)t} \left(2\pi\right)^{n-1} \delta^{n-1}(\mathbf{k}_1 - \mathbf{k_2}). \tag{2.4.10}$$

It is a requirement that the modes $\Phi_1$ and $\Phi_2$ be orthonormal, or, using the inner product:

$$\langle \Phi_1, \Phi_2 \rangle = \delta^{n-1}(\mathbf{k}_1 - \mathbf{k}_2), \tag{2.4.11}$$

which selects the normalisation factor to be

$$\Phi_0 = \frac{1}{\sqrt{2\omega(2\pi)^{n-1}}}, \tag{2.4.12}$$

which gives the *classical* field mode to be

$$\Phi_{\mathbf{k}}(\boldsymbol{x}, t) = \frac{1}{\sqrt{2\omega(2\pi)^{n-1}}} e^{-i\omega t + i\mathbf{k}\cdot\boldsymbol{x}}. \tag{2.4.13}$$

To quantise the classical field, we promote the fields to be operator-valued distributions, i.e. $\Phi(\boldsymbol{x}, t) \to \widehat{\Phi}(\boldsymbol{x}, t)$ and subject the field operators to equal-time commutation relations

$$\left[\widehat{\Phi}(\boldsymbol{x}, t), \widehat{\Phi}(\boldsymbol{x}', t)\right] = 0, \tag{2.4.14a}$$

$$\left[\widehat{\pi}(\boldsymbol{x}, t), \widehat{\pi}(\boldsymbol{x}', t)\right] = 0, \tag{2.4.14b}$$

$$\left[\widehat{\Phi}(\boldsymbol{x}, t), \widehat{\pi}(\boldsymbol{x}', t)\right] = i\delta^{n-1}(\boldsymbol{x} - \boldsymbol{x}'), \tag{2.4.14c}$$

where the operator $\widehat{\pi}$ is called the conjugate momentum, defined as

$$\widehat{\pi}(\boldsymbol{x}, t) = \partial_t \widehat{\Phi}(\boldsymbol{x}, t). \tag{2.4.15}$$

The field modes (2.4.13) and their complex conjugates form a complete orthonormal basis, and we can thus expand the quantised field $\widehat{\Phi}$ in terms of the orthonormal modes as

$$\begin{aligned}\widehat{\Phi}(\boldsymbol{x},t) &= \int \mathrm{d}^{n-1}\mathbf{k}\left(\hat{a}(\mathbf{k})\widehat{\Phi}_{\mathbf{k}}(\boldsymbol{x},t)+\hat{a}^{\dagger}(\mathbf{k})\widehat{\Phi}^{\dagger}_{\mathbf{k}}(\boldsymbol{x},t)\right)\\ &= \int \frac{\mathrm{d}^{n-1}\mathbf{k}}{\sqrt{2\omega(2\pi)^{n-1}}}\left(\hat{a}(\mathbf{k})e^{-i\omega t+i\mathbf{k}\cdot\boldsymbol{x}}+\hat{a}^{\dagger}(\mathbf{k})e^{i\omega t-i\mathbf{k}\cdot\boldsymbol{x}}\right). \end{aligned} \tag{2.4.16}$$

The operators $\hat{a}(\mathbf{k})$ and $\hat{a}^{\dagger}(\mathbf{k})$ are the annihilation and creation operators, respectively, subject to the canonical commutation relations

$$\left[\hat{a}(\mathbf{k}),\hat{a}(\mathbf{k}')\right]=0, \tag{2.4.17a}$$

$$\left[\hat{a}^{\dagger}(\mathbf{k}),\hat{a}^{\dagger}(\mathbf{k}')\right]=0, \tag{2.4.17b}$$

$$\left[\hat{a}(\mathbf{k}),\hat{a}^{\dagger}(\mathbf{k}')\right]=(2\pi)^{n-1}\delta^{n-1}(\mathbf{k}-\mathbf{k}'). \tag{2.4.17c}$$

In flat space-time, a unique[10], global ground state $|0\rangle$ can be defined by the effect of the annihilation operator upon it:

$$\hat{a}(\mathbf{k})|0\rangle=0, \quad \forall\,\mathbf{k}. \tag{2.4.18}$$

Throughout this thesis, as it is in the literature, the ground state will be referred to as the *vacuum state*; the vacuum state has no field quanta (i.e. particles) present, carries zero momentum and naïvely, one might expect it to also carry no energy, given there are no particles present. However, as we will see, this is not manifestly the case; in flat space, we must redefine the zero-point energy (detailed below) to be zero and only then the flat space vacuum has zero energy. In curved spaces, we instead think of the vacuum state as the state with the lowest *possible* energy - see section 2.6.1.

Recall the stress-energy tensor (2.2.43) for a general curved space-time. Reducing this to the flat space-time version (by replacing the curved space metrics with the flat space metrics and setting the coupling constant to zero), we have

$$\widehat{T}^{\mathbb{M}}_{\mu\nu}=\partial_{\mu}\widehat{\Phi}\partial_{\nu}\widehat{\Phi}-\frac{1}{2}\eta_{\mu\nu}\eta^{\alpha\beta}\partial_{\alpha}\widehat{\Phi}\partial_{\beta}\widehat{\Phi}-\frac{1}{2}\eta_{\mu\nu}m^{2}\widehat{\Phi}^{2}, \tag{2.4.19}$$

[10]Unique in the sense that it is the ground state on which *all* inertial observers agree.

from which we can define the Hamiltonian energy density operator as

$$\widehat{H} \equiv \int_{\mathcal{M}} \mathrm{d}^{n-1}\boldsymbol{x}\, \widehat{T}^{\mathbb{M}}_{tt} = \frac{1}{2}\sum_{\mathbf{k}} \left[\hat{a}^{\dagger}(\mathbf{k})\hat{a}(\mathbf{k}) + \hat{a}(\mathbf{k})\hat{a}^{\dagger}(\mathbf{k})\right]\omega, \tag{2.4.20a}$$

switching to using discretised sum notation rather than integral representations of operators à la [45]. Using the canonical commutation relations (2.4.17), this can be expressed as

$$\widehat{H} = \sum_{\mathbf{k}} \left(\hat{a}^{\dagger}(\mathbf{k})\hat{a}(\mathbf{k}) + \frac{1}{2}\right)\omega. \tag{2.4.20b}$$

Taking the expectation value of the Hamiltonian operator (2.4.20) (i.e. by acting on the operator with the bra and ket vacuum state) yields the energy density in the vacuum (or the zero-point energy density), given by

$$\langle 0|\widehat{H}|0\rangle = \frac{1}{2}\sum_{\mathbf{k}} \omega, \tag{2.4.21}$$

using the definition of the vacuum state. Clearly, not only is the zero-point energy (2.4.21) non-zero, but it appears to be divergent; this is due to $\omega$ having no upper bound and thus the zero-point energy can become arbitrarily large. This issue will plague the subject of quantum field theories in curved space-times; in flat space, this can be circumvented. The energy density (2.4.21) is unmeasurable in non-gravitational physics; this means, without affecting observable quantities, we are free to *renormalise* the zero-point energy by any (even infinite) amount. We therefore discard the $\frac{1}{2}\sum_{\mathbf{k}}\omega$ term and *define* the zero-point energy to be zero in flat space-time. In curved space-times, the divergent parts of the zero-point energy have considerably more complicated forms and thus the problem of renormalisation is not as straightforward. The issue of divergent zero-point energy is not unique to canonical quantisation procedures; as we will see in the next section, it also besets any attempts at quantising using the Green function approach.

As discussed above, the notion of renormalising the zero-point energy is somewhat heuristic; we simply 'discard the infinities'. In fact, in flat space-time, this procedure can be formalised by introducing (Wick) *normal ordering* [383]. Denoted by colons either side of

the operator, i.e $:\widehat{\mathscr{Q}}:$, normal ordering works by taking any product of creation and annihilation operators and arranging them such that the annihilation operators always lie to the right of the creation operators [45, 87, 299, 383], i.e.

$$:\hat{a}\hat{a}^\dagger: = \hat{a}^\dagger\hat{a}, \quad :\hat{a}^\dagger\hat{a}: = \hat{a}^\dagger\hat{a}, \quad :\hat{a}\hat{a}\hat{a}^\dagger\hat{a}\hat{a}^\dagger\hat{a}^\dagger: = \hat{a}^\dagger\hat{a}^\dagger\hat{a}^\dagger\hat{a}\hat{a}\hat{a} \quad \text{etc.} \tag{2.4.22}$$

If we take the Hamiltonian energy density operator (2.4.20a) and apply normal ordering, we have

$$:\widehat{H}: = \int_{\mathcal{M}} \mathrm{d}^{n-1}\boldsymbol{x} :\widehat{T}^{\mathbb{M}}_{tt}: = \frac{1}{2}\sum_{\mathbf{k}} \left[:\hat{a}^\dagger(\mathbf{k})\hat{a}(\mathbf{k}): + :\hat{a}(\mathbf{k})\hat{a}^\dagger(\mathbf{k}):\right]\omega, \tag{2.4.23}$$

which, after correctly arranging the annihilation and creation operators, reduces to

$$:\widehat{H}: = \sum_{\mathbf{k}} \left[\hat{a}^\dagger(\mathbf{k})\hat{a}(\mathbf{k})\right]\omega. \tag{2.4.24}$$

If we now take the vacuum expectation value, due to the normal ordering this is now zero:

$$\langle 0|:\widehat{H}:|0\rangle = \langle 0|\sum_{\mathbf{k}} \left[\hat{a}^\dagger(\mathbf{k})\hat{a}(\mathbf{k})\right]\omega|0\rangle = 0, \tag{2.4.25}$$

which is, in essence, the renormalisation procedure we heuristically introduced above. In fact, the vacuum expectation value of *any* normal-ordered operator is, by definition, zero:

$$\langle 0|:\widehat{\mathscr{Q}}:|0\rangle = 0, \tag{2.4.26}$$

where the operator $\widehat{\mathscr{Q}}$ may be scalar-, vector- or tensor-valued. In particular, the vacuum expectation value of the normal-ordered, flat space-time stress-energy tensor (2.4.19) is also zero

$$\langle 0|:\widehat{T}^{\mathbb{M}}_{\mu\nu}:|0\rangle = 0. \tag{2.4.27}$$

Normal ordering is not unique to the vacuum state $|0\rangle$. Indeed, one can take expectation values of normal ordered operators in any state $|\psi\rangle$; they are finite but not necessarily zero.

## § 2.5 Flat space-time expectation values and Green functions

In sections 1.1 and 2.4, it was argued that we can uniquely specify a quantum field theory by constructing a suitable Green function; this is the Wightman reconstruction theorem [343, 384, 385]. In this section we first derive the explicit form of the Hadamard Green function using two different methods, before relating this to the other Green functions of interest.

The Hadamard Green function is defined as either the vacuum expectation value of the anti-commutator of a scalar field (at two distinct, but geodesically connected points), or as a solution to the homogeneous Klein-Gordon equation (2.4.3) (with certain boundary conditions applied). We will start by deriving the Hadamard Green function as the vacuum expectation value of the anti-commutator of the scalar field, before deriving it by exploiting maximal symmetry of flat space in conjunction with Klein-Gordon equation. The Hadamard Green function derived in the vacuum will henceforth be known as the *vacuum Hadamard Green function*, since each Hadamard Green function is unique for the state it is calculated in. Recall the mode-sum expansion of the scalar field (2.4.16). In the following analysis we will collapse the scalar products and write the fields using four-vector notation, so

$$x = (t, \boldsymbol{x}), \quad \text{and} \quad k = (\omega(\mathbf{k}), \mathbf{k}), \tag{2.5.1}$$

and

$$x \cdot k = -t\omega + \boldsymbol{x} \cdot \mathbf{k}. \tag{2.5.2}$$

We also drop the explicit functional dependence of the creation and annihilation operators, and denote the ones for the field at different points by primes, i.e.

$$\hat{a}(\mathbf{k}) \to \hat{a}_{\mathbf{k}}, \quad \hat{a}(\mathbf{k}') \to \hat{a}_{\mathbf{k}'}. \tag{2.5.3}$$

The vacuum Hadamard Green function is defined as the vacuum expectation value of the

anti-commutator of the scalar field:

$$G^{(1)}(x,x') = \langle 0|\{\widehat{\Phi}(x)\widehat{\Phi}(x')\}|0\rangle = \langle 0|\widehat{\Phi}(x)\widehat{\Phi}(x')|0\rangle + \langle 0|\widehat{\Phi}(x')\widehat{\Phi}(x)|0\rangle. \tag{2.5.4}$$

Since the roles of the space-time coordinates $x$ and $x'$ are the same (up to an interchange of the prime), we can calculate one of the expectation values above and easily generalise to the other. Recall that the scalar field decomposition (2.4.16) is written in terms of annihilation $\hat{a}$ and creation $\hat{a}^\dagger$ operators, which act on the vacuum state $|0\rangle$ as

$$\langle 0|\hat{a}^\dagger_{\mathbf{k}} = 0, \qquad \hat{a}_{\mathbf{k}}|0\rangle = 0. \tag{2.5.5}$$

Taking the expectation value of the product $\widehat{\Phi}(x)\widehat{\Phi}(x')$, we have

$$\begin{aligned}\langle 0|\widehat{\Phi}(x)\widehat{\Phi}(x')|0\rangle &= \int\int \frac{\mathrm{d}^{n-1}\mathbf{k}\,\mathrm{d}^{n-1}\mathbf{k}'}{2(2\pi)^{n-1}\sqrt{\omega\omega'}}\left[\langle 0|\hat{a}_{\mathbf{k}}e^{ik\cdot x}\hat{a}^\dagger_{\mathbf{k}'}e^{-ik'\cdot x'}|0\rangle\right], \\ &= \int\int \frac{\mathrm{d}^{n-1}\mathbf{k}\,\mathrm{d}^{n-1}\mathbf{k}'}{2(2\pi)^{n-1}\sqrt{\omega\omega'}}\langle 0|\hat{a}_{\mathbf{k}}\hat{a}^\dagger_{\mathbf{k}'}|0\rangle e^{i(k\cdot x - k'\cdot x')}.\end{aligned} \tag{2.5.6}$$

Using the canonical commutation relations (2.4.17) and the fact that

$$\langle 0|\hat{a}^\dagger_{\mathbf{k}'}\hat{a}_{\mathbf{k}}|0\rangle = 0, \tag{2.5.7}$$

we can deduce that

$$\langle 0|\hat{a}_{\mathbf{k}}\hat{a}^\dagger_{\mathbf{k}'}|0\rangle = \delta^{(n-1)}(\mathbf{k}-\mathbf{k}'), \tag{2.5.8}$$

where we have additionally used the fact that the vacuum state is normalised, i.e.

$$\langle 0|0\rangle = 1. \tag{2.5.9}$$

Returning to the expectation value (2.5.6), using the result (2.5.8), we can write it as

$$\langle 0|\widehat{\Phi}(x)\widehat{\Phi}(x')|0\rangle = \int\int \frac{\mathrm{d}^{n-1}\mathbf{k}\,\mathrm{d}^{n-1}\mathbf{k}'}{2(2\pi)^{n-1}\sqrt{\omega\omega'}}\delta^{(n-1)}(\mathbf{k}-\mathbf{k}')e^{i(k\cdot x - k'\cdot x')}, \tag{2.5.10}$$

and after integrating the $\mathbf{k}'$ integral using the delta function, we have

$$\langle 0|\widehat{\Phi}(x)\widehat{\Phi}(x')|0\rangle = \int \frac{\mathrm{d}^{n-1}\mathbf{k}}{2\omega(2\pi)^{n-1}}e^{ik\cdot(x-x')}. \tag{2.5.11}$$

In a similar fashion, the expectation value $\langle 0|\widehat{\Phi}(x')\widehat{\Phi}(x)|0\rangle$ is found to be

$$\langle 0|\widehat{\Phi}(x')\widehat{\Phi}(x)|0\rangle = \int \frac{\mathrm{d}^{n-1}\mathbf{k}}{2\omega(2\pi)^{n-1}} e^{-ik\cdot(x-x')}. \tag{2.5.12}$$

Combining the expectation values (2.5.11) and (2.5.12), we find the momentum space integral representation of the vacuum Hadamard Green function to be

$$G^{(1)}(x,x') = \langle 0|\{\widehat{\Phi}(x)\widehat{\Phi}(x')\}|0\rangle = \int \frac{\mathrm{d}^{n-1}\mathbf{k}}{2\omega(2\pi)^{n-1}} \left[e^{ik\cdot(x-x')} + e^{-ik\cdot(x-x')}\right]. \tag{2.5.13}$$

We have therefore constructed the Hadamard Green function using the explicit mode-sum expansions of the fields. We next construct this using a different, but equally as valid, method.

The Hadamard Green function is a solution to the homogeneous wave equation, which in our case is the flat space Klein-Gordon equation (2.4.3):

$$\left(-\partial_\mu\partial^\mu + m^2\right) G^{(1)}(x,x') = 0. \tag{2.5.14}$$

Since Minkowski space exhibits Poincaré invariance (and in particular there exists a unique Poincaré invariant vacuum state), we can make an ansatz that the vacuum Hadamard Green function depends only on the biscalar quantity[11] $\sigma(x,x')$, defined by

$$\sigma(x,x') = \frac{1}{2}\eta_{\mu\nu}(x-x')^\mu(x-x')^\nu, \tag{2.5.15}$$

and thus write

$$G^{(1)}(x,x') = f(\sigma). \tag{2.5.16}$$

Using the chain rule, we can write the coordinate derivatives as derivatives in $\sigma$, by noting that

$$\partial_\mu f(\sigma) = f'(\sigma)(x-x')_\mu, \qquad \partial^\mu\partial_\mu f(\sigma) = 2\sigma f''(\sigma) + nf'(\sigma), \tag{2.5.17}$$

where a prime (on anything but the coordinate $x$) denotes differentiation with respect to $\sigma$. Substituting into the Klein-Gordon equation (2.5.14), we have

$$2\sigma f''(\sigma) + nf'(\sigma) - m^2 f(\sigma) = 0. \tag{2.5.18}$$

[11] This is known as *Synge's world function*, and will be introduced in more detail in section 2.7.

Next, we make a coordinate transformation to the *proper distance*, $s(x, x')$, given by

$$\sigma(x, x') = \frac{1}{2} s(x, x')^2, \tag{2.5.19}$$

so that the differential equation (2.5.18) reads

$$\frac{\mathrm{d}^2 f}{\mathrm{d}s^2} + \frac{n-1}{s}\frac{\mathrm{d}f}{\mathrm{d}s} - m^2 f = 0. \tag{2.5.20}$$

Identifying with the standard modified Bessel equation [280], we find the general solution to be a linear combination of modified Bessel functions of the first ($I_\upsilon$) and second kind ($K_\upsilon$):

$$f(s) = \mathfrak{G}_1 (ms)^{-\upsilon} I_\upsilon(ms) + \mathfrak{G}_2 (ms)^{-\upsilon} K_\upsilon(ms), \tag{2.5.21}$$

where $\upsilon = (n-2)/2$, and $\mathfrak{G}_i$ are constants to be determined. We next examine the behaviour at large space-like separation (corresponding to $s \to \infty$), where the modified Bessel functions have asymptotic behaviour [280]

$$I_\upsilon(ms) \sim \frac{e^{ms}}{\sqrt{2\pi ms}}, \qquad K_\upsilon(ms) \sim \sqrt{\frac{\pi}{2ms}} e^{-ms}. \tag{2.5.22}$$

The *cluster decomposition principle* [343, 382] states that vacuum fluctuations at two points (space-like) separated by a huge distance should be uncorrelated, or, in other words, as $s \to \infty$, the Hadamard Green function $G^{(1)}$ must vanish. This fixes the constant $\mathfrak{G}_1 \equiv 0$ in the solution (2.5.21), since, the modified Bessel function of the first kind is exponentially growing in the limit $s \to \infty$ whilst the modified Bessel function of the second kind is exponentially decaying in the same limit.

The other constant is fixed by using one of two ways. Either, one could take the momentum integral form of the Hadamard Green function (2.5.13) and use the *Schwinger proper time method* [331], which essentially replaces the $\omega = \sqrt{|\mathbf{k}|^2 + m^2}$ factors with Gaussian integrals of the form [280, 331]

$$\frac{1}{A} = \frac{1}{\sqrt{\pi}} \int_0^\infty \frac{\mathrm{d}p}{\sqrt{p}} e^{-pA^2}, \tag{2.5.23}$$

explicitly evaluates the integral over $\mathbf{k}$ and then compares the resulting integral with the integral form of the modified Bessel function of the second kind [280]

$$K_\upsilon(z) = \frac{1}{2}\left(\frac{z}{2}\right)^\upsilon \int_0^\infty \mathrm{d}p\, p^{-\upsilon-1} e^{-\left(p+\frac{z^2}{4p}\right)}, \tag{2.5.24}$$

in order to match the constants. This method is rather common in QFT-based approaches, for example in [45]. However, this relies on using the momentum-space integral form of the Hadamard Green function. The second method, one which is independent of the momentum-space integral form of the Hadamard Green function, relies on standard techniques for dealing with Green functions and is a standard differential equations technique; it is somewhat independent of QFT. Essentially, one takes the Hadamard Green function (2.5.21) (with $\mathfrak{G}_1 = 0$) and substitutes this back into the Klein-Gordon equation (2.5.14). One would then assume that the Laplacian term $\partial_\mu \partial^\mu$ dominates, before treating the resulting equation

$$\partial_\mu \partial^\mu f(s) = 0, \tag{2.5.25}$$

as a Poisson equation and applying Gauss' law to solve it as if it were a point source differential equation. Standard PDE textbooks detail this approach, for example [35, 133].

The upshot is that the constant $\mathfrak{G}_2$ is given by [45, 103]

$$\mathfrak{G}_2 = \frac{m^{n-2}}{(2\pi)^{n/2}} \tag{2.5.26}$$

and thus, the Hadamard Green function is given in terms of the modified Bessel function of the second kind as

$$G^{(1)}(x,x') = \frac{1}{(2\pi)^{n/2}} \left(\frac{m}{\sqrt{2\sigma(x,x')}}\right)^{(n-2)/2} K_{\frac{n-2}{2}}\left(m\sqrt{2\sigma(x,x')}\right). \tag{2.5.27}$$

An important case of the Hadamard Green function is the massless limit. The asymptotics of the Bessel function for small arguments are [280]

$$K_\upsilon(z) \sim \frac{\Gamma(\upsilon)}{2}\left(\frac{2}{z}\right)^\upsilon, \quad |z| \to 0 \tag{2.5.28}$$

This is only valid for $\upsilon > 0$; the Hadamard Green function (2.5.27) has $\upsilon = (n-2)/2$, which implies that $n > 2$. For $\upsilon = 0$ ($n = 2$), the Bessel function behaves logarithmically, and the Hadamard Green function (2.5.27) continues to grow as the space-like separation of its two points increases, violating the cluster decomposition principle [86, 343, 382]. This is known as an *infrared divergence*, and means that massless particles in (1+1)-dimensions cannot exist [86]. The following analysis of the Hadamard Green function in the massless limit is therefore valid only for $n > 2$.

Expanding the Hadamard Green function (2.5.27), using the asymptotic behaviour of the Bessel function (2.5.28), for $m \to 0$ we have

$$G^{(1)}(x,x') \sim \frac{1}{(2\pi)^{n/2}} \left( \frac{m}{\sqrt{2\sigma(x,x')}} \right)^{(n-2)/2} \frac{\Gamma(\frac{n-2}{2})}{2} \left( \frac{2}{m\sqrt{2\sigma(x,x')}} \right)^{(n-2)/2}, \tag{2.5.29}$$

and, after simplifying factors, we have the massless Hadamard Green function [106, 220, 305]

$$G^{(1)}(x,x') = \frac{\Gamma(\frac{n-2}{2})}{2(2\pi)^{n/2}} \frac{1}{\sigma(x,x')^{(n-2)/2}}. \tag{2.5.30}$$

We now therefore have the form of the Hadamard Green function in terms of either the biscalar $\sigma$ or as a momentum space integral (2.5.13) (see also equation (2.5.39)) - both are valid and are useful in different contexts.

Once we have the Hadamard Green function, it is straightforward to reconstruct the other (quantum field theory) Green functions of note. For example, in the decomposition (2.5.4), after the second equals sign the left expectation value is known as the *positive frequency Wightman Green function* and the right expectation value is the *negative frequency Wightman Green function*, i.e.

$$G^{+}(x,x') = \langle 0|\widehat{\Phi}(x)\widehat{\Phi}(x')|0\rangle, \qquad \text{positive frequency Wightman Green function,} \tag{2.5.31a}$$

$$G^{-}(x,x') = \langle 0|\widehat{\Phi}(x')\widehat{\Phi}(x)|0\rangle, \qquad \text{negative frequency Wightman Green function.} \tag{2.5.31b}$$

These can be used to construct the *Pauli-Jordan* (known also as *Schwinger*) Green function, which is the vacuum expectation value of the commutator of two fields, as

$$iG(x,x') = \langle 0|[\widehat{\Phi}(x), \widehat{\Phi}(x')]|0\rangle = G^{+}(x,x') - G^{-}(x,x'), \tag{2.5.32}$$

and the Hadamard Green function can be stated explicitly using the Wightman functions as

$$G^{(1)}(x,x') = G^{+}(x,x') + G^{-}(x,x'). \tag{2.5.33}$$

The *Feynman propagator* can likewise be defined as

$$G_F(x,x') = \langle 0|\mathcal{T}(\widehat{\Phi}(x)\widehat{\Phi}(x'))|0\rangle, \tag{2.5.34a}$$

where the operator $\mathcal{T}$ indicates that the fields are time-ordered, i.e. if the fields have time coordinates $t$ and $t'$ respectively, then

$$\mathcal{T}(\widehat{\Phi}(x), \widehat{\Phi}(x')) = \begin{cases} \widehat{\Phi}(x)\widehat{\Phi}(x'), & \text{if} \quad t > t', \\ \widehat{\Phi}(x')\widehat{\Phi}(x), & \text{if} \quad t' > t. \end{cases} \tag{2.5.34b}$$

The Feynman propagator can be written in terms of the positive and negative frequency Wightman functions as

$$G_F(x,x') = \Theta(t-t')G^{+}(x,x') + \Theta(t'-t)G^{-}(x,x'), \tag{2.5.34c}$$

where $\Theta$ is the Heaviside function, defined as

$$\Theta(t-t') = \begin{cases} 1, & t > t', \\ 0, & t' > t. \end{cases} \tag{2.5.34d}$$

In the temporal coincidence limit, i.e. when $t = t'$, time ordering is not possible and we define (by convention) [45, 377]

$$G_F(x,x')|_{t'=t} = G^{+}(x,x'). \tag{2.5.34e}$$

There are two final Green functions of interest, which are constructed with respect to the Pauli-Jordan Green function as

$$G_R(x,x') = -\,\Theta(t-t')G(x,x'), \tag{2.5.35a}$$

$$G_A(x,x') = \Theta(t'-t)G(x,x'). \tag{2.5.35b}$$

These are known as the *retarded* and *advanced* Green functions, respectively. Their average,

$$\overline{G}(x,x') = \frac{1}{2}\left[G_R(x,x') + G_A(x,x')\right], \tag{2.5.36}$$

can be used to express the Feynman Green function as

$$G_F(x,x') = -\overline{G}(x,x') - \frac{1}{2}iG^{(1)}(x,x'). \tag{2.5.37}$$

Whilst we have constructed the Green functions on flat space-time using the Minkowski vacuum state $|0\rangle$, it is straightforward to generalise the Green functions to curved space-times - see section 2.7.

One may expect, based on the fact we have named the other Green functions *Green functions*, that they satisfy the inhomogeneous wave equation, as is the (mathematical) definition of Green functions [172, 173]. However, a peculiarity of some quantum field theory Green functions (such as the Hadamard Green function) is that they are, by definition, *not* Green functions, since they solve the *homogeneous* wave equation. Of the other QFT-Green functions introduced in this section, the Pauli-Jordon and Wightman Green functions satisfy the homogeneous wave equation, i.e.

$$\left(-\partial_\mu\partial^\mu + m^2\right)\mathscr{G}(x,x') = 0, \tag{2.5.38a}$$

where $\mathscr{G} = \{G, G^{(1)}, G^{\pm}\}$. The remaining Green functions satisfy an inhomogeneous wave equation,

$$\left(-\partial_\mu\partial^\mu + m^2\right)G_F(x,x') = -\delta^n(x-x'), \tag{2.5.38b}$$

$$\left(-\partial_\mu\partial^\mu + m^2\right)G_{R/A}(x,x') = \delta^n(x-x'). \tag{2.5.38c}$$

Owing to the presence of a Dirac-delta source term, the Feynman, advanced and retarded Green functions describe the propagation of field disturbances under certain boundary conditions.

Just as the Hadamard Green function (2.5.13) has a momentum space integral representation (by expressing the fields in terms of their mode-sum expansions), so too do the other Green functions. In fact, every Green function considered in this section can be represented as [45]

$$\mathscr{G}(x,x') = \frac{1}{(2\pi)^n}\int \mathrm{d}^n k \frac{e^{-ik\cdot x}}{-\omega^2 + |\mathbf{k}|^2 + m^2}, \tag{2.5.39}$$

where $|\mathbf{k}|^2 = (k^1)^2 + (k^2)^2 + \cdots + (k^{n-1})^2$. The integral (2.5.39) has poles at $\omega = \pm\sqrt{|\mathbf{k}|^2 + m^2}$, and can be performed as a contour integral in $\omega$ by deforming the contour around the poles. The way in which the contour is deformed specifies which of the various Green functions is obtained. Figure 2.2 shows the various choices of contour and their resulting Green function. For example, by choosing the "figure-8" contour (red contour in the second figure of figure 2.2) and performing the integral in $\omega$, the Hadamard Green function (2.5.13) is recovered.

Whilst the Green functions have been constructed in the Minkowski vacuum, it is possible to construct them in any quantum state. The Minkowski vacuum, and the resulting Green functions, describe a system at zero temperature. For systems with nonzero temperature, we thus need a different quantum state and resulting Green functions. Whilst the Minkowski vacuum is a pure state, a state with nonzero temperature cannot be described by a pure state, but rather one that is statistically distributed across all pure states. Suppose we have a state that is at constant inverse temperature $\beta = 1/T$, with $T$ being the local temperature. The corresponding Green functions are then defined as the average (across all pure states) of the expectation value of the product of field operators in the pure states [1, 45, 113, 136, 215, 216, 251, 294, 299]. In short, we can replace the vacuum state with a grand canonical ensemble of states and define the thermal Green functions by replacing the vacuum expectation value (of the Green functions) with the ensemble average

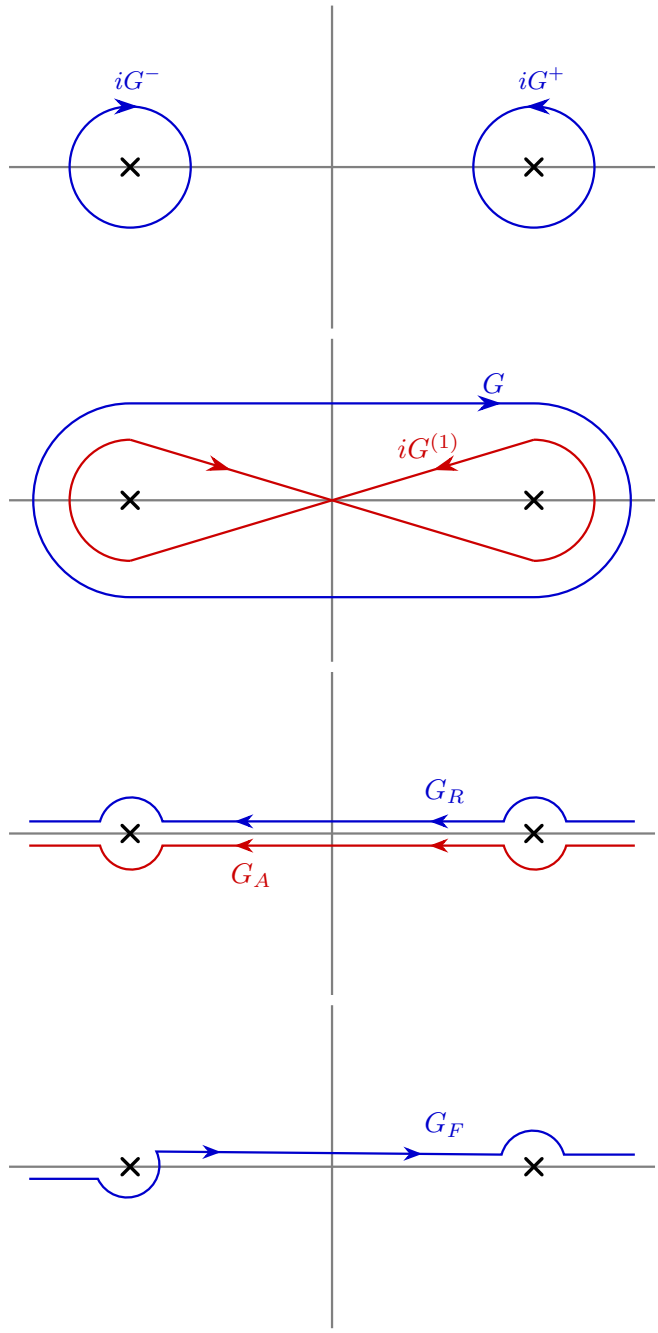


Figure 2.2: Examples of the possible deformed contours in the complex $\omega$ plane for the integral (2.5.39). Each is associated with a different Green function; the top gives the Wightman functions; the second gives the Pauli-Jordan (blue) and Hadamard (red) Green functions; the third gives the retarded (blue) and advanced (red) Green functions; and the bottom gives the Feynman Green function. The poles, represented by the crosses, are at the points $\omega = \pm\sqrt{|\mathbf{k}|^2 + m^2}$, and are located on the real line. Figures adapted from [45].

$\langle\cdot\rangle_\beta$. For example, the Wightman functions (2.5.31) in a thermal state are defined as

$$G^+_\beta(x,x') = \langle\widehat{\Phi}(x)\widehat{\Phi}(x')\rangle_\beta, \tag{2.5.40a}$$

$$G^-_\beta(x,x') = \langle\widehat{\Phi}(x')\widehat{\Phi}(x)\rangle_\beta, \tag{2.5.40b}$$

and satisfy the periodicity property [45]

$$G^\pm_\beta(t,\boldsymbol{x};t',\boldsymbol{x}') = G^\mp_\beta(t+i\beta,\boldsymbol{x};t',\boldsymbol{x}'). \tag{2.5.41}$$

Recall the definition of the Hadamard Green function (2.5.33). Swapping the vacuum expectation value with the ensemble average yields the corresponding thermal Hadamard Green function. If we then impose a shift by $i\beta$ in the time coordinate and expand this in terms of the Wightman functions, we have

$$G^{(1)}_\beta(t+i\beta,\boldsymbol{x};t',\boldsymbol{x}') = G^+_\beta(t+i\beta,\boldsymbol{x};t',\boldsymbol{x}') + G^-_\beta(t+i\beta,\boldsymbol{x};t',\boldsymbol{x}'), \tag{2.5.42}$$

and then inverting the periodicity condition (2.5.41) yields

$$G^{(1)}_\beta(t+i\beta,\boldsymbol{x};t',\boldsymbol{x}') = G^-_\beta(x,x') + G^+_\beta(x,x') = G^{(1)}_\beta(x,x'). \tag{2.5.43}$$

Therefore, the thermal Hadamard Green function is *also* periodic in the time coordinate with period $i\beta$. This fact is exploited heavily when constructing the thermal expectation value of the stress-energy tensor on anti-de Sitter space; see chapter 5.

It is possible to find functional or integral representations of Green functions in the ensemble state $\langle\cdot\rangle_\beta$, and some are simpler than others. For example, take the Pauli-Jordan Green function (2.5.32). The Pauli-Jordan Green function is the expectation value of the commutator, which gives the expectation value of a real or complex number and not an operator. The expectation value of a number is the number itself, since there are no operators acting on the state. Adopting the nomenclature of Dirac [113], we refer to these as *c-numbers* (classical or commuting numbers), they are defined to be deterministic quantities that do *not* fluctuate, and thus their expectation values are state-independent [113, 216, 294, 299].

Using the fact that the commutator is a c-number, it follows that the thermal and vacuum Pauli-Jordan Green functions are equal, i.e.

$$iG_\beta(x,x') = iG(x,x') = [\widehat{\Phi}(x), \widehat{\Phi}(x')], \tag{2.5.44}$$

where, by virtue of their being c-numbers, we have expressed both as just the commutator and dropped the state dependence[12]. We can express the Pauli-Jordan Green function in integral form by writing its Fourier transform as [45]

$$iG_\beta(x,x') = \frac{1}{2\pi}\int_{-\infty}^{\infty} \mathrm{d}\omega\, c(\omega) e^{-i\omega(t-t')} \tag{2.5.45}$$

where $c(\omega)$[13] is the momentum space integral form of the Green functions (2.5.39), evaluated on an appropriate contour (see figure 2.2). In the literature, this is often referred to as the *spectral function*; we adopt this terminology. For the following analysis, we do not require the explicit form of the spectral function, but we assume that it is an odd function in $\omega$ [45]. In a similar fashion, we can write the Fourier transform of the Wightman functions (2.5.31) in terms of spectral functions $g^\pm$ as

$$G^\pm_\beta(x,x') = \frac{1}{2\pi}\int_{-\infty}^{\infty} \mathrm{d}\omega\, g^\pm(\omega) e^{-i\omega(t-t')}. \tag{2.5.46}$$

Using the definition of the Pauli-Jordan Green function (2.5.32) in terms of the Wightman functions, and writing these in terms of their Fourier transforms, we have

$$\frac{1}{2\pi}\int_{-\infty}^{\infty} \mathrm{d}\omega\, c(\omega) e^{-i\omega(t-t')} = \frac{1}{2\pi}\int_{-\infty}^{\infty} \mathrm{d}\omega\, g^+(\omega) e^{-i\omega(t-t')} - \frac{1}{2\pi}\int_{-\infty}^{\infty} \mathrm{d}\omega\, g^-(\omega) e^{-i\omega(t-t')}, \tag{2.5.47}$$

from which it follows

$$c(\omega) = g^+(\omega) - g^-(\omega). \tag{2.5.48}$$

[12] We cannot do this in general; the commutator is not always a c-number. For example, for the case of interacting scalar fields, the commutator is a *q-number* [299].

[13] Here, $c(\omega)$ should technically be $c(\omega; \boldsymbol{x}, \boldsymbol{x}')$ to reflect its dependence on the space-time points $\boldsymbol{x}$ and $\boldsymbol{x}'$. However, for brevity we drop this dependence; this also applies to the functions $g^\pm(\omega)$.

Now recall the periodicity property of the thermal Wightman functions (2.5.41). Writing this in terms of the Fourier transforms yields

$$\begin{aligned} G^{-}(t+i\beta,\boldsymbol{x};t',\boldsymbol{x}') &= \frac{1}{2\pi}\int_{-\infty}^{\infty} \mathrm{d}\omega\, g^{-}(\omega) e^{-i\omega(t+i\beta-t')} \\ &= \frac{1}{2\pi}\int_{-\infty}^{\infty} \mathrm{d}\omega\, g^{-}(\omega) e^{\beta\omega} e^{-i\omega(t-t')}, \end{aligned} \tag{2.5.49}$$

from which we acquire the relation

$$g^{+}(\omega) = e^{\beta\omega} g^{-}(\omega), \tag{2.5.50}$$

between the spectral functions of the positive and negative frequency, thermal Wightman functions. Combining this with the relation (2.5.48), after a little algebraic manipulation we can express the Wightman spectral functions in terms of the Pauli-Jordan spectral function as

$$g^{\pm}(\omega) = \pm c(\omega)\left[1 - e^{\mp\beta\omega}\right]^{-1}. \tag{2.5.51}$$

Substituting these back into the Fourier transform of the thermal Wightman functions (2.5.46), we can express both the positive and negative frequency variants in terms of the Pauli-Jordan spectral function as

$$G^{\pm}_{\beta}(x,x') = \pm\frac{1}{2\pi}\int_{-\infty}^{\infty} \mathrm{d}\omega\, \frac{c(\omega)}{1-e^{\mp\beta\omega}} e^{-i\omega(t-t')}. \tag{2.5.52}$$

From these integral forms it is possible to construct integral forms of the other thermal Green functions. In part II of this thesis, we exclusively use the thermal Hadamard Green function on anti-de Sitter space. Therefore, we will just derive the explicit integral form of the thermal Hadamard Green function. The thermal Hadamard Green function, using the definition (2.5.33) in terms of the Wightman functions, can be expressed neatly as the sum of the thermal Wightman functions, i.e.

$$G^{(1)}_{\beta}(x,x') = G^{+}_{\beta}(x,x') + G^{-}_{\beta}(x,x'). \tag{2.5.53}$$

Using the Fourier transforms of the thermal Wightman functions (2.5.46), we can express the thermal Hadamard Green function as

$$\begin{aligned} G_\beta^{(1)}(x,x') &= \frac{1}{2\pi}\int_{-\infty}^{\infty} \mathrm{d}\omega\, c(\omega) e^{-i\omega(t-t')}\left[\frac{1}{1-e^{-\beta\omega}} - \frac{1}{1-e^{\beta\omega}}\right] \\ &= \frac{1}{2\pi}\int_{-\infty}^{\infty} \mathrm{d}\omega\, c(\omega) e^{-i\omega(t-t')} \coth\left(\tfrac{1}{2}\beta\omega\right). \end{aligned} \tag{2.5.54}$$

We can express the hyperbolic cotangent as an infinite sum (where we use the Heaviside function to combine the negative and positive frequency and summation index terms) as

$$\begin{aligned} \coth\left(\tfrac{1}{2}\beta\omega\right) &= \left[\Theta(\omega) - \Theta(-\omega)\right] \sum_{j=-\infty}^{\infty} e^{-|j|\beta|\omega|} \\ &= \left[\Theta(\omega) - \Theta(-\omega)\right] + 2\left[\Theta(\omega) - \Theta(-\omega)\right] \sum_{j=1}^{\infty} e^{-j\beta|\omega|}. \end{aligned} \tag{2.5.55}$$

Substituting this back into the thermal Hadamard function (2.5.54), we have

$$G_\beta^{(1)}(x,x') = \frac{1}{2\pi}\int_{-\infty}^{\infty} \mathrm{d}\omega\, c(\omega) e^{-i\omega(t-t')} \left[\Theta(\omega) - \Theta(-\omega)\right] \sum_{j=-\infty}^{\infty} e^{-|j|\beta|\omega|}. \tag{2.5.56}$$

It is straightforward to recover the vacuum Hadamard Green function in similar notation, by taking the limit as $\beta \to \infty$ of the thermal Hadamard function (2.5.56):

$$\begin{aligned} G^{(1)}(x,x') &= \lim_{\beta\to\infty} G_\beta^{(1)}(x,x') \\ &= \frac{1}{2\pi}\lim_{\beta\to\infty}\int_{-\infty}^{\infty} \mathrm{d}\omega\, c(\omega) e^{-i\omega(t-t')} \coth\left(\tfrac{1}{2}\beta\omega\right) \\ &= \frac{1}{2\pi}\int_{-\infty}^{\infty} \mathrm{d}\omega\, c(\omega) e^{-i\omega(t-t')} \left[\Theta(\omega) - \Theta(-\omega)\right], \end{aligned} \tag{2.5.57}$$

where, in the last line, we have expanded the hyperbolic cotangent according to the second line of the expansion (2.5.55). The appearance of the Heaviside functions allude to the fact that the integral will depend on whether we have a positive $\omega > 0$ or negative $\omega < 0$ frequency. Returning to the thermal Hadamard function (2.5.56), we assume we can pull the summation in front of the integral, and combine the time-step $(t - t')$ and frequency

shift ($|j|\beta|\omega|$) exponents. This yields

$$\begin{aligned} G^{(1)}_{\beta}(x,x') &= \sum_{j=-\infty}^{\infty} \frac{1}{2\pi} \int_{-\infty}^{\infty} \mathrm{d}\omega\, c(\omega) e^{-i\omega(t-t')-|j|\beta|\omega|} \left[\Theta(\omega) - \Theta(-\omega)\right] \\ &= \sum_{j=-\infty}^{\infty} G^{(1)}(t - ij\beta, \boldsymbol{x}; t', \boldsymbol{x}'), \end{aligned} \tag{2.5.58}$$

where to achieve the second equality: the method of images [157, 379] is used to analytically extend the frequency $|\omega|$ to both its positive and negative domains; to similarly extend the summation index across positive and negative integers we use the same method; and we have compared the resulting expression to the corresponding vacuum function (2.5.57). Finally, since the sum over $j$ is across *all* integers positive and negative, we can flip the sign of the summation index without loss of generality to arrive at the standard *Matsubara sum* [45, 115, 157, 379]

$$G^{(1)}_{\beta}(x,x') = \sum_{j=-\infty}^{\infty} G^{(1)}(t + ij\beta, \boldsymbol{x}; t', \boldsymbol{x}'). \tag{2.5.59}$$

This is a very powerful object; once we have an explicit form of the vacuum Hadamard Green function, we can perform an infinite sum in the shifted imaginary time direction to find a corresponding form for the thermal Hadamard Green function. This is used extensively in part II of this thesis.

## § 2.6 Quantum field theory on curved space-times

Having (briefly) detailed the canonical quantisation procedure for scalar fields in flat space in section 2.4.1, we now proceed to consider the canonical quantisation procedure of scalar fields on a general curved space. It is worth mentioning that, in this thesis, we do not work with canonical quantisation and instead focus purely on the Green function approach, as outlined for fields in flat space in section 2.5; we detail the curved space Green function approach in detail in section 2.7. Rather, this section will be a schematic overview of the

canonical quantisation procedure for fields in curved space-time; we refer the reader to the numerous textbooks and articles on the subject, for example, amongst others, [45, 157, 271, 293, 374].

To quantise fields on a general curved space-time, we follow a similar procedure to the quantisation of scalar fields on flat space-time, the starting point of which is finding the field equation of motion. For a general curved space-time, this was already derived in section 2.2.3, in particular equation (2.2.55). For completeness, this is included below:

$$\left(-\Box_g + m^2 + \xi R\right)\Phi = 0, \tag{2.6.1}$$

where the box operator $\Box_g$, known as the curved space Laplacian or d'Alembertian, is given by

$$\Box_g = \nabla_\mu \nabla^\mu = g^{\mu\nu}\left(\partial_\mu \partial_\nu - \Gamma^\lambda_{\mu\nu}\partial_\lambda\right). \tag{2.6.2}$$

The Christoffel symbols $\Gamma^\lambda_{\mu\nu}$ (2.1.9) were previously defined in section 2.1. After fixing the field equation, we can then find mode solutions and follow the general canonical quantisation procedure. This is detailed next.

### 2.6.1 Canonical quantisation

The starting point for the schematic canonical quantisation procedure in general curved spaces is to generalise the flat space Klein-Gordon inner product (2.4.5). We do this by upgrading the coordinate derivative to the covariant connection[14] and altering the domain of integration. We can therefore define the curved space Klein-Gordon inner product as

$$\langle \Phi_1, \Phi_2 \rangle = -i \int_\Sigma \Phi_1 \overleftrightarrow{\nabla}_\mu \Phi_2^* \sqrt{-g}\; n^\mu \, \mathrm{d}\Sigma, \tag{2.6.3}$$

where the operator $\overleftrightarrow{\nabla}$ is defined by

$$\Phi_1 \overleftrightarrow{\nabla}_\mu \Phi_2^* := \Phi_1 \overleftrightarrow{\nabla}_\mu \Phi_2^* - \Phi_2^* \overleftrightarrow{\nabla}_\mu \Phi_1. \tag{2.6.4}$$

[14] Although, since we are only considering scalar fields, we need not impose this.

The domain of integration is now a non-compact, space-like Cauchy surface $\Sigma$ with unit normal $n^\mu$, *provided we have global hyperbolicity.* Global hyperbolicity is a key requirement for quantised fields to be well-defined; as we will see later (see chapter 4; in particular sections 4.2 and 4.5), anti-de Sitter space is *not* globally hyperbolic and hence constructing a QFT has added complications, though these can be sidestepped. It can be shown that the Klein-Gordon inner product (2.6.3) is independent of the choice of Cauchy surface, provided we have global hyperbolicity [190, 373]. Without global hyperbolicity, the inner product can still be well-defined and independent of the choice of space-like hypersurface[15] [205]; for example, in anti-de Sitter space, this is achieved by applying suitable boundary conditions to the field [31] (see section 4.5).

With a well-defined inner product, the next step in the canonical quantisation procedure is to find mode solutions to the Klein-Gordon equation (2.6.1) in curved space-times. Assuming that there is an orthonormal basis of modes, we expand the field in terms of the annihilation and creation operators as

$$\widehat{\Phi}(\boldsymbol{x}, t) = \sum_i \left[\hat{a}_i f_i(\boldsymbol{x}, t) + \hat{a}_i^\dagger f_i^*(\boldsymbol{x}, t)\right], \tag{2.6.5}$$

where the intermediate steps (i.e. promoting the field to an operator valued distribution and imposing equal-time commutation relations) are skipped for brevity but still hold. A minor difference to the analysis in the flat space-time case is that we now use the index $i$ to label the modes, instead of explicitly expanding into the frequency-momentum form. Additionally, whilst the $i$-index is a continuum index (in $(n-1)$-spatial dimensions), we have adopted the treatment of Birrell and Davies [45] and expanded the mode solution as a discrete sum rather than a continuous integral. In the expansion (2.6.5), the $f_i$ are positive frequency modes, and the $f_i^*$ are the negative frequency modes. As before, the annihilation and creation operators obey the canonical commutation relations (which are

[15] Without global hyperbolicity, Cauchy surfaces cannot exist, so we relax the domain of integration to be some space-like hypersurface instead.

now written using the index $i$ notation for modes)

$$[\hat{a}_i, \hat{a}_j] = 0, \tag{2.6.6a}$$

$$[\hat{a}_i^\dagger, \hat{a}_j^\dagger] = 0, \tag{2.6.6b}$$

$$[\hat{a}_i, \hat{a}_j^\dagger] = \delta^{n-1}(i-j) =: \delta_{ij}. \tag{2.6.6c}$$

As in flat space, the annihilation operator can be used to define a 'vacuum' state[16] $|0_f\rangle$ that is annihilated by all annihilation operators:

$$\hat{a}_i|0_f\rangle = 0. \tag{2.6.7}$$

To ensure the modes are normalised, the curved space Klein-Gordon inner product (2.6.3) is utilised.

In flat space-time, there is a natural set of field modes, however in curved space-time, there is, in general, a potential ambiguity [156]. This is because the Minkowski vacuum (2.4.18) is defined as being invariant under the Poincaré group of transformations, whilst in curved space-time, the Poincaré group is no longer a symmetry of the space-time [362]. Without Poincaré invariance, there is no natural definition of positive frequency modes (in a general curved space-time[17]) and therefore there is an inherent ambiguity with the definition of field modes. Suppose then that there is another orthonormal basis of modes with respect to which we can expand the field:

$$\widehat{\Phi}(\boldsymbol{x}, t) = \sum_j \left[\hat{b}_j h_j(\boldsymbol{x}, t) + \hat{b}_j^\dagger h_j^*(\boldsymbol{x}, t)\right], \tag{2.6.8}$$

where $\hat{b}$ and $\hat{b}^\dagger$ are also annihilation and creation operators satisfying the canonical commutation relations (2.6.6). We can therefore define *another* vacuum state that is annihilated

[16] This is the nomenclature we use to refer to a ground state with the lowest possible energy; as we will see later, this doesn't necessarily preclude the possibility of the 'vacuum' state containing particles, unlike the situation in flat space.

[17] Specific choices of space-time *may* have natural choices of positive frequency modes; for example, static space-times [45, 374].

by the annihilation operator $\hat{b}$ as

$$\hat{b}_j|0_h\rangle = 0. \tag{2.6.9}$$

Since the modes $f_i$ and $h_i$ both form orthonormal bases, we can expand both in terms of the other as

$$h_j = \sum_i \left[\alpha_{ji} f_i + \beta_{ji} f_i^*\right], \tag{2.6.10a}$$

$$f_i = \sum_j \left[\alpha_{ji}^* h_j - \beta_{ji} h_j^*\right], \tag{2.6.10b}$$

where the coefficients $\alpha_{ij}$ and $\beta_{ij}$ are defined as the Klein-Gordon inner product between the modes $f_i$ and $h_i$:

$$\alpha_{ij} = \langle h_i, f_j\rangle, \qquad \beta_{ij} = -\langle h_i, f_j^*\rangle. \tag{2.6.11}$$

In addition, the coefficients are subject to the relations

$$\sum_k \left[\alpha_{ik}\alpha_{jk}^* - \beta_{ik}\beta_{jk}^*\right] = \delta_{ij}, \tag{2.6.12}$$

$$\sum_k \left[\alpha_{ik}\beta_{jk} - \beta_{ik}\alpha_{jk}\right] = 0. \tag{2.6.13}$$

The transformations (2.6.10) are known as *Bogoliubov transformations* [45, 157, 271], and the coefficients (2.6.11) are the corresponding *Bogoliubov coefficients*. By orthogonality of the field modes, we can express the annihilation operators $\hat{a}$ and $\hat{b}$ in terms of one another (and their respective creation operators); the relations are

$$\hat{a}_i = \sum_j \left[\alpha_{ji}\hat{b}_j + \beta_{ji}^*\hat{b}_j^\dagger\right], \tag{2.6.14a}$$

$$\hat{b}_j = \sum_i \left[\alpha_{ji}^*\hat{a}_i - \beta_{ji}^*\hat{a}_i^\dagger\right], \tag{2.6.14b}$$

whilst the corresponding expressions for the creation operators are found by taking the hermitian conjugate of the transformations (2.6.14).

Let us now consider a system in the '$f$-vacuum' state, $|0_f\rangle$, which is the state where no particles are found by an observer with respect to the $f_i$ basis modes. Using the

decomposition (2.6.14b), and the $h_j$ basis number operator $\widehat{N}_j = \hat{b}_j^\dagger \hat{b}_j$, we can calculate the number of particles in $f$-vacuum as seen by an observer using the $h_j$ basis modes; this is

$$\langle 0_f | \widehat{N}_j | 0_f \rangle = \sum_i |\beta_{ij}|^2. \tag{2.6.15}$$

If *any* of the coefficients $\beta_{ij}$ are nonzero, then the observer using the $h_j$ modes will see particles in a vacuum as defined by an observer using the $f_i$ modes; this is straightforwardly generalised to any sets of modes and the corresponding vacua.

Therefore, the notion of particles and vacua are on a general curved space-time are observer dependent, and thus there does not exist a unique vacuum state on a general curved space-time. It is important to note that one could apply the same logic to flat space-time, since, one can similarly define multiple bases of modes. In flat space-time, for inertial observers, the Bogoliubov coefficients are zero and thus all inertial observers agree on the definition of the vacuum state. However, if one were to instead consider an accelerating observer in Minkowski space, the Bogoliubov coefficients are nonzero and the accelerating observer sees particles in the 'vacuum' state as defined by the inertial observer. This is the *Unruh effect* [361].

For the purpose of this thesis, however, in later chapters when working on anti-de Sitter space, we choose to use the global anti-de Sitter space vacuum. This is the unique vacuum state that is defined using global anti-de Sitter space coordinates (see section 4.1; equations (4.1.3) and (4.1.6)) and is the state that respects the underlying maximal symmetry (see section 4.3) of anti-de Sitter space; one could perhaps consider this as the anti-de Sitter space equivalent of the Poincaré invariant vacuum on flat space. Note that any expectation values constructed in this (anti-de Sitter space) vacuum state will depend on any boundary conditions applied to the field (which are required to bypass the issue of non-global hyperbolicity of anti-de Sitter space); see sections 4.2, 4.5, 4.6 and chapter 5.

## § 2.7 Curved space-time expectation values and Hadamard renormalisation

Having (schematically) quantised the field on a general curved space-time in section 2.6.1, we now generalise the Green function approach in section 2.5 so that we can calculate expectation values in curved space-time. Thankfully, there is not much that needs to be changed.

We make the assumption that there exists a (not necessarily unique) ground state $|0\rangle$ and that there exists a global time coordinate that can be used to unambiguously define the order of events in time. Then, under these assumptions, the Green functions in section 2.5 are valid on any general curved space-time that possesses such a vacuum state and global time coordinate. The definitions of the Green functions as expectation values of (various products of) scalar fields are valid on any space-time that exhibit global hyperbolicity. For later purposes, we note that the universal covering space of anti-de Sitter space-time, CadS, has a global time coordinate and ground state and thus the Green functions in this section are well defined there (see chapter 4 for more detail). In flat space-time, the various Green functions satisfy either the homogeneous or inhomogeneous Klein-Gordon equation, as in (2.5.38). To generalise this to curved space-time, we upgrade the coordinate derivatives to covariant derivatives, modify the mass term to include a coupling to gravity, and, for the inhomogeneous solutions, include a factor of $\sqrt{-g}$, where $g$ is the metric determinant; this comes from the definition of the Dirac-delta function as an integral over (curved) space. The Klein-Gordon equations for the curved space-time Green functions are therefore

$$\left(-\nabla_\mu\nabla^\mu + m^2 + \xi R\right)\mathscr{G}(x,x') = 0 \tag{2.7.1a}$$

for $\mathscr{G} = \{G, G^{(1)}, G^{\pm}\}$, and

$$\left(-\nabla_\mu\nabla^\mu + m^2 + \xi R\right)G_F(x,x') = -\frac{1}{\sqrt{-g}}\delta^n(x-x'), \tag{2.7.1b}$$

$$\left(-\nabla_\mu\nabla^\mu + m^2 + \xi R\right)G_{R/A}(x,x') = \frac{1}{\sqrt{-g}}\delta^n(x-x'). \tag{2.7.1c}$$

Using these Green functions, expectation values of (products of various) scalar field operators can be calculated.

In Minkowski space, the vacuum expectation value (2.4.21) of the Hamiltonian operator (which gives the zero-point energy density) is divergent. The cure for this was to redefine the zero-point energy and instead consider differences in energy levels. A similar divergence is found in curved space-times; however redefining the zero-point energy is no longer a viable approach. This is because the zero-point energy density is given by the vacuum expectation value of the curved space stress-energy tensor (2.2.43)

$$E \sim \langle 0|\widehat{T}_{\tau\tau}|0\rangle. \tag{2.7.2}$$

In a curved space-time, the stress-energy tensor is a dynamical object, acting as a source in the Einstein equations (2.2.40), and thus influences the space-time curvature. Hence we cannot simply discard the zero-point energy; instead, we need to employ a *renormalisation procedure* to make sense of the divergent expectation values.

There are many different such procedures in the literature. The first attempt was the *Pauli-Villers* approach [296], followed closely by the *DeWitt-Schwinger* method [105, 106, 108, 331]. Other methods include *dimensional renormalisation* [47, 348], *zeta-function regularisation* [130, 189] and the *adiabatic approach* [290]. In this thesis, we are concerned with a sixth method: *Hadamard renormalisation* [84, 103, 219, 369, 371]. Hadamard renormalisation is a technique that relies upon representing propagators (i.e. *suitable* Green functions) in the so-called *Hadamard form* by expressing them in terms of the *Hadamard parametrix*. Decanini and Folacci [103] devised a suitable approach (following on from earlier work by Christensen [84], Fulling [158, 159], Sweeney [159] and Wald [158, 159, 219, 369, 371]) for the Hadamard renormalisation process in a general, $n$-dimensional curved space-time, in some general Hadamard state $|\psi\rangle$ (which will be defined later), using the Feynman propagator (2.5.34) as the fundamental object. In this thesis, we instead use the anticommutator, i.e. the Hadamard Green function, as the fundamental object.

The overall schematic of Hadamard renormalisation is to take Feynman (or indeed the Hadamard) Green function and separate it into its singular and regular parts, before removing the singular part by subtracting the Hadamard parametrix (this will be defined later). It is known that the singular parts are state-independent and thus purely geometric, whereas the regular part is state-dependent [219]. In the renormalisation, we discard the state-independent parts and retain the state-dependent parts.

In this thesis, we work directly with the Hadamard Green function, not the Feynman Green function; this needs to be justified. Recall the connection between the Feynman and Hadamard Green functions (2.5.37), reproduced here for clarity:

$$G_F(x,x') = -\overline{G}(x,x') - \frac{i}{2}G^{(1)}(x,x'). \tag{2.7.3}$$

The average of the advanced and retarded Green functions, $\overline{G}(x,x')$, only has support on the lightcone, and thus vanishes for points that are space- or time-like separated [267]. This means that all of the short-distance singularity structure of $G_F$ is contained within $\frac{i}{2}G^{(1)}$. In addition, the singularity structure of the Feynman Green function is complex-valued, owing to the time ordering in its definition (2.5.34). To sidestep this, in [103], $-i$ multiplied by the Feynman Green function is used in the renormalisation procedure; since the singularity structures are the same up to a multiplication of $i/2$, we can safely replace $-iG_F(x,x')$ with $\frac{1}{2}G^{(1)}(x,x')$ in the resulting renormalisation procedure as detailed in [103], provided we also remove the $i\epsilon$ prescription as in [103].

In order to facilitate the Hadamard renormalisation procedure, we need to formally introduce three important quantities: *Synge's world function* [347], the *geodetic distance* and the *van Vleck-Morette determinant* [365]. The first two were already briefly touched upon in section 2.5. The geodetic distance $s(x,x')$, or *proper distance*, is the geodesic interval separating two distinct space-time points $x$ and $x'$. Synge's world function $\sigma(x,x')$ can be defined by its relation to the geodetic distance as [347]

$$\sigma(x,x') = \frac{1}{2}\left[s(x,x')\right]^2. \tag{2.7.4}$$

Assuming that the points $x$ and $x'$ are in a normal neighbourhood and are connected by some (affinely parameterised) unique geodesic $\chi(\lambda)$ such that $\chi(\lambda_1) = x$ and $\chi(\lambda_2) = x'$, Synge's world function can be written as [305]

$$\sigma(x, x') = \frac{1}{2}(\lambda_2 - \lambda_1) \int_\chi \mathrm{d}\lambda \, g_{\mu\nu} \zeta^\mu \zeta^\nu, \tag{2.7.5}$$

where $\lambda$ is the affine parameter and $\zeta = \frac{\mathrm{d}\chi}{\mathrm{d}\lambda}$ is a vector tangent to the unique geodesic $\chi(\lambda)$. The world function also satisfies the differential equation [103, 305]

$$2\sigma = \sigma^{;\mu} \sigma_{;\mu}. \tag{2.7.6}$$

Synge's world function can be used to classify worldlines connecting the two points $x$ and $x'$, and thus we can say that if

$$\sigma(x, x') < 0, \qquad \{x, x'\} \text{ are time-like separated,} \tag{2.7.7a}$$

$$\sigma(x, x') = 0, \qquad \{x, x'\} \text{ are light-like separated,} \tag{2.7.7b}$$

$$\sigma(x, x') > 0, \qquad \{x, x'\} \text{ are space-like separated.} \tag{2.7.7c}$$

Considering the relation (2.7.4) between the geodetic distance and Synge's world function, it is clear that the geodetic distance is imaginary-valued when the points are connected by a time-like worldline, and real otherwise. In chapter 4, when we specialise to anti-de Sitter space, we can choose either time- or space-like separation without loss of generality due to the underlying maximal symmetry of the space (see section 4.3). It is for the reasons outlined above that we elect to use space-like separated points.

There are further quantities that provide information about the geodesics connecting the space-time points $x$ and $x'$. For example, the van Vleck-Morette determinant $\Delta(x, x')$ tells us about how the geodesics $\chi(\lambda)$ emanating from $x = \chi(\lambda_1)$ converge or disperse at the point $x' = \chi(\lambda_2)$ [367]. It is defined as [103, 365, 367]

$$\Delta(x, x') = [-g(x)]^{-1/2} \det\{\sigma_{;\mu\nu'}(x, x')\} \left[-g(x')\right]^{-1/2}, \tag{2.7.8}$$

where $g(x)$ and $g(x')$ are the determinants of the metric at $x$ and $x'$ respectively. The van Vleck-Morette determinant satisfies the boundary condition

$$\lim_{x' \to x} \Delta(x, x') = 1, \tag{2.7.9}$$

and in $n$-dimensions, satisfies the differential equation [103, 365, 367]

$$\Box_g \sigma = n - 2\Delta^{-1/2} \Delta^{1/2}_{;\mu} \sigma^{;\mu}. \tag{2.7.10}$$

With Synge's world function and the van Vleck-Morette determinant, it is possible to construct the Hadamard form of the Hadamard Green function. In general, this depends upon the number of space-time dimensions one is working in, with it split between the three cases of: $n = 2$; $n > 2$ even; and $n$ odd in [103]. In order to unburden the transcription somewhat, we introduce two piecewise-defined coefficients

$$\digamma = \begin{cases} 0, & \text{if } n \text{ is odd}, \\ 1, & \text{if } n \text{ is even} \end{cases} \tag{2.7.11}$$

and

$$\widetilde{\digamma} = \begin{cases} 1, & \text{if} \quad n \neq 2, \\ 0, & \text{if} \quad n = 2 \end{cases} \tag{2.7.12}$$

so that we can combine the three cases into one equation. Using these constants, the Hadamard Green function has Hadamard parametrix [103, 182]

$$G^{(1)}(x, x') = \alpha_n \left( \frac{\widetilde{\digamma} U(x, x')}{[\sigma(x, x')]^{(n-2)/2}} + \digamma V(x, x') \ln|\sigma(x, x')| + W(x, x') \right), \tag{2.7.13}$$

where the constant $\alpha_n$ is defined by

$$\alpha_n = \begin{cases} \frac{1}{2\pi}, & n = 2, \\ \dfrac{\Gamma(\frac{n-2}{2})}{(2\pi)^{n/2}}, & n > 2. \end{cases} \tag{2.7.14}$$

The Hadamard parametrix is *defined* as the short distance singularity structure (i.e. the near-coincidence limit) of the Hadamard Green function in some suitable quantum state

$|\psi\rangle$. In fact, any state which has a Hadamard Green function that expands as the Hadamard parametrix in the near-coincidence limit is known as a Hadamard state [63, 146, 219, 224, 374]; such states are considered a set of physically reasonable states [65, 145, 219, 265, 308]. If we expand the Hadamard parametrix (2.7.13) into its leading-order, near-coincidence limit behaviour (for which one must momentarily instate an $i\epsilon$ prescription in the argument of the logarithm), we recover the Hadamard Green function of Minkowski space (2.5.30).

The Hadamard biscalars $U(x,x')$, $V(x,x')$ and $W(x,x')$ are biscalars regular in the coincidence limit and symmetric under the interchange $x \longleftrightarrow x'$. They are defined in terms of sums of coefficients multiplied by Synge's world function, i.e.

$$U(x,x') = \sum_{j=0}^{\mathfrak{J}} U_j(x,x')\sigma^j(x,x'), \tag{2.7.15}$$

$$V(x,x') = \sum_{j=0}^{\infty} V_j(x,x')\sigma^j(x,x'), \tag{2.7.16}$$

$$W(x,x') = \sum_{j=0}^{\infty} W_j(x,x')\sigma^j(x,x'), \tag{2.7.17}$$

where the upper limit of the sum for $U(x,x')$ is dependent on the number of space-time dimensions, and is given by

$$\mathfrak{J} = \begin{cases} \infty, & \text{if } n \text{ is odd,} \\ \frac{n-2}{2}, & \text{if } n \text{ is even.} \end{cases} \tag{2.7.18}$$

The coefficients $U_j$, $V_j$ and $W_j$ can be determined by using the fact that they satisfy certain recursion relations [103]. These will be detailed below, split between the three cases of: $n = 2$; $n > 2$ even; and $n$ odd. First, however, we define the Klein-Gordon differential operator

$$\mathbf{K} := \Box_g - m^2 - \xi R, \tag{2.7.19}$$

for later ease of transcription.

In two space-time dimensions, the coefficients $V_j$ satisfy the relations [103]

$$2(j+1)^2 V_{j+1} + 2(j+1)V_{j+1;\mu}\sigma^{;\mu} - 2(j+1)V_{j+1}\Delta^{-1/2}\Delta^{1/2}_{;\mu}\sigma^{;\mu} + \mathbf{K}\, V_j = 0, \quad j \in \mathbb{N}, \tag{2.7.20}$$

with initial term

$$V_0 = -\Delta^{1/2}. \tag{2.7.21}$$

Likewise, the coefficients $W_j$ satisfy the recursion relations [103]

$$\begin{aligned} &2(j+1)^2 W_{j+1} + 2(j+1)W_{j+1;\mu}\sigma^{;\mu} - 2(j+1)W_{j+1}\Delta^{-1/2}\Delta^{1/2}_{;\mu}\sigma^{;\mu} \\ &\quad +4(j+1)V_{j+1} + 2V_{j+1;\mu}\sigma^{;\mu} - 2V_{j+1}\Delta^{-1/2}\Delta^{1/2}_{;\mu}\sigma^{;\mu} + \mathbf{K}\, W_j = 0. \end{aligned} \tag{2.7.22}$$

In even space-time dimensions greater than two, the corresponding recursion relations are [103]

$$\begin{aligned} &(j+1)(2j+4-n)U_{j+1} + (2j+4-n)U_{j+1;\mu}\sigma^{;\mu} \\ &\quad -(2j+4-n)U_{j+1}\Delta^{-1/2}\Delta^{1/2}_{;\mu}\sigma^{;\mu} + \mathbf{K}\, U_j = 0, \quad j = 0, 1, \ldots, \frac{n-6}{2}, \end{aligned} \tag{2.7.23}$$

for $U_j$, with initial term

$$U_0 = \Delta^{1/2}. \tag{2.7.24}$$

For later use, the $n = 4$ case simplifies considerably to

$$U(x, x') = \Delta^{1/2}(x, x'), \tag{2.7.25}$$

where we have an exact form for the Hadamard biscalar $U(x, x')$ and do *not* require recursion relations. The coefficients $V_j$ satisfy the relations [103]

$$\begin{aligned} &(j+1)(2j+n)V_{j+1} + 2(j+1)V_{j+1;\mu}\sigma^{;\mu} \\ &\quad -2(j+1)V_{j+1}\Delta^{-1/2}\Delta^{1/2}_{;\mu}\sigma^{;\mu} + \mathbf{K}\, V_j = 0, \quad j \in \mathbb{N}, \end{aligned} \tag{2.7.26}$$

with boundary condition

$$(n-2)V_0 + 2V_{0;\mu}\sigma^{;\mu} - 2V_0\Delta^{-1/2}\Delta^{1/2}_{;\mu}\sigma^{;\mu} + \mathbf{K}\, U_{\frac{n-4}{2}} = 0. \tag{2.7.27}$$

Finally, the $W_j$ coefficients satisfy the recursion relations [103]

$$(j+1)(2j+n)W_{j+1} + 2(j+1)W_{j+1;\mu}\sigma^{;\mu} - 2(j+1)W_{j+1}\Delta^{-1/2}\Delta^{1/2}_{;\mu}\sigma^{;\mu}$$

$$+(4j+2+n)V_{j+1}+2V_{j+1;\mu}\sigma^{;\mu}-2V_{j+1}\Delta^{-1/2}\Delta^{1/2}_{;\mu}\sigma^{;\mu}+\mathbf{K}\,W_j=0,\quad j\in\mathbb{N}. \tag{2.7.28}$$

The last case to consider is when the space-time dimension is odd. The recursion relations for the coefficients $U_j$ are given by

$$\begin{aligned}(j+1)(2j+4-n)U_{j+1}&+(2j+4-n)U_{j+1;\mu}\sigma^{;\mu}\\ &-(2j+4-n)U_{j+1}\Delta^{-1/2}\Delta^{1/2}_{;\mu}\sigma^{;\mu}+\mathbf{K}\,U_j=0,\quad j\in\mathbb{N},\end{aligned} \tag{2.7.29}$$

which have a boundary condition

$$U_0=\Delta^{1/2}. \tag{2.7.30}$$

In odd dimensions, $V(x,x')\equiv 0$ and thus there are no recursion relations for the $V_j$ coefficients. The relations for the final coefficients, $W_j$, are

$$\begin{aligned}(j+1)(2j+n)W_{j+1}&+2(j+1)W_{j+1;\mu}\sigma^{;\mu}\\ &-2(j+1)W_{j+1}\Delta^{-1/2}\Delta^{1/2}_{;\mu}\sigma^{;\mu}+\mathbf{K}\,W_j=0,\quad j\in\mathbb{N}.\end{aligned} \tag{2.7.31}$$

To obtain the explicit form of the coefficients, the corresponding recursion relations for $U_j$ and $V_j$ should be integrated along the unique geodesic connecting the points $x$ and $x'$ and, consequently, the coefficients $U_j$ and $V_j$ are uniquely determined and purely geometric, depending only on the geometry along the geodesic [103]. However, we do not find a similar condition for the coefficients $W_j$. Indeed, these coefficients are neither purely geometrical nor uniquely defined. Worse still, the initial coefficient $W_0$ is undetermined by the recursion relations for $W_j$ and is thus completely arbitrary. This arbitrariness extends to the other coefficients $W_j$ ($j\geq 1$), since they are determined by the initial coefficient $W_0$ through their recursion relations. This arbitrariness can be thought of as encoding information about the quantum state dependence of the Hadamard Green function entirely within the symmetric biscalar $W(x,x')$ [103]. We can therefore conclude that the Hadamard form comprises a state-independent, purely geometric part (made up of the $U(x,x')$ and $V(x,x')$ parts) and a state-dependent part (made up of the $W(x,x')$ part). The geometric part is divergent in

the coincidence limit $x' \to x$, whilst the state-dependent part is regular there. We can use this to decompose the Hadamard Green function into its *singular* and *regular* parts. We define the singular part as

$$G^{(1)}_{\text{sing}} = \alpha_n \left( \frac{\widetilde{\digamma} U(x,x')}{[\sigma(x,x')]^{(n-2)/2}} + \digamma V(x,x') \ln|\sigma(x,x')| \right), \tag{2.7.32}$$

whilst the regular part is given by the simple expression

$$G^{(1)}_{\text{reg}}(x,x') = \alpha_n W(x,x'), \tag{2.7.33}$$

where the constants $\digamma$ (2.7.11) and $\widetilde{\digamma}$ (2.7.12) were defined earlier to control the space-time dimension number dependence. Whilst we touched upon it briefly at the start of this section, the reason for extracting the regular and singular parts of the Hadamard parametrix will be illustrated below.

Let us suppose we wish to take the expectation value of the square of the field in a quantum state $|\psi\rangle$. Using the definition of the Hadamard Green function (2.5.4), we can write this as

$$\langle\psi|\widehat{\Phi}^2|\psi\rangle = \lim_{x'\to x} \frac{1}{2} G^{(1)}(x,x'). \tag{2.7.34}$$

However, the Hadamard Green function is divergent in coincidence limit, so the notion of the expectation value of the square of the field is meaningless. This pathological behaviour comes from the purely geometric part of the Hadamard Green function. In the analysis above, we have extracted the singular (geometric) and regular (state-dependent) parts of the Hadamard Green function. Wald [369, 371, 374] showed that it is however possible to cure the pathological divergence issue, and thus give a meaningful expression for expectation values of the coincidence limit of products of field operators. The resulting expectation value is the *renormalised* expectation value (with respect to the Hadamard condition). The renormalisation prescription, as laid out by Christensen [84], Wald [369, 371, 374] and Decanini and Folacci [103], is to essentially discard the singular part of the Hadamard Green function and keep only the regular part. Figure 2.3 shows this process for a scalar function,

$$\langle\psi|\widehat{Q}(x)|\psi\rangle = \lim_{x'\to x} \mathcal{Q}(x,x') \left[\frac{1}{2}G^{(1)}(x,x')\right]$$

$$\Big\downarrow \text{ remove singular part}$$

$$\lim_{x'\to x} \mathcal{Q}(x,x') \left[\frac{1}{2}G^{(1)}(x,x') - \frac{1}{2}G^{(1)}_{\text{sing}}(x,x')\right]$$

$$\Big\downarrow \text{ replace difference with regular part}$$

$$\lim_{x'\to x} \mathcal{Q}(x,x') \left[\frac{1}{2}G^{(1)}_{\text{reg}}(x,x')\right] \longrightarrow \langle\psi|\widehat{Q}(x)|\psi\rangle_{\text{ren}}$$

Figure 2.3: Schematic flowchart for the Hadamard renormalisation procedure for a scalar operator $\widehat{Q}(x)$ in a general Hadamard state $|\psi\rangle$. The operator $\mathcal{Q}_{\mu\nu}$ is some general differential operator that depends on the two space- or time-like separated points $x$ and $x'$.

and figure 2.4 shows this process for a general rank-2 tensor. Returning to the expectation value of the square of the field (2.7.34), we can therefore construct the renormalised expectation value (of the square) of the field as

$$\langle\psi|\widehat{\Phi}^2|\psi\rangle_{\text{ren}} = \lim_{x'\to x}\left[\frac{1}{2}G^{(1)}_{\text{reg}}(x,x')\right] = \frac{\alpha_n}{2}\lim_{x'\to x} W(x,x'), \tag{2.7.35}$$

where $W(x,x')$ is the state-dependent Hadamard biscalar (2.7.17), with recursion relations (2.7.22) for space-times of dimension $n=2$, (2.7.28) for space-times of dimensions $n>2$ even, and (2.7.31) for space-times of odd dimension.

This pathological divergence issue is not unique to the expectation value of $\Phi^2$, it also plagues *any* expectation value (as defined as some scalar or tensor operator acting on the

Hadamard Green function) in a general curved space-time. For example, the expectation value of the stress-energy tensor can be defined as a differential operator acting on the Hadamard Green function. This is therefore *also* plagued by the divergent behaviour in the coincidence limit. Indeed, to see this explicitly, we define the expectation value of the stress-energy tensor in some Hadamard state as

$$\langle\psi|\widehat{T}_{\mu\nu}|\psi\rangle = \lim_{x'\to x} \mathcal{T}_{\mu\nu}(x,x')\left[\frac{1}{2}G^{(1)}(x,x')\right], \tag{2.7.36a}$$

where the operator $\mathcal{T}_{\mu\nu}$ is obtained by point-splitting the classical expression for the stress-energy tensor (2.2.43), and is given by [84, 103]

$$\begin{aligned}\mathcal{T}_{\mu\nu} = &\ (1-2\xi)\, g_{\nu}{}^{\nu'}\nabla_{\mu}\nabla_{\nu'} + \left(2\xi - \frac{1}{2}\right) g_{\mu\nu} g^{\gamma\varrho'}\nabla_{\gamma}\nabla_{\varrho'} - 2\xi g_{\mu}{}^{\mu'} g_{\nu}{}^{\nu'}\nabla_{\mu'}\nabla_{\nu'} \\ &+ 2\xi g_{\mu\nu} g^{\gamma\varrho}\nabla_{\gamma}\nabla_{\varrho} + \xi\left(R_{\mu\nu} - \frac{1}{2}R g_{\mu\nu}\right) - \frac{1}{2}g_{\mu\nu}m^2,\end{aligned} \tag{2.7.36b}$$

and where the metric $g_{\mu\nu'}$ is the *bivector of parallel transport*, and is defined by the differential equation [45, 84, 103, 105, 106, 109]

$$g_{\mu\nu';\rho}\sigma^{;\rho} = 0, \tag{2.7.36c}$$

and boundary condition

$$\lim_{x'\to x} g_{\mu\nu'} = g_{\mu\nu}. \tag{2.7.36d}$$

Since the Hadamard Green function is divergent in the coincidence limit, the expectation value of the stress-energy tensor (2.7.36) is also divergent and thus meaningless. To remedy this, we follow the same procedure as for the square of the field, i.e. we discard the singular parts of the Hadamard Green function, apply the differential operator $\mathcal{T}_{\mu\nu}$ (2.7.36b) to the regular part, take the coincidence limit and define this as our renormalised stress-energy tensor expectation value (see figure 2.4). Explicitly, this process yields

$$\begin{aligned}\langle\psi|\widehat{T}_{\mu\nu}|\psi\rangle_{\text{ren}} &= \lim_{x'\to x} \mathcal{T}_{\mu\nu}(x,x')\left[\frac{1}{2}G^{(1)}_{\text{reg}}(x,x')\right] \\ &= \frac{\alpha_n}{2}\lim_{x'\to x} \mathcal{T}_{\mu\nu}(x,x')W(x,x').\end{aligned} \tag{2.7.37}$$

The explicit form of the renormalised stress-energy tensor (2.7.37), in terms of the Hadamard biscalar $W(x, x')$ and its series coefficients, can be found by acting with the differential operator $\mathcal{T}_{\mu\nu}$ (2.7.36b) on $W(x, x')$. In a general, $n$-dimensional, curved space-time, the renormalised expectation value of the stress-energy tensor can be written in the form [103]

$$\langle\psi|\widehat{T}_{\mu\nu}|\psi\rangle_{\text{ren}} = \frac{\alpha_n}{2}\left[-w_{\mu\nu} + \frac{1}{2}\left(1-2\xi\right)w_{;\mu\nu} + \frac{1}{2}\left(2\xi - \frac{1}{2}\right)g_{\mu\nu}\Box_g w + \xi R_{\mu\nu} w\right]. \quad (2.7.38)$$

If we take the covariant derivative of this renormalised stress-energy tensor, we find that

$$\nabla^\mu\langle\psi|\widehat{T}_{\mu\nu}|\psi\rangle_{\text{ren}} \neq 0, \quad (2.7.39)$$

i.e. the renormalised stress-energy tensor is *not* conserved. When we take the covariant derivative of the left-hand-side of the Einstein equations (2.2.40), we find they *are* conserved. If a renormalised stress-energy tensor is to replace the classical stress-energy tensor in the Einstein equations (2.2.40), then it is sensible to require that any renormalised stress-energy tensor also be conserved. This was, in part, the motivation behind a set of axioms constructed to select finite, well-defined and physically meaningful renormalised stress-energy tensors. These axioms were instigated by Christensen [84], before being fully developed by Wald [369, 370, 371], and are known as *Wald's axioms for the renormalised stress-energy tensor*. The axioms are summarised as:

❶ **Conservation:** The renormalised stress-energy tensor expectation value must be locally conserved, i.e. $\nabla^\mu\langle\psi|\widehat{T}_{\mu\nu}|\psi\rangle = 0$. This follows from conservation of the left-hand-side of the Einstein equations (2.2.40); see the text above.

❷ **Causality:** Given an "in" state (i.e. one in the asymptotic past) at some point $q$, the renormalised stress-energy tensor $\langle\psi|\widehat{T}_{\mu\nu}|\psi\rangle_{\text{ren}}$ must depend only on events in the causal past of the point $q$. Likewise, for some "out" state (i.e. one defined in the asymptotic future) at a point $q'$, the expectation value $\langle\psi|\widehat{T}_{\mu\nu}|\psi\rangle_{\text{ren}}$ must only depend on events in the causal future of $q'$.

❸ **Consistency:** For two orthogonal states satisfying $\langle\Psi|\Psi'\rangle = 0$, the matrix element given by $\langle\Psi|\widehat{T}_{\mu\nu}|\Psi'\rangle$ must agree with the formal expression, that gives a finite and unambiguous answer.

❹ **Normal ordering:** In the flat space limit, the renormalised stress-energy tensor must reduce to the normal-ordered stress-energy tensor expectation value, i.e $\langle\psi|\widehat{T}^{\mathbb{M}}_{\mu\nu}|\psi\rangle_{\text{ren}} = \langle\psi|{:}\widehat{T}^{\mathbb{M}}_{\mu\nu}{:}|\psi\rangle$. See section 2.4.1 for more detail, in particular equation (2.4.27).

Any renormalised stress-energy tensor satisfying these axioms is thus unique, up to the addition of a locally conserved, geometric tensor $\widetilde{\Theta}_{\mu\nu}$. This follows from a uniqueness theorem by Wald [369, 370, 371] who proved that, if we have two renormalised stress-energy tensor (expectation values) $\langle\psi|\widehat{T}^{(A)}_{\mu\nu}|\psi\rangle$ and $\langle\psi|\widehat{T}^{(B)}_{\mu\nu}|\psi\rangle$, then their difference is some locally conserved and purely geometric tensor

$$\langle\psi|\widehat{T}^{(A)}_{\mu\nu}|\psi\rangle - \langle\psi|\widehat{T}^{(B)}_{\mu\nu}|\psi\rangle = \widetilde{\Theta}_{\mu\nu}. \tag{2.7.40}$$

Henceforth, we assume that any renormalised stress-energy tensor satisfies Wald's axioms and is therefore unique up to the addition of the locally conserved, geometric tensor $\widetilde{\Theta}_{\mu\nu}$.

The renormalised stress-energy tensor (2.7.38), therefore, does *not* satisfy Wald's axioms. In order to remedy this, we add a counter term $v_1 g_{\mu\nu}$ so that the renormalised stress-energy tensor (2.7.38) is locally conserved, and we add the tensor $\Theta_{\mu\nu}$, since any renormalised stress-energy tensor is only unique up to such a tensor. We therefore have the *conserved*, renormalised stress-energy tensor

$$\begin{aligned}\langle\psi|\widehat{T}_{\mu\nu}|\psi\rangle_{\text{ren}} = \frac{\alpha_n}{2}\Bigg[&-w_{\mu\nu} + \frac{1}{2}\left(1-2\xi\right)w_{;\mu\nu} \\ &+\frac{1}{2}\left(2\xi - \frac{1}{2}\right)g_{\mu\nu}\Box_g w + \xi R_{\mu\nu}w - \digamma\, g_{\mu\nu}v_1\Bigg] + \Theta_{\mu\nu},\end{aligned} \tag{2.7.41}$$

where

$$v_1 = \lim_{x'\to x} V_1(x,x'), \tag{2.7.42}$$

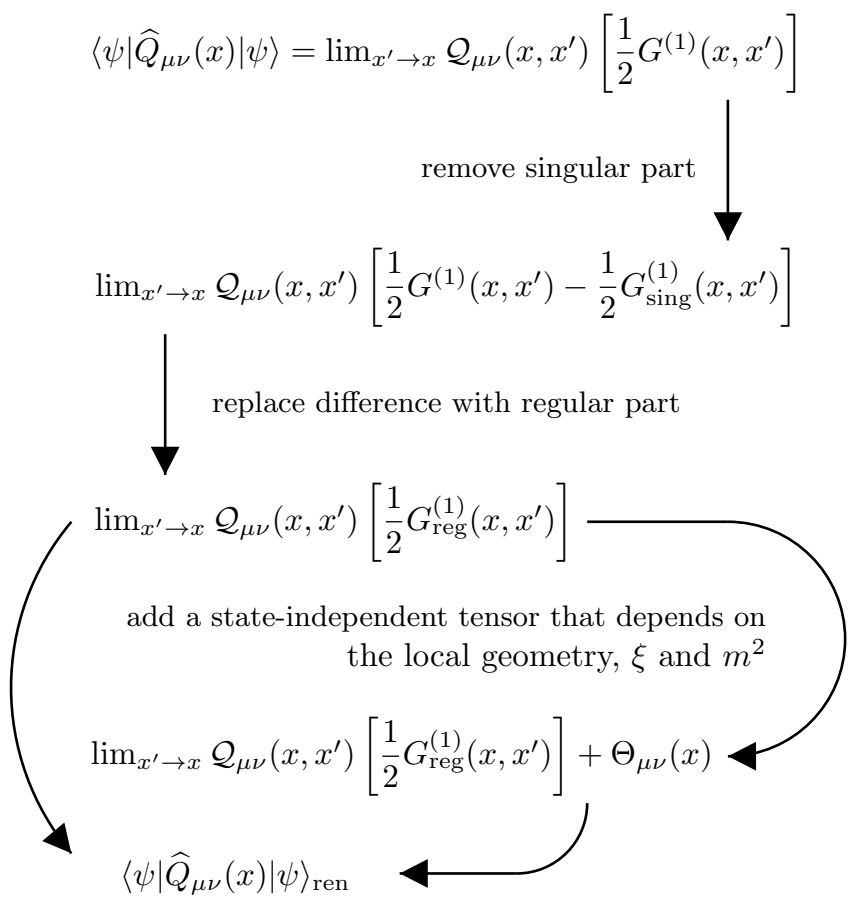


Figure 2.4: Schematic flowchart for the Hadamard renormalisation procedure for a rank-2 operator $\widehat{Q}_{\mu\nu}(x)$ in a general Hadamard state $|\psi\rangle$. The differential operator $\mathcal{Q}_{\mu\nu}(x,x')$ depends, in general, on the two space- or time-like separated points $x$ and $x'$. The addition of the state-independent tensor $\Theta_{\mu\nu}$ is *not* required for a meaningful expectation value, but is necessary for a well-defined renormalised stress-energy tensor according to Wald's axioms [369, 370, 371]. See the text for more detail.

is a function that only appears in even dimensions (hence the reintroduction of the parity-control constant $\digamma$ (2.7.11)), and will depend explicitly on the number of space-time dimensions. Additionally, we have the scalar and tensor functions

$$w(x) = \lim_{x' \to x} W(x, x'), \tag{2.7.43a}$$

$$w_{\mu\nu}(x) = \lim_{x' \to x} W(x, x')_{;\mu\nu}, \tag{2.7.43b}$$

which are built out of the Hadamard biscalar $W(x, x')$ (and derivatives thereof), and will also explicitly depend upon the space-time dimension and quantum state $|\psi\rangle$. The trace of (2.7.43b) can be written as (dropping the functional dependence)

$$w_{\mu}{}^{\mu} = \left(m^2 + \xi R\right) w - \digamma(n+2)v_1. \tag{2.7.44}$$

This will provide a consistency check when performing explicit computations - see chapter 5. Finally, as discussed above, the geometric tensor $\Theta_{\mu\nu}$ is included to ensure uniqueness, and is itself covariantly conserved in odd dimensions:

$$\Theta^{\mu\nu}{}_{;\nu} = 0, \tag{2.7.45}$$

whilst, in even dimensions, it is subject to the differential equation

$$\nabla^{\mu}\left[\Theta_{\mu\nu} - \frac{n\alpha_n}{4} g_{\mu\nu} v_1\right] = 0, \tag{2.7.46}$$

where $\alpha_n$ (2.7.14) was defined previously. The tensor $\Theta_{\mu\nu}$ can additionally be absorbed into the left-hand-side of the Einstein equations (2.2.40) (since it is purely geometric in nature), and can thus be thought of as an effective action term. We therefore leave any further discussion about the tensor $\Theta_{\mu\nu}$ to chapter 3, and in particular section 3.2.

Since the functions in the renormalised stress-energy tensor (2.7.41) depend on the explicit number of space-time dimensions, here and henceforth we will only consider three- and four-dimensional space-times, since these are the focus of the later chapters of this thesis. In three dimensions, the function $v_1$ is zero. In four dimensions, the function $v_1$ is given in

terms of the mass $m$, coupling constant $\xi$, Ricci scalar $R$, Ricci tensor $R_{\mu\nu}$ and Riemann tensor $R_{\mu\nu\rho\varrho}$ as [103]

$$\begin{aligned} v_1 = &\frac{1}{8}m^4 + \frac{1}{4}\left(\xi - \frac{1}{6}\right)m^2 R - \frac{1}{24}\left(\xi - \frac{1}{5}\right)\Box_g R \\ &+ \frac{1}{8}\left(\xi - \frac{1}{6}\right)^2 R^2 - \frac{1}{720}R_{\mu\nu}R^{\mu\nu} + \frac{1}{720}R_{\mu\nu\rho\varrho}R^{\mu\nu\rho\varrho}. \end{aligned} \tag{2.7.47}$$

Since the scalar $w(x)$ and tensor $w_{\mu\nu}(x)$ depend on the space-time point $x$ and the quantum state $|\psi\rangle$, in order to find their explicit expressions, one needs to make a choice of space-time to work in. We therefore leave these until part II of the thesis, where we work on anti-de Sitter space.

For the remainder of this thesis, as well as restricting ourselves to three- and four-dimensional space-times, we are also only interested in massless and conformally coupled scalar fields. The function $v_1$ (2.7.47) reduces somewhat in this limit, and is given by

$$v_1|_{m=0,\,\xi=\xi_c} = \frac{1}{720}\left(\Box_g R - R_{\mu\nu}R^{\mu\nu} + R_{\mu\nu\rho\varrho}R^{\mu\nu\rho\varrho}\right). \tag{2.7.48}$$

Now, by taking the trace of the renormalised stress-energy tensor (2.7.37), we find

$$\langle\psi|\widehat{T}_\mu{}^\mu|\psi\rangle_{\text{ren}} = \frac{1}{2}\alpha_n n \digamma v_1 + \Theta_\mu{}^\mu. \tag{2.7.49}$$

It can be shown that, in the massless and conformally coupled case, the tensor $\Theta_{\mu\nu}$ is zero in three dimensions (see section 3.2); in addition, the quantity $v_1$ will vanish in three dimensions. Therefore, in three dimensions, the trace of the renormalised stress-energy tensor is zero, as was the case for its classical counterpart. However, in four dimensions, the trace reduces to [103]

$$\langle\psi|\widehat{T}_\mu{}^\mu|\psi\rangle_{\text{ren}} = \frac{v_1}{4\pi^2}, \tag{2.7.50}$$

which is nonzero, very much unlike its classical counterpart. This phenomenon is called the *trace anomaly* [45, 103, 157, 374].

### 2.7.1 Renormalisation by state subtraction

Before concluding this chapter, it is necessary to mention a specific case of the Hadamard renormalisation procedure, *state subtraction*. This is the method that will be used when renormalising the stress-energy tensor in anti-de Sitter space in part II of the thesis. The state subtraction procedure will be sketched below.

Let us assume that we have two, distinct Hadamard states, $|\Psi\rangle$ and $|\Psi'\rangle$. Now, as we have discussed already in this section, all Hadamard states will have the same short-distance singularity structure. We can construct the expectation values of any, say, rank-2 tensor (or scalar, for that matter) in these states, in the usual manner as

$$\langle\Psi|\widehat{Q}_{\mu\nu}(x)|\Psi\rangle = \lim_{x'\to x} \mathcal{Q}_{\mu\nu}(x,x')\left[\frac{1}{2}G^{(1)}(x,x')\right] \tag{2.7.51a}$$

$$\langle\Psi'|\widehat{Q}_{\mu\nu}(x)|\Psi'\rangle = \lim_{x'\to x} \mathcal{Q}_{\mu\nu}(x,x')\left[\frac{1}{2}G'^{(1)}(x,x')\right], \tag{2.7.51b}$$

where $G^{(1)}(x,x')$ is the Hadamard Green function constructed in the state $|\Psi\rangle$, and similarly $G'^{(1)}(x,x')$ is the Hadamard Green function constructed in the state $|\Psi'\rangle$. In addition, $\mathcal{Q}_{\mu\nu}(x,x')$ is some general differential operator that depends on the space-time points $x$ and $x'$. By taking the difference of the two expectation values (2.7.51), we have

$$\begin{aligned}\langle\Psi|\widehat{Q}_{\mu\nu}(x)|\Psi\rangle - \langle\Psi'|\widehat{Q}_{\mu\nu}(x)|\Psi'\rangle &= \lim_{x'\to x} \mathcal{Q}_{\mu\nu}(x,x')\left[\frac{1}{2}G^{(1)}(x,x') - \frac{1}{2}G'^{(1)}(x,x')\right] \\ &= \lim_{x'\to x} \mathcal{Q}_{\mu\nu}(x,x')\left[\frac{1}{2}G^{(1)}_{\text{sing}}(x,x') - \frac{1}{2}G'^{(1)}_{\text{sing}}(x,x')\right. \\ &\qquad \left. + \frac{1}{2}G^{(1)}_{\text{reg}}(x,x') - \frac{1}{2}G'^{(1)}_{\text{reg}}(x,x')\right].\end{aligned} \tag{2.7.52}$$

Since the singular parts will be identical, i.e.

$$G^{(1)}_{\text{sing}}(x,x') = G'^{(1)}_{\text{sing}}(x,x'), \tag{2.7.53}$$

the difference (2.7.52) reduces to

$$\langle\Psi|\widehat{Q}_{\mu\nu}(x)|\Psi\rangle - \langle\Psi'|\widehat{Q}_{\mu\nu}(x)|\Psi'\rangle = \lim_{x'\to x} \mathcal{Q}_{\mu\nu}(x,x')\left[\frac{1}{2}G^{(1)}_{\text{reg}}(x,x') - \frac{1}{2}G'^{(1)}_{\text{reg}}(x,x')\right], \tag{2.7.54}$$

and we can thus split the limit into two as

$$\langle\Psi|\widehat{Q}_{\mu\nu}(x)|\Psi\rangle - \langle\Psi'|\widehat{Q}_{\mu\nu}(x)|\Psi'\rangle = \lim_{x'\to x} \mathcal{Q}_{\mu\nu}(x,x')\left[\frac{1}{2}G^{(1)}_{\text{reg}}(x,x')\right] - \lim_{x'\to x} \mathcal{Q}_{\mu\nu}(x,x')\left[\frac{1}{2}G'^{(1)}_{\text{reg}}(x,x')\right]. \quad (2.7.55)$$

Recognising that the quantities on the right-hand-side are in fact the definition of the renormalised expectation values, we can deduce that

$$\langle\Psi|\widehat{Q}_{\mu\nu}(x)|\Psi\rangle - \langle\Psi'|\widehat{Q}_{\mu\nu}(x)|\Psi'\rangle = \langle\Psi|\widehat{Q}_{\mu\nu}(x)|\Psi\rangle_{\text{ren}} - \langle\Psi'|\widehat{Q}_{\mu\nu}(x)|\Psi'\rangle_{\text{ren}}. \quad (2.7.56)$$

This is a very powerful tool, since it allows us to effectively sidestep the part of the renormalisation procedure where we extract information about the regular and singular parts of the Green function, and instead directly construct, for example, *physically meaningful* renormalised stress-energy tensors by considering differences between expectation values of the stress-energy tensor in Hadamard states. The major advantage of using state subtraction is that the renormalisation only needs to be performed once. For example, in chapter 5, we construct thermal expectation values of the stress-energy tensor (in some state $|\beta\rangle$ at fixed inverse temperature $\beta$) by constructing them as

$$\langle\beta|\widehat{T}_{\mu\nu}|\beta\rangle_{\text{ren}} := \underbrace{\left[\langle\beta|\widehat{T}_{\mu\nu}|\beta\rangle - \langle 0|\widehat{T}_{\mu\nu}|0\rangle\right]}_{\text{state subtraction}} + \underbrace{\left[\langle 0|\widehat{T}_{\mu\nu}|0\rangle_{\text{ren}}\right]}_{\text{already renormalised}}, \quad (2.7.57)$$

where we perform the renormalisation in the vacuum state $|0\rangle$, since in anti-de Sitter space, this is the state that has the most symmetries (see part II).

## § 2.8 Summary

In this chapter, we have introduced some of the background theory necessary for this thesis. In particular, we have briefly covered Einstein's theory of general relativity and quantum field theory on both flat and curved space-times.

In section 2.1, we started by introducing the basic theory that underpins much of this thesis, and we outlined the conventions in use throughout this thesis. We defined the Riemann tensor, Christoffel symbols, the Ricci tensor and Ricci scalar, and the Levi-Civita connection. In addition, we defined the Weyl tensor and three second-order curvature invariants: the Kretschmann scalar, the Chern-Pontryagin scalar and the Euler scalar. Much of the scope of this thesis surround space-times which are maximally symmetric, and thus we also introduced the concept of maximal symmetry and properties maximally-symmetric space-times exhibit. Finally, we defined and discussed global hyperbolicity.

Section 2.2 was dedicated to the classical theory used throughout this thesis. We began, in section 2.2.1, by briefly outlining the basics of classical field theory, deriving the Euler-Lagrange equations from Hamilton's principle of least action. We paid particular care when discussing the boundary terms that arise in this analysis. Next, in section 2.2.2, we derived the Einstein field equations in the absence of matter, starting with the Einstein-Hilbert action and exploiting variational principles. Additionally, by using the contracted Bianchi identity, we showed that the left-hand-side of the Einstein field equations must be covariantly conserved. In section 2.2.3, we introduced matter into the Einstein field equations in the form of scalar fields. We started by discussing the stress-energy tensor, how it is derived and where it fits in the Einstein field equations. In section 2.2.3.1, we briefly mentioned the classical energy conditions, how these are used to specify physical models of matter, and situations in which they are violated. Next, in section 2.2.3.2, we discussed scalar fields; in particular, we derived the classical stress-energy tensor for a massive and generally-coupled scalar field. By considering conservation of the stress-energy tensor, we derived the mass-shell condition for the scalar field in the form of a Klein-Gordon equation. Finally, in section 2.2.3.3, we briefly mentioned the perfect-fluid matter model.

To mark the end of the classical theory, in section 2.3 we introduced the concept of orthonormal frames in general relativity and relativistic kinetic theory. We defined vielbeins and showed how we can use suitable vielbeins to represent stress-energy tensors in terms of

the thermometer frame decomposition. We next introduced the basic theory for relativistic kinetic theory, which we used to model matter as a thermal gas of noninteracting, bosonic particles, distributed according to the Bose-Einstein distribution. Furthermore, we constructed a macroscopic stress-energy tensor in terms of momentum-space integrals. Then, in sections 2.3.1 and 2.3.2 we explicitly constructed the macroscopic stress-energy tensor in three and four space-time dimensions, respectively. Finally, in section 2.3.3, we showed a simple example of using relativistic kinetic theory to model a rigidly-rotating thermal distribution in Minkowski space-time.

For the remaining sections of this chapter, we switched our attention towards quantum theory. In section 2.4, we introduced quantum field theory on flat space-time. In particular, in section 2.4.1 we outlined the canonical quantisation procedure for scalar fields, expressing the quantised field in terms of annihilation and creation operators as a continuous integral over momentum-space. Recalling the classical stress-energy tensor for a scalar field, we constructed the Hamiltonian energy density operator for a quantum scalar field, and showed that taking the expectation value of this operator in a vacuum state yields infinite energy density. Finally, we discussed how, in flat space-time, this pathological behaviour can be cured by a process called normal ordering.

In section 2.5, we introduced an alternative method for quantising fields, the propagator approach and the Wightman reconstruction theorem. This entails using various Green functions to construct expectation values of operators in generic quantum states. We motivated this by constructing the Hadamard Green function in terms of the canonically quantised field as the vacuum expectation value of the anticommutator of the field at two space-time points. We then showed that the same Hadamard Green function can be constructed using the flat-space Klein-Gordon equation, and expressed the Green function as a two-point function that depends on Synge's world function. We then stated the remaining Green functions of interest, i.e. the positive and negative Wightman Green functions, the Pauli-Jordan Green function, the Feynman Green function and the advanced

and retarded Green functions. We discussed how the Green functions are all solutions to either the homogeneous or inhomogeneous Klein-Gordon equation, and how we could express them in terms of momentum-space (contour) integrals provided we made a suitable choice of contour. Up to this point, the Green functions discussed were defined in a vacuum state; in order to extend the (Hadamard) Green function to a general thermal state, we derived the Matsubara sum, constructing the thermal Hadamard Green function as an infinite sum of vacuum Hadamard Green functions.

Next, in section 2.6, we turned our attention away from quantum field theory on flat space-time to quantum field theory on general curved space-times. In particular, in section 2.6.1, we schematically described the canonical quantisation procedure for scalar fields on a general curved space-time. We discussed the notions of particles and vacua on general curved space-times being nonunique and in particular observer-dependent.

Finally, in section 2.7, we detailed the Green function approach for quantum field theory on curved space-times. We started by upgrading the flat space Green functions of section 2.5 to curved space Green functions, which satisfy the (in)homogeneous curved space Klein-Gordon equation. We discussed how, as in flat space, the 'vacuum' expectation value is divergent. However, unlike in flat space-time, curing this pathological behaviour is difficult. We therefore discussed different renormalisation schemes one could use to cure this pathological behaviour, before detailing the Hadamard renormalisation prescription as laid out in [103]. In the process, we briefly mentioned Hadamard states and Wald's axioms for a renormalised stress-energy tensor. Finally, in section 2.7.1, we discussed the state-subtraction renormalisation procedure, which is the scheme used extensively in chapter 5 of this thesis.

# Chapter 3

# Towards quantum gravity

"In the beginning the Universe was created.
This has made a lot of people very angry and been widely regarded as a bad move."

*Douglas Adams*

In this chapter we briefly introduce some different approaches to quantum gravity (in section 3.1), and pay particular attention to the semi-classical regime (section 3.2). We then, in section 3.3, outline the method of using analytical approximations to the renormalised stress-energy tensor in an effort to solve the semi-classical Einstein equations. Similarly, in section 3.4, we outline the perturbative approach for solving the semi-classical Einstein equations and then, in section 3.5, we detail the quantum corrections based approach, which is the focus of part III of this thesis. Finally, in section 3.6 we show how the semi-classical regime simplifies under the assumption of maximal symmetry (of the background space-time), and derive the simplified linearised, quantum-corrected Einstein equations and the full, nonlinear, quantum-corrected Einstein equations.

## § 3.1 Different approaches

The dynamics of gravity at the macroscopic level, such as stars and planets, are described by the classical Einstein equations, which we constructed in section 2.2.2 in the absence of matter content, and then in section 2.2.3 when matter was included in the form of the stress-energy tensor. For completeness, we reproduce them here as

$$G_{\mu\nu}[g] + \Lambda g_{\mu\nu} = \kappa T_{\mu\nu}[g], \tag{3.1.1}$$

where the factors of $[g]$ indicate that each tensor is constructed with respect to the metric $g_{\mu\nu}$ (this becomes important later).

Some of the philosophical and heuristic discussion of quantum gravity was presented in chapter 1. The idea behind a full theory of quantum gravity is a theory in which both the left- and right-hand-sides of the Einstein equations (3.1.1) describe gravitational propagation on both the macroscopic and microscopic (i.e. at scales below the Planck length) scales. In a mathematical sense, this amounts to essentially quantising both the left- and right-hand-sides of the Einstein equations (3.1.1). There are many different approaches in

the literature at broaching this problem; perhaps the most popularised[1] is *string theory* [346, 366]. String theory replaces the notion of point particles with higher dimensional, vibrating strings and is an attempt at unifying *all* of the fundamental forces. One major drawback, currently, with string theory is the lack of experimental verification [277]; the energy scales required to verify any prediction made by string theory currently far exceed those available to us. Since this thesis is not about string theory, very little else will be said (apart from a minor discussion in chapter 4 due to the key role of anti-de Sitter space in string theory), and instead the reader is referred to many reviews and textbooks, such as, amongst others, [37, 46, 174, 175, 226, 306, 307, 394].

Another popular approach is that of *loop quantum gravity* [30, 323, 324]. This is a slightly less ambitious approach than string theory, since it does not (initially) attempt to unify all of the fundamental forces. Instead, it focuses on quantising the gravitational field itself, by discretising space-time and considering integrals around loops (hence the name), with each node of the discretised network representing a volume of space and each connection a surface. Loop quantum gravity also suffers from a lack of experimental validation; in fact, *all* theories of quantum gravity do. There are many great reviews and textbooks on loop quantum gravity, see, for example [160, 322, 325, 352].

There are of course other approaches in the literature. For example, there is the *causal sets* approach [48, 195, 345]. This works in a similar way to loop quantum gravity in so much as it treats space-time as a discrete set of points that are elements of a causal set. Events on space-time are then connected by causality relations. Another, somewhat similar approach, is that of *causal dynamical triangulations* [6, 7, 8], which is a nonperturbative approach that approximates curved space-time by a lattice of higher-dimensional triangles, and enforces causality by requiring a well-defined time direction in every configuration. There is the

[1] Some estimates in the literature have the overall proportion of people working on string theory (out of the quantum gravity community) as high as 85%. There are two books from 2006 that discuss the 'over-allocation of resources' to string theory and its sociological impact: [336, 387].

*asymptotic safety regime* [121, 312, 376], which posits that there exists a high-energy scale at which gravity becomes "safe" from divergences due to renormalisation effects. There are many other approaches as well. One could undoubtedly spend countless time listing each in detail, but instead, the reader is referred to two review papers [204, 337] that cover the (main) different approaches to quantum gravity, and any predictions a valid theory must make.

A further approach, one that we take in this thesis, is considering a semi-classical theory: one in which the matter is quantised but the space-time remains classical. The space-time dynamics are still governed by the classical Einstein equations, whilst the propagation of matter is now governed by the theory of *quantum field theory in curved space-times* [45, 138, 157, 271, 293, 374]. Quantum field theory in curved space-times has led to some rather interesting discoveries, such as: *Hawking radiation* [187, 188], which predicts the evaporation of black holes, by considering spontaneous particle and anti-particle creation on the horizon of a black hole; and the *Unruh effect* [361], which shows that uniformly accelerating observers in Minkowski space-time will see a 'thermal bath' of particles where an inertial observer sees a vacuum. Quantum field theory on curved space-times was discussed in more detail in chapter 2; in particular, sections 2.6 and 2.7.

The semi-classical regime works by, essentially, replacing the classical stress-energy tensor in the Einstein equations (3.1.1) with an expectation value of the stress-energy tensor operator in some quantum state $|\psi\rangle$:

$$T_{\mu\nu} \longrightarrow \langle\psi|\widehat{T}_{\mu\nu}[g]|\psi\rangle, \tag{3.1.2}$$

so that the Einstein equations would look something akin to

$$G_{\mu\nu}[g] + \Lambda g_{\mu\nu} = \kappa\langle\psi|\widehat{T}_{\mu\nu}[g]|\psi\rangle. \tag{3.1.3}$$

This is not a simple fix, however. As we have discussed in detail in section 2.7, the notion of an expectation value in a general curved space is fraught with issues. To remedy this,

one must *renormalise* the expectation value so that it is physically meaningful (see section 2.7), though even this introduces more issues. We therefore discuss, in more detail, the semi-classical theory of quantum gravity in the next section.

## § 3.2 The semi-classical regime

The 'semi-classical' Einstein equations (3.1.3), as they are, are somewhat otiose; the expectation value of the stress-energy tensor on the right-hand-side is physically meaningless. The solution to this is to renormalise the stress-energy tensor - this procedure was discussed in detail in section 2.7. Assuming we have already performed this renormalisation, we replace the expectation value on the right-hand-side of the Einstein equations (3.1.3) with its renormalised expectation value:

$$G_{\mu\nu}[g] + \Lambda g_{\mu\nu} = \kappa \langle \psi | \widehat{T}_{\mu\nu}[g] | \psi \rangle_{\text{ren}} + \Theta_{\mu\nu}[g], \tag{3.2.1}$$

where the extra tensor $\Theta_{\mu\nu}$ arises in the renormalisation procedure (again, see section 2.7). This extra tensor is purely geometrical, and depends only on the space-time and parameters of the theory (i.e. mass $m$ and coupling $\xi$), and not the quantum state. We can therefore move this over to the left-hand-side of the Einstein equations

$$G_{\mu\nu}[g] + \Lambda g_{\mu\nu} - \Theta_{\mu\nu}[g] = \kappa \langle \psi | \widehat{T}_{\mu\nu}[g] | \psi \rangle_{\text{ren}}, \tag{3.2.2}$$

so that, heuristically at least, we have an equation that is essentially "classical=quantum". In addition, this new tensor $\Theta_{\mu\nu}$ can be considered as the result of an *effective action*; i.e. we modify the Einstein-Hilbert action (2.2.12) to include an effective Lagrangian density that depends on the parameters of the theory:

$$\mathcal{S} = \int \mathrm{d}^n x \sqrt{-g} \left[ \frac{1}{2\kappa} (R - 2\Lambda) + \mathscr{L}_{\text{RSET}} + \mathscr{L}_{\text{eff}} \right]. \tag{3.2.3}$$

By variational principles, one can recover the Einstein equations (3.2.2), by choosing suitable Lagrangian densities $\mathscr{L}_{\text{RSET}}$ and $\mathscr{L}_{\text{eff}}$. In general, it is not known what Lagrangian

density $\mathscr{L}_{\text{RSET}}$ would produce a renormalised expectation value of the stress-energy tensor, $\langle\psi|\widehat{T}_{\mu\nu}[g]|\psi\rangle_{\text{ren}}$, but it is assumed that one exists. On the other hand, the effective Lagrangian density $\mathscr{L}_{\text{eff}}$ (which gives rise to the tensor $\Theta_{\mu\nu}$ in the Einstein equations (3.2.2), by varying with respect to the metric) can be specified by considering dimensional arguments of the theory. This is detailed next. First, however, it is worth making a minor clarification. In the literature, some authors may consider the combination $\mathscr{L}_{\text{RSET}} + \mathscr{L}_{\text{eff}}$ as the effective Lagrangian. In addition, there are choices of $\mathscr{L}_{\text{RSET}}$ which give rise to analytical approximations of the renormalised stress-energy tensor; see section 3.3 for more detail.

In order to correctly specify the effective Lagrangian density $\mathscr{L}_{\text{eff}}$, we momentarily reinstate Newton's constant, but keep the speed of light $c$ and Planck constant $\hbar$ dimensionless. In this case, dimensional analysis shows that

$$[c] = 1 \implies LT^{-1} = 1 \iff L = T, \tag{3.2.4}$$

and

$$[\hbar] = 1 \implies ML^2T^{-1} = ML = 1 \iff L = M^{-1}. \tag{3.2.5}$$

Newton's constant $G_N$ now has dimensions

$$[G_N] = M^{-1}L^{n-1}T^{-2} = M^{-n+2}, \tag{3.2.6}$$

and thus the constant $\kappa$ (that appears as a prefactor in the Einstein-Hilbert Lagrangian density (2.2.11)) must then have dimensions

$$[\kappa] = [G_N] = M^{-n+2}. \tag{3.2.7}$$

Since the Ricci tensor and cosmological constant have dimensions

$$[R] = [\Lambda] = L^{-2} = M^2, \tag{3.2.8}$$

the Einstein-Hilbert Lagrangian density in the action (3.2.3) must have dimensions of $M^n$. Therefore, in order for dimensions to correctly match up in the action (3.2.3), it must be

the case that both the Lagrangian densities $\mathscr{L}_{\text{RSET}}$ and $\mathscr{L}_{\text{eff}}$ have dimensions

$$[\mathscr{L}_{\text{RSET}}] = [\mathscr{L}_{\text{eff}}] = M^n. \tag{3.2.9}$$

Since the Einstein-Hilbert Lagrangian term leads to the left-hand-side of the classical Einstein equations (2.2.40), and the Lagrangian density $\mathscr{L}_{\text{RSET}}$ leads to the renormalised-stress-energy tensor by construction, we assume that these have the correct dimensions. We now focus on the effective Lagrangian density $\mathscr{L}_{\text{eff}}$, which, when varied with respect to the metric, will yield the tensor $\Theta_{\mu\nu}$.

Since Newton's constant has dimensions $M^{-n+2}$ and $L = M^{-1}$, we can deduce that Synge's world function (2.7.4), $\sigma(x, x')$, which depends on the square of a distance, must have dimensions of $L^2 = M^{-2}$. If we now consider the Hadamard parametrix (2.7.13), (reproduced here for clarity)

$$G^{(1)}(x, x') \sim U(x, x')\sigma^{(2-n)/2} + V(x, x') \ln|\sigma| + W(x, x'), \tag{3.2.10}$$

it is clear that the argument of the logarithm is dimensionful, and in fact has dimensions of $M^{-2}$ [103]. In order to make it dimensionless, we rescale the argument of the logarithm by multiplying by the square of the mass scale, $\mathfrak{M}^2$. Using standard logarithm rules, we can then split the logarithm into two terms and absorb the $\ln \mathfrak{M}^2$ term into the Hadamard biscalar $W(x, x')$, i.e.

$$\begin{aligned} V(x, x') \ln|\sigma(x, x')| &\mapsto V(x, x') \ln|\mathfrak{M}^2 \sigma(x, x')|, \\ \implies W(x, x') &\mapsto W(x, x') - V(x, x') \ln \mathfrak{M}^2. \end{aligned} \tag{3.2.11}$$

In the renormalisation process (see section 2.7), the singular and regular parts of the Hadamard Green function are extracted. The singular parts comprise of the terms

$$G^{(1)}_{\text{sing}}(x, x') \sim U(x, x')\sigma^{(2-n)/2} + V(x, x') \ln|\sigma|, \tag{3.2.12}$$

and the regular parts now consist of

$$G^{(1)}_{\text{reg}}(x, x') \sim W(x, x') - V(x, x') \ln \mathfrak{M}^2, \tag{3.2.13}$$

since $V(x,x')\ln\mathfrak{M}^2$ is regular in the coincidence limit. However, since the extra contribution $V(x,x')\ln\mathfrak{M}^2$ does not encode any information about the quantum state dependence (only $W(x,x')$ does), we consider this as a contribution to the geometric tensor $\Theta_{\mu\nu}$ that arises due to the ambiguities in the renormalisation process. We therefore write

$$\Theta_{\mu\nu}(x) = \widetilde{\Theta}_{\mu\nu}(x) + \Theta^{\mathfrak{M}^2}_{\mu\nu}(x), \tag{3.2.14}$$

where

$$\Theta^{\mathfrak{M}^2}_{\mu\nu}(x) = -\frac{\alpha_n}{2}\lim_{x'\to x}\mathcal{T}_{\mu\nu}(x,x')V(x,x')\ln\mathfrak{M}^2, \tag{3.2.15}$$

with $\alpha_n$ (2.7.14) and $\mathcal{T}_{\mu\nu}$ (2.7.36b) given earlier. The new tensor $\widetilde{\Theta}_{\mu\nu}(x)$ is also purely geometric and conserved, and is determined by further dimensional analysis; this will be detailed later in this section. The tensor $\Theta^{\mathfrak{M}^2}_{\mu\nu}$ is normally referred to as the mass-scale ambiguity [103], and is only present in even dimension space-times, since the logarithm term in the Hadamard parametrix (2.7.13) only exists in even dimension space-times. In three dimensions, it therefore vanishes, whilst in four dimensions, it is given by [103]

$$\begin{aligned}\Theta^{\mathfrak{M}^2}_{\mu\nu} = \frac{\ln\mathfrak{M}^2}{16\pi^2}\Bigg\{&\frac{1}{180}\left[90\left(\xi-\frac{1}{6}\right)^2-1\right]{}^{\widetilde{\Theta}}\mathcal{H}^{(1)}_{\mu\nu} - \frac{1}{60}{}^{\widetilde{\Theta}}\mathcal{H}^{(2)}_{\mu\nu}\\ &-\left(\xi-\frac{1}{6}\right)m^2\left[R_{\mu\nu}-\frac{1}{2}Rg_{\mu\nu}\right]+\frac{1}{4}m^4g_{\mu\nu}\Bigg\},\end{aligned} \tag{3.2.16}$$

where the tensors ${}^{\widetilde{\Theta}}\mathcal{H}^{(j)}_{\mu\nu}$ will be defined later (see equation (3.2.25)). In the massless and conformally-coupled case, this reduces to

$$\Theta^{\mathfrak{M}^2}_{\mu\nu} = -\frac{\ln\mathfrak{M}^2}{2880\pi^2}\left\{{}^{\widetilde{\Theta}}\mathcal{H}^{(1)}_{\mu\nu} + 3\,{}^{\widetilde{\Theta}}\mathcal{H}^{(2)}_{\mu\nu}\right\}. \tag{3.2.17}$$

In higher dimensions, the mass-scale ambiguity tensor is given in [103].

We next determine the tensor $\widetilde{\Theta}_{\mu\nu}$ by considering further dimensional analysis. Since we have split the tensor $\Theta_{\mu\nu}$ (3.2.14) into the mass-scale ambiguity and another tensor, $\widetilde{\Theta}_{\mu\nu}$, we can write the Lagrangian density $\mathscr{L}_{\text{eff}}$ as

$$\mathscr{L}_{\text{eff}} = \mathscr{L}_{\widetilde{\Theta}} + \mathscr{L}_{\Theta^{\mathfrak{M}^2}}, \tag{3.2.18}$$

where $\mathscr{L}_{\Theta^{\mathfrak{M}^2}}$ is the Lagrangian density that will give the mass-scale ambiguity tensor (3.2.15) when considering variations with respect to the metric; the Lagrangian density $\mathscr{L}_{\widetilde{\Theta}}$ is found using dimensional arguments. Since the Lagrangian density $\mathscr{L}_{\text{eff}}$ has dimensions $M^n$ [103], it must be the case that the Lagrangian density $\mathscr{L}_{\widetilde{\Theta}}$ must also have dimensions of $M^n$ [103]. The tensor $\widetilde{\Theta}_{\mu\nu}$ can then be constructed by considering variational arguments using the Lagrangian density $\mathscr{L}_{\widetilde{\Theta}}$, by writing the variation of the action corresponding to the Lagrangian density $\mathscr{L}_{\widetilde{\Theta}}$ as

$$^{\widetilde{\Theta}}\mathcal{S}_{\mu\nu} \coloneqq \frac{1}{\sqrt{-g}}\frac{\delta}{\delta g^{\mu\nu}}\int \mathrm{d}^n x\sqrt{-g}\mathscr{L}_{\widetilde{\Theta}}, \tag{3.2.19}$$

where the tensor $\widetilde{\Theta}_{\mu\nu}$ is then given by a linear combination of all possible variations of the actions $^{\widetilde{\Theta}}\mathcal{S}_{\mu\nu}$ that are constructed with Lagrangian densities having dimensions of $M^n$. Using the facts that $[g_{\mu\nu}] = 1$ and $[R] = [R_{\mu\nu}] = [R_{\mu\nu\rho\varrho}] = M^2$ along with the relations (2.2.16), it is then possible to specify suitable Lagrangian densities, i.e. Lagrangian densities $\mathscr{L}_{\widetilde{\Theta}}$ that have dimensions $M^n$. Since these will depend on the number of space-time dimensions, we now specialise to three- and four-dimensional space-times, since these are the focus of this thesis, to construct the relevant Lagrangian densities and resulting (effective) actions.

In three dimensions, the only suitable Lagrangian densities are [103]

$$\mathscr{L}_{\widetilde{\Theta}} = \{m^3, mR\}, \tag{3.2.20}$$

whose functional derivatives are

$$\mathscr{L}^{(1)}_{\widetilde{\Theta}} = m^3 \implies {}^{\widetilde{\Theta}}\mathcal{S}^{(1)}_{\mu\nu} = \frac{1}{2}m^3 g_{\mu\nu}, \tag{3.2.21}$$

$$\mathscr{L}^{(2)}_{\widetilde{\Theta}} = mR \implies {}^{\widetilde{\Theta}}\mathcal{S}^{(2)}_{\mu\nu} = -m\left(R_{\mu\nu} - \frac{1}{2}Rg_{\mu\nu}\right), \tag{3.2.22}$$

and thus [103]

$$\widetilde{\Theta}_{\mu\nu} = {}^{\widetilde{\Theta}}\mathcal{S}^{(1)}_{\mu\nu} + {}^{\widetilde{\Theta}}\mathcal{S}^{(2)}_{\mu\nu} = \vartheta_1 m^3 g_{\mu\nu} + \vartheta_2 m\left(R_{\mu\nu} - \frac{1}{2}Rg_{\mu\nu}\right), \tag{3.2.23}$$

where the $\vartheta_j$ are arbitrary constants. In four dimensions, the suitable Lagrangian densities are given by [103]

$$\mathscr{L}_{\widetilde{\Theta}} = \{m^4, m^2 R, R^2, R_{\mu\nu}R^{\mu\nu}, R_{\mu\nu\rho\varrho}R^{\mu\nu\rho\varrho}\}. \tag{3.2.24}$$

Their functional derivatives are given by [103]

$$\mathscr{L}^{(1)}_{\widetilde{\Theta}} = m^4 \qquad \Longrightarrow \quad {}^{\widetilde{\Theta}}\mathcal{S}^{(1)}_{\mu\nu} = \frac{1}{2}m^4 g_{\mu\nu}, \tag{3.2.25a}$$

$$\mathscr{L}^{(2)}_{\widetilde{\Theta}} = m^2 R \qquad \Longrightarrow \quad {}^{\widetilde{\Theta}}\mathcal{S}^{(2)}_{\mu\nu} = -m^2\left(R_{\mu\nu} - \frac{1}{2}Rg_{\mu\nu}\right), \tag{3.2.25b}$$

$$\mathscr{L}^{(3)}_{\widetilde{\Theta}} = R^2 \qquad \Longrightarrow \quad {}^{\widetilde{\Theta}}\mathcal{H}^{(1)}_{\mu\nu} = 2R_{;\mu\nu} - 2RR_{\mu\nu} + \left(\frac{1}{2}R^2 - 2\Box_g R\right)g_{\mu\nu}, \tag{3.2.25c}$$

$$\mathscr{L}^{(4)}_{\widetilde{\Theta}} = R_{\mu\nu}R^{\mu\nu} \qquad \Longrightarrow \quad {}^{\widetilde{\Theta}}\mathcal{H}^{(2)}_{\mu\nu} = R_{;\mu\nu} - \Box_g R_{\mu\nu} - 2R^{\rho\varrho}R_{\rho\mu\varrho\nu} + \frac{1}{2}\left(R_{\rho\varrho}R^{\rho\varrho} - \Box_g R\right)g_{\mu\nu}, \tag{3.2.25d}$$

$$\begin{aligned}\mathscr{L}^{(5)}_{\widetilde{\Theta}} = R_{\mu\nu\rho\varrho}R^{\mu\nu\rho\varrho} \qquad \Longrightarrow \quad {}^{\widetilde{\Theta}}\mathcal{H}^{(3)}_{\mu\nu} &= 2R_{;\mu\nu} - 4\Box_g R_{\mu\nu} + 4R^{\rho}{}_{\mu}R_{\rho\nu} - 4R^{\rho\varrho}R_{\rho\mu\varrho\nu} \\ &\quad - 2R^{\rho\varrho\lambda}{}_{\mu}R_{\rho\varrho\lambda\nu} + \frac{1}{2}R_{\rho\varrho\lambda\varsigma}R^{\rho\varrho\lambda\varsigma}g_{\mu\nu},\end{aligned} \tag{3.2.25e}$$

where, with foresight and to match the literature, we have named the latter three functional derivatives as $\mathcal{H}$ rather than $\mathcal{S}$. Therefore, we can construct the geometric tensor $\widetilde{\Theta}_{\mu\nu}$, in terms of five arbitrary constants $\vartheta_j$, as [103]

$$\widetilde{\Theta}_{\mu\nu} = \vartheta_1 m^4 g_{\mu\nu} + \vartheta_2 m^2\left(R_{\mu\nu} - \frac{1}{2}Rg_{\mu\nu}\right) + \vartheta_3\,{}^{\widetilde{\Theta}}\mathcal{H}^{(1)}_{\mu\nu} + \vartheta_4\,{}^{\widetilde{\Theta}}\mathcal{H}^{(2)}_{\mu\nu} + \vartheta_5\,{}^{\widetilde{\Theta}}\mathcal{H}^{(3)}_{\mu\nu}. \tag{3.2.26}$$

In four dimensions, we can, in addition, define a Gauss-Bonnet Lagrangian density [82, 120, 233, 245, 262]

$$\mathscr{L}_{\mathrm{GB}} = R^2 - 4R_{\mu\nu}R^{\mu\nu} + R_{\mu\nu\rho\varrho}R^{\mu\nu\rho\varrho} \tag{3.2.27}$$

whose integral over a closed Riemannian manifold $\mathcal{M}$ gives the *Euler characteristic* (for the manifold)

$$\chi(\mathcal{M}) \coloneqq \frac{1}{32\pi^2}\int_{\mathcal{M}} \mathrm{d}^4x\sqrt{-g}\,\mathscr{L}_{\mathrm{GB}}. \tag{3.2.28}$$

This is useful because the Euler characteristic is a topological invariant [82, 120] and thus its variation (and hence the variation of the Gauss-Bonnet Lagrangian density $\mathscr{L}_{\mathrm{GB}}$)

with respect to the metric is zero [82, 120, 262]. We can also rewrite the Gauss-Bonnet Lagrangian density using the Lagrangian densities (3.2.25c)-(3.2.25e) as

$$\mathscr{L}_{\mathrm{GB}} = \mathscr{L}^{(3)}_{\widetilde{\Theta}} - 4\mathscr{L}^{(4)}_{\widetilde{\Theta}} + \mathscr{L}^{(5)}_{\widetilde{\Theta}}, \tag{3.2.29}$$

and by varying with respect to the metric, we have[2]

$$0 = {}^{\widetilde{\Theta}}\mathcal{H}^{(1)}_{\mu\nu} - 4{}^{\widetilde{\Theta}}\mathcal{H}^{(2)}_{\mu\nu} + {}^{\widetilde{\Theta}}\mathcal{H}^{(3)}_{\mu\nu}. \tag{3.2.30}$$

Therefore, we can express one of ${}^{\widetilde{\Theta}}\mathcal{H}^{(i)}$ in terms of the other two, and therefore, without loss of generality, we can set one of $\vartheta_j$ $(j = 3, 4, 5)$ equal to zero in the tensor (3.2.26). The locally conserved, geometric tensors ${}^{\widetilde{\Theta}}\mathcal{H}^{(i)}_{\mu\nu}$ play a very important role in semi-classical theories of quantum gravity - they will be discussed in somewhat more detail later in this section.

Similar expressions for the tensor $\widetilde{\Theta}_{\mu\nu}$ can be found in higher dimensions. Roughly speaking, one can write the $n$-dimensional tensor $\widetilde{\Theta}_{\mu\nu}$ in the form [103]

$$\widetilde{\Theta}_{\mu\nu} = \vartheta_1 m^n g_{\mu\nu} + \vartheta_2 m^{n-2}\left(R_{\mu\nu} - \frac{1}{2}Rg_{\mu\nu}\right) + \sum_{j=1}^{n-1}\vartheta_{j+2}{}^{\widetilde{\Theta}}\mathcal{H}^{(j)}_{\mu\nu}. \tag{3.2.31}$$

The tensors ${}^{\widetilde{\Theta}}\mathcal{H}^{(j)}_{\mu\nu}$ are built out of Lagrangian densities that have dimensions of $M^n$, and in general have terms including the Ricci scalar, Ricci tensor, Riemann tensor and the metric. In addition, in odd dimensions, the tensors ${}^{\widetilde{\Theta}}\mathcal{H}^{(j)}_{\mu\nu}$ include a factor of the mass $m$ to some positive power. Using this in conjunction with the expression (3.2.31), it is clear that the tensor $\widetilde{\Theta}_{\mu\nu}$ vanishes in the massless case for odd-dimensional space-times, and reduces to terms only including the tensors ${}^{\widetilde{\Theta}}\mathcal{H}^{(j)}_{\mu\nu}$ in the even-dimensional case. In four dimensions, we have already shown that one of the tensors ${}^{\widetilde{\Theta}}\mathcal{H}^{(j)}_{\mu\nu}$ can be removed by considering the variation of the Gauss-Bonnet Lagrangian density. In six dimensions, a similar argument is made by considering the cubic Lovelock Lagrangian density [103, 245]

$$\mathscr{L}_{\mathrm{L}} = R^3 - 12RR_{\mu\nu}R^{\mu\nu} + 16R_{\mu\nu}R^{\mu}{}_{\gamma}R^{\nu\gamma} + 24R_{\mu\nu}R_{\gamma\varrho}R^{\mu\gamma\nu\varrho} + 3RR_{\mu\nu\gamma\varrho}R^{\mu\nu\gamma\varrho}$$

[2]This relation can also be found using the Bianchi identities.

$$- 24R_{\mu\nu}R^{\mu}{}_{\gamma\varrho\lambda}R^{\nu\gamma\varrho\lambda} + 4R_{\mu\nu\gamma\varrho}R^{\mu\nu\lambda\alpha}R^{\gamma\varrho}{}_{\lambda\alpha} - 8R_{\mu\nu\gamma\varrho}R^{\mu}{}_{\lambda}{}^{\nu}{}_{\alpha}R^{\gamma\lambda\varrho\alpha}. \tag{3.2.32}$$

This argument is then easily extendible[3] to $n$ (even) dimensions, using the $n^{\text{th}}$ order Lovelock Lagrangian density [245]

$$\mathscr{L}_{\mathrm{L}(n)} = \frac{1}{2^n}\delta^{\mu_1\nu_1\ldots\mu_n\nu_n}_{\gamma_1\varrho_1\ldots\gamma_n\varrho_n}\prod_{i=1}^{n}R^{\gamma_i\varrho_i}_{\mu_i\nu_i}, \tag{3.2.33}$$

where the delta is the generalised Kronecker delta of rank-$2n$.

To obtain the *full, semi-classical Einstein equations* in $n$-dimensions and for a scalar field of mass $m$ and coupling $\xi$, one would add the tensors (3.2.15) and (3.2.31) to the left-hand-side of the Einstein equations (3.2.2) (in place of the tensor $\Theta_{\mu\nu}$), to get equations that are of the form[4]

$$G_{\mu\nu}[g] + \Lambda g_{\mu\nu} + \vartheta_1 m^n g_{\mu\nu} + \vartheta_2 m^{n-2}G_{\mu\nu}[g] + \sum_{j=1}^{n-1}\vartheta_{j+2}\widetilde{\Theta}\mathcal{H}^{(j)}_{\mu\nu}[g] + \Theta^{\mathfrak{M}^2}_{\mu\nu}[g] = \kappa\langle\psi|\widehat{T}_{\mu\nu}[g]|\psi\rangle_{\text{ren}}. \tag{3.2.34}$$

In order to further simplify the SCEE (3.2.34), we can combine some of the terms into renormalisations of constants of the theory. In particular, we can absorb the $\vartheta_1 m^n g_{\mu\nu}$ term into a renormalisation of the cosmological constant, and write

$$\Lambda_{\text{ren}} = \Lambda + \vartheta_1 m^n. \tag{3.2.35}$$

Likewise, we can absorb the $\vartheta_2 m^{n-2}G_{\mu\nu}[g]$ term into a redefinition of Newton's constant, which in essence means we renormalise the constant $\kappa$, by setting $\kappa \mapsto \kappa_{\text{ren}}$. Under these renormalisations, the SCEE (3.2.34) now read

$$G_{\mu\nu}[g] + \Lambda_{\text{ren}}g_{\mu\nu} + \sum_{j=1}^{n-1}\vartheta_{j+2}\widetilde{\Theta}\mathcal{H}^{(j)}_{\mu\nu}[g] + \Theta^{\mathfrak{M}^2}_{\mu\nu}[g] = \kappa_{\text{ren}}\langle\psi|\widehat{T}_{\mu\nu}[g]|\psi\rangle_{\text{ren}}. \tag{3.2.36}$$

For transcriptional ease and brevity, we will henceforth drop the 'ren' subscripts on the cosmological constant and the constant $\kappa$, but understand that when we refer to the cosmological constant or constant $\kappa$ henceforth, we mean the renormalised version. In any

[3]Whilst not rigorously proven, this is justified *a posteriori*.

[4]NB: This is very much a schematic form of the full SCEE.

case, when we consider massless fields, these contributions vanish identically and the renormalised and unrenormalised cosmological constant and constant $\kappa$ coincide.

In the remainder of this thesis (in particular parts II and III), as well as restricting ourselves to three- and four-dimensional space-times, we are also only interested in massless and conformally-coupled scalar fields. In three dimensions, we have already mentioned that the mass ambiguity (which gives rise to the tensor $\Theta_{\mu\nu}^{\mathfrak{M}^2}$) is not present. In addition to this, it is obvious that the remaining conserved tensor, $\widetilde{\Theta}_{\mu\nu}$ (3.2.23) is also zero in the massless limit. Therefore, in three dimensions, for massless and conformally coupled scalar fields, there is no extra conserved tensor, and the semi-classical Einstein equations read

$$G_{\mu\nu}[g] + \Lambda g_{\mu\nu} = \kappa \langle \psi | \widehat{T}_{\mu\nu}[g] | \psi \rangle_{\text{ren}}. \tag{3.2.37}$$

It is a different story in four dimensions. Unlike in three dimensions, where the mass-scale ambiguity tensor $\Theta_{\mu\nu}^{\mathfrak{M}^2}$ vanishes identically, in four dimensions, it is nonzero and depends on the tensors ${}^{\widetilde{\Theta}}\mathcal{H}_{\mu\nu}^{(1)}$ and ${}^{\widetilde{\Theta}}\mathcal{H}_{\mu\nu}^{(2)}$; in particular it is given by the relation (3.2.17). However, since the prefactor of equation (3.2.17) is constant (it depends only on the logarithm of the square of the mass scale $\mathfrak{M}$), we can absorb these extra terms into the constants $\vartheta_3$ and $\vartheta_4$ in the tensor $\widetilde{\Theta}_{\mu\nu}$ (3.2.26).

In addition, whilst in three dimensions, the tensor $\widetilde{\Theta}_{\mu\nu}$ vanishes in the massless and conformally-coupled limit, in four dimensions, it does *not* vanish. Indeed, in the tensor $\widetilde{\Theta}_{\mu\nu}$ (3.2.26), the first two terms vanish identically in the massless limit, whilst (two of) the tensors $\mathcal{H}_{\mu\nu}^{(i)}$ remain, meaning the renormalised stress-energy tensor in four dimensions for a massless and conformally-coupled scalar field will carry an ambiguity in tow, in the form of the tensors $\mathcal{H}_{\mu\nu}^{(i)}$. The semi-classical Einstein equations in this case reduce to (dropping the pre-superscript $\widetilde{\Theta}$ on the tensors ${}^{\widetilde{\Theta}}\mathcal{H}_{\mu\nu}^{(j)}$ here and henceforth for brevity):

$$G_{\mu\nu}[g] + \Lambda g_{\mu\nu} + \vartheta_1 \mathcal{H}_{\mu\nu}^{(1)}[g] + \vartheta_2 \mathcal{H}_{\mu\nu}^{(2)}[g] = \kappa \langle \psi | \widehat{T}_{\mu\nu}[g] | \psi \rangle_{\text{ren}}, \tag{3.2.38}$$

where the tensors $\mathcal{H}_{\mu\nu}^{(1)}$ (3.2.25c) and $\mathcal{H}_{\mu\nu}^{(2)}$ (3.2.25d) were given previously, but are repro-

duced here for clarity:

$$\mathcal{H}^{(1)}_{\mu\nu} = 2R_{;\mu\nu} - 2RR_{\mu\nu} + \left(\frac{1}{2}R^2 - 2\Box_g R\right) g_{\mu\nu}, \tag{3.2.39a}$$

$$\mathcal{H}^{(2)}_{\mu\nu} = R_{;\mu\nu} - \Box_g R_{\mu\nu} - 2R^{\gamma\varrho}R_{\gamma\mu\varrho\nu} + \frac{1}{2}\left(R_{\gamma\varrho}R^{\gamma\varrho} - \Box_g R\right) g_{\mu\nu}. \tag{3.2.39b}$$

The tensors (3.2.39) involve derivatives of the metric tensor up to and including fourth order. When these tensors are included, finding a fully self-consistent solution to the semi-classical Einstein equations (3.2.38) is challenging. In this case, we mean by "self-consistent" the notion that the renormalised stress-energy tensor is computed on the same background space-time on which the curvature tensors are defined. One particular issue with solutions including the fourth-order tensors $\mathcal{H}^{(j)}_{\mu\nu}$ is that they give rise to *runaway solutions* [292, 335, 344]. Runaway solutions are solutions that include terms that exponentially grow even in the absence of matter or energy and will eventually destabilise the space-time geometry; they are understandably deemed unphysical. In particular it was shown by Simon [335] that *any* theory that attempts to add higher-order curvature terms beyond second-order will be either nonlocal (and thus needs to be treated as a perturbative problem) or possess runaway solutions [335].

Nevertheless, it is possible to find rigorous work in the literature regarding consistent solutions to the full semi-classical Einstein equations, particularly in both $(2+1)$ and $(3+1)$ dimensions. For example, Sanders found solutions using a background Einstein static universe [326], Pinamonti (and collaborators) have produced extensive work using cosmological models [94, 259, 300, 301] as well as Juarez-Aubry [208] and Gottschalk [171], and there is some recent work by Juarez-Aubrey in static space-times [209, 213], anti-de Sitter space-time [212] and more general work on semi-classical regimes [210, 211, 214].

There are many different lines of attack in the literature to sidestep the inherent difficulties in solving the full semi-classical Einstein equations, of which we will detail three: *analytical approximations to the renormalised stress-energy tensor* in section 3.3; *perturbative approaches* involving the background metric in section 3.4; and *quantum corrections* to the

semi-classical Einstein equations in section 3.5. In the literature, it is frequently the case that a combination of each method may be used due to the complexity of the semi-classical Einstein equations (3.6.8). In fact, in this thesis, we use a combination of all three at one point or another; whilst the primary focus is on the quantum corrections regime, we employ a perturbative approach (to the quantum-corrected Einstein equations; see section 3.5) in chapters 7 and 8, as well as using a relativistic kinetic theory stress-energy tensor as an analytic approximation alongside the quantum field theory renormalised stress-energy tensor when solving the quantum-corrected Einstein equations.

## § 3.3 Analytical approximations to the renormalised stress-energy tensor

One approach to working with semi-classical theories of gravity is to employ some analytic approximation to the renormalised stress-energy tensor on the right-hand-side of the full semi-classical Einstein equations (3.2.34). This analytic approximation would be valid on a general class of space-time metrics, and as a result it would be possible for the right-hand-side of the semi-classical Einstein equations (3.2.34) to be written in terms of a number of unknown metric functions. The idea is then to take the semi-classical Einstein equations (3.2.34), now written in terms of unknown metric functions on *both* sides, and solve for the unknown metric functions.

One recent example in the literature is to use a Polyakov approximation [135, 286], which results from an $s$-wave approximation (that neglects back-scattering [135]) to the renormalised stress-energy tensor on static and spherically symmetric space-times. This approximation was initiated in $1+1$ dimensions, before being uplifted (by the $s$-wave approximation) to $3+1$ dimensions. The advantage of this particular approximation is that it involves only second-order derivatives of the metric, and hence the reduced semi-classical Einstein equations (i.e. setting $\vartheta_j = 0$ in the full semi-classical Einstein equations (3.2.34)) can be solved in a self-consistent manner. This particular approximation has been

used to find solutions to the semi-classical Einstein equations corresponding to spherically-symmetric, semi-classical stars and black holes, as well as solutions that represent stable and horizonless geometries and even exotic solutions such as wormholes. See, for example [24, 25, 26, 27, 40, 72, 80, 196] for a selection of recent works employing this approximation.

A follow-on from the Polyakov approximation (that is valid *only* in the $s$-wave sector) was the development of an Anderson-Hiscock-Samuel (AHS) approximation [20], which is a fourth-order Wentzel–Kramers–Brillouin (WKB) approximation. Whilst the full AHS approximation still involved fourth-order derivatives of the metric (and thus possessed run-away solutions), it has proved tractable to solve the order-reduced semi-classical Einstein equations that involve only second-order derivatives of the metric. This has led to solutions corresponding to semi-classical stars [23, 27].

Other analytical approximations used in the literature include adiabatic methods for cosmological scenarios [259], and taking advantage of the trace anomaly (of the renormalised stress-energy tensor) in four dimensions to induce an effective action [29, 260, 279]; in particular by using the Riegert-Mottola-Vaulin (RMV) approximation [73]. The trace anomaly approach works by generating four-dimensional renormalised stress-energy tensor approximations through a pair of auxiliary scalar fields. These scalar fields then satisfy higher-order equations of motion, with the specific boundary conditions imposed on these auxiliary fields yielding different renormalised stress-energy tensors. The leading-order terms of these renormalised stress-energy tensors mimic the behaviour of different vacuum states [29].

Finally, other notable analytic approximation methods in the literature are via the Page approximation [60, 155, 283] for massless scalar fields, and the DeWitt-Schwinger approximation [105, 106, 331] for massive fields. These work by explicitly specifying Lagrangian densities $\mathscr{L}_{\mathrm{RSET}}$ that, when varied with respect to the metric, give the approximate renormalised stress-energy tensor (see equation (3.2.3) and discussion thereof). There are a

plethora of papers that detail the construction of analytical approximations to the renormalised stress-energy tensor using the DeWitt-Schwinger expansion. In particular, see [39, 252, 253, 254, 255, 256, 257, 258, 350]. Both the DeWitt-Schwinger and Page approximations have also had particular success for asymptotically-anti-de Sitter black holes [350], though this was coupled with a perturbative approach, assuming that the approximations were valid at first order. This demonstrates that the three methods do not live in a vacuum; more often than not, a combination of each may be used, such is the complexity of the semi-classical problem.

In this thesis, when considering the quantum-corrected Einstein equations (these are introduced in section 3.5), we employ an analytical approximation to the renormalised stress-energy tensor in the form of a relativistic kinetic theory stress-energy tensor (see section 2.3). Whilst perhaps not as sophisticated as, say, a Polyakov approximation, using the RKT-SET provides reasonable results, particularly in the high temperature regime. A detailed treatment of the specific RKT-SET and how well this approximates the QFT renormalised stress-energy tensor is given in chapter 5, in particular section 5.3.4.

## § 3.4 Perturbative approaches

Another popular approach to (self-consistently) solving the full semi-classical Einstein equations is to treat the (unknown) metric as a perturbative expansion in the Planck constant $\hbar$, expanding as

$$g_{\mu\nu} = g^0_{\mu\nu} + \hbar g^{(1)}_{\mu\nu} + \mathcal{O}(\hbar^2), \tag{3.4.1}$$

where $g^0$ is the background space-time metric and $g^{(1)}$ is the first-order correction to the metric. In perturbative approaches, one usually assumes that the renormalised stress-energy tensor is also of first order in the Planck constant, and that the higher-order curvature tensors $\mathcal{H}^{(j)}_{\mu\nu}$ are also corrections to first order, i.e. we assume that the constants $\vartheta_j$ are of order $\mathcal{O}(\hbar)$. We additionally assume that the (renormalised) cosmological constant

$\Lambda$ and (renormalised) constant $\kappa$ can be expanded in a similar fashion as

$$\Lambda \mapsto \Lambda + \hbar\Lambda^{(1)} + \mathcal{O}(\hbar^2), \tag{3.4.2}$$

$$\kappa \mapsto \kappa + \hbar\kappa^{(1)} + \mathcal{O}(\hbar^2). \tag{3.4.3}$$

To zeroth order, the semi-classical Einstein equations (3.2.36) will read

$$G_{\mu\nu}[g^0] + \Lambda g^0_{\mu\nu} = 0, \tag{3.4.4}$$

whilst to first order, they read

$$G^{(1)}_{\mu\nu} + \Lambda^{(1)} g^{(1)}_{\mu\nu} + \sum_{j=1}^{n-1} \vartheta_j \mathcal{H}^{(j)}_{\mu\nu}[g^{(0)}] + \Theta^{\mathfrak{M}^2}_{\mu\nu}[g^{(0)}] = \kappa\langle\psi|\widehat{T}_{\mu\nu}[g^{(0)}]|\psi\rangle_{\text{ren}}, \tag{3.4.5}$$

which are a set of linear (by construction) equations for the (first-order) perturbed metric $g^{(1)}_{\mu\nu}$ and are second-order in time derivatives [148, 350]. The notation $G^{(1)}_{\mu\nu}$ refers to the fact that this is the linearised perturbation of the Einstein tensor. In practical uses (see chapters 7 and 8), we frequently employ the notation $\delta G_{\mu\nu}$ etc. The linearised semi-classical Einstein equations (3.4.5) involve, as a source term, the renormalised stress-energy tensor computed on the fixed space-time metric $g^0_{\mu\nu}$.

Particularly pertinent to this thesis are massless and conformally coupled quantum scalar fields. For these fields, in three- and four-dimensional space-times, the (perturbed) semi-classical Einstein equations are

$$G^{(1)}_{\mu\nu} + \Lambda^{(1)} g^{(1)}_{\mu\nu} = \kappa\langle\psi|\widehat{T}_{\mu\nu}[g^{(0)}]|\psi\rangle_{\text{ren}}, \tag{3.4.6}$$

in three dimensions, and

$$G^{(1)}_{\mu\nu} + \Lambda^{(1)} g^{(1)}_{\mu\nu} + \vartheta_1 \mathcal{H}^{(1)}_{\mu\nu}[g^{(0)}] + \vartheta_2 \mathcal{H}^{(2)}_{\mu\nu}[g^{(0)}] = \kappa\langle\psi|\widehat{T}_{\mu\nu}[g^{(0)}]|\psi\rangle_{\text{ren}}, \tag{3.4.7}$$

in four dimensions, with the tensors $\mathcal{H}^{(j)}$ (3.2.39) unchanged.

Even in the perturbative approach, solving the reduced (perturbed) semi-classical Einstein equations (3.4.5) remains a challenging problem on account of the complexity of the renormalised stress-energy tensor. This is even considering the recent development of efficient

methods of computing the renormalised stress-energy tensor on certain backgrounds, e.g. black hole backgrounds (see, for example, [28, 241, 242, 351]). This is why it is common to also employ some analytic approximation to the renormalised stress-energy tensor; see section 3.3. There has been some recent success when considering the Bañados-Teitelboim-Zanelli (BTZ) black hole [76, 78] - we discuss this in further detail in section 6.5.

## § 3.5 Quantum corrections

The *quantum-corrected* regime is where the bulk of the focus of this thesis lies, especially in part III. The quantum-corrected regime is not overly dissimilar from the perturbative approach detailed in section 3.4, in the sense that the renormalised stress-energy tensor is calculated on some fixed, classical background, and acts as a source term to solve for the *quantum-corrected metric*, whose curvature tensors appear on the left-hand-side of the semi-classical Einstein equations (3.2.36). The quantum-corrected Einstein equations read

$$G_{\mu\nu}[g^{\mathrm{QC}}] + \Lambda^{\mathrm{QC}} g^{\mathrm{QC}}_{\mu\nu} + \sum_{j=1}^{n-1} \vartheta_j \mathcal{H}^{(j)}_{\mu\nu}[g^0] + \Theta^{\mathfrak{M}^2}_{\mu\nu}[g^0] = \kappa^{\mathrm{QC}} \langle \psi | \widehat{T}_{\mu\nu}[g^0] | \psi \rangle_{\mathrm{ren}}, \tag{3.5.1}$$

where $g^0$ is the fixed, classical space-time background on which the renormalised stress-energy tensor (and ensuing extra tensors) is computed. For massless and conformally-coupled quantum scalar fields, the quantum-corrected Einstein equations read

$$G_{\mu\nu}[g^{\mathrm{QC}}] + \Lambda^{\mathrm{QC}} g^{\mathrm{QC}}_{\mu\nu} + \sum_{j=1}^{n-1} \vartheta_j \widetilde{\Theta} \mathcal{H}^{(j)}_{\mu\nu}[g^0] = \kappa^{\mathrm{QC}} \langle \psi | \widehat{T}_{\mu\nu}[g^0] | \psi \rangle_{\mathrm{ren}}, \tag{3.5.2}$$

since the mass-ambiguity tensor disappears (see section 3.2). In three dimensions, they simplify further to

$$G_{\mu\nu}[g^{\mathrm{QC}}] + \Lambda^{\mathrm{QC}} g^{\mathrm{QC}}_{\mu\nu} = \kappa^{\mathrm{QC}} \langle \psi | \widehat{T}_{\mu\nu}[g^0] | \psi \rangle_{\mathrm{ren}}. \tag{3.5.3}$$

We will henceforth refer to (3.5.3) as the *three-dimensional quantum-corrected Einstein equations* (QCEE), and they are used extensively in chapter 7. In four dimensions, the

quantum-corrected Einstein equations (3.5.2) similarly reduce, but still include some of the ambiguity-induced tensors. They are

$$G_{\mu\nu}[g^{\mathrm{QC}}] + \Lambda^{\mathrm{QC}} g^{\mathrm{QC}}_{\mu\nu} + \vartheta_1 \mathcal{H}^{(1)}_{\mu\nu}[g^0] + \vartheta_2 \mathcal{H}^{(2)}_{\mu\nu}[g^0] = \kappa^{\mathrm{QC}} \langle \psi | \widehat{T}_{\mu\nu}[g^0] | \psi \rangle_{\mathrm{ren}}, \tag{3.5.4}$$

and we will refer to these as the *four-dimensional, quantum-corrected Einstein equations*; these will be used in chapters 8 and 9, after a brief treatment in section 3.6 (where we argue that we can set $\vartheta_1 = \vartheta_2 = 0$).

In recent times, there has been considerable success utilising this approach for black hole space-times. For example, the BTZ black hole [32, 33] has had considerable attention. See, for example, [76, 78, 243, 248, 249, 334]. The quantum-corrected BTZ black hole plays an important role in chapter 7, where we consider (linear) quantum corrections to three-dimensional anti-de Sitter space-time, using the BTZ metric as a starting point for the solitonic interpretation; this is of particular relevance since the BTZ black hole is asymptotic to three-dimensional anti-de Sitter space. In chapter 6, in particular section 6.5, we briefly review the quantum-corrected BTZ black hole as developed in [78]. In the next section, we specialise to maximally symmetric space-times since anti-de Sitter space, the main focus of this thesis, is maximally symmetric.

## § 3.6 Semi-classical gravity and quantum-corrected geometry on maximally symmetric spaces

In this thesis, we are interested in background space-times which are maximally symmetric, in particular we are primarily concerned with anti-de Sitter space-time. In this section we, therefore, take the semi-classical Einstein equations (3.2.34), the linearised semi-classical Einstein equations (3.4.5) and the quantum-corrected Einstein equations (3.5.1), and show how they simplify when considering maximally-symmetric background space-times. In particular, we show that, without loss of generality, we can discard the extra tensors

arising from the ambiguity in the renormalisation procedure, i.e. $\mathcal{H}^{(j)}_{\mu\nu}$ (3.2.19) and $\Theta^{\mathfrak{M}^2}_{\mu\nu}$ (3.2.15). In addition, since in the remainder of this thesis we consider only massless and conformally-coupled scalar fields, we restrict ourselves to that case for the remainder of this chapter. The maximal symmetry arguments presented below will also be valid for massive and generally-coupled scalar fields, but we leave these for transcriptional ease.

Suppose we have an $n$-dimensional, maximally-symmetric space-time. In section 2.1, we gave the Riemann tensor (with $\mathscr{K}$ a constant) in any maximally-symmetric space-time as

$$R_{\mu\nu\gamma\varrho} = \mathscr{K}\left(g_{\mu\gamma}g_{\nu\varrho} - g_{\mu\varrho}g_{\nu\gamma}\right), \tag{3.6.1}$$

and Ricci scalar and tensor

$$R = \mathscr{K}\, n(n-1), \quad R_{\mu\nu} = \mathscr{K}\,(n-1)g_{\mu\nu}. \tag{3.6.2}$$

Since the tensors $\mathcal{H}^{(j)}_{\mu\nu}$ (3.2.19) arising from the renormalisation ambiguity are defined in terms of (products of) the Riemann tensor, Ricci tensor and Ricci scalar, the tensors $\mathcal{H}^{(j)}_{\mu\nu}$ will also be proportional to the metric tensor when evaluated on the background, maximally-symmetric space-time. For example, the tensors $\mathcal{H}^{(1)}_{\mu\nu}$ and $\mathcal{H}^{(2)}_{\mu\nu}$ (3.2.39) that appear in the four-dimensional semi-classical Einstein equations (3.2.38) reduce to

$$\mathcal{H}^{(1)}_{\mu\nu} = -2\mathscr{K}^2 n(n-1)^2 g_{\mu\nu} + \frac{1}{2}\mathscr{K}^2 n^2(n-1)^2 g_{\mu\nu} = \frac{1}{2}\mathscr{K}^2 n(n-1)^2(n-4)g_{\mu\nu} \overset{n=4}{=} 0, \tag{3.6.3}$$

using the fact that the Levi-Civita connection preserves the metric and that the covariant derivative of a constant is zero. Similarly, for the tensor $\mathcal{H}^{(2)}_{\mu\nu}$, we have

$$\begin{aligned}\mathcal{H}^{(2)}_{\mu\nu} &= -\,2\mathscr{K}^2(n-1)\underbrace{g^{\gamma\lambda}R_{\gamma\mu\lambda\nu}}_{=R_{\mu\nu}} - \frac{1}{2}\mathscr{K}^2 n(n-1)^2 g_{\mu\nu} \\ &= -\,\frac{1}{2}\mathscr{K}^2(n-1)^2(4\mathscr{K}+n)g_{\mu\nu} \overset{n=4}{=} -18\mathscr{K}^2(\mathscr{K}+1)g_{\mu\nu}.\end{aligned} \tag{3.6.4}$$

Recall the four-dimensional semi-classical Einstein equations (3.2.38). Under the assumption of (background) maximal symmetry, we have shown that the tensors $\mathcal{H}^{(j)}_{\mu\nu}$ are directly

proportional to the metric tensor (and in particular $\mathcal{H}^{(1)}_{\mu\nu} = 0$), and thus we can write the four-dimensional semi-classical Einstein equations as

$$G_{\mu\nu}[g] + \Lambda g_{\mu\nu} - 18\vartheta_2 \mathscr{K}^2(\mathscr{K}+1)g_{\mu\nu} = \kappa\langle\psi|\widehat{T}_{\mu\nu}[g]|\psi\rangle_{\text{ren}}. \tag{3.6.5}$$

Since both $\mathscr{K}$ and $\vartheta_2$ are constants, we can absorb the extra term into a redefinition of the cosmological constant, so that the four-dimensional semi-classical Einstein equations read

$$G_{\mu\nu}[g] + \widetilde{\Lambda} g_{\mu\nu} = \kappa\langle\psi|\widehat{T}_{\mu\nu}[g]|\psi\rangle_{\text{ren}}, \tag{3.6.6}$$

where

$$\widetilde{\Lambda} = \Lambda - 18\vartheta_2 \mathscr{K}^2(\mathscr{K}+1). \tag{3.6.7}$$

Therefore, in maximally-symmetric spaces, it is sufficient to consider the semi-classical Einstein equations in the absence of the extra renormalisation-ambiguity-induced-tensors. This is justified by absorbing the extra tensors into a redefinition of the cosmological constant (and therefore the vacuum energy of the space-time), and thus we can set the constants $\vartheta_j = 0$ in the full, semi-classical Einstein equations (3.2.34) and consider instead the reduced semi-classical Einstein equations

$$G_{\mu\nu}[g] + \widetilde{\Lambda} g_{\mu\nu} = \kappa\langle\psi|\widehat{T}_{\mu\nu}[g]|\psi\rangle_{\text{ren}}. \tag{3.6.8}$$

Here and henceforth, on account of the fact that in this thesis we only work with maximally-symmetric space-times, we refer to equations (3.6.8) as the semi-classical Einstein equations (SCEE).

Whilst in the above analysis we have assumed we are in a four-dimensional, maximally symmetric space-time, it is straightforward enough to generalise this to $n$ dimensions. Indeed, the higher-dimensional terms in the full semi-classical Einstein equations (3.2.34), i.e. the tensors $\mathcal{H}^{(j)}_{\mu\nu}$ $(j = 3, \ldots, n-1)$, are constructed from the Riemann tensor, Ricci tensor, Ricci scalar and derivatives (and products) thereof. Therefore, they will all also be directly proportional to the metric tensor, and by extending the arguments given above, we can

absorb every one of these terms into a redefinition of the cosmological constant. It is therefore sufficient to consider the semi-classical Einstein equations (3.6.8) in $n$-dimensional, maximally symmetric space-times.

In the bulk of this thesis, i.e. parts II and III, we assume we are in a situation whereby there exists some 'vacuum' state $|0\rangle$ that preserves the underlying maximal symmetry of the space-time, and that, in addition, there exists a thermal state $|\beta\rangle$ which does *not* necessarily preserve the underlying maximal symmetry of the space-time. *A priori*, it seems that the discarding of the extra renormalisation-ambiguity-induced-tensors may not be valid. However, by constructing the renormalised stress-energy tensor in a thermal state via state subtraction (see section 2.7.1) this problem can be sidestepped.

Suppose we have a state $|0\rangle$ that preserves the underlying maximal symmetry of the (background) space-time. The semi-classical Einstein equations (3.6.8) take the form

$$G_{\mu\nu}[g] + \widetilde{\Lambda} g_{\mu\nu} = \kappa \langle 0|\widehat{T}_{\mu\nu}[g]|0\rangle_{\text{ren}}. \tag{3.6.9}$$

In a maximal-symmetry-preserving state $|0\rangle$, the renormalised stress-energy tensor must be proportional to the metric tensor. In the maximal-symmetry-preserving vacuum state $|0\rangle$, we therefore write the renormalised stress-energy tensor as

$$\langle 0|\widehat{T}_{\mu\nu}[g]|0\rangle_{\text{ren}} = \mathcal{C} g_{\mu\nu}, \tag{3.6.10}$$

where $\mathcal{C}$ is some position-independent constant. Now let us construct the renormalised stress-energy tensor in some 'thermal' state $|\beta\rangle$, using the state subtraction procedure as in equation (2.7.57), i.e.

$$\langle \beta|\widehat{T}_{\mu\nu}[g]|\beta\rangle_{\text{ren}} = \Big[\langle \beta|\widehat{T}_{\mu\nu}[g]|\beta\rangle_{\text{ren}} - \langle 0|\widehat{T}_{\mu\nu}[g]|0\rangle_{\text{ren}}\Big] + \langle 0|\widehat{T}_{\mu\nu}[g]|0\rangle_{\text{ren}}. \tag{3.6.11}$$

Since the renormalisation-ambiguity-induced-tensors ($\mathcal{H}^{(j)}_{\mu\nu}$ etc) are state-independent, the term in the square brackets in equation (3.6.11) will not induce any extra ambiguous tensors since they will be cancelled in the difference. Furthermore, since the remaining

term, $\langle 0|\widehat{T}_{\mu\nu}[g]|0\rangle_{\text{ren}}$, is constructed in a state preserving the maximal symmetry of the background space-time, it must take the form (3.6.10) and thus does not induce any further ambiguous tensors. Therefore, the renormalised stress-energy tensor (3.6.11) constructed in a thermal state using state subtraction will not induce any extra ambiguous tensors, and it is therefore sufficient to consider the semi-classical Einstein equations

$$G_{\mu\nu}[g] + \Lambda_{\text{ren}}\, g_{\mu\nu} = \kappa\langle\beta|\widehat{T}_{\mu\nu}[g]|\beta\rangle_{\text{ren}} - \kappa\langle 0|\widehat{T}_{\mu\nu}[g]|0\rangle_{\text{ren}}, \tag{3.6.12}$$

where

$$\Lambda_{\text{ren}}\, g_{\mu\nu} = \widetilde{\Lambda} g_{\mu\nu} - \kappa\langle 0|\widehat{T}_{\mu\nu}[g]|0\rangle_{\text{ren}} \implies \Lambda_{\text{ren}} = \widetilde{\Lambda} - \kappa\mathcal{C}, \tag{3.6.13}$$

is the renormalised cosmological constant, assuming the vacuum renormalised stress-energy tensor takes the form (3.6.10). The redefined cosmological constant $\widetilde{\Lambda}$ arises from taking the background theory cosmological constant and absorbing the renormalisation-ambiguity-induced-tensors that are proportional to the metric tensor (including the mass-dependent term (3.2.35), though this vanishes in our cases of interest). In practice, we do not perform this redefinition; instead we discard the renormalisation-ambiguity-induced-tensors and treat $\widetilde{\Lambda}$ as the background cosmological constant. We are justified in doing this by virtue of the following. Firstly, in three-dimensions, the tensors $\mathcal{H}^{(j)}_{\mu\nu}$ vanish identically and thus $\vartheta_2 = 0$ and hence $\widetilde{\Lambda} = \Lambda$. In four-dimensions, the cosmological constant $\widetilde{\Lambda}$ (3.6.7) only has an extra term proportional to the constant $\mathscr{K}$ cubed. This is therefore a simple rescaling of the background vacuum energy and thus doesn't introduce any new physics. In order to simplify calculations, we thus set $\vartheta_2 = 0$ in the cosmological constant (3.6.7) and consider $\widetilde{\Lambda} = \Lambda$.

Even the reduced semi-classical Einstein equations (3.6.8), (3.6.9) and (3.6.12) are difficult to self-consistently solve, due to the nonlinearity of the Einstein tensor (see the discussion at the end of section 3.2). In this thesis we take two different approaches to simplifying the problem. In chapters 7 and 8, we attempt to solve the (reduced) linearised semi-classical

Einstein equations

$$G^{(1)}_{\mu\nu} + \Lambda_{\rm ren} g^{(1)}_{\mu\nu} = \kappa \langle \psi | \widehat{T}_{\mu\nu}[g^{(0)}] | \psi \rangle_{\rm ren} - \kappa \langle 0 | \widehat{T}_{\mu\nu}[g^{(0)}] | 0 \rangle_{\rm ren}, \tag{3.6.14}$$

sourced by (the difference between) renormalised stress-energy tensors in some Hadamard state $|\psi\rangle$ and a background-maximal-symmetry-preserving state $|0\rangle$. We will refer to the linearised semi-classical Einstein equations (3.6.14) as the *linearised, quantum-corrected Einstein equations*[5] (LQCEE). The other method we employ, specifically in chapter 9, is to solve the (nonlinear) *quantum-corrected Einstein equations* (QCEE), given by (in maximally symmetric background space-times)

$$G_{\mu\nu}[g^{\rm QC}] + \Lambda_{\rm ren} g^{\rm QC}_{\mu\nu} = \kappa \langle \psi | \widehat{T}_{\mu\nu}[g^{(0)}] | \psi \rangle_{\rm ren} - \kappa \langle 0 | \widehat{T}_{\mu\nu}[g^{(0)}] | 0 \rangle_{\rm ren}, \tag{3.6.15}$$

using the (difference between) renormalised stress-energy tensors in some Hadamard state $|\psi\rangle$ and the background-maximal-symmetry-preserving state $|0\rangle$, as the source term.

In particular, in part III of this thesis, we take the Hadamard state $|\psi\rangle$ to be either the (maximal-symmetry-preserving) vacuum state $|0\rangle$ or the thermal Hadamard state $|\beta\rangle$ in both the LQCEE and QCEE. When using the background-maximal-symmetry preserving vacuum state $|0\rangle$, the difference on the right-hand-side of the LQCEE (3.6.14) and QCEE (3.6.15) vanishes provided we have already renormalised the cosmological constant; the problem is therefore somewhat trivial. This was discussed earlier in this section. Nevertheless, we still explicitly show this (using the QCEE) in chapter 6 when taking the background space-time to be anti-de Sitter space; in particular see section 6.3. When constructing the renormalised stress-energy tensor in the thermal Hadamard state, we assume that the renormalisation of the cosmological constant (from the vacuum RSET) has already

[5] Technically, these are not linearised, quantum-corrected Einstein equations but rather linearised, semi-classical Einstein equations. However, since the renormalised stress-energy tensor on the right-hand-side is constructed on the background space-time and is used to solve for a different metric (the first order perturbation, in particular), it is our nomenclature to refer to these as linearised, quantum-corrected Einstein equations.

been completed, and thus the LQCEE are

$$G^{(1)}_{\mu\nu} + \Lambda_{\rm ren} g^{(1)}_{\mu\nu} = \kappa \langle \beta | \widehat{T}_{\mu\nu}[g^{(0)}] | \beta \rangle_{\rm ren} - \kappa \langle 0 | \widehat{T}_{\mu\nu}[g^{(0)}] | 0 \rangle_{\rm ren}, \tag{3.6.16}$$

where $G^{(1)}_{\mu\nu}$ is the (first-order) linearised perturbation of the Einstein tensor. Furthermore, the QCEE are given by

$$G_{\mu\nu}[g^{\rm QC}] + \Lambda g^{\rm QC}_{\mu\nu} = \kappa \langle \beta | \widehat{T}_{\mu\nu}[g^{(0)}] | \beta \rangle_{\rm ren} - \kappa \langle 0 | \widehat{T}_{\mu\nu}[g^{(0)}] | 0 \rangle_{\rm ren}. \tag{3.6.17}$$

## § 3.7 Summary

In this chapter, we have (briefly) introduced some of the approaches in the literature towards forming a full theory of quantum gravity. We have paid particular attention to semi-classical approaches, since this is the focus of the thesis, and derived the full semi-classical Einstein equations (including, in particular, the extra renormalisation-ambiguity-induced-tensors); we have also discussed different methods employed in the literature in order to solve, simplify or reduce the semi-classical regime, such as analytical approximations to the renormalised stress-energy tensor (section 3.3), perturbative treatments (section 3.4) and quantum corrections (section 3.5). Since much of the scope of this thesis surrounds anti-de Sitter space (as the title suggests), which is a maximally-symmetric space-time, we show (in section 3.6) how the semi-classical regime simplifies when considering maximally-symmetric background space-times. In particular, we argue that the extra renormalisation-ambiguity-induced-tensors can safely be discarded without loss of generality, and explicitly present the linearised, quantum-corrected Einstein equations and the full nonlinear quantum-corrected Einstein equations under these assumptions.

# Part II

# Quantum field theory on anti-de Sitter space-time

# Chapter 4

# Anti-de Sitter space-time

"Any sufficiently advanced technology is indistinguishable from magic."

*Arthur C. Clarke*

Anti-de Sitter space-time is a maximally symmetric solution to the classical Einstein field equations (2.2.33), with a constant, negative cosmological constant. Maximal symmetry refers to the fact that no point in the space-time is preferred above another, and cannot be distinguished in any way. Meanwhile, a constant, negative cosmological constant implies that the rate of the expansion of the universe should be decelerating. This is at odds with recent observations [298]. If the rate of expansion is indeed decelerating, then null rays can reach the space-time boundary in a finite affine parameter. As a result, boundary conditions must be imposed on the time-like boundary (see section 4.5).

Anti-de Sitter space-time has been studied extensively in recent years. One reason for such attention is undoubtedly its role in the adS/CFT correspondence, first posited in 1997 by Maldecena [247] and developed by Witten [386]. A comprehensive review can be found in [2]. Essentially, the adS/CFT correspondence states that any supersymmetric Yang-Mills theory on four dimensional Minkowski space-time is dual to a type IIB closed superstring theory on $\mathrm{adS}_5 \times \mathcal{S}_5$, where $\mathcal{S}_5$ is the standard five-sphere. Schematically, this is because the conformal boundary on adS is locally flat. This essentially means that a conformal field theory (such as Yang-Mills) on the boundary of an $(n+1)$-dimensional adS space-time is equivalent to a theory of quantum gravity (in particular a string theory) in the bulk. Although there are limited rigorous results[1], the attractiveness of the adS/CFT correspondence lies in the fact that there exists a dictionary translating between the CFT on the boundary and the QFT in the bulk. This has huge ramifications in the race to postulate a theory of quantum gravity, since it allows one to formulate certain objects in whichever theory it is easier to do so, before translating to the other. In particular one could potentially ascertain information about quantum gravity in adS by translating objects from the CFT in Minkowski space-time.

[1]There is a rigorous proof of the correspondence between QFTs in the bulk of adS and the boundary of adS. See [309, 310]. However, to the author's knowledge, there is no *rigorous* proof of the correspondence from a string theory perspective.

The layout of this chapter is as follows. In section 4.1 we review the basic geometry of anti-de Sitter space and fix a specific coordinate chart; this is not intended to be a detailed treatment, and the reader is instead referred to many great different sources, such as [41, 167, 190, 269] for more detailed discussions of anti-de Sitter space. Section 4.2 details the conformal structure of anti-de Sitter space, and the conformal relationship between anti-de Sitter space and the Einstein static universe. We discuss, in section 4.3, the maximal symmetry of anti-de Sitter space and general properties of maximally symmetric space-times. In section 4.4 we make a coordinate transformation to a rigidly rotating frame and discuss the orthonormal bases for the frame, which we call *vielbeins*. Following this we discuss, in section 4.5, the necessity for boundary conditions on the conformal adS boundary, and describe how these are applied by mapping to the ESU. In section 4.6 we detail the quantisation procedure for conformally-coupled scalar fields on anti-de Sitter space-time and construct the Hadamard Green function. Then, in section 4.7 we briefly discuss quantum states on anti-de Sitter space, paying particular attention to rigidly-rotating states. Finally, in section 4.8, we summarise the content of the chapter.

## § 4.1 Geometry

One can visualise $n$-dimensional adS ($\mathrm{adS}_n$) as an $n$-dimensional, single-sheeted hyperboloid embedded in an $(n+1)$-dimensional flat space $\mathbb{R}^{(n-1,2)}$ with a metric that has two time-like components and $n-1$ space-like components, i.e. $\eta_{\mu\nu} = \mathrm{Diag}\{-1, 1, \ldots, 1, -1\}$. By introducing global coordinates $\chi^\alpha$, $\alpha \in \{0, 1, \ldots, n\}$, we can write the equation for the hyperboloid in the embedding space as the quasi-sphere

$$-\left(\chi^0\right)^2 + \left(\chi^1\right)^2 + \left(\chi^2\right)^2 + \cdots + \left(\chi^{n-1}\right)^2 - \left(\chi^n\right)^2 = -a^{-2}, \tag{4.1.1}$$

where $a$ is a constant quantity of dimensions of inverse length, and is the inverse radius of the waist of the hyperboloid. The quantity $-a^2$ is the inverse radius of curvature [190, 341], and the quantity $a$ will be henceforth known as the inverse adS length scale. In all numerical

calculations in this thesis (and indeed many in the literature), we set $a = 1$. Whilst this is primarily for ease of computation, this has the added benefit of rescaling the characteristic units so that the radius of curvature is dimensionless and all physical quantities are then expressed in terms of units of the inverse radius of curvature.

In terms of the coordinates $\chi^\alpha$, the metric on the embedding space is written as

$$\mathrm{d}s^2 = -\left(\mathrm{d}\chi^0\right)^2 + \left(\mathrm{d}\chi^1\right)^2 + \left(\mathrm{d}\chi^2\right)^2 + \cdots + \left(\mathrm{d}\chi^{n-1}\right)^2 - \left(\mathrm{d}\chi^n\right)^2 . \tag{4.1.2}$$

A set of suitable, intrinsic and dimensionless coordinates to parameterise adS space-time is the set of hyperspherical coordinates, given by

$$\begin{aligned}
&\tau, && \text{a timelike coordinate,} && -\pi \leq \tau \leq \pi, \\
&\rho, && \text{a radial coordinate,} && 0 \leq \rho < \pi/2, \\
&\theta_j, && \text{polar coordinates,} && 0 \leq \theta_j \leq \pi, \quad j = 1, 2, \ldots, n-3, \\
&\phi, && \text{an azimuthal coordinate,} && 0 \leq \phi < 2\pi,
\end{aligned} \tag{4.1.3}$$

where the coordinates in the embedding space of $\mathrm{adS}_n$ are given as

$$\begin{aligned}
\chi^0 &= a^{-1}\cos(\tau)\sec(\rho), \\
\chi^1 &= a^{-1}\tan(\rho)\cos(\theta_1), \\
\chi^2 &= a^{-1}\tan(\rho)\sin(\theta_1)\cos(\theta_2), \\
\chi^3 &= a^{-1}\tan(\rho)\sin(\theta_1)\sin(\theta_2)\cos(\phi), \\
&\vdots \\
\chi^{n-2} &= a^{-1}\tan(\rho)\sin(\theta_1)\sin(\theta_2)\cdots\sin(\theta_{n-3})\cos(\phi), \\
\chi^{n-1} &= a^{-1}\tan(\rho)\sin(\theta_1)\sin(\theta_2)\cdots\sin(\theta_{n-3})\sin(\phi), \\
\chi^n &= a^{-1}\sin(\tau)\sec(\rho).
\end{aligned} \tag{4.1.4}$$

The advantage of these coordinates over, say, sausage coordinates [41], is that they are *global* coordinates, in the sense that they cover the whole of the hyperboloid and thus

cover all of anti-de Sitter space. Taking the derivatives of the $\chi^i$ (4.1.4), we have

$$\begin{aligned}
\mathrm{d}\chi^0 &= a^{-1}\left[-\sin(\tau)\sec(\rho)\,\mathrm{d}\tau + \cos(\tau)\sec(\rho)\tan(\rho)\,\mathrm{d}\rho\right],\\
\mathrm{d}\chi^1 &= a^{-1}\left[\sec^2(\rho)\cos(\theta_1)\,\mathrm{d}\rho - \tan(\rho)\sin(\theta_1)\,\mathrm{d}\theta_1\right],\\
&\vdots\\
\mathrm{d}\chi^{n-1} &= a^{-1}\left[\sec^2(\rho)\sin(\theta_1)\sin(\theta_2)\cdots\sin(\theta_{n-3})\sin(\phi)\,\mathrm{d}\rho\right.\\
&\qquad + \tan(\rho)\cos(\theta_1)\sin(\theta_2)\cdots\sin(\theta_{n-3})\sin(\phi)\,\mathrm{d}\theta_1\\
&\qquad + \tan(\rho)\sin(\theta_1)\cos(\theta_2)\cdots\sin(\theta_{n-3})\sin(\phi)\,\mathrm{d}\theta_2\\
&\qquad \vdots\\
&\qquad \left. + \tan(\rho)\sin(\theta_1)\sin(\theta_2)\cdots\sin(\theta_{n-3})\cos(\phi)\,\mathrm{d}\phi\right],\\
\mathrm{d}\chi^n &= a^{-1}\left[\cos(\tau)\sec(\rho)\,\mathrm{d}\tau + \sin(\tau)\sec(\rho)\tan(\rho)\,\mathrm{d}\rho\right],
\end{aligned} \tag{4.1.5}$$

and by substituting these into the metric on the embedding space (4.1.2), we find the metric induced on $\mathrm{adS}_n$ is

$$\mathrm{d}s^2 = a^{-2}\sec^2(\rho)\left(-\mathrm{d}\tau^2 + \mathrm{d}\rho^2 + \sin^2(\rho)\left\{\mathrm{d}\theta_1^2 + \sum_{i=2}^{n-3}\mathrm{d}\theta_i^2\prod_{j=1}^{i-1}\sin^2(\theta_j) + \mathrm{d}\phi^2\prod_{j=1}^{n-3}\sin^2(\theta_j)\right\}\right). \tag{4.1.6}$$

In this thesis, we are primarily interested in three- and four-dimensional anti-de Sitter space-time. The metric (4.1.6) in three dimensions reads

$$\mathrm{d}s^2 = a^{-2}\sec^2(\rho)\left[-\mathrm{d}\tau^2 + \mathrm{d}\rho^2 + \sin^2(\rho)\,\mathrm{d}\phi^2\right], \tag{4.1.7}$$

whilst in four dimensions, it is

$$\mathrm{d}s^2 = a^{-2}\sec^2(\rho)\left[-\mathrm{d}\tau^2 + \mathrm{d}\rho^2 + \sin^2(\rho)\,\mathrm{d}\theta^2 + \sin^2(\rho)\sin^2(\theta)\,\mathrm{d}\phi^2\right]. \tag{4.1.8}$$

An important limit of anti-de Sitter space is the 'zero curvature' limit, i.e. the limit in which anti-de Sitter space reduces to Minkowski space. Since the cosmological constant of anti-de Sitter space is proportional to $a^2$ (see section 4.3), and the cosmological constant

of Minkowski space is identically zero, the 'zero curvature' limit corresponds to the limit $a \to 0$. However, if one were simply to take the metric (4.1.6), the $a^{-2}$ prefactor would diverge in the $a \to 0$ limit, rendering the result meaningless. To recover flat space in the limit $a \to 0$, we have to make a minor coordinate change. The coordinates $\tau$ and $\rho$ are dimensionless. If we make them dimensionful under the transformations

$$\mathcal{T} = a^{-1}\tau, \quad \mathcal{R} = a^{-1}\rho, \tag{4.1.9}$$

where $a$ has dimensions of inverse length (and thus $\mathcal{T}$ and $\mathcal{R}$ have dimensions of length), then the metric (4.1.6) transforms to

$$\begin{aligned} \mathrm{d}s^2 &= \sec^2(a\mathcal{R}) \\ &\times \left( -\mathrm{d}\mathcal{T}^2 + \mathrm{d}\mathcal{R}^2 + a^{-2}\sin^2(a\mathcal{R}) \left\{ \mathrm{d}\theta_1^2 + \sum_{i=2}^{n-3} \mathrm{d}\theta_i^2 \prod_{j=1}^{i-1} \sin^2(\theta_j) + \mathrm{d}\phi^2 \prod_{j=1}^{n-3} \sin^2(\theta_j) \right\} \right). \end{aligned} \tag{4.1.10}$$

Now taking the limit $a \to 0$, using the facts that $\lim_{a\to 0} \sec^2(a\mathcal{R}) = 1$ and, in addition, $\lim_{a\to 0} a^{-2}\sin^2(a\mathcal{R}) = \mathcal{R}^2$, the metric (4.1.10) reduces to

$$\mathrm{d}s^2 = -\mathrm{d}\mathcal{T}^2 + \mathrm{d}\mathcal{R}^2 + \mathcal{R}^2 \left\{ \mathrm{d}\theta_1^2 + \sum_{i=2}^{n-3} \mathrm{d}\theta_i^2 \prod_{j=1}^{i-1} \sin^2(\theta_j) + \mathrm{d}\phi^2 \prod_{j=1}^{n-3} \sin^2(\theta_j) \right\}, \tag{4.1.11}$$

which is simply the Minkowski space metric in $\{\mathcal{T}, \mathcal{R}, \theta_1, \ldots, \theta_{n-3}, \phi\}$ coordinates. Therefore, flat space-time is recovered from anti-de Sitter space in the limit $a \to 0$, *provided* we make suitable coordinate transforms such that the temporal and radial coordinates have dimensions of length.

In figure 4.1, the hyperboloid corresponding to two-dimensional adS is shown embedded in three-dimensional Minkowski space-time. The inverse radius of curvature is visualised as the inverse radius of the waist of the hyperboloid. Since anti-de Sitter space-time is maximally symmetric, all points on the hyperboloid are indistinguishable; there is nothing special about any one part of the hyperboloid. Despite this, figure 4.1 seems to suggest

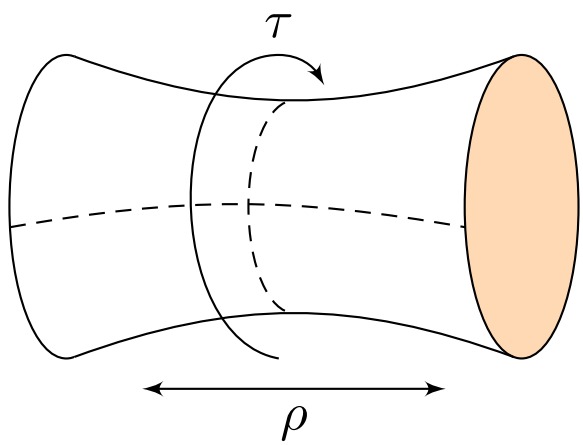


Figure 4.1: Anti-de Sitter space-time visualised as a single-sheeted hyperboloid, embedded in three-dimensional Minkowski space-time with $n-2$ angular coordinates suppressed. Figure adapted from [13].

that the waist is a unique part of the hyperboloid; however, this is a visual quirk of the embedding in Minkowski space, since one tends to interpret the hyperboloid as if it were a surface embedded in Euclidean space. We have used the line element (4.1.6) to visualise the hyperboloid in figure 4.1. In this case, the transverse sections are parameterised by the time coordinate $\tau$, whilst the radial coordinate parametrises the longitudinal sections of the hyperboloid. Additionally, the $n-2$ suppressed angular coordinates $\theta_i$ and $\phi$ are hyperspherical coordinates that label the $n-3$ angles of inclination and the azimuthal angle respectively.

An interesting feature of anti-de Sitter space is that it possesses unphysical, closed time-like curves. This is seen most easily by the coordinate choice (4.1.3), where the time coordinate is periodic with period $2\pi$, but can also be observed from the circular symmetry of the hyperboloid in figure 4.1. The existence of closed time-like curves renders anti-de Sitter space a non-physically viable choice of space-time. However, this can be remedied by moving to the covering space of anti-de Sitter, which is discussed in the next section.

## § 4.2 Conformal structure

The existence of closed time-like curves is unappealing. However, it is possible to remove the periodicity in the time coordinate by "unwrapping" the hyperboloid of anti-de Sitter and moving to the universal covering space, denoted by $\mathrm{CadS}_n$ [31, 190]. The domain of the time-like coordinate in the covering space is then $-\infty < \tau < \infty$. In figure 4.2, the Carter-Penrose diagrams for both pure anti-de Sitter and the universal covering space are shown (suppressing all but the time-like coordinate $\tau$ and the space-like coordinate $\rho$). The null rays, represented by blue lines, can reach the time-like boundary $\mathscr{I}$ in finite coordinate time. This means that neither anti-de Sitter space nor its universal covering space are globally hyperbolic space-times. Global hyperbolicity of a space-time was discussed in section 2.1 following [372], but will be outlined here for completeness. Global hyperbolicity of a space-time is equivalent to the requirement that there exists a Cauchy surface within the space-time. A Cauchy surface is defined as a closed achronal (i.e. no point on the surface is within the past or future light-cone of any other point, or equivalently, there does not exist a time-like or null geodesic that connects the two points) surface whose domain of dependence, $\mathcal{D}(\Sigma)$, is given by the full space-time. If we now apply this to the Carter-Penrose diagrams shown in figure 4.2, we can see the lack of global hyperbolicity clearly; the shaded red region is the domain of dependence $\mathcal{D}(\Sigma)$ of the surface $\Sigma$, which is clearly not the full space-time.

Furthermore, we can consider a (classical or quantum) field theory defined by a wave equation, such as the Klein-Gordon equation (2.4.3). If the space-time is globally hyperbolic, then there exists a Cauchy surface. We can therefore specify initial data (for the wave equation) on the Cauchy surface which can be uniquely propagated throughout space-time, entirely on time-like and null geodesics. In contrast, if the space-time is *not* globally hyperbolic, then there does not exist a Cauchy surface. If we consider some (non-Cauchy) hypersurface $\Sigma$, then initial data specified on the hypersurface $\Sigma$ cannot be uniquely evolved

throughout the whole space-time, but can be uniquely evolved throughout the domain of dependence $\mathcal{D}(\Sigma)$. If we apply this to (the universal covering space of) anti-de Sitter space, shown in figure 4.2, this is clear to see. If initial data is specified on the hypersurface $\Sigma$, then it can be uniquely evolved throughout its domain of dependence $\mathcal{D}(\Sigma)$ (shaded red region), but will hit its limit of evolution at the null curves (blue lines). From a field theory point of view, this lack of global hyperbolicity can be remedied, however. If one applies certain conditions on the time-like boundary, it is possible that any initial data specified on the hypersurface $\Sigma$ will have a unique evolution throughout the whole space-time, meaning the field theory will be well-defined. This will be discussed in section 4.5.

A further issue is that the boundary of anti-de Sitter space at $\rho = \pi/2$ is not actually part of the adS space-time. This can prevent the imposition of boundary conditions at the space-time boundary [205, 206]. Nevertheless, this issue can be bypassed. In order to preserve the global causal structure of anti-de Sitter space-time, it is the case that the metric of adS is everywhere conformal to the metric of some other space-time. This is in fact possible for any space-time [177]. Therefore, (C)adS must be conformally related to some other space-time; the space-time in question is the Einstein Static Universe (ESU). To see this, consider the following argument. In $n$-dimensions, the ESU can be represented by an $n$-dimensional cylinder embedded in $(n+1)$-dimensional Minkowski space [190], subject to the condition

$$\left(\varsigma^0\right)^2 + \left(\varsigma^1\right)^2 + \cdots + \left(\varsigma^{n-1}\right)^2 + \left(\varsigma^n\right)^2 = a^{-2}, \tag{4.2.1}$$

where $a^{-1}$ is the radius of the cylinder. The metric for the embedding space is given by the standard $(n+1)$-dimensional line element for Minkowski space,

$$\mathrm{d}s^2 = -\left(\mathrm{d}\varsigma^0\right)^2 + \left(\mathrm{d}\varsigma^1\right)^2 + \cdots + \left(\mathrm{d}\varsigma^{n-1}\right)^2 + \left(\mathrm{d}\varsigma^n\right)^2. \tag{4.2.2}$$

By choosing the following intrinsic dimensionless coordinates

$$\tau \in (-\infty, \infty), \quad \rho \in [0, \pi), \quad \theta_j \in [0, \pi],\ j = 1, \ldots, n-3, \quad \phi \in [0, 2\pi), \tag{4.2.3}$$

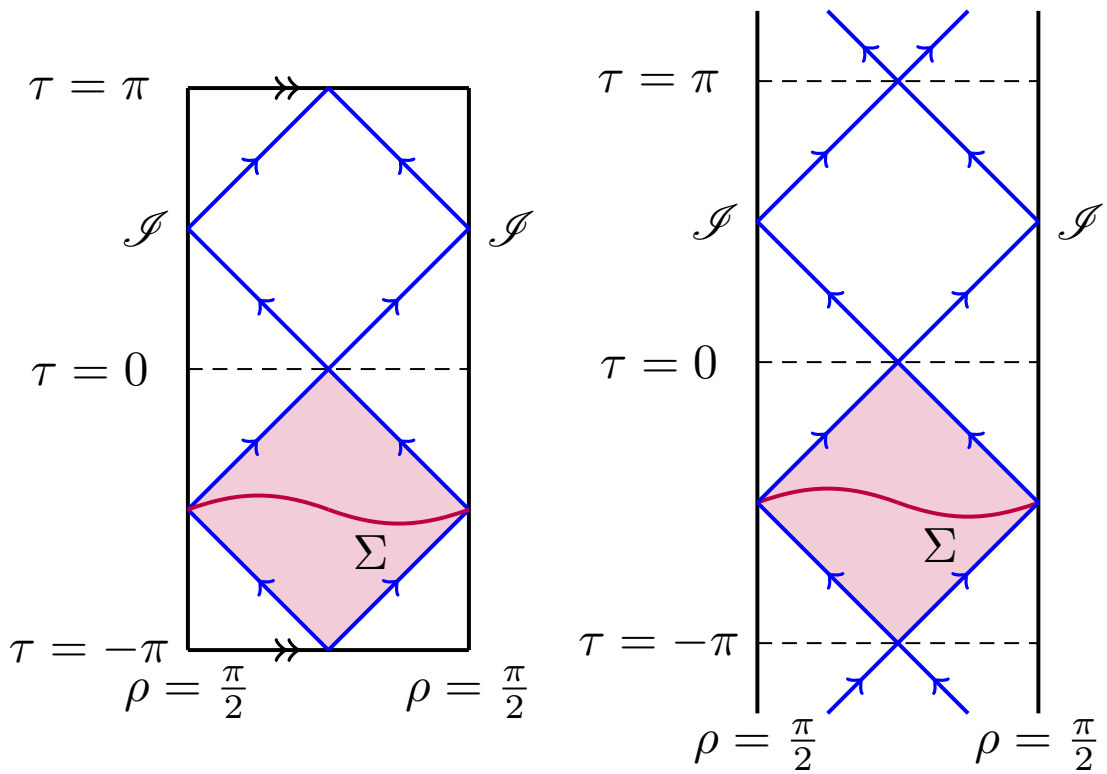


Figure 4.2: Carter-Penrose diagram of pure anti-de Sitter space-time (left) and its universal covering space (right). The time periodicity of pure-adS is shown by virtue of the horizontal lines with arrows being identified. The blue lines represent null rays, whilst the red curve is a space-like hypersurface $\Sigma$ within its domain of dependence $\mathcal{D}(\Sigma)$, which is denoted by the shaded pink region. For $\Sigma$ to be a Cauchy surface, boundary data must be specified on $\mathscr{I}$ to allow it to uniquely propagate into the future (and from the past). Figures adapted from [31].

we can write the general coordinates in the embedding space as

$$\begin{aligned}
\varsigma^0 &= a^{-1}\tau, \\
\varsigma^1 &= a^{-1}\sin(\rho)\cos(\theta_1), \\
\varsigma^2 &= a^{-1}\sin(\rho)\sin(\theta_1)\cos(\theta_2), \\
\varsigma^3 &= a^{-1}\sin(\rho)\sin(\theta_1)\sin(\theta_2)\cos(\phi), \\
&\vdots \\
\varsigma^{n-2} &= a^{-1}\sin(\rho)\sin(\theta_1)\sin(\theta_2)\cdots\sin(\theta_{n-3})\cos(\phi), \\
\varsigma^{n-1} &= a^{-1}\sin(\rho)\sin(\theta_1)\sin(\theta_2)\cdots\sin(\theta_{n-3})\sin(\phi), \\
\varsigma^{n} &= a^{-1}\cos(\rho).
\end{aligned} \tag{4.2.4}$$

By taking the derivatives, we arrive at the metric of the ESU in $n$-dimensions,

$$\mathrm{d}s^2 = a^{-2}\left(-\mathrm{d}\tau^2 + \mathrm{d}\rho^2 + \sin^2(\rho)\left\{\mathrm{d}\theta_1^2 + \sum_{i=2}^{n-3}\mathrm{d}\theta_i^2\prod_{j=1}^{i-1}\sin^2(\theta_j) + \mathrm{d}\phi^2\prod_{j=1}^{n-3}\sin^2(\theta_j)\right\}\right). \tag{4.2.5}$$

Comparing this with the line element of (C)adS (4.1.6), it is clear that the two are conformally related via the transformation

$$g_{\mu\nu}^{\mathrm{ESU}} = \Omega^2 g_{\mu\nu}^{\mathrm{adS}}, \quad \Omega^2 = \cos(\rho). \tag{4.2.6}$$

Considering the coordinate ranges of the adS radial coordinate $\rho_{\mathrm{adS}}$ (4.1.3) and ESU radial coordinate $\rho_{\mathrm{ESU}}$ (4.2.3), we see that adS is conformal to *half* of the ESU, since the coordinate ranges are

$$\rho_{\mathrm{adS}} \in [0, \pi/2), \qquad \rho_{\mathrm{ESU}} \in [0, \pi). \tag{4.2.7}$$

Furthermore, we see that not only is adS conformal to half of the ESU, but the adS boundary is also part of the ESU. Therefore, provided we alter the domains for each coordinate, we can map between the two space-times. This is particularly useful in light of the fact that the ESU *is* globally hyperbolic [190]. Being globally hyperbolic, there

exists a Cauchy surface that can be uniquely evolved throughout the space-time, so initial data can uniquely propagate through the space-time, which makes quantisation possible. Additionally, due to the mapping, the (C)adS boundary is now part of the space-time and as such, boundary conditions can be imposed without issue. The mapping of anti-de Sitter space onto the ESU is shown in figure 4.3. The fact that the boundary is included within the ESU and the ESU is globally hyperbolic make quantisation on (C)adS much more tractable, since we can first quantise on the ESU and then map to (C)adS via the mapping (4.2.6) (provided one is working with a conformally-coupled scalar field). This will be discussed in more detail in section 4.6.

## § 4.3 Maximal symmetry and the geodesic interval

A particularly appealing property of anti-de Sitter space is that it is maximally symmetric. This renders certain calculations easier to perform - see, in particular, section 4.6 and chapter 5. In section 2.1, a brief overview of maximal symmetry was presented. In this section, we extend this discussion to anti-de Sitter space and mention the important properties of anti-de Sitter space that follow from maximal symmetry.

There are many useful properties of maximally symmetric spaces. For example, as mentioned in section 2.1, the Riemann tensor can always be expressed as [341]

$$R_{\mu\nu\alpha\beta} = \frac{R}{n(n-1)}(g_{\mu\nu}g_{\alpha\beta} - g_{\mu\beta}g_{\nu\alpha}), \tag{4.3.1}$$

whilst the Ricci tensor is given by

$$R_{\mu\nu} = \mathscr{K}(n-1)g_{\mu\nu}, \tag{4.3.2}$$

where $R$ is the Ricci scalar and $\mathscr{K}$ is the radius of curvature. The radius of curvature $\mathscr{K}$ can be found (owing to its definition) by considering the embedding equation (4.1.1), from which we deduce that $\mathscr{K} = -a^2$. Using this in conjunction with the form of the Ricci

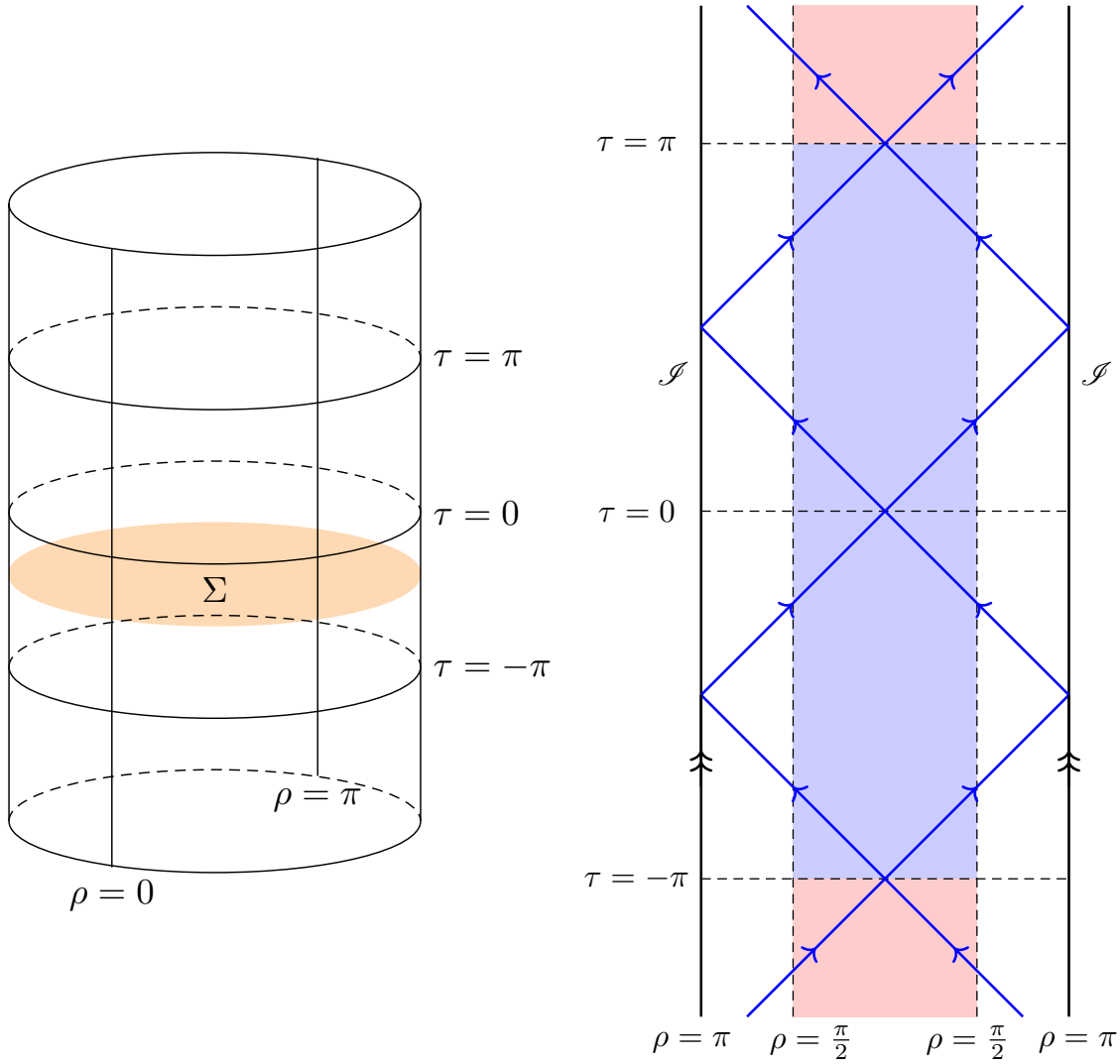


Figure 4.3: The two-dimensional ESU cylinder shown embedded in three dimensional Minkowski space, with the angular dimensions suppressed (left) and the Carter-Penrose diagram of the ESU (right). The ESU is a globally hyperbolic space-time [190], and as such, there exists a Cauchy surface $\Sigma$ that can be uniquely evolved through the ESU space-time. The Carter-Penrose diagram demonstrates the conformal mapping between the ESU and anti-de Sitter space (purple region) and the universal covering space of adS (red region). The blue lines are null rays, and the arrows on the time-like boundary $\mathscr{I}$ indicate that $\rho = \pi$ is identified. Diagrams adapted from [13].

scalar (2.1.28) for maximally symmetric spaces, we find the Ricci scalar for anti-de Sitter space is

$$R = -a^2 n(n-1), \tag{4.3.3}$$

whilst the Ricci tensor is

$$R_{\mu\nu} = -a^2(n-1)g_{\mu\nu}, \tag{4.3.4}$$

and the Riemann tensor is

$$R_{\mu\nu\alpha\beta} = -a^2(g_{\mu\nu}g_{\alpha\beta} - g_{\mu\beta}g_{\nu\alpha}). \tag{4.3.5}$$

Anti-de Sitter space is a vacuum solution to the Einstein field equations (2.2.33) [190]. We can use this fact to express the cosmological constant in terms of the (inverse) adS length scale $a$. Indeed, by contracting the vacuum Einstein equations (2.2.33) with the inverse metric tensor, we find

$$R - \frac{n}{2}R = -n\Lambda, \tag{4.3.6}$$

which rearranges to give

$$\Lambda = \frac{R(n-2)}{2n}. \tag{4.3.7}$$

Inserting the Ricci tensor (4.3.3), we therefore find the following relation for the cosmological constant:

$$\Lambda = -\frac{a^2}{2}(n-1)(n-2). \tag{4.3.8}$$

Another useful property resulting from maximal symmetry arises when considering the geodesic interval. Consider some biscalar $b(x, x')$ which depends on two space-time points $\{x, x'\}$ that are connected by a unique geodesic in the maximally symmetric space. Provided the biscalar preserves the underlying maximal symmetry, without loss of generality we may express the biscalar as

$$b(0, s), \quad \text{where} \quad s = s(x, x'), \tag{4.3.9}$$

is the *geodetic* interval separating the two space-time points. In such settings, it is true that biscalars are reducible to scalars [5], meaning that we can express the biscalar as

$$b(x, x') \to b(s). \tag{4.3.10}$$

There are instances within the literature where the related invariant distance

$$\sigma(x, x') = \frac{1}{2}[s(x, x')]^2, \tag{4.3.11}$$

is used instead. This distance is known as Synge's world function [347] - see section 2.7 for more detail. In this thesis, we are interested in the case where the points in the geodetic interval are space-like separated, since in this case Synge's world function is positive and thus the geodetic distance $s(x, x')$ is real-valued. Since anti-de Sitter space is maximally symmetric, we could just have easily chosen time-like separation without loss of generality, however in this case Synge's world function would be negative and thus the geodetic distance would be complex-valued, making calculations potentially more difficult. On anti-de Sitter space, the geodetic interval for space-like separated points is given by [4, 5, 221]

$$s(x, x') = a^{-1} \arccos\left(\frac{\cos(\tau - \tau') - \sin(\rho)\sin(\rho')\cos(\gamma_n)}{\cos(\rho)\cos(\rho')}\right), \tag{4.3.12a}$$

where $\gamma_n$ is the angular separation on the $(n-2)$-dimensional sphere. In this thesis, we are only interested in three- and four-dimensional adS. In these cases, the angular separation function is given by

$$\cos(\gamma_3) = \cos\big(\phi - \phi'\big), \tag{4.3.12b}$$

$$\cos(\gamma_4) = \cos(\theta)\cos\big(\theta'\big) + \sin(\theta)\sin\big(\theta'\big)\cos\big(\phi - \phi'\big). \tag{4.3.12c}$$

From these expressions, we can explicitly write down the functional form of the Synge's world function as [221]

$$\sigma(x, x') = \frac{1}{2a^2}\left[\arccos\left(\frac{\cos(\tau - \tau') - \sin(\rho)\sin(\rho')\cos(\gamma_n)}{\cos(\rho)\cos(\rho')}\right)\right]^2, \tag{4.3.13}$$

where the $\cos(\gamma_n)$ terms are given in equations (4.3.12b) and (4.3.12c). We can also explicitly write down the van Vleck-Morette determinant (see section 2.7 for more details) in $n$-dimensional anti-de Sitter space using the world function (4.3.13) as [5, 221]

$$\Delta(x, x') = \left[a\sqrt{2\sigma}\csc\left(a\sqrt{2\sigma}\right)\right]^{n-1}, \tag{4.3.14}$$

which agrees with the result in [4] for $n = 4$. In section 5.1, we make extensive use of a third, invariant biscalar which is related to the geodetic distance $s(x, x')$ as

$$Z(x, x') = \cos\big(a\, s(x, x')\big). \tag{4.3.15}$$

We use the quantities defined in this section - the geodetic distance (4.3.12), Synge's world function (4.3.13), the van Vleck-Morette determinant (4.3.14) and the biscalar (4.3.15) - extensively in chapter 5 to compute various expectation values of the scalar field and stress-energy tensor.

## § 4.4 Anti-de Sitter space in rotating coordinates and vielbeins

Of interest to us in this thesis is the study of rigidly rotating quantum states in anti-de Sitter space-time, and in particular expectation values constructed in such states. It is therefore necessary to introduce some theory regarding scalar fields in a rigidly rotating quantum state on anti-de Sitter space. In this section we focus on the classical aspects, in particular the geometric structure. In contrast, in section 4.7, the quantum aspects are discussed; we first set out the motivation for studying rigidly rotating states before discussing the states themselves. For simplicity, we only present results for three- and four-dimensional anti-de Sitter space.

In order to facilitate the study of rigidly rotating states on anti-de Sitter space, it is necessary to introduce co-rotating coordinates

$$\widetilde{\tau} = \tau, \quad \widetilde{\rho} = \rho, \quad \widetilde{\phi} = \phi - \Omega\tau, \qquad \mathrm{adS}_3, \tag{4.4.1a}$$

$$\widetilde{\tau} = \tau, \quad \widetilde{\rho} = \rho, \quad \widetilde{\theta} = \theta, \quad \widetilde{\phi} = \phi - \Omega\tau, \qquad \text{adS}_4, \tag{4.4.1b}$$

where the rotation is rigid and occurs only in the azimuthal coordinate, with constant angular speed $\Omega$. For brevity, here and henceforth the tilde on the new co-rotating coordinates will be dropped. While this makes it more difficult to distinguish between the co-rotating and nonrotating coordinates, context will instead be used to distinguish between the two. Taking the new co-rotating coordinates, we can substitute these into the corresponding line elements for three- (4.1.7) and four-dimensional (4.1.8) anti-de Sitter space to yield the metrics in co-rotating coordinates as

$$\mathrm{d}s^2 = a^{-2}\sec^2(\rho)\left\{-\left[1-\Omega^2\sin^2(\rho)\right]\mathrm{d}\tau^2 + \mathrm{d}\rho^2 + 2\Omega\sin^2(\rho)\,\mathrm{d}\tau\,\mathrm{d}\phi + \sin^2(\rho)\,\mathrm{d}\phi^2\right\}, \tag{4.4.2}$$

for three-dimensional anti-de Sitter space, and

$$\begin{aligned}\mathrm{d}s^2 = a^{-2}\sec^2(\rho)\Big\{&-\left[1-\Omega^2\sin^2(\rho)\sin^2(\theta)\right]\mathrm{d}\tau^2 + \mathrm{d}\rho^2 \\ &+2\Omega\sin^2(\rho)\sin^2(\theta)\,\mathrm{d}\tau\,\mathrm{d}\phi + \sin^2(\rho)\,\mathrm{d}\theta^2 + \sin^2(\rho)\sin^2(\theta)\,\mathrm{d}\phi^2\Big\},\end{aligned} \tag{4.4.3}$$

for four-dimensional anti-de Sitter space. The metrics in co-rotating coordinates both have a Lorentz factor-type term in the time-like coordinate. For later convenience, we define these as

$$\Gamma_{(3)} \coloneqq \left[1-\Omega^2\sin^2(\rho)\right]^{-1/2}, \tag{4.4.4a}$$

$$\Gamma_{(4)} \coloneqq \left[1-\Omega^2\sin^2(\rho)\sin^2(\theta)\right]^{-1/2}. \tag{4.4.4b}$$

We will henceforth refer to metrics in co-rotating coordinates as rotating[2] metrics, for example, equation (4.4.3) is the four-dimensional rotating anti-de Sitter space metric. In the interest of clarity therefore, we will refer to the line elements (4.1.7) and (4.1.8) as three- and four-dimensional, nonrotating anti-de Sitter space, respectively.

[2]It is important to note that by choosing this nomenclature, we are not saying that the space-time itself is rotating, since this is a misnomer; the nomenclature is simply introduced in the interest of brevity.

There is an important point that needs mentioning with regards to the rigidly rotating coordinate mapping (4.4.1). In analogy with the flat space Lorentz factor

$$\gamma = \frac{1}{\sqrt{1 - \frac{v^2}{c^2}}}, \tag{4.4.5}$$

which diverges as the velocity $v$ approaches the speed of light $c$, the Lorentz factors (4.4.4) also diverge when, in three and four dimensions respectively,

$$\Omega^2 \sin^2(\rho) = 1, \tag{4.4.6a}$$

$$\Omega^2 \sin^2(\rho) \sin^2(\theta) = 1. \tag{4.4.6b}$$

This is referred to as the *speed-of-light surface* (oft abbreviated SOL in the literature), and plays an important role when considering rotational quantum states on anti-de Sitter space. Throughout the remainder of this thesis, we always assume that we never breach the speed-of-light surface, i.e.

$$\Omega^2 \sin^2(\rho) \ngeq 1, \tag{4.4.7a}$$

$$\Omega^2 \sin^2(\rho) \sin^2(\theta) \ngeq 1. \tag{4.4.7b}$$

Using the fact that $\sin^2(\chi) \in [0, 1] \quad \forall \chi$, the condition for the absence of the speed-of-light surface reduces to (in both cases)

$$\Omega \ngeq 1. \tag{4.4.8}$$

We therefore only consider the case when the angular rotation speed is in the range $0 \leq \Omega < 1$. In the above analysis, the speed-of-light surface was defined in analogy with the divergence of the Lorentz factor in flat space; in general, it is defined as the surface outside which rigidly-rotating observers are rotating at speeds greater than the speed of light. In practice, the speed-of-light surface is defined by the requirement that the coefficient of the time-like component of the metric is zero [234]. This was discussed in more detail in section 2.3.3.

In chapter 5, along with computing quantum field theory expectation values of the stress-energy tensors, we compute relativistic kinetic theory stress-energy tensors by performing momentum space integrals in some orthonormal frame. The general theory of RKT, as well as the concept of orthonormal frames, was discussed in detail in section 2.3. In order to perform the explicit computations of the momentum space integrals in chapter 5, we must make a suitable choice of frame, characterised by vielbein vectors and corresponding one-forms. Recall that throughout this thesis, indices in brackets refer to frame vectors, which are embedded in Minkowski space with metric $\eta_{(a)(b)}$.

The choice of frame is not necessarily unique; provided it is orthonormal, i.e. subject to the condition

$$g_{\mu\nu} e^{\mu}_{(a)} e^{\nu}_{(b)} = \eta_{(a)(b)}, \tag{4.4.9}$$

it is a perfectly valid choice. Similarly, the corresponding one-forms are then subject to the condition

$$g^{\mu\nu} w^{(a)}_{\mu} w^{(b)}_{\nu} = \eta^{(a)(b)}, \tag{4.4.10}$$

and are found by contracting with the space-time and Minkowski metric:

$$w^{(a)}_{\mu} = g_{\mu\nu} \eta^{(a)(b)} e^{\nu}_{(b)}. \tag{4.4.11}$$

Since the choice of frame is not unique, we must make some initial assumptions about the form of the vielbein vector fields. This is easier for the nonrotating space-times, since by orthonormality, the metric tensor can be reconstructed as

$$\mathrm{d}s^2 = g_{\mu\nu}\, \mathrm{d}x^{\mu}\, \mathrm{d}x^{\nu} = \eta_{(a)(b)} w^{(a)}_{\mu} w^{(b)}_{\nu}\, \mathrm{d}x^{\mu}\, \mathrm{d}x^{\nu}, \tag{4.4.12}$$

and thus the vielbein frame one-forms are identified by comparing, component by component, with the metric tensor. In four dimensions, the set of basis one-forms are therefore

$$w^{(\tau)}_{\mu}\, \mathrm{d}x^{\mu} = a^{-1} \sec(\rho)\, \mathrm{d}\tau, \quad w^{(\rho)}_{\mu}\, \mathrm{d}x^{\mu} = a^{-1} \sec(\rho)\, \mathrm{d}\rho, \quad w^{(\theta)}_{\mu}\, \mathrm{d}x^{\mu} = a^{-1} \cot(\rho)\, \mathrm{d}\theta,$$
$$w^{(\phi)}_{\mu}\, \mathrm{d}x^{\mu} = a^{-1} \tan(\rho) \sin(\theta)\, \mathrm{d}\phi, \tag{4.4.13}$$

which have the corresponding vector fields

$$e^{\mu}_{(\tau)}\partial_\mu = a\cos(\rho)\partial_\tau, \quad e^{\mu}_{(\rho)}\partial_\mu = a\cos(\rho)\partial_\rho, \quad e^{\mu}_{(\theta)}\partial_\mu = a\cot(\rho)\partial_\theta,$$
$$e^{\mu}_{(\phi)}\partial_\mu = a\cot(\rho)\csc(\theta)\partial_\phi. \quad (4.4.14)$$

This is our *vierbein* for nonrotating, four-dimensional anti-de Sitter space-time. In three dimensions, we have a similar story, with the basis one-forms

$$\mathfrak{w}^{(\tau)}_{\mu}\,\mathrm{d}x^\mu = a^{-1}\sec(\rho)\,\mathrm{d}\tau, \quad \mathfrak{w}^{(\rho)}_{\mu}\,\mathrm{d}x^\mu = a^{-1}\sec(\rho)\,\mathrm{d}\rho, \quad \mathfrak{w}^{(\phi)}_{\mu}\,\mathrm{d}x^\mu = a^{-1}\tan(\rho)\,\mathrm{d}\phi, \quad (4.4.15)$$

and corresponding vector fields

$$\mathfrak{e}^{\mu}_{(\tau)}\partial_\mu = a\cos(\rho)\partial_\tau, \quad \mathfrak{e}^{\mu}_{(\rho)}\partial_\mu = a\cos(\rho)\partial_\rho, \quad \mathfrak{e}^{\mu}_{(\phi)}\partial_\mu = a\cot(\rho)\sin(\rho)\partial_\phi, \quad (4.4.16)$$

providing a *dreibein* for nonrotating, three-dimensional anti-de Sitter space-time.

It is not so simple when we switch to rotating anti-de Sitter space. Since we require the frame to be rigidly rotating, we make the following ansatz for the vierbein vector fields:

$$\mathring{e}^{\mu}_{(\tau)}\partial_\mu = \mathscr{A}(\rho,\theta,\Omega)\partial_\tau, \quad \mathring{e}^{\mu}_{(\rho)}\partial_\mu = \mathscr{B}(\rho,\theta,\Omega)\partial_\rho, \quad \mathring{e}^{\mu}_{(\theta)}\partial_\mu = \mathscr{C}(\rho,\theta,\Omega)\partial_\theta,$$
$$\mathring{e}^{\mu}_{(\phi)}\partial_\mu = \mathscr{D}(\rho,\theta,\Omega)\partial_\tau + \mathscr{E}(\rho,\theta,\Omega)\partial_\phi. \quad (4.4.17)$$

This choice of ansatz then corresponds to a frame that is rigidly rotating in the azimuthal coordinate $\phi$ with angular speed $\Omega$. To find constraints on the unknown functions $\mathscr{A}, \mathscr{B}, \mathscr{C}, \mathscr{D}$ and $\mathscr{E}$, we can use the condition (4.4.9). For example, taking the $(\tau)$-vector field and contracting with the rotating adS metric (4.4.3), we have

$$g_{\mu\nu}\mathring{e}^{\mu}_{(\tau)}\mathring{e}^{\nu}_{(\tau)} = \eta_{(\tau)(\tau)} = -1, \quad \Longrightarrow \quad [\mathring{e}^{\tau}_{(\tau)}]^2 = -\frac{1}{g_{\tau\tau}} \quad \Longrightarrow \quad \mathscr{A} = [-g_{\tau\tau}]^{-1/2}, \quad (4.4.18)$$

after dropping the functional dependence of $\mathscr{A}$ for brevity, which will be continued henceforth. In a similar fashion, we find

$$g_{\mu\nu}\mathring{e}^{\mu}_{(\rho)}\mathring{e}^{\nu}_{(\rho)} = \eta_{(\rho)(\rho)} \quad \Longrightarrow \quad \mathscr{B} = [g_{\rho\rho}]^{-1/2},$$

$$g_{\mu\nu}\mathring{e}^{\mu}_{(\theta)}\mathring{e}^{\nu}_{(\theta)} = \eta_{(\theta)(\theta)} \qquad \Longrightarrow \qquad \mathscr{C} = [g_{\theta\theta}]^{-1/2}. \tag{4.4.19}$$

Note that at any point where there is a squareroot, we are required to make a choice of sign. Since either is valid, without loss of generality, we choose the positive squareroot. The final vierbein vector field, $\mathring{e}^{\bullet}_{(\phi)}$, is not as simple as the previous three due to it having components in both the $\tau$ and $\phi$ slots, and thus having two unknown functions $\mathscr{D}$ and $\mathscr{E}$. This means that we require two equations to determine both $\mathscr{D}$ and $\mathscr{E}$. The first is

$$\begin{aligned} &g_{\mu\nu}\mathring{e}^{\mu}_{(\phi)}\mathring{e}^{\nu}_{(\phi)} = \eta_{(\phi)(\phi)} = 1 \qquad \Longleftrightarrow \\ &g_{\tau\tau}\mathring{e}^{\tau}_{(\phi)}\mathring{e}^{\tau}_{(\phi)} + 2g_{\tau\phi}\mathring{e}^{\tau}_{(\phi)}\mathring{e}^{\phi}_{(\phi)} + g_{\phi\phi}\mathring{e}^{\phi}_{(\phi)}\mathring{e}^{\phi}_{(\phi)} = 1, \end{aligned} \tag{4.4.20}$$

and then substituting in the ansatz (4.4.17), we have

$$-a^{-2}\sec^2(\rho)\Gamma^{-2}_{(4)}\mathscr{D}^2 + 2a^{-2}\Omega\tan^2(\rho)\sin^2(\theta)\mathscr{D}\mathscr{E} + a^{-2}\tan^2(\rho)\sin^2(\theta)\mathscr{E}^2 = 1. \tag{4.4.21}$$

The second equation is found by taking advantage of the orthonormality of the vierbein basis, i.e.

$$g_{\mu\nu}\mathring{e}^{\mu}_{(\tau)}\mathring{e}^{\nu}_{(\phi)} = \eta_{(\tau)(\phi)} = 0. \tag{4.4.22}$$

Performing the contraction over space-time indices, we have

$$g_{\tau\tau}\mathring{e}^{\tau}_{(\tau)}\mathring{e}^{\tau}_{(\phi)} + g_{\tau\phi}\mathring{e}^{\tau}_{(\tau)}\mathring{e}^{\phi}_{(\phi)} = 0, \tag{4.4.23}$$

and then substituting in the metric components and vierbein vector fields, we find

$$-a^{-2}\sec^2(\rho)\Gamma^{-2}_{(4)}\mathscr{D} + a^{-2}\Omega\tan^2(\rho)\sin^2(\theta)\mathscr{E} = 0 \qquad \Longrightarrow \qquad \mathscr{D} = \Gamma^{2}_{(4)}\Omega\sin^2(\rho)\sin^2(\theta)\mathscr{E}. \tag{4.4.24}$$

Finally, by substituting equation (4.4.24) into equation (4.4.21) and simplifying, the following functional form for $\mathscr{E}$ is yielded:

$$\mathscr{E} = a\Gamma^{-1}_{(4)}\cot(\rho)\csc(\theta), \tag{4.4.25}$$

from which, we find the functional form of $\mathscr{D}$ is

$$\mathscr{D} = a\Gamma_{(4)}\,\Omega\cos(\rho)\sin(\rho)\sin(\theta). \tag{4.4.26}$$

Combining all of the above, and simplifying factors where possible, we therefore have the vierbein basis

$$\mathring{e}^{\mu}_{(\tau)}\partial_\mu = a\Gamma_{(4)}\cos(\rho)\partial_\tau, \quad \mathring{e}^{\mu}_{(\rho)}\partial_\mu = a\cos(\rho)\partial_\rho, \quad \mathring{e}^{\mu}_{(\theta)}\partial_\mu = a\cot\rho\,\partial_\theta,$$
$$\mathring{e}^{\mu}_{(\phi)}\partial_\mu = a\Gamma_{(4)}\cos(\rho)\sin(\rho)\sin(\theta)\left[\Omega\,\partial_\tau + \Gamma^{-2}_{(4)}\csc^2(\rho)\csc^2(\theta)\partial_\phi\right], \quad (4.4.27)$$

for four-dimensional rotating anti-de Sitter space. By using the relation (4.4.11), the basis can be inverted to find the corresponding one-forms, which are

$$\mathring{w}^{(\tau)}_{\mu}\,\mathrm{d}x^\mu = a^{-1}\Gamma^{-1}_{(4)}\sec(\rho)\left[\mathrm{d}\tau - \Omega\Gamma^2_{(4)}\sin^2(\rho)\sin^2(\theta)\,\mathrm{d}\phi\right], \quad \mathring{w}^{(\rho)}_{\mu}\,\mathrm{d}x^\mu = a^{-1}\sec(\rho)\,\mathrm{d}\rho,$$
$$\mathring{w}^{(\theta)}_{\mu}\,\mathrm{d}x^\mu = a^{-1}\tan(\rho)\,\mathrm{d}\theta, \quad \mathring{w}^{(\phi)}_{\mu}\,\mathrm{d}x^\mu = a^{-1}\Gamma_{(4)}\tan(\rho)\sin(\theta)\,\mathrm{d}\phi. \quad (4.4.28)$$

Following the same procedure as for the vierbein above, we find the following dreibein basis for three-dimensional rotating anti-de Sitter space

$$\mathring{\mathfrak{e}}^{\mu}_{(\tau)}\partial_\mu = a\Gamma_{(3)}\cos(\rho)\partial_\tau, \quad \mathring{\mathfrak{e}}^{\mu}_{(\rho)}\partial_\mu = a\cos(\rho)\partial_\rho,$$
$$\mathring{\mathfrak{e}}^{\mu}_{(\phi)}\partial_\mu = a\Gamma_{(3)}\cos(\rho)\sin(\rho)\left[\Omega\partial_\tau + \Gamma^{-2}_{(3)}\csc^2(\rho)\partial_\phi\right], \quad (4.4.29)$$

with corresponding one-forms

$$\mathring{\mathfrak{w}}^{(\tau)}_{\mu}\,\mathrm{d}x^\mu = a^{-1}\Gamma^{-1}_{(3)}\sec(\rho)\left[\mathrm{d}\tau - \Omega\Gamma^2_{(3)}\sin^2(\rho)\,\mathrm{d}\phi\right], \quad \mathring{\mathfrak{w}}^{(\rho)}_{\mu}\,\mathrm{d}x^\mu = a^{-1}\sec(\rho)\,\mathrm{d}\rho,$$
$$\mathring{\mathfrak{w}}^{(\phi)}_{\mu}\,\mathrm{d}x^\mu = a^{-1}\Gamma_{(3)}\tan(\rho)\,\mathrm{d}\phi. \quad (4.4.30)$$

## § 4.5 Boundary conditions

The lack of global hyperbolicity of both anti-de Sitter and its global covering space necessitate the imposition of boundary conditions at the time-like boundary $\mathscr{I}$ in order that any quantum field theory on these spaces be both physically meaningful and well-posed [31, 34, 42, 163, 205, 206, 372].

Quantisation on anti-de Sitter space was first discussed in [31] (see section 4.6 for more detail) for a massless scalar field conformally coupled to the ESU subject to *transparent* or *reflective* boundary conditions at the anti-de Sitter space boundary, which lies within the ESU (see section 4.2 for more details). Figure 4.4 shows the Carter-Penrose diagram for the ESU with the coloured curves representing propagating field modes subject to different boundary conditions. In particular, the Carter-Penrose diagram on the left (of figure 4.4) depicts field modes that are subject to transparent boundary conditions; this is where the field modes are permitted to pass beyond the anti-de Sitter space boundary at $\rho = \pi/2$ before continuing around the ESU cylinder, reappearing at the other side. In contrast, the two reflective cases (right of figure 4.4) - *Dirichlet* boundary conditions and *Neumann* boundary conditions - are such that the field modes are entirely contained within the anti-de Sitter space and are not permitted to pass through the boundary, and instead 'reflect back', hence the name. The reflective boundary conditions take their usual definitions; when Dirichlet boundary conditions are applied, the field modes must be zero at the space-time boundary, and when Neumann boundary conditions are applied, the normal derivative of the field modes at the boundary must be zero. Note that these are for the field modes defined on the ESU; the corresponding mathematical interpretation for the conformal field modes on (C)adS is much more involved, and not particularly illuminating [31]. The reflective boundary conditions, therefore, amount to requiring that '*there is no net flux across [the anti-de Sitter space boundary]*' [31].

In this thesis, we do not concern ourselves with canonical quantisation and field mode decomposition; instead, to fully specify a QFT, we construct a Hadamard Green function. To that end, we require an alternative way of thinking about boundary conditions. Instead of considering the behaviour of the field modes, we consider the behaviour of the Hadamard Green function in certain limits (e.g. as the space-time boundary is approached), and by exploiting either the method of images or by decomposing the Hadamard Green function into its short-distance singularity structure and comparing with the Hadamard form [5, 31].

This is discussed in more detail when constructing the Hadamard Green function in section 4.6.

There are, of course, other boundary conditions that can be applied to the scalar field modes at the time-like boundary. One such choice that has gained some attention in recent times is that of Robin (or mixed) boundary conditions, first posed in [206] (on anti-de Sitter space) as a linear combination of Dirichlet and Neumann boundary conditions, parameterised by a Robin parameter. Recent studies in quantum scalar field theory on anti-de Sitter space imposing Robin boundary conditions have focussed on computing expectation values of the vacuum polarisation [268, 274] and the stress-energy tensor [266, 275], charge superradiance [229], and Unruh-DeWitt detectors [302, 303] amongst others. There are many other different, valid boundary conditions that can be applied to the quantum field modes, which all give rise to a substantial set of quantum states that can be studied on anti-de Sitter space backgrounds. See, for example, [92, 93, 95, 96, 102, 163]. In this thesis, we are only interested in the boundary conditions first set out in [31], namely Dirichlet, Neumann and transparent boundary conditions.

## § 4.6 Quantisation

Quantisation on anti-de Sitter space has been studied in great depth since the late 1970s, initiated for both massive and massless scalar fields conformally coupled to four-dimensional anti-de Sitter space [31]. Recent advances have been made in performing the quantisation procedure for massive scalar fields with general coupling to $n$-dimensional anti-de Sitter space [221], and for Dirac fermion fields minimally coupled [89] or more generally coupled [13, 165] to anti-de Sitter space. There has been substantial work quantising (charged and uncharged) scalar fields with different boundary conditions on anti-de Sitter space either by mode construction techniques [55, 266, 267] or Hadamard renormalisation [93, 95, 275], as well as more rigorous work [57, 91, 96]. Due to its central role in the adS/CFT

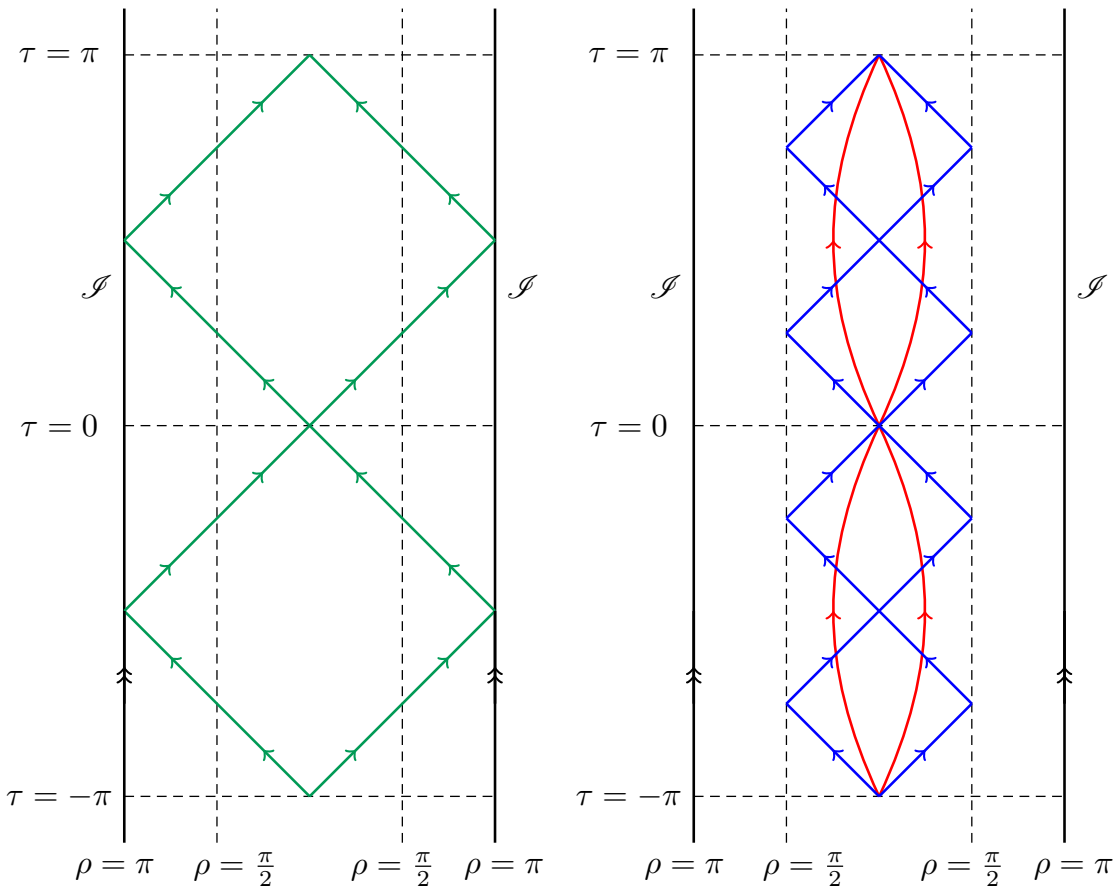


Figure 4.4: Carter-Penrose diagrams of the transparent (left) and reflective (right) boundary conditions applied to anti-de Sitter space, mapped onto the ESU. The green and blue lines are null geodesics, whilst the red lines are time-like geodesics. (C)adS is the region contained within the dashed lines at $\rho = \pi/2$, and the vertical lines with arrows are identified. Figures adapted from [13].

correspondence, field quantisation on anti-de Sitter space has received much attention in the literature, and the references above are certainly not exhaustive.

The focus of this thesis is not on the construction of scalar or fermionic quantum field theories on anti-de Sitter space, but rather the construction (chapter 5) and subsequent use (part III) of expectation values performed in states on anti-de Sitter space. As such, not much detail will be included in this section; instead, a brief overview of the quantisation procedure will be presented in the case of a massless, conformally-coupled quantum scalar field, following [31], and the general procedure outlined in section 2.6.1.

We start by defining the action for a massless, real quantum scalar field $\Phi$ conformally-coupled to $\mathrm{adS}_n$ as

$$\mathcal{S}[\Phi, g] = -\frac{1}{2}\int \mathrm{d}^n x\sqrt{-g}(g^{\mu\nu}\Phi_{;\mu}\Phi_{;\nu} + \xi_c R\Phi^2), \tag{4.6.1}$$

where $g$ is the determinant of the metric,

$$g \coloneqq \det g_{\mu\nu}, \tag{4.6.2}$$

with $\xi_c$ being the conformal coupling constant between the scalar field and classical gravitational field, defined in $n$ dimensions as

$$\xi_c = \frac{n-2}{4(n-1)}, \tag{4.6.3}$$

and $R$ denotes the Ricci scalar curvature of the classical background space-time. By varying the action (4.6.1) with respect to the field, we find the field equation of motion is given by the curved space-time Klein-Gordon equation,

$$\left(-\Box_g + \xi_c R\right)\Phi(x) = 0, \tag{4.6.4}$$

where $\Box_g$ is the curved space-time d'Alembertian operator, defined by

$$\Box_g\Phi(x) = \frac{1}{\sqrt{-g}}\left(\sqrt{-g}\, g^{\mu\nu}\Phi_{,\nu}\right)_{,\mu}. \tag{4.6.5}$$

In the case of anti-de Sitter space using the coordinate chart (4.1.3) and metric (4.1.6), it is given as [220]

$$\Box_g \Phi(x) = -a^2 \cot^2(\rho) \left\{ \sin^2(\rho)\partial_\tau^2 - (n-2)\tan(\rho)\partial_\rho^2 - (n-2)\sum_{j=1}^{n-3} \cot(\theta_j)\partial_{\theta_j} \right.$$
$$\left. - \sum_{j=1}^{n-3}\prod_{p=1}^{j-1} \csc^2(\theta_p) - \prod_{j=1}^{n-3} \csc^2(\theta_j)\partial_\phi^2 \right\} \Phi(x). \quad (4.6.6)$$

Recall that, as anti-de Sitter space and its universal covering space are not globally hyperbolic, Cauchy data can not be uniquely evolved throughout the space-time. This is due to the natural time-like boundary. We have shown in section 4.2 that mapping to the ESU bypasses the issue of global hyperbolicity, and in section 4.5 we have discussed that the imposition of boundary conditions upon the adS boundary via the conformal mapping (4.2.6) between the ESU and (C)adS renders Cauchy data uniquely evolvable on anti-de Sitter space. In section 2.6.1, the necessity of uniquely evolvable Cauchy data (and thus a Cauchy surface) for the existence of meaningful quantum field theories is discussed in a little more detail. The upshot here, and the argument of [31], is that it is a valid procedure to first quantise the field on the ESU and then use the conformal mapping (4.2.6) to map back to anti-de Sitter space to yield a physically viable and acceptable quantum field theory. The reason this holds is that the Klein-Gordon equation (4.6.4) is invariant under conformal mappings provided the field is assigned a conformal weight of $-1$. That is to say,

$$\Phi^{\mathrm{ESU}} = \Omega^{-1}\Phi^{\mathrm{adS}}, \quad (4.6.7)$$

so that if $\Phi^{\mathrm{adS}}$ is a solution to the Klein-Gordon equation in anti-de Sitter space, then $\Phi^{\mathrm{ESU}}$ is a solution to the Klein-Gordon equation on the appropriate half of the ESU, satisfying the equation

$$\left(-\Box_g^{\mathrm{ESU}} + \xi_c R^{\mathrm{ESU}}\right)\Phi^{\mathrm{ESU}}(x) = 0. \quad (4.6.8)$$

Therefore, to continue the canonical quantisation procedure of fields in anti-de Sitter space, one would follow the general canonical quantisation procedure (using field modes) for fields

in the ESU (as outlined in section 2.6.1), and then use the conformal mapping (4.2.6), (4.6.7) to map the quantised fields back onto anti-de Sitter space. As discussed at the start of this section, the canonical quantisation procedure on anti-de Sitter space has had much attention in the literature recently. We do not deal with the canonical quantisation procedure of fields in anti-de Sitter space in this thesis, and we instead refer the reader to the many citations included at the start of this section.

However, as already discussed in sections 1.1 and 2.5, we can fully specify a quantum field theory by constructing a Hadamard Green function. For this reason, we include the construction of the Hadamard Green function on anti-de Sitter space; it is also extensively used in chapter 5. We start by exploiting the maximal symmetry of anti-de Sitter space to construct the Hadamard Green function, before using the conformal mapping (4.2.6), (4.6.7) to construct the corresponding Hadamard Green function on the ESU, given by the mapping

$$G^{(1)}_{\mathrm{adS}}(x,x') = \Omega(x)\Omega(x')G^{(1)}_{\mathrm{ESU}}(x,x'). \tag{4.6.9}$$

This is necessary since, as outlined in [31], when transparent boundary conditions are applied to the field, there is energy leakage outside the space-time, which is considered unphysical. To remedy this, reflective boundary conditions are instead applied; however, since the boundary $\rho = \pi/2$ is not part of the anti-de Sitter space-time, and the Hadamard Green function is not valid there, the reflective boundary conditions can only be applied to the ESU Hadamard Green function. To that end, after constructing the Hadamard Green function on anti-de Sitter space and mapping to the Hadamard Green function on the ESU (4.6.9), we apply the boundary conditions (which fixes constants later on in the process, see discussion below equation (4.6.18)) to the ESU Hadamard Green function before mapping this back to the anti-de Sitter space Hadamard Green function. This is outlined as a flowchart in figure 4.5.

Due to the underlying maximal symmetry of anti-de Sitter space, as shown in section 4.3 any biscalar depending on two uniquely, geodesically-connected space-time points can be

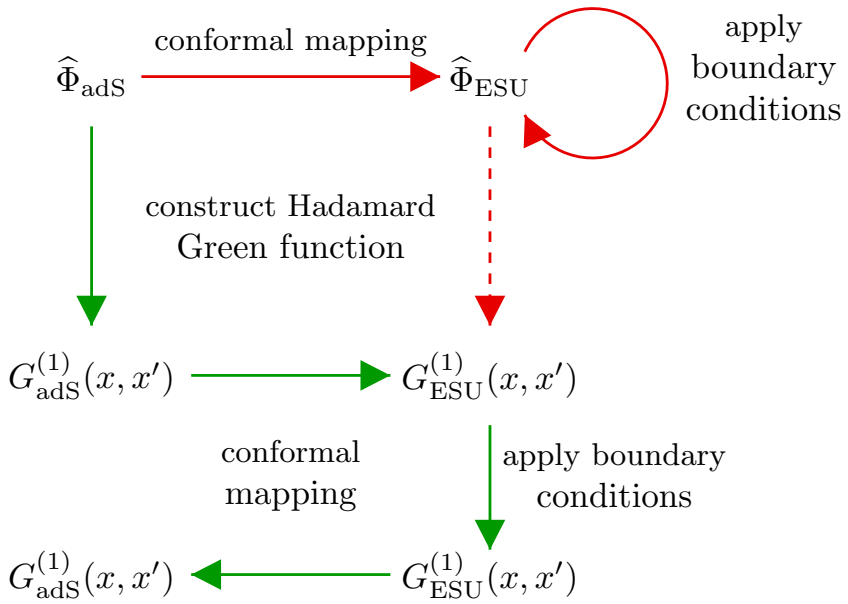


Figure 4.5: Flowchart for the conformal mapping procedure between anti-de Sitter space and the ESU, in order to construct the Hadamard Green function of a quantum scalar field on anti-de Sitter space with suitable boundary conditions applied. There are two possible paths: red and green. The red path relies on mapping the field in anti-de Sitter space to the ESU, applying boundary conditions to the field in the ESU and constructing the Hadamard Green function of the ESU from the field. The other path, the green path, is a more common procedure. One starts by constructing the Hadamard Green function of anti-de Sitter space (exploiting maximal symmetry), before mapping this to the Hadamard Green function of the ESU, applying suitable boundary conditions to the ESU Hadamard Green function before mapping back to the Hadamard Green function of anti-de Sitter space (which now has correct boundary behaviour).

expressed as a scalar. Using this, the Hadamard Green function (2.5.4) can be expressed as a function of the geodetic interval $s(x, x')$ (4.3.12), and hence we can write

$$G^{(1)}(x, x') = G^{(1)}(s(x, x')) = f(Z(x, x')) = f(Z), \tag{4.6.10}$$

where $Z(x, x')$ (4.3.15) is a biscalar depending on the two geodesically-connected space-time points. The Hadamard Green function is a homogeneous solution to the curved space-time Klein-Gordon equation

$$(-\Box_g + \xi_c R)\, G^{(1)}(x, x') = 0. \tag{4.6.11}$$

By exploiting the maximal symmetry of anti-de Sitter space, we can rewrite the Klein-Gordon equation as:

$$\left[-\frac{\mathrm{d}^2}{\mathrm{d}s^2} + a(1-n)\cot(as)\frac{\mathrm{d}}{\mathrm{d}s} + \xi_c R\right] G^{(1)}(s) = 0, \tag{4.6.12}$$

and by making the change of variables (justified by equation (4.6.10)) [5]

$$\widetilde{Z} = \cos^2(as/2), \tag{4.6.13}$$

we have the hypergeometric equation

$$\left[\widetilde{Z}(1-\widetilde{Z})\frac{\mathrm{d}^2}{\mathrm{d}\widetilde{Z}^2} + \left\{\mathfrak{z}_3 - (\mathfrak{z}_1 + \mathfrak{z}_2 + 1)\,\widetilde{Z}\right\}\frac{\mathrm{d}}{\mathrm{d}\widetilde{Z}} - \mathfrak{z}_1\mathfrak{z}_2\right] f(\widetilde{Z}) = 0, \tag{4.6.14}$$

where the constants $\mathfrak{z}_i$ depend on the number of space-time dimensions and are given by [5]

$$\mathfrak{z}_1 = \frac{n}{2}, \qquad \mathfrak{z}_2 = \frac{n-2}{2}, \qquad \mathfrak{z}_3 = \frac{n}{2}. \tag{4.6.15}$$

The most general solution to the hypergeometric equation (4.6.14) is a linear combination of two linearly independent solutions [280]; in our case this is [280]

$$f(\widetilde{Z}) = \mathfrak{F}_1\, {}_2F_1\left(\frac{n}{2}, \frac{n-2}{2}; \frac{n}{2}; \widetilde{Z}\right) + \mathfrak{F}_2\, \widetilde{Z}^{(2-n)/2}\, {}_2F_1\left(1, 0; 2 - \frac{n}{2}; \widetilde{Z}\right), \tag{4.6.16}$$

where ${}_2F_1$ is the hypergeometric function and the $\mathfrak{F}_i$ are constants to be determined by considering the short- and long-distance singularity structure when compared to the Hadamard

form and by using the method of images, respectively [5]. For later convenience, we make a further transformation to the argument of the hypergeometric function:

$$\widetilde{Z} = \frac{1+Z}{2}, \tag{4.6.17}$$

where $Z$ is the invariant biscalar related to the geodetic distance, defined in equation (4.3.15). The solution (4.6.16) therefore reads, after evaluating the hypergeometric functions,

$$f(Z) = \frac{\widetilde{\mathfrak{F}}_1}{(1-Z)^{(n-2)/2}} + \frac{\widetilde{\mathfrak{F}}_2}{(1+Z)^{(n-2)/2}}, \tag{4.6.18}$$

where the new constants $\widetilde{\mathfrak{F}}_i$ are related to the old constants $\mathfrak{F}_i$ by the relation $\widetilde{\mathfrak{F}}_i = 2^{(n-2)/2}\mathfrak{F}_i$. All that remains is to fix the constants $\widetilde{\mathfrak{F}}_i$, which will depend on the space-time dimensions and any boundary conditions applied to the field. In [31], the authors use a rather elegant approach in order to fix the constants. Whilst the details will be omitted here, the upshot is that, by considering the analogy of a box in Minkowski space-time, one can fix the constants by separately considering transparent and reflective boundary conditions. By expanding the Hadamard Green function into its short distance singularity structure and comparing with the Hadamard form, in the case of transparent boundary conditions, $\widetilde{\mathfrak{F}}_2 = 0$ and $\widetilde{\mathfrak{F}}_1 \neq 0$, so that the Hadamard Green function has the same singularity structure as the Hadamard Green function in Minkowski space [31]. In contrast, by using the method of images, it can be shown that both $\widetilde{\mathfrak{F}}_i \neq 0$ when reflective boundary conditions are applied [5, 31]. The explicit form of the constants is then found by matching the leading-order divergences of the solution (4.6.18) with the corresponding divergences of the Hadamard Green function in Minkowski space-time [5, 31, 221]. The upshot is that the short-distance singularity structure of the Hadamard Green function (4.6.18) fixes the constant $\widetilde{\mathfrak{F}}_1$, and the boundary conditions applied to the quantum scalar field fix the constant $\widetilde{\mathfrak{F}}_2$.

The Hadamard Green function for a conformally-coupled scalar field, in $n$-dimensions, is

therefore given as [5, 31, 221]

$$G^{(1)}(x,x') = \frac{a^{n-2}\Gamma\left(\frac{n}{2}-1\right)}{2(2\pi)^{n/2}}\left\{\frac{1}{[1-Z(x,x')]^{(n-2)/2}} + \frac{\lambda}{[1+Z(x,x')]^{(n-2)/2}}\right\}, \tag{4.6.19}$$

where we have inserted the factor of $\lambda$ in order to control the boundary conditions, with

$$\lambda = \begin{cases} +1, & \text{Dirichlet boundary conditions,} \\ 0, & \text{Transparent boundary conditions,} \\ -1, & \text{Neumann boundary conditions.} \end{cases} \tag{4.6.20}$$

## § 4.7 Quantum states on anti-de Sitter space

In this section, we will present a brief outline of quantum states on anti-de Sitter space and their important properties. The study of quantum states on anti-de Sitter space has been covered extensively in the literature; the purpose of this chapter is not to repeat or re-derive any of the important results but just outline some of the important features used in this thesis.

As outlined in section 2.6.1, in a general curved space-time the notion of a vacuum is ambiguous and observer-dependent. Throughout this thesis, we work with the unique global 'vacuum' state that is anti-de Sitter invariant, i.e. respects the underlying maximal symmetry of anti-de Sitter space. In chapter 5, we consider both the vacuum and a *thermal* state in anti-de Sitter space when computing expectation values. As mentioned in section 2.6.1, an observer in one state (defined by one set of scalar field modes) may see particles in a vacuum as defined by an observer in another state (defined by another set of scalar field modes). Since particles will have some intrinsic energy, we can interpret non-vacuum states as thermal states at some non-zero, finite temperature. In anti-de Sitter space, for scalar fields, thermal states can be interpreted as free bosonic radiative fields at finite temperature [4]. An important consequence of the thermalisation of anti-de Sitter space is the resulting

symmetry breaking. During his investigation of thermal equilibrium in gravitational fields, Tolman found that the local temperature $\widetilde{\beta}$ as measured by an observer is dependent on the gravitational field at the site of the measurement [357, 359]. Indeed, the Tolman relation for a static metric (using global anti-de Sitter space coordinates (4.1.3)),

$$\widetilde{\beta}\sqrt{-g_{\tau\tau}} = \overline{\beta} \in \mathbb{R}, \tag{4.7.1}$$

where $\overline{\beta}$ is some real constant, gives the local inverse temperature in anti-de Sitter space to be

$$\widetilde{\beta} \propto \cos(\rho). \tag{4.7.2}$$

This clearly breaks the maximal symmetry that the global vacuum possesses, since it distinguishes a preferred origin at which the thermal radiation pools [4].

Somewhat recently, it was shown that, in anti-de Sitter space, the vacuum as defined by an observer rigidly rotating on the polar axis about a scalar field in the global adS vacuum coincides with the (nonrotating) global adS vacuum [222], provided no speed-of-light surface formed. These results are in accordance with the corresponding ones on Minkowski space [116, 240], where the global nonrotating and rotating vacua coincide. For a rotating thermal state to be well defined in Minkowski space-time, an artificial boundary must be installed, and in particular, must be within the speed-of-light surface (as defined in sections 2.3.3 and 4.4) [116]. Since anti-de Sitter space has a natural boundary, the study of (rigidly) rotating thermal states is a sensible field of work. Provided the angular speed of the rotation is not sufficiently high such that a speed-of-light surface forms, it is expected that the rotating thermal states on anti-de Sitter space will also be well-defined [222]. It is upon this assumption that we construct expectation values of the stress-energy tensor in rotating thermal states in chapter 5, in particular sections 5.1.2 and 5.2.2.

## § 4.8 Summary

In this chapter, we have introduced anti-de Sitter space-time, a maximally-symmetric, vacuum solution to the classical Einstein equations (2.2.40).

In section 4.1, we reviewed its basic geometry and specified a global coordinate chart. In addition, using this coordinate chart we constructed the familiar global anti-de Sitter space metric, and showed that, in a suitable limit, this reduces to the Minkowski space metric.

Next, in section 4.2, we reviewed anti-de Sitter space's conformal structure, and in particular the conformal relation to (half of) the Einstein static universe. In the same section, we discussed the fact that anti-de Sitter space is *non*globally hyperbolic, and how the conformal mapping to the ESU allows one to circumvent some of the issues this causes.

In section 4.3, we discussed one of the most important features of anti-de Sitter space: its maximal symmetry. In particular, using the classical vacuum Einstein equations (2.2.33), we were able to write the cosmological constant of anti-de Sitter space purely in terms of its (inverse) radius of curvature and the number of space-time dimensions. Furthermore, we discussed how any biscalar (that depends on two uniquely-connected space-time points) on a maximally-symmetric space can be considered as a scalar of the geodetic distance. We then wrote down the geodetic interval on anti-de Sitter space, before using this to construct Synge's world function. We then used Synge's world function to write down the van Vleck-Morette determinant in anti-de Sitter space.

Next, in section 4.4, we discussed rigid rotation on anti-de Sitter space, and how the anti-de Sitter space metric changes when undergoing rigid rotation. In analogy with the flat-space Lorentz factor, we detailed the emergence of a speed-of-light surface for sufficiently high angular speed. We also explicitly constructed vielbeins; an orthonormal frame for anti-de Sitter space. In particular we constructed a static dreibein and vierbein, and a rigidly-rotating dreibein and vierbein.

In section 4.5, we discussed the role of boundary conditions in anti-de Sitter space. Since anti-de Sitter space is nonglobally hyperbolic, boundary conditions are required to ensure unique propagation of data throughout the space-time; without this, any QFT would be ill-posed. Since the time-like boundary of anti-de Sitter space is not part of the manifold, we discussed how one imposes boundary conditions by conformally mapping the quantum field onto the ESU, applying the boundary conditions to the field on the ESU, before reverting this conformal mapping to find the corresponding quantum field (subject to boundary conditions) on anti-de Sitter space.

Next, in section 4.6, we briefly detailed the canonical quantisation procedure for uncharged scalar fields on anti-de Sitter space. Following this, we explicitly constructed the (vacuum) Hadamard Green function on anti-de Sitter space, by exploiting maximal-symmetry arguments to rewrite the Klein-Gordon equation as a hypergeometric equation, expressing the result in terms of the hypergeometric function ${}_2F_1$.

Finally, in section 4.7, we briefly covered quantum states on anti-de Sitter space-time. In particular, we discussed how thermal states on anti-de Sitter space are defined, and how they break the maximal symmetry of anti-de Sitter space. In addition, we discussed recent results that showed the nonrotating and rigidly-rotating anti-de Sitter space vacua coincide, provided no speed-of-light surface forms.

# Chapter 5

# Stress-energy tensor renormalisation

"Just when you think you've answered all the questions, another one smacks you in the face. Life, life, life."

*Dexter Morgan*

In this chapter, we perform the renormalisation procedure (as laid out in section 2.7) for massless and conformally-coupled scalar fields on three- and four-dimensional anti-de Sitter space. In section 5.1.1 we start by reviewing the construction for a static scalar field as first done in [4]. Next, in section 5.1.2 we perform the renormalisation procedure for a scalar field undergoing rigid rotation (in four dimensions) using the state subtraction renormalisation procedure (see section 2.7.1). In sections 5.2.1 and 5.2.2 we perform the (state subtraction) renormalisation procedure for scalar fields in three-dimensional anti-de Sitter space that are static or undergoing rigid rotation, respectively. Then, in section 5.3, we construct relativistic kinetic theory stress-energy tensors for static and rigidly-rotating three- and four-dimensional anti-de Sitter space. In particular, in section 5.3.4 we compare the stress-energy tensors arising from the renormalisation procedure and the RKT based approach.

## § 5.1 Four-dimensional anti-de Sitter space-time

### 5.1.1 Static fields

The vacuum and thermal expectation values for a stress-energy tensor in four-dimensional anti-de Sitter space have been known since 1978 and 1987, respectively. In [4], the renormalisation procedure is performed for a massless and conformally-coupled scalar field theory.

The vacuum Hadamard Green function (4.6.19), given in terms of two space-like separated points in four-dimensional anti-de Sitter space-time is [4, 31]

$$ {}_{(4,\not{\Omega})}G_0^{(1)}(x,x') = -\frac{a^2}{8\pi^2}\left([1 - {}_{(4,\not{\Omega})}Z(x,x')]^{-1} + \lambda[1 + {}_{(4,\not{\Omega})}Z(x,x')]^{-1}\right), \tag{5.1.1} $$

where the $\lambda$ term controls the boundary conditions applied to the field; $\lambda = 1$ refers to Dirichlet boundary conditions, $\lambda = -1$ refers to Neumann boundary conditions and $\lambda = 0$ refers to transparent boundary conditions. The function ${}_{(4,\not{\Omega})}Z(x,x')$ is an invariant biscalar (the general definition of which is found in equation (4.3.15)) dependent on the

space-like separated points (and hence the coordinates of adS) and defined as

$$
\begin{aligned}
{}_{(4,\mathfrak{Q})}Z(x,x') &= \frac{1}{\cos(\rho)\cos(\rho')} \\
&\times \left[\cos\big(\tau-\tau'\big) - \sin(\rho)\sin\big(\rho'\big)\left\{\cos(\theta)\cos\big(\theta'\big) + \sin(\theta)\sin\big(\theta'\big)\cos\big(\phi-\phi'\big)\right\}\right]. \quad (5.1.2)
\end{aligned}
$$

Following [4], we demand that the adS origin ($\rho = 0$) is held at a finite temperature $T = 1/\beta$. Since it is a general property of thermal Hadamard Green functions that they are periodic in imaginary time (see section 2.5), we impose the following form on the thermal Hadamard Green function:

$$
{}_{(4,\mathfrak{Q})}G^{(1)}_{\beta}(x,x') = -\frac{a^2}{4\pi^2}\left[J_\beta(\tau-\tau';\rho,\rho') + \lambda J_\beta(\tau-\tau'+\pi;-\rho,\rho')\right], \quad (5.1.3)
$$

where

$$
J_\beta(\tau-\tau';\rho,\rho') = \sum_{n=-\infty}^{\infty}\left[1 - {}_{(4,\mathfrak{Q})}Z(\tau-\tau'+ia\beta n;\rho,\rho';\mho,\mho')\right]^{-1}, \quad (5.1.4)
$$

so that the thermal Hadamard Green function is indeed periodic in $(\tau-\tau')$, with imaginary period $ia\beta$. Before continuing further from this point, it is important to address a minor point arising in the notation within the Matsubara sum (5.1.4): the notation for the functional dependence of $Z(x,x')$ changes here. This is simply a typographical choice that we are justified in making, since the $\tau$ and $\tau'$ dependence of the function $Z(x,x')$ is actually always $\tau-\tau'$ due to its definition, meaning we can take the two coordinates $\tau,\tau'$ and redefine them as one coordinate $\tau-\tau'$. Additionally, the $\mho,\mho'$ notation simply refers to the angular coordinates, $\theta,\theta',\phi,\phi'$.

There are two relations of note here. Firstly,

$$
J_\beta(\tau-\tau';\rho,\rho') = J_\beta(\tau-\tau'+2\pi;\rho,\rho') \quad (5.1.5)
$$

reflects the real-time periodicity of adS, whilst

$$
J_\beta(\tau-\tau';\rho,\rho') = J_\beta(\tau-\tau'+ia\beta;\rho,\rho') \quad (5.1.6)
$$

reflects the thermal imaginary-time periodicity. In fact, the imaginary time periodicity is a consequence of the fact that any scalar field in equilibrium at some inverse temperature $\beta$ has a (Hadamard) Green function that is also periodic in time with a period $i\beta$ [4, 45]. This is exactly what was imposed by writing the thermal Hadamard Green function as in equation (5.1.3).

Since the function $J_\beta$ is doubly periodic, and in fact is meromorphic, it is an elliptic function [4]. Using a fundamental theorem of elliptic functions [381], the function $J_\beta$ is entirely determined by and can be expressed in terms of the location and residues of its poles - and therefore so can the thermal Green's function ${}_{(4,\mathfrak{A})}G^{(1)}_\beta(x,x')$. The upshot is that the thermal Hadamard Green function can be written as [4]

$$
\begin{aligned}
{}_{(4,\mathfrak{A})}G^{(1)}_\beta(x,x') = -\frac{a^2}{4\pi^2}\Bigg[&[1-{}_{(4,\mathfrak{A})}Z(x,x')]^{-1}+\lambda[1+{}_{(4,\mathfrak{A})}Z(x,x')]^{-1} \\
&-4\cos\rho\cos\rho'\sum_{k=1}^{\infty}\left(\frac{\sin(k\eta(\rho,\rho';\mho,\mho'))}{\sin(\eta(\rho,\rho';\mho,\mho'))}+\lambda(-1)^k\frac{\sin(k\eta(-\rho,\rho';\mho,\mho'))}{\sin(\eta(-\rho,\rho';\mho,\mho'))}\right)\frac{\cos(k[\tau-\tau'])}{\exp(ka\beta)-1}\Bigg],
\end{aligned}
\tag{5.1.7}
$$

where $\tau-\tau' = \pm\eta(\rho,\rho';\mho,\mho')$, with

$$
\eta(\rho,\rho';\mho,\mho') = \cos^{-1}(\cos\rho\cos\rho'+\sin\rho\sin\rho'[\cos\theta\cos\theta'+\sin\theta\sin\theta'\cos(\phi-\phi')]) \tag{5.1.8}
$$

representing the locations of the poles of $J_\beta$. As shown in [4], once the exact form of the thermal Hadamard Green function is known, it is somewhat straightforward to compute the vacuum and thermal expectation values of both the vacuum polarisation of the field and the stress-energy tensor. This is done by exploiting the well-known Hadamard parametrix of the thermal Hadamard Green function (given in general by equation (2.7.13)), which in four space-time dimensions (for a massless and conformally-coupled scalar field) is [103],

$$
G^{(1)}_\beta(x,x') = (2\pi)^{-2}\left(\Delta^{1/2}\sigma^{-1}+W(x,x')\right), \tag{5.1.9}
$$

where $\sigma$ is half the square of the geodesic distance between the points $x$ and $x'$ (i.e. Synge's world function), and $\Delta$ is the van Vleck-Morette determinant, given by equations (4.3.13)

and (4.3.14) respectively. In terms of the biscalar ${}_{(4,\not{\Omega})}Z(x,x')$ (5.1.2), they can be explicitly written as (see section 4.3) [4]

$$\sigma(x,x') = 6R^{-1}\left[\arccos\left({}_{(4,\not{\Omega})}Z(x,x')\right)\right]^2, \qquad \Delta = \left(\frac{1}{6}R\sigma\right)^{3/2}\csc^3\left(\left[\frac{1}{6}R\sigma\right]^{1/2}\right), \tag{5.1.10}$$

where $R = 12a^2$ is the Ricci scalar. The information required to construct both expectation values of interest is contained within the symmetric biscalar $W(x,x')$ from equation (5.1.9). As laid out in section 2.7, to isolate this we subtract the contribution of the Hadamard parametrix from the geodesic distance and the Van Vleck determinant from the thermal Hadamard Green function (the singular parts), i.e. we consider

$$W(x,x') = 4\pi^2 G^{(1)}_{\beta}(x,x') - \Delta^{1/2}\sigma^{-1}. \tag{5.1.11}$$

We can then expand $W$ into its short distance structure,

$$W(x,x') = \omega(x) - \frac{1}{2}\omega_\mu(x)\partial^\mu\sigma + \frac{1}{2}\omega_{\mu\nu}(x)\partial^\mu\sigma\partial^\nu\sigma + \dots \tag{5.1.12}$$

where

$$\omega(x) = \lim_{x'\to x} W(x,x'), \qquad \omega_\mu(x) = \partial_\mu\omega(x), \qquad \omega_{\mu\nu}(x) = \lim_{x'\to x}\nabla_\mu\nabla_\nu W(x,x'). \tag{5.1.13}$$

To calculate these quantities, one needs to use the thermal Hadamard Green function (5.1.7) together with the geodesic separation and the Van Vleck determinant (5.1.10) and compare with the short distance expansion (5.1.12). Once the explicit form of $W(x,x')$ has been found, the vacuum and thermal expectation values of the vacuum polarisation and the stress-energy tensor can be computed. Given in terms of the short distance expansion quantities, these are [43, 61, 103]

$$\langle\widehat{\Phi}^2\rangle = \left(8\pi^2\right)^{-1}\omega(x) \tag{5.1.14}$$

for the vacuum polarisation and

$$\langle\widehat{T}_{\mu\nu}\rangle = \left(8\pi^2\right)^{-1}\left[-\omega_{\mu\nu} + \frac{1}{2}g_{\mu\nu}\omega_\delta{}^\delta + \left(-\frac{1}{12}g_{\mu\nu}\Box + \frac{1}{3}\nabla_\mu\nabla_\nu + \frac{1}{2}a^2 g_{\mu\nu}\right)\omega - \frac{1}{30}a^4 g_{\mu\nu}\right] \tag{5.1.15}$$

for the stress-energy tensor. One can calculate the quantities $\omega$ and $\omega_{\mu\nu}$. These are given by [4]

$$ {}_{(4,\not{\Omega})}\omega(x) = a^2\left[\frac{1}{3} + 4\cos^2(\rho) f_1(a\beta)\right] + a^2\lambda\left[-\frac{1}{2} + 2\cot(\rho) S_0(a\beta,\rho)\right] \tag{5.1.16} $$

and

$$ \begin{aligned} {}_{(4,\not{\Omega})}\omega_{\mu\nu}(x) =& \frac{a^4}{3}\left\{\left[-\frac{17}{40} + 4\left(\cos^2(\rho) - 3\right)\cos^2(\rho) f_1(a\beta) - 4\cos^4(\rho) f_3(a\beta)\right] g_{\mu\nu}\right. \\ & - 8\cos^4(\rho)\left[f_1(a\beta) + 2f_3(a\beta)\right]\mathfrak{t}_\mu\mathfrak{t}_\nu + \left[6\sin^2(2\rho) f_1(a\beta,\rho)\right]\mathfrak{p}_\mu\mathfrak{p}_\nu\Big\} \\ & + \frac{a^4\lambda}{4}\cot^2(\rho)\left\{\left[\tan^2(\rho) - 2\csc(2\rho)\left(2\sin^2(\rho) + 1\right) S_0(a\beta,\rho)\right.\right. \\ & + 4C_1(a\beta,\rho)\Big] g_{\mu\nu} - \left[2\csc(2\rho) S_0(a\beta,\rho) - 4\cos(2\rho) C_1(a\beta,\rho)\right. \\ & + 8\sin(2\rho) S_2(a\beta,\rho)\Big]\mathfrak{t}_\mu\mathfrak{t}_\nu + \left[6\csc(2\rho) S_0(a\beta,\rho)\right. \\ & \left.\left. - 4\left(2\sin^2(\rho) + 3\right) C_1(a\beta,\rho) - 8\sin(2\rho) S_2(a\beta,\rho)\right]\mathfrak{p}_\mu\mathfrak{p}_\nu\right\}. \end{aligned} \tag{5.1.17} $$

Here, the following functions and vectors are introduced for convenience:

$$ f_m(x) = \sum_{n=1}^{\infty} n^m \left(e^{nx} - 1\right)^{-1}, \tag{5.1.18} $$

$$ S_m(x,\rho) = \sum_{n=1}^{\infty} n^m (-1)^n \left(e^{nx} - 1\right)^{-1} \sin(2n\rho), \tag{5.1.19} $$

$$ C_m(x,\rho) = \sum_{n=1}^{\infty} n^m (-1)^n \left(e^{nx} - 1\right)^{-1} \cos(2n\rho), \tag{5.1.20} $$

are rapidly converging infinite sums; and

$$ \mathfrak{t}_\bullet = (a^{-1}\sec\rho, 0, 0, 0), \qquad \mathfrak{p}_\bullet = (0, a^{-1}\sec\rho, 0, 0), \tag{5.1.21} $$

are unit length time-like and radial vector fields, introduced to write the expression for both $\omega_{\mu\nu}$ and the expectation value of the stress-energy tensor in a geometric form. Upon substitution of these quantities into equations (5.1.14) and (5.1.15), we find the following expressions for the thermal expectation values; though the details of such a computation

will not be shown here for brevity. The upshot is that the thermal expectation value of the vacuum polarisation value is given by [4]

$$\langle\widehat{\Phi}^2\rangle_\beta = \frac{a^2}{8\pi^2}\left[\frac{1}{3} + 4\cos^2(\rho)f_1(a\beta)\right] + \frac{a^2\lambda}{8\pi^2}\left[-\frac{1}{2} + 2\cot(\rho)S_0(a\beta,\rho)\right] \tag{5.1.22}$$

while the thermal expectation value of the stress-energy tensor takes the rather unwieldy form[1] [4]

$$\begin{aligned}
{}_{(4,\mathfrak{A})}\langle\widehat{T}_{\mu\nu}\rangle_\beta = \frac{a^4}{8\pi^2}&\left(\left[-\frac{1}{120} + \frac{4}{3}\cos^4(\rho)f_3(a\beta)\right]g_{\mu\nu} + \left[\frac{16}{3}\cos^4(\rho)f_3(a\beta)\right]\mathfrak{t}_\mu\mathfrak{t}_\nu\right)\\
&+ \frac{a^4\lambda}{48\pi^2}\cot(\rho)\left\{\left[-\csc^2(\rho)\cos(2\rho)S_0(a\beta,\rho) + 2\cot(\rho)C_1(a\beta,\rho)\right.\right.\\
&+ \left.4\cos^2(\rho)S_2(a\beta,\rho)\right]g_{\mu\nu} + \left[\left(3-\cot^2(\rho)\right)S_0(a\beta,\rho)\right.\\
&+ \left.2\cot(\rho)\left(3-2\cos^2(\rho)\right)C_1(a\beta,\rho) + 12\cos^2(\rho)S_2(a\beta,\rho)\right]\mathfrak{t}_\mu\mathfrak{t}_\nu\\
&+ \left[\left(3\csc^2(\rho)-4\right)S_0(a\beta,\rho) + 2\cot(\rho)\left(2\sin^2(\rho)-3\right)C_1(a\beta,\rho)\right.\\
&- \left.\left.4\cos^2(\rho)S_2(a\beta,\rho)\right]\mathfrak{p}_\mu\mathfrak{p}_\nu\right\}.
\end{aligned} \tag{5.1.23}$$

We are also interested in the vacuum expectation values of both of these quantities. Rather than repeat the preceding analysis, it is easier to simply take the zero temperature limit (corresponding to $\beta \to \infty$) of the thermal expectation values. For the vacuum polarisation, we find that the vacuum expectation value is

$$\langle\widehat{\Phi}^2\rangle_0 = \frac{a^2}{8\pi^2}\left[\frac{1}{3} - \frac{1}{2}\lambda\right], \tag{5.1.24}$$

where $\lambda$ still controls the boundary conditions applied to the field. These are in accordance with those found in [221, 267] for Dirichlet boundary conditions. Meanwhile, the zero temperature limit for the stress-energy tensor is given by the surprisingly simple expression

$${}_{(4,\mathfrak{A})}\langle\widehat{T}_{\mu\nu}\rangle_0 = -\frac{a^4}{960\pi^2}g_{\mu\nu}. \tag{5.1.25}$$

[1] There is a typographical error in the original paper [4], whereby a factor of $\cot(\rho)$ is missing from the overall factor at the start of the second line (private communication, C. Kent, S. Namasivayan and E. Winstanley). This is corrected in equation (5.1.23).

What is particularly remarkable is that the vacuum expectation value for the stress-energy tensor does not actually depend on the choice of boundary conditions, and is merely a constant multiple of the metric. This seems to suggest that the vacuum state respects the underlying maximal symmetry of anti-de Sitter space-time. This fact is something that is exploited when considering back-reaction effects, see part III of this thesis.

In Figure 5.1, the non-zero components of the thermal expectation value of the stress-energy tensor (with one index up and one down) are shown. The plot for $\langle \widehat{T}_{\phi}{}^{\phi} \rangle_{\beta}$ is not shown since this is identical to that of $\langle \widehat{T}_{\theta}{}^{\theta} \rangle_{\beta}$. In particular, $-\langle \widehat{T}_{\tau}{}^{\tau} \rangle_{\beta}$ is plotted in Figure 5.1a since this represents the energy density of the matter [13]. Whilst the vacuum expectation value of the stress-energy tensor is maximally symmetric (and, in fact, constant), the thermal expectation value is *not* maximally symmetric. This can be seen in Figure 5.1 by virtue of the fact that the distribution of the thermal expectation value tends to 'clump' towards the origin ($\rho = 0$) and then tend towards the vacuum expectation value at the boundary. Also of note is the fact that the plots of $\langle \widehat{T}_{\rho}{}^{\rho} \rangle_{\beta}$ (5.1b) and $\langle \widehat{T}_{\theta}{}^{\theta} \rangle_{\beta}$ (5.1c) look remarkably similar. One might assume, based on these plots alone, that they are identical - which is certainly how it looks to the naked eye. However, there are differences between the two of order $10^{-3}$. This can be seen in, for example, figure 5.42 when a quantity called the pressure deviator is plotted - see section 5.3.4 for more details.

Figures 5.2 and 5.3 show the very same quantities but for Neumann and transparent boundary conditions, respectively. Yet again, whilst to the naked eye these plots look almost identical to the Dirichlet plots, there are, in fact, differences to the order of $10^{-3}$. This is most easily seen in figure 5.4, where the components are plotted for one fixed value of the inverse temperature with all three boundary conditions.

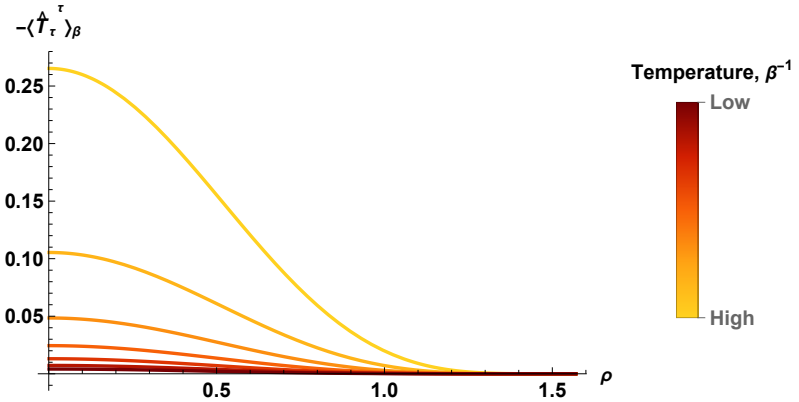


(a) $-\langle \widehat{T}_\tau{}^\tau \rangle$

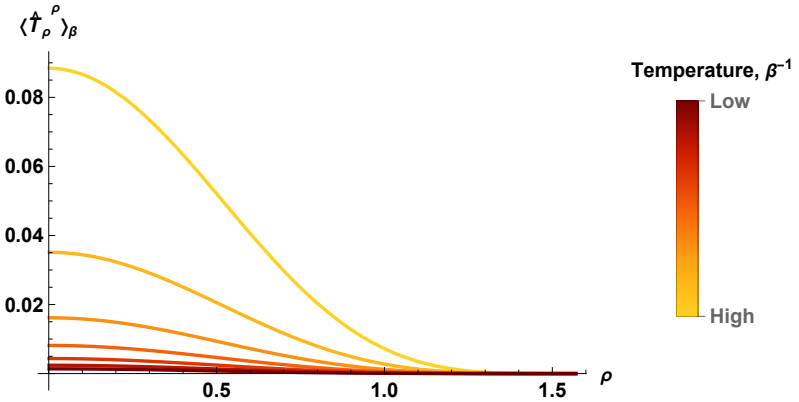


(b) $\langle \widehat{T}_\rho{}^\rho \rangle$

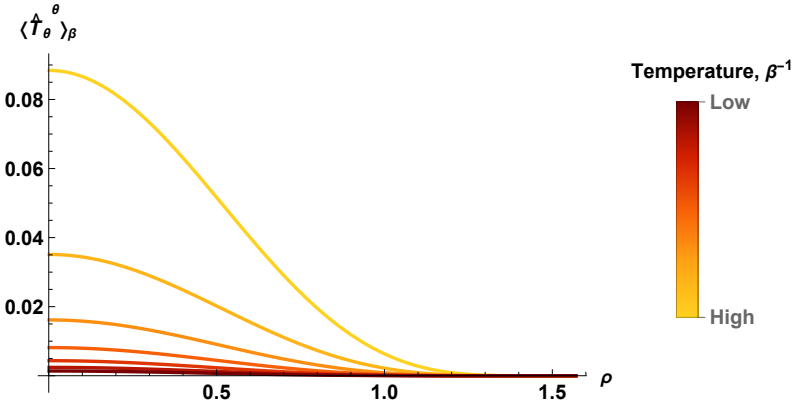


(c) $\langle \widehat{T}_\theta{}^\theta \rangle$

Figure 5.1: Plots for the components of the thermal expectation value of the stress-energy tensor, keeping the adS length scale $a = 1$ while varying the inverse temperature within the range $\beta \in [\pi/3, 5\pi/6]$. These plots are for the case of Dirichlet boundary conditions.

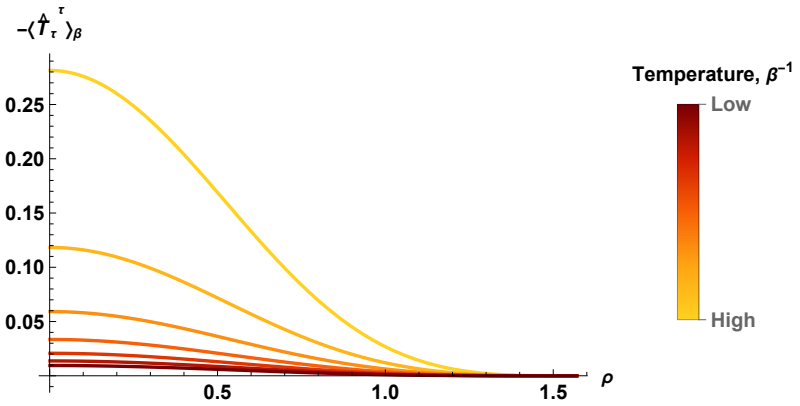


(a) $-\langle \widehat{T}_\tau{}^\tau \rangle$

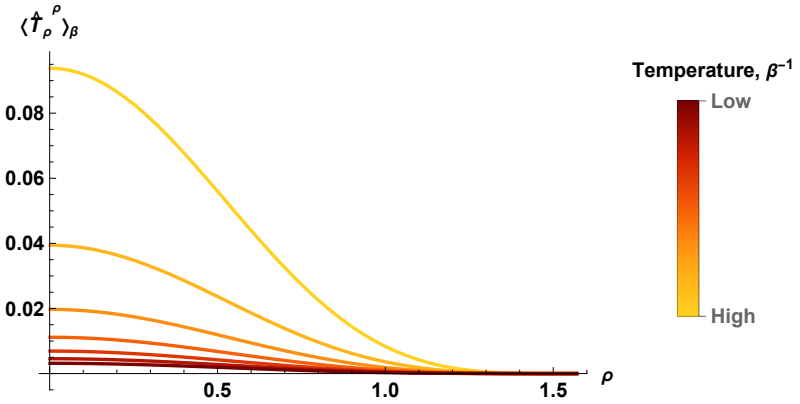


(b) $\langle \widehat{T}_\rho{}^\rho \rangle$

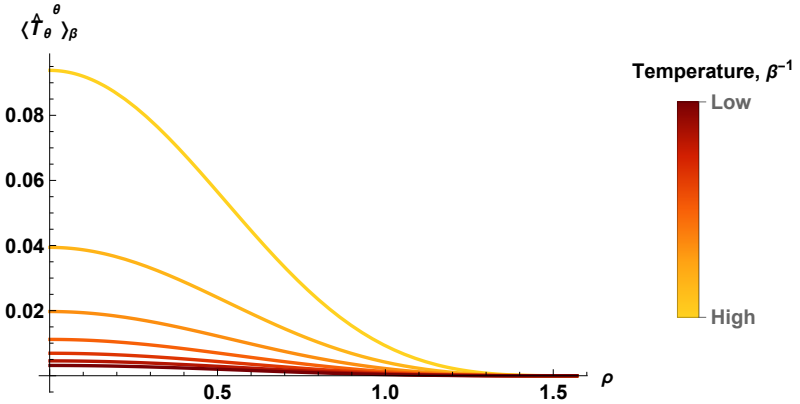


(c) $\langle \widehat{T}_\theta{}^\theta \rangle$

Figure 5.2: Plots for the components of the thermal expectation value of the stress-energy tensor, keeping the adS length scale $a = 1$ while varying the inverse temperature within the range $\beta \in [\pi/3, 5\pi/6]$. These plots are for the case of Neumann boundary conditions.

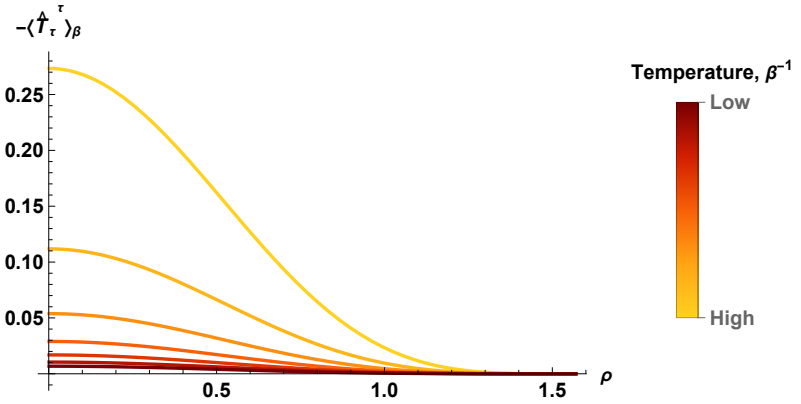


(a) $-\langle \widehat{T}_\tau{}^\tau \rangle$

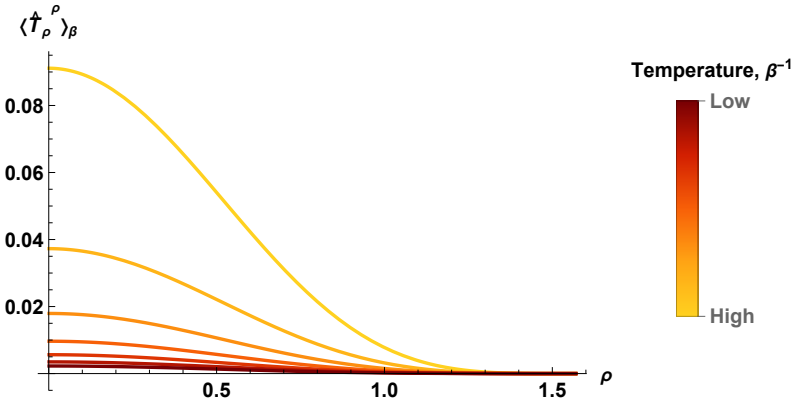


(b) $\langle \widehat{T}_\rho{}^\rho \rangle$

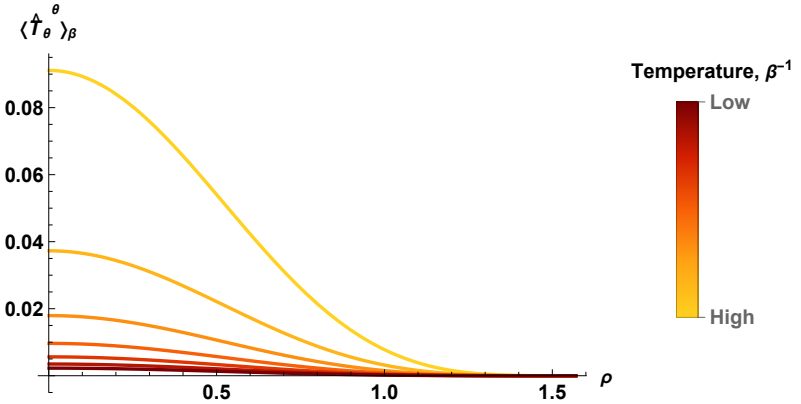


(c) $\langle \widehat{T}_\theta{}^\theta \rangle$

Figure 5.3: Plots for the components of the thermal expectation value of the stress-energy tensor, keeping the adS length scale $a = 1$ while varying the inverse temperature within the range $\beta \in [\pi/3, 5\pi/6]$. These plots are for the case of transparent boundary conditions.

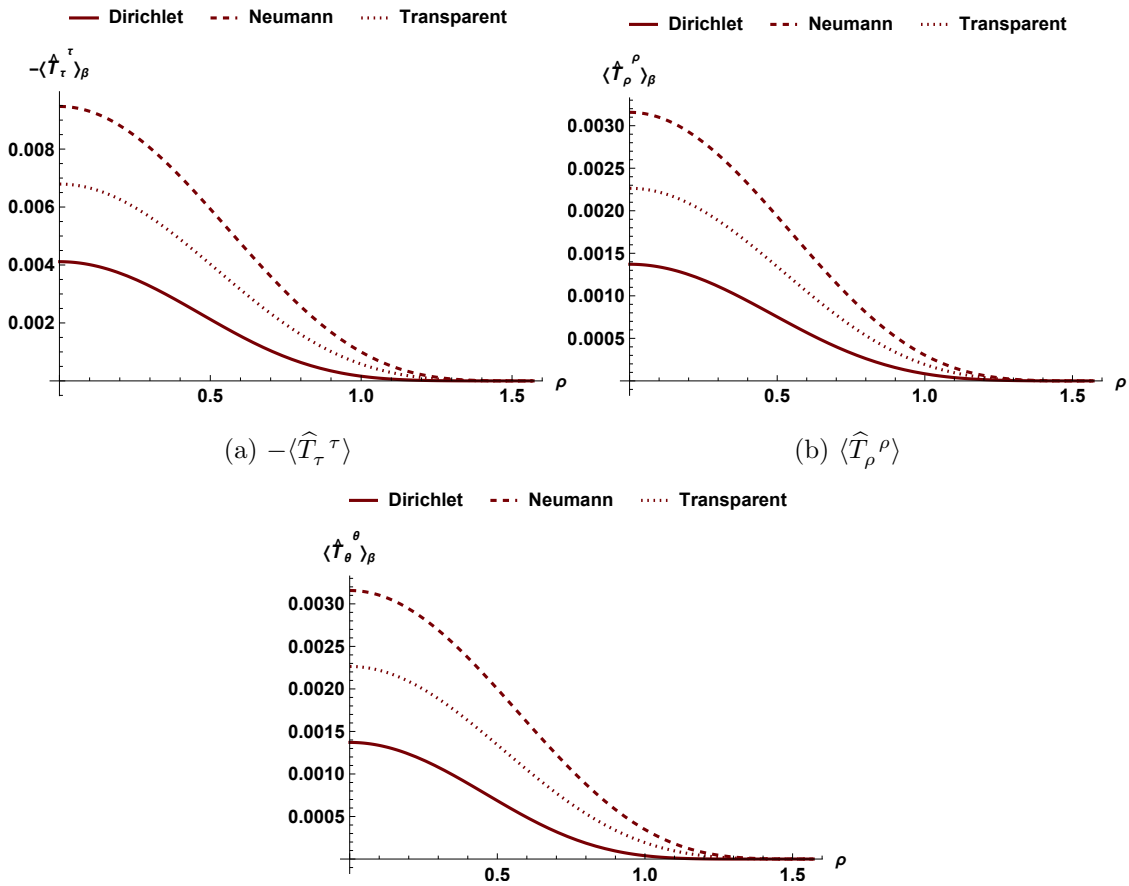


(a) $-\langle \widehat{T}_\tau{}^\tau \rangle$ (b) $\langle \widehat{T}_\rho{}^\rho \rangle$

(c) $\langle \widehat{T}_\theta{}^\theta \rangle$

Figure 5.4: Plots for the components of the thermal expectation value of the stress-energy tensor, keeping the adS length scale $a = 1$ and inverse temperature $\beta = 5\pi/6$ fixed. These plots show the differences in each component between the three cases of boundary conditions. For each, Dirichlet boundary conditions are represented by a solid line; Neumann boundary conditions by a dashed line; and transparent by a dotted line.

### 5.1.2 Rigidly-rotating fields

The method of renormalising the stress-energy tensor for a rigidly-rotating, quantum scalar field in four-dimensional anti-de Sitter space-time will follow a slightly different procedure to that in the previous section. Unlike in [4] for static fields in four-dimensional anti-de Sitter space-time, the act of 'removing the infinities' (the act of renormalisation) was done by exploiting the well-known form of the Hadamard parametrix of the thermal Hadamard Green function and writing the Matsubara sum in terms of elliptic functions. Instead, here we take a slightly different approach to renormalisation: state subtraction. Whilst the general procedure can be found in section 2.7.1, here the specific calculation details are laid out. We start by recalling the vacuum Hadamard Green function (4.6.19), which in four dimensions is

$$ {}_{(4,\Omega)}G_0^{(1)}(x,x') = \frac{a^2}{8\pi^2}\left[\frac{1}{{}_{(4,\Omega)}Z(x,x')-1} - \frac{\lambda}{{}_{(4,\Omega)}Z(x,x')+1}\right], \tag{5.1.26} $$

where $\lambda$ controls the boundary conditions applied to the field: $\lambda = 1$ refers to Dirichlet boundary conditions; $\lambda = -1$ for Neumann boundary conditions; and $\lambda = 0$ for transparent boundary conditions. For more detail on the boundary conditions, see chapter 4; in particular sections 4.2, 4.5 and 4.6.

We must make a small caveat before proceeding. The vacuum Hadamard Green function (5.1.26) is constructed with respect to the *non*rotating anti-de Sitter space vacuum, but we wish to construct the renormalised stress-energy tensor for a rigidly-rotating scalar field. Thankfully, it was shown that the rigidly-rotating and nonrotating vacua on anti-de Sitter space coincide, provided no speed-of-light surface forms [222] - see section 4.7 for more details.

Since we are considering a (bosonic) scalar field theory, the vacuum Hadamard Green function is a scalar. This means that to find the vacuum Hadamard Green function for rotating anti-de Sitter space-time, we can just perform a coordinate mapping from nonrotating to

rotating anti-de Sitter space-time. To find the rotating vacuum Hadamard Green function in, say, a fermionic field theory, the vacuum Hadamard Green function would be a spinor and so making the coordinate transformation would be insufficient [15]. Since we make the rotation in the angular coordinate $\phi$ in the metric (4.4.3), we can use the same mapping in the vacuum Hadamard Green function. Ergo, we make the transformation $\phi \mapsto \phi + \Omega\tau$ in the vacuum Hadamard Green function. The upshot is that the symmetric biscalar ${}_{(4,\Omega)}Z(x,x')$ is defined as

$$
\begin{aligned}
{}_{(4,\Omega)}Z(x,x') &= \frac{1}{\cos\rho\cos\rho'}\times \\
&\left[\cos\left(\tau-\tau'\right) - \sin\rho\sin\rho'\left\{\cos(\theta)\cos\left(\theta'\right) + \sin(\theta)\sin\left(\theta'\right)\cos\left(\phi-\phi'+\Omega\left[\tau-\tau'\right]\right)\right\}\right].
\end{aligned}
\tag{5.1.27}
$$

The biscalar depends on two space-like separated points in the space-time, and is written in terms of the adS coordinates as defined in section 4.3; see equation (4.3.15).

The next step is to construct the thermal Hadamard Green function. Analogously to section 5.1.1 and [4], the thermal Hadamard Green function is assembled by performing a Matsubara sum of the vacuum Hadamard Green function. In our case, we have

$$
{}_{(4,\Omega)}G^{(1)}_{\beta}(x,x') = \sum_{j=-\infty}^{\infty} {}_{(4,\Omega)}G^{(1)}_{0}(\tau+ij\beta,\tau',\rho,\rho',\theta,\theta',\phi,\phi'). \tag{5.1.28}
$$

It is at this step where the difference in methods between this section and those in section 5.1.1, [4] and [103], is most stark. In [4], the fact that the thermal Hadamard Green function can be written in terms of doubly periodic functions is exploited, before developing this function into its short-distance singularity structure and subtracting the relevant Hadamard parametrix. Since it is not true in general that functions (in particular the vacuum Hadamard Green function) can be written in terms of doubly periodic elliptical functions, it proves easier to follow a different method [103] that holds in more general cases. As it is true that both the vacuum and thermal Hadamard Green functions for a space-time have the same short-distance singularity structure (see section 2.7), we employ

state subtraction (see section 2.7.1 for details). This simply amounts to subtracting the vacuum Hadamard Green function from the thermal Hadamard Green function:

$$\begin{aligned} {}_{(4,\Omega)}W(x,x') &= {}_{(4,\Omega)}G^{(1)}_{\beta}(x,x') - {}_{(4,\Omega)}G^{(1)}_{0}(x,x') \\ &= \sum_{j\neq 0} {}_{(4,\Omega)}G^{(1)}_{0}(\tau + ij\beta, \tau', \rho, \rho', \theta, \theta', \phi, \phi'), \end{aligned} \tag{5.1.29}$$

and as can be seen in the last line of the above equation, rather conveniently amounts to removing the $j = 0$ term from the sum. For later convenience, we define the following thermal summand:

$${}_{(4,\Omega)}W^{j}(x,x') = {}_{(4,\Omega)}G^{(1)}_{0}(\tau + ij\beta, \tau', \rho, \rho', \theta, \theta', \phi, \phi') \tag{5.1.30}$$

so that

$${}_{(4,\Omega)}W(x,x') = \sum_{j\neq 0} {}_{(4,\Omega)}W^{j}(x,x'). \tag{5.1.31}$$

Provided $j \neq 0$, the thermal summand (5.1.30) is regular in the (short-distance) coincidence limit.

It is at this stage that it proves pertinent to make a minor clarification. By definition, the thermal expectation value of a stress-energy tensor must include contributions from the vacuum expectation value [250], since in the zero temperature limit (of the thermal expectation value), the vacuum expectation value must be recovered. However, by using state subtraction to find the thermal expectation value, we remove the vacuum expectation value. This is because, as shown in [222], the vacuum expectation value for rigidly rotating states on anti-de Sitter space-time is identical to the nonrotating vacuum expectation value, provided that the rate of rotation is such that the space-time does not form a speed-of-light surface [222]. If we use equation (5.1.29) as the propagator with which the expectation value (2.7.37) is constructed, the resulting expectation value is not quite the full thermal expectation value; we would still need the contribution from the vacuum expectation value. Thankfully, we can simply add the vacuum expectation value (5.1.25) to the resulting expectation value to yield the full thermal expectation value.

The general form of the thermal expectation value of the stress-energy tensor (2.7.37) still requires that we find the short distance expansion coefficients of the propagator (5.1.29). We proceed by first finding the short distance expansion coefficients of the thermal mode (5.1.30), before constructing the expectation value of the stress-energy tensor in terms of $j$ and then summing over $j$ at the end. Recall that in general these are given by equation (2.7.43) in section 2.7. We begin by writing down the thermal summand explicitly,

$$\begin{aligned}
{}_{(4,\Omega)}W^j(x,x') = \frac{a^2}{8\pi^2}\Big[&-1+\sec(\rho)\sec\big(\rho'\big)\Big\{\cos\big(\tau-\tau'+ij\beta\big)\\
&-\big(\cos(\theta)\cos\big(\theta'\big)+\cos\big(\phi-\phi'-\tau'\Omega+(\tau+ij\beta)\Omega\big)\sin(\theta)\sin\big(\theta'\big)\big)\Big\}\Big]^{-1}\\
&-\frac{a^2\lambda}{8\pi^2}\Big[1+\sec(\rho)\sec\big(\rho'\big)\Big\{\cos\big(\tau-\tau'+ij\beta\big)\\
&-\big(\cos(\theta)\cos\big(\theta'\big)+\cos\big(\phi-\phi'-\tau'\Omega+(\tau+ij\beta)\Omega\big)\sin(\theta)\sin\big(\theta'\big)\big)\Big\}\Big]^{-1}
\end{aligned} \tag{5.1.32}$$

before then taking the coincidence limit, leading to

$$\begin{aligned}
&{}_{(4,\Omega)}\omega^j(x) =\\
&\quad\frac{a^2}{8\pi^2}\Big[\big(-1+\cosh(j\beta)\sec^2(\rho)-\cos^2(\theta)\tan^2(\rho)-\cosh(j\beta\Omega)\sin^2(\theta)\tan^2(\rho)\big)^{-1}\\
&\quad-\lambda\left(1+\cosh(j\beta)\sec^2(\rho)-\cos^2(\theta)\tan^2(\rho)-\cosh(j\beta\Omega)\sin^2(\theta)\tan^2(\rho)\right)^{-1}\Big]\,.
\end{aligned} \tag{5.1.33}$$

Certain expressions show up multiple times, so for brevity and convenience, we define

$$\mathcal{A}_{(\pm,4,\Omega)} \coloneqq \pm1+\cosh(j\beta)\sec^2(\rho)-\cos^2(\theta)\tan^2(\rho)-\cosh(j\beta\Omega)\sin^2(\theta)\tan^2(\rho), \tag{5.1.34a}$$

and

$$\widetilde{\mathcal{A}}_{(4)} \coloneqq 1-\cosh^2(j\beta)\sec^2(\rho)+\cos^2(\theta)\tan^2(\rho)+\cosh^2(j\beta\Omega)\sin^2(\theta)\tan^2(\rho), \tag{5.1.34b}$$

$$\mathcal{S}_{(4)} \coloneqq \sinh(j\beta)-\Omega\sinh(j\beta\Omega)\sin^2(\theta)\sin^2(\rho), \tag{5.1.34c}$$

$$\mathcal{C}_{(4)} \coloneqq \cos^2(\theta)-\cosh(j\beta)+\cosh(j\beta\Omega)\sin^2(\theta), \tag{5.1.34d}$$

$$\Gamma_{(4)} \coloneqq \left[1-\Omega^2\sin^2(\theta)\sin^2(\rho)\right]^{-1/2}. \tag{5.1.34e}$$

The 4 in the subscript refers to the dimension whilst the $\Omega$ refers to the rotation. Although we use it here to simplify algebraic expressions, $\Gamma_{(4)}$ (4.4.4b) was previously defined in section 4.4 as the Lorentz factor. Despite its use here, there is not necessarily anything physically significant about its appearance in certain expressions.

We can therefore rewrite ${}_{(4,\Omega)}\omega^j(x)$ in the following concise form using the newly defined quantities above:

$$ {}_{(4,\Omega)}\omega^j(x) = \frac{a^2}{8\pi^2}\left[\mathcal{A}^{-1}_{(-,4,\Omega)} - \lambda\,\mathcal{A}^{-1}_{(+,4,\Omega)}\right]. \tag{5.1.35} $$

The next step is to compute the second covariant derivative, before then taking the coincidence limit. The intermediary steps will be omitted, but this results in the following nonzero components:

$$ \begin{aligned} {}_{(4,\Omega)}\omega^j_{\tau\tau} =& \frac{a^2\sec^2(\rho)}{8\pi^2\mathcal{A}^3_{(-,4,\Omega)}\Gamma^2_{(4)}}\left[\mathcal{A}^2_{(-,4,\Omega)} + \mathcal{A}_{(-,4,\Omega)} - 2\Gamma^2_{(4)}\sec^2(\rho)\mathcal{S}^2_{(4)}\right] \\ &- \frac{a^2\sec^2(\rho)}{8\pi^2\mathcal{A}^3_{(+,4,\Omega)}\Gamma^2_{(4)}}\left[\mathcal{A}^2_{(+,4,\Omega)} - \mathcal{A}_{(+,4,\Omega)} - 2\Gamma^2_{(4)}\sec^2(\rho)\mathcal{S}^2_{(4)}\right], \end{aligned} \tag{5.1.36a} $$

$$ {}_{(4,\Omega)}\omega^j_{\tau\rho} = \frac{a^2 i\sec^4(\rho)\tan(\rho)}{4\pi^2\mathcal{A}^3_{(-,4,\Omega)}\mathcal{A}^3_{(+,4,\Omega)}}\mathcal{C}_{(4)}\mathcal{S}_{(4)}\left[\mathcal{A}^3_{(+,4,\Omega)} - \lambda\mathcal{A}^3_{(-,4,\Omega)}\right], \tag{5.1.36b} $$

$$ {}_{(4,\Omega)}\omega^j_{\tau\theta} = -\frac{a^2 i\cos(\theta)\sin(\theta)\sec^2(\rho)\tan^2(\rho)}{4\pi^2\mathcal{A}^3_{(-,4,\Omega)}\mathcal{A}^3_{(+,4,\Omega)}}\left[1-\cosh(j\beta\Omega)\right]\mathcal{S}_{(4)}\left[\mathcal{A}^3_{(+,4,\Omega)} - \lambda\mathcal{A}^3_{(-,4,\Omega)}\right], \tag{5.1.36c} $$

$$ \begin{aligned} {}_{(4,\Omega)}\omega^j_{\tau\phi} =& -\frac{a^2\sin^2(\theta)\tan^2(\rho)}{8\pi^2\mathcal{A}^3_{(-,4,\Omega)}}\left[\Omega\mathcal{A}^2_{(-,4,\Omega)} + \Omega\mathcal{A}_{(-,4,\Omega)} - 2\sinh(j\beta\Omega)\sec^2(\rho)\mathcal{S}_{(4)}\right] \\ &+ \frac{a^2\lambda\sin^2(\theta)\tan^2(\rho)}{8\pi^2\mathcal{A}^3_{(+,4,\Omega)}}\left[\Omega\mathcal{A}^2_{(+,4,\Omega)} - \Omega\mathcal{A}_{(+,4,\Omega)} - 2\sinh(j\beta\Omega)\sec^2(\rho)\mathcal{S}_{(4)}\right], \end{aligned} \tag{5.1.36d} $$

$$ \begin{aligned} {}_{(4,\Omega)}\omega^j_{\rho\rho} =& -\frac{a^2\sec^2(\rho)}{8\pi^2\mathcal{A}^3_{(-,4,\Omega)}}\left[\mathcal{A}^2_{(-,4,\Omega)} + \mathcal{A}_{(-,4,\Omega)} - 2\sec^2(\rho)\tan^2(\rho)\mathcal{C}^2_{(4)}\right] \\ &+ \frac{a^2\lambda\sec^2(\rho)}{8\pi^2\mathcal{A}^3_{(+,4,\Omega)}}\left[\mathcal{A}^2_{(+,4,\Omega)} - \mathcal{A}_{(+,4,\Omega)} - 2\sec^2(\rho)\tan^2(\rho)\mathcal{C}^2_{(4)}\right], \end{aligned} \tag{5.1.36e} $$

$$
{}_{(4,\Omega)}\omega^{j}_{\rho\theta} = -\frac{a^2\cos(\theta)\sin(\theta)\sec^2(\rho)\tan^3(\rho)}{4\pi^2\mathcal{A}^3_{(-,4,\Omega)}\mathcal{A}^3_{(+,4,\Omega)}}\left[1-\cosh(j\beta\Omega)\right]\mathcal{C}_{(4)}\left[\mathcal{A}^3_{(+,4,\Omega)}-\lambda\mathcal{A}^3_{(-,4,\Omega)}\right], \tag{5.1.36f}
$$

$$
{}_{(4,\Omega)}\omega^{j}_{\rho\phi} = -\frac{a^2 i\sinh(j\beta\Omega)\sin^2(\theta)\sec^2(\rho)\tan^3(\rho)}{4\pi^2\mathcal{A}^3_{(-,4,\Omega)}\mathcal{A}^3_{(+,4,\Omega)}}\mathcal{C}_{(4)}\left[\mathcal{A}^3_{(+,4,\Omega)}-\lambda\mathcal{A}^3_{(-,4,\Omega)}\right], \tag{5.1.36g}
$$

$$
\begin{aligned}
{}_{(4,\Omega)}\omega^{j}_{\theta\theta} = &-\frac{a^2\tan^2(\rho)}{8\pi^2\mathcal{A}^3_{(-,4,\Omega)}}\left[\mathcal{A}^2_{(-,4,\Omega)}+\mathcal{A}_{(-,4,\Omega)}-2\{1-\cosh(j\beta\Omega)\}^2\cos^2(\theta)\sin^2(\theta)\tan^2(\rho)\right]\\
&+\frac{a^2\tan^2(\rho)}{8\pi^2\mathcal{A}^3_{(+,4,\Omega)}}\left[\mathcal{A}^2_{(+,4,\Omega)}-\mathcal{A}_{(+,4,\Omega)}-2\{1-\cosh(j\beta\Omega)\}^2\cos^2(\theta)\sin^2(\theta)\tan^2(\rho)\right],
\end{aligned} \tag{5.1.36h}
$$

$$
{}_{(4,\Omega)}\omega^{j}_{\theta\phi} = \frac{a^2 i\sinh(j\beta\Omega)\cos(\theta)\sin^3(\theta)\tan^4(\rho)}{4\pi^2\mathcal{A}^3_{(-,4,\Omega)}\mathcal{A}^3_{(+,4,\Omega)}}\left[1-\cosh(j\beta\Omega)\right]\left[\mathcal{A}^3_{(+,4,\Omega)}-\lambda\mathcal{A}^3_{(-,4,\Omega)}\right], \tag{5.1.36i}
$$

$$
\begin{aligned}
{}_{(4,\Omega)}\omega^{j}_{\phi\phi} = &-\frac{a^2\sin^2(\theta)\tan^2(\rho)}{8\pi^2\mathcal{A}^3_{(-,4,\Omega)}}\left[\mathcal{A}^2_{(-,4,\Omega)}+\mathcal{A}_{(-,4,\Omega)}+2\sinh^2(j\beta\Omega)\sin^2(\theta)\tan^2(\rho)\right]\\
&+\frac{a^2\lambda\sin^2(\theta)\tan^2(\rho)}{8\pi^2\mathcal{A}^3_{(+,4,\Omega)}}\left[\mathcal{A}^2_{(+,4,\Omega)}-\mathcal{A}_{(+,4,\Omega)}+2\sinh^2(j\beta\Omega)\sin^2(\theta)\tan^2(\rho)\right].
\end{aligned} \tag{5.1.36j}
$$

There are a few things of note here. Firstly, the off-diagonal components are symmetric under the interchange of the their indices, owing to the torsion-free property of the covariant derivative. Perhaps more interestingly, however, is the appearance of imaginary coefficients in some of the components. Initially, it may seem concerning; after all, we want a real-valued renormalised stress-energy tensor. The quantities in question are in fact the individual $j$-terms, which we will sum over for $j \neq 0$. It is clear that $\mathcal{C}_{(4)}$ is even, whilst $\mathcal{S}_{(4)}$ is odd in $j$. This means that when we perform the sum, these components will vanish.

There is a consistency check we can perform on the above components. Recall equation (2.7.44), from [103], which states that the trace of the coincidence limit of the second covariant derivative of ${}_{(4,\Omega)}W(x,x')$ is proportional to its coincidence limit. For a four-

dimensional massless and conformally coupled scalar field theory, we have

$$ {}_{(4,\Omega)}\omega^{j\,\mu}_{\mu} = \frac{1}{6} R\, {}_{(4,\Omega)}\omega^{j}, \tag{5.1.37} $$

with $R = -12a^2$ the Ricci scalar. The trace can be computed as

$$ {}_{(4,\Omega)}\omega^{j\,\mu}_{\mu} = -\frac{a^4}{4\pi^2 \mathcal{A}_{(-,4,\Omega)}\mathcal{A}_{(+,4,\Omega)}} \left[\mathcal{A}_{(+,4,\Omega)} - \lambda \mathcal{A}_{(-,4,\Omega)}\right], \tag{5.1.38} $$

from which it should be clear to see that equation (5.1.37) holds. A minor clarification: normally, this holds for the whole contribution to the stress-energy tensor (i.e. the sum over $j \neq 0$), however, in this case it holds for each $j$-term in the sum. This is not something that is necessarily true in general.

From here, the next step is to compute the second covariant derivative of the coincidence limit. Whilst the details of such a computation will be omitted for brevity, this results in the following nonzero components:

$$ \begin{aligned} \nabla_\tau \nabla_\tau \left[{}_{(4,\Omega)}\omega^{j}\right] =& \frac{a^2 \tan^2(\rho)}{4\pi^2 \mathcal{A}^2_{(-,4,\Omega)}} \left[\mathcal{A}_{(-,4,\Omega)} \left\{1 - \Omega^2 \sin^2(\theta)\right\}\right. \\ &+ \left(1-\Omega^2\right)\left\{1 - \cosh(j\beta\Omega)\right\}\sin^2(\theta)\Big] \\ &- \frac{a^2 \lambda \tan^2(\rho)}{4\pi^2 \mathcal{A}^2_{(+,4,\Omega)}} \left[\mathcal{A}_{(+,4,\Omega)} \left\{1 - \Omega^2 \sin^2(\theta)\right\}\right. \\ &+ \left(1-\Omega^2\right)\left\{1 - \cosh(j\beta\Omega)\right\}\sin^2(\theta) - 2\left\{1 - \Omega^2 \sin^2(\theta)\right\}\Big], \end{aligned} \tag{5.1.39a} $$

$$ \begin{aligned} \nabla_\tau \nabla_\phi \left[{}_{(4,\Omega)}\omega^{j}\right] =& -\frac{a^2 \Omega \sin^2(\theta)\tan^2(\rho)}{4\pi^2 \mathcal{A}^2_{(-,4,\Omega)}} \left[\mathcal{A}_{(-,4,\Omega)} + 1 - \cosh(j\beta\Omega)\right], \\ &+ \frac{a^2 \lambda \Omega \sin^2(\theta)\tan^2(\rho)}{4\pi^2 \mathcal{A}^2_{(+,4,\Omega)}} \left[\mathcal{A}_{(+,4,\Omega)} - 1 - \cosh(j\beta\Omega)\right], \end{aligned} \tag{5.1.39b} $$

$$ \begin{aligned} \nabla_\rho \nabla_\rho \left[{}_{(4,\Omega)}\omega^{j}\right] =& -\frac{a^2}{4\pi^2 \mathcal{A}^3_{(-,4,\Omega)}} \Big[\mathcal{A}^2_{(-,4,\Omega)} \left\{1 - 2\tan^2(\rho)\right\} \\ &+ \mathcal{A}_{(-,4,\Omega)} \left\{1 - \cosh(j\beta\Omega)\right\}\left\{1 - 6\tan^2(\rho)\right\}\sin^2(\theta) \\ &-4\left\{1 - \cosh(j\beta\Omega)\right\}^2 \sin^4(\theta)\tan^2(\rho)\Big] \\ &+ \frac{a^2 \lambda}{4\pi^2 \mathcal{A}^3_{(+,4,\Omega)}} \Big[\mathcal{A}^2_{(+,4,\Omega)} \left\{1 - 2\tan^2(\rho)\right\} \end{aligned} $$

$$
\begin{aligned}
&- \mathcal{A}_{(+,4,\Omega)} \left\{2 - [1-\cosh(j\beta\Omega)]\sin^2(\theta)\right\} \left\{1 - 6\tan^2(\rho)\right\} \\
&- 4\left\{2 - [1-\cosh(j\beta\Omega)]\sin^2(\theta)\right\}^2 \tan^2(\rho)\Big], \qquad (5.1.39c)
\end{aligned}
$$

$$
\begin{aligned}
\nabla_\rho \nabla_\theta \left[{}_{(4,\Omega)}\omega^j\right] = &- \frac{a^2\cos(\theta)\sin(\theta)\tan(\rho)}{4\pi^2\mathcal{A}^3_{(-,4,\Omega)}} \{1-\cosh(j\beta\Omega)\} \left[\mathcal{A}_{(-,4,\Omega)}\left\{1 - 3\tan^2(\rho)\right\}\right. \\
&+ 4\{1-\cosh(j\beta\Omega)\}\sin^2(\theta)\tan^2(\rho)\Big], \\
&+ \frac{a^2\lambda\cos(\theta)\sin(\theta)\tan(\rho)}{4\pi^2\mathcal{A}^3_{(+,4,\Omega)}} \{1-\cosh(j\beta\Omega)\} \left[\mathcal{A}_{(+,4,\Omega)}\left\{1 - 3\tan^2(\rho)\right\}\right. \\
&- 4\left\{2 - [1-\cosh(j\beta\Omega)]\sin^2(\theta)\right\}\tan^2(\rho)\Big], \qquad (5.1.39d)
\end{aligned}
$$

$$
\begin{aligned}
\nabla_\theta \nabla_\theta \left[{}_{(4,\Omega)}\omega^j\right] = &- \frac{a^2\tan^2(\rho)}{4\pi^2\mathcal{A}^3_{(-,4,\Omega)}} \Big[\mathcal{A}^2_{(-,4,\Omega)} + \mathcal{A}_{(-,4,\Omega)}\{1-\cosh(j\beta\Omega)\}\cos^2(\theta) \\
&- 4\{1-\cosh(j\beta\Omega)\}^2\cos^2(\theta)\sin^2(\theta)\tan^2(\rho)\Big] \\
&+ \frac{a^2\lambda\tan^2(\rho)}{4\pi^2\mathcal{A}^3_{(+,4,\Omega)}} \Big[\mathcal{A}^2_{(+,4,\Omega)} - \mathcal{A}_{(+,4,\Omega)}\left\{2 - [1-\cosh(j\beta\Omega)]\cos^2(\theta)\right\} \\
&- 4\{1-\cosh(j\beta\Omega)\}^2\cos^2(\theta)\sin^2(\theta)\tan^2(\rho)\Big], \qquad (5.1.39e)
\end{aligned}
$$

$$
\begin{aligned}
\nabla_\phi \nabla_\phi \left[{}_{(4,\Omega)}\omega^j\right] = &- \frac{a^2\sin^2(\theta)\tan^2(\rho)}{4\pi^2\mathcal{A}^2_{(-,4,\Omega)}} \left[\mathcal{A}_{(-,4,\Omega)} + 1 - \cosh(j\beta\Omega)\right] \\
&+ \frac{a^2\lambda\sin^2(\theta)\tan^2(\rho)}{4\pi^2\mathcal{A}^2_{(+,4,\Omega)}} \left[\mathcal{A}_{(+,4,\Omega)} - 1 - \cosh(j\beta\Omega)\right]. \qquad (5.1.39f)
\end{aligned}
$$

There is not much worth remarking upon here. The only points worth mentioning are that there are no imaginary parts since ${}_{(4,\Omega)}\omega^j$ is manifestly real, and somewhat surprisingly, the $\rho\rho$-component is the most complicated.

The next step is to apply the covariant d'Alembertian operator to the coincidence limit. This amounts to taking the trace of equation (5.1.39), resulting in the following expression:

$$
\begin{aligned}
\nabla_\mu \nabla^\mu \left[{}_{(4,\Omega)}\omega^j(x)\right] &= \Box\left[{}_{(4,\Omega)}\omega^j(x)\right] \\
&= - \frac{a^4}{4\pi^2\mathcal{A}^3_{(-,4,\Omega)}} \Big[\mathcal{A}^2_{(-,4,\Omega)} - 2\mathcal{A}_{(-,4,\Omega)}\{2 + \cosh(j\beta) + \cosh(j\beta\Omega)\} \\
&\qquad - 4\widetilde{\mathcal{A}}_{(4)}\Big]
\end{aligned}
$$

$$+\frac{a^4\lambda}{4\pi^2\mathcal{A}^3_{(+,4,\Omega)}}\Big[\mathcal{A}^2_{(+,4,\Omega)}-2\mathcal{A}_{(+,4,\Omega)}\left\{-1+\cosh(j\beta)+\cosh(j\beta\Omega)\right\} - 4\widetilde{\mathcal{A}}_{(4)}\Big]. \tag{5.1.40}$$

We now have all of the constituent parts, allowing us to finally construct the $j$-summand of the thermal expectation value of the stress-energy tensor. Recall from section 2.7 the form of the renormalised stress-energy tensor (2.7.37) in terms of the short-distance coefficients $\omega$ and $\omega_{\mu\nu}$. Specialised to four-dimensional, rigidly-rotating anti-de Sitter space-time we have

$${}_{(4,\Omega)}\langle\widehat{T}^j_{\mu\nu}\rangle_\beta=-{}_{(4,\Omega)}\omega^j_{\mu\nu}+\frac{1}{3}\nabla_\mu\nabla_\nu\left[{}_{(4,\Omega)}\omega^j\right]-\frac{1}{12}\left(\Box\left[{}_{(4,\Omega)}\omega^j\right]+6a^2\,{}_{(4,\Omega)}\omega^j\right)g_{\mu\nu}, \tag{5.1.41}$$

along with

$${}_{(4,\Omega)}\langle\widehat{T}_{\mu\nu}\rangle_\beta=\sum_{j\neq 0}{}_{(4,\Omega)}\langle\widehat{T}^j_{\mu\nu}\rangle_\beta. \tag{5.1.42a}$$

To compute the full thermal expectation value for the stress-energy tensor, one would need to perform the sum over $j\neq 0$.

Below, the nonzero components (for single $j$-summands) are presented. Since the expressions for the components are rather long, we have defined new quantities to aid in the transcription of the components into a more readable form; these are defined immediately proceeding each component. We begin with the $\tau\tau$-component, which is given as

$$\begin{aligned}{}_{(4,\Omega)}\langle\widehat{T}^j_{\tau\tau}\rangle_\beta=&-\frac{a^2\sec^2(\rho)}{24\pi^2\mathcal{A}^3_{(-,4,\Omega)}}\left[\mathcal{A}^2_{(-,4,\Omega)}\mathcal{B}_{(4,\Omega;\,\tau\tau,-,2)}+\mathcal{A}_{(-,4,\Omega)}\mathcal{B}_{(4,\Omega;\,\tau\tau,-,1)}-2\mathcal{B}_{(4,\Omega;\,\tau\tau,-,0)}\right]\\&+\frac{a^2\lambda\sec^2(\rho)}{24\pi^2\mathcal{A}^3_{(+,4,\Omega)}}\left[\mathcal{A}^2_{(+,4,\Omega)}\mathcal{B}_{(4,\Omega;\,\tau\tau,+,2)}+\mathcal{A}_{(+,4,\Omega)}\mathcal{B}_{(4,\Omega;\,\tau\tau,+,1)}-2\mathcal{B}_{(4,\Omega;\,\tau\tau,+,0)}\right],\end{aligned} \tag{5.1.42b}$$

where we have defined (recalling that $\Gamma_{(4)}$ was defined in equation (5.1.34e))

$$\mathcal{B}_{(4,\Omega;\,\tau\tau,-,2)}=3\Gamma^{-2}_{(4)}-1-\left[2-3\Omega^2\sin^2(\theta)\right]\sin^2(\rho), \tag{5.1.42c}$$

$$\begin{aligned}\mathcal{B}_{(4,\Omega;\,\tau\tau,-,1)} =& 3\Gamma_{(4)}^{-2} - [2+\cosh(j\beta)+\cosh(j\beta\Omega)] \\ & - \left[2 - 2\cosh(j\beta\Omega) - \Omega^2\left\{4+\cosh(j\beta)-\cosh(j\beta\Omega)\right\}\right]\sin^2(\theta)\sin^2(\rho),\end{aligned} \tag{5.1.42d}$$

$$\begin{aligned}\mathcal{B}_{(4,\Omega;\,\tau\tau,-,0)} =& \widetilde{\mathcal{A}}_{(4)}\Gamma_{(4)}^{-2} + 3\sec^2(\rho)\mathcal{S}_{(4)}^2 \\ & + 2\Omega^2\sin^2(\theta)\sin^2(\rho)\tan^2(\rho)\left[1-2\sinh^2(j\beta\Omega)\sin^2(\theta)\right],\end{aligned} \tag{5.1.42e}$$

$$\mathcal{B}_{(4,\Omega;\,\tau\tau,+,2)} = -\,\mathcal{B}_{(4,\Omega;\,\tau\tau,-,2)}, \tag{5.1.42f}$$

$$\mathcal{B}_{(4,\Omega;\,\tau\tau,+,1)} = -\,\mathcal{B}_{(4,\Omega;\,\tau\tau,-,1)} + 6\Gamma_{(4)}^{-2} - 3 - \left[4-7\Omega^2\sin^2(\theta)\right]\sin^2(\rho), \tag{5.1.42g}$$

$$\mathcal{B}_{(4,\Omega;\,\tau\tau,+,0)} = -\,\mathcal{B}_{(4,\Omega;\,\tau\tau,-,0)}. \tag{5.1.42h}$$

The next component we consider is the $\tau\phi$-component. This can be written down in terms of the $\phi\phi$-component, which will be given further down. We have

$${}_{(4,\Omega)}\langle\widehat{T}^j_{\tau\phi}\rangle_\beta = -\frac{a^2\sinh(j\beta)\sinh(j\beta\Omega)\sec^2(\rho)\tan^2(\rho)}{4\pi^2\mathcal{A}^3_{(-,4,\Omega)}\mathcal{A}^3_{(+,4,\Omega)}}\left[\mathcal{A}^3_{(+,4,\Omega)} - \lambda\mathcal{A}^3_{(-,4,\Omega)}\right] - \Omega\,{}_{(4,\Omega)}\langle\widehat{T}^j_{\phi\phi}\rangle_\beta. \tag{5.1.42i}$$

Next is the $\rho\rho$-component, given by

$$\begin{aligned}{}_{(4,\Omega)}\langle\widehat{T}^j_{\rho\rho}\rangle_\beta =& \frac{a^2}{24\pi^2\mathcal{A}^3_{(-,4,\Omega)}}\left[6\mathcal{A}^2_{(-,4,\Omega)}\tan^2(\rho) - \mathcal{B}_{(4,\Omega;\,\rho\rho,-,1)} + \mathcal{B}_{(4,\Omega;\,\rho\rho,-,0)}\sec^2(\rho)\right] \\ & - \frac{a^2\lambda}{24\pi^2\mathcal{A}^3_{(+,4,\Omega)}}\left[6\mathcal{A}^2_{(+,4,\Omega)}\tan^2(\rho) - \mathcal{B}_{(4,\Omega;\,\rho\rho,+,1)} + \mathcal{B}_{(4,\Omega;\,\rho\rho,+,0)}\sec^2(\rho)\right],\end{aligned} \tag{5.1.42j}$$

where

$$\begin{aligned}\mathcal{B}_{(4,\Omega;\,\rho\rho,-,1)} =& \cosh(j\beta)\sec^2(\rho)\left\{1+12\sec^2(\rho)\right\} \\ & - [1-\cosh(j\beta\Omega)]\left\{\sec^2(\rho) - 2\sin^2(\theta)\left[1-6\tan^2(\rho)\right]\right\},\end{aligned} \tag{5.1.42k}$$

$$\begin{aligned}\mathcal{B}_{(4,\Omega;\,\rho\rho,-,0)} =& 6\left\{1-\cosh(j\beta)\sec^2(\rho)\right\}^2 - 8\left\{1-\cosh^2(j\beta)\sec^2(\rho)\right\} \\ & + 2\left\{1-\cosh(j\beta\Omega)\right\}^2\sin^2(\theta)\sin^2(\rho)\left\{4\sin^2(\theta)+3\cos^2(\theta)\sec^4(\rho)\right\} \\ & - 2\tan^2(\rho)\left\{\cos^2(\theta)+\cosh^2(j\beta\Omega)\sin^2(\theta)\right\}\left[1+3\sec^2(\rho)\right],\end{aligned} \tag{5.1.42l}$$

$$\mathcal{B}_{(4,\Omega;\,\rho\rho,+,1)} = \mathcal{B}_{(4,\Omega;\,\rho\rho,-,1)} + 4\cos^2(\theta)\left\{4-3\sec^4(\rho)\right\} - 3\left\{4-9\sec^2(\rho)\right\}, \tag{5.1.42m}$$

$$\begin{aligned}\mathcal{B}_{(4,\Omega;\,\rho\rho,+,0)} =& \mathcal{B}_{(4,\Omega;\,\rho\rho,-,0)} + 4\cosh(j\beta)\left\{4 + 6\sec^2(\rho) + \cos^2(\theta)\left[4 - 3\sec^4(\rho)\right]\right\} \\ &+ 4\cosh(j\beta\Omega)\sin^2(\theta)\sin^2(\rho)\left\{4\sin^2(\theta) + 3\cos^2(\theta)\sec^4(\rho)\right\} \\ &+ 4\left\{4\cos^2(\rho) + \cos^2(\theta)\left[4 - 3\sec^2(\rho)\right] - \cos^4(\theta)\sin^2(\rho)\left[4 - 3\sec^4(\rho)\right]\right\}.\end{aligned} \tag{5.1.42n}$$

For the $\rho\theta$-component, we have

$$\begin{aligned}{}_{(4,\Omega)}\langle\widehat{T}^j_{\rho\theta}\rangle_\beta =& -\frac{a^2\cos(\theta)\sin(\theta)\tan(\rho)}{12\pi^2\mathcal{A}^3_{(-,4,\Omega)}}\left[1 - \cosh(j\beta\Omega)\right]\left[\mathcal{A}_{(-,4,\Omega)} - \mathcal{B}_{(4,\Omega;\,\rho\theta,-,0)}\right] \\ &+ \frac{a^2\lambda\cos(\theta)\sin(\theta)\tan(\rho)}{12\pi^2\mathcal{A}^3_{(+,4,\Omega)}}\left[1 - \cosh(j\beta\Omega)\right]\left[\mathcal{A}_{(+,4,\Omega)} + \mathcal{B}_{(4,\Omega;\,\rho\theta,+,0)}\right],\end{aligned} \tag{5.1.42o}$$

where

$$\mathcal{B}_{(4,\Omega;\,\rho\theta,-,0)} = \{1 - \cosh(j\beta\Omega)\}\sin^2(\theta)\tan^2(\rho), \tag{5.1.42p}$$

$$\mathcal{B}_{(4,\Omega;\,\rho\theta,+,0)} = \left\{2 - [1 - \cosh(j\beta\Omega)]\sin^2(\theta)\right\}\tan^2(\rho). \tag{5.1.42q}$$

The $\theta\theta$-component is given as

$$\begin{aligned}{}_{(4,\Omega)}\langle\widehat{T}^j_{\theta\theta}\rangle_\beta =& -\frac{a^2\tan^2(\rho)}{24\pi^2\mathcal{A}^3_{(-,4,\Omega)}}\left[\mathcal{A}_{(-,4,\Omega)}\mathcal{B}_{(4,\Omega;\,\theta\theta,-,1)} + 2\mathcal{B}_{(4,\Omega;\,\theta\theta,-,0)}\right] \\ &+ \frac{a^2\lambda\tan^2(\rho)}{24\pi^2\mathcal{A}^3_{(+,4,\Omega)}}\left[\mathcal{A}_{(+,4,\Omega)}\mathcal{B}_{(4,\Omega;\,\theta\theta,+,1)} + 2\mathcal{B}_{(4,\Omega;\,\theta\theta,+,0)}\right],\end{aligned} \tag{5.1.42r}$$

where

$$\mathcal{B}_{(4,\Omega;\,\theta\theta,-,1)} = -1 + \cosh(j\beta) + \cosh(j\beta\Omega) + 2\cos^2(\theta)\left[1 - \cosh(j\beta\Omega)\right], \tag{5.1.42s}$$

$$\mathcal{B}_{(4,\Omega;\,\theta\theta,-,0)} = 1 - \cosh^2(j\beta\Omega)\sec^2(\rho) + \left[\cos^2(\theta) + \cosh(j\beta\Omega)\sin^2(\theta)\right]^2\tan^2(\rho), \tag{5.1.42t}$$

$$\mathcal{B}_{(4,\Omega;\,\theta\theta,+,1)} = \mathcal{B}_{(4,\Omega;\,\theta\theta,-,1)} - 1, \tag{5.1.42u}$$

$$\mathcal{B}_{(4,\Omega;\,\theta\theta,+,0)} = \mathcal{B}_{(4,\Omega;\,\theta\theta,-,0)}. \tag{5.1.42v}$$

Finally, for the $\phi\phi$-component, we have

$${}_{(4,\Omega)}\langle\widehat{T}^j_{\phi\phi}\rangle_\beta = -\frac{a^2\sin^2(\theta)\tan^2(\rho)}{24\pi^2\mathcal{A}^3_{(-,4,\Omega)}}\left[\mathcal{A}_{(-,4,\Omega)}\mathcal{B}_{(4,\Omega;\,\phi\phi,-,1)} + 2\mathcal{B}_{(4,\Omega;\,\phi\phi,-,0)}\right]$$

$$+\frac{a^2\lambda\sin^2(\theta)\tan^2(\rho)}{24\pi^2\mathcal{A}^3_{(+,4,\Omega)}}\left[\mathcal{A}_{(+,4,\Omega)}\mathcal{B}_{(4,\Omega;\,\phi\phi,+,1)}+2\mathcal{B}_{(4,\Omega;\,\phi\phi,+,0)}\right], \tag{5.1.42w}$$

where

$$\mathcal{B}_{(4,\Omega;\,\phi\phi,-,1)} = 1+\cosh(j\beta)-\cosh(j\beta\Omega), \tag{5.1.42x}$$

$$\begin{aligned}\mathcal{B}_{(4,\Omega;\,\phi\phi,-,0)} =& 1-\cosh^2(j\beta)\sec^2(\rho)+\cos^2(\theta)\tan^2(\rho)+\cosh^2(j\beta\Omega)\sin^2(\theta)\tan^2(\rho)\\ &-3\sinh^2(j\beta\Omega)\sin^2(\theta)\tan^2(\rho),\end{aligned} \tag{5.1.42y}$$

$$\mathcal{B}_{(4,\Omega;\,\phi\phi,+,1)} = \mathcal{B}_{(4,\Omega;\,\phi\phi,-,1)}-1, \tag{5.1.42z}$$

$$\mathcal{B}_{(4,\Omega;\,\phi\phi,+,0)} = \mathcal{B}_{(4,\Omega;\,\phi\phi,-,0)}. \tag{5.1.42aa}$$

To find the full components, one would need to perform the infinite sum over $j \neq 0$. However, algebraically speaking, it is intractable to compute this in closed form. For the purposes of producing plots therefore, we proceed numerically - see below.

There are a few things upon which it is worth remarking. Firstly, in order to satisfy Wald's axioms (see section 2.7), the renormalised stress-energy tensor must satisfy conservation, i.e.

$$\nabla^{\mu}{}_{(4,\Omega)}\langle\widehat{T}_{\mu\nu}\rangle_{\beta} = 0. \tag{5.1.43}$$

Since the renormalised stress-energy tensor components for individual $j$-summands are continuous[2], we can interchange the order of the covariant derivative and summation over $j$. That is, we can perform the differentiation upon the single $j$-summand expressions first, before summing:

$$\nabla^{\mu}\left[\sum_{j\neq 0}{}_{(4,\Omega)}\langle\widehat{T}^{j}_{\mu\nu}\rangle_{\beta}\right] = \sum_{j\neq 0}\left[\nabla^{\mu}{}_{(4,\Omega)}\langle\widehat{T}^{j}_{\mu\nu}\rangle_{\beta}\right]. \tag{5.1.44}$$

Using this method, we find that all four of the components of the conservation equation are nonzero. Whilst initially this may seem concerning - after all this would suggest that the renormalised stress-energy tensor does not satisfy Wald's axioms and therefore is not

[2]Strictly speaking, we also require uniform convergence. Whilst not rigorous, we only consider the individual $j$-summands.

valid - we notice that all four of these components are odd functions in $j$. Thus these sum to zero and conservation does indeed hold.

Second, computing the trace brings up an interesting point. Whilst for a four-dimensional conformally-coupled scalar field theory one would normally have a trace anomaly for the renormalised stress-energy tensor, we actually have a zero trace. This is due to the renormalisation prescription chosen: it is true in general that the trace is state-independent [371], so using state subtraction means we will have a zero trace. We find a similar phenomenon when evaluating the zero temperature ($\beta \to \infty$) limit. Taking the limit $\beta \to \infty$ of the stress-energy tensor components (5.1.42) yields zero across the board. Mathematically speaking, this is because each $j$-term in the sum converges fairly rapidly toward zero, owing to the fact that the quantities $\mathcal{A}_{(\pm,4,\Omega)}$ (5.1.34a) tend toward infinity quicker than the coefficients $\mathcal{B}_{(4,\Omega;\bullet,\pm,\bullet)}$. However, this is just a manifestation of using a state-subtraction renormalisation procedure. Indeed, the renormalised stress-energy tensor components (5.1.42) are *constructed* as the difference between the thermal and vacuum (5.1.25) expectation values. This therefore gives a check on the validity of the renormalised stress-energy tensor components.

Another point worth mentioning is with regards to the underlying structure of the renormalised stress-energy tensor. In the nonrotating four-dimensional case, the stress-energy tensor (5.1.23) is proportional to the metric plus contributions proportional to time- and space-like vectors. This means that the structure (i.e. where there are zeroes and where there are not) of the metric and the renormalised stress-energy tensor match. It is not unreasonable to therefore suggest that we may have a similar case here; however, the stress-energy tensor has nonzero $\rho\theta$- and $\theta\rho$-components, whereas the $\rho\theta$- and $\theta\rho$-components of the metric are zero.

Finally, we consider the functional dependence of the stress-energy tensor components. Whilst for the nonrotating case, the components of the renormalised stress-energy tensor

(5.1.23) had functional dependence only on $\rho$, applying a rigid rotation to the field (and metric tensor) results in the components of the renormalised stress-energy tensor (for four-dimensional, rotating anti-de Sitter space-time) having functional dependence on both $\rho$ and $\theta$. As such, in figures 5.5, 5.6, 5.7, 5.8, 5.9 and 5.10, the components are plotted as functions of $\rho$ and $\theta$, for three different values of the angular speed $\Omega$. In order to plot the components of the stress-energy tensor, we were forced to make a choice of summation range; for our purposes, terminating the sum at $j = \pm 100$ was sufficient (see appendix A for more details on numerical checks employed in this thesis). Before we consider the below figures, in particular the figures 5.5, 5.6, 5.7, 5.8, 5.9 and 5.10, we need to make one minor clarification. These plots are all produced for the case of Dirichlet boundary conditions. This is somewhat of an arbitrary choice; we could have just as well produced these plots for Neumann or transparent boundary conditions. Qualitatively, the plots arising from considering Neumann or transparent boundary conditions look the same - this is discussed in more detail in section 5.3.4. A word of warning regarding the following plots, however: it is not trivial to compare the figures in this thesis, say, for example, figures 5.1a and 5.5, since the plots for the nonrotating case are of the components with mixed indices, whereas for the rotating case they are both indices down. This is something that will also be addressed in section 5.3.4. Finally, all of the following figures show the thermal expectation value minus the vacuum expectation value (5.1.25), which is constant.

Figure 5.5 shows ${}_{(4,\Omega)}\langle \widehat{T}_{\tau\tau} \rangle$ as a function of both $\rho$ and $\theta$, for three different angular rotation speeds: $\Omega = 0$, $\Omega = 0.5$, and $\Omega = 0.96$. The $\Omega = 0$ case is just a function of $\rho$ and is independent of $\theta$. Although not immediately obvious, the $\Omega = 0.5$ case is not independent of $\theta$, and in fact, figures 5.5a and 5.5b are not the same. The $\Omega = 0$ case being independent of $\theta$ is entirely to be expected; we should require that taking the angular rotation speed to zero would reproduce the results in Section 5.1.1. Despite plotting the mixed indices $\tau\tau$-component in figure 5.1 and both indices down in figure 5.5a, and with different inverse temperatures, it is obvious that they both have the same profile. Indeed,

when considering the covariant $\tau\tau$-component of the rotating renormalised stress-energy tensor, with angular speed $\Omega = 0$, and the corresponding nonrotating component at some fixed inverse temperature, we see that the plots match up to an additive nonzero constant, corresponding to the vacuum expectation value absent in the rotating plots but included in the plots for the nonrotating renormalised stress-energy tensor (5.1.23). Again, this is due to the state subtraction renormalisation prescription we use in this case. As the angular rotation speed increases, we see an interesting phenomenon. What can only be described as a hump starts to form away from the origin and towards the space-time boundary at $\rho = \pi/2$, localised around the equatorial plane $\theta = \pi/2$. This feature is most apparent at high angular speeds; in particular figure 5.5c. Whilst it may seem that this is a local maximum based on the viewing angle of the plot, the maximum remains at the origin, $\rho = 0$. In fact, this remains the case at *all* values of both $\Omega$ and $\theta$. This tells us that for the $\tau\tau$-component, there is no angular dependence at $\rho = 0$, which means the rotation has no effect on the axis. This is also true of the $\rho = \pi/2$ axis.

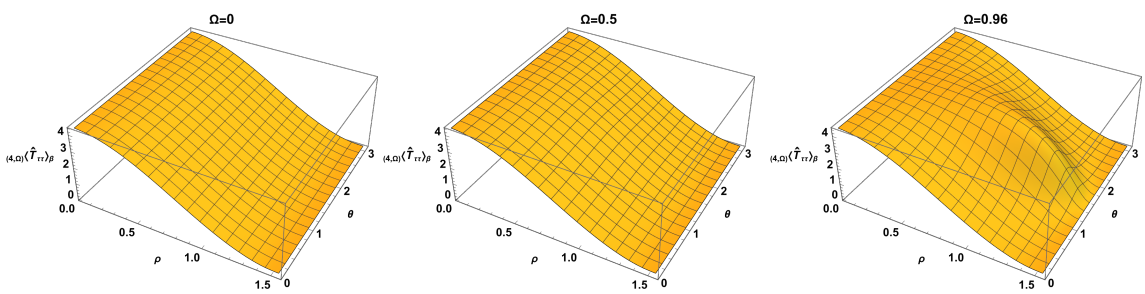


(a) $\Omega = 0$ (b) $\Omega = 0.5$ (c) $\Omega = 0.96$

Figure 5.5: The $\tau\tau$-component of the renormalised stress-energy tensor. The inverse adS length scale $a = 1$ is kept fixed, as is the inverse temperature $\beta = \pi/6$. The angular rotation speed $\Omega$ is varied. Dirichlet boundary conditions are applied to the field.

Figure 5.6 shows the corresponding plots, but for the (negative) $\tau\phi$-component. At $\Omega = 0$, we have an entirely flat surface at 0; this is to be expected since the nonrotating stress-

energy tensor has no $\tau\phi$-component. As the angular speed increases, the local (absolute) maximum moves towards the space-time boundary, $\rho = \pi/2$, along the equatorial plane $\theta = \pi/2$. These components are always negative.

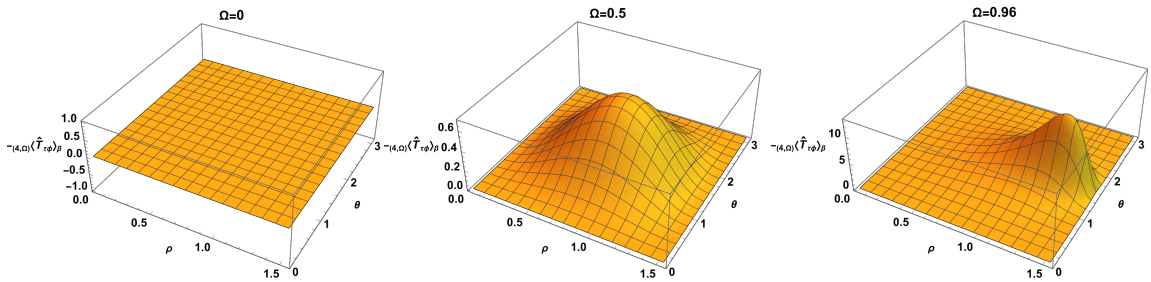


(a) $\Omega = 0$ (b) $\Omega = 0.5$ (c) $\Omega = 0.96$

Figure 5.6: Minus the $\tau\phi$-component of the renormalised stress-energy tensor. The inverse adS length scale $a = 1$ is kept fixed, as is the inverse temperature $\beta = \pi/6$. The angular rotation speed $\Omega$ is varied. Dirichlet boundary conditions are applied to the field.

In figure 5.7, we see some similar features as the $\tau\tau$-component exhibited by the $\rho\rho$-component. The major difference is that the emergent hump does actually change the global maximum by quite some way. It is also verifiable that the $\Omega = 0$ case corresponds to the nonrotating renormalised stress-energy tensor minus the vacuum expectation value. Meanwhile, figure 5.8 shows the $\rho\theta$-component. These have perhaps the most interesting features of all the components. At $\Omega = 0$, the figure shows a constant zero surface, as is expected. It is once the angular speed is increased that the interesting features emerge. Unlike all of the other components, which are symmetric about the equatorial plane, the $\rho\theta$-component is in fact antisymmetric about the equatorial plane. This is to be expected, since we have an odd number of $\theta$ indices, and the coordinate $\theta$ changes orientation when crossing the equatorial plane, whereas the coordinate $\rho$ does not. Additionally, at all values of $\Omega$ and $\beta$, the component is zero on the equatorial plane. We do, however, observe the same behaviour as the other components when the angular speed is increased: the local

maximum (and minimum, in this case) tend towards $\rho = \pi/2$. An additional interesting feature is that this component is vanishing along the axes of rotation ($\theta = 0, \pi$). The last point to mention about this component is the relative magnitude compared to, for example, the $\rho\rho$-component. Since the $\rho\theta$ metric component is zero, the expectation was that the corresponding renormalised stress-energy tensor component might also be zero. Whilst this is clearly not the case, we can observe that the relative magnitude of the $\rho\theta$-component of the renormalised stress-energy tensor is between at least one and three orders of magnitude smaller than the other stress-energy tensor components. This is something of which we later take advantage when considering a stress-energy tensor from relativistic kinetic theory and whether it could provide a good approximation to the renormalised stress-energy tensor from QFT. See section 5.3.4.

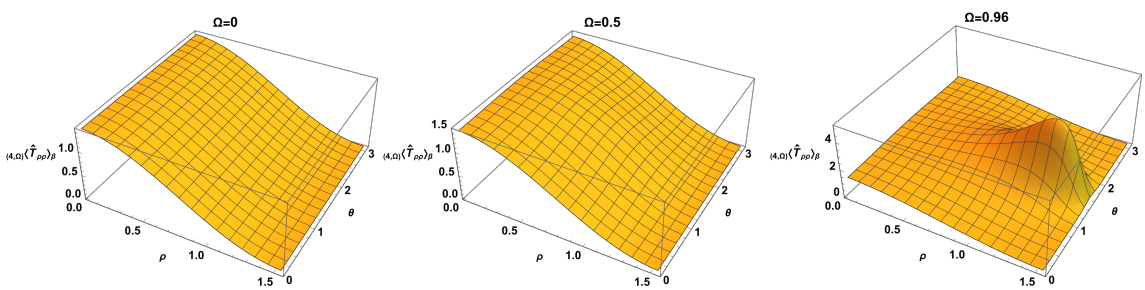


(a) $\Omega = 0$ (b) $\Omega = 0.5$ (c) $\Omega = 0.96$

Figure 5.7: The $\rho\rho$-component of the renormalised stress-energy tensor. The inverse adS length scale $a = 1$ is kept fixed, as is the inverse temperature $\beta = \pi/6$. The angular rotation speed $\Omega$ is varied. Dirichlet boundary conditions are applied to the field.

In figure 5.9 the $\theta\theta$-component is shown. This exhibits the same behaviour as all of the other components with regards to the shifting of the maximum as the angular speed increases. The major difference between this and, say, the $\rho\rho$-component, is the profile at lower angular speeds. The $\rho\rho$-component looks solitonic at lower angular speeds (i.e., the plot is clumped toward the origin $\rho = 0$ and tends toward zero as $\rho$ increases), whereas the

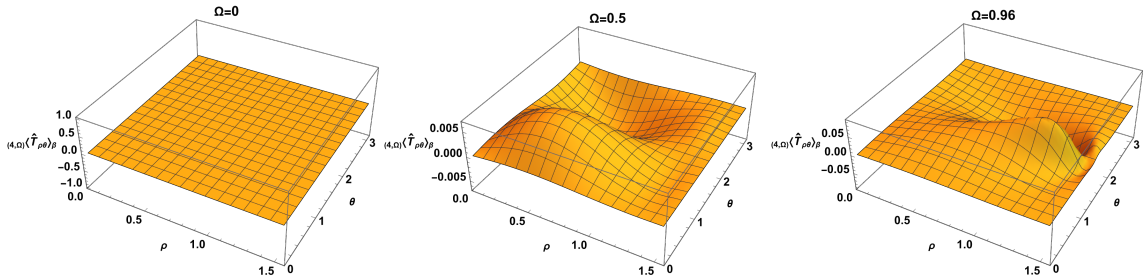


(a) $\Omega = 0$ (b) $\Omega = 0.5$ (c) $\Omega = 0.96$

Figure 5.8: The $\rho\theta$-component of the renormalised stress-energy tensor. The inverse adS length scale $a = 1$ is kept fixed, as is the inverse temperature $\beta = \pi/6$. The angular rotation speed $\Omega$ is varied. Dirichlet boundary conditions are applied to the field.

maximum of the $\theta\theta$-component appears to be somewhere around $\rho = \pi/4$. This is due to the structure of the adS metric (4.4.3); with both indices down, $g_{\theta\theta} = 0$ at $\rho = 0$, and this is reflected in the corresponding renormalised stress-energy tensor component. As we approach higher angular speeds, however, the two components start to look more similar, with the biggest difference occurring at $\rho = 0$.

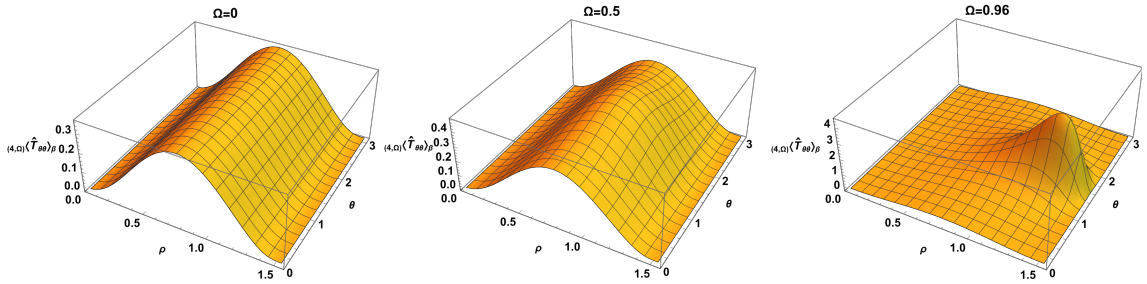


(a) $\Omega = 0$ (b) $\Omega = 0.5$ (c) $\Omega = 0.96$

Figure 5.9: The $\theta\theta$-component of the renormalised stress-energy tensor. The inverse adS length scale $a = 1$ is kept fixed, as is the inverse temperature $\beta = \pi/6$. The angular rotation speed $\Omega$ is varied. Dirichlet boundary conditions are applied to the field.

The final component shown, in figure 5.10, is ${}_{(4,\Omega)}\langle\widehat{T}_{\phi\phi}\rangle_\beta$. The feature that the maximum shifts as the angular speed increases is perhaps most obvious with this component. At $\Omega = 0$ the profile is that of a hump, symmetric in both $\rho$ and $\theta$. As the angular speed increases, this hump becomes a sharp spike localised at roughly $\rho = \pi/2 - 0.4$, $\theta = \pi/2$. The only other point worth mentioning is the profile at $\Omega = 0$. Unlike every other component, that are all constant in $\theta$ at $\Omega = 0$, the $\phi\phi$-component seemingly is not. This is simply due to the structure of the adS metric (4.4.3); for both indices down, the $\phi\phi$-component has a contribution of $\sin^2(\theta)$ from the metric.

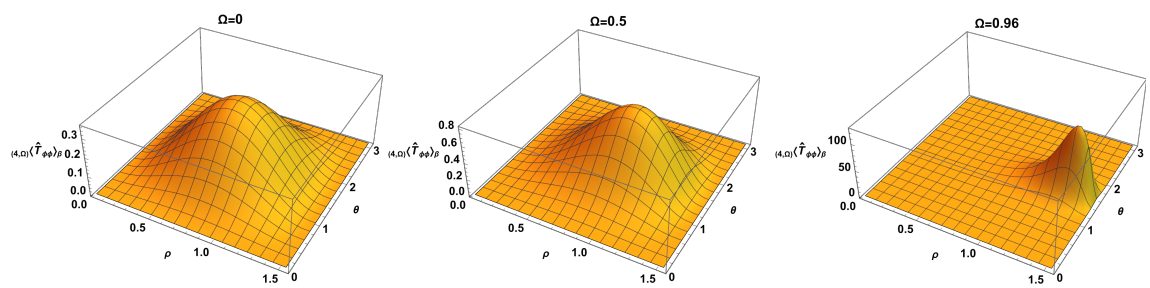


(a) $\Omega = 0$ (b) $\Omega = 0.5$ (c) $\Omega = 0.96$

Figure 5.10: The $\phi\phi$-component of the renormalised stress-energy tensor. The inverse adS length scale $a = 1$ is kept fixed, as is the inverse temperature $\beta = \pi/6$. The angular rotation speed $\Omega$ is varied. Dirichlet boundary conditions are applied to the field.

The final figure presented, figure 5.11, shows all six nonzero components, at a fixed inverse temperature and angular speed, as well a fixed value of $\theta$. For all the components, this is on the equatorial plane $\theta = \pi/2$, except for ${}_{(4,\Omega)}\langle\widehat{T}_{\rho\theta}\rangle_\beta$, which is evaluated at $\theta = 6\pi/25$ since it is identically zero on the equatorial plane. Instead, $\theta = 6\pi/25$ corresponds (roughly) to the location of the maximum value of the component. In this figure, it is the boundary conditions that vary. In each sub-figure, the component is shown for all three boundary conditions. In each case, Neumann boundary conditions take the largest (absolute) value, Dirichlet boundary conditions the lowest and transparent boundary conditions lies roughly halfway between the others. In all cases, we have used a higher inverse temperature than in

the previous figures as the difference between the boundary conditions is easier to discern at lower temperatures. One can of course conclude from this that the boundary conditions play less of an important role as the temperature increases, and the renormalised stress-energy tensor is instead dominated by temperature and rotational effects. This was discussed in [266].

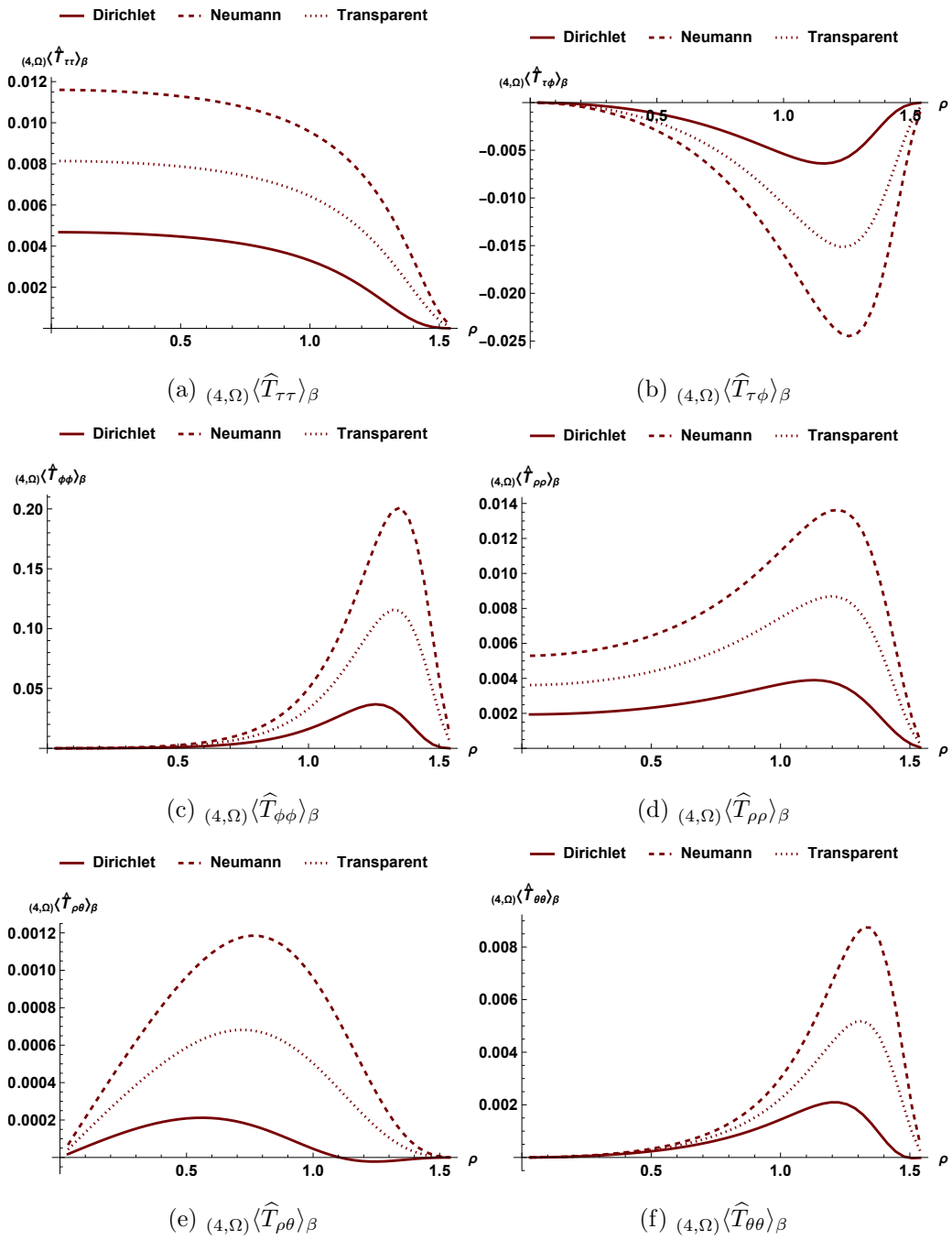


(a) $_{(4,\Omega)}\langle\widehat{T}_{\tau\tau}\rangle_\beta$ (b) $_{(4,\Omega)}\langle\widehat{T}_{\tau\phi}\rangle_\beta$

(c) $_{(4,\Omega)}\langle\widehat{T}_{\phi\phi}\rangle_\beta$ (d) $_{(4,\Omega)}\langle\widehat{T}_{\rho\rho}\rangle_\beta$

(e) $_{(4,\Omega)}\langle\widehat{T}_{\rho\theta}\rangle_\beta$ (f) $_{(4,\Omega)}\langle\widehat{T}_{\theta\theta}\rangle_\beta$

Figure 5.11: The renormalised stress-energy tensor components at angular rotation speed $\Omega = 0.96$ either on the equatorial plane, $\theta = \pi/2$, or at $\theta = 6\pi/25$ (for the $\rho\theta$-component). The inverse adS length scale $a = 1$ is kept fixed, as is the inverse temperature $\beta = 5\pi/6$. The boundary conditions applied to the field are varied.

## § 5.2 Three-dimensional anti-de Sitter space-time

### 5.2.1 Static fields

The renormalisation procedure used for the case of nonrotating three-dimensional anti-de Sitter space-time will be almost identical to that used in the previous section, section 5.1.2. To avoid repetition, many details will be omitted from this section regarding the general procedure, and we will instead present the calculations. Any points where this differs from that of the previous section, comments will be made. We begin in the same manner with the vacuum Hadamard Green function (4.6.19), which in three dimensions is

$$ {}_{(3,\mathcal{Q})}G_0^{(1)}(x,x') = \frac{a}{4\sqrt{2}\pi}\left[\frac{1}{\sqrt{{}_{(3,\mathcal{Q})}Z(x,x')-1}} - \frac{\lambda}{\sqrt{{}_{(3,\mathcal{Q})}Z(x,x')+1}}\right]. \tag{5.2.1} $$

As was the case previously, $\lambda$ refers to the boundary conditions with: $\lambda = 1$ referring to Dirichlet boundary conditions; $\lambda = -1$ referring to Neumann boundary conditions; and $\lambda = 0$ referring to transparent boundary conditions.

One might question why the method used in [4] does not work here in the three-dimensional case. After all, we still have double periodicity in the vacuum Hadamard Green function. The issue arises due to the square root in the vacuum Green's function; an elliptic function must be meromorphic [236], and for a function to be meromorphic, it needs to have countably many poles. Since we have to introduce a branch cut to make the function $(Z \pm 1)^{-1}$ single-valued, the function fails to be (globally[3]) meromorphic, and is thus not elliptic. The method used in [4] relied on the thermal Hadamard Green function being elliptic to express it purely in terms of the location and residues of its poles. Hence, we use the state subtraction renormalisation procedure in this case.

[3]Functions can be locally meromorphic. For example, the function $\sqrt{z}$ is meromorphic on an open set that includes $z = 0$. However, since we need the vacuum Hadamard Green function to be elliptic everywhere, we need it to be globally meromorphic.

The corresponding symmetric biscalar ${}_{(3,\mathfrak{Q})}Z(x,x')$ (4.3.15), again depending on two space-like separated points, is given in terms of the adS coordinates (4.1.3) as

$$ {}_{(3,\mathfrak{Q})}Z(x,x') = \frac{1}{\cos(\rho)\cos(\rho')}\left[\cos\big(\tau-\tau'\big) - \sin(\rho)\sin\big(\rho'\big)\cos\big(\phi-\phi'\big)\right]. \tag{5.2.2} $$

To find the thermal Hadamard Green function, we again perform a Matsubara sum [45, 103, 250] of the vacuum Hadamard Green function,

$$ {}_{(3,\mathfrak{Q})}G^{(1)}_{\beta}(x,x') = \sum_{j=-\infty}^{\infty} {}_{(3,\mathfrak{Q})}G^{(1)}_{0}(\tau+ij\beta,\tau',\rho,\rho',\phi,\phi'), \tag{5.2.3} $$

before renormalising using state subtraction. This corresponds to removing the $j=0$ term from the sum, yielding

$$ {}_{(3,\mathfrak{Q})}W(x,x') = {}_{(3,\mathfrak{Q})}G^{(1)}_{\beta}(x,x') - {}_{(3,\mathfrak{Q})}G^{(1)}_{0}(x,x') = \sum_{j\neq 0} {}_{(3,\mathfrak{Q})}G^{(1)}_{0}(\tau+ij\beta,\tau',\rho,\rho',\phi,\phi'). \tag{5.2.4} $$

As was the case for rotating four-dimensional anti-de Sitter space-time, due to the use of state subtraction, the expectation value yielded by using the propagator (5.2.4) will not be the full thermal expectation value. Rather, it will be the thermal minus vacuum expectation value. Somewhat fortuitously, as shown in [221, 275], the vacuum expectation value for a massless, conformally coupled scalar field in three-dimensional anti-de Sitter space-time is zero.

To simplify things, we again work firstly with the individual, general $j$-terms in the sum and then sum over $j\neq 0$ at the end. Each expression below, unless specified otherwise, will be the corresponding $j$-term of each quantity. The thermal summand, ${}_{(3,\mathfrak{Q})}W^{j}(x,x')$, is given by

$$ \begin{aligned} &{}_{(3,\mathfrak{Q})}W^{j}(x,x') = \\ &\frac{a}{4\sqrt{2}\pi}\left[\left\{-1+\cosh\big(j\beta-i\tau+i\tau'\big)\sec(\rho)\sec\big(\rho'\big)-\cos\big(\phi-\phi'\big)\tan(\rho)\tan\big(\rho'\big)\right\}^{-1/2}\right] \\ &-\frac{a\lambda}{4\sqrt{2}\pi}\left[\left\{1+\cosh\big(j\beta-i\tau+i\tau'\big)\sec(\rho)\sec\big(\rho'\big)-\cos\big(\phi-\phi'\big)\tan(\rho)\tan\big(\rho'\big)\right\}^{-1/2}\right]. \end{aligned} \tag{5.2.5} $$

Recall that, in order to construct expectation values of the stress-energy tensor, we require the 'short distance expansion coefficients' (2.7.43), given as the coincidence limit of the biscalar $W(x,x')$ and the coincidence limit of the second covariant derivative of the biscalar $W(x,x')$. The coincidence limit of the thermal summand in equation (5.2.5) is given by the following expression:

$$
\begin{aligned}
{}_{(3,\not{\Omega})}\omega^{j}(x) = \frac{a}{4\sqrt{2}\pi}\times \\
\left[\left(-1+\cosh(j\beta)\sec^2(\rho)-\tan^2(\rho)\right)^{-1/2} - \lambda\left(1+\cosh(j\beta)\sec^2(\rho)-\tan^2(\rho)\right)^{-1/2}\right].
\end{aligned}
\tag{5.2.6}
$$

One check we can perform at this point is to take the analogous expression in the rotating four-dimensional case, and a) set the angular speed to zero and b) transform to three-dimensions by setting the azimuthal coordinate, $\theta$, to be on the equatorial plane; that is, set $\theta = \pi/2$. Performing this check on equation (5.1.33), one can easily verify that this is true. In analogy to the rotating four-dimensional case, certain expressions show up multiple times, so for brevity and convenience, we define

$$
\mathcal{A}_{(\pm,3,\not{\Omega})} := \pm 1 + \cosh(j\beta)\sec^2(\rho) - \tan^2(\rho). \tag{5.2.7}
$$

Taking equation (5.1.34a) and setting $\Omega = 0$ and $\theta = \pi/2$, it is clear that equation (5.2.7) is recovered. Using these new quantities, we can rewrite the coincidence limit ${}_{(3,\not{\Omega})}\omega^{j}(x)$ into the following simple form:

$$
{}_{(3,\not{\Omega})}\omega^{j}(x) = \frac{a}{4\sqrt{2}\pi}\left[\mathcal{A}_{(-,3,\not{\Omega})}^{-1/2} - \lambda\mathcal{A}_{(+,3,\not{\Omega})}^{-1/2}\right]. \tag{5.2.8}
$$

As in the rotating four-dimensional case, obtaining ${}_{(3,\not{\Omega})}\omega_{\mu\nu}(x)$ is more tricky. Skipping the details of the calculation for brevity, it has the following non-zero components:

$$
\begin{aligned}
{}_{(3,\not{\Omega})}\omega^{j}_{\tau\tau} = & \frac{a}{16\sqrt{2}\pi\mathcal{A}_{(-,3,\not{\Omega})}^{5/2}}\Big[2\mathcal{A}^2_{(-,3,\not{\Omega})}\tan^2(\rho) + 2\mathcal{A}_{(-,3,\not{\Omega})}\cosh(j\beta)\sec^2(\rho) \\
& - 3\sinh^2(j\beta)\sec^4(\rho)\Big]
\end{aligned}
$$

$$
\begin{aligned}
&- \frac{a\lambda}{16\sqrt{2}\pi\mathcal{A}_{(+,3,\not{\Omega})}^{5/2}} \left[2\mathcal{A}_{(+,3,\not{\Omega})}\sec^2(\rho)\left\{\cosh(j\beta) + (1-\cosh(j\beta))^2\tan^2(\rho)\right\}\right. \\
&\left. - 3\sinh^2(j\beta)\sec^4(\rho)\right], \qquad (5.2.9a)\\
{}_{(3,\not{\Omega})}\omega^j_{\tau\rho} =& \frac{3ai\sinh(j\beta)\sec^2(\rho)\tan(\rho)}{16\sqrt{2}\pi\mathcal{A}_{(-,3,\not{\Omega})}^{3/2}\mathcal{A}_{(+,3,\not{\Omega})}^{5/2}}\left[\mathcal{A}_{(+,3,\not{\Omega})}^{5/2} - \lambda\mathcal{A}_{(-,3,\not{\Omega})}^{5/2}\right], \qquad (5.2.9b)\\
{}_{(3,\not{\Omega})}\omega^j_{\rho\rho} =& \frac{a}{16\sqrt{2}\pi\mathcal{A}_{(-,3,\not{\Omega})}^{3/2}}\left[\mathcal{A}_{(-,3,\not{\Omega})}\{5\tan^2(\rho) - 2\sec^2(\rho)\} + 2\cosh(j\beta)\sec^2(\rho)\right.\\
&\left. - 2\sec^2(\rho)\mathcal{A}_{(+,3,\not{\Omega})}\right]\\
&+ \frac{a\lambda}{16\sqrt{2}\pi\mathcal{A}_{(+,3,\not{\Omega})}^{5/2}}\left[\mathcal{A}_{(+,3,\not{\Omega})}^2\sec^2(\rho) + \mathcal{A}_{(+,3,\not{\Omega})}\sec^4(\rho)\{\cosh(j\beta)-1\}\right.\\
&\left. - 3\mathcal{A}_{(-,3,\not{\Omega})}^2\tan^2(\rho)\right], \qquad (5.2.9c)\\
{}_{(3,\not{\Omega})}\omega^j_{\phi\phi} =& -\frac{a\tan^2(\rho)}{8\sqrt{2}\pi\mathcal{A}_{(-,3,\not{\Omega})}^{3/2}}\left[\mathcal{A}_{(-,3,\not{\Omega})} + 1\right]\\
&+ \frac{a\lambda\tan^2(\rho)}{16\sqrt{2}\pi\mathcal{A}_{(+,3,\not{\Omega})}^{3/2}}\left[\mathcal{A}_{(+,3,\not{\Omega})} + \sec^2(\rho)\{\cosh(j\beta)-1\}\right]. \qquad (5.2.9d)
\end{aligned}
$$

The only non-zero off-diagonal component of the above tensor is the $\tau\rho$-component, which has an imaginary value. Much in the same way as for the rotating four-dimensional case, when we perform the sum over $j \neq 0$ this disappears due to the fact that $\sinh(j\beta)$ is an odd function in $j$, while $\mathcal{A}_{(\pm,3,\not{\Omega})}$ is even. The trace of the above tensor can be calculated as

$$
{}_{(3,\not{\Omega})}\omega^j_{\mu}{}^{\mu} = -\frac{3a^3}{16\sqrt{2}\pi}\left[\mathcal{A}_{(-,3,\not{\Omega})}^{-1/2} - \lambda\mathcal{A}_{(+,3,\not{\Omega})}^{-1/2}\right], \qquad (5.2.10)
$$

allowing us to complete the same consistency check (2.7.44) as before. For three-dimensional anti-de Sitter space-times, the Ricci scalar and coupling constant take different values. With the Ricci scalar, $R = -6a^2$, the trace is given in terms of the coincidence limit as

$$
{}_{(3,\not{\Omega})}\omega^j_{\mu}{}^{\mu}(x) - \frac{1}{8}R\,{}_{(3,\not{\Omega})}\omega^j(x) = 0, \qquad (5.2.11)
$$

which when considering equations (5.2.8) and (5.2.10), clearly holds. The same caveat as in the previous case still holds: this is to be satisfied when summing over $j \neq 0$ and not

necessarily for each $j$, it just so happens that in this case it does in fact hold term by term. The second covariant derivative of the coincidence limit only has three non-zero components, given by

$$\nabla_\tau\nabla_\tau\left[{}_{(3,\not{\Omega})}\omega^j\right] = \frac{a\tan^2(\rho)}{4\sqrt{2}\pi\mathcal{A}^{1/2}_{(-,3,\not{\Omega})}\mathcal{A}^{3/2}_{(+,3,\not{\Omega})}}\left[\mathcal{A}^{3/2}_{(+,3,\not{\Omega})} - \lambda\mathcal{A}^{3/2}_{(-,3,\not{\Omega})}\right], \tag{5.2.12a}$$

$$\begin{aligned}\nabla_\rho\nabla_\rho\left[{}_{(3,\not{\Omega})}\omega^j\right] =& \frac{a\sec^2(\rho)}{4\sqrt{2}\pi\mathcal{A}^{1/2}_{(-,3,\not{\Omega})}\mathcal{A}^{5/2}_{(+,3,\not{\Omega})}}\Big[-\mathcal{A}^{5/2}_{(+,3,\not{\Omega})}\cos(2\rho) \\ &+ \lambda\left(\mathcal{A}^{5/2}_{(-,3,\not{\Omega})}\cos(2\rho) + \mathcal{A}^{3/2}_{(-,3,\not{\Omega})}\{3-\cos(2\rho)\}\right)\Big],\end{aligned} \tag{5.2.12b}$$

$$\nabla_\phi\nabla_\phi\left[{}_{(3,\not{\Omega})}\omega^j\right] = \frac{a\tan^2(\rho)}{4\sqrt{2}\pi\mathcal{A}^{1/2}_{(-,3,\not{\Omega})}\mathcal{A}^{3/2}_{(+,3,\not{\Omega})}}\left[-\mathcal{A}^{3/2}_{(+,3,\not{\Omega})} + \lambda\mathcal{A}^{3/2}_{(-,3,\not{\Omega})}\right]. \tag{5.2.12c}$$

The final part to compute is the trace of the above tensor, i.e. apply the box operator to the coincidence limit of the thermal summand. This yields

$$\begin{aligned}\nabla_\mu\nabla^\mu\left[{}_{(3,\not{\Omega})}\omega^j\right] &= \Box\left[{}_{(3,\not{\Omega})}\omega^j(x)\right] \\ &= -\frac{a^3}{8\sqrt{2}\pi}\Big[2\mathcal{A}^{-1/2}_{(-,3,\not{\Omega})} + 2\mathcal{A}^{-3/2}_{(-,3,\not{\Omega})}\{\cosh(j\beta)-1\} \\ &\quad - \lambda\mathcal{A}_{(-,3,\not{\Omega})}\left\{\mathcal{A}^{-3/2}_{(+,3,\not{\Omega})}[3+\cos(2\rho)] + 12\mathcal{A}^{-5/2}_{(+,3,\not{\Omega})}\sin^2(\rho)\right\}\Big].\end{aligned} \tag{5.2.13}$$

Finally, we can assemble the $j$-term of the thermal expectation value of the stress-energy tensor, using equation (2.7.37). For a three-dimensional, massless and conformally-coupled scalar field this reads

$${}_{(3,\not{\Omega})}\langle\widehat{T}^j_{\mu\nu}\rangle_\beta = -{}_{(3,\not{\Omega})}\omega^j_{\mu\nu} + \frac{3}{8}\nabla_\mu\nabla_\nu\left[{}_{(3,\not{\Omega})}\omega^j\right] - \frac{1}{8}\left(\Box\left[{}_{(3,\not{\Omega})}\omega^j\right] + 2a^2{}_{(3,\not{\Omega})}\omega^j\right)g_{\mu\nu}. \tag{5.2.14}$$

Putting everything together, we can write the thermal expectation value of the stress-energy tensor as

$${}_{(3,\not{\Omega})}\langle\widehat{T}_{\mu\nu}\rangle_\beta = \sum_{j\neq 0}{}_{(3,\not{\Omega})}\langle\widehat{T}^j_{\mu\nu}\rangle_\beta, \tag{5.2.15a}$$

where

$${}_{(3,\not{\Omega})}\langle\widehat{T}^j_{\mu\nu}\rangle_\beta = -\frac{a}{32\sqrt{2}\pi}\left\{{}_{(3,\not{\Omega})}\varpi^j_{\mu\nu}[\mathcal{A}_{(-,3,\not{\Omega})}] - \lambda\,{}_{(3,\not{\Omega})}\varpi^j_{\mu\nu}[\mathcal{A}_{(+,3,\not{\Omega})}]\right\}. \tag{5.2.15b}$$

The tensor ${}_{(3,\not{2})}\varpi^{j}_{\mu\nu}$ is introduced to write the components of the renormalised stress-energy tensor in a succinct and convenient way. The $\tau\tau$-component is defined as

$$ {}_{(3,\not{2})}\varpi^{j}_{\tau\tau}[\mathcal{A}_{(\pm,3,\not{2})}] := -\frac{1}{\mathcal{A}^{5/2}_{(\pm,3,\not{2})}}\left\{\mathcal{B}_{(3,\not{2};\,\tau\tau,2)}\mathcal{A}^{2}_{(\pm,3,\not{2})} + \mathcal{B}_{(3,\not{2};\,\tau\tau,1)}\mathcal{A}_{(\pm,3,\not{2})} + \mathcal{B}_{(3,\not{2};\,\tau\tau,0)}\right\}, \tag{5.2.15c} $$

where we have defined the following coefficients:

$$ \mathcal{B}_{(3,\not{2};\,\tau\tau,2)} := 2\sec^{2}(\rho), \tag{5.2.15d} $$

$$ \mathcal{B}_{(3,\not{2};\,\tau\tau,1)} := -\cosh(j\beta)\left[\sec^{2}(\rho) + 5\sec^{4}(\rho)\right] - 3\sec^{2}(\rho) + 5\sec^{4}(\rho), \tag{5.2.15e} $$

$$ \mathcal{B}_{(3,\not{2};\,\tau\tau,0)} := 3\tan^{2}(\rho)\sec^{4}(\rho)\left[\cosh(j\beta) - 1\right]^{2} + 6\sinh^{2}(j\beta)\sec^{2}(\rho). \tag{5.2.15f} $$

The $\rho\rho$-component can be displayed in a similar fashion, as

$$ {}_{(3,\not{2})}\varpi^{j}_{\rho\rho}[\mathcal{A}_{(\pm,3,\not{2})}] := \frac{\sec^{2}(\rho)}{\mathcal{A}^{3/2}_{(\pm,3,\not{2})}}\left\{2\mathcal{A}_{(\pm,3,\not{2})} - \mathcal{B}_{(3,\not{2};\,\rho\rho,0)}\right\}, \tag{5.2.15g} $$

where the new coefficient is defined as

$$ \mathcal{B}_{(3,\not{2};\,\rho\rho,0)} := \cosh(j\beta)\left[1 + 2\sec^{2}(\rho)\right] + 3 - 2\sec^{2}(\rho). \tag{5.2.15h} $$

Finally the last component, the $\theta\theta$-component, is given by

$$ {}_{(3,\not{2})}\varpi^{j}_{\phi\phi}[\mathcal{A}_{(\pm,3,\not{2})}] := \frac{\tan^{2}(\rho)}{\mathcal{A}^{5/2}_{(\pm,3,\not{2})}}\left\{2\mathcal{A}^{2}_{(\pm,3,\not{2})} + \mathcal{B}_{(3,\not{2};\,\phi\phi,1)}\mathcal{A}_{(\pm,3,\not{2})} + 3\tan^{2}(\rho)\,\mathcal{B}_{(3,\not{2};\,\phi\phi,0)}\right\}, \tag{5.2.15i} $$

where the coefficients are

$$ \mathcal{B}_{(3,\not{2};\,\phi\phi,1)} := \cosh(j\beta)\left[2 - 5\sec^{2}(\rho)\right] - 6 + 5\sec^{2}(\rho), \tag{5.2.15j} $$

$$ \mathcal{B}_{(3,\not{2};\,\phi\phi,0)} := \sec^{2}(\rho)\left[\cosh(j\beta) - 1\right]^{2}. \tag{5.2.15k} $$

Unlike the rotating four-dimensional case in section 5.1.2, there are no surprises in the structure of the renormalised stress-energy tensor. There are only three nonzero components and they are on the diagonal of the renormalised stress-energy tensor, matching the

structure of the adS metric (4.1.7), which is also diagonal. The components depend only on $\rho$; in the low temperature limit $\beta \to \infty$ the renormalised stress-energy tensor tends towards zero, as is expected. This is due, in part, to the fact that the functions $\mathcal{A}_{(\pm,3,\not{\ell})}$ tend towards infinity faster than the coefficients $\mathcal{B}_{(3,\not{\ell};\bullet,\bullet)}$. More importantly, though, is that to apply state subtraction, we removed the vacuum expectation value of the stress-energy tensor and so, while ordinarily we would expect that taking the zero temperature limit of a thermal expectation value would yield the vacuum expectation value, we instead yield zero. This fact is true in general of state subtraction renormalisation; for three-dimensional anti-de Sitter space-time, the vacuum expectation value of the stress-energy tensor (5.2.15) is zero anyway [221, 275].

Below, the renormalised stress-energy tensor components are plotted. Figure 5.12 shows the three nonzero components ${}_{(3,\not{\ell})}\langle\widehat{T}_{\tau\tau}\rangle_\beta$, ${}_{(3,\not{\ell})}\langle\widehat{T}_{\rho\rho}\rangle_\beta$, and ${}_{(3,\not{\ell})}\langle\widehat{T}_{\phi\phi}\rangle_\beta$. In a similar fashion as the four-dimensional rotating case, we first show the components with Dirichlet boundary conditions applied to the field, before showing a plot of each component at a fixed inverse temperature, comparing the three boundary conditions. This is for the same reasons as previously, and again will become more clear in section 5.3.4. For all three components, we see that as the temperature is increased, the values of the components increase. The $\tau\tau$- and $\rho\rho$-components both take their maximum values at the origin $\rho = 0$, and approach zero at the space-time boundary. On the other hand, at both the origin and space-time boundary $\rho = \pi/2$, the $\phi\phi$-component is zero. This is simply due to the underlying metric structure: at $\rho = 0$, we have that $g_{\phi\phi} = 0$. A slightly strange feature of figure 5.12c is that just before the space-time boundary, the stress-energy tensor component dips below zero before reaching zero at the boundary itself.

Figure 5.13 shows each nonzero renormalised stress-energy tensor component at a fixed inverse temperature, $\beta = 5\pi/6$, with the boundary conditions varied between Dirichlet, Neumann and transparent. In each case, Neumann boundary conditions take the highest value; Dirichlet boundary conditions take the lowest value; and transparent boundary con-

ditions lie somewhere between the two. The dip below the axis of ${}_{(3,\mathfrak{Q})}\langle\widehat{T}_{\phi\phi}\rangle_\beta$ interestingly only occurs for the case of Dirichlet boundary conditions. In addition, the rate at which the components tend towards zero as $\rho \to \pi/2$ is greatest for the case of Dirichlet boundary conditions, whilst the case of Neumann boundary conditions is the slowest.

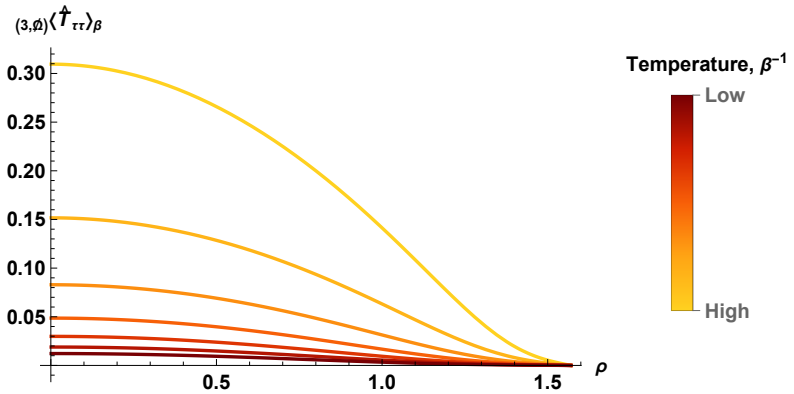


(a) $_{(3,\emptyset)}\langle \widehat{T}_{\tau\tau}\rangle_\beta$

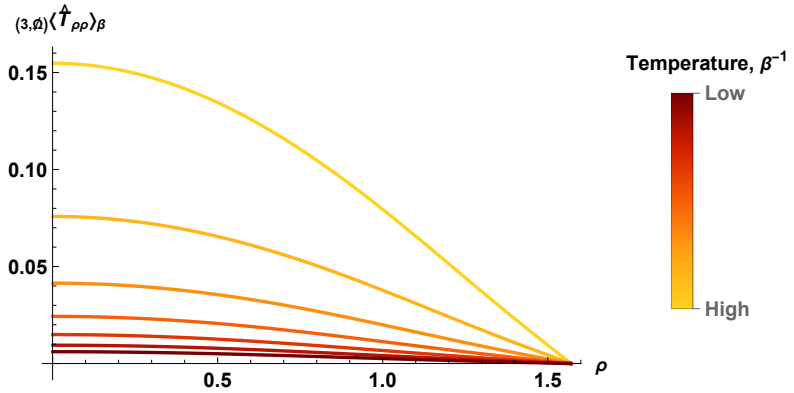


(b) $_{(3,\emptyset)}\langle \widehat{T}_{\rho\rho}\rangle_\beta$

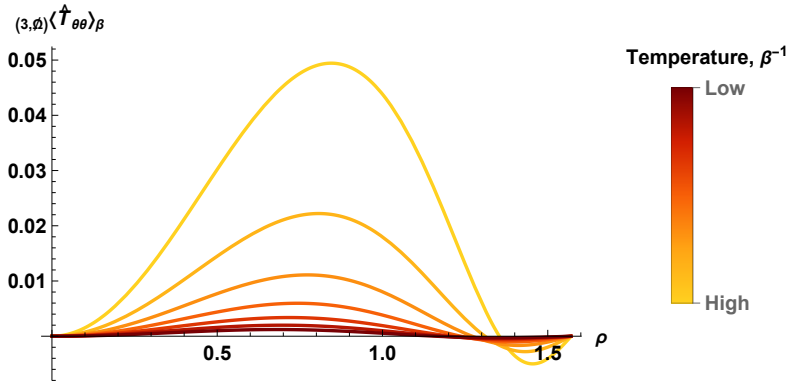


(c) $_{(3,\emptyset)}\langle \widehat{T}_{\phi\phi}\rangle_\beta$

Figure 5.12: The components of the renormalised stress-energy tensor. The inverse adS length scale is kept fixed at $a = 1$. The inverse temperature is varied within the range $\beta \in [\pi/3, 5\pi/6]$. Dirichlet boundary conditions are applied to the field.

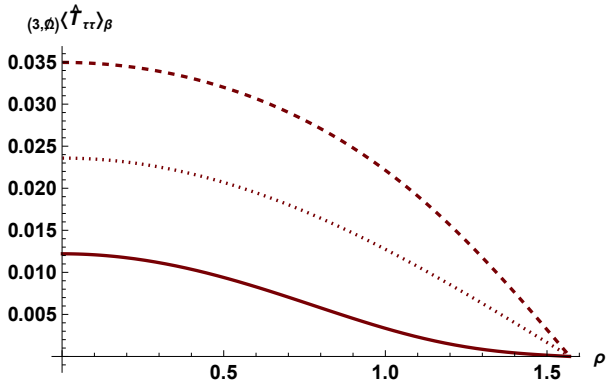


(a) $_{(3,\mathcal{D})}\langle \widehat{T}_{\tau\tau} \rangle_\beta$

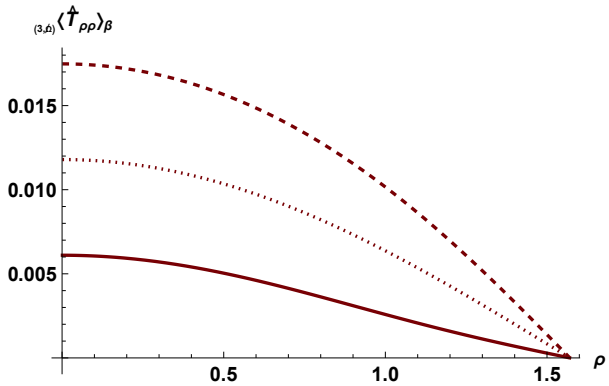


(b) $_{(3,\mathcal{D})}\langle \widehat{T}_{\rho\rho} \rangle_\beta$

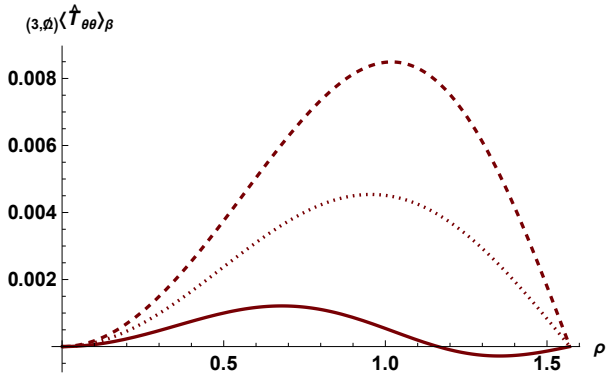


(c) $_{(3,\mathcal{D})}\langle \widehat{T}_{\phi\phi} \rangle_\beta$

Figure 5.13: Plots for the components of the renormalised stress-energy tensor. The inverse adS length scale is kept fixed at $a = 1$, as is the inverse temperature at $\beta = 5\pi/6$. The boundary conditions applied to the field are varied, with the solid line corresponding to Dirichlet boundary conditions; the dashed line to Neumann boundary conditions; and the dotted line to transparent boundary conditions.

### 5.2.2 Rigidly-rotating fields

The last case we consider is that of rigidly-rotating fields in three-dimensional anti-de Sitter space-time. We start by writing down the vacuum Hadamard Green function (4.6.19), which in three space-time dimensions is

$$ {}_{(3,\Omega)}G_0^{(1)}(x,x') = \frac{a}{4\sqrt{2}\pi}\left[\frac{1}{\sqrt{{}_{(3,\Omega)}Z(x,x')-1}} - \frac{\lambda}{\sqrt{{}_{(3,\Omega)}Z(x,x')+1}}\right], \tag{5.2.16} $$

where the symmetric biscalar ${}_{(3,\Omega)}Z(x,x')$ (4.3.15), in three dimensions, is

$$ {}_{(3,\Omega)}Z(x,x') = \frac{1}{\cos(\rho)\cos(\rho')}\times \\ \left[\cos\big(\tau-\tau'\big) - \sin(\rho)\sin\big(\rho'\big)\left\{\cos\big(\phi-\phi'\big)\cos\big(\Omega[\tau-\tau']\big) - \sin\big(\phi-\phi'\big)\sin\big(\Omega[\tau-\tau']\big)\right\}\right]. \tag{5.2.17} $$

Analogously to the rotating four-dimensional case, since the vacuum Hadamard Green function is a scalar quantity, we have simply applied the coordinate mapping $\phi \mapsto \phi + \Omega\tau$ in the coordinate dependence of the biscalar. As it has been in the other three cases, $\lambda$ again controls the boundary conditions applied to the field; $\lambda = 1$ for Dirichlet boundary conditions, $\lambda = -1$ for Neumann boundary conditions and $\lambda = 0$ for transparent boundary conditions. We construct the thermal Hadamard Green function by performing a Matsubara sum of the vacuum Hadamard Green function,

$$ {}_{(3,\Omega)}G_\beta^{(1)}(x,x') = \sum_{j=-\infty}^{\infty} {}_{(3,\Omega)}G_0^{(1)}(t+ij\beta,t',\rho,\rho',\phi,\phi'). \tag{5.2.18} $$

The renormalisation procedure of choice is yet again state subtraction (see section 2.7.1), by taking the difference between expectation values in a thermal state and the global (nonrotating) anti-de Sitter space vacuum state; we use the nonrotating vacuum state since, as discussed in section 4.7, the rotating and nonrotating vacua on anti-de Sitter space coincide, provided no speed-of-light surface forms [222]. Additionally, the vacuum expectation value of the stress-energy tensor in the global (three-dimensional) anti-de Sitter

space vacuum is identically zero [221, 275] Therefore, we consider the difference between the thermal and vacuum Hadamard Green functions:

$$\begin{aligned} {}_{(3,\Omega)}W(x,x') &= {}_{(3,\Omega)}G^{(1)}_{\beta}(x,x') - {}_{(3,\Omega)}G^{(1)}_{0}(x,x') \\ &= \sum_{j\neq 0} {}_{(3,\Omega)}G^{(1)}_{0}(t+ij\beta,t',\rho,\rho',\phi,\phi'). \end{aligned} \tag{5.2.19}$$

We define a thermal summand ${}_{(3,\Omega)}W^{j}(x,x')$ such that

$${}_{(3,\Omega)}W(x,x') = \sum_{j\neq 0} {}_{(3,\Omega)}W^{j}(x,x'), \tag{5.2.20}$$

where the thermal summand is given by

$${}_{(3,\Omega)}W^{j}(x,x') = {}_{(3,\Omega)}G^{(1)}_{0}(\tau+ij\beta,\tau',\rho,\rho',\phi,\phi'). \tag{5.2.21}$$

Explicitly in terms of the adS coordinates, this is

$$\begin{aligned} {}_{(3,\Omega)}W^{j}(x,x') =& \frac{a}{4\sqrt{2}\pi}\Big[\big\{-1+\cosh\big(j\beta-i\tau+i\tau'\big)\sec(\rho)\sec\big(\rho'\big) \\ &- \cos\big(\phi-\phi'+[ij\beta+\tau-\tau']\Omega\big)\tan(\rho)\tan\big(\rho'\big)\big\}^{-1/2} \\ &- \lambda\big\{1+\cosh\big(j\beta-i\tau+i\tau'\big)\sec(\rho)\sec\big(\rho'\big) \\ &- \cos\big(\phi-\phi'+[ij\beta+\tau-\tau']\Omega\big)\tan(\rho)\tan\big(\rho'\big)\big\}^{-1/2}\Big]. \end{aligned} \tag{5.2.22}$$

In order to construct the thermal expectation value of the stress-energy tensor, we need to find the coincidence limit of the difference (5.2.19) and the coincidence limit of the second covariant derivative of the difference (5.2.19). The coincidence limit of the difference (5.2.19) is given by

$$\begin{aligned} {}_{(3,\Omega)}\omega^{j}(x) = \frac{a}{4\sqrt{2}\pi}\Big[&\big\{-1+\cosh(j\beta)\sec^2(\rho)-\cosh(j\beta\Omega)\tan^2(\rho)\big\}^{-1/2} \\ &- \lambda\big\{1+\cosh(j\beta)\sec^2(\rho)-\cosh(j\beta\Omega)\tan^2(\rho)\big\}^{-1/2}\Big]. \end{aligned} \tag{5.2.23}$$

It is easily verified that by taking the limit $\Omega \to 0$, the nonrotating expression (5.2.6) is recovered. For brevity, we, in an identical way as for the nonrotating case, define the

following quantities

$$\mathcal{A}_{(\pm,3,\Omega)} := \pm 1 + \cosh(j\beta)\sec^2(\rho) - \cosh(j\beta\Omega)\tan^2(\rho), \tag{5.2.24}$$

and

$$\Gamma_{(3)} := \left[1 - \Omega^2 \sin^2(\rho)\right]^{-1/2}, \tag{5.2.25}$$

$$\mathcal{C}_{(3)} := \cosh(j\beta) - \cosh(j\beta\Omega), \tag{5.2.26}$$

$$\widetilde{\mathcal{C}}_{(3)} := \cosh(j\beta) - \cosh(j\beta\Omega)\sin^2(\rho), \tag{5.2.27}$$

$$\mathcal{S}_{(3)} := \sinh(j\beta) - \Omega\sinh(j\beta\Omega)\sin^2(\rho). \tag{5.2.28}$$

Again, by taking the nonrotating limit $\Omega \to 0$, the corresponding nonrotating expressions (5.2.7) are recovered for $\mathcal{A}_{(\pm,3,\bullet)}$. We can therefore, in analogy with the nonrotating case, rewrite the expression for the coincidence limit as follows,

$${}_{(3,\Omega)}\omega^j(x) = \frac{a}{4\sqrt{2}\pi}\left[\mathcal{A}_{(-,3,\Omega)}^{-1/2} - \lambda\mathcal{A}_{(+,3,\Omega)}^{-1/2}\right]. \tag{5.2.29}$$

Meanwhile, the tensor ${}_{(3,\Omega)}\omega^j_{\mu\nu}$ has nonzero components

$$\begin{aligned}
{}_{(3,\Omega)}\omega^j_{\tau\tau} =& \frac{a\sec^4(\rho)}{16\sqrt{2}\pi\mathcal{A}_{(-,3,\Omega)}^{5/2}}\left[2\mathcal{A}_{(-,3,\Omega)}\sec^2(\rho)\Gamma_{(3)}^{-2}\widetilde{\mathcal{C}}_{(3)} - 3\mathcal{S}_{(3)}^2\right] \\
&- \frac{a\lambda\sec^4(\rho)}{16\sqrt{2}\pi\mathcal{A}_{(+,3,\Omega)}^{5/2}}\left[2\mathcal{A}_{(+,3,\Omega)}\sec^2(\rho)\Gamma_{(3)}^{-2}\widetilde{\mathcal{C}}_{(3)} - 3\mathcal{S}_{(3)}^2\right],
\end{aligned} \tag{5.2.30a}$$

$${}_{(3,\Omega)}\omega^j_{t\rho} = \frac{3ia\sec^4(\rho)\tan(\rho)}{16\sqrt{2}\pi\mathcal{A}_{(-,3,\Omega)}^{5/2}\mathcal{A}_{(+,3,\Omega)}^{5/2}}\mathcal{C}_{(3)}\mathcal{S}_{(3)}\left[\lambda\mathcal{A}_{(-,3,\Omega)}^{5/2} - \mathcal{A}_{(+,3,\Omega)}^{5/2}\right], \tag{5.2.30b}$$

$$\begin{aligned}
{}_{(3,\Omega)}\omega^j_{t\phi} =& -\frac{a\sec^2(\rho)\tan^2(\rho)}{16\sqrt{2}\pi\mathcal{A}_{(-,3,\Omega)}^{5/2}}\left[2\mathcal{A}_{(-,3,\Omega)}\Omega\widetilde{\mathcal{C}}_{(3)} - 3\sinh(j\beta\Omega)\mathcal{S}_{(3)}\right] \\
&+ \frac{a\lambda\sec^2(\rho)\tan^2(\rho)}{16\sqrt{2}\pi\mathcal{A}_{(+,3,\Omega)}^{5/2}}\left[2\mathcal{A}_{(+,3,\Omega)}\Omega\widetilde{\mathcal{C}}_{(3)} - 3\sinh(j\beta\Omega)\mathcal{S}_{(3)}\right],
\end{aligned} \tag{5.2.30c}$$

$$\begin{aligned}
{}_{(3,\Omega)}\omega^j_{\rho\rho} =& -\frac{a\sec^4(\rho)}{16\sqrt{2}\pi\mathcal{A}_{(-,3,\Omega)}^{5/2}}\left[2\mathcal{A}_{(-,3,\Omega)}\widetilde{\mathcal{C}}_{(3)} - 3\tan^2(\rho)\mathcal{C}_{(3)}^2\right] \\
&+ \frac{a\lambda\sec^4(\rho)}{16\sqrt{2}\pi\mathcal{A}_{(+,3,\Omega)}^{5/2}}\left[2\mathcal{A}_{(+,3,\Omega)}\widetilde{\mathcal{C}}_{(3)} - 3\tan^2(\rho)\mathcal{C}_{(3)}^2\right],
\end{aligned} \tag{5.2.30d}$$

$$
\begin{aligned}
{}_{(3,\Omega)}\omega^{j}_{\rho\theta} =& \frac{3ia\sinh(j\beta\Omega)\sec^2(\rho)\tan^3(\rho)}{16\sqrt{2}\pi\mathcal{A}^{5/2}_{(-,3,\Omega)}\mathcal{A}^{5/2}_{(+,3,\Omega)}}\mathcal{C}_{(3)}\left[\lambda\mathcal{A}^{5/2}_{(-,3,\Omega)} - \mathcal{A}^{5/2}_{(+,3,\Omega)}\right], \qquad (5.2.30e)\\
{}_{(3,\Omega)}\omega^{j}_{\phi\phi} =& -\frac{a\sec^2(\rho)\tan^2(\rho)}{16\sqrt{2}\pi\mathcal{A}^{5/2}_{(-,3,\Omega)}}\left[2\mathcal{A}_{(-,3,\Omega)}\widetilde{\mathcal{C}}_{(3)} + 3\sinh^2(j\beta\Omega)\sin^2(\rho)\right]\\
&+\frac{a\sec^2(\rho)\tan^2(\rho)}{16\sqrt{2}\pi\mathcal{A}^{5/2}_{(+,3,\Omega)}}\left[2\mathcal{A}_{(+,3,\Omega)}\widetilde{\mathcal{C}}_{(3)} + 3\sinh^2(j\beta\Omega)\sin^2(\rho)\right]. \qquad (5.2.30f)
\end{aligned}
$$

Taking the trace, we have that

$$
{}_{(3,\Omega)}\omega^{j\ \mu}_{\mu} = -\frac{3a^3}{16\sqrt{2}\pi}\left[\mathcal{A}^{-1/2}_{(-,3,\Omega)} - \lambda\mathcal{A}^{-1/2}_{(+,3,\Omega)}\right], \qquad (5.2.31)
$$

whereby we can verify that the consistency check (2.7.44) is satisfied. The second covariant derivative of the coincidence limit has nonzero components,

$$
\nabla_\tau\nabla_\tau\left[{}_{(3,\Omega)}\omega^{j}\right] = \frac{a\left(1-\Omega^2\right)}{4\sqrt{2}\pi\mathcal{A}^{3/2}_{(-,3,\Omega)}\mathcal{A}^{3/2}_{(+,3,\Omega)}}\sec^2(\rho)\tan^2(\rho)\mathcal{C}_{(3)}\left[\mathcal{A}^{3/2}_{(+,3,\Omega)} - \lambda\mathcal{A}^{3/2}_{(-,3,\Omega)}\right], \qquad (5.2.32a)
$$

$$
\nabla_\tau\nabla_\phi\left[{}_{(3,\Omega)}\omega^{j}\right] = -\frac{a\Omega}{4\sqrt{2}\pi\mathcal{A}^{3/2}_{(-,3,\Omega)}\mathcal{A}^{3/2}_{(+,3,\Omega)}}\sec^2(\rho)\tan^2(\rho)\mathcal{C}_{(3)}\left[\mathcal{A}^{3/2}_{(+,3,\Omega)} - \lambda\mathcal{A}^{3/2}_{(-,3,\Omega)}\right], \qquad (5.2.32b)
$$

$$
\begin{aligned}
\nabla_\rho\nabla_\rho\left[{}_{(3,\Omega)}\omega^{j}\right] =& \frac{a\sec^4(\rho)}{8\sqrt{2}\pi\mathcal{A}^{5/2}_{(-,3,\Omega)}}\mathcal{C}_{(3)}\left[\mathcal{A}_{(-,3,\Omega)}\{\cos(2\rho)-3\} + 6\tan^2(\rho)\right]\\
&-\frac{a\lambda\sec^4(\rho)}{8\sqrt{2}\pi\mathcal{A}^{5/2}_{(+,3,\Omega)}}\mathcal{C}_{(3)}\left[\mathcal{A}_{(+,3,\Omega)}\{\cos(2\rho)-3\} + 6\tan^2(\rho)\right], \qquad (5.2.32c)
\end{aligned}
$$

$$
\nabla_\phi\nabla_\phi\left[{}_{(3,\Omega)}\omega^{j}\right] = -\frac{a}{4\sqrt{2}\pi\mathcal{A}^{3/2}_{(-,3,\Omega)}\mathcal{A}^{3/2}_{(+,3,\Omega)}}\sec^2(\rho)\tan^2(\rho)\mathcal{C}_{(3)}\left[\mathcal{A}^{3/2}_{(+,3,\Omega)} - \lambda\mathcal{A}^{3/2}_{(-,3,\Omega)}\right], \qquad (5.2.32d)
$$

and taking the trace (corresponding to applying the covariant d'Alembertian operator to the coincidence limit) yields the somewhat concise expression:

$$
\begin{aligned}
\nabla_\mu\nabla^\mu\left[{}_{(3,\Omega)}\omega^{j}(x)\right] =& \Box\left[{}_{(3,\Omega)}\omega^{j}(x)\right]\\
=& \frac{a^3\sec^2(\rho)}{4\sqrt{2}\pi\mathcal{A}^{5/2}_{(-,3,\Omega)}}\mathcal{C}_{(3)}\left[\mathcal{A}_{(-,3,\Omega)}\{\cos(2\rho)-3\} + 3\tan^2(\rho)\mathcal{C}_{(3)}\right]
\end{aligned}
$$

$$- \frac{a^3 \lambda \sec^2(\rho)}{4\sqrt{2}\pi \mathcal{A}_{(+,3,\Omega)}^{5/2}} \mathcal{C}_{(3)} \left[ \mathcal{A}_{(+,3,\Omega)} \{\cos(2\rho) - 3\} + 3\tan^2(\rho) \mathcal{C}_{(3)} \right]. \tag{5.2.33}$$

Recall that the renormalised stress-energy tensor for a three-dimensional massless and conformally-coupled quantum scalar field is given in section 2.7, by equation (2.7.37). For rigidly-rotating fields in three-dimensional anti-de Sitter space-time, we have that the $j$-summand of the renormalised stress-energy tensor is constructed as

$${}_{(3,\Omega)}\langle \widehat{T}^j_{\mu\nu} \rangle_\beta = -{}_{(3,\Omega)}\omega^j_{\mu\nu} + \frac{3}{8} \nabla_\mu \nabla_\nu \left[ {}_{(3,\Omega)}\omega^j \right] - \frac{1}{8} \left( \Box \left[ {}_{(3,\Omega)}\omega^j \right] + 2a^2 {}_{(3,\Omega)}\omega^j \right) g_{\mu\nu}. \tag{5.2.34}$$

Assembling the constituent parts, we can write the $j$-summand of the renormalised stress-energy tensor as

$${}_{(3,\Omega)}\langle \widehat{T}^j_{\mu\nu} \rangle_\beta(\rho) = -\frac{a}{32\sqrt{2}\pi} \left\{ {}_{(3,\Omega)}\varpi^j_{\mu\nu}[\mathcal{A}_{(-,3,\Omega)}] - \lambda \, {}_{(3,\Omega)}\varpi^j_{\mu\nu}[\mathcal{A}_{(+,3,\Omega)}] \right\}, \tag{5.2.35a}$$

where the tensor ${}_{(3,\Omega)}\varpi^j_{\mu\nu}$ is inserted to aid in the transcription of the renormalised stress-energy tensor components. Below, each component will be given, along with any new quantities defined to further aid in the transcription. Starting with the $\tau\tau$-component, we have

$${}_{(3,\Omega)}\varpi^j_{\tau\tau}[\mathcal{A}_{(\pm,3,\Omega)}] := -\frac{1}{\mathcal{A}_{(\pm,3,\Omega)}^{5/2}} \left\{ \mathcal{B}_{(3,\Omega;\,\tau\tau,2)} \mathcal{A}^2_{(\pm,3,\Omega)} + \mathcal{B}_{(3,\Omega;\,\tau\tau,1)} \mathcal{A}_{(\pm,3,\Omega)} + \mathcal{B}_{(3,\Omega;\,\tau\tau,0)} \right\}, \tag{5.2.35b}$$

where the coefficients $\mathcal{B}_{(3,\Omega;\,\tau\tau,\bullet)}$ are given by

$$\mathcal{B}_{(3,\Omega;\,\tau\tau,2)} := 2\Gamma_{(3)}^{-2} \sec^2(\rho), \tag{5.2.35c}$$

$$\begin{aligned} \mathcal{B}_{(3,\Omega;\,\tau\tau,1)} :=& \mathcal{C}_{(3)} \left[ 2\Omega^2 - (1 + 7\Omega^2)\sec^2(\rho) - 5(1 - \Omega^2)\sec^4(\rho) \right] \\ & - 4\Gamma_{(3)}^{-2} \cosh(j\beta\Omega) \sec^2(\rho), \end{aligned} \tag{5.2.35d}$$

$$\mathcal{B}_{(3,\Omega;\,\tau\tau,0)} := 3\Gamma_{(3)}^{-2} \mathcal{C}^2_{(3)} \tan^2(\rho) \sec^4(\rho) + 6\sec^4(\rho) \mathcal{S}^2_{(3)}. \tag{5.2.35e}$$

The $\tau\theta$-component can be written in terms of the $\phi\phi$-component, which is given below. It is

$$ {}_{(3,\Omega)}\varpi^{j}_{\tau\phi}[\mathcal{A}_{(\pm,3,\Omega)}] = \Omega\, {}_{(3,\Omega)}\varpi^{j}_{\phi\phi}[\mathcal{A}_{(\pm,3,\Omega)}] - \frac{6}{\mathcal{A}^{5/2}_{(\pm,3,\Omega)}} \sec^2(\rho)\tan^2(\rho)\sinh(j\beta)\sinh(j\beta\Omega). \tag{5.2.35f} $$

The $\rho\rho$-component is given by

$$ {}_{(3,\Omega)}\varpi^{j}_{\rho\rho}[\mathcal{A}_{(\pm,3,\Omega)}] := \frac{\sec^2(\rho)}{\mathcal{A}^{3/2}_{(\pm,3,\Omega)}} \left\{ 2\mathcal{A}_{(\pm,3,\Omega)} - \mathcal{B}_{(3,\Omega;\,\rho\rho,0)} \right\}, \tag{5.2.35g} $$

where

$$ \mathcal{B}_{(3,\Omega;\,\rho\rho,0)} := \mathcal{C}_{(3)} \left[ 1 + 2\sec^2(\rho) \right] - 4\cosh(j\beta\Omega). \tag{5.2.35h} $$

Finally, the $\phi\phi$-component is as follows:

$$ {}_{(3,\Omega)}\varpi^{j}_{\phi\phi}[\mathcal{A}_{(\pm,3,\Omega)}] := \frac{\tan^2(\rho)}{\mathcal{A}^{5/2}_{(\pm,3,\Omega)}} \left\{ 2\mathcal{A}^2_{(\pm,3,\Omega)} + \mathcal{B}_{(3,\Omega;\,\phi\phi,1)}\mathcal{A}_{(\pm,3,\Omega)} + 3\tan^2(\rho)\,\mathcal{B}_{(3,\Omega;\,\phi\phi,0)} \right\} \tag{5.2.35i} $$

where the coefficients $\mathcal{B}_{(3,\Omega;\,\phi\phi,\bullet)}$ are given by

$$ \mathcal{B}_{(3,\Omega;\,\phi\phi,1)} := \mathcal{C}_{(3)} \left[ 2 - 5\sec^2(\rho) \right] - 4\cosh(j\beta\Omega), \tag{5.2.35j} $$

$$ \mathcal{B}_{(3,\Omega;\,\phi\phi,0)} := \mathcal{C}^2_{(3)} \sec^2(\rho) - 2\sinh^2(j\beta\Omega). \tag{5.2.35k} $$

The most obvious first point to address here is with regards to the nonrotating limit $\Omega \to 0$. Starting with the off-diagonal component, it is clear that in the limit $\Omega \to 0$, ${}_{(3,\Omega)}\varpi^{j}_{\tau\phi} = 0$. This is to be expected; after all there are no off-diagonal terms in the nonrotating renormalised stress-energy tensor (5.2.15). Additionally, in the nonrotating limit, we have that

$$ \Gamma_{(3)} \to 1, \quad \text{and} \quad \mathcal{C}_{(3)} \to \cosh(j\beta) - 1, \tag{5.2.36} $$

from which it should be clear to see that the nonrotating tensor components ${}_{(3,\not{\Omega})}\varpi^{j}_{\bullet\bullet}$ (5.2.15c,5.2.15g,5.2.15i) are recovered.

In spite of the fact that we have rigidly-rotated the quantum scalar field and the metric tensor, we still only have dependence on the $\rho$ coordinate. This is at odds with the results for rotating four-dimensional anti-de Sitter space-time, where adding rotation induced extra functional dependence on the $\theta$ coordinate. It is not unreasonable, therefore, to suggest that we would have multivariable dependence in the rotating three-dimensional case. However, the induced coordinate dependence in the four-dimensional case is *not* the coordinate upon which we apply the rigid rotation (i.e. $\phi$), but rather the angular coordinate $\theta$ which appears in the metric tensor (4.4.3). Since the three-dimensional metric (4.4.2) does not have explicit dependence on $\theta$, we have no induced angular coordinate dependence. Therefore, the plots presented below will be a selection of two-dimensional graphs at various angular speeds, rather than surface plots. This lack of extra functional dependence of the renormalised stress-energy tensor is one of the key reasons we focus on quantum corrections to rotating anti-de Sitter space in three-dimensions - see chapter 7.

Figure 5.14 shows the $\tau\tau$-component of the renormalised stress-energy tensor at angular speeds of $\Omega = 0.5$ and $\Omega = 0.96$. Unlike in the four-dimensional rotating case, we elect not to show the $\Omega = 0$ case, since this corresponds directly to figure 5.12a. As the angular speed is increased, the profile of the curves change. In particular, for higher angular speeds the component decreases less rapidly to zero as the space-time boundary is approached, and seems to plateau in a neighbourhood around the origin. As expected, increasing the temperature increases the magnitude of the component. The maximum value that the component takes is always at the origin $\rho = 0$, and tends toward zero at the space-time boundary $\rho = \pi/2$.

In figure 5.15, we show the $\rho\rho$-component of the renormalised stress-energy tensor. This behaves in a similar fashion to that of the $\tau\tau$-component in terms of its temperature dependence. The major difference is that as the angular speed is increased, the maximum of the $\rho\rho$-component shifts away from the origin and toward the space-time boundary. The component is still zero at the space-time boundary, however. A minor clarification must

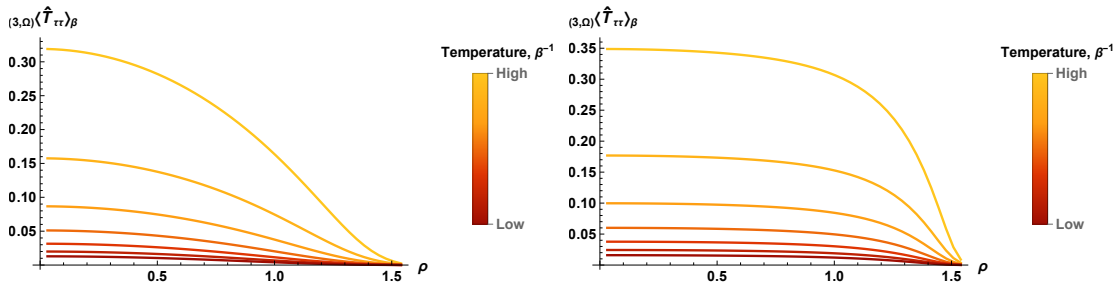


(a) $\Omega = 0.5$ (b) $\Omega = 0.96$

Figure 5.14: The $\tau\tau$-component of the renormalised stress-energy tensor at two different angular speeds $\Omega$. The inverse adS length scale is kept fixed at $a = 1$. The inverse temperature is varied within the range $\beta \in [\pi/3, 5\pi/6]$. Dirichlet boundary conditions are applied to the field.

be made at this point. It appears, based on figure 5.15b, that the component takes a nonzero value at the space-time boundary. This is merely a limitation of the numerics and, in particular, the mesh for $\rho$ used. It simply reflects the fact that the $\rho$ mesh ceases at approximately $\rho = \pi/2 - 10^{-3}$, since numerical evaluation directly at $\rho = \pi/2$ produced irredeemable divergences. From the construction, we know this not to be the case; since we require that the components be zero on the boundary, we can safely remove these divergences and chalk it up to numerical error.

The next figure shown, figure 5.16, is of the (negative) $\tau\phi$-component. Unlike both the $\tau\tau$- and $\rho\rho$-components which take a nonzero value at the origin, the $\tau\phi$-component is zero at both the origin and space-time boundary. As the angular speed is increased, the (absolute) maximum starts to shift away from around $\rho = \pi/2$ toward the boundary.

Figure 5.17 shows the final nonzero component, ${}_{(3,\Omega)}\langle \widehat{T}_{\phi\phi} \rangle_\beta$. The profile of this component is similar to that of the (negative) $\tau\phi$ component and shares some of the same features. Namely, as the angular speed is increased, the location of the maximum tends towards the space-time boundary. The major difference is the behaviour just before the boundary for

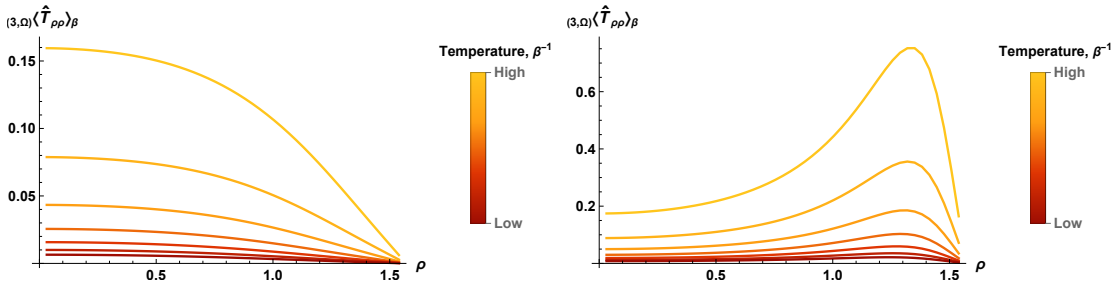


(a) $\Omega = 0.5$ (b) $\Omega = 0.96$

Figure 5.15: The $\rho\rho$-component of the renormalised stress-energy tensor at two different angular speeds $\Omega$. The inverse adS length scale is kept fixed at $a = 1$. The inverse temperature is varied within the range $\beta \in [\pi/3, 5\pi/6]$. Dirichlet boundary conditions are applied to the field.

the $\Omega = 0.5$ case, where the component seemingly becomes negative before hitting zero at the boundary.

There is one feature of the plots (figures 5.14-5.17) that every component of the renormalised stress-energy tensor (5.2.35) seems to exhibit. Indeed, as the angular speed is increased, the plots seem to suggest that the quantum matter starts to clump toward the space-time boundary. This is behaviour one would expect to observe when considering (nonrelativistic) centripetal motion.

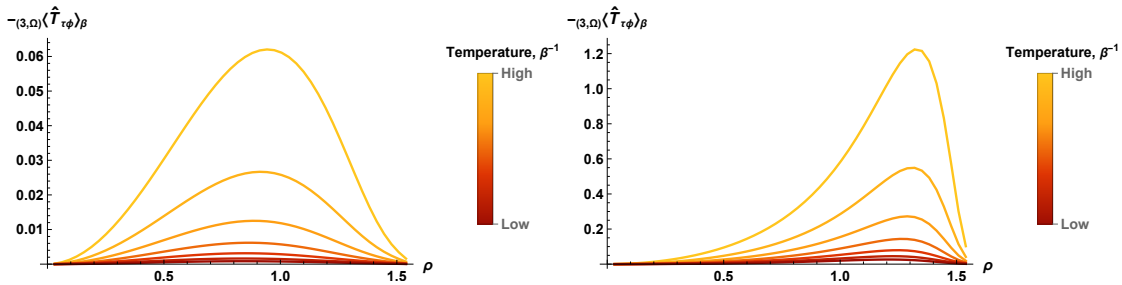


(a) $\Omega = 0.5$ (b) $\Omega = 0.96$

Figure 5.16: The negative $\tau\phi$-component of the renormalised stress-energy tensor at two different angular speeds $\Omega$. The inverse adS length scale is kept fixed at $a = 1$. The inverse temperature is varied within the range $\beta \in [\pi/3, 5\pi/6]$. Dirichlet boundary conditions are applied to the field.

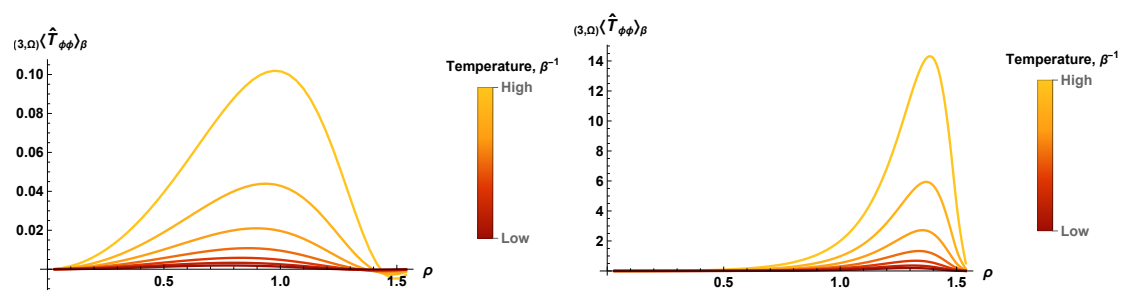


(a) $\Omega = 0.5$ (b) $\Omega = 0.96$

Figure 5.17: The $\phi\phi$-component of the renormalised stress-energy tensor at two different angular speeds $\Omega$. The inverse adS length scale is kept fixed at $a = 1$. The inverse temperature is varied within the range $\beta \in [\pi/3, 5\pi/6]$. Dirichlet boundary conditions are applied to the field.

## § 5.3 A brief interlude: QFT vs RKT

In section 2.3, results for a stress-energy tensor in a relativistic kinetic theory, for certain three- and four-dimensional space-times was presented. Here, we specialise to the four cases of anti-de Sitter space-time considered in the previous sections: three- and four-dimensional rigidly-rotating and static adS. We then transform these RKT-stress-energy tensors (RKT-SETs) into a rigidly-rotating frame, described by the orthonormal dreibein (4.4.16,4.4.29) or vierbein (4.4.14,4.4.27) basis vectors, found in section 4.4. To aid in the comparison between RKT and QFT, in section 5.3.3 we transform the renormalised stress-energy tensors found in sections 5.1 and 5.2 into the same frame. We compare plots of the different stress-energy tensors for both QFT and RKT in the thermometer frame (2.3.3), as discussed in section 2.3, allowing us to compare physical attributes of the two theories. A brief word on nomenclature: since we are using RKT to model a quantum scalar field as a distribution of particles, we refer to the quantum scalar field modelled by RKT as both a field and distribution interchangeably.

### 5.3.1 RKT in four-dimensional anti-de Sitter space

Recall that from equation 2.3.34, for four-dimensional space-times, the RKT-SET is given by

$$ {}^{\mathrm{RKT}}_{(4,\bullet)}\widehat{T}^{(a)(b)} = \frac{\pi^2}{90\widetilde{\beta}^4}\mathrm{Diag}\{3,1,1,1\}, \tag{5.3.1} $$

where $\widetilde{\beta}$ is the local inverse temperature, given by the Tolman relation [357, 359]

$$ \widetilde{\beta} = \beta\sqrt{-g_{\tau\tau}}. \tag{5.3.2} $$

In the following two subsections, we will write down the RKT-SET explicitly for both static and rigidly-rotating distributions in four-dimensional anti-de Sitter space-time. Whilst we will inevitably use the frame components to compare with the QFT stress-energy tensors,

we will also convert the RKT-SETs into space-time coordinates for use in computing back-reaction effects. This is done by using the vierbeins (4.4.14,4.4.27) in section 4.4 to contract with the RKT-SET in the following way:

$$ {}^{\text{RKT}}_{(4,\bullet)}\widehat{T}^{\mu\nu} = {}^{\text{RKT}}_{(4,\bullet)}\widehat{T}^{(a)(b)} e^{\mu}_{(a)} e^{\nu}_{(b)}. \tag{5.3.3} $$

Note that in the rotating case, one would use the (rotating) vierbein $\mathring{e}^{\bullet}_{(\bullet)}$ (4.4.27) rather than the (nonrotating) vierbein $e^{\bullet}_{(\bullet)}$ (4.4.14).

#### 5.3.1.1 Static distributions

In static (i.e. nonrotating) space-times, the Lorentz factor as defined in (4.4.4b) is equal to one. The local temperature in this case is

$$ \widetilde{\beta} = \beta a^{-1} \sec(\rho). \tag{5.3.4} $$

This means that the RKT-SET in the frame takes the simple form

$$ {}^{\text{RKT}}_{(4,\not{\Omega})}\widehat{T}^{(a)(b)} = \frac{a^4\pi^2}{90\beta^4}\cos^4(\rho)\text{Diag}\{3,\ 1,\ 1,\ 1\}. \tag{5.3.5} $$

To find the RKT-SET in space-time coordinates, we must contract, with respect to the Minkowski metric, the RKT-SET (5.3.5) with the vierbein (4.4.14). This yields

$$ {}^{\text{RKT}}_{(4,\not{\Omega})}\widehat{T}^{\tau\tau} = e^{\tau}_{(a)} e^{\tau}_{(b)} {}^{\text{RKT}}_{(4,\not{\Omega})}\widehat{T}^{(a)(b)} = e^{\tau}_{(\tau)} e^{\tau}_{(\tau)} {}^{\text{RKT}}_{(4,\not{\Omega})}\widehat{T}^{(\tau)(\tau)} = 3a^2 {}_{(4,\not{\Omega})}\mathcal{N}\cos^2(\rho), \tag{5.3.6} $$

$$ {}^{\text{RKT}}_{(4,\not{\Omega})}\widehat{T}^{\rho\rho} = e^{\rho}_{(a)} e^{\rho}_{(b)} {}^{\text{RKT}}_{(4,\not{\Omega})}\widehat{T}^{(a)(b)} = e^{\rho}_{(\rho)} e^{\rho}_{(\rho)} {}^{\text{RKT}}_{(4,\not{\Omega})}\widehat{T}^{(\rho)(\rho)} = a^2 {}_{(4,\not{\Omega})}\mathcal{N}\cos^2(\rho), \tag{5.3.7} $$

$$ {}^{\text{RKT}}_{(4,\not{\Omega})}\widehat{T}^{\theta\theta} = e^{\theta}_{(a)} e^{\theta}_{(b)} {}^{\text{RKT}}_{(4,\not{\Omega})}\widehat{T}^{(a)(b)} = e^{\theta}_{(\theta)} e^{\theta}_{(\theta)} {}^{\text{RKT}}_{(4,\not{\Omega})}\widehat{T}^{(\theta)(\theta)} = a^2 {}_{(4,\not{\Omega})}\mathcal{N}\cot^2(\rho), \tag{5.3.8} $$

$$ {}^{\text{RKT}}_{(4,\not{\Omega})}\widehat{T}^{\phi\phi} = e^{\phi}_{(a)} e^{\phi}_{(b)} {}^{\text{RKT}}_{(4,\not{\Omega})}\widehat{T}^{(a)(b)} = e^{\phi}_{(\phi)} e^{\phi}_{(\phi)} {}^{\text{RKT}}_{(4,\not{\Omega})}\widehat{T}^{(\phi)(\phi)} = a^2 {}_{(4,\not{\Omega})}\mathcal{N}\csc^2(\theta)\cot^2(\rho), \tag{5.3.9} $$

where we have defined

$$ {}_{(4,\not{\Omega})}\mathcal{N} := \frac{a^4\pi^2}{90\beta^4}\cos^4(\rho). \tag{5.3.10} $$

The contravariant RKT-SET can thus be written as

$$ {}^{\text{RKT}}_{(4,\not{\Omega})}\widehat{T}^{\bullet\bullet} = \frac{a^6\pi^2}{90\beta^4}\cos^6(\rho)\,\text{Diag}\left\{3,\ 1,\ \csc^2(\rho),\ \csc^2(\theta)\csc^2(\rho)\right\}, \tag{5.3.11} $$

and by lowering the indices using the anti-de Sitter space metric (4.1.8), the covariant RKT-SET is given by

$$ {}^{\text{RKT}}_{(4,\Omega)}\widehat{T}_{\bullet\bullet} = \frac{a^2\pi^2}{90\beta^4}\cos^2(\rho)\,\text{Diag}\left\{3,\,1,\,\sin^2(\rho),\,\sin^2(\theta)\sin^2(\rho)\right\}. \tag{5.3.12} $$

#### 5.3.1.2 Rigidly-rotating distributions

For the RKT-SET in the frame, one simply needs to substitute the local inverse temperature into equation (5.3.1), using equation (5.3.2). From the metric (4.4.3), we have that

$$ g_{\tau\tau} = -a^{-2}\sec^2(\rho)\left[1-\Omega^2\sin^2(\rho)\sin^2(\theta)\right], \tag{5.3.13} $$

and so the RKT-SET (in the frame) can be written as

$$ \begin{aligned} {}^{\text{RKT}}_{(4,\Omega)}\widehat{T}^{(a)(b)} &= \frac{a^4\pi^2}{90\beta^4}\cos^4(\rho)\left[1-\Omega^2\sin^2(\rho)\sin^2(\theta)\right]^{-2}\text{Diag}\{3,1,1,1\} \\ &= \frac{a^4\pi^2\Gamma^4_{(4)}}{90\beta^4}\cos^4(\rho)\text{Diag}\{3,1,1,1\}, \end{aligned} \tag{5.3.14} $$

where $\Gamma_{(4)}$ is the Lorentz factor (4.4.4b) defined in section 4.4. For ease of transcription henceforth, we define the prefactor in equation (5.3.14) to be the quantity

$$ {}_{(4,\Omega)}\mathcal{N} := \frac{\pi^2 a^4\Gamma^4_{(4)}}{90\beta^4}\cos^4(\rho). \tag{5.3.15} $$

In figure 5.18 below, ${}_{(4,\Omega)}\mathcal{N}$ is shown as a surface plot for a fixed inverse global temperature $\beta = \pi/6$ and angular speeds $\Omega = 0.5$ and $\Omega = 0.96$. For both angular speeds, the maximum is at the origin $\rho = 0$. Whilst ${}_{(4,\Omega)}\mathcal{N}$ depends on $\theta$ for the $\Omega = 0.5$ case, this is not overly apparent from figure 5.18a. As the angular speed increases, the $\theta$ dependence becomes more obvious. Indeed, at high angular speeds, a hump emerges on the equatorial plane $\theta = \pi/2$ near to the space-time boundary, $\rho = \pi/2$.

To find the RKT-SET in space-time coordinates, we need to contract with the relevant vierbein (4.4.27) using equation (5.3.3). The nonzero components of the RKT-SET in

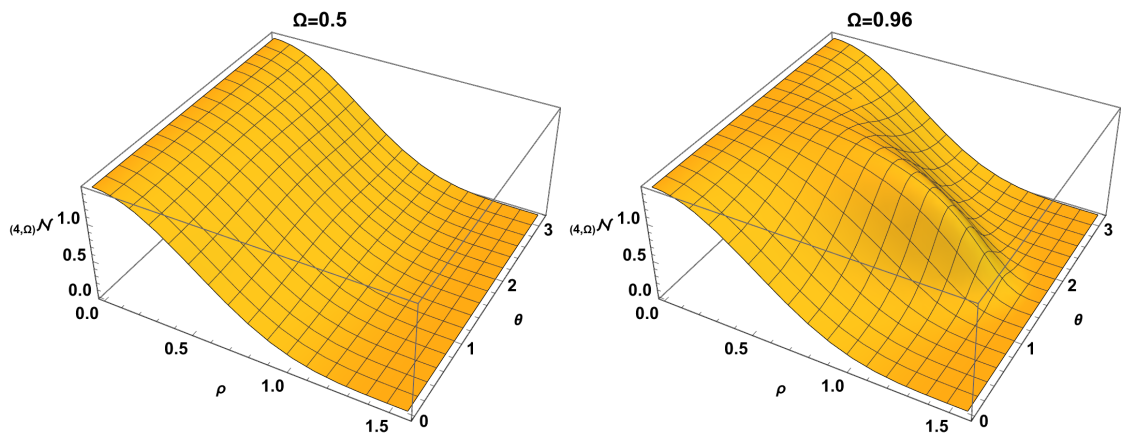


(a) $\Omega = 0.5$ (b) $\Omega = 0.96$

Figure 5.18: Surface plots of the rotating four-dimensional adS RKT-SET prefactor (5.3.15). The adS length scale is fixed, $a = 1$, as well as the global inverse temperature $\beta = \pi/6$. The angular speed is varied.

space-time coordinates are calculated below. Starting with the $\tau\tau$-component, we have

$$\begin{aligned}
{}^{\text{RKT}}_{(4,\Omega)}\widehat{T}^{\tau\tau} &= \mathring{e}^{\tau}_{(a)}\mathring{e}^{\tau}_{(b)}\,{}^{\text{RKT}}_{(4,\Omega)}\widehat{T}^{(a)(b)} \\
&= \mathring{e}^{\tau}_{(\tau)}\mathring{e}^{\tau}_{(\tau)}\,{}^{\text{RKT}}_{(4,\Omega)}\widehat{T}^{(\tau)(\tau)} + \mathring{e}^{\tau}_{(\tau)}\mathring{e}^{\tau}_{(\phi)}\,{}^{\text{RKT}}_{(4,\Omega)}\widehat{T}^{(\tau)(\phi)} \\
&\quad + \mathring{e}^{\tau}_{(\phi)}\mathring{e}^{\tau}_{(\tau)}\,{}^{\text{RKT}}_{(4,\Omega)}\widehat{T}^{(\phi)(\tau)} + \mathring{e}^{\tau}_{(\phi)}\mathring{e}^{\tau}_{(\phi)}\,{}^{\text{RKT}}_{(4,\Omega)}\widehat{T}^{(\phi)(\phi)} \\
&= 3a^2\,{}_{(4,\Omega)}\mathcal{N}\Gamma^2_{(4)}\cos^2(\rho) + a^2\,{}_{(4,\Omega)}\mathcal{N}\Gamma^2_{(4)}\Omega^2\sin^2(\theta)\cos^2(\rho)\sin^2(\rho) \\
&= {}_{(4,\Omega)}\mathcal{N}a^2\cos^2(\rho)\left\{4\Gamma^2_{(4)} - 1\right\}. \qquad (5.3.16)
\end{aligned}$$

The other diagonal components are easier to calculate. They are

$$\begin{aligned}
{}^{\text{RKT}}_{(4,\Omega)}\widehat{T}^{\rho\rho} &= \mathring{e}^{\rho}_{(a)}\mathring{e}^{\rho}_{(b)}\,{}^{\text{RKT}}_{(4,\Omega)}\widehat{T}^{(a)(b)} = \mathring{e}^{\rho}_{(\rho)}\mathring{e}^{\rho}_{(\rho)}\,{}^{\text{RKT}}_{(4,\Omega)}\widehat{T}^{(\rho)(\rho)} = {}_{(4,\Omega)}\mathcal{N}a^2\cos^2(\rho), \qquad (5.3.17) \\
{}^{\text{RKT}}_{(4,\Omega)}\widehat{T}^{\theta\theta} &= \mathring{e}^{\theta}_{(a)}\mathring{e}^{\theta}_{(b)}\,{}^{\text{RKT}}_{(4,\Omega)}\widehat{T}^{(a)(b)} = \mathring{e}^{\theta}_{(\theta)}\mathring{e}^{\theta}_{(\theta)}\,{}^{\text{RKT}}_{(4,\Omega)}\widehat{T}^{(\theta)(\theta)} = {}_{(4,\Omega)}\mathcal{N}a^2\cot^2(\rho), \qquad (5.3.18) \\
{}^{\text{RKT}}_{(4,\Omega)}\widehat{T}^{\phi\phi} &= \mathring{e}^{\phi}_{(a)}\mathring{e}^{\phi}_{(b)}\,{}^{\text{RKT}}_{(4,\Omega)}\widehat{T}^{(a)(b)} = \mathring{e}^{\phi}_{(\phi)}\mathring{e}^{\phi}_{(\phi)}\,{}^{\text{RKT}}_{(4,\Omega)}\widehat{T}^{(\phi)(\phi)} = {}_{(4,\Omega)}\mathcal{N}\Gamma^{-2}_{(4)}a^2\csc^2(\theta)\cos^2(\rho)\csc^2(\rho). \qquad (5.3.19)
\end{aligned}$$

The only nonzero off-diagonal component is

$$ {}^{\mathrm{RKT}}_{(4,\Omega)}\widehat{T}^{\tau\phi} = \mathring{e}^{\tau}_{(a)}\mathring{e}^{\phi}_{(b)}\widehat{T}^{(a)(b)} = \mathring{e}^{\tau}_{(\phi)}\mathring{e}^{\phi}_{(\phi)}\widehat{T}^{(\phi)(\phi)} = {}_{(4,\Omega)}\mathcal{N}a^2\Omega\cos^2(\rho). \tag{5.3.20} $$

Combining these, and reinstating ${}_{(4,\Omega)}\mathcal{N}$ using equation (5.3.15), we can write down the contravariant RKT-SET in matrix form as

$$ {}^{\mathrm{RKT}}_{(4,\Omega)}\widehat{T}^{\bullet\bullet} = \frac{a^6\pi^2\Gamma^4_{(4)}}{90\beta^4}\cos^6(\rho)\begin{pmatrix} 4\Gamma^2_{(4)}-1 & 0 & 0 & \Omega \\ 0 & 1 & 0 & 0 \\ 0 & 0 & \csc^2(\rho) & 0 \\ \Omega & 0 & 0 & \Gamma^{-2}_{(4)}\csc^2(\theta)\csc^2(\rho) \end{pmatrix}. \tag{5.3.21} $$

In section 2.3.3, we constructed the contravariant RKT-SET for rigidly-rotating distributions in Minkowski space, in rotating cylindrical coordinates. Additionally, in section 4.1 it was shown that the (rigidly-rotating) flat space metric can be recovered from the (rigidly-rotating) anti-de Sitter space in the limit $a \to 0$, provided we dimensionalise the radial and temporal coordinates. If we take the contravariant RKT-SET (5.3.21), dimensionalise the radial (and temporal) coordinate and switch from spherical to cylindrical coordinates in the usual way, we recover the contravariant Minkowski space RKT-SET (2.3.42).

By contracting with the space-time metric (4.4.3), we can lower the indices and write down the covariant RKT-SET as

$$ {}^{\mathrm{RKT}}_{(4,\Omega)}\widehat{T}_{\bullet\bullet} = \frac{a^2\pi^2\Gamma^4_{(4)}}{90\beta^4}\cos^2(\rho)\begin{pmatrix} 3\Gamma^{-2}_{(4)} & 0 & 0 & 3\Gamma^{-2}_{(4)}-3 \\ 0 & 1 & 0 & 0 \\ 0 & 0 & \sin^2(\rho) & 0 \\ 3\Gamma^{-2}_{(4)}-3 & 0 & 0 & \sin^2(\theta)\sin^2(\rho)\left[4\Gamma^2_{(4)}-3\right] \end{pmatrix}. \tag{5.3.22} $$

Figures 5.19 to 5.23 show the components of the covariant RKT-SET in space-time coordinates, all at a fixed inverse global temperature $\beta = \pi/6$. In particular, figure 5.19 shows the $\tau\tau$-component. For both $\Omega = 0.5$ and $\Omega = 0.96$, the overall profile is solitonic, in so much as it takes its global maximum at the origin and tends towards zero at the space-time

boundary. As the angular speed is increased, a hump around the equatorial plane $\theta = \pi/2$ forms. However, the hump is not as sharp as, say, the one formed for the RKT prefactor shown in figure 5.18b.

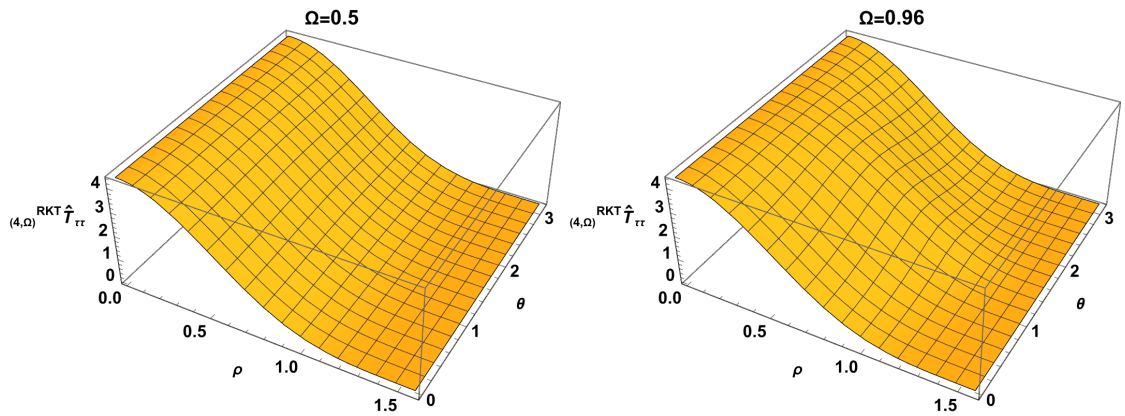


(a) $\Omega = 0.5$ (b) $\Omega = 0.96$

Figure 5.19: Surface plots of the $\tau\tau$-component of the rotating four-dimensional adS RKT-SET. The adS length scale is fixed, $a = 1$, as well as the global inverse temperature $\beta = \pi/6$. The angular speed is varied.

Figure 5.20 shows minus the $\tau\phi$-component. Unlike for the $\tau\tau$-component, the $\tau\phi$-component is zero at both the origin and space-time boundary. Additionally, it is zero for both $\theta = 0$ and $\theta = \pi$, meaning the rotation has no effect on the axes. The global maximum of the $\tau\phi$-component is on the equatorial plane, and as angular speed is increased, this maximum starts to shift towards the space-time boundary.

In figure 5.21, we see the $\rho\rho$-component of the covariant RKT-SET. This shares some features with the $\tau\tau$-component; they have similar profiles, both have their maximum at the origin, both are zero at the space-time boundary and as the angular speed is increased, both form a hump on the equatorial plane. The main difference is in the severity of said hump; the hump that forms in the $\rho\rho$-component is much more sharp, and indeed noticeable, than the emergent hump in the $\tau\tau$-component.

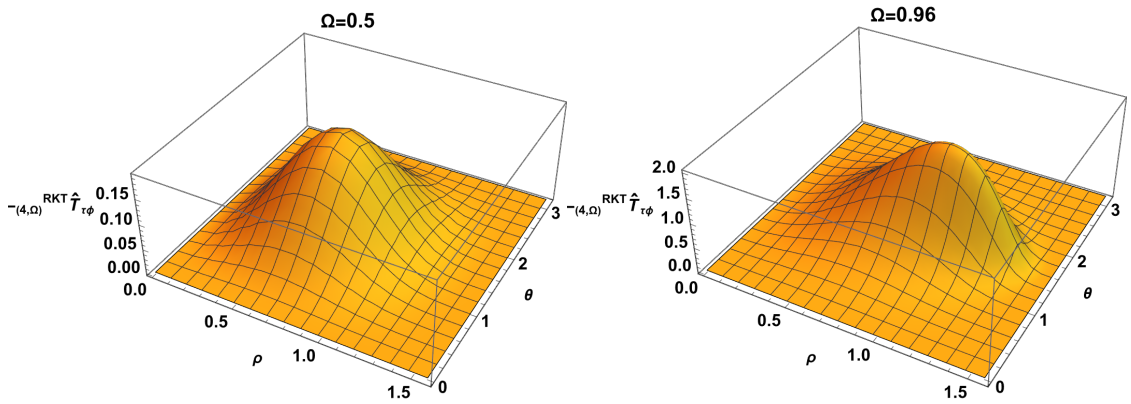


(a) $\Omega = 0.5$ (b) $\Omega = 0.96$

Figure 5.20: Minus the $\tau\phi$-component of the rotating four-dimensional adS RKT-SET. The adS length scale is fixed, $a = 1$, as well as the global inverse temperature $\beta = \pi/6$. The angular speed is varied.

The $\theta\theta$-component, shown in figure 5.22, has an interesting profile. Whilst similar to the $\tau\phi$-component in that it is zero at both the origin and space-time boundary, it is not identically zero at $\theta = 0$ and $\theta = \pi$, meaning the rotation does have an effect on the axes. The global maximum of the $\theta\theta$-component is on the equatorial plane away from both $\rho = 0$ and $\rho = \pi/2$, and as angular speed is increased, this maximum tends towards the space-time boundary $\rho = \pi/2$.

The final component, ${}^{\text{RKT}}_{(4,\Omega)}\widehat{T}_{\phi\phi}$, is shown in figure 5.23. This has a very similar profile to the $\tau\phi$-component. It is zero on all four axes, $\rho = 0, \pi/2$ and $\theta = 0, \pi$. The global maximum is thus away from the axes, and, as angular speed is increased, starts to shift towards the space-time boundary $\rho = \pi/2$. An extra point to note is that the difference in magnitudes between the maximum in figures 5.23a and 5.23b is much higher than the corresponding differences for the other components. For example, the difference in global maximum between angular speeds $\Omega = 0.5$ and $\Omega = 0.96$ for both the $\tau\tau$- and $\rho\rho$-components is approximately $\sim 1$; the difference for the $\theta\theta$-components is $\sim 3$; for the $\tau\phi$-component it

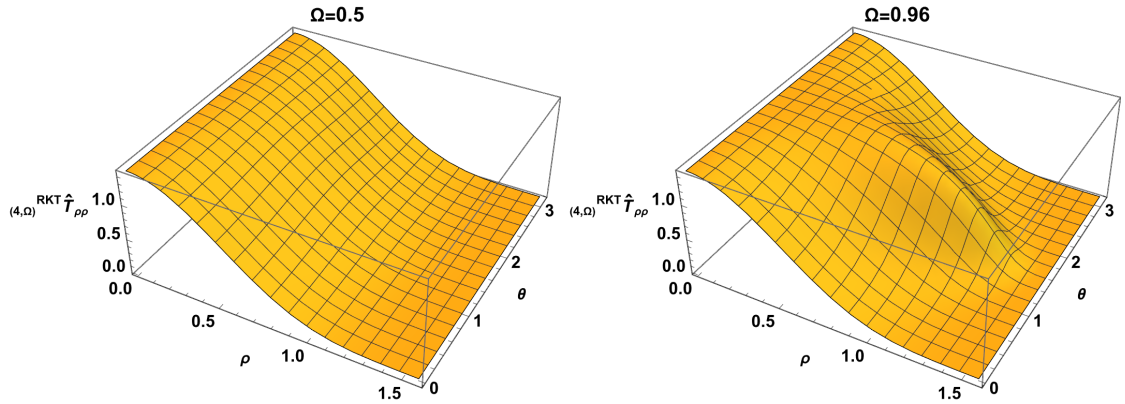


(a) $\Omega = 0.5$ (b) $\Omega = 0.96$

Figure 5.21: Surface plots of the $\rho\rho$-component of the rotating four-dimensional adS RKT-SET. The adS length scale is fixed, $a = 1$, as well as the global inverse temperature $\beta = \pi/6$. The angular speed is varied.

is $\sim 10$ times; whereas for the $\phi\phi$-component it is $\sim 30$ times larger. This suggests that the rotation has the greatest effect on the $\phi\phi$-component of the RKT-SET.

### 5.3.2 RKT in three-dimensional anti-de Sitter space

Recall that for three-dimensional space-times, the RKT-SET is given by (2.3.22)

$$ {}^{\mathrm{RKT}}_{(3,\bullet)}\widehat{T}^{(a)(b)} = \frac{\zeta(3)}{2\pi\widetilde{\beta}^3}\mathrm{Diag}\{2,1,1\}, \tag{5.3.23} $$

where $\widetilde{\beta}$ is the local inverse temperature, given by equation (2.3.7) [357, 359], and $\zeta(3)$ is Apéry's constant (2.3.23) [21, 280].

In the following two subsections, we will write down the RKT-SET explicitly for both static and rigidly-rotating distributions in three-dimensional anti-de Sitter space-time. As for the four-dimensional case, we will use frame coordinates to compare the RKT-SETs with the corresponding renormalised stress-energy tensors (5.2.15,5.2.35). Nevertheless, we compute the RKT-SET in space-time coordinates for use in considering back-reaction

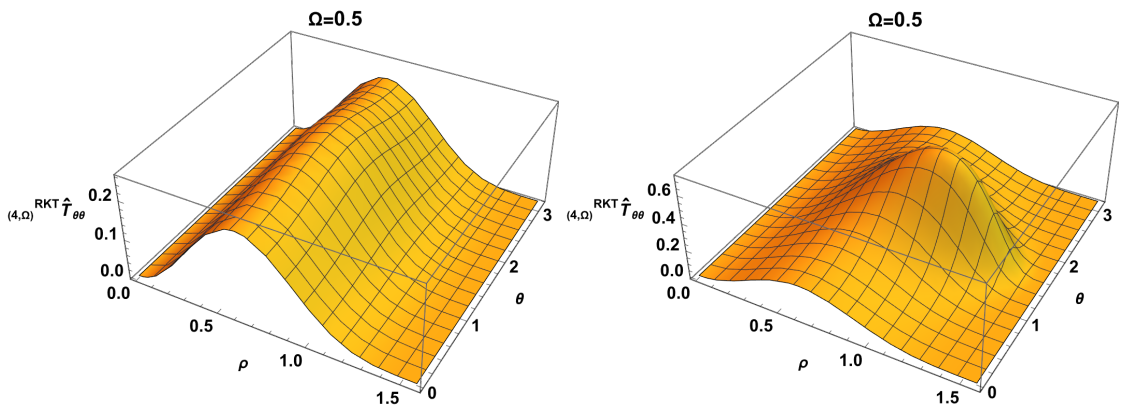


(a) $\Omega = 0.5$ (b) $\Omega = 0.96$

Figure 5.22: Surface plots of the $\theta\theta$-component of the rotating four-dimensional adS RKT-SET. The adS length scale is fixed, $a = 1$, as well as the global inverse temperature $\beta = \pi/6$. The angular speed is varied.

effects in part III of this thesis. To write the RKT-SET in space-time coordinates, we use the rotating (4.4.29) and nonrotating (4.4.29) dreibeins in conjunction with the relation (2.3.13).

#### 5.3.2.1 Static distributions

For static (i.e. nonrotating) three-dimensional anti-de Sitter space-time, the local temperature is given by

$$\widetilde{\beta} = \beta a^{-1} \sec(\rho), \tag{5.3.24}$$

and so the macroscopic stress-energy tensor (RKT-SET) in the frame is simply

$$\underset{(3,\mathcal{Q})}{\mathrm{RKT}}\widehat{T}^{(a)(b)} = \frac{a^3\zeta(3)}{2\pi\beta^3}\cos^3(\rho)\mathrm{Diag}\{2,\,1,\,1\}. \tag{5.3.25}$$

Contracting this SET with the dreibein (4.4.16), with respect to the Minkowski metric, we yield the RKT-SET in space-time coordinates. For brevity, we define the prefactor as the

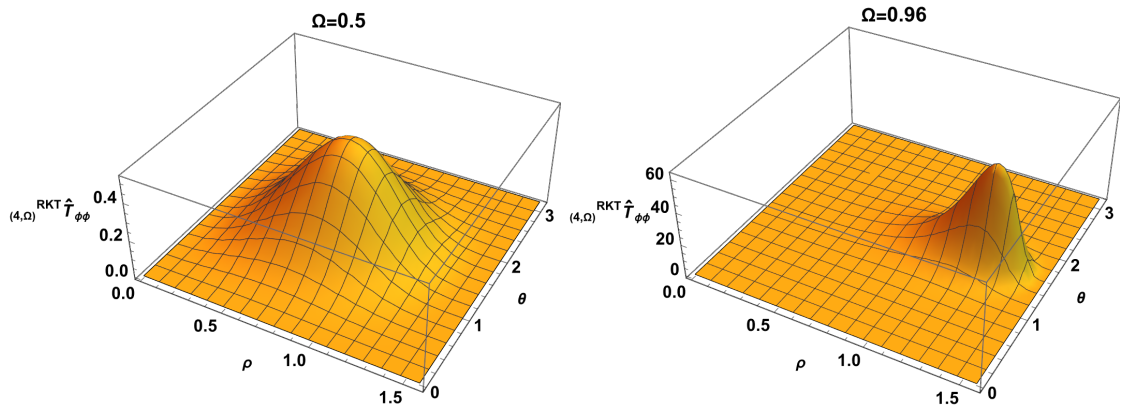


(a) $\Omega = 0.5$ (b) $\Omega = 0.96$

Figure 5.23: Surface plots of the $\phi\phi$-component of the rotating four-dimensional adS RKT-SET. The adS length scale is fixed, $a = 1$, as well as the global inverse temperature $\beta = \pi/6$. The angular speed is varied.

quantity

$$ {}_{(3,\mathfrak{Q})}\mathcal{N} := \frac{a^3\zeta(3)}{2\pi\beta^3}\cos^3(\rho). \tag{5.3.26} $$

The components are then calculated as follows:

$$ {}^{\mathrm{RKT}}_{(3,\mathfrak{Q})}\widehat{T}^{\tau\tau} = \mathfrak{e}^{\tau}_{(a)}\mathfrak{e}^{\tau}_{(b)}\,{}^{\mathrm{RKT}}_{(3,\mathfrak{Q})}\widehat{T}^{(a)(b)} = \mathfrak{e}^{\tau}_{(\tau)}\mathfrak{e}^{\tau}_{(\tau)}\,{}^{\mathrm{RKT}}_{(3,\mathfrak{Q})}\widehat{T}^{(\tau)(\tau)} = 2a^2\,{}_{(3,\mathfrak{Q})}\mathcal{N}\cos^2(\rho), \tag{5.3.27} $$

$$ {}^{\mathrm{RKT}}_{(3,\mathfrak{Q})}\widehat{T}^{\rho\rho} = \mathfrak{e}^{\rho}_{(a)}\mathfrak{e}^{\rho}_{(b)}\,{}^{\mathrm{RKT}}_{(3,\mathfrak{Q})}\widehat{T}^{(a)(b)} = \mathfrak{e}^{\rho}_{(\rho)}\mathfrak{e}^{\rho}_{(\rho)}\,{}^{\mathrm{RKT}}_{(3,\mathfrak{Q})}\widehat{T}^{(\rho)(\rho)} = a^2\,{}_{(3,\mathfrak{Q})}\mathcal{N}\cos^2(\rho), \tag{5.3.28} $$

$$ {}^{\mathrm{RKT}}_{(3,\mathfrak{Q})}\widehat{T}^{\phi\phi} = \mathfrak{e}^{\phi}_{(a)}\mathfrak{e}^{\phi}_{(b)}\,{}^{\mathrm{RKT}}_{(3,\mathfrak{Q})}\widehat{T}^{(a)(b)} = \mathfrak{e}^{\phi}_{(\phi)}\mathfrak{e}^{\phi}_{(\phi)}\,{}^{\mathrm{RKT}}_{(3,\mathfrak{Q})}\widehat{T}^{(\phi)(\phi)} = a^2\,{}_{(3,\mathfrak{Q})}\mathcal{N}\cot^2(\rho). \tag{5.3.29} $$

After reinstating the prefactor (5.3.26), we can write down the contravariant RKT-SET as

$$ {}^{\mathrm{RKT}}_{(3,\mathfrak{Q})}\widehat{T}^{\bullet\bullet} = \frac{a^5\zeta(3)}{2\pi\beta^3}\cos^5(\rho)\,\mathrm{Diag}\left\{2,\ 1,\ \csc^2(\rho)\right\}. \tag{5.3.30} $$

Lowering the indices using the anti-de Sitter space metric (4.1.7), we have that the covariant RKT-SET is simply

$$ {}^{\mathrm{RKT}}_{(3,\mathfrak{Q})}\widehat{T}_{\bullet\bullet} = \frac{a\zeta(3)}{2\pi\beta^3}\cos(\rho)\,\mathrm{Diag}\left\{2,\ 1,\ \sin^2(\rho)\right\}. \tag{5.3.31} $$

Plots of the space-time coordinate components of the RKT-SET will not be shown, since (5.3.31) takes a simple form. All three nonzero components are zero at the space-time boundary. The global maxima of the $\tau\tau$- and $\rho\rho$-components are at the origin; whereas the $\phi\phi$-component is zero at the origin and has its global maximum away from both the origin and boundary. For all three nonzero components, the temperature dependence is cubic.

#### 5.3.2.2 Rigidly-rotating distributions

For rigidly-rotating three-dimensional anti-de Sitter space-time, the local temperature is

$$\widetilde{\beta} = \beta a^{-1} \sec(\rho) \left[1 - \Omega^2 \sin^2(\rho)\right]^{1/2} = \beta a^{-1} \Gamma_{(3)}^{-1} \sec(\rho), \tag{5.3.32}$$

where the Lorentz factor $\Gamma_{(3)}$ was given in equation (4.4.4a). Substituting this into equation (5.3.23) we yield the RKT-SET in the frame, which is

$$\underset{(3,\Omega)}{\mathrm{RKT}}\widehat{T}^{(a)(b)} = \frac{a^3 \zeta(3) \Gamma_{(3)}^3}{2\pi\beta^3} \cos^3(\rho) \mathrm{Diag}\left\{2,\, 1,\, 1\right\}. \tag{5.3.33}$$

For later ease of transcription, we define the prefactor in equation (5.3.33) as the quantity

$$_{(3,\Omega)}\mathcal{N} := \frac{a^3 \zeta(3) \Gamma_{(3)}^3}{2\pi\beta^3} \cos^3(\rho). \tag{5.3.34}$$

Figure 5.24 shows this prefactor as a function of $\rho$ and $\Omega$ at a fixed inverse temperature $\beta = \pi/6$. As the angular speed is increased towards $\Omega = 1$ (such that a speed of light surface forms at the space-time boundary), the surface tends towards a constant value $108\zeta(3)/\pi^4 \approx 1.33$. For zero angular speed, the function is proportional to $\cos^3(\rho)$.

If we wish to find the RKT-SET in space-time coordinates, as set out in the relation (2.3.13), we must contract with a suitable orthonormal basis; we use the dreibein (4.4.29) given in section 4.4. The nonzero components of the RKT-SET are calculated below, starting with the $\tau\tau$-component:

$$\underset{(3,\Omega)}{\mathrm{RKT}}\widehat{T}^{\tau\tau} = \mathring{\mathfrak{e}}^{\tau}_{(a)} \mathring{\mathfrak{e}}^{\tau}_{(b)} \underset{(3,\Omega)}{\mathrm{RKT}}\widehat{T}^{(a)(b)}$$

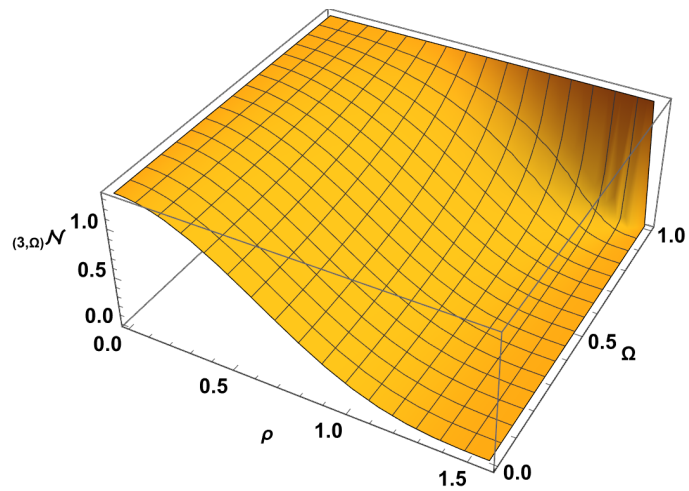


Figure 5.24: Surface plot of the rotating three-dimensional adS RKT-SET prefactor. The adS length scale is fixed, $a = 1$, as well as the global inverse temperature $\beta = \pi/6$. The angular speed is varied.

$$
\begin{aligned}
&= \mathring{\mathfrak{e}}^{\tau}_{(\tau)}\mathring{\mathfrak{e}}^{\tau}_{(\tau)}\,{}^{\mathrm{RKT}}_{(3,\Omega)}\widehat{T}^{(\tau)(\tau)} + \mathring{\mathfrak{e}}^{\tau}_{(\tau)}\mathring{\mathfrak{e}}^{\tau}_{(\phi)}\,{}^{\mathrm{RKT}}_{(3,\Omega)}\widehat{T}^{(\tau)(\phi)} \\
&\quad + \mathring{\mathfrak{e}}^{\tau}_{(\phi)}\mathring{\mathfrak{e}}^{\tau}_{(\tau)}\,{}^{\mathrm{RKT}}_{(3,\Omega)}\widehat{T}^{(\phi)(\tau)} + \mathring{\mathfrak{e}}^{\tau}_{(\phi)}\mathring{\mathfrak{e}}^{\tau}_{(\phi)}\,{}^{\mathrm{RKT}}_{(3,\Omega)}\widehat{T}^{(\phi)(\phi)} \\
&= 2a^2\,{}_{(3,\Omega)}\mathcal{N}\Gamma^2_{(3)}\cos^2(\rho) + a^2\,{}_{(3,\Omega)}\mathcal{N}\Gamma^2_{(3)}\Omega^2\cos^2(\rho)\sin^2(\rho) \\
&= {}_{(3,\Omega)}\mathcal{N}a^2\cos^2(\rho)\left\{3\Gamma^2_{(3)} - 1\right\}. \qquad (5.3.35)
\end{aligned}
$$

The other nonzero components of the RKT-SET in space-time coordinates are

$$
{}^{\mathrm{RKT}}_{(3,\Omega)}\widehat{T}^{\rho\rho} = \mathring{\mathfrak{e}}^{\rho}_{(a)}\mathring{\mathfrak{e}}^{\rho}_{(b)}\,{}^{\mathrm{RKT}}_{(3,\Omega)}\widehat{T}^{(a)(b)} = \mathring{\mathfrak{e}}^{\rho}_{(\rho)}\mathring{\mathfrak{e}}^{\rho}_{(\rho)}\,{}^{\mathrm{RKT}}_{(3,\Omega)}\widehat{T}^{(\rho)(\rho)} = {}_{(3,\Omega)}\mathcal{N}a^2\cos^2(\rho), \qquad (5.3.36)
$$

$$
{}^{\mathrm{RKT}}_{(3,\Omega)}\widehat{T}^{\phi\phi} = \mathring{\mathfrak{e}}^{\phi}_{(a)}\mathring{\mathfrak{e}}^{\phi}_{(b)}\,{}^{\mathrm{RKT}}_{(3,\Omega)}\widehat{T}^{(a)(b)} = \mathring{\mathfrak{e}}^{\phi}_{(\phi)}\mathring{\mathfrak{e}}^{\phi}_{(\phi)}\,{}^{\mathrm{RKT}}_{(3,\Omega)}\widehat{T}^{(\phi)(\phi)} = {}_{(3,\Omega)}\mathcal{N}\Gamma^{-2}_{(3)}a^2\cos^2(\rho)\csc^2(\rho), \qquad (5.3.37)
$$

$$
{}^{\mathrm{RKT}}_{(3,\Omega)}\widehat{T}^{\tau\phi} = \mathring{\mathfrak{e}}^{\tau}_{(a)}\mathring{\mathfrak{e}}^{\phi}_{(b)}\,{}^{\mathrm{RKT}}_{(3,\Omega)}\widehat{T}^{(a)(b)} = \mathring{\mathfrak{e}}^{\tau}_{(\phi)}\mathring{\mathfrak{e}}^{\phi}_{(\phi)}\,{}^{\mathrm{RKT}}_{(3,\Omega)}\widehat{T}^{(\phi)(\phi)} = {}_{(3,\Omega)}\mathcal{N}a^2\Omega\cos^2(\rho). \qquad (5.3.38)
$$

Reinstating ${}_{(3,\Omega)}\mathcal{N}$ using equation (5.3.34), we can write down, in matrix form, the con-

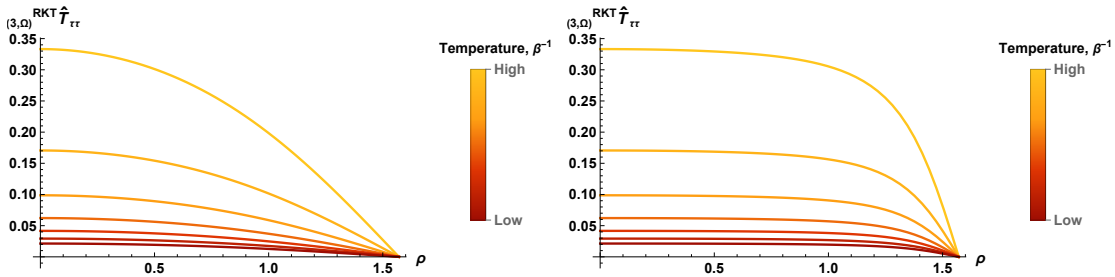


(a) $\Omega = 0.5$ (b) $\Omega = 0.96$

Figure 5.25: The $\tau\tau$-component of the RKT-SET. The angular speed and inverse temperature are varied, while the inverse adS length scale is fixed at $a = 1$. The inverse temperature range is $\beta \in [\pi/3, 5\pi/6]$.

travariant RKT-SET as

$$ {}^{\text{RKT}}_{(3,\Omega)}\widehat{T}^{\bullet\bullet} = \frac{a^5\zeta(3)\Gamma^3_{(3)}}{2\pi\beta^3}\cos^5\rho \begin{pmatrix} 3\Gamma^2_{(3)} - 1 & 0 & \Omega \\ 0 & 1 & 0 \\ \Omega & 0 & \Gamma^{-2}_{(3)}\csc^2\rho \end{pmatrix}. \tag{5.3.39} $$

Likewise, by contracting with the space-time metric (4.4.2), we can write down the covariant RKT-SET in matrix form as

$$ {}^{\text{RKT}}_{(3,\Omega)}\widehat{T}_{\bullet\bullet} = \frac{a\zeta(3)\Gamma^3_{(3)}}{2\pi\beta^3}\cos\rho \begin{pmatrix} 2\Gamma^{-2}_{(3)} & 0 & -2\Omega\sin^2(\rho) \\ 0 & 1 & 0 \\ -2\Omega\sin^2(\rho) & 0 & \sin^2(\rho)\left[3\Gamma^2_{(3)} - 2\right] \end{pmatrix}. \tag{5.3.40} $$

Figure 5.25 shows the $\tau\tau$-component of the RKT-SET. As the temperature is increased, the value of the component increases. For higher angular speeds, we see that a plateau forms around the origin $\rho = 0$, and the higher the speed, the farther the plateau extends towards the boundary at $\rho = \pi/2$. For all angular speeds, the global maximum is at the origin, and the component is zero on the boundary.

In figure 5.26, we see minus the $\tau\phi$-component of the RKT-SET. Similarly to the $\tau\tau$-component, the component increases (in magnitude) as the temperature is increased. One

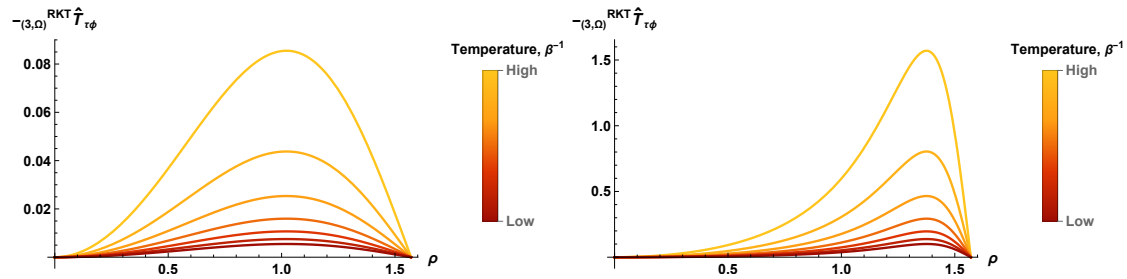


(a) $\Omega = 0.5$ (b) $\Omega = 0.96$

Figure 5.26: Minus the $\tau\phi$-component of the RKT-SET, plotted for two values of the angular speed, and with inverse temperature varied in the range $\beta \in [\pi/3, 5\pi/6]$. The inverse adS length scale is fixed at $a = 1$.

difference between the two components, however, is that for the $\tau\phi$-component, it is zero at the origin and takes its (absolute) maximum value away from both the origin and space-time boundary. As the angular speed is increased, this maximum starts to shift towards the space-time boundary.

Figure 5.27, meanwhile, shows the $\rho\rho$-component of the RKT-SET. This has some interesting features. At lower angular speeds, the component resembles the $\tau\tau$-component, in so much as it has a similar overall profile; the location of the global maximum is the same (at the origin); and it is zero on the boundary. As the angular speed is increased, however, it begins to resemble minus the $\tau\phi$-component in profile. Indeed, at high angular speeds the global maximum shifts away from the origin and is located close to the space-time boundary. Although the $\rho\rho$-component is zero on the space-time boundary, the major difference between the $\rho\rho$- and $\tau\phi$-components is the behaviour at the origin; whilst the $\tau\phi$-component is zero at the origin, the $\rho\rho$-component remains nonzero at the origin.

The final component, the $\phi\phi$-component, is shown in figure 5.28. The profile of the $\phi\phi$-component closely resembles that of the (negative) $\tau\phi$-component. Both are zero at both the origin and space-time boundary and take their respective maximum values away from

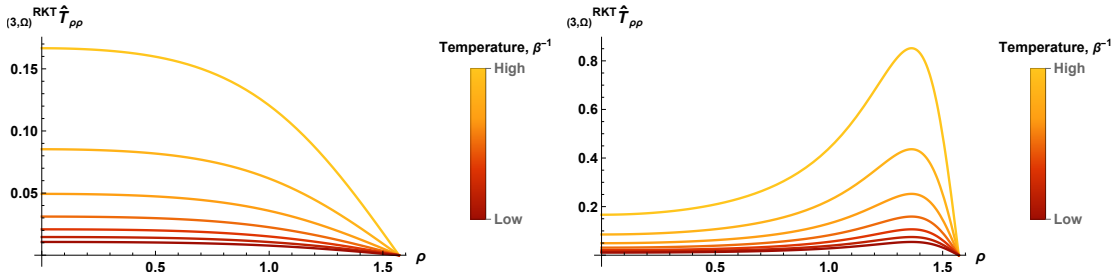


(a) $\Omega = 0.5$ (b) $\Omega = 0.96$

Figure 5.27: The $\rho\rho$-component of the RKT-SET, for two values of the angular speed, and with inverse temperature varied in the range $\beta \in [\pi/3, 5\pi/6]$. The inverse adS length scale is fixed at $a = 1$.

the boundary and origin. As the angular speed increases, this maximum starts to shift toward the space-time boundary.

### 5.3.3 QFT in the frame: three- and four-dimensional anti-de Sitter space

The purpose of this subsection is to convert the renormalised stress-energy tensors found in sections 5.1 and 5.2 into frame components for use in comparisons with the corresponding RKT results. The RKT-SETs constructed in sections 5.3.1 and 5.3.2 neglect vacuum energy effects [13, 16], since there is no classical vacuum energy. This is manifested by the zero temperature limit $\beta \to \infty$; in which they are identically zero. To that end, to aid in the comparison with the corresponding QFT stress-energy tensors, we consider only the difference in renormalised stress-energy tensor values between both nonrotating and rigidly-rotating thermal states, and the vacuum state on anti-de Sitter space-time. Since the renormalisation procedure employed in sections 5.1.2, 5.2.1 and 5.2.2 was state subtraction, there is nothing more we need to do; the expectation values are already the difference between thermal and vacuum. Conversely, for the nonrotating, four-dimensional stress-energy tensor (5.1.23), we need to subtract the vacuum expectation value (5.1.25).

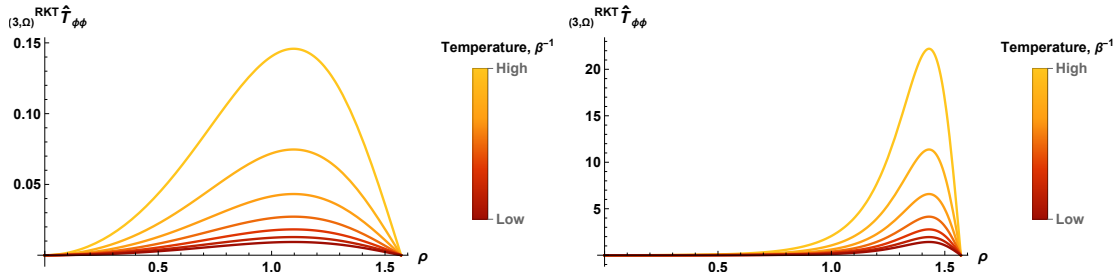


(a) $\Omega = 0.5$ (b) $\Omega = 0.96$

Figure 5.28: The $\phi\phi$-component of the RKT-SET, plotted for two values of the angular speed, and with inverse temperature varied in the range $\beta \in [\pi/3, 5\pi/6]$. The inverse adS length scale is fixed at $a = 1$.

Here and henceforth, the difference between thermal and vacuum expectation values of the stress-energy tensor will be referred to as the QFT-RSET.

Note that this subsection will merely be a presentation of the results for self-completeness. Since the expressions for the various renormalised stress-energy tensors are rather long, they will not be reproduced here; instead, the contractions with the basis one-forms will be written out explicitly, with the stress-energy tensor components kept implicit. The comparisons between the RKT and QFT results, and analyses of these, can be found in section 5.3.4.

#### 5.3.3.1 Static fields in four dimensions

To find the QFT-RSET for static fields in four-dimensional anti-de Sitter space in the frame, we first need to take the thermal expectation value (5.1.23) and subtract the vacuum expectation value (5.1.25). We can then use the one-forms (4.4.28) for the vierbein (4.4.27) to contract, with respect to the adS metric (4.1.8), the difference in thermal and vacuum expectation values. This will yield the QFT-RSET for static fields in four-dimensional

anti-de Sitter space in the orthonormal frame. This is

$$ {}^{\mathrm{QFT}}_{(4,\not{\Omega})}\widehat{T}^{(a)(b)} = w^{(a)}_{\mu} w^{(b)}_{\nu} \, {}^{\mathrm{QFT}}_{(4,\not{\Omega})}\widehat{T}^{\mu\nu}, \tag{5.3.41} $$

where we have defined the difference in thermal and vacuum expectation values, i.e. the QFT-RSET, as

$$ {}^{\mathrm{QFT}}_{(4,\not{\Omega})}\widehat{T}_{\mu\nu} = {}_{(4,\not{\Omega})}\langle \widehat{T}_{\mu\nu} \rangle_{\beta} - {}_{(4,\not{\Omega})}\langle \widehat{T}_{\mu\nu} \rangle_{0}. \tag{5.3.42} $$

Since the vierbein one-forms (4.4.28) form an orthonormal basis for a diagonal metric, the frame components of the QFT-RSET are just the mixed indices components of the renormalised stress-energy tensor. Explicitly,

$$ {}^{\mathrm{QFT}}_{(4,\not{\Omega})}\widehat{T}^{(\tau)(\tau)} = -{}^{\mathrm{QFT}}_{(4,\not{\Omega})}\widehat{T}_{\tau}{}^{\tau}, \tag{5.3.43} $$

$$ {}^{\mathrm{QFT}}_{(4,\not{\Omega})}\widehat{T}^{(\rho)(\rho)} = {}^{\mathrm{QFT}}_{(4,\not{\Omega})}\widehat{T}_{\rho}{}^{\rho}, \tag{5.3.44} $$

$$ {}^{\mathrm{QFT}}_{(4,\not{\Omega})}\widehat{T}^{(\theta)(\theta)} = {}^{\mathrm{QFT}}_{(4,\not{\Omega})}\widehat{T}_{\theta}{}^{\theta}, \tag{5.3.45} $$

$$ {}^{\mathrm{QFT}}_{(4,\not{\Omega})}\widehat{T}^{(\phi)(\phi)} = {}^{\mathrm{QFT}}_{(4,\not{\Omega})}\widehat{T}_{\phi}{}^{\phi}. \tag{5.3.46} $$

In section 5.1.1, figures were presented for the mixed indices components of the renormalised stress-energy tensor. Plots will therefore not be reproduced, since figures 5.1-5.4 already show these components.

#### 5.3.3.2 Rigidly-rotating fields in four dimensions

Since we have used state subtraction, the renormalised stress-energy tensor (5.1.42) is already the difference between thermal and vacuum states. In spite of this, to make notation consistent, we will redefine

$$ {}^{\mathrm{QFT}}_{(4,\Omega)}\widehat{T}_{\mu\nu} = {}_{(4,\Omega)}\langle \widehat{T}_{\mu\nu} \rangle_{\beta}, \tag{5.3.47} $$

as the QFT-RSET, since this is the difference between thermal and vacuum expectation values. Contracting with the one-forms (4.4.28), we have

$$ {}^{\mathrm{QFT}}_{(4,\Omega)}\widehat{T}^{(a)(b)} = \mathring{w}^{(a)}_{\mu} \mathring{w}^{(b)}_{\nu} \, {}^{\mathrm{QFT}}_{(4,\Omega)}\widehat{T}^{\mu\nu}. \tag{5.3.48} $$

The nonzero components of the QFT-RSET are given by the following expressions:

$$
\begin{aligned}
{}^{\mathrm{QFT}}_{(4,\Omega)}\widehat{T}^{(\tau)(\tau)} &= \mathring{w}^{(\tau)}_{\mu}\mathring{w}^{(\tau)}_{\nu}\,{}^{\mathrm{QFT}}_{(4,\Omega)}\widehat{T}^{\mu\nu} \\
&= \mathring{w}^{(\tau)}_{\tau}\mathring{w}^{(\tau)}_{\tau}\,{}^{\mathrm{QFT}}_{(4,\Omega)}\widehat{T}^{\tau\tau} + 2\mathring{w}^{(\tau)}_{\tau}\mathring{w}^{(\tau)}_{\phi}\,{}^{\mathrm{QFT}}_{(4,\Omega)}\widehat{T}^{\tau\phi} + \mathring{w}^{(\tau)}_{\phi}\mathring{w}^{(\tau)}_{\phi}\,{}^{\mathrm{QFT}}_{(4,\Omega)}\widehat{T}^{\phi\phi} \\
&= a^{-2}\sec^2(\rho)\left[\Gamma^{-2}_{(4)}\,{}^{\mathrm{QFT}}_{(4,\Omega)}\widehat{T}^{\tau\tau} - 2\Omega\sin^2(\theta)\sin^2(\rho)\,{}^{\mathrm{QFT}}_{(4,\Omega)}\widehat{T}^{\tau\phi}\right. \\
&\qquad \left. + \Gamma^{2}_{(4)}\sin^4(\theta)\sin^4(\rho)\,{}^{\mathrm{QFT}}_{(4,\Omega)}\widehat{T}^{\phi\phi}\right], \qquad (5.3.49)
\end{aligned}
$$

$$
\begin{aligned}
{}^{\mathrm{QFT}}_{(4,\Omega)}\widehat{T}^{(\tau)(\phi)} &= \mathring{w}^{(\tau)}_{\mu}\mathring{w}^{(\phi)}_{\nu}\,{}^{\mathrm{QFT}}_{(4,\Omega)}\widehat{T}^{\mu\nu} \\
&= \mathring{w}^{(\tau)}_{\tau}\mathring{w}^{(\phi)}_{\phi}\,{}^{\mathrm{QFT}}_{(4,\Omega)}\widehat{T}^{\tau\phi} + \mathring{w}^{(\tau)}_{\phi}\mathring{w}^{(\phi)}_{\phi}\,{}^{\mathrm{QFT}}_{(4,\Omega)}\widehat{T}^{\phi\phi} \\
&= a^{-2}\sin(\theta)\sec(\rho)\tan(\rho)\left[{}^{\mathrm{QFT}}_{(4,\Omega)}\widehat{T}^{\tau\phi} - \Omega\Gamma^{2}_{(4)}\sin^2(\theta)\sin^2(\rho)\,{}^{\mathrm{QFT}}_{(4,\Omega)}\widehat{T}^{\phi\phi}\right], \qquad (5.3.50)
\end{aligned}
$$

$$
\begin{aligned}
{}^{\mathrm{QFT}}_{(4,\Omega)}\widehat{T}^{(\rho)(\rho)} &= \mathring{w}^{(\rho)}_{\mu}\mathring{w}^{(\rho)}_{\nu}\,{}^{\mathrm{QFT}}_{(4,\Omega)}\widehat{T}^{\mu\nu} \\
&= \mathring{w}^{(\rho)}_{\rho}\mathring{w}^{(\rho)}_{\rho}\,{}^{\mathrm{QFT}}_{(4,\Omega)}\widehat{T}^{\rho\rho} \\
&= a^{-2}\sec^2(\rho)\,{}^{\mathrm{QFT}}_{(4,\Omega)}\widehat{T}^{\rho\rho}, \qquad (5.3.51)
\end{aligned}
$$

$$
\begin{aligned}
{}^{\mathrm{QFT}}_{(4,\Omega)}\widehat{T}^{(\rho)(\theta)} &= \mathring{w}^{(\rho)}_{\mu}\mathring{w}^{(\theta)}_{\nu}\,{}^{\mathrm{QFT}}_{(4,\Omega)}\widehat{T}^{\mu\nu} \\
&= \mathring{w}^{(\rho)}_{\rho}\mathring{w}^{(\theta)}_{\theta}\,{}^{\mathrm{QFT}}_{(4,\Omega)}\widehat{T}^{\rho\theta} \\
&= a^{-2}\sec(\rho)\tan(\rho)\,{}^{\mathrm{QFT}}_{(4,\Omega)}\widehat{T}^{\rho\theta}, \qquad (5.3.52)
\end{aligned}
$$

$$
\begin{aligned}
{}^{\mathrm{QFT}}_{(4,\Omega)}\widehat{T}^{(\theta)(\theta)} &= \mathring{w}^{(\theta)}_{\mu}\mathring{w}^{(\theta)}_{\nu}\,{}^{\mathrm{QFT}}_{(4,\Omega)}\widehat{T}^{\mu\nu} \\
&= \mathring{w}^{(\theta)}_{\theta}\mathring{w}^{(\theta)}_{\theta}\,{}^{\mathrm{QFT}}_{(4,\Omega)}\widehat{T}^{\theta\theta} \\
&= a^{-2}\tan^2(\rho)\,{}^{\mathrm{QFT}}_{(4,\Omega)}\widehat{T}^{\theta\theta}, \qquad (5.3.53)
\end{aligned}
$$

$$
\begin{aligned}
{}^{\mathrm{QFT}}_{(4,\Omega)}\widehat{T}^{(\phi)(\phi)} &= \mathring{w}^{(\phi)}_{\mu}\mathring{w}^{(\phi)}_{\nu}\,{}^{\mathrm{QFT}}_{(4,\Omega)}\widehat{T}^{\mu\nu} \\
&= \mathring{w}^{(\phi)}_{\phi}\mathring{w}^{(\phi)}_{\phi}\,{}^{\mathrm{QFT}}_{(4,\Omega)}\widehat{T}^{\phi\phi} \\
&= a^{-2}\Gamma^{2}_{(4)}\sin^2(\theta)\tan^2(\rho)\,{}^{\mathrm{QFT}}_{(4,\Omega)}\widehat{T}^{\phi\phi}. \qquad (5.3.54)
\end{aligned}
$$

#### 5.3.3.3 Static fields in three dimensions

In a similar fashion to the rigidly-rotating, four-dimensional result above, we redefine the thermal expectation value (5.2.15) to be the QFT-RSET, given by

$$ {}^{\mathrm{QFT}}_{(3,\not{\Omega})}\widehat{T}_{\mu\nu} = {}_{(3,\not{\Omega})}\langle \widehat{T}_{\mu\nu}\rangle_{\beta}, \tag{5.3.55} $$

so that, after contracting with the one-forms (4.4.15), the QFT-RSET (5.2.15) in frame components is

$$ {}^{\mathrm{QFT}}_{(3,\not{\Omega})}\widehat{T}^{(a)(b)} = \mathfrak{w}^{(a)}_{\mu}\mathfrak{w}^{(b)}_{\nu}\,{}^{\mathrm{QFT}}_{(3,\not{\Omega})}\widehat{T}^{\mu\nu}. \tag{5.3.56} $$

In a similar fashion to the nonrotating four-dimensional case, since the dreibein forms an orthonormal basis for a diagonal metric, converting the QFT-RSET (5.3.55) to frame components simply corresponds to lowering one index using the space-time metric (4.1.7). The QFT-RSET components in the frame are therefore just the mixed indices space-time coordinate components:

$$ {}^{\mathrm{QFT}}_{(3,\not{\Omega})}\widehat{T}^{(\tau)(\tau)} = -{}^{\mathrm{QFT}}_{(3,\not{\Omega})}\widehat{T}_{\tau}{}^{\tau}, \tag{5.3.57} $$

$$ {}^{\mathrm{QFT}}_{(3,\not{\Omega})}\widehat{T}^{(\rho)(\rho)} = {}^{\mathrm{QFT}}_{(3,\not{\Omega})}\widehat{T}_{\rho}{}^{\rho}, \tag{5.3.58} $$

$$ {}^{\mathrm{QFT}}_{(3,\not{\Omega})}\widehat{T}^{(\phi)(\phi)} = {}^{\mathrm{QFT}}_{(3,\not{\Omega})}\widehat{T}_{\phi}{}^{\phi}. \tag{5.3.59} $$

#### 5.3.3.4 Rigidly-rotating fields in three dimensions

Finally, for rigidly-rotating fields in three-dimensional anti-de Sitter space-time, the difference in thermal and vacuum expectation values of the stress-energy tensor, i.e. the QFT-RSET, for consistency is redefined as

$$ {}^{\mathrm{QFT}}_{(3,\Omega)}\widehat{T}_{\mu\nu} = {}_{(3,\Omega)}\langle \widehat{T}_{\mu\nu}\rangle_{\beta}. \tag{5.3.60} $$

Contracting with the dreibein one-forms (4.4.30), the QFT-RSET (5.2.35) in frame components is

$$ {}^{\mathrm{QFT}}_{(3,\Omega)}\widehat{T}^{(a)(b)} = \mathring{\mathfrak{w}}^{(a)}_{\mu}\mathring{\mathfrak{w}}^{(b)}_{\nu}\,{}^{\mathrm{QFT}}_{(3,\Omega)}\widehat{T}^{\mu\nu}. \tag{5.3.61} $$

The nonzero components of the QFT-RSET in the frame are given by

$$\begin{aligned}
{}^{\mathrm{QFT}}_{(3,\Omega)}\widehat{T}^{(\tau)(\tau)} &= \mathring{\mathfrak{w}}^{(\tau)}_{\mu}\mathring{\mathfrak{w}}^{(\tau)}_{\nu}\,{}^{\mathrm{QFT}}_{(3,\Omega)}\widehat{T}^{\mu\nu} \\
&= \mathring{\mathfrak{w}}^{(\tau)}_{\tau}\mathring{\mathfrak{w}}^{(\tau)}_{\tau}\,{}^{\mathrm{QFT}}_{(3,\Omega)}\widehat{T}^{\tau\tau} + 2\mathring{\mathfrak{w}}^{(\tau)}_{\tau}\mathring{\mathfrak{w}}^{(\tau)}_{\phi}\,{}^{\mathrm{QFT}}_{(3,\Omega)}\widehat{T}^{\tau\phi} + \mathring{\mathfrak{w}}^{(\tau)}_{\phi}\mathring{\mathfrak{w}}^{(\tau)}_{\phi}\,{}^{\mathrm{QFT}}_{(3,\Omega)}\widehat{T}^{\phi\phi} \\
&= a^{-2}\sec^2(\rho)\left[\Gamma^{-2}_{(3)}\,{}^{\mathrm{QFT}}_{(3,\Omega)}\widehat{T}^{\tau\tau} - 2\Omega\sin^2(\rho)\,{}^{\mathrm{QFT}}_{(3,\Omega)}\widehat{T}^{\tau\phi} + \Omega^2\Gamma^2_{(3)}\sin^4(\rho)\,{}^{\mathrm{QFT}}_{(3,\Omega)}\widehat{T}^{\phi\phi}\right],
\end{aligned} \tag{5.3.62}$$

$$\begin{aligned}
{}^{\mathrm{QFT}}_{(3,\Omega)}\widehat{T}^{(\tau)(\phi)} &= \mathring{\mathfrak{w}}^{(\tau)}_{\mu}\mathring{\mathfrak{w}}^{(\phi)}_{\nu}\,{}^{\mathrm{QFT}}_{(3,\Omega)}\widehat{T}^{\mu\nu} \\
&= \mathring{\mathfrak{w}}^{(\tau)}_{\tau}\mathring{\mathfrak{w}}^{(\phi)}_{\phi}\,{}^{\mathrm{QFT}}_{(3,\Omega)}\widehat{T}^{\tau\phi} + \mathring{\mathfrak{w}}^{(\tau)}_{\phi}\mathring{\mathfrak{w}}^{(\phi)}_{\phi}\,{}^{\mathrm{QFT}}_{(3,\Omega)}\widehat{T}^{\phi\phi} \\
&= a^{-2}\sec(\rho)\tan(\rho)\left[{}^{\mathrm{QFT}}_{(3,\Omega)}\widehat{T}^{\tau\phi} - \Omega\Gamma^2_{(3)}\sin^2(\rho)\,{}^{\mathrm{QFT}}_{(3,\Omega)}\widehat{T}^{\phi\phi}\right],
\end{aligned} \tag{5.3.63}$$

$$\begin{aligned}
{}^{\mathrm{QFT}}_{(3,\Omega)}\widehat{T}^{(\rho)(\rho)} &= \mathring{\mathfrak{w}}^{(\rho)}_{\mu}\mathring{\mathfrak{w}}^{(\rho)}_{\nu}\,{}^{\mathrm{QFT}}_{(3,\Omega)}\widehat{T}^{\mu\nu} \\
&= \mathring{\mathfrak{w}}^{(\rho)}_{\rho}\mathring{\mathfrak{w}}^{(\rho)}_{\rho}\,{}^{\mathrm{QFT}}_{(3,\Omega)}\widehat{T}^{\rho\rho} \\
&= a^{-2}\sec^2(\rho)\,{}^{\mathrm{QFT}}_{(3,\Omega)}\widehat{T}^{\rho\rho},
\end{aligned} \tag{5.3.64}$$

$$\begin{aligned}
{}^{\mathrm{QFT}}_{(3,\Omega)}\widehat{T}^{(\phi)(\phi)} &= \mathring{\mathfrak{w}}^{(\phi)}_{\mu}\mathring{\mathfrak{w}}^{(\phi)}_{\nu}\,{}^{\mathrm{QFT}}_{(3,\Omega)}\widehat{T}^{\mu\nu} \\
&= \mathring{\mathfrak{w}}^{(\phi)}_{\phi}\mathring{\mathfrak{w}}^{(\phi)}_{\phi}\,{}^{\mathrm{QFT}}_{(3,\Omega)}\widehat{T}^{\phi\phi} \\
&= a^{-2}\Gamma^2_{(3)}\tan^2(\rho)\,{}^{\mathrm{QFT}}_{(3,\Omega)}\widehat{T}^{\phi\phi}.
\end{aligned} \tag{5.3.65}$$

### 5.3.4 Stress-energy tensor comparisons between RKT and QFT

In this subsection, the QFT-RSETs (5.1.23,5.1.42,5.2.15,5.2.35) will be compared with the RKT-SETs (5.3.12,5.3.22,5.3.31,5.3.40). Since we want to ascertain whether RKT is a good approximation to QFT for modelling quantum matter in space-time, we need to assess how well the physical properties of the two theories match. Moreover, we want to quantify quantum effects by assessing deviations from the classical RKT model. The best way to do this is to employ the thermometer frame decomposition from section 2.3. This allows us to extract physical quantities from both theories, such as the energy density and isotropic pressure. Recall that the thermometer frame decomposition for a massless particle in a rigidly-rotating thermal state is given in equation (2.3.3). Inverting this decomposition (the

details of which are contained within section 2.3), we can extract the following quantities [19, 36, 363]:

$$E = u_{(a)}u_{(b)}\widehat{T}^{(a)(b)}, \tag{5.3.66}$$

$$P = \frac{1}{n-1}\Delta^{(a)(b)}\widehat{T}^{(a)(b)}, \tag{5.3.67}$$

$$W^{(a)} = -\Delta^{(a)(b)}u^{(c)}\widehat{T}_{(b)(c)}, \tag{5.3.68}$$

$$\Pi^{(a)(b)} = \left[\Delta^{(a)(c)}\Delta^{(b)(d)} - \frac{1}{n-1}\Delta^{(a)(b)}\Delta^{(c)(d)}\right]\widehat{T}_{(c)(d)}, \tag{5.3.69}$$

where $u^{(\bullet)}$ is the fluid velocity and

$$\Delta^{(a)(b)} = u^{(a)}u^{(b)} + \eta^{(a)(b)}, \tag{5.3.70}$$

is a projector on the hypersurface orthogonal to the fluid velocity. The energy density is represented by $E$, the isotropic pressure is $P$, the heat flux is $W^{(\bullet)}$ while $\Pi^{(\bullet)(\bullet)}$ denotes the anisotropic pressure, sometimes also referred to as the pressure deviator [13, 266]. Since we are considering massless particles, we also have the relation $E = (n-1)P$. As discussed in section 2.3, both the heat flux and anisotropic pressure vanish identically in RKT. Thus we may quantify quantum effects by considering the nonzero components of the heat flux and anisotropic pressure. In both three- and four-dimensions, the only nonzero component of the heat flux is in the $\phi$ direction. This quantity is always negative, indicating that the heat flux is opposite to the direction of the rotation in the rigidly rotating frame. Meanwhile, the only nonzero components of the anisotropic pressure in three-dimensions are the $\rho\rho$- and $\phi\phi$-components, satisfying

$$\Pi^{(\rho)(\rho)} + \Pi^{(\phi)(\phi)} = 0. \tag{5.3.71}$$

For four-dimensional space-times, there are four nonzero components of the anisotropic pressure: $\Pi^{(\rho)(\rho)}$, $\Pi^{(\rho)(\theta)}$, $\Pi^{(\theta)(\theta)}$ and $\Pi^{(\phi)(\phi)}$, additionally satisfying

$$\Delta_{(a)(b)}\Pi^{(a)(b)} = \Pi^{(\rho)(\rho)} + \Pi^{(\theta)(\theta)} + \Pi^{(\phi)(\phi)} = 0. \tag{5.3.72}$$

This simply comes from the fact that, by definition, the anisotropic pressure is traceless.

In the below subsections, we have split the cases of three- and four-dimensional anti-de Sitter space-times, and we will consider both in turn. Since the nonrotating stress-energy tensors can be obtained by setting the angular speed $\Omega$ to zero in the corresponding rotating stress-energy tensors, no distinction will be made between the rotating and nonrotating cases. For the vast majority of the figures in the subsections below, they will be for the three values of $\Omega = 0, 0.5, 0.96$ unless specified otherwise. In both the three- and four-dimensional cases, the pressure and energy density are related by an integer multiple. Hence, they both share exactly the same qualitative features. To that end, the pressure will not be considered or shown in the following subsections. This means there are three physical quantities of interest: the energy density, heat flux and anisotropic pressure.

#### 5.3.4.1 Four-dimensional anti-de Sitter space-time

In four-dimensional anti-de Sitter space-time and, by extension, in the vierbein frame, we have dependence on two coordinates; the radial coordinate $\rho$ and the polar angular coordinate $\theta$. To help distinguish between temperature, angular speed, boundary condition and coordinate dependence the proceeding plots will either be on the equatorial plane $\theta = \pi/2$ or for varying $\theta$. Each quantity will be considered in turn, starting with its behaviour on the equatorial plane before considering the case where $\theta$ is no longer fixed.

Figures 5.29-5.33 show the energy density for a selection of angular speeds and inverse temperatures, while figure 5.34 shows the energy density for varied $\theta$ when Dirichlet boundary conditions are applied. Figure 5.35 shows the difference in energy densities of the RKT-SET and QFT-RSETs, for all three boundary conditions considered. Figures 5.36-5.39 show the (negative) heat flux on the equatorial plane and figures 5.40-5.41 show the heat flux for varying $\theta$. Lastly figures 5.42-5.45, 5.47-5.50 and 5.53 show the anisotropic pressure components on the equatorial plane, and figures 5.46, 5.51, 5.52, 5.54, 5.55, 5.56 and 5.57

show the various nonzero anisotropic pressure components for varied $\theta$. In four-dimensional anti-de Sitter space-time, the anisotropic pressure has four nonzero components: $\Pi^{(\rho)(\rho)}$, $\Pi^{(\theta)(\theta)}$, $\Pi^{(\phi)(\phi)}$ and $\Pi^{(\rho)(\theta)}$. Since the anisotropic pressure is traceless, one of the repeated indices components can be expressed as a sum of the other two. To that end, for the equatorial plane plots, only $\Pi^{(\rho)(\rho)}$ and $\Pi^{(\phi)(\phi)}$ are shown. Additionally, the $\rho\theta$-component of the anisotropic pressure is antisymmetric under the mapping $\theta \to \pi - \theta$ and is zero on the equatorial plane, so will only be shown as a surface.

Below, we will describe each figure in detail and point out any interesting features of note, starting with the energy density, then the heat flux and finally the anisotropic pressure.

**Energy density**

Figure 5.29 shows the energy density on the equatorial plane. The solid lines represent the QFT-RSETs, whilst the dashed lines are the corresponding RKT-SETs. The left-hand-side plots show the SETs at lower temperatures, whilst the right-hand-side plots show the SETs at higher temperatures. What is clear is that, regardless of angular speed, the best agreement between QFT and RKT comes at the higher temperatures. This is actually a theme that is repeated throughout all of the different quantities, regardless of boundary conditions applied to the field or angular rotation speed chosen. This is a consequence of the fact that at lower temperatures, quantum effects become more significant and at higher temperatures there are more particles, and thus the quantum matter begins to resemble a classical gas of energetic particles, or in other words, an RKT [178]. As the angular speed is increased, the quantum matter starts to become more evenly distributed across the space-time. The energy density always has a maximum at the origin, a value independent of the angular speed, and monotonically decays toward zero at the boundary; this happens for all values of the inverse temperature $\beta$ and angular speed $\Omega$ chosen. The rate of decay decreases for increasing angular speed. This also occurs regardless of the boundary conditions applied to the field; we see the same phenomenon for Neumann (figure 5.30)

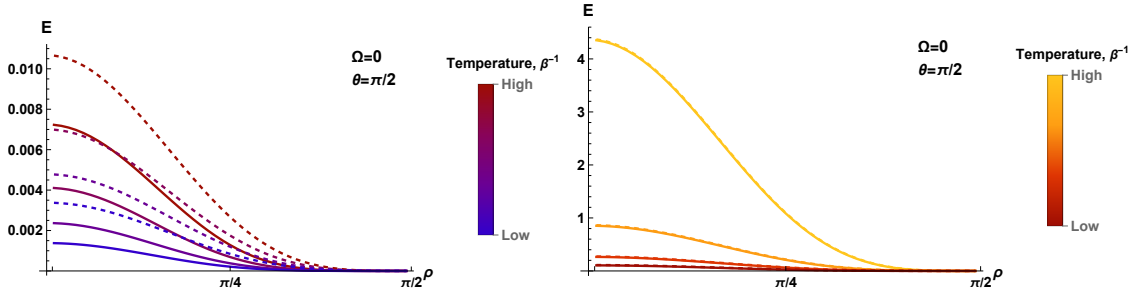


(a) $\Omega = 0$

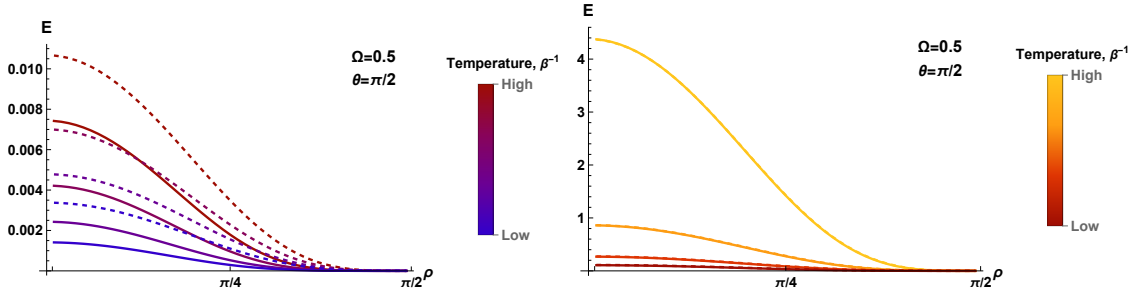


(b) $\Omega = 0.5$

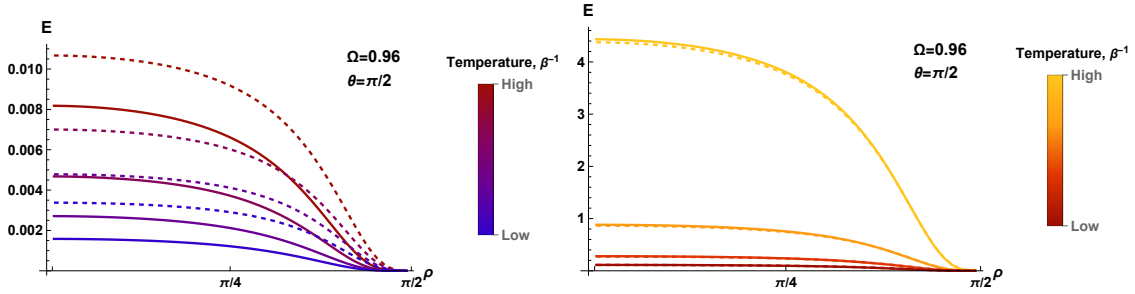


(c) $\Omega = 0.96$

Figure 5.29: Energy density of the QFT-RSET (solid) and RKT-SET (dashed) on the equatorial plane $\theta = \pi/2$. The angular speed is varied, whilst the inverse temperature is in the range $\beta \in [\pi/6, 5\pi/12] \cup [3\pi/4, \pi]$ for the right and left plots respectively. The inverse adS length scale is fixed at $a = 1$, whilst Dirichlet boundary conditions are applied to the field.

and transparent (figure 5.31) boundary conditions. For lower temperatures at all angular speeds considered, the QFT-RSET arising from the field with Dirichlet boundary conditions applied is consistently and considerably lower than its RKT counterpart. In contrast, for the case of Neumann boundary conditions, the QFT-RSET produces an energy density somewhat larger than the result from RKT. This suggests that if we force the field to decay to zero at the boundary, the system has, on average, less energy. On the other hand, if we allow the field to take some nonzero value at the boundary, and a zero flux across, the system has more energy. Figure 5.31 shows the energy density when the field is allowed to freely move through the boundary. We see that in this case, even at lower temperatures, the QFT-RSETs and RKT-SETs agree quite well. At high temperatures, they are virtually indistinguishable at the scales considered. As the angular speed is increased, the RKT-SET goes from being a slight overestimate to a slightly more considerable underestimate.

Figure 5.32 shows the energy density for two fixed inverse temperatures, with solid lines representing the RKT energy density and dashed lines the QFT-RSET energy density. The large dashed line corresponds to Dirichlet boundary conditions, whilst the medium dashed line is for Neumann boundary conditions and the small dashed line for transparent boundary conditions. Figure 5.33 shows the absolute difference in energy densities between the QFT and RKT SETs, for the same choices of angular speed and fixed inverse temperature. We see that for lower temperatures, at any angular speed, transparent boundary conditions represent the best approximation to the RKT energy density. In contrast, at higher temperatures, as the angular speed is increased, the best approximation to the RKT energy density goes from transparent at lower speeds to Dirichlet at higher speeds. This is particularly apparent in figure 5.33 where, for $\Omega = 0$, the curve representing transparent boundary conditions is at least one order of magnitude smaller than the curves representing either Dirichlet and Neumann boundary conditions. Meanwhile, for angular speed $\Omega = 0.96$, figure 5.33 shows that Dirichlet boundary conditions represent the best approximation to the RKT energy density, given that the absolute difference between the

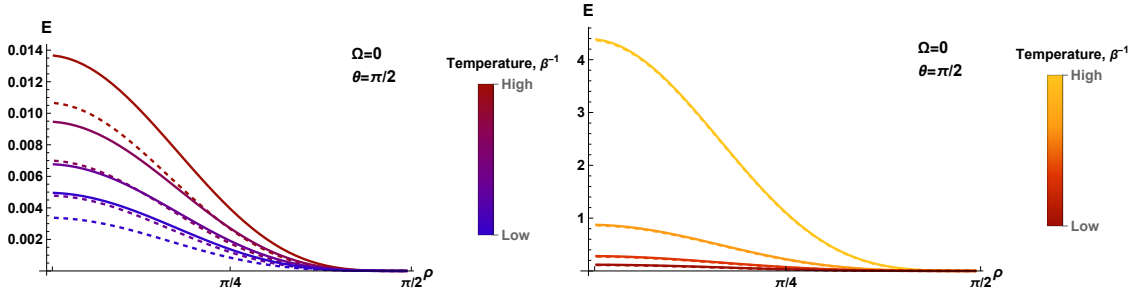


(a) $\Omega = 0$

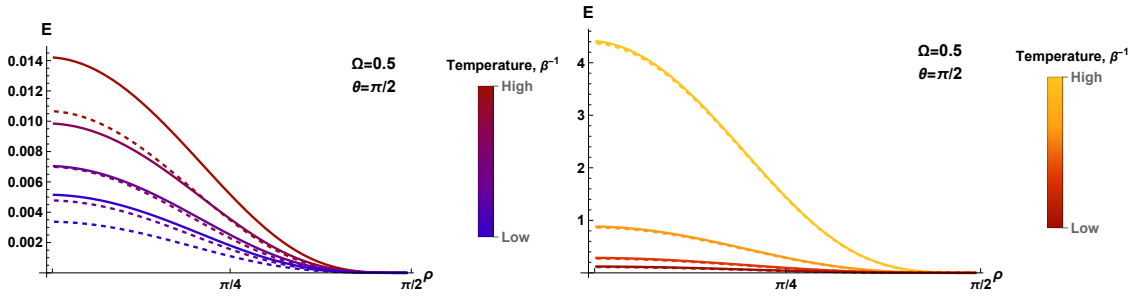


(b) $\Omega = 0.5$

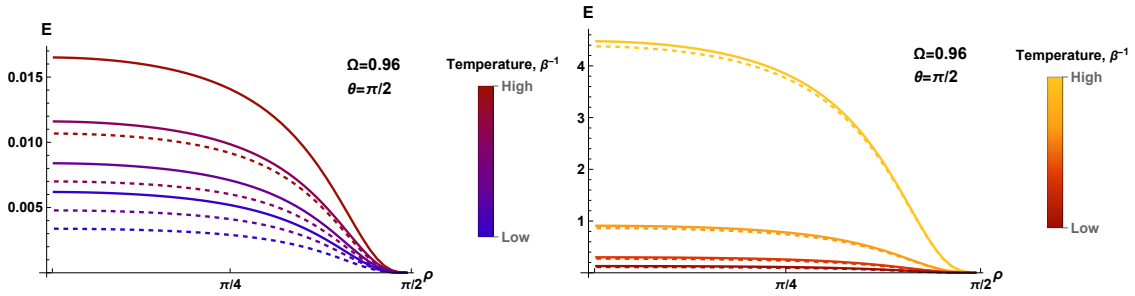


(c) $\Omega = 0.96$

Figure 5.30: Energy density of the QFT-RSET (solid) and RKT-SET (dashed) on the equatorial plane $\theta = \pi/2$. The angular speed is varied, whilst the inverse temperature is in the range $\beta \in [\pi/6, 5\pi/12] \cup [3\pi/4, \pi]$ for the right and left plots respectively. The inverse adS length scale is fixed at $a = 1$, whilst Neumann boundary conditions are applied to the field.

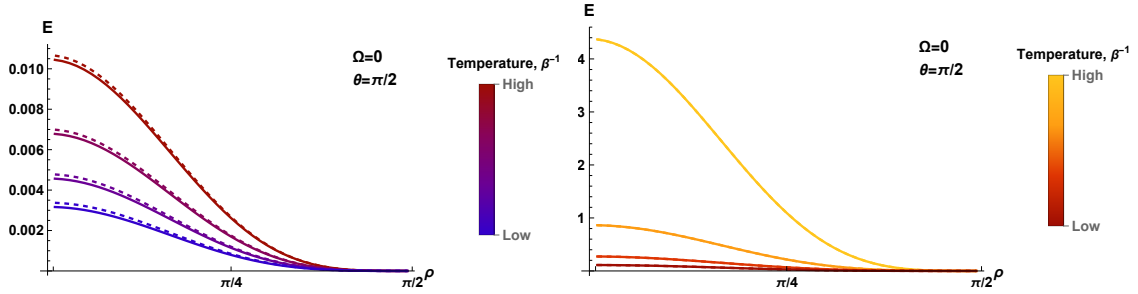


(a) $\Omega = 0$

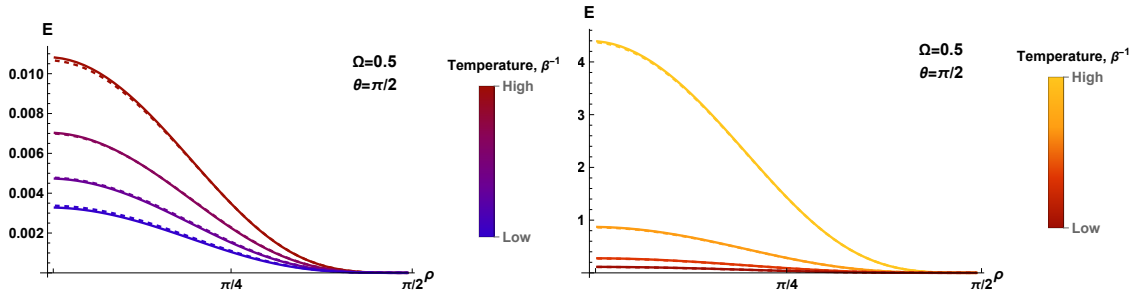


(b) $\Omega = 0.5$

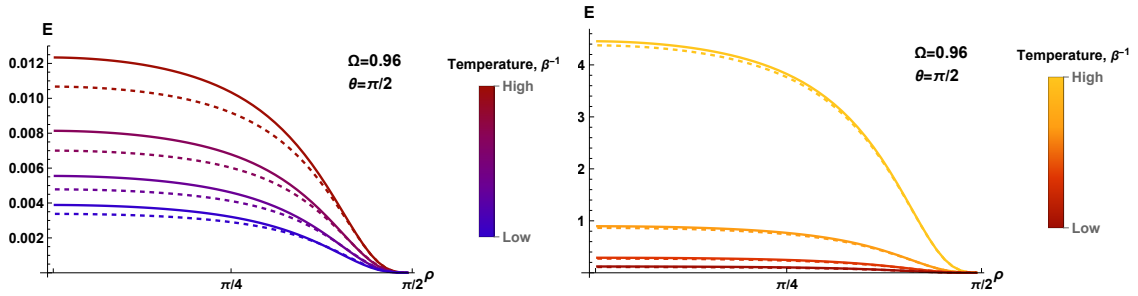


(c) $\Omega = 0.96$

Figure 5.31: Energy density of the QFT-RSET (solid) and RKT-SET (dashed) on the equatorial plane $\theta = \pi/2$. The angular speed is varied, whilst the inverse temperature is in the range $\beta \in [\pi/6, 5\pi/12] \cup [3\pi/4, \pi]$ for the right and left plots respectively. The inverse adS length scale $a = 1$ is fixed, whilst transparent boundary conditions are applied to the field.

RKT and QFT energy densities is lowest. One interesting point is that this is not true across the entire space-time; rather, close to the boundary the absolute difference in energy densities is lowest for transparent boundary conditions. This change is also noticeable in the $\Omega = 0.5$ case. Close to the origin, the absolute difference in energy densities is lowest when Dirichlet boundary conditions are applied, but at around $\rho = \pi/8$ this switches so that the absolute difference is lowest for the case of transparent boundary conditions. In all cases considered, the absolute difference in energy densities between QFT and RKT is approximately the same for both Dirichlet and Neumann boundary conditions close to the boundary $\rho = \pi/2$, with the closest agreement occurring for lower angular speeds.

When we do not restrict to the equatorial plane, the energy density has the same qualitative features regardless of the boundary conditions applied to the field. To that end, the surface plots shown in figure 5.34 are only for the case of Dirichlet boundary conditions. In figure 5.34, we observe that for zero angular speed, the energy density is actually independent of $\theta$. As the angular speed is increased, a hump around the equatorial plane starts to emerge, and, for high angular speeds, this emergent hump is largest. It is worth pointing out that this emergent hump does not change the maximum of the energy density; this is always at the origin $\rho = 0$. The energy density is always zero on the boundary $\rho = \pi/2$.

To understand the effect on the energy density (across the whole range of $\theta$) of changing the boundary conditions, we consider figure 5.35. The energy density of the RKT-SET looks qualitatively the same; instead of plotting the RKT-SET energy density, figure 5.35 shows the difference between the QFT-RSETs and RKT-SET, for all three choices of boundary conditions. In particular, the top row shows the difference in energy densities between the QFT-RSET with Dirichlet boundary conditions applied, and the RKT-SET. The middle row shows the same but with Neumann boundary conditions, and the bottom row with transparent boundary conditions. For all angular speeds considered, Neumann and transparent boundary conditions provide an overestimate in the energy density compared to RKT, whilst for lower angular speeds, Dirichlet boundary conditions provide an under-

estimate. However, at higher angular speeds, Dirichlet boundary conditions provide an overestimate (except for a small hump on the equatorial plane) in the energy density when compared to the RKT, albeit one that is roughly an order of magnitude less than the case of zero angular speed. For vanishing angular speed, we observe that QFT-RSET arising from transparent boundary conditions gives the closest approximation to the RKT-SET, but at high angular speeds the QFT-RSET corresponding to Dirichlet boundary conditions is actually the best approximation to the RKT-SET. For an angular speed of $\Omega = 0.5$, the difference in energy densities between the QFT-RSETs and RKT-SET is the same order of magnitude for both Dirichlet and transparent boundary conditions. At all angular speeds considered, Neumann boundary conditions provide the worst approximation to the RKT-SET.

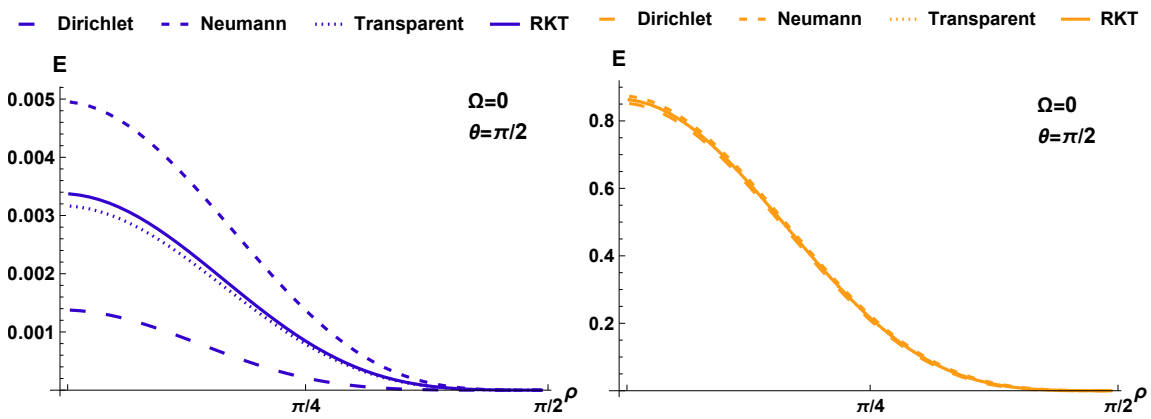


(a) $\Omega = 0$

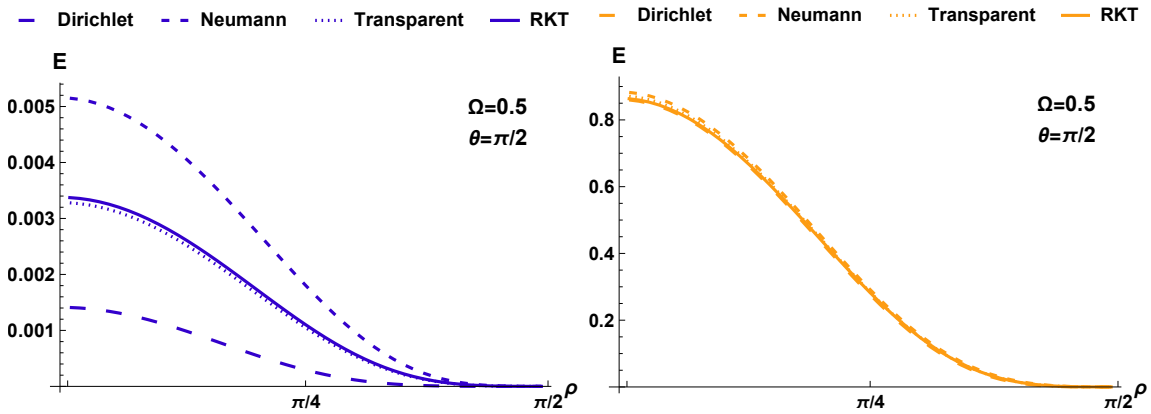


(b) $\Omega = 0.5$

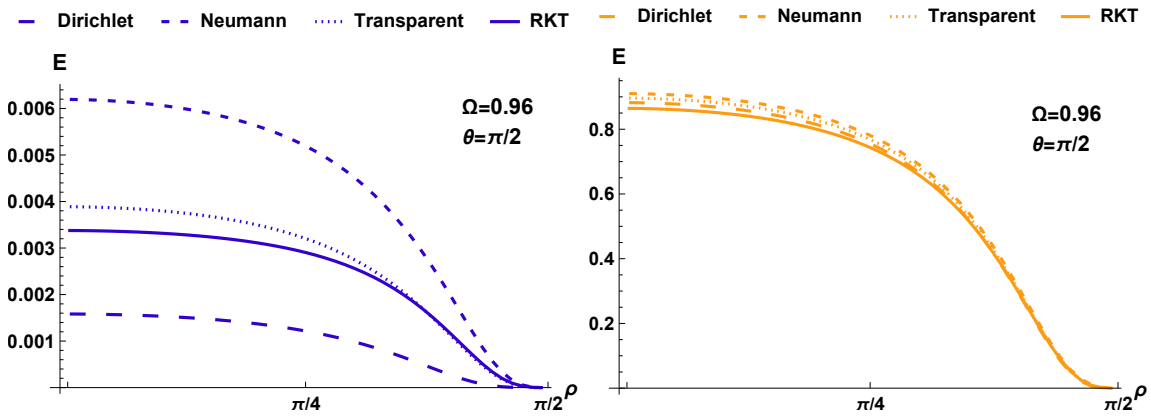


(c) $\Omega = 0.96$

Figure 5.32: Energy density of the QFT-RSET and RKT-SET on the equatorial plane. The angular speed is varied, whilst the inverse temperature is fixed at either $\beta = \pi$ (left) or $\beta = \pi/4$ (right). The inverse adS length scale $a = 1$ is fixed, and the boundary conditions are varied.

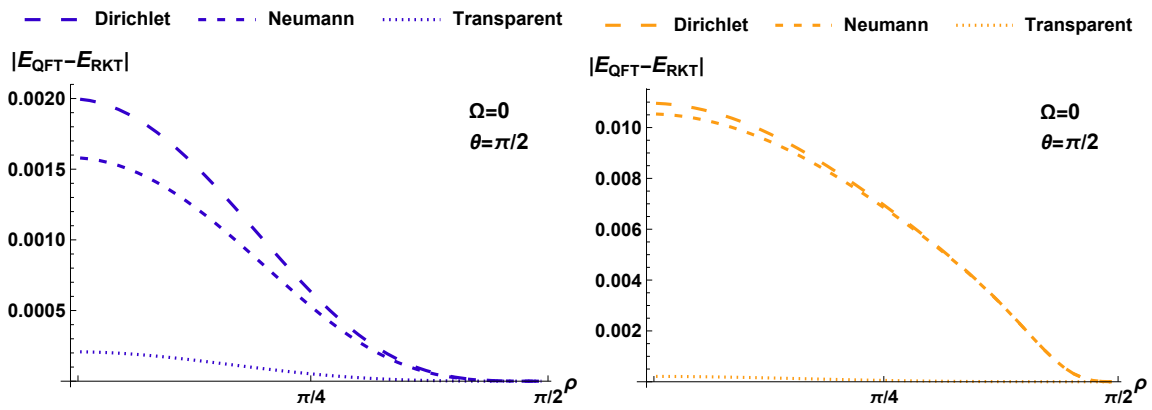


(a) $\Omega = 0$

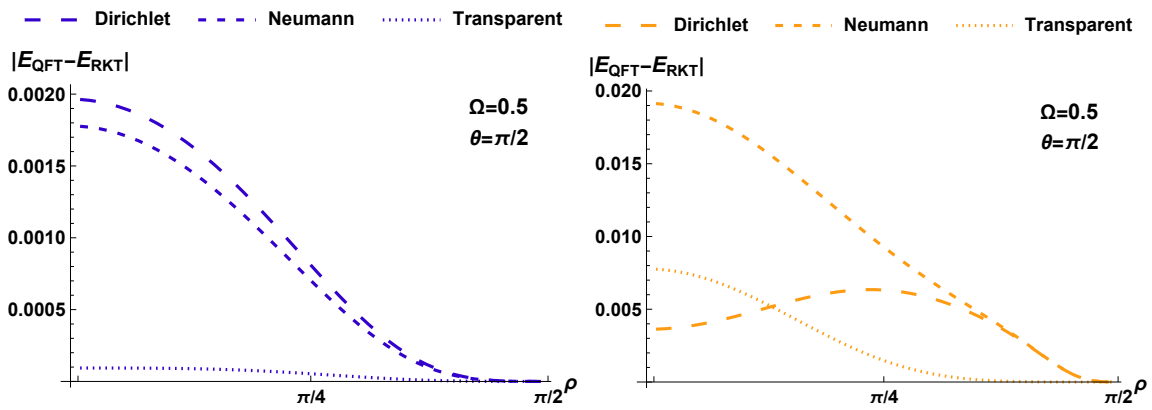


(b) $\Omega = 0.5$

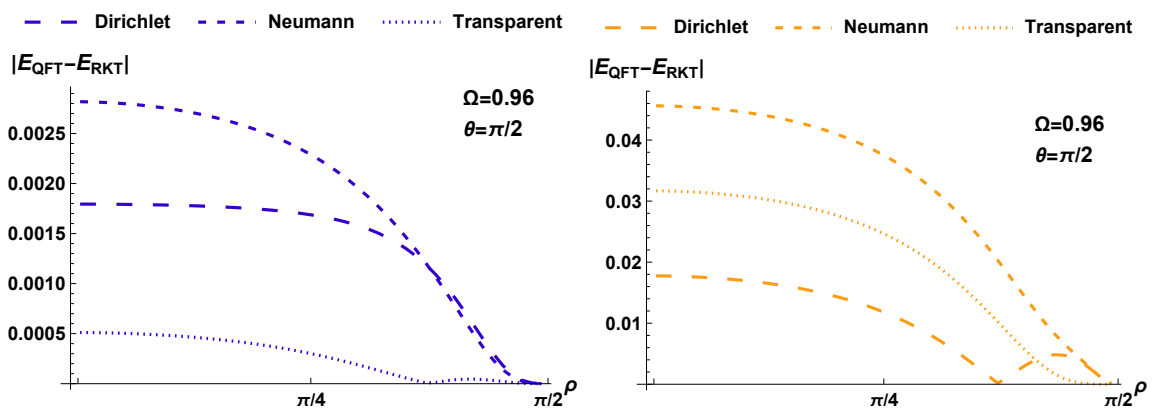


(c) $\Omega = 0.96$

Figure 5.33: The difference in energy densities between the QFT-RSETs and RKT-SET on the equatorial plane. The angular speed is varied, whilst the inverse temperature is fixed at either $\beta = \pi$ (left) or $\beta = \pi/4$ (right). The inverse adS length scale $a = 1$ is fixed, and the boundary conditions are varied.

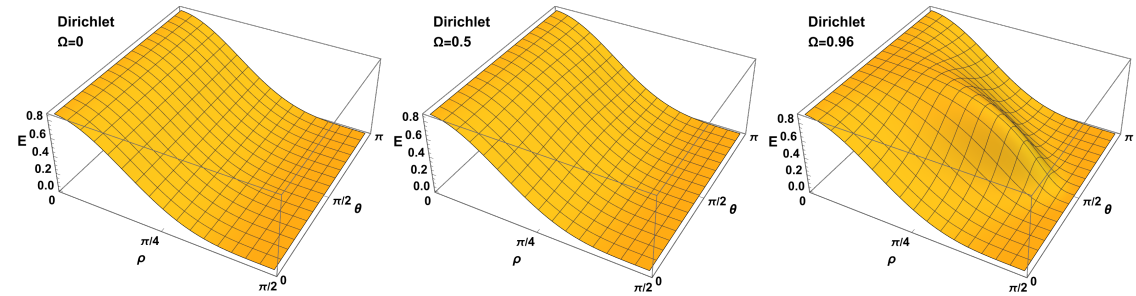


Figure 5.34: Surface plot of the energy density of the QFT-RSET. The inverse temperature is held fixed at $\beta = \pi/4$ as is the inverse adS length scale $a = 1$. The angular speed is varied, while Dirichlet boundary conditions are applied to the field.

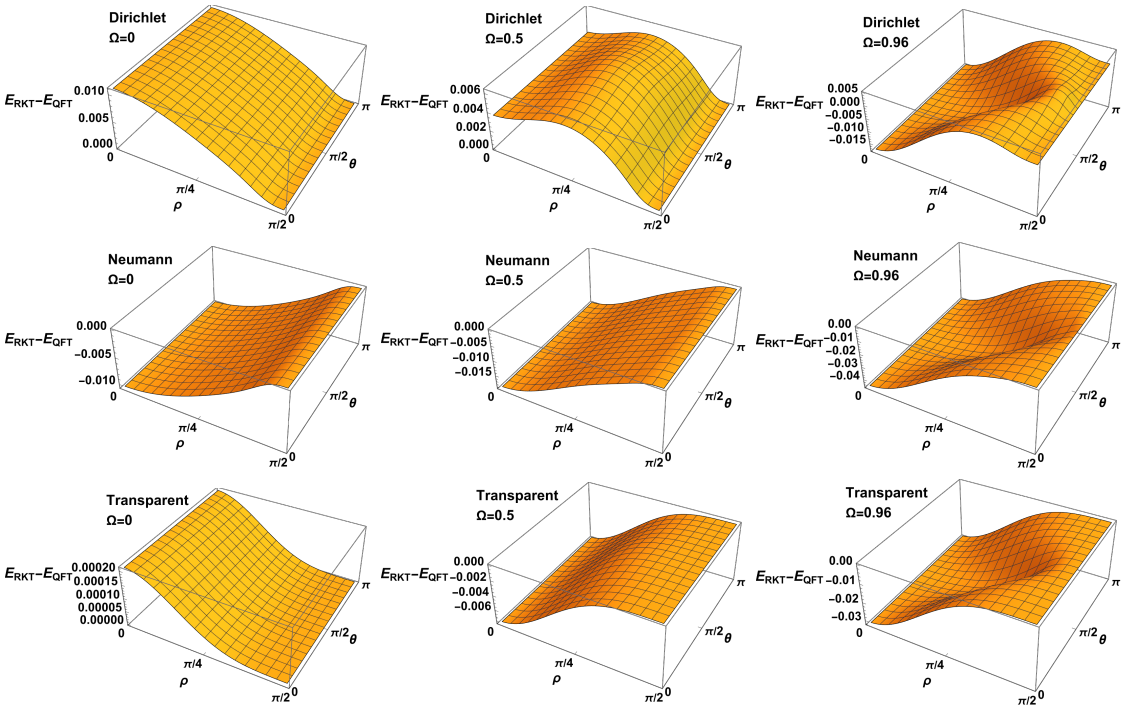


Figure 5.35: Surface plot of the difference in energy densities of the QFT-RSET and RKT-SET. The inverse temperature is held fixed at $\beta = \pi/4$ as is the inverse adS length scale $a = 1$. The angular speed and boundary conditions varied.

**Heat flux**

The next quantity to consider is the heat flux. Since it is always negative, minus the heat flux is shown instead. The heat flux vanishes identically for RKT, and is thus a measure of quantum deviations from the classical RKT. Figure 5.36 shows the heat flux when Dirichlet boundary conditions are applied to the field; figure 5.37 shows the heat flux for Neumann boundary conditions; and finally the heat flux for transparent boundary conditions is shown in figure 5.38. In all cases considered, we see that the heat flux is zero both at the origin and on the boundary, whilst attaining its maximum magnitude somewhere inbetween. As the angular speed is increased, this maximum starts to shift toward the boundary $\rho = \pi/2$. This maximum magnitude is at least one order of magnitude smaller than that of the energy density. For $\Omega = 0$, the heat flux vanishes identically, which suggests it is a rotational effect. In figures 5.36-5.38 the top line of plots instead show the heat flux at $\Omega = 0.02$. We see that whilst it keeps the same overall shape, the order of magnitude is very small, as is to be expected.

There is no real qualitative difference between the three boundary conditions, instead, they differ by a small numerical factor. Figure 5.39 illustrates this point well. It shows the heat flux at two fixed temperatures and the same selection of angular speeds. We see that, regardless of temperature or angular speed, the heat flux corresponding to Dirichlet boundary conditions is always the smallest. This means that it provides the closest approximation to the RKT-SET. More importantly, however, is that this suggests that Dirichlet boundary conditions exhibit the smallest quantum effects of the three boundary conditions, since it deviates least from the classical RKT model. Another feature is that at higher temperatures, regardless of angular speed, there is less fluctuation between the three boundary conditions, in so much as the heat fluxes are much closer in size than for the lower temperatures considered. For all values of the temperature and angular speed considered, the magnitude of the heat flux for Dirichlet boundary conditions was smallest, whilst Neumann boundary conditions produced the highest heat flux, with transparent boundary conditions

lying somewhere inbetween. This indicates that applying Neumann boundary conditions to the field produces more quantum effects (since the heat flux measures a quantum deviation from the classical model) than the other two boundary conditions considered.

Figure 5.40 shows the heat flux as a function of both $\rho$ and $\theta$. However, the heat flux is only shown for the case of Dirichlet boundary conditions; the cases of Neumann and transparent boundary conditions differ from Dirichlet boundary conditions by a small numerical factor. Mimicking the behaviour on the equatorial plane, the heat flux shown in figure 5.40 is zero at both $\rho = 0$ and $\rho = \pi$, attaining its absolute maximum on the equatorial plane, at a value of $\rho$ that increases as the angular speed increases. In figure 5.41, the difference in heat flux for Dirichlet and Neumann, and Dirichlet and transparent boundary conditions is shown. We see, from figure 5.41, that Dirichlet boundary conditions produce the absolute smallest heat flux, since the difference between the heat fluxes shown in the figure are all positive. The difference in heat fluxes between Dirichlet and Neumann boundary conditions is roughly double in magnitude the corresponding difference between Dirichlet and transparent boundary conditions, indicating that the heat flux corresponding to transparent boundary conditions is of a more comparable size with the heat flux for Dirichlet boundary conditions than the heat flux corresponding to Neumann boundary conditions.

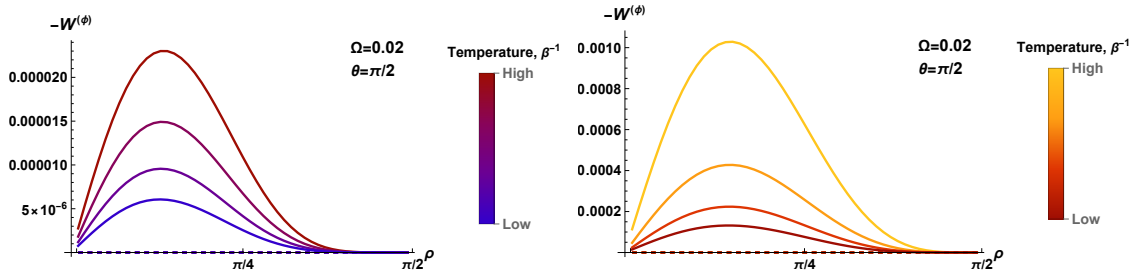


(a) $\Omega = 0.02$

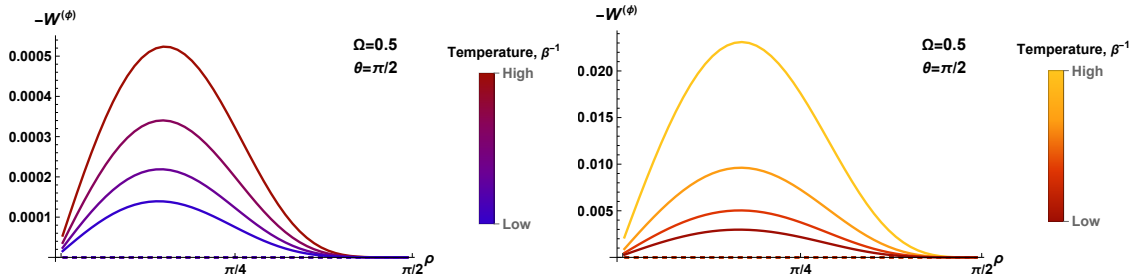


(b) $\Omega = 0.5$

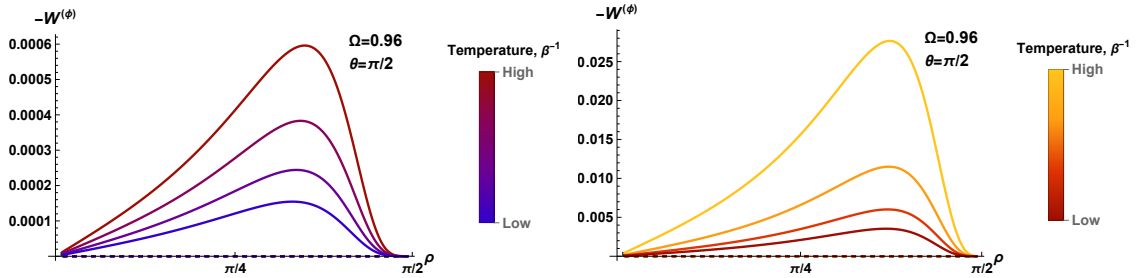


(c) $\Omega = 0.96$

Figure 5.36: Minus the heat flux on the equatorial plane $\theta = \pi/2$. The angular speed is varied, whilst the inverse temperature is in the range $\beta \in [\pi/6, 5\pi/12] \cup [3\pi/4, \pi]$ for the right and left plots respectively. The inverse adS length scale is fixed at $a = 1$, whilst Dirichlet boundary conditions are applied to the field. The solid lines correspond to the QFT-RSET, and the dashed lines correspond to the RKT-SET (which is identically zero).

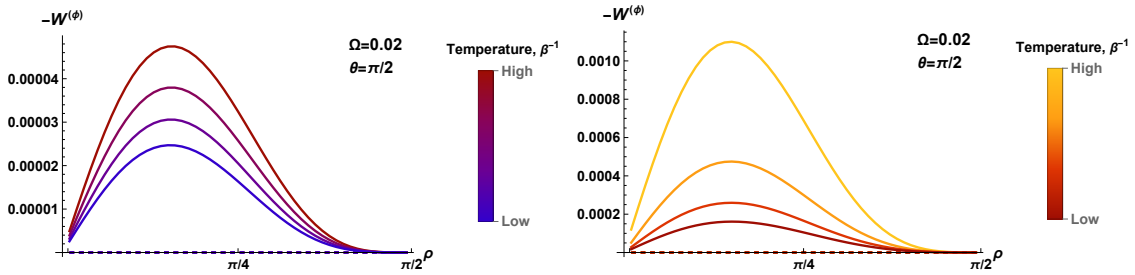


(a) $\Omega = 0.02$

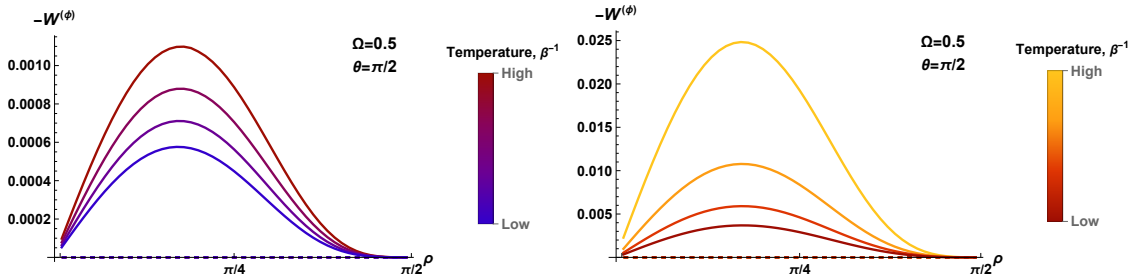


(b) $\Omega = 0.5$

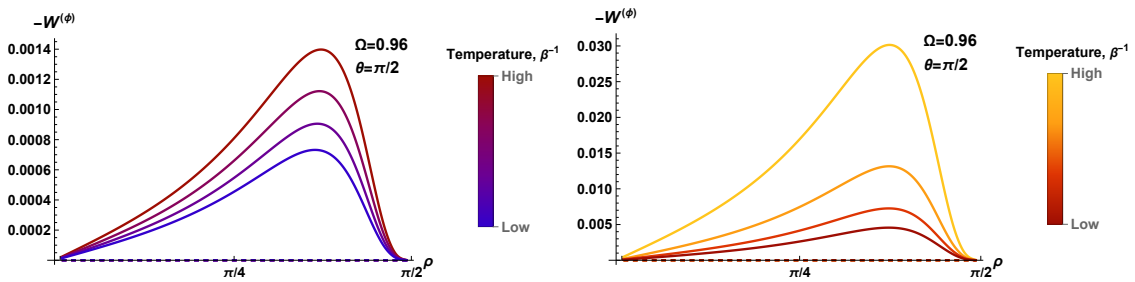


(c) $\Omega = 0.96$

Figure 5.37: Minus the heat flux on the equatorial plane $\theta = \pi/2$. The angular speed is varied, whilst the inverse temperature is in the range $\beta \in [\pi/6, 5\pi/12] \cup [3\pi/4, \pi]$ for the right and left plots respectively. The inverse adS length scale is fixed at $a = 1$, whilst Neumann boundary conditions are applied to the field. The solid lines correspond to the QFT-RSET, and the dashed lines correspond to the RKT-SET (which is identically zero).

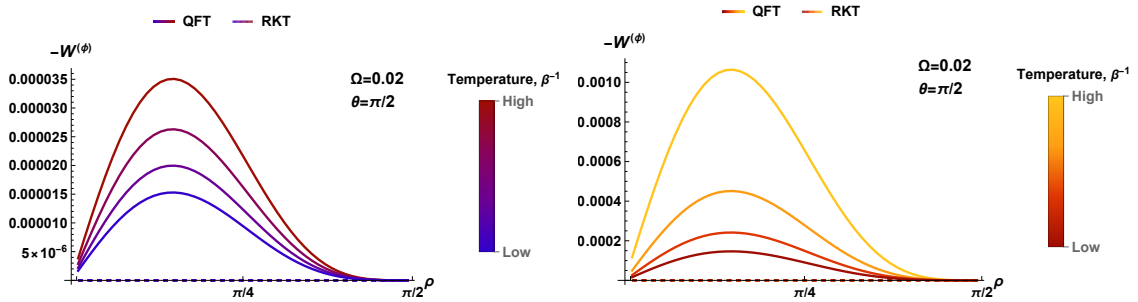


(a) $\Omega = 0.02$

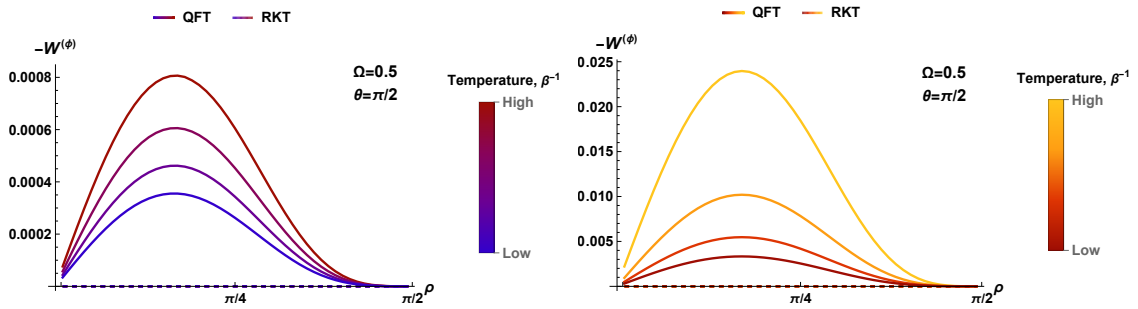


(b) $\Omega = 0.5$

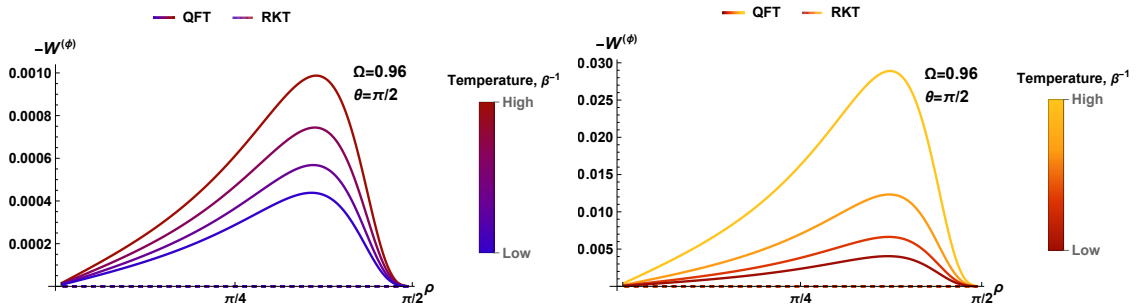


(c) $\Omega = 0.96$

Figure 5.38: Minus the heat flux on the equatorial plane $\theta = \pi/2$. The angular speed is varied, whilst the inverse temperature is in the range $\beta \in [\pi/6, 5\pi/12] \cup [3\pi/4, \pi]$ for the right and left plots respectively. The inverse adS length scale is fixed at $a = 1$, whilst transparent boundary conditions are applied to the field. The solid lines correspond to the QFT-RSET, and the dashed lines correspond to the RKT-SET (which is identically zero).

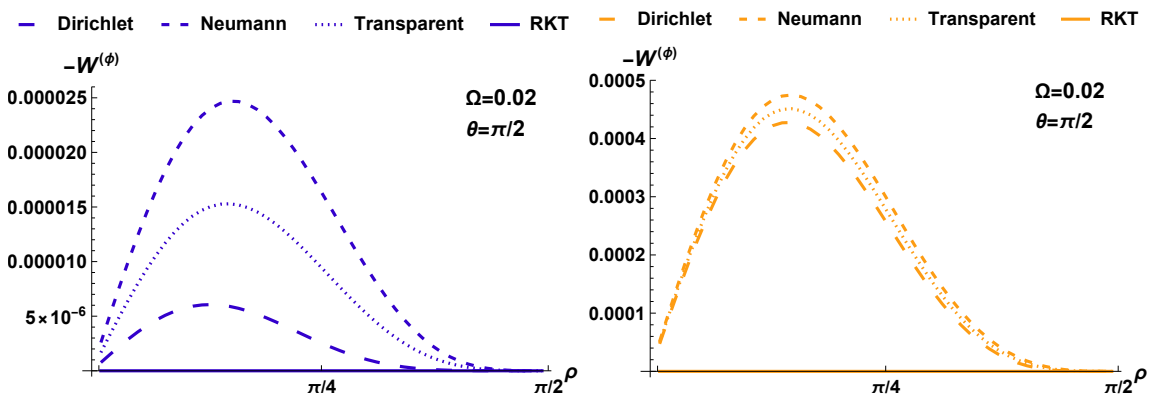


(a) $\Omega = 0.02$

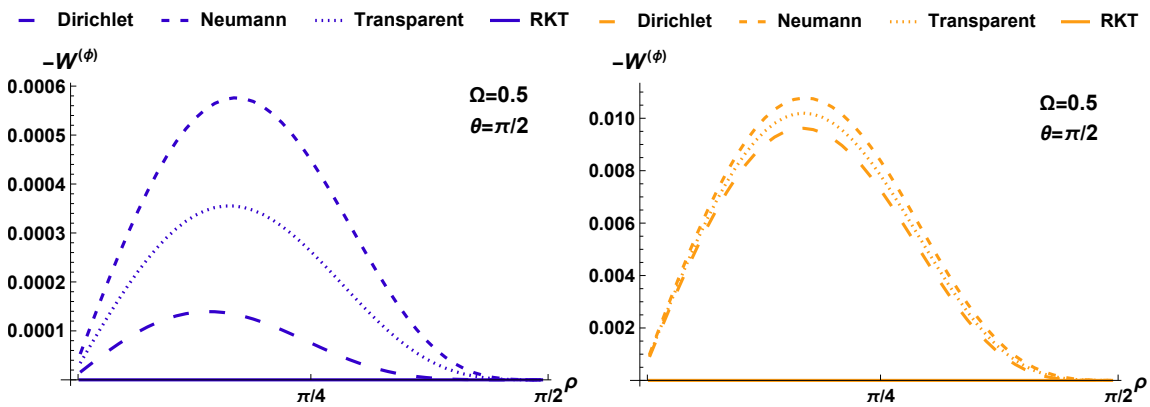


(b) $\Omega = 0.5$

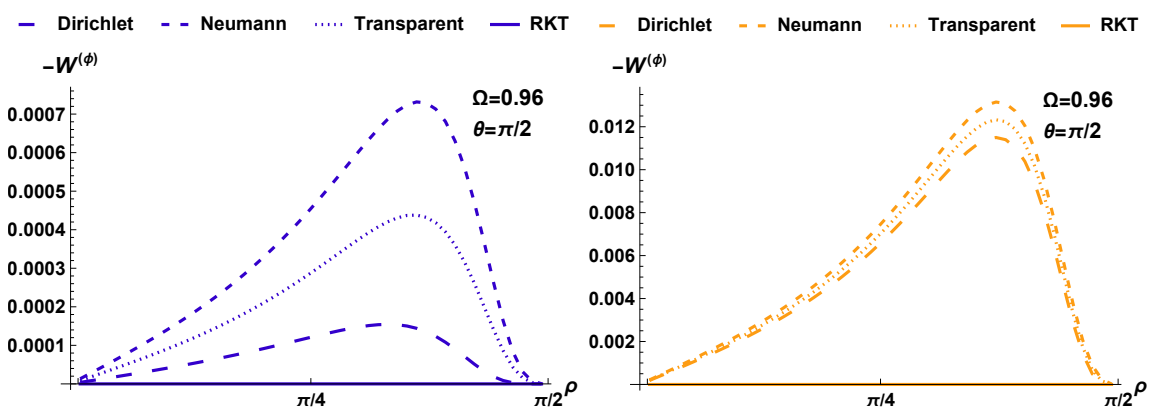


(c) $\Omega = 0.96$

Figure 5.39: Minus the heat flux plots on the equatorial plane. The angular speed is varied, whilst the inverse temperature is fixed at either $\beta = \pi$ (left) or $\beta = \pi/4$ (right). The inverse adS length scale $a = 1$ is fixed, and the boundary conditions are varied.

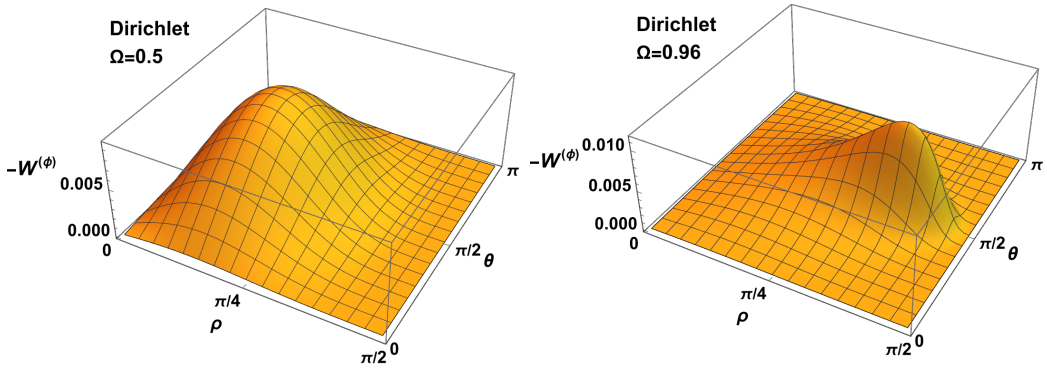


Figure 5.40: Surface plot of minus the heat flux. The inverse temperature is held fixed at $\beta = \pi/4$ as is the inverse adS length scale $a = 1$. The angular speed is varied and boundary conditions are Dirichlet.

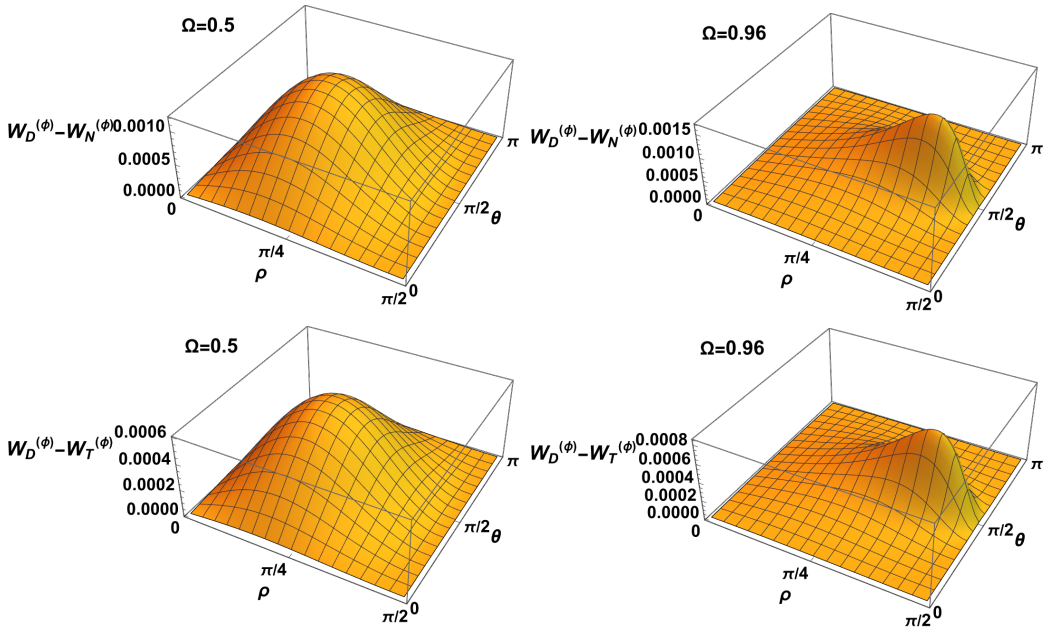


Figure 5.41: Difference in heat fluxes for the differing boundary conditions. The inverse temperature is held fixed at $\beta = \pi/4$ as is the inverse adS length scale $a = 1$, while the angular speed is varied.

### Anisotropic pressure

The final quantity to consider is the anisotropic pressure (and combinations of its components). We start with the component $\Pi^{(\rho)(\rho)}$, which is shown in figures 5.42-5.45. Figure 5.42 shows the $\rho\rho$-component of the anisotropic pressure with Dirichlet boundary conditions applied to the field; figure 5.43 for Neumann boundary conditions; transparent boundary conditions are shown in figure 5.44; and figure 5.45 shows the anisotropic pressure component $\Pi^{(\rho)(\rho)}$ at a fixed inverse temperature in order to compare the effect of changing the boundary conditions. For zero rotation, $\Pi^{(\rho)(\rho)}$ is identically zero for transparent boundary conditions, whilst $\Pi^{(\rho)(\rho)}$ for Dirichlet and Neumann boundary conditions are exactly the negative of each other - this no longer holds when rotation is included. For ease of comparison, therefore, we have shown $-\Pi^{(\rho)(\rho)}$ for the case of Neumann boundary conditions with angular speed $\Omega = 0$. In this case, we see that the anisotropic pressure component is zero at both the origin and space-time boundary, and takes its maximum away from both. For higher temperatures, this maximum is closer to the space-time boundary. As the angular speed is increased, we see some interesting effects. For all three boundary conditions, $\Pi^{(\rho)(\rho)}$ takes a nonzero value at the origin, corresponding to its global maximum; though, if $\Omega$ is sufficiently small, the global maximum will not be at the origin, otherwise there would be a continuity error somewhere between $\Omega = 0$ and $\Omega = 0.5$. It is still zero at the space-time boundary, however for the case of Neumann and transparent boundary conditions (at lower temperatures) the component drops below the axis and increases toward zero. This rate of increase is marginally faster for transparent boundary conditions than for Neumann boundary conditions. At higher temperatures, the anisotropic pressure component for the case of Neumann boundary conditions still drops below the axis, however for transparent boundary conditions it no longer does. At higher temperatures, the anisotropic pressure component $\Pi^{(\rho)(\rho)}$ begins to resemble the energy density in profile. Considering once more figure 5.45, we see another interesting effect. For all angular speeds considered, the anisotropic pressure components corresponding to the

three different boundary conditions all meet at two distinct points - one that is independent of the angular speed (the boundary $\rho = \pi/2$) and one that varies based on $\Omega$. For zero angular speed, this second point is at the origin $\rho = 0$ and, as the angular speed is increased, it starts to shift towards the boundary $\rho = \pi/2$. The temperature does not have any effect on the value of $\rho$ that these points occur; the temperature only affects the magnitude of the pressure deviator component of these points. Since there are no other points where only two of the boundary conditions meet (recall that for $\Omega = 0$, figure shows the absolute value of the component), one can postulate that these are two unique points in the space-time where there is no dependence on the boundary conditions. There is not anything necessarily physically significant about this; it is most likely a quirk of the functional dependence of the anisotropic pressure component.

Figure 5.46 shows the anisotropic pressure component $\Pi^{(\rho)(\rho)}$ in a grid, where the rows correspond to the differing boundary conditions and the columns refer to the varying angular speeds. As on the equatorial plane, for zero angular speed $\Pi^{(\rho)(\rho)}$ is identically zero for transparent boundary conditions, whilst $\Pi^{(\rho)(\rho)}$ for Dirichlet and Neumann boundary conditions are negatives of each other. As the angular speed is increased, for all three boundary conditions, a bump localised at $\rho = 0$ and around $\theta = \pi/2$ begins to form. For higher angular speeds, the bump is more defined, and at the highest angular speed considered, the global maximum of the component is the same for all three cases of boundary conditions. Regardless of boundary conditions, angular speed or temperature, $\Pi^{(\rho)(\rho)}$ is always zero on the boundary $\rho = \pi/2$.

The next anisotropic pressure component we shall consider is $\Pi^{(\phi)(\phi)}$. Figures 5.47, 5.48 and 5.49 show this component at various temperaures and angular speeds, for Dirichlet, Neumann and transparent boundary conditions respectively. Note that, for the case of Dirichlet boundary conditions and zero rotation, $-\Pi^{(\phi)(\phi)}$ is instead plotted, since it is everywhere negative. In a similar fashion to the component $\Pi^{(\rho)(\rho)}$, for zero rotation, $\Pi^{(\phi)(\phi)}$ when Dirichlet and Neumann boundary conditions are applied are exact negatives

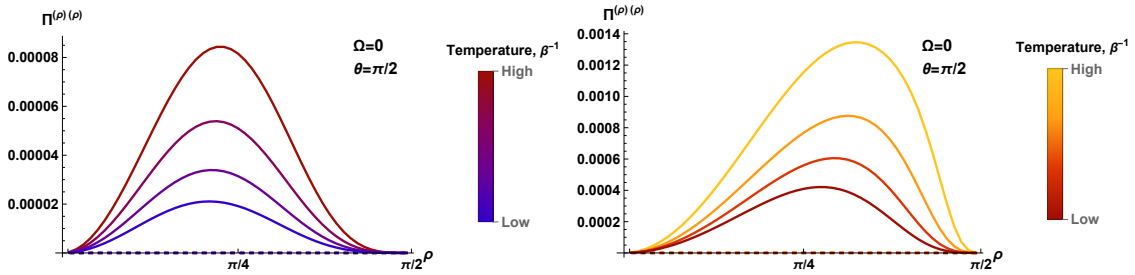


(a) $\Omega = 0$

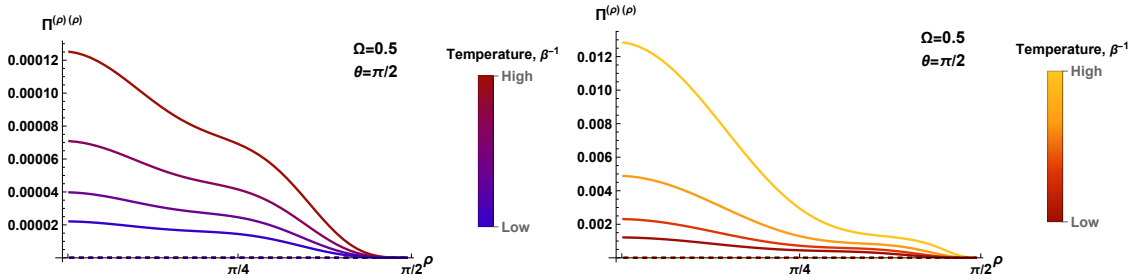


(b) $\Omega = 0.5$

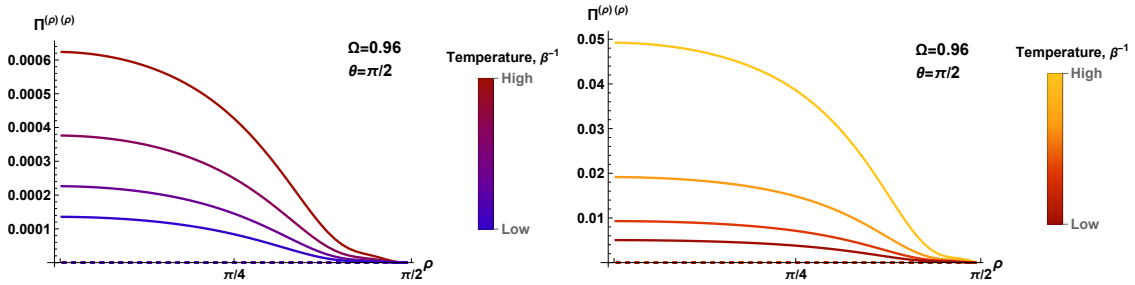


(c) $\Omega = 0.96$

Figure 5.42: The $\rho\rho$-component of the pressure deviator, plotted on the equatorial plane $\theta = \pi/2$. The angular speed is varied, whilst the inverse temperature is in the range $\beta \in [\pi/6, 5\pi/12] \cup [3\pi/4, \pi]$ for the right and left plots respectively. The inverse adS length scale is fixed at $a = 1$, whilst Dirichlet boundary conditions are applied to the field. The solid lines correspond to the QFT-RSET, and the dashed lines correspond to the RKT-SET (which is identically zero).

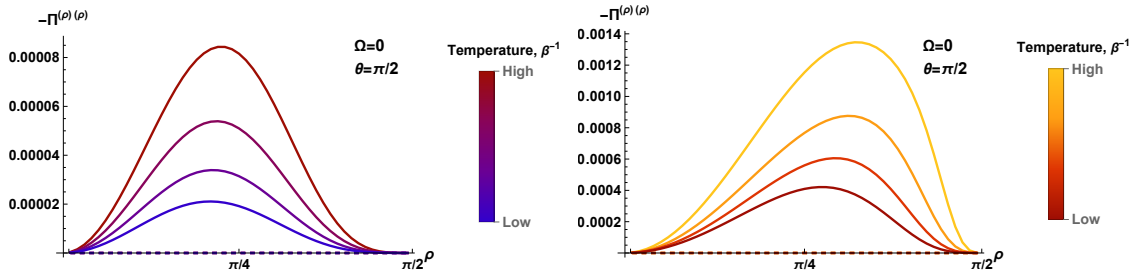


(a) $\Omega = 0$

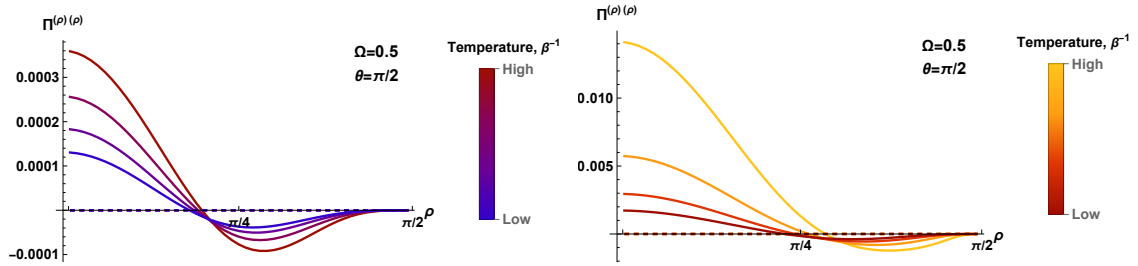


(b) $\Omega = 0.5$

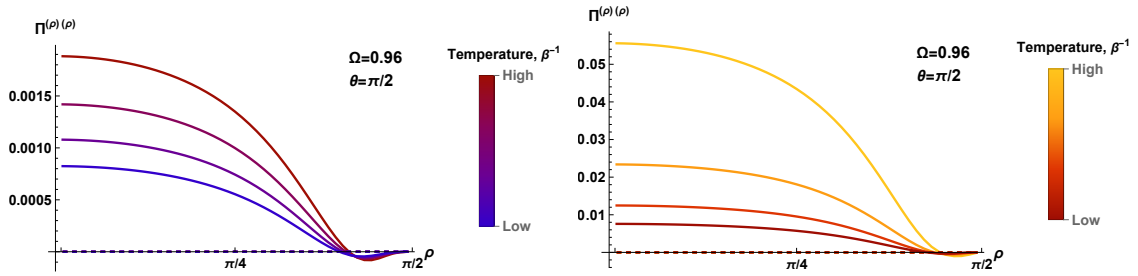


(c) $\Omega = 0.96$

Figure 5.43: Plots of the pressure deviator $\rho\rho$-component, on the equatorial plane $\theta = \pi/2$. The angular speed is varied, whilst the inverse temperature is in the range $\beta \in [\pi/6, 5\pi/12] \cup [3\pi/4, \pi]$ for the right and left plots respectively. The inverse adS length scale is fixed at $a = 1$, whilst Neumann boundary conditions are applied to the field. For the angular speed of $\Omega = 0$, minus the pressure deviator is instead plotted. The solid lines correspond to the QFT-RSET, and the dashed lines correspond to the RKT-SET (which is identically zero).

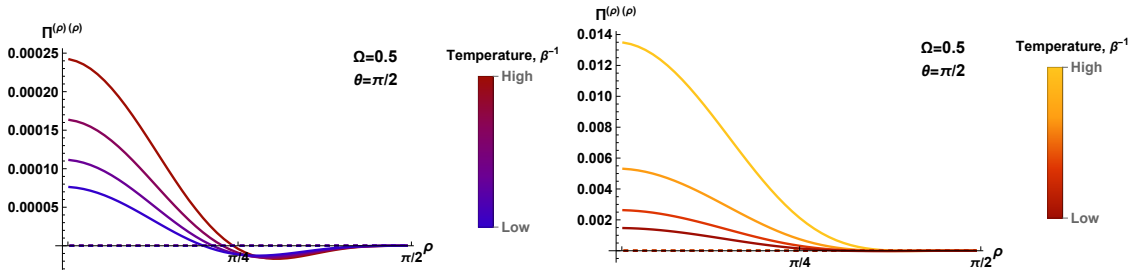


(a) $\Omega = 0.5$

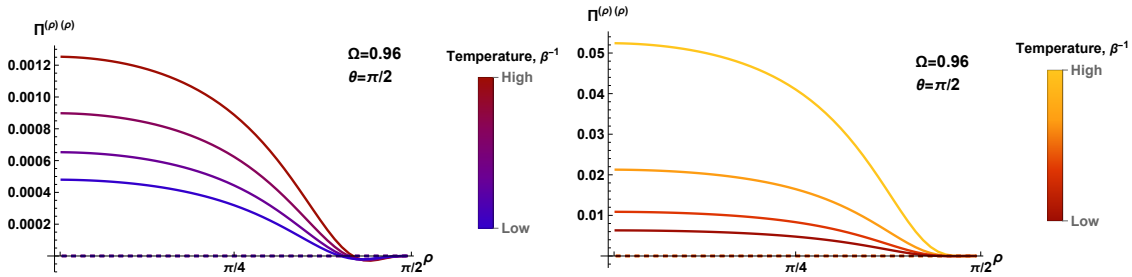


(b) $\Omega = 0.96$

Figure 5.44: The $\rho\rho$-component of the pressure deviator on the equatorial plane $\theta = \pi/2$. The angular speed is varied, whilst the inverse temperature is in the range $\beta \in [\pi/6, 5\pi/12] \cup [3\pi/4, \pi]$ for the right and left plots respectively. The inverse adS length scale is fixed at $a = 1$, whilst transparent boundary conditions are applied to the field. The pressure deviator is identically zero for an angular speed of $\Omega = 0$, hence its exclusion in this figure. The solid lines correspond to the QFT-RSET, and the dashed lines correspond to the RKT-SET (which is identically zero).

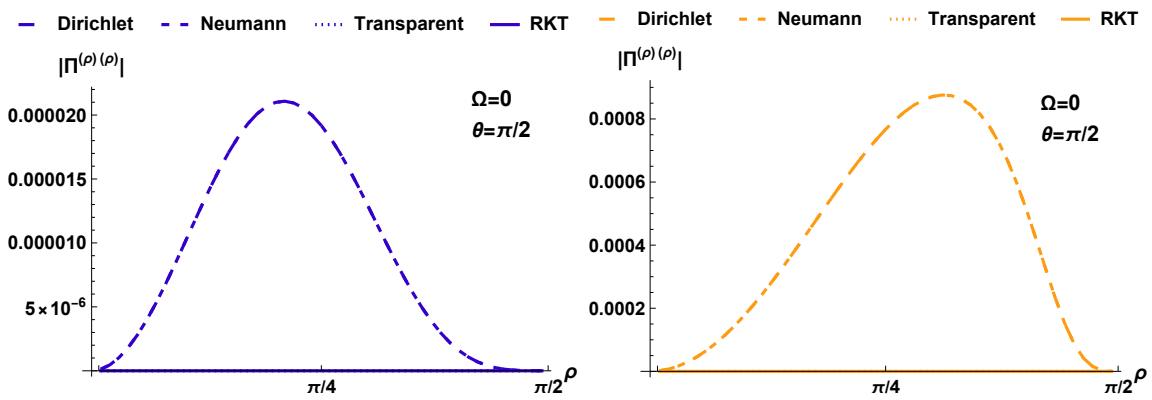


(a) $\Omega = 0$

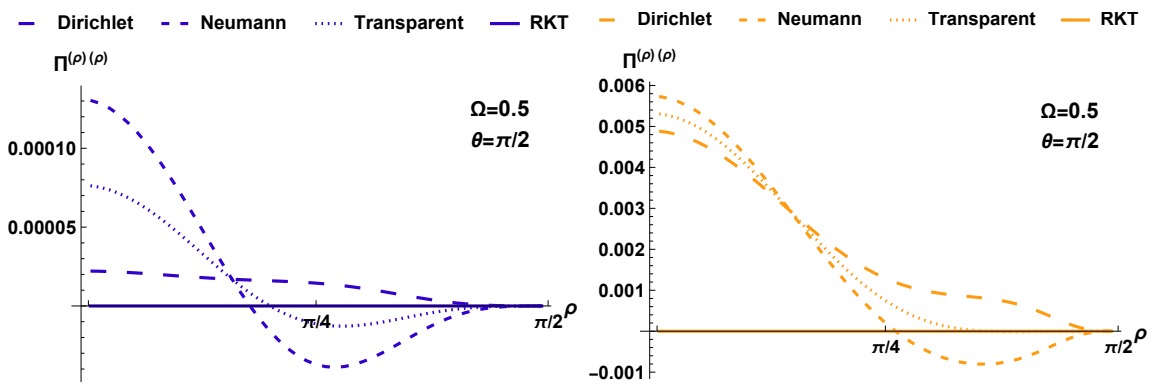


(b) $\Omega = 0.5$

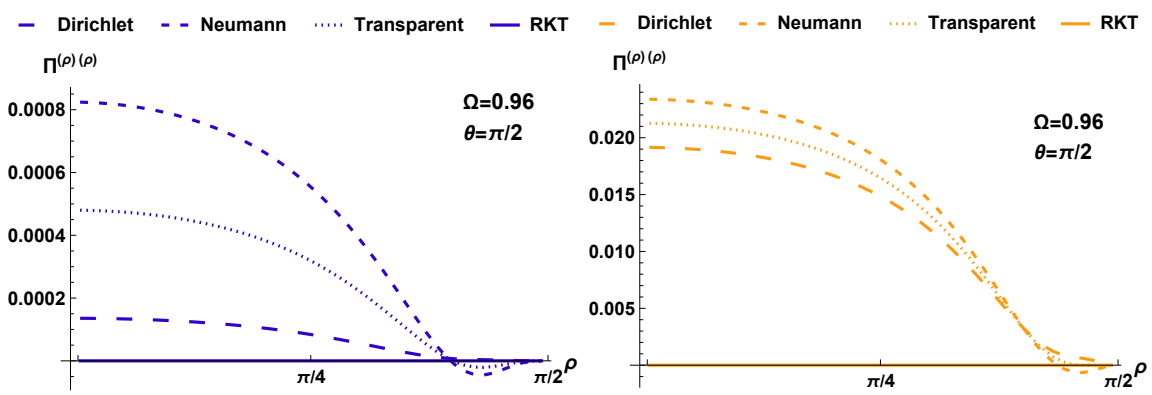


(c) $\Omega = 0.96$

Figure 5.45: Pressure deviator $\rho\rho$-component plots on the equatorial plane. The angular speed is varied, whilst the inverse temperature is fixed at either $\beta = \pi$ (left) or $\beta = \pi/4$ (right). The inverse adS length scale $a = 1$ is fixed, and the boundary conditions are varied. For $\Omega = 0$, we show the absolute value of the pressure deviator component.

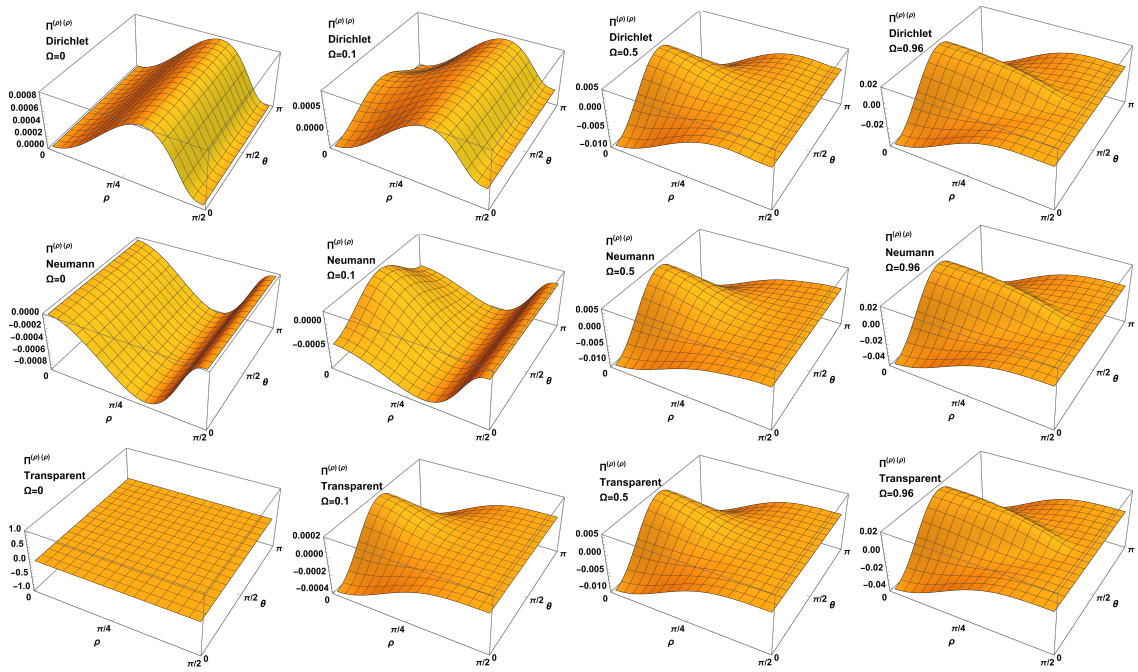


Figure 5.46: The $\rho\rho$-component of the pressure deviator, plotted at a fixed inverse temperature $\beta = \pi/4$. The inverse adS length scale is fixed $a = 1$, whilst both the angular speed and boundary conditions are varied.

of each other, whilst $\Pi^{(\phi)(\phi)} \equiv 0$ for transparent boundary conditions - hence there are no $\Omega = 0$ plots in figure 5.49. As the angular speed is increased, $\Pi^{(\phi)(\phi)}$ for Neumann and transparent boundary conditions take the same, solitonic profile, and differ by a constant multiple. At higher temperatures, these begin to resemble the energy density in shape. At lower temperatures and for lower angular speeds, we observe that the curves do not take their global maximum at the origin and instead have a peak close to $\rho = \pi/4$. As the system gains energy, either through increased temperature or angular speed, this feature gets flattened out, and the global maximum is then found at the origin $\rho = 0$. This feature is not present for the case of Dirichlet boundary conditions. Instead, for nonzero rotation, the curves look solitonic in so much as they take their global maximum at the origin $\rho = 0$ and tend toward zero at the boundary. This is with the caveat that, in order to ensure continuity for $\Omega \in (0, 1/2)$, for sufficiently small $\Omega \neq 0$ this is not the case, and some interpolating behaviour is present (which is verifiable by plotting lower values of $\Omega$, though these are not shown here). The major difference between Dirichlet, Neumann and transparent boundary conditions for nonzero rotation is that $\Pi^{(\phi)(\phi)}$ is not everywhere positive for Dirichlet boundary conditions, and in fact drops below the $\rho$-axis close to the boundary. The extent to which this happens is decreased as the angular speed is increased. Considering figure 5.50, we see that, for each value of angular speed and temperature considered, the curves corresponding to Dirichlet boundary conditions are the smallest, Neumann the largest and transparent somewhere inbetween. Recall that $\Pi^{(\phi)(\phi)}$ at $\Omega = 0$ is everywhere negative for the case of Dirichlet boundary conditions, so although not immediately obvious from figure 5.50, this still holds. As the temperature is increased, the variance between the scales of each curve decreases; that is, at higher temperatures they are much closer together.

The final figure for the $\phi\phi$-component of the anisotropic pressure, figure 5.51, shows $\Pi^{(\phi)(\phi)}$ for varying polar angle $\theta$. This is presented as a grid of plots, where the columns correspond to different angular speeds, whilst the rows are for the three different boundary conditions.

Unlike the component $\Pi^{(\rho)(\rho)}$, as angular speed is increased, no hump forms on the origin $\rho = 0$ around the equatorial plane. Instead, the value of $\Pi^{(\phi)(\phi)}$ at the origin is always independent of $\theta$ and, as the angular speed is increased, increases away from the origin and toward its global maximum. However, it only reaches its global maximum for sufficiently high angular speed. Note that this is only for the case of Neumann boundary conditions; in the cases of Dirichlet and transparent boundary conditions, $\Pi^{(\phi)(\phi)}$ always has its global maximum at the origin $\rho = 0$. For example, at $\Omega = 0.1$, the global maximum occurs around $\rho \sim \pi/4$ for Neumann boundary conditions, whereas it is a global minimum for the case of Dirichlet boundary conditions. Once the angular speed is high enough, all three cases start to look similar in profile, and in fact tend towards the energy density in shape. This suggests that at high angular speeds, rotational effects are dominant over effects corresponding to the boundary conditions. In all cases considered, whether that be on the equatorial plane or across the full range of $\theta$, the anisotropic pressure component $\Pi^{(\phi)(\phi)}$ is always at least the smallest in magnitude for Dirichlet boundary conditions, indicating that Dirichlet boundary conditions produce the smallest quantum effects.

The next anisotropic pressure component to consider is $\Pi^{(\theta)(\theta)}$. Since the anisotropic pressure is traceless, the $\theta\theta$-component can be expressed as a sum of the $\rho\rho$- and $\phi\phi$-components. Hence we omit the equatorial plane plots of $\Pi^{(\theta)(\theta)}$. In spite of this, in figure 5.52 we still show the component $\Pi^{(\theta)(\theta)}$ as a function of both $\rho$ and $\theta$, since it displays some interesting features. Whereas for the $\Pi^{(\rho)(\rho)}$ component we had a hump form on the origin around the equatorial plane, instead, for the $\Pi^{(\theta)(\theta)}$ component, we see a sink form in the same place. Also in analogy with the $\rho\rho$-component, for sufficiently high angular speed this sink then corresponds to the global minimum of the component. The magnitude of this minimum is roughly twice as large for the cases of Neumann and transparent boundary conditions than it is for Dirichlet boundary conditions. For zero rotation, we have that $\Pi^{(\theta)(\theta)} = \Pi^{(\phi)(\phi)}$, which is easily verified by comparing figures 5.51 and 5.52. When we increase the angular speed, it is clear that this no longer holds, simply

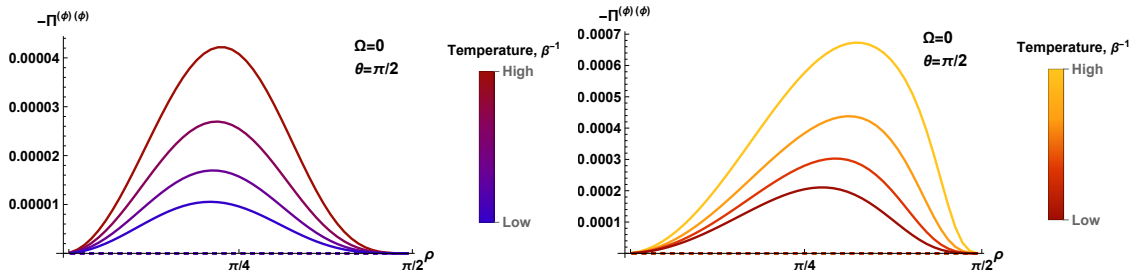


(a) $\Omega = 0$

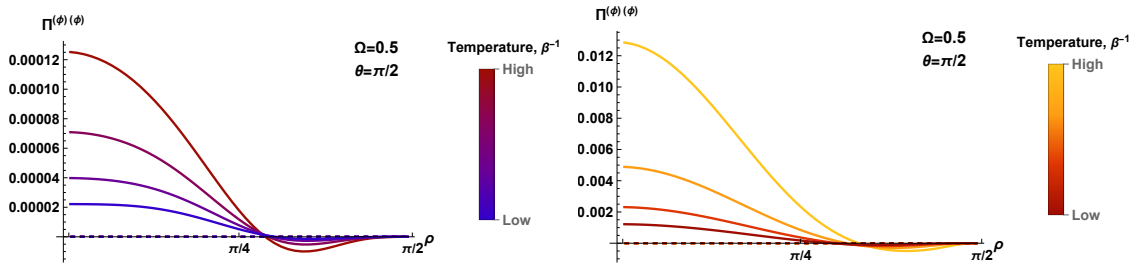


(b) $\Omega = 0.5$

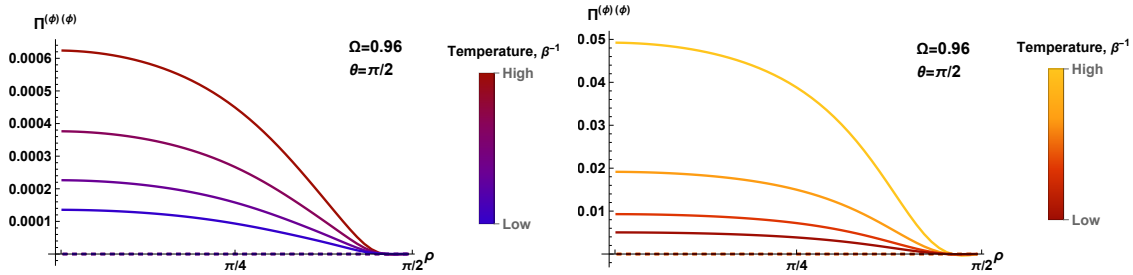


(c) $\Omega = 0.96$

Figure 5.47: The $\phi\phi$-component of the pressure deviator, plotted on the equatorial plane $\theta = \pi/2$. The angular speed is varied, whilst the inverse temperature is in the range $\beta \in [\pi/6, 5\pi/12] \cup [3\pi/4, \pi]$ for the right and left plots respectively. The inverse adS length scale is fixed at $a = 1$, whilst Dirichlet boundary conditions are applied to the field. For $\Omega = 0$, minus the pressure deviator component is plotted since it is everywhere negative. The solid lines correspond to the QFT-RSET, and the dashed lines correspond to the RKT-SET (which is identically zero).

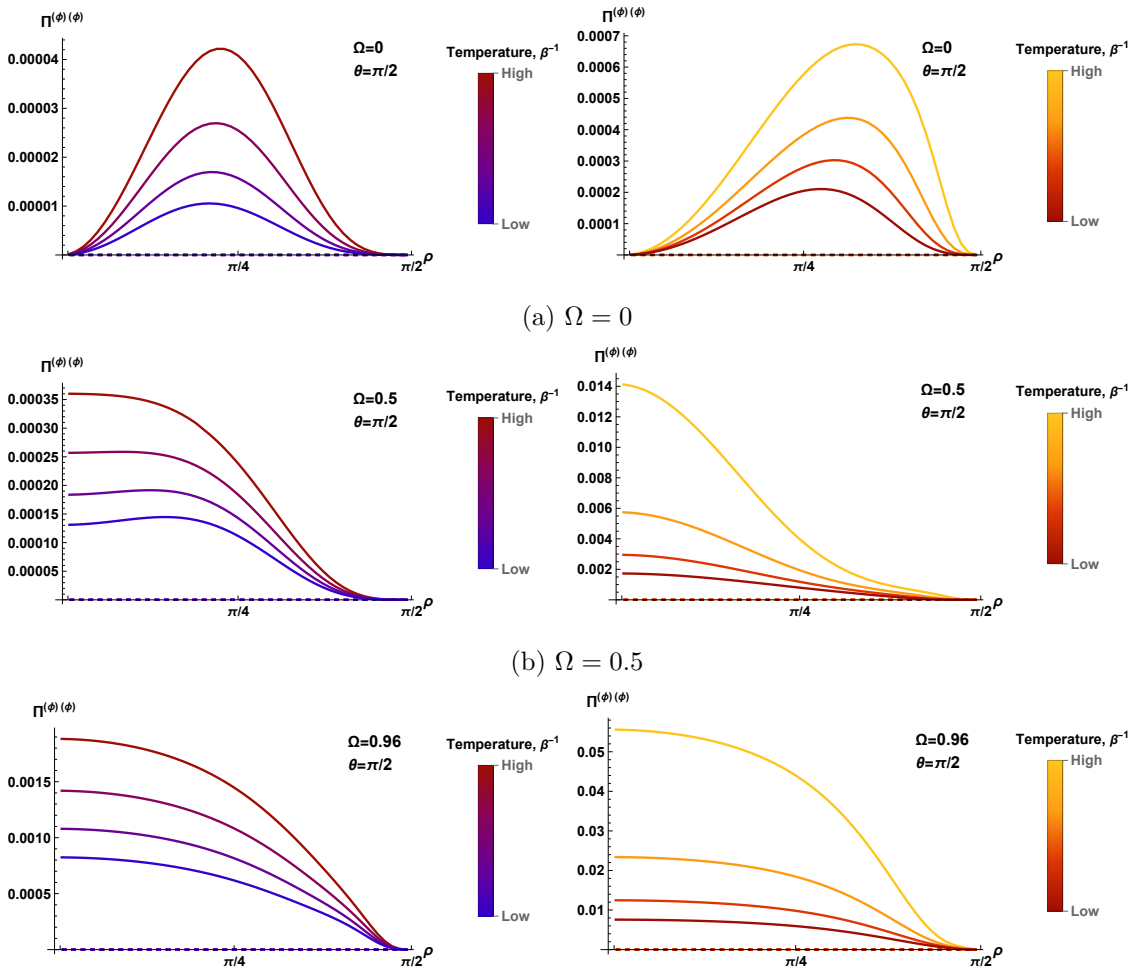


(a) $\Omega = 0$

(b) $\Omega = 0.5$

(c) $\Omega = 0.96$

Figure 5.48: The pressure deviator $\phi\phi$-component, on the equatorial plane $\theta = \pi/2$. The angular speed is varied, whilst the inverse temperature is in the range $\beta \in [\pi/6, 5\pi/12] \cup [3\pi/4, \pi]$ for the right and left plots respectively. The inverse adS length scale is fixed at $a = 1$, whilst Neumann boundary conditions are applied to the field. The solid lines correspond to the QFT-RSET, and the dashed lines correspond to the RKT-SET (which is identically zero).

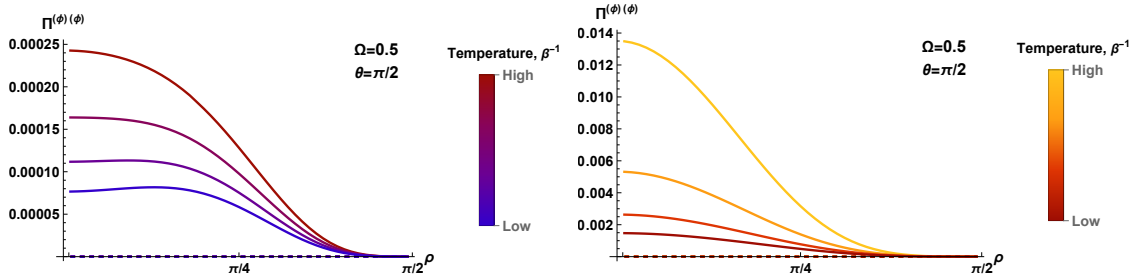


(a) $\Omega = 0.5$

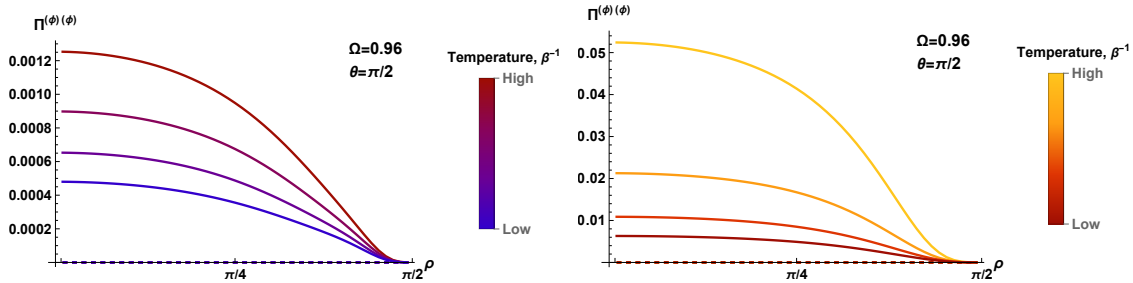


(b) $\Omega = 0.96$

Figure 5.49: The $\phi\phi$-component of the pressure deviator on the equatorial plane $\theta = \pi/2$. The angular speed is varied, whilst the inverse temperature is in the range $\beta \in [\pi/6, 5\pi/12] \cup [3\pi/4, \pi]$ for the right and left plots respectively. The inverse adS length scale is fixed at $a = 1$, whilst transparent boundary conditions are applied to the field. When there is no rotation ($\Omega = 0$), the pressure deviator vanishes for transparent boundary conditions, hence the exclusion of plots corresponding to $\Omega = 0$ here. The solid lines correspond to the QFT-RSET, and the dashed lines correspond to the RKT-SET (which is identically zero).

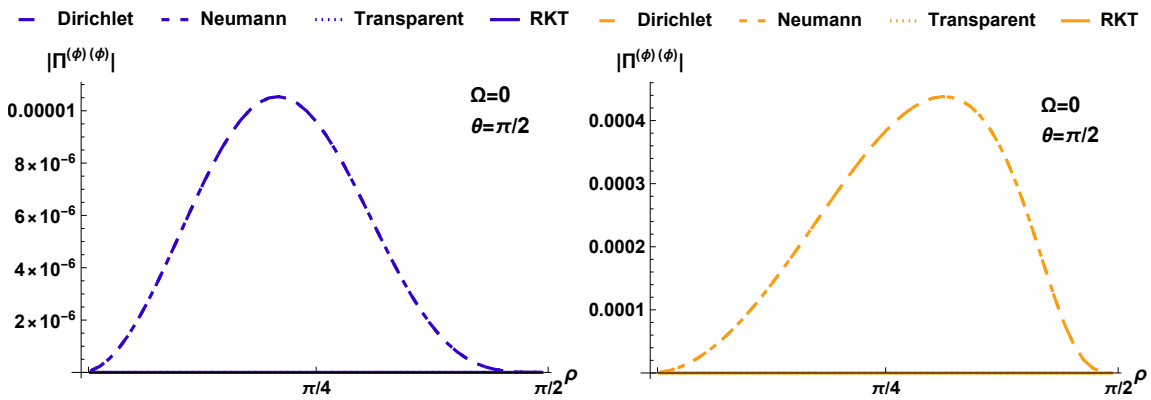


(a) $\Omega = 0$

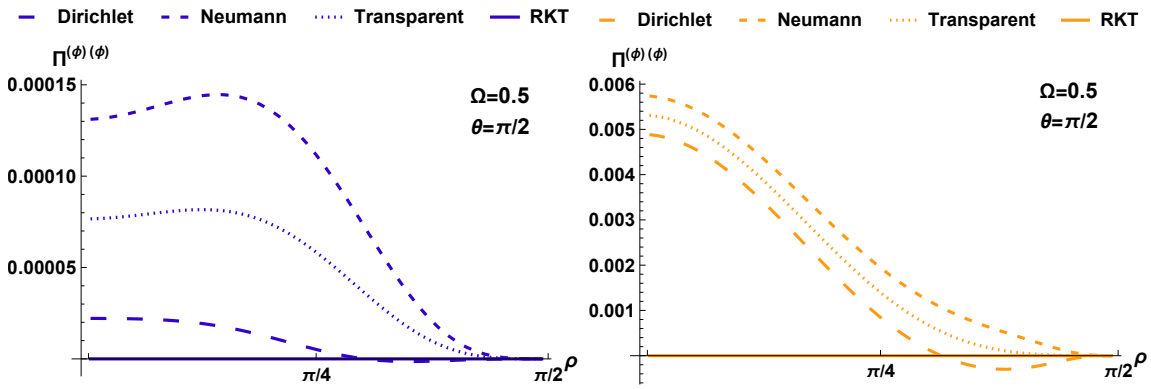


(b) $\Omega = 0.5$

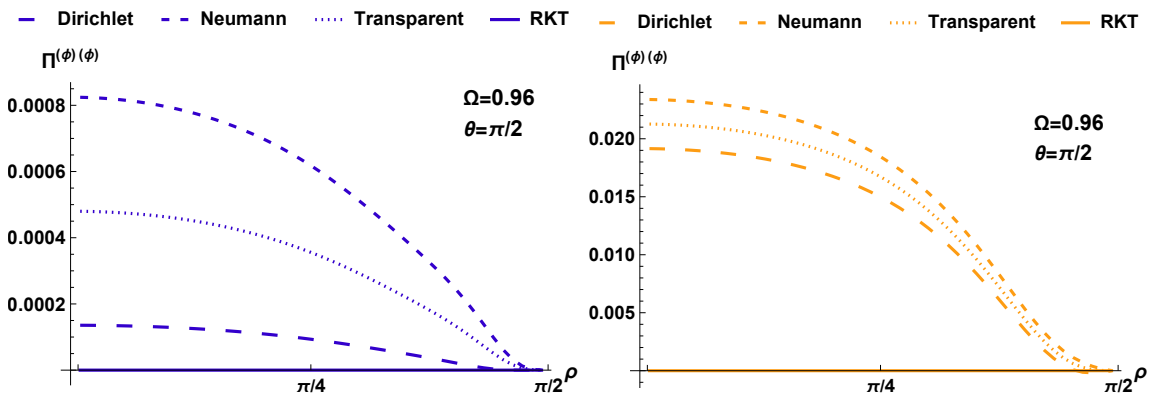


(c) $\Omega = 0.96$

Figure 5.50: Pressure deviator $\phi\phi$-component plots on the equatorial plane. The angular speed is varied, whilst the inverse temperature is fixed at either $\beta = \pi$ (left) or $\beta = \pi/4$ (right). The inverse adS length scale $a = 1$ is fixed, and the boundary conditions are varied. When $\Omega = 0$, the absolute value of the pressure deviator component is plotted.

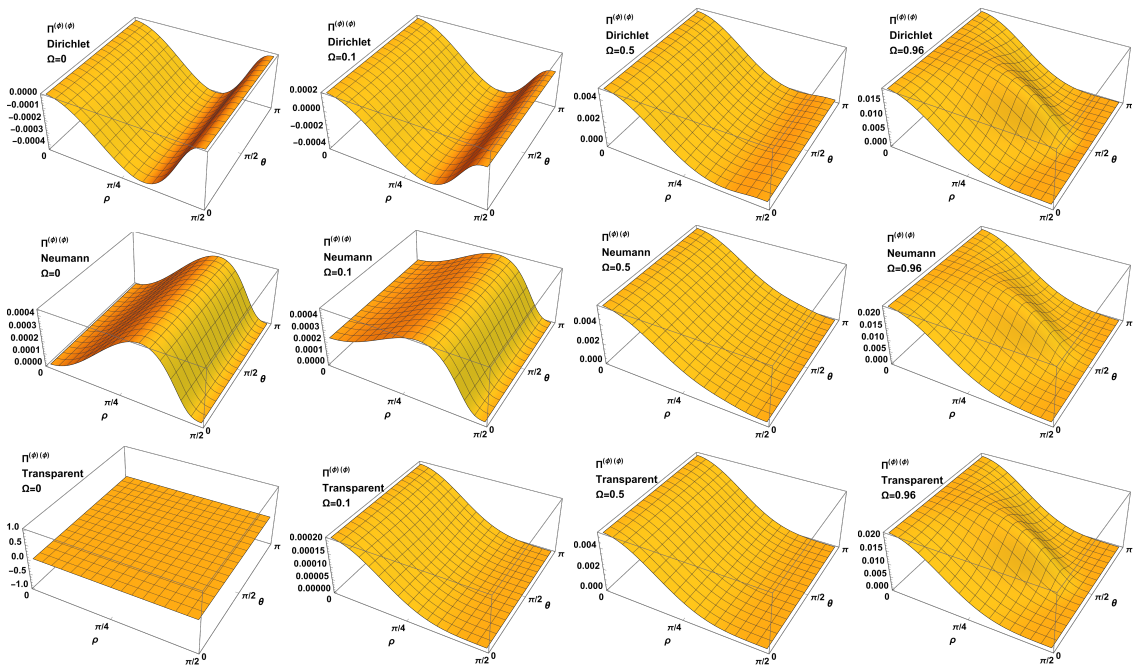


Figure 5.51: Surface plot of the pressure deviator component $\Pi^{(\phi)(\phi)}$. The inverse temperature $\beta = \pi/4$ and inverse adS length scale $a = 1$ are fixed. Both the angular speed and boundary conditions are varied.

by comparing the profile of the two components at nonzero angular speed, regardless of boundary conditions. This means that the quantity $\Pi^{(\phi)(\phi)} - \Pi^{(\theta)(\theta)}$ represents an angular deviation, since at zero angular speed the difference is zero, but for nonzero angular speed, the difference is likewise nonzero. Figure 5.53 shows the difference for two choices of angular speed and two choices of temperature. As the angular speed is increased, the curves tend toward zero as $\rho \to \pi/2$ at a slower rate. In contrast, as the temperature is increased, the magnitude of the difference increases. Figure 5.54 shows the difference in components as a function of $\rho$ and $\theta$. It is clear that, regardless of angular speed, the difference is always zero on the poles $\theta = 0, \pi$ and at the boundary $\rho = \pi/2$, meaning the rotation has no effect there. On the other hand, the rotation seemingly has the largest effect at the origin $\rho = 0$, with a hump forming around the equatorial plane. As the angular speed is increased, not only does the magnitude of this hump increase, but it starts to extend out towards the boundary along the equatorial plane, meaning it decays to zero at a slower rate for higher angular speeds. This feature was also observed in the equatorial plane plots. Since the corresponding differences in components $\Pi^{(\phi)(\phi)} - \Pi^{(\theta)(\theta)}$ for Neumann and transparent boundary conditions are qualitatively the same, in figure 5.55 the difference between the the quantity $\Pi^{(\phi)(\phi)} - \Pi^{(\theta)(\theta)}$ for Dirichlet and both Neumann and transparent boundary conditions is shown. For both Neumann and transparent boundary conditions, the difference is positive regardless of the angular speed, indicating that the rotation had the least effect on the QFT-RSETs corresponding to Dirichlet boundary conditions. The magnitude of the difference is highest for Neumann boundary conditions, indicating the rotation had a larger effect on the QFT-RSET corresponding to Neumann boundary conditions, with the QFT-RSET corresponding to transparent boundary conditions lying somewhere inbetween.

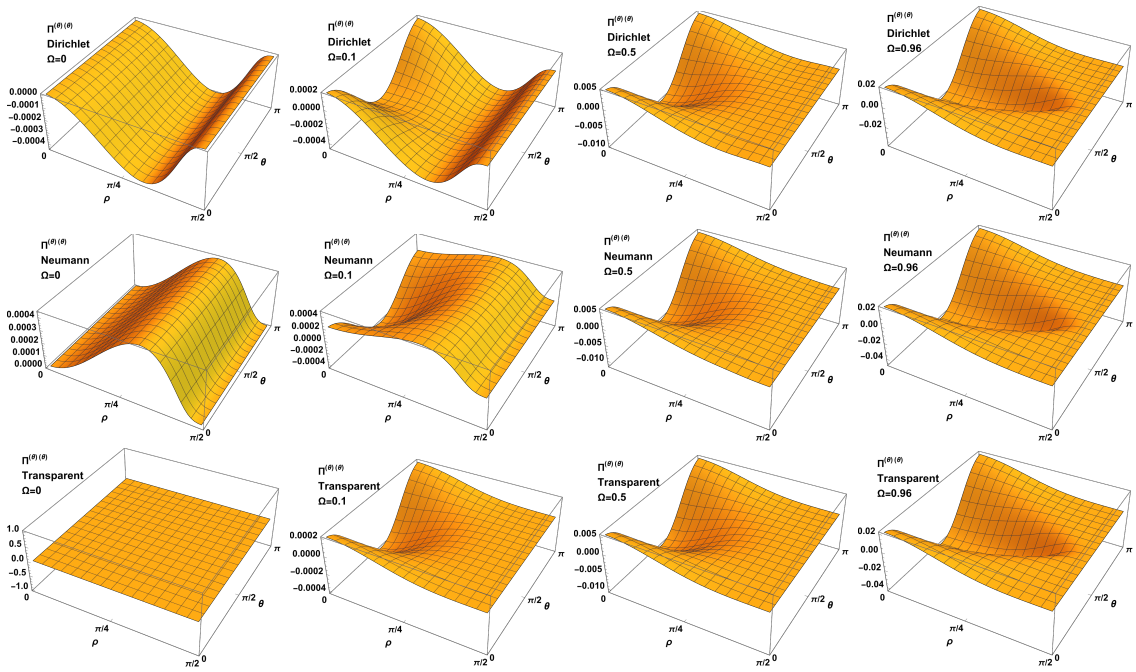


Figure 5.52: Surface plot of the pressure deviator component $\Pi^{(\theta)(\theta)}$. The inverse temperature $\beta = \pi/4$ and inverse adS length scale $a = 1$ are fixed. Both the angular speed and boundary conditions are varied.

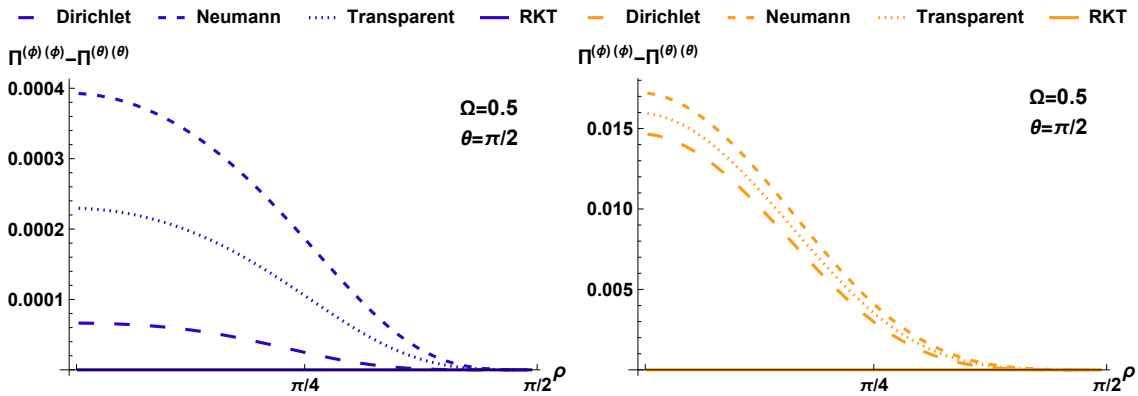


(a) $\Omega = 0.5$

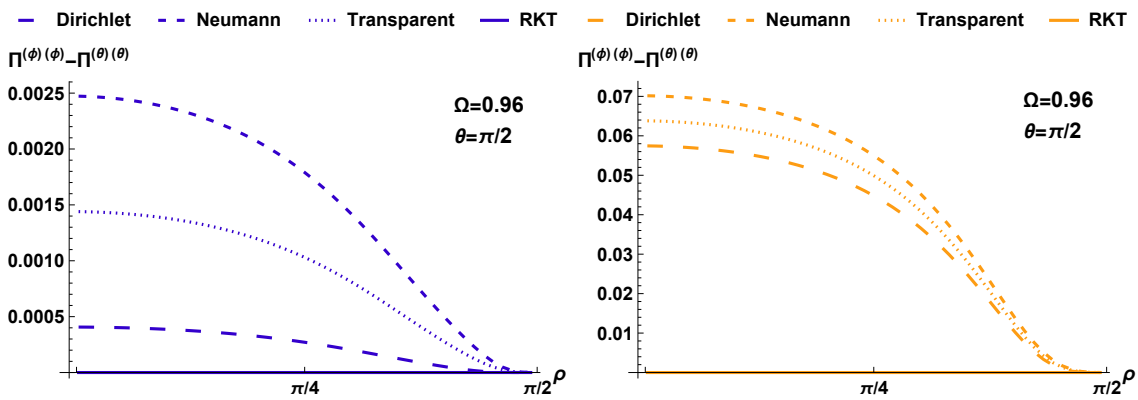


(b) $\Omega = 0.96$

Figure 5.53: The difference between the $\phi\phi$- and $\theta\theta$-components of the pressure deviator on the equatorial plane $\theta = \pi/2$. The angular speed is varied, whilst the inverse temperature is fixed at either $\beta = \pi$ (left plots) or $\beta = \pi/4$ (right plots). The inverse adS length scale is fixed at $a = 1$, whilst the boundary conditions are varied.

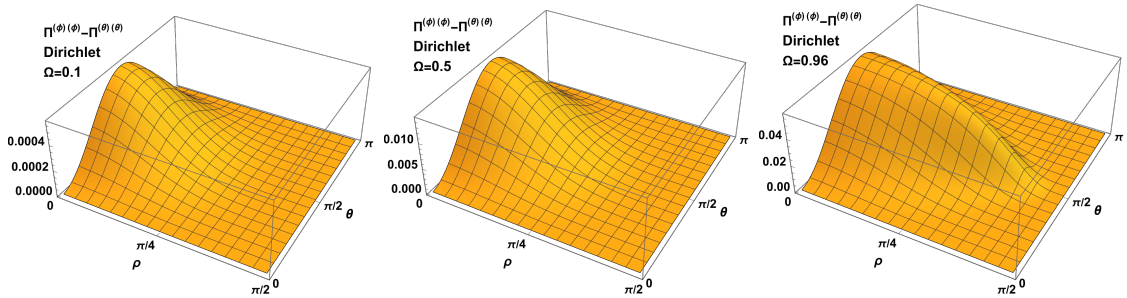


Figure 5.54: The difference in pressure deviator components $\Pi^{(\phi)(\phi)}$ and $\Pi^{(\theta)(\theta)}$. The inverse temperature $\beta = \pi/4$ and inverse adS length scale $a = 1$ are fixed. The angular speed is varied and Dirichlet boundary conditions are applied to the field.

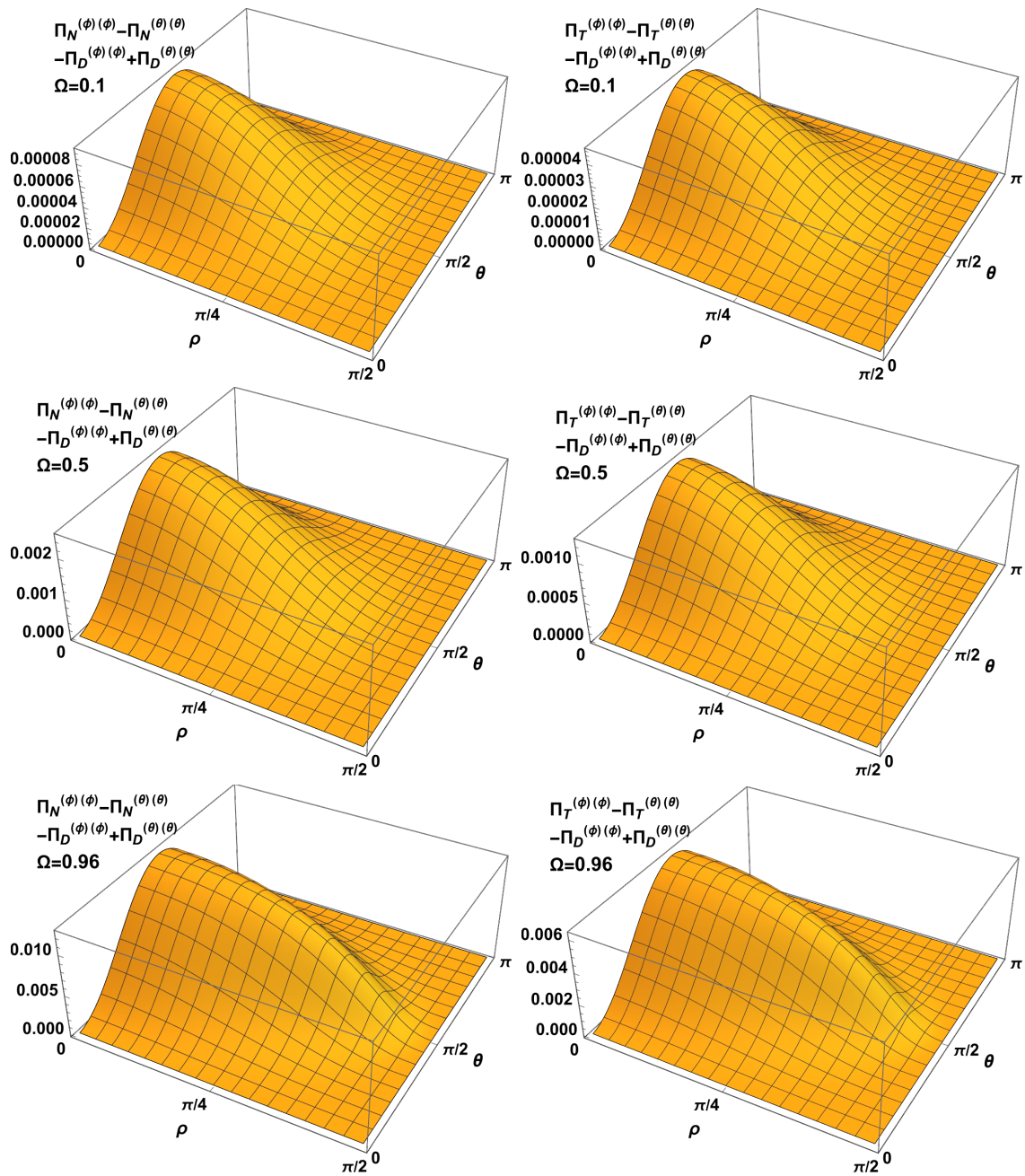


Figure 5.55: Differences in pressure deviator components $\Pi^{(\phi)(\phi)}$ and $\Pi^{(\theta)(\theta)}$, between the differing boundary conditions. The inverse temperature $\beta = \pi/4$ and inverse adS length scale $a = 1$ are fixed. The angular speed is varied.

The final nonzero component of the anisotropic pressure is $\Pi^{(\rho)(\theta)}$. Unlike the situation observed for a quantum fermion field, where $\Pi^{(\rho)(\theta)}$ is identically zero [15, 19], this is not the case for a quantum scalar field. As mentioned in the prelude to this subsection, $\Pi^{(\rho)(\theta)}$ is antisymmetric under the mapping $\theta \to \pi - \theta$ and is thus zero on the equatorial plane. Figure 5.56 shows $\Pi^{(\rho)(\theta)}$ as a surface plot for the case of Dirichlet boundary conditions. The component $\Pi^{(\rho)(\theta)}$ vanishes not only on the equatorial plane, but also on the axis of rotation and at the boundary $\rho = \pi/2$, as illustrated in figure 5.56. The absolute maximum of the component always occurs at the origin $\rho = 0$, at $\theta = \pi/4$ and $\theta = 3\pi/4$. The effect of increasing the angular speed is only to increase the magnitude of the absolute maxima. Away from the origin, as the angular speed is increased the component decays towards zero as $\rho \to \pi/2$ at a slower rate. The corresponding plots for Neumann and transparent boundary conditions look qualitatively similar and hence, figure 5.57 shows the difference in $\Pi^{(\rho)(\theta)}$ between Dirichlet and both Neumann and transparent boundary conditions. The difference in the component $\Pi^{(\rho)(\theta)}$ for the differing boundary conditions is always negative relative to the corresponding component $\Pi^{(\rho)(\theta)}$ for Dirichlet boundary conditions in figure 5.56. This means that the component arising from Dirichlet boundary conditions always has a smaller magnitude than the corresponding component for both Neumann and transparent boundary conditions. Additionally, the difference is larger between Dirichlet and Neumann boundary conditions than between Dirichlet and transparent boundary conditions, indicating that the component $\Pi^{(\rho)(\theta)}$ takes the largest magnitude for the case of Neumann boundary conditions. In a similar fashion to the other anisotropic pressure components, since they can be construed as a measure of quantum deviation, Dirichlet boundary conditions produce the least significant quantum effects; whilst Neumann boundary conditions produce the most significant quantum effects; and transparent boundary conditions produces quantum effects with a significance somewhere between Dirichlet and Neumann boundary conditions (when measured by the magnitude of the anisotropic pressure components).

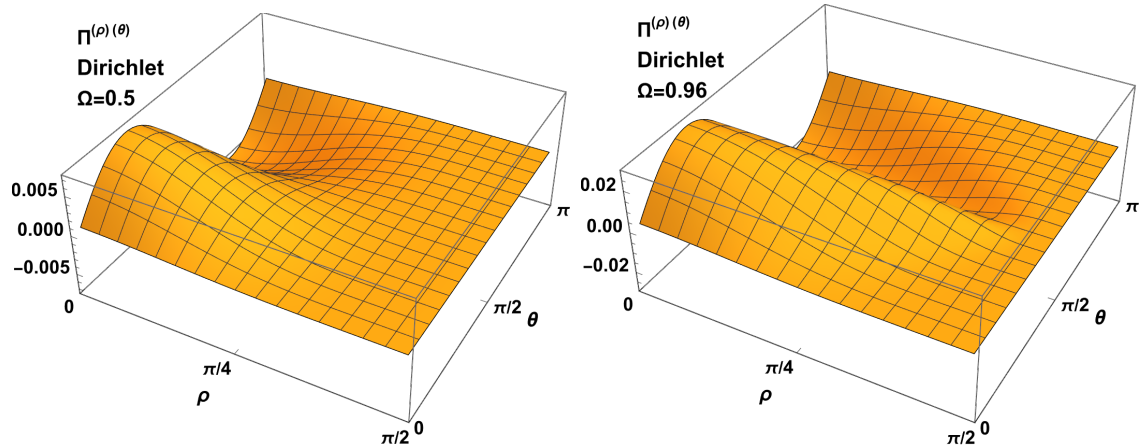


Figure 5.56: The pressure deviator component $\Pi^{(\rho)(\theta)}$. The inverse temperature $\beta = \pi/4$ and inverse adS length scale $a = 1$ are fixed. The angular speed is varied, whilst Dirichlet boundary conditions are applied to the field.

We make one final, general comment regarding the various pressure deviator components. In general, as the angular speed is increased, the magnitude of the pressure deviator components also increases, regardless of boundary conditions or temperature. This alludes to the fact that the angular speed has a greater effect on the pressure deviator than the temperature or choice of boundary condition.

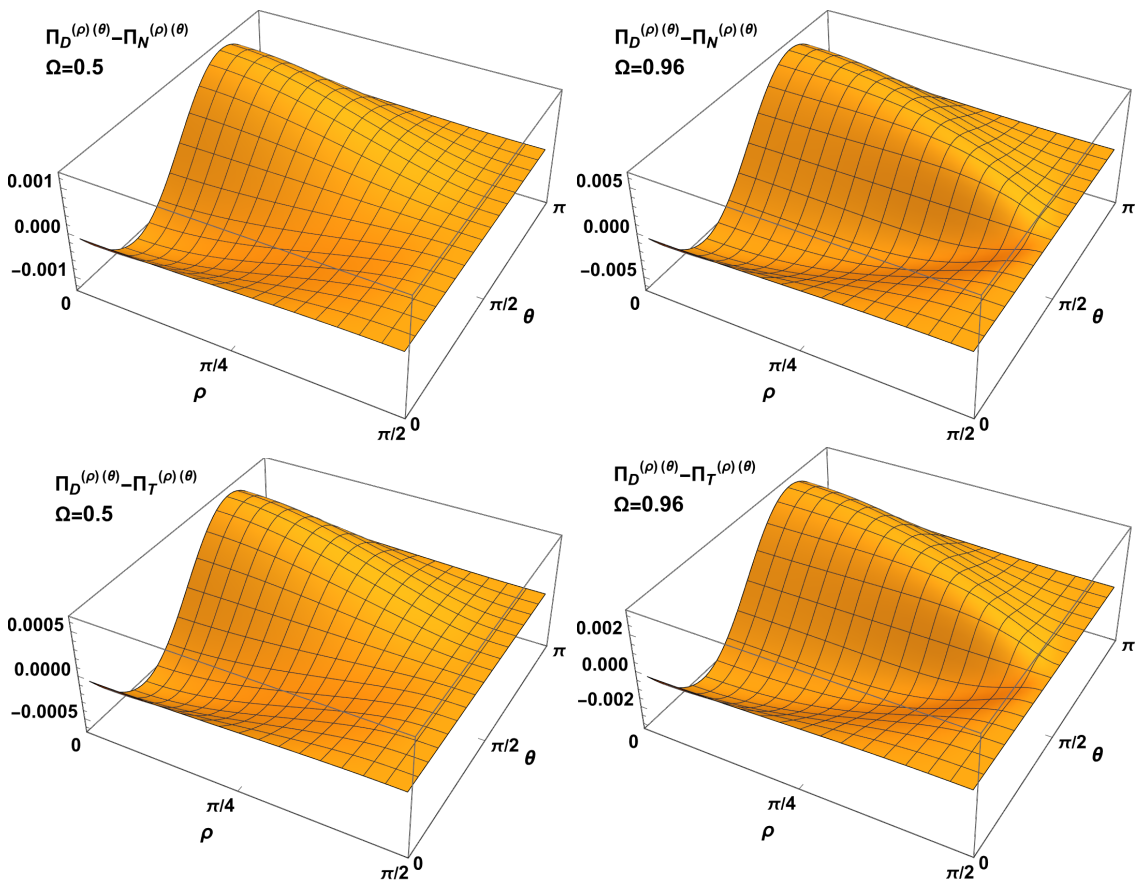


Figure 5.57: Differences in pressure deviator component $\Pi^{(\rho)(\theta)}$ between the differing boundary conditions. The inverse temperature $\beta = \pi/4$ and inverse adS length scale $a = 1$ are fixed. The angular speed is varied.

#### 5.3.4.2 Three-dimensional anti-de Sitter space-time

We now turn our attention to the case of three-dimensional anti-de Sitter space-time. Again, we will split the proceeding analyses into the three physical quantities of interest: energy density, heat flux and anisotropic pressure. Figures 5.58-5.62 show the energy density, figures 5.63-5.66 show the heat flux and the anisotropic pressure is shown in figures 5.67-5.70.

**Energy density**

Figure 5.58 shows the energy density when Dirichlet boundary conditions are applied to the field. The energy density has the same solitonic profile in three-dimensions as it does in four-dimensions, taking its global maximum at the origin and decaying to zero at the boundary. The rate of decay decreases as the angular speed increases. The agreement between the QFT-RSETs and RKT-SET is better for higher temperatures, as was the case in four-dimensions. The major difference between three- and four-dimensions is that the difference between the RKT and QFT results is slightly bigger in three- rather than four-dimensions.

Figure 5.59 shows the energy density when Neumann boundary conditions are applied to the field. Whereas for Dirichlet boundary conditions the RKT was an overestimate (for most angular speeds) to the QFT energy density (to varying degrees depending on the temperature), when Neumann boundary conditions are applied the RKT-SET is an underestimate to the QFT-RSET energy density for all angular speeds and inverse temperatures. Even at higher temperatures, where the QFT-RSET corresponding to Dirichlet boundary conditions gives very close agreement with the RKT-SET, the QFT-RSET corresponding to Neumann boundary conditions is considerably less well approximated by the RKT-SET. For example, for an angular speed of $\Omega = 0.96$ and at an inverse temperature of $\beta = \pi/6$, the percentage difference in global maxima of the energy density between the QFT and RKT is: $\sim 3\%$ for Dirichlet boundary conditions; $\sim 11\%$ for Neumann boundary condi-

tions; and $\sim 7\%$ for transparent boundary conditions. Whilst this suggests that Dirichlet boundary conditions give the best approximation to RKT, this is actually only the case for high angular speeds. At lower angular speeds, the QFT-RSET energy density arising from transparent boundary conditions - given in figure 5.60 - appears to be a closer approximation to the RKT-SET.

To investigate this further, in figure 5.61 the energy density is shown at two fixed inverse temperatures for varying angular speed. At lower angular speeds and temperature, it is clear that transparent boundary conditions give the best agreement to the RKT-SET. Conversely, at higher angular speeds, Dirichlet boundary conditions give the best agreement to the RKT-SET, regardless of temperature. This indicates that angular speed is a more important factor than temperature when it comes to comparing the QFT-RSET with the RKT-SET.

To understand the effect of changing the boundary conditions on the energy density further, figure 5.62 shows the absolute value of the difference in energy densities of the QFT-RSETs and RKT-SET. For no rotation, regardless of temperature, the difference corresponding to transparent boundary conditions is always the lowest, whereas the difference corresponding to Neumann boundary conditions is the highest and the difference corresponding to Dirichlet boundary conditions lies somewhere inbetween, although closer to the curve corresponding to Neumann rather than transparent boundary conditions. As the angular speed increases, an interplay between Dirichlet and transparent boundary conditions ensues; at lower temperatures the difference in energy densities is lowest for transparent boundary conditions but, as the temperature increases, the difference is lower for Dirichlet boundary conditions close to the origin but the difference for transparent boundary conditions is then the lowest closer to the boundary. Conversely, at the highest angular speed considered, the difference corresponding to Dirichlet boundary conditions is the lowest across most of the range of $\rho$, where the difference corresponding to transparent boundary conditions is marginally lower very close to the boundary.

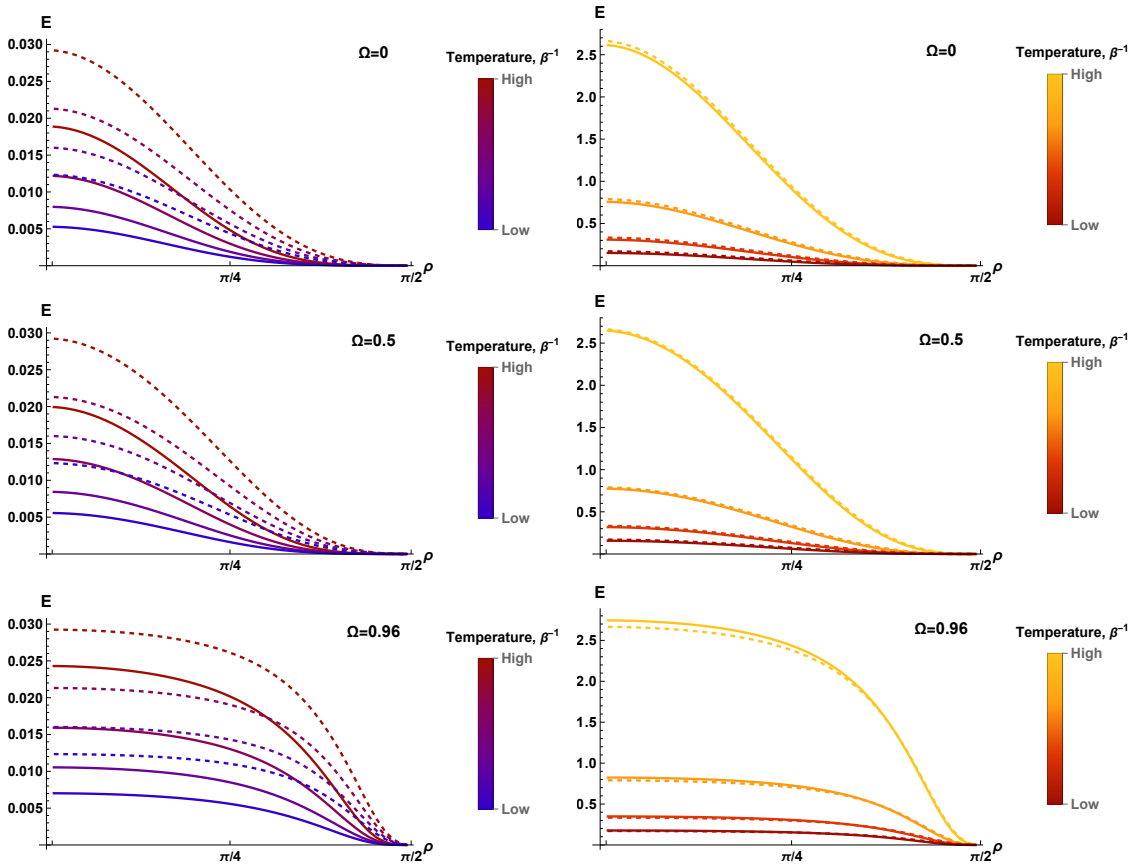


Figure 5.58: Energy density of the QFT-RSET (solid) and RKT-SET (dashed) in three-dimensional anti-de Sitter space-time. The inverse temperature is in the range $\beta \in [\pi/6, 5\pi/12] \cup [3\pi/4, \pi]$ for the right and left plots respectively. The angular speed is varied and Dirichlet boundary conditions are applied to the field. The inverse adS length scale is fixed $a = 1$.

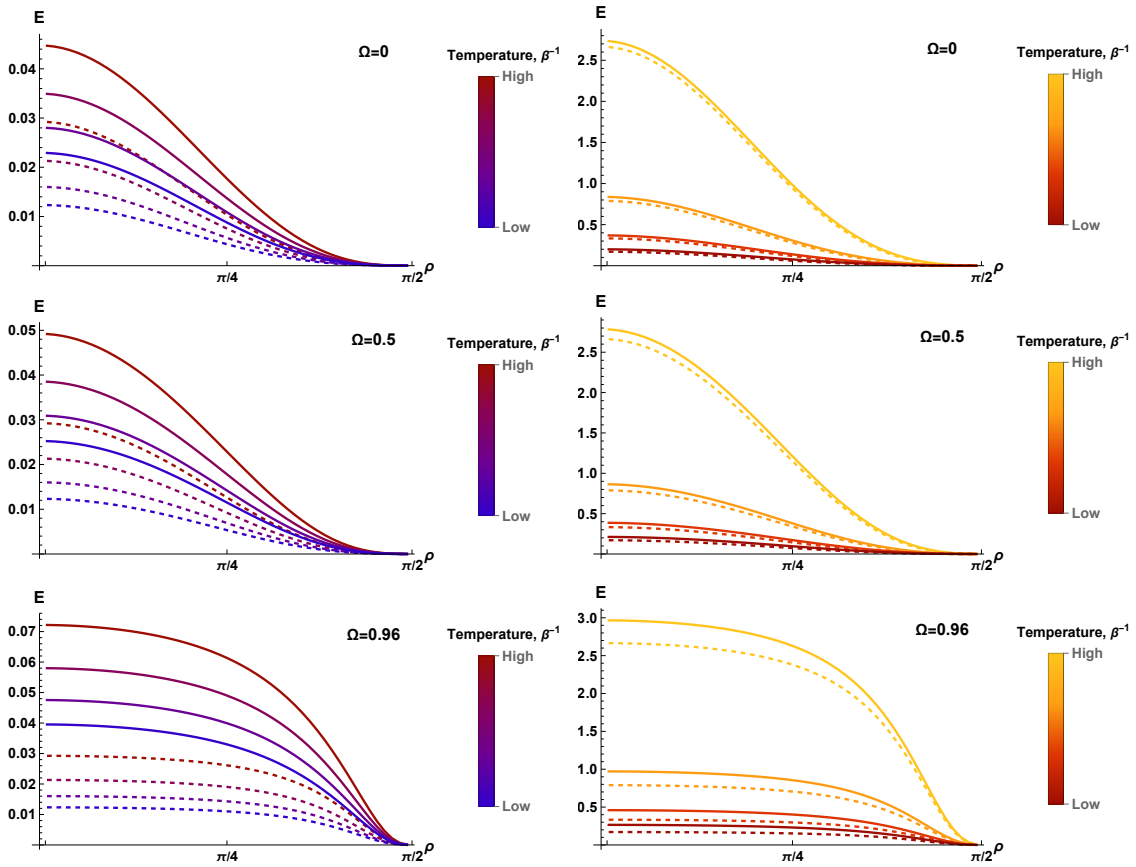


Figure 5.59: Energy density of the QFT-RSET (solid) and RKT-SET (dashed) in three-dimensional anti-de Sitter space-time. The inverse temperature is in the range $\beta \in [\pi/6, 5\pi/12] \cup [3\pi/4, \pi]$ for the right and left plots respectively. The angular speed is varied and Neumann boundary conditions are applied to the field. The inverse adS length scale is fixed $a = 1$.

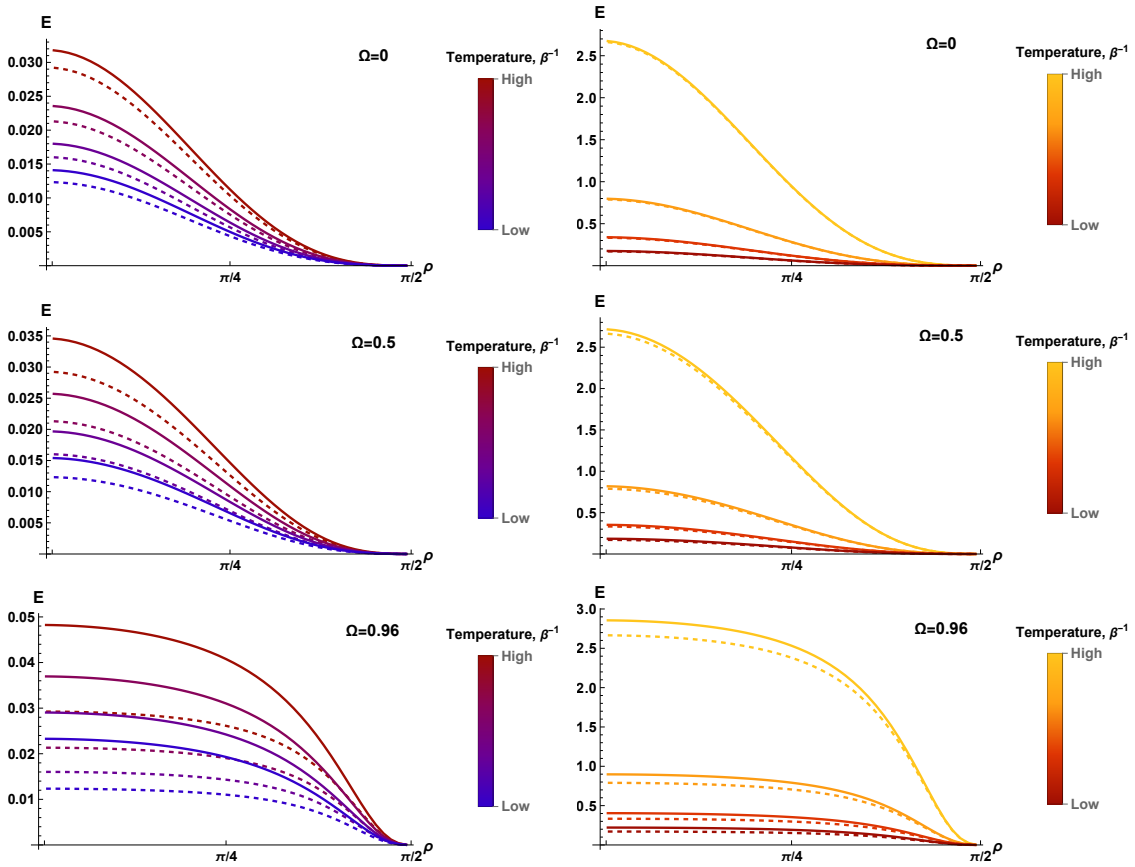


Figure 5.60: Energy density of the QFT-RSET (solid) and RKT-SET (dashed) in three-dimensional anti-de Sitter space-time. The inverse temperature is in the range $\beta \in [\pi/6, 5\pi/12] \cup [3\pi/4, \pi]$ for the right and left plots respectively. The angular speed is varied and transparent boundary conditions are applied to the field. The inverse adS length scale is fixed $a = 1$.

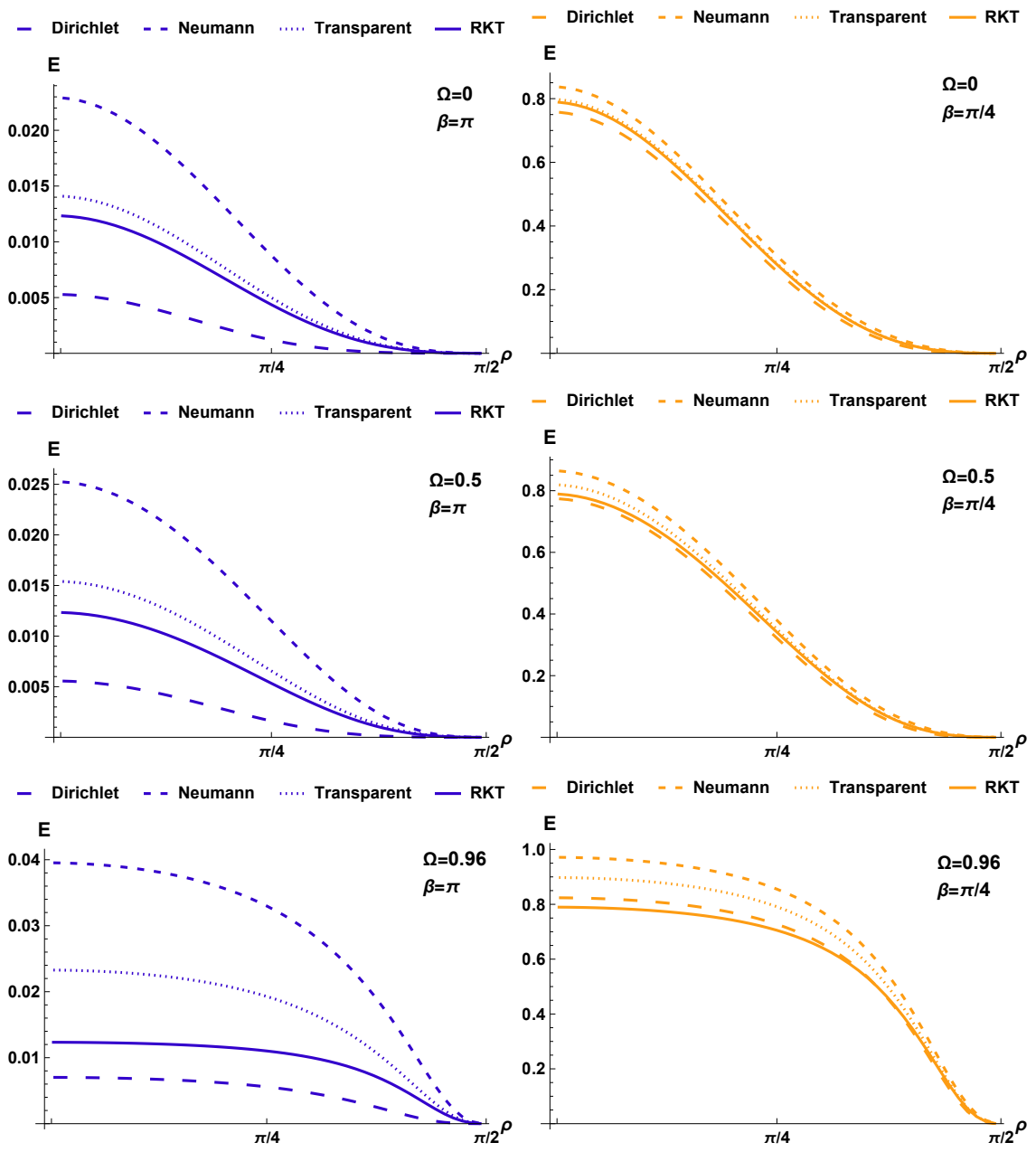


Figure 5.61: Energy density of the QFT-RSETs (dashed lines) and RKT-SET (solid line) at two fixed inverse temperatures, $\beta = \pi$ (left column) or $\beta = \pi/4$ (right column). The angular speed and boundary conditions applied to the field are varied, whilst the inverse adS length scale is kept fixed $a = 1$.

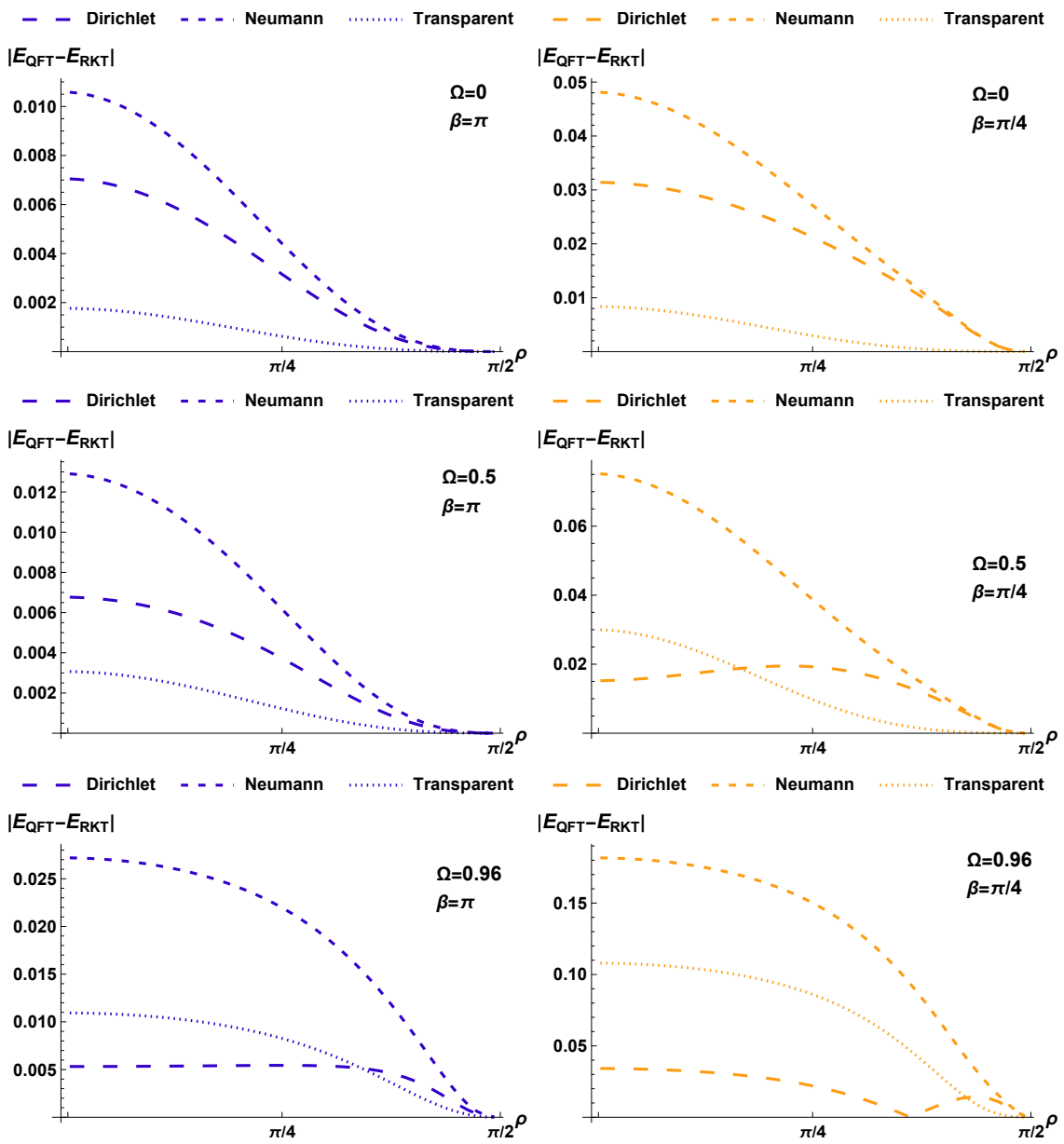


Figure 5.62: Magnitude of the differences in the energy densities of the QFT-RSETs and RKT-SET at two fixed inverse temperatures, $\beta = \pi$ (left column) or $\beta = \pi/4$ (right column). The angular speed and boundary conditions applied to the field are varied, whilst the inverse adS length scale is kept fixed $a = 1$.

**Heat flux**

The next quantity we consider is the heat flux. This is always negative so in figures 5.63-5.66 minus the heat flux is shown instead. Figure 5.63 shows the heat flux when Dirichlet boundary conditions are applied to the field. Since the heat flux is identically zero for nonrotating quantum states, in the top row we have shown the heat flux for a very low angular speed $\Omega = 0.02$ instead. As can be seen, at very low angular speeds the magnitude of the heat flux is very small, with the absolute maximum of the heat flux taking a value of $\sim 10^{-6}$ for lower temperatures and $\sim 10^{-4}$ for higher temperatures. As the angular speed increases, the order of magnitude increases to a maximum of $\sim 10^{-3}$ (low temperatures) and $\sim 10^{-2}$ (high temperatures) at $\Omega = 0.5$. As the angular speed increases further, the effect on the heat flux is not to increase the overall order of magnitude, but rather the location of the absolute maximum shifts away from the origin and towards the boundary. For all cases of angular speed, the heat flux is zero at both the origin and on the boundary.

These features are also mirrored by the heat flux corresponding to Neumann boundary conditions (figure 5.64) and transparent boundary conditions (figure 5.65). The major difference between the boundary conditions is that in the case of Dirichlet boundary conditions, the curves representing the heat flux at different temperatures are quite spread out, whereas for the cases of Neumann and transparent boundary conditions these tend to clump together. This potentially indicates that the temperature has slightly less of an effect on the heat flux for the cases of Neumann and transparent boundary conditions than for the case of Dirichlet boundary conditions. For an angular speed of $\Omega = 0.5$, the largest curve of the low temperature plots (left column) has a slight divot close to the absolute maximum for the cases of Neumann and transparent boundary conditions. This is not physically significant and likely just an anomalous data point.

Finally, figure 5.66 shows the heat flux at two fixed inverse temperatures for the three different boundary conditions. In all cases considered (of inverse temperature and angular

speed), the magnitude of the heat flux is always lowest for Dirichlet boundary conditions and highest for Neumann boundary conditions, with transparent boundary conditions lying somewhere inbetween the two.

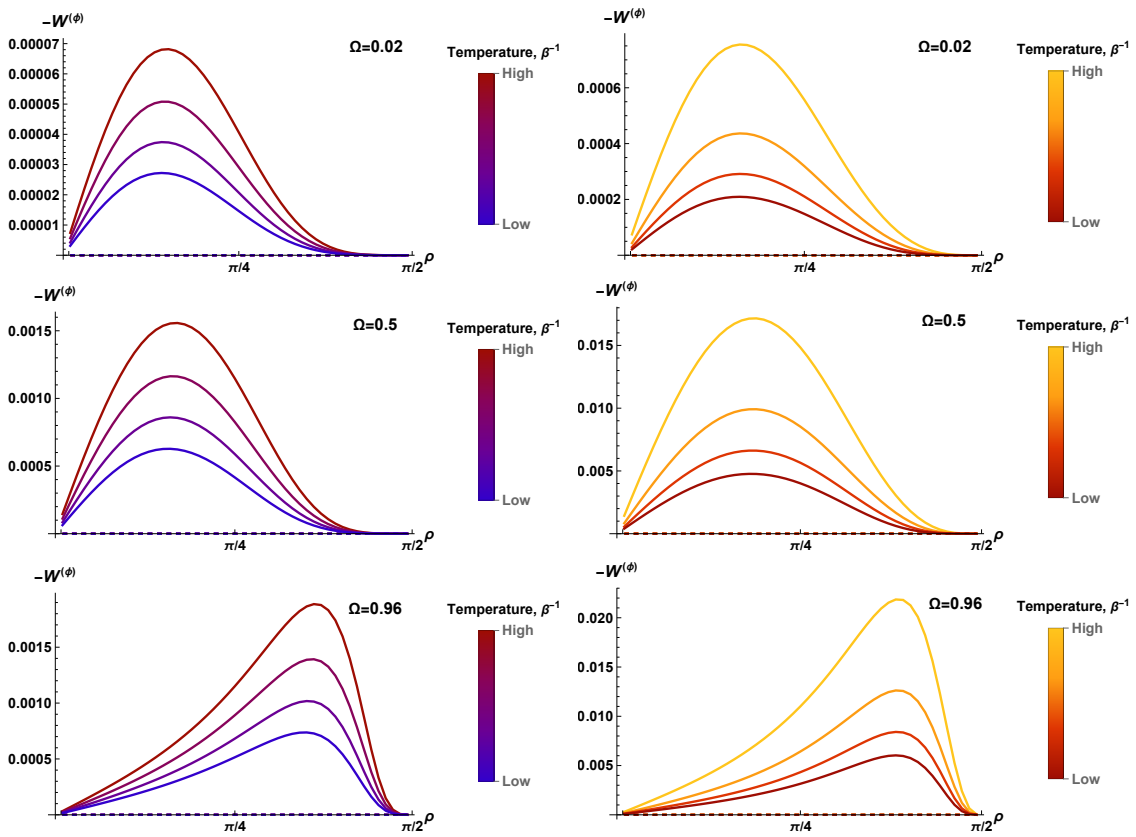


Figure 5.63: Heat fluxes of the QFT-RSET (solid) and RKT-SET (dashed - identically zero). The inverse temperature is varied in the range $\beta \in [\pi/6, 5\pi/12] \cup [3\pi/4, \pi]$ for the right and left plots respectively. The angular speed is varied and the inverse adS length scale is fixed $a = 1$. Dirichlet boundary conditions are applied to the field.

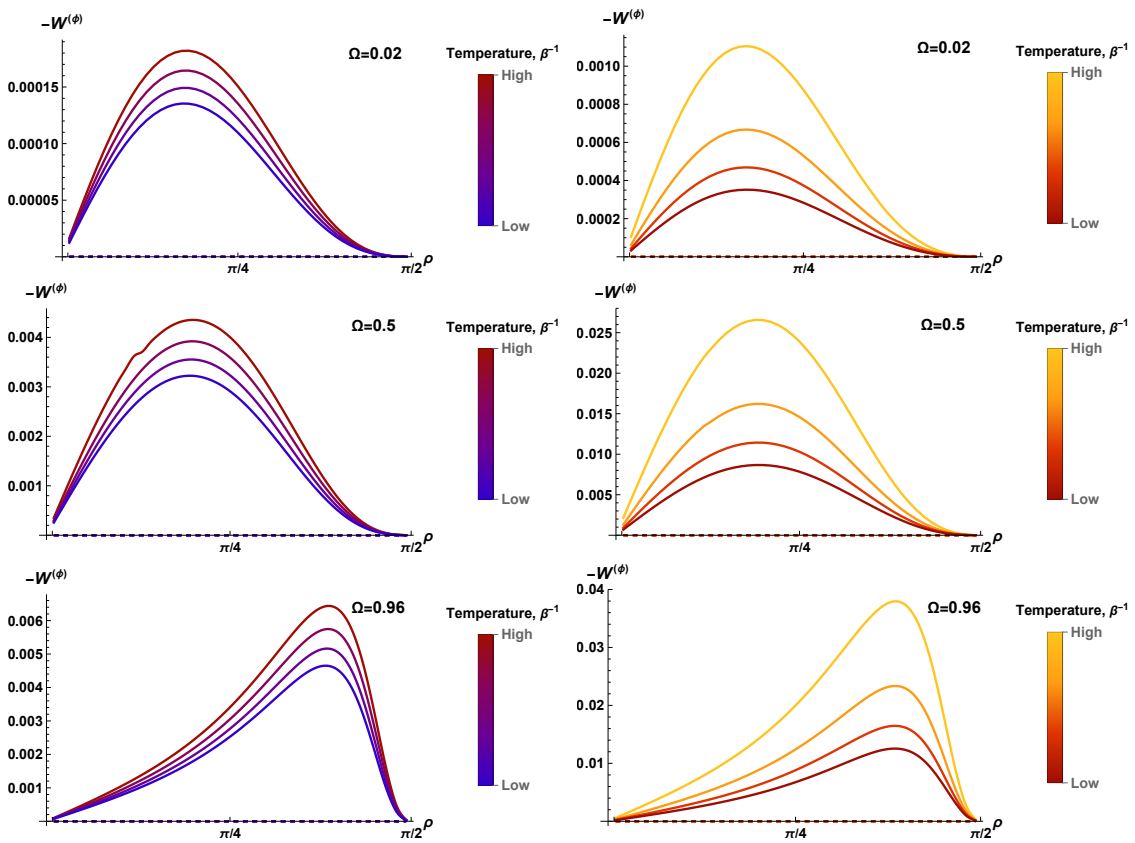


Figure 5.64: Heat fluxes of the QFT-RSET (solid) and RKT-SET (dashed - identically zero). The inverse temperature is varied in the range $\beta \in [\pi/6, 5\pi/12] \cup [3\pi/4, \pi]$ for the right and left plots respectively. The angular speed is varied and the inverse adS length scale is fixed $a = 1$. Neumann boundary conditions are applied to the field.

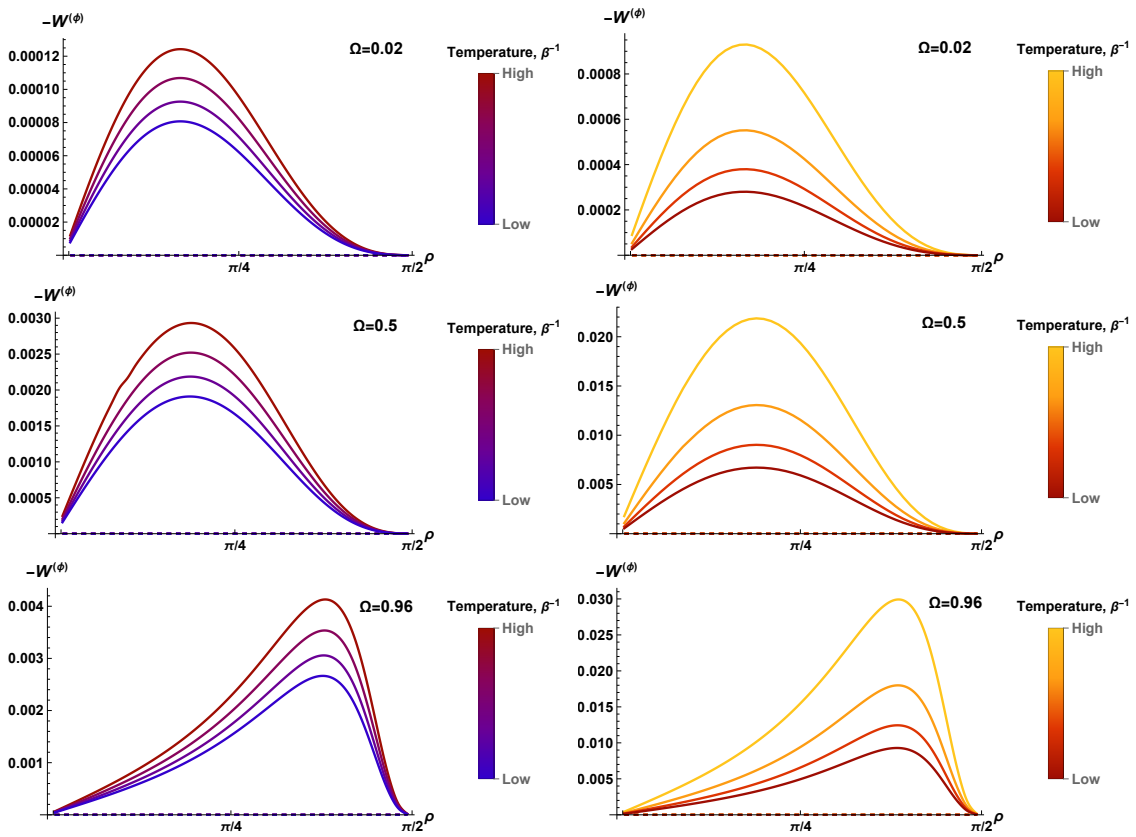


Figure 5.65: Heat fluxes of the QFT-RSET (solid) and RKT-SET (dashed - identically zero). The inverse temperature is varied in the range $\beta \in [\pi/6, 5\pi/12] \cup [3\pi/4, \pi]$ for the right and left plots respectively. The angular speed is varied and the inverse adS length scale is fixed $a = 1$. Transparent boundary conditions are applied to the field.

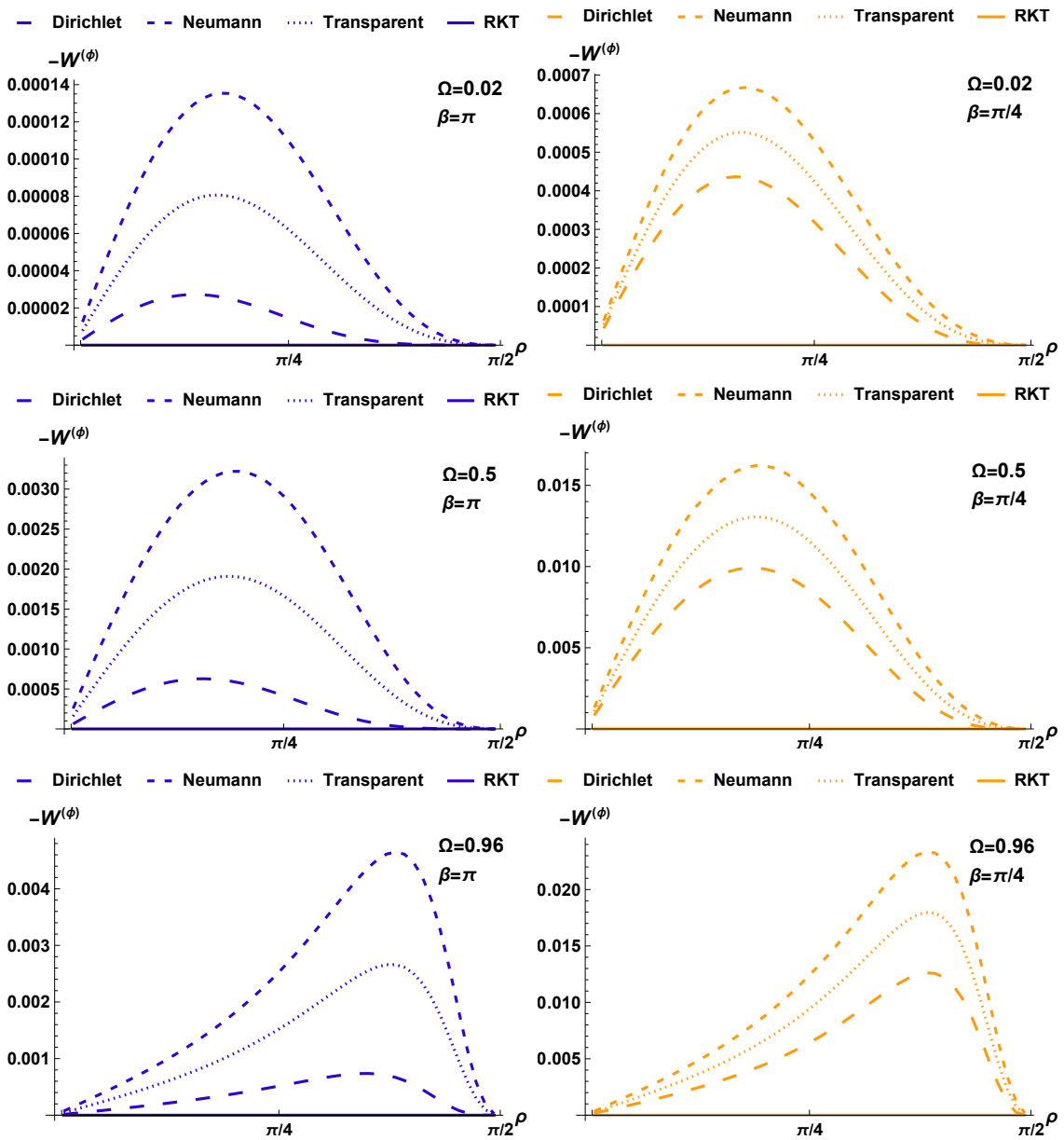


Figure 5.66: Heat fluxes of the QFT-RSET for the three different cases of boundary conditions. The inverse temperature is either $\beta = \pi$ (left column) or $\beta = \pi/4$ (right column). The angular speed is varied whilst the inverse adS length scale is kept fixed $a = 1$.

**Anisotropic pressure**

The final quantity to consider is the anisotropic pressure. Unlike in four-dimensions, where there were four nonzero components of the anisotropic pressure, in three-dimensions there are only two: $\Pi^{(\rho)(\rho)}$ and $\Pi^{(\phi)(\phi)}$. Additionally, they are subject to a tracelessness condition $\Pi^{(\rho)(\rho)} + \Pi^{(\phi)(\phi)} = 0$. To that end, in the proceeding figures, we elect to show only one of these components, since the other is directly related and will thus have the same features.

Figure 5.67 shows the anisotropic pressure when Dirichlet boundary conditions are applied to the field; figure 5.68 is the anisotropic pressure when Neumann boundary conditions are applied; and finally, for transparent boundary conditions applied to the field, figure 5.69 shows the anisotropic pressure. For all cases of inverse temperature and angular speed considered, the anisotropic pressure is zero at both the origin and on the boundary. Additionally, the component takes its absolute maximum between the two, with the effect of increasing the angular speed corresponding to a shifting of the location of this absolute maximum, moving away from the origin and towards the boundary. Increasing the angular speed seemingly has no effect on the magnitude of the absolute maximum; instead, this is dominated by the temperature dependence.

We now return our attention to figure 5.67, which shows the pressure deviator (component) for Dirichlet boundary conditions. We see that, at high angular speeds, the anisotropic pressure component begins below the $\rho$ axis, before switching at around $\rho = 3\pi/8$, increasing to its absolute maximum before rapidly decaying to zero on the boundary. The relative difference in magnitudes of the negative and positive portions is larger for higher temperatures; that is, at higher temperatures the anisotropic pressure component dips below the $\rho$ axis to a lesser extent than at lower temperatures. What is remarkable is that we do not see this feature for the cases of Neumann (figure 5.68) or transparent (figure 5.69) boundary conditions. Instead, they always remain positive for all $\rho$, with the exception of the case of zero rotation. Indeed, at zero angular speed (top row) the anisotropic pressure

component for Neumann boundary conditions is exactly the negative of the corresponding component for Dirichlet boundary conditions, and is identically zero for transparent boundary conditions. That is why, on the top row of figure 5.69, the angular speed is $\Omega = 0.02$ and not $\Omega = 0$. For all nonzero angular speeds and temperatures, the anisotropic pressure component $\Pi^{(\rho)(\rho)}$ is negative for Neumann and transparent boundary conditions and, as such, figures 5.68 and 5.69 show the negative of this component, corresponding to $-\Pi^{(\rho)(\rho)} = \Pi^{(\phi)(\phi)}$.

As was the case for the heat flux, the temperature seems to have less of an effect on the anisotropic pressure for the cases of Neumann and transparent boundary conditions, since the curves for varying temperature are much closer together compared to the corresponding curves for Dirichlet boundary conditions. Also in a similar fashion to the heat flux, there is a slight kink in the highest temperature curve of the left column plots, most likely corresponding to an anomalous data point rather than a physically significant feature.

Finally, figure 5.70 shows the absolute value of the anisotropic pressure components at two fixed values of the inverse temperature. It is clear from these figures that for zero rotation, the anisotropic pressure components for Dirichlet and Neumann boundary conditions are exact negatives of each other and, as the angular speed is increased, this is no longer the case. For the low temperature plots (left column), regardless of angular speed, the component corresponding to Dirichlet boundary conditions always takes the lowest magnitude of the three boundary conditions. Conversely, at the higher temperature considered (right column), the component corresponding to Dirichlet boundary conditions only takes the lowest magnitude for the highest angular speed considered ($\Omega = 0.96$), and even then, this is not true very close to the boundary - the component corresponding to transparent boundary conditions takes the lowest absolute value here. Since the component corresponding to Neumann boundary conditions always has the highest magnitude in the anisotropic pressure, this indicates that Neumann boundary conditions produce the most significant quantum effects and, depending on the temperature and angular speed, either

Dirichlet or transparent boundary conditions produce the least significant quantum effects (when measuring the size of quantum effects based upon the magnitude of the anisotropic pressure).

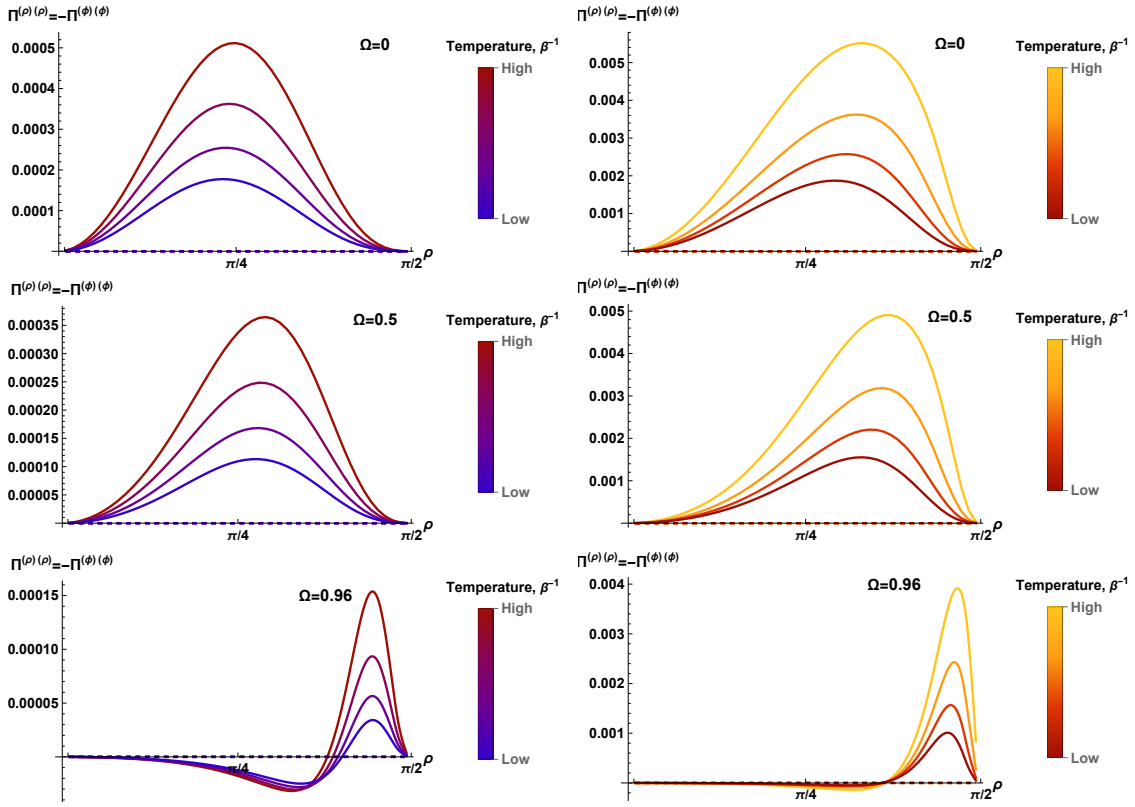


Figure 5.67: The nonzero components of the anisotropic pressure of the QFT-RSET (solid lines) - it is identically zero for the RKT-SET (dashed lines). Dirichlet boundary conditions are applied to the field and the inverse adS length scale is kept fixed $a = 1$. The angular speed and inverse temperature are varied, with the latter in the range $\beta \in [\pi/6, 5\pi/12] \cup [3\pi/4, \pi]$, for the right and left plots respectively.

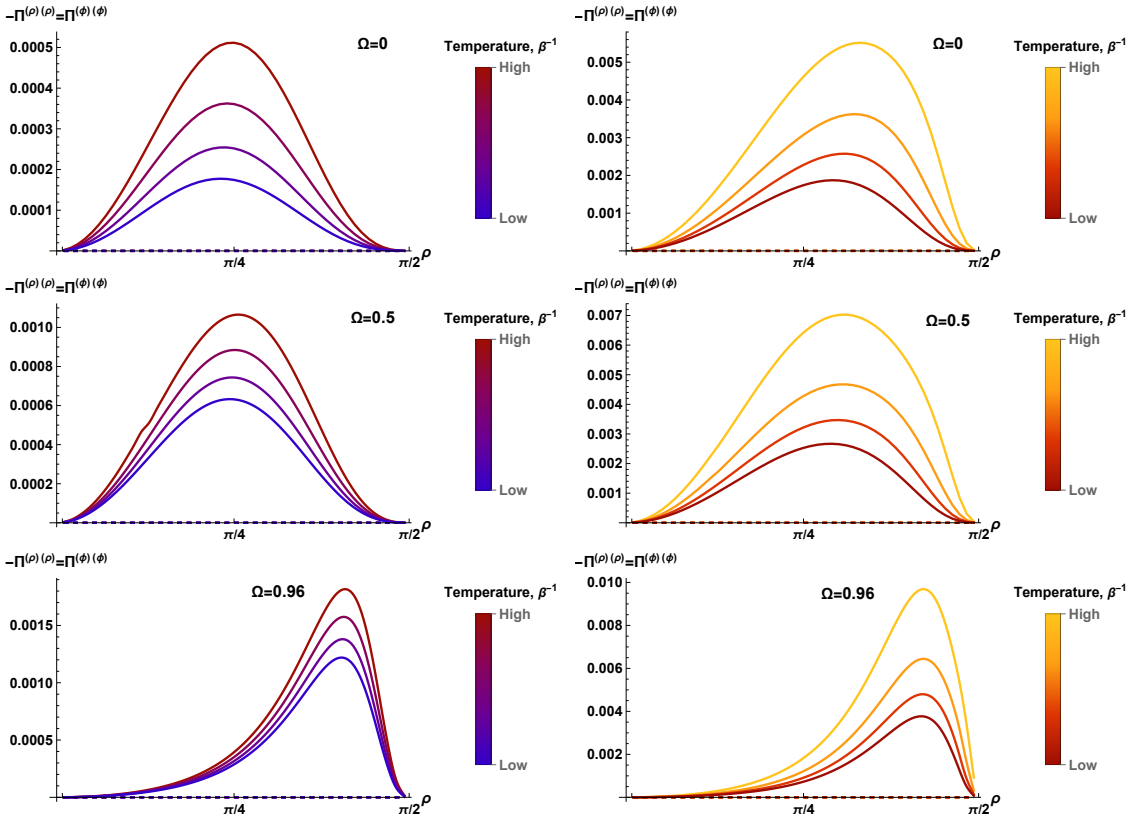


Figure 5.68: The nonzero components of the anisotropic pressure of the QFT-RSET - it is identically zero for the RKT-SET. Neumann boundary conditions are applied to the field and the inverse adS length scale is kept fixed $a = 1$. The angular speed and inverse temperature are varied, with the latter in the range $\beta \in [\pi/6, 5\pi/12] \cup [3\pi/4, \pi]$, for the right and left plots respectively.

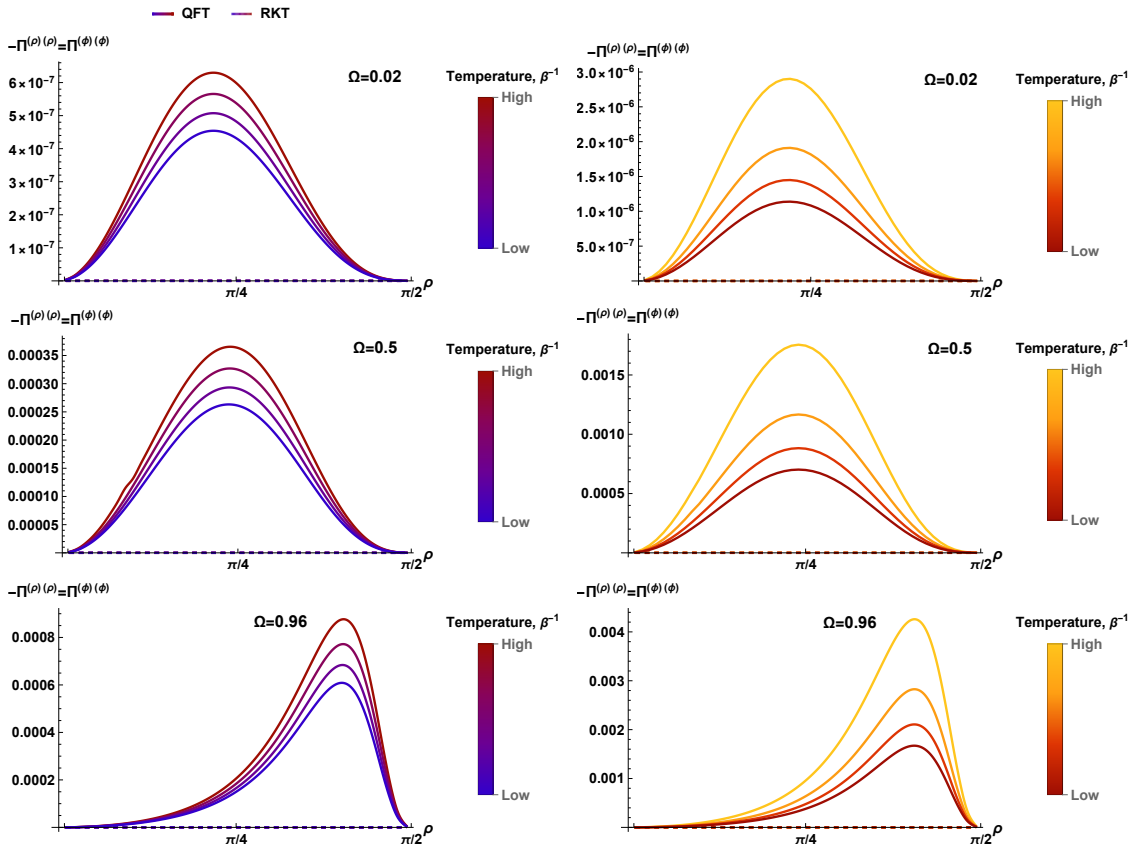


Figure 5.69: The nonzero components of the anisotropic pressure of the QFT-RSET - it is identically zero for the RKT-SET. Transparent boundary conditions are applied to the field and the inverse adS length scale is kept fixed $a = 1$. The angular speed and inverse temperature are varied, with the latter in the range $\beta \in [\pi/6, 5\pi/12] \cup [3\pi/4, \pi]$, for the right and left plots respectively.

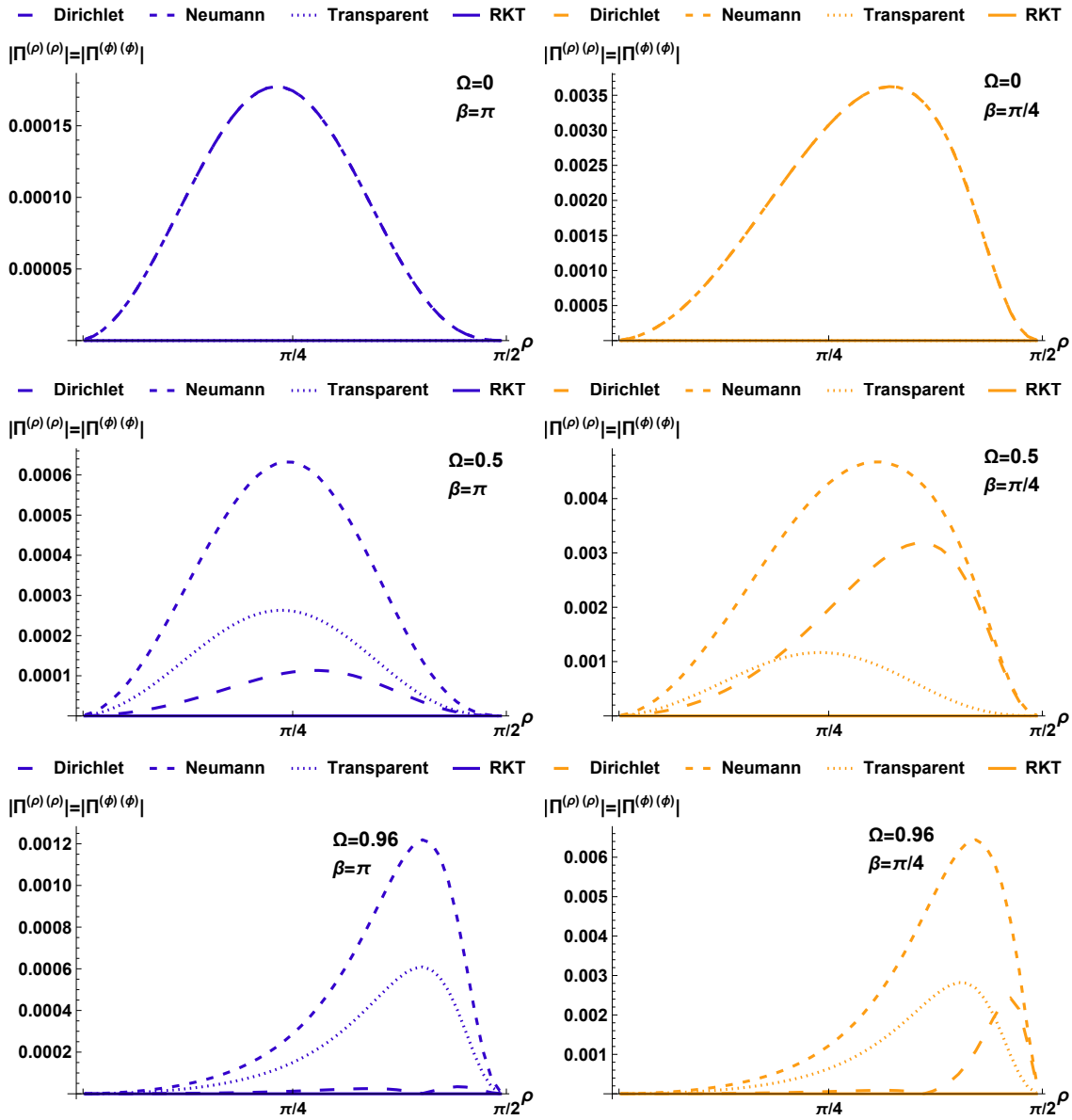


Figure 5.70: The absolute value of the nonzero anisotropic pressure components of the QFT-RSETs, for the three different boundary conditions of interest. The inverse temperature is either $\beta = \pi$ (left column) or $\beta = \pi/4$ (right column). The inverse adS length scale is kept fixed, whilst the angular speed is varied.

## § 5.4 Is RKT a suitable approximation to QFT? Summary of the chapter

In this chapter, the renormalised stress-energy tensor has been constructed in three- and four-dimensional anti-de Sitter space-time, in a thermal Hadamard state $|\beta\rangle$ using state subtraction with respect to the global anti-de Sitter space vacuum. This was done for static and rigidly-rotating, massless and conformally-coupled quantum scalar fields satisfying Dirichlet, Neumann or transparent boundary conditions at the space-time boundary. We have found semi-analytic expressions for all four renormalised stress-energy tensors, expressed in terms of the inverse temperature $\beta$ (of the quantum state in which the RSETs were constructed), the global anti-de Sitter space radial coordinate $\rho$, the polar angular coordinate $\theta$ and the angular speed $\Omega$ (of the rigid rotation (4.4.1)). In addition, by specifying suitable vielbeins (in section 4.4), we have written these renormalised stress-energy tensors in terms of the thermometer frame (2.3.3) in order for us to evaluate the physical quantities (2.3.4).

We also considered the general relativistic kinetic theoretic stress-energy tensor (2.3.11) (constructed in section 2.3), which models the scalar field as a classical gas of noninteracting bosonic particles. We gave the RKT-SETs in terms of the thermometer frame (2.3.3), before using the vielbeins constructed in section 4.4 to find the corresponding RKT-SETs in global anti-de Sitter space coordinates, for three- and four-dimensional, (non)rotating anti-de Sitter space.

Using the RKT-SETs and the RSETs in the thermometer frame, in section 5.3.4, we compared the RKT-SETs with the corresponding RSETs. We found that, at high temperatures (and all values of the angular speed), the RKT-SETs were good approximations of the RSETs. At lower temperatures, the agreement between the RKT-SETs and the RSETs was no longer as strong; quantum effects became more significant. This result is in accordance with the findings for both scalars [13] and fermions [16] in nonrotating anti-de Sitter space. These results are not unexpected; by increasing the temperature of

the quantum state, we are, in effect, increasing the number of quantum particles in the state. Any large number of quantum particles will be well approximated by a classical gas of particles.

Furthermore, it was found that the RKT-SET best approximated the QFT-RSET when transparent boundary conditions were applied to the quantum scalar field. This is an interesting result. One can postulate, perhaps, that this is due to the distribution function chosen in order to model the classical gas. Since transparent boundary conditions essentially allow the quantum scalar field to pass beyond the anti-de Sitter space boundary, we are effectively 'losing' information about the quantum scalar field, and in particular the total energy (within the adS boundary) will decrease. Likewise, using the Bose-Einstein distribution (2.3.6) to model the classical gas of particles, we did not impose any boundary conditions (at the adS boundary) on the distribution function itself, meaning the gas of particles was also allowed to pass beyond the anti-de Sitter space boundary. It is therefore clear why the RKT-SET best approximates the QFT-RSET when the field satisfies transparent boundary conditions. If we were to improve the approximation when reflective boundary conditions are imposed on the quantum field, we would have to modify the Bose-Einstein distribution (2.3.6) in such a way to artificially insert a boundary and impose suitable (reflective) conditions on the distribution function there, to ensure the classical gas of particles cannot pass beyond this boundary. The explicit conditions one would need to impose on the distribution function are currently unclear, but it would be interesting to investigate this further.

By decomposing the stress-energy tensors into the thermometer frame (2.3.3), we were able to extract four physical quantities that describe both theories: the energy density, pressure, heat flux and anisotropic pressure. For a massless, conformally-coupled scalar field, the pressure and energy density are always related by an integer multiple, and thus we neglected the pressure in the analyses of the stress-energy tensors. In a classical theory, the heat flux and anisotropic pressure are always zero, and so we used these as measures of

quantum deviation from the classical RKT model. The stress-energy tensors corresponding to rigidly-rotating quantum states have a more complicated form than the corresponding nonrotating stress-energy tensors, with a nonzero azimuthal heat flux component, and extra independent anisotropic pressure components. Furthermore, in the case of rigidly rotating fermions, the anisotropic pressure contains only diagonal elements [15, 19]; this is unlike the situation we find for scalar fields, where the anisotropic pressure has nonzero off-diagonal components (in four dimensions). It is surprising that the stress-energy tensor for the quantum scalar field has fewer symmetries than the stress-energy tensor for the quantum fermion field [19].

In the case of the quantum scalar field, we find that the qualitative behaviour of the energy density (and hence the pressure) is independent of the inverse temperature $\beta$ and angular speed $\Omega$. We find that they always have a maximum at the anti-de Sitter space origin, and monotonically decrease towards the space-time boundary. This in contrast with the situation for rigidly rotating fermions, where it was found that the location of the maximum moved towards the boundary as the angular speed increased [15]. We therefore conclude that the (rigid) rotation has a less dramatic effect on scalar fields than it does on fermion fields; this is perhaps due to the nonzero spin of a fermion field coupling to the rigid rotation.

We explored how each stress-energy tensor (in particular their components) depends on: the space-time and frame coordinates; angular speed of the rigid rotation; the inverse temperature of the quantum state and the bosonic gas; and the boundary conditions applied to the quantum scalar field. Of the dependent variables that we varied in the analyses (angular speed $\Omega$ and inverse temperature $\beta$), we found that the inverse temperature had the greatest effect on the magnitude of the stress-energy components, whilst the angular speed had the greatest effect on the qualitative behaviour. In addition, we found that the rigid-rotation broke the symmetry of the system, and that, at higher temperatures, the boundary conditions had less of an effect on the stress-energy tensor components (in

particular the thermometer frame decomposition); this is in accordance with results found in [266] for a nonrotating, conformally-coupled quantum scalar field on four-dimensional anti-de Sitter space, when the scalar field satisfies Robin boundary conditions at the spacetime boundary.

The next step in this thesis, in part III, is to take the stress-energy tensors constructed in this chapter and use them as source terms in both the linearised (chapters 7 and 8) and nonlinear (chapter 9) quantum-corrected Einstein equations.

# Part III

# Quantum-corrected anti-de Sitter space-time

# Chapter 6

# Quantum-corrected maximally symmetric space-times

"If people do not believe that mathematics is simple, it is only because they do not realise how complicated life is."

*John Von Neumann*

In this chapter, we present some simple solutions of the quantum-corrected Einstein equations (3.6.15) when the background space-time is maximally symmetric. In section 6.1, we consider the simplest possible background space-time: Minkowski space-time (i.e. flat space-time); in section 6.2, we consider de Sitter space-time; whilst in section 6.3 the background space-time is taken to be anti-de Sitter space-time; and, in section 6.4, we consider the Einstein static universe[1]; finally, in section 6.5, we consider the Bañados-Teitelboim-Zanelli (BTZ) space-time[2]. We consider the cases when the quantum scalar field is in either: a thermal state - Minkowski, the ESU and BTZ; or the vacuum state - Minkowski, the ESU, de Sitter, anti-de Sitter and the BTZ space-time.

## § 6.1 Minkowski space-time

In this section, we consider solutions to the QCEE (3.6.15) when the background space-time is four-dimensional Minkowski space, with line element

$$\mathrm{d}s^2 = -\,\mathrm{d}t^2 + \mathrm{d}x^2 + \mathrm{d}y^2 + \mathrm{d}z^2. \tag{6.1.1}$$

Throughout most of this thesis, we have only considered massless particles. However, for quantum-corrections to Minkowski space-time, we will also consider massive particles, since the vacuum and thermal expectation values of the stress-energy tensor have the same structure. This will be detailed in the following section.

### 6.1.1 RSET on Minkowski space-time

To compute the renormalised stress-energy tensor, we require the Hadamard Green function (2.5.27), which we constructed already in section 2.5 for the Minkowski vacuum state. For

[1]The author is aware that the ESU is indeed not maximally symmetric. Its inclusion is argued in the corresponding section of this chapter, section 6.4.

[2]Whilst the BTZ space-time is not globally maximally-symmetric, it is locally isometric to anti-de Sitter space and thus locally maximally-symmetric. It is for these reasons we justify its inclusion in this chapter.

clarity, this will be reproduced here, given in terms of the modified Bessel function of the second kind as

$$G_0^{(1)}(x,x') = \frac{1}{4\pi^2}\frac{m}{\sqrt{2\sigma(x,x')}}K_1\left(m\sqrt{2\sigma(x,x')}\right), \tag{6.1.2}$$

where we have inserted the zero subscript to indicate that this is the vacuum Hadamard Green function, and $\sigma(x,x')$ is Synge's world function between two space-like separated points $x = (t,\mathbf{x})$ and $x' = (t',\mathbf{x}')$, given in Minkowski space-time as

$$\sigma(x,x') = \frac{1}{2}(x-x')^2 = \frac{1}{2}\eta_{\mu\nu}(x^\mu - x'^\mu)(x^\nu - x'^\nu), \tag{6.1.3}$$

where $\eta_{\mu\nu}$ is the Minkowski metric. The (vacuum) Hadamard Green function (6.1.2) only depends on Synge's world function and thus the separation of the two space-like separated points $x$ and $x'$; we can thus treat the vacuum Hadamard Green function as a scalar, not a biscalar. This is due to the maximal symmetry of Minkowski space-time.

To construct the corresponding thermal Hadamard Green function (at fixed inverse temperature $\beta$), one must perform a Matsubara sum of the vacuum Hadamard Green function:

$$G_\beta^{(1)}(x,x') = \sum_{j=-\infty}^{\infty} G_0^{(1)}(t+ij\beta,\boldsymbol{x};t',\boldsymbol{x}'). \tag{6.1.4}$$

To find the thermal and vacuum expectation values of the stress-energy tensor, the following coincidence limit is performed [45]

$$\langle\widehat{T}_{\mu\nu}\rangle_{0/\beta} = \lim_{x'\to x}\left\{\mathcal{T}_{\mu\nu}\left[G_{0/\beta}^{(1)}(x,x')\right]\right\}, \tag{6.1.5a}$$

where the operator $\mathcal{T}_{\mu\nu}$ is given as

$$\mathcal{T}_{\mu\nu} = \delta_\nu^{\ \nu'}\partial_\mu\partial_{\nu'} - \frac{1}{2}\eta_{\mu\nu}\eta^{\gamma\delta}\partial_\gamma\partial_{\delta'} - \frac{1}{2}\eta_{\mu\nu}m^2. \tag{6.1.5b}$$

When the coincidence limit $x' \to x$ is taken, both the vacuum and thermal expectation values (6.1.5) are infinite. In Minkowski space-time, this is resolved by setting the vacuum expectation value of the stress-energy tensor (the zero-point energy density) equal to zero - see section 2.4. For the thermal expectation values, state subtraction is then utilised;

because the vacuum and thermal states both share the same, state-independent, short-distance singularity structure, by taking the difference between the thermal and vacuum Green functions, the resulting difference will not have any singularities and the coincidence limit will therefore be finite (see section 2.7.1). Since the vacuum Hadamard Green function corresponds to the $j = 0$ term in the Matsubara sum (6.1.4), the difference between the thermal and vacuum Hadamard Green functions is then

$$G_\beta^{(1)}(x, x') = \sum_{j\neq 0} G_0^{(1)}(t + ij\beta, \boldsymbol{x}; t', \boldsymbol{x}'), \tag{6.1.6}$$

in the same way as in chapter 5. We are therefore considering the difference between the thermal and vacuum expectation values of the stress-energy tensor, which we denote as

$$\langle :\widehat{T}_{\mu\nu}: \rangle_\beta \equiv \langle \widehat{T}_{\mu\nu} \rangle_\beta - \langle \widehat{T}_{\mu\nu} \rangle_0, \tag{6.1.7}$$

where the colons either side of the stress-energy tensor refer to normal ordering.

The thermal expectation values of the stress-energy tensor take the perfect fluid form

$$\langle :\widehat{T}_{\mu\nu}: \rangle_\beta = \mathrm{Diag}\left\{E(\beta), P(\beta), P(\beta), P(\beta)\right\}, \tag{6.1.8}$$

where the energy density $E(\beta)$ and pressure $P(\beta)$ for a quantum scalar field are given by the relations [13]

$$E(\beta) - 3P(\beta) = \frac{m^3}{2\pi^2} \sum_{j=1}^{\infty} \frac{1}{j} K_1(mj\beta), \qquad P(\beta) = \frac{m^2}{2\pi^2\beta^2} \sum_{j=1}^{\infty} \frac{1}{j^2} K_2(mj\beta), \tag{6.1.9}$$

where $K_\upsilon$ are modified Bessel functions. By using the asymptotic properties of the modified Bessel functions as $|z| \to 0$, namely [280]

$$K_\upsilon(z) \sim \frac{\Gamma(\upsilon)}{2} \left(\frac{2}{z}\right)^\upsilon, \qquad 0 < |z| \ll \sqrt{\upsilon + 1}, \quad \upsilon > 0, \tag{6.1.10}$$

we find the following expressions for the energy density and pressure in the massless case:

$$E(\beta)\rfloor_{m=0} = 3P(\beta)\rfloor_{m=0} = \frac{\pi^2}{30\beta^4}. \tag{6.1.11}$$

What is particularly remarkable is that thermal expectation value of the stress-energy tensor is identical to the RKT-SET for four-dimensional Minkowski space-time [13]. In the massless case, this is most easily seen by comparing the thermal expectation value of the stress-energy tensor (6.1.8) with the RKT-SET (5.3.12) computed in section 5.3.1. In addition, one could take the RKT-SET (2.3.42) computed for rigidly-rotating distributions on Minkowski space-time and set the angular speed to zero, $\Omega \to 0$. For the massive case, see [9, 12, 207].

### 6.1.2 Quantum-corrected Einstein equations

Now that we have the vacuum and thermal expectation values of the stress-energy tensor, we can solve the quantum-corrected Einstein equations. We will first focus on the QCEE when the scalar field is in the vacuum state, before considering the case when the scalar field is in a thermal state at inverse temperature $\beta$. Recall the general form of the QCEE (3.6.15). When using Minkowski space-time as the background, and the vacuum expectation value of the stress-energy tensor as the source, the QCEE read

$$G_{\mu\nu} = \langle \widehat{T}_{\mu\nu} \rangle_0. \tag{6.1.12}$$

Since the expectation value of the stress-energy tensor in the Minkowski vacuum is zero by construction, the QCEE now read

$$G_{\mu\nu} = 0, \tag{6.1.13}$$

which are precisely the classical Einstein equations for Minkowski space-time. Therefore, there are no quantum-corrections in this case, and the back-reaction problem is trivial.

This is not the case when we consider the quantum scalar field in the thermal state. The QCEE in this case then read, after raising an index for later convenience:

$$G_{\mu}{}^{\nu} = \langle \widehat{T}_{\mu}{}^{\nu} \rangle_\beta. \tag{6.1.14}$$

By taking advantage of the structure of the stress-energy tensor (6.1.8), we can isolate a contribution proportional to the metric, yielding

$$G_{\mu}{}^{\nu} = P(\beta)\delta_{\mu}{}^{\nu} - \mathrm{Diag}\{E(\beta) + P(\beta), 0, 0, 0\}. \tag{6.1.15}$$

By moving the term proportional to the metric over to the left-hand-side of the QCEE, we induce a negative cosmological constant

$$\widetilde{\Lambda} = -P(\beta), \tag{6.1.16}$$

such that the modified QCEE now read

$$G_{\mu}{}^{\nu} + \widetilde{\Lambda}\delta_{\mu}{}^{\nu} = -[E(\beta) + P(\beta)]\mathrm{Diag}\{1, 0, 0, 0\}. \tag{6.1.17}$$

The stress-energy tensor on the right-hand-side now has the pressureless dust form. There are a number of solutions to the classical Einstein equations that have a negative cosmological constant with a classical stress-energy tensor corresponding to pressureless dust, such as a Friedmann-Lemaître-Robertson-Walker type solution [190], or the Gödel solution [170]. However, since the induced negative cosmological constant changes the asymptotic behaviour and global structure of the space-time, we do not consider this case further, and leave it to future work.

## § 6.2 De Sitter space-time

De Sitter space-time is a vacuum solution to the classical Einstein equations with a positive cosmological constant $\Lambda = 3a^2 > 0$, with $a$ being the inverse radius of curvature. The metric of de Sitter space-time is given as [100, 101]

$$\mathrm{d}s^2 = a^{-2}\sec^2(\tau)\left[-\mathrm{d}\tau^2 + \mathrm{d}\rho^2 + \sin^2(\rho)\,\mathrm{d}\theta^2 + \sin^2(\rho)\sin^2(\theta)\,\mathrm{d}\phi^2\right]. \tag{6.2.1}$$

Solutions to the full semi-classical Einstein equations have been studied in great detail in the literature for solutions of de Sitter type, see, for example, [94, 171, 208]. Here, however,

we take the less ambitious approach of finding the quantum-corrected metric rather than considering solutions to the full SCEE.

### 6.2.1 RSET on de Sitter

To construct the renormalised stress-energy tensor on de Sitter space-time, we require the Hadamard Green function $G^{(1)}$, which is a solution of the Klein-Gordon equation

$$(-\Box_g + \xi_c R)\, G^{(1)}(x, x') = 0, \tag{6.2.2}$$

where $R = 12a^2$ is the Ricci scalar curvature of de Sitter space, $\xi_c = 1/6$ is the conformal coupling constant and $\Box_g = \nabla_\mu \nabla^\mu$ is the curved space-time d'Alembertian operator. By exploiting the maximal symmetry of de Sitter space, one can rewrite the Klein-Gordon equation so that the Hadamard Green function is given as the solution to the differential equation [3, 166]

$$\left[\left(Z^2 - 1\right) \frac{\mathrm{d}^2}{\mathrm{d}Z^2} + 4Z \frac{\mathrm{d}}{\mathrm{d}Z} + 2\right] f(Z) = 0, \tag{6.2.3}$$

where

$$Z(x, x') = \cos\big(a\, s(x, x')\big) \tag{6.2.4}$$

is a function of the geodetic distance $s(x, x')$ between two points $x$ and $x'$ connected by a unique geodesic in the maximally symmetric space. This holds since the Hadamard Green function is a function of the geodetic interval $s(x, x')$ by de Sitter invariance, and thus [3, 166]

$$G^{(1)}(x, x') = G^{(1)}(s(x, x')) = f(Z(x, x')) = f(Z). \tag{6.2.5}$$

A solution of the differential equation (6.2.3) is given by the hypergeometric function

$$f(Z) = {}_2F_1(1, 2, 2, [Z + 1]/2) = \frac{2}{1 - Z}, \tag{6.2.6}$$

and another solution is given by the hypergeometric function

$$f(Z) = {}_2F_1(2, 1, 2, [Z + 1]/2) = {}_2F_1(1, 2, 2, [Z + 1]/2), \tag{6.2.7}$$

where the second equality follows from properties of the hypergeometric function [280]. However, both solutions (6.2.6) and (6.2.7) are identical. A linearly independent solution is therefore given by $f(-Z)$, since the differential equation (6.2.3) is invariant under the map $Z \to -Z$ [3]. The general solution is then a linear combination of the two linearly independent solutions, given by

$$F(Z) = \mathfrak{f}_1 f(Z) + \mathfrak{f}_2 f(-Z), \tag{6.2.8}$$

where the constants $\mathfrak{f}_1$ and $\mathfrak{f}_2$ are fixed by the choice of state. We next describe how we fix this choice of state.

On the static patch of de Sitter space-time, there is a cosmological horizon, and thus there is a preferred temperature which corresponds to the temperature across said cosmological horizon [3, 169]. This preferred temperature fixes the unique de Sitter-invariant (i.e. maximally symmetric) quantum state in de Sitter space, given by the Bunch-Davies vacuum state [67, 83], also known as the "unique" vacuum of Schomblond [328]. We will not go into any more detail regarding the Bunch-Davies vacuum state; instead, see [3, 67]. Henceforth, we therefore only consider expectation values constructed in the Bunch-Davies vacuum, since it preserves the underlying maximal symmetry of de Sitter space. Note that other states on de Sitter space exist, and one can construct expectation values in these states, however we will not go into any detail on them in this thesis - instead, see, for example, [3, 270]. In the Bunch-Davies state, the Hadamard Green function $G^{(1)}(x, x')$ is only singular if its points $x$ and $x'$ are null separated, i.e. $x$ lies on the lightcone of $x'$. Recall the solution (6.2.8), and the relationship between the biscalar $Z$ and the geodetic distance (6.2.4). Since the hypergeometric function $f(Z)$ (6.2.6) is singular for $Z = 1$ (and $f(-Z)$ is singular for $Z = -1$), and the biscalar $Z$ is unity only when the space-time points are null separated (since the geodetic distance would then be zero), we can deduce that the contribution from $f(-Z)$ must be zero, since the Hadamard Green function can only be singular for null separated points. Therefore, $\mathfrak{f}_2 = 0$. To fix $\mathfrak{f}_1$, one would expand the

Hadamard Green function (6.2.8) into its short-distance singularity structure and match the leading-order divergences with the Hadamard parametrix (2.7.13). The constants in the linear combination (6.2.8) are thus given by [3, 328]

$$\mathfrak{f}_1 = \frac{a^2}{8\pi^2}, \quad \text{and} \quad \mathfrak{f}_2 = 0. \tag{6.2.9}$$

Therefore, the solution (6.2.8) (after substituting in the hypergeometric function (6.2.6)) reduces to

$$F(Z) = \frac{a^2}{4\pi^2}\frac{1}{1-Z}. \tag{6.2.10}$$

This leads to the following expression for the Hadamard Green function (inverting the transformation (6.2.5)) [3, 328]:

$$G^{(1)}(x,x') = \frac{a^2}{4\pi^2}\frac{1}{1-Z(x,x')}. \tag{6.2.11}$$

What is particularly remarkable is that the Hadamard Green function in the Bunch-Davies vacuum on de Sitter space-time exactly mimics the Hadamard Green function (5.1.1) in the vacuum state on anti-de Sitter space-time when $\lambda = 0$ (i.e. when transparent boundary conditions are applied to the field), under the length-scale transformation $a \to ia$. This is due to the dependence of the biscalar $Z(x,x')$ on the geodetic distance in de Sitter space (6.2.4) being exactly the same as the dependence in anti-de Sitter space (4.3.15), up to a Wick rotation of the radius of curvature [5]. Since the geodetic distance in anti-de Sitter space is the direct analytical continuation of the geodetic distance in de Sitter space [58], then the biscalar $Z(x,x')$ in both space-times is the same up to a redefinition of the domain of $Z$ with regards to the branch cut (i.e. which side of the branch cut $Z$ is taken to lie in) [5, 58]. Therefore, the Hadamard Green functions in de Sitter space and anti-de Sitter space are directly related by the Wick rotation $a \to ia$ *provided maximal symmetry is preserved*[3] [5, 58]. Additionally, since the differential operator one applies to the Hadamard Green

[3]For example, this would not hold when considering a thermal state in anti-de Sitter space since it breaks the underlying maximal symmetry of adS.

function to find the expectation value of the stress-energy tensor is linear in the Hadamard Green function, the vacuum expectation values of the stress-energy tensor in de Sitter and anti-de Sitter space are *also* directly related by the Wick rotation $a \to ia$. This means, to find the vacuum expectation value of the stress-energy tensor on de Sitter space-time, we can simply take the corresponding vacuum expectation value (5.1.25) on anti-de Sitter space-time, and perform the Wick rotation $a \to ia$. This results in the following vacuum expectation value of the stress-energy tensor:

$$\langle \widehat{T}_\mu{}^\nu \rangle_0 = \frac{a^2}{960\pi^2} \delta_\mu{}^\nu, \tag{6.2.12}$$

which, as expected, is proportional to the metric tensor and thus respects the underlying maximal symmetry of the Bunch-Davies vacuum state [67]. This result is in accordance with [67, 283, 349].

### 6.2.2 Quantum-corrected Einstein equations

Now that we have the vacuum expectation value of the stress-energy tensor, we are in a position to consider solutions to the QCEE, using the vacuum expectation value (6.2.12) as a source term. The QCEE, in this case, then read

$$G_\mu{}^\nu + \Lambda \delta_\mu{}^\nu = \frac{a^2}{960\pi^2} \delta_\mu{}^\nu, \tag{6.2.13}$$

and by combining the contributions proportional to the metric, the QCEE read

$$G_\mu{}^\nu + \widetilde{\Lambda} \delta_\mu{}^\nu = 0, \tag{6.2.14}$$

where the renormalised cosmological constant is given by

$$\widetilde{\Lambda} = 3a^2 - \frac{a^2}{960\pi^2} = \frac{a^2}{960\pi^2} \left(2880\pi^2 - 1\right) \approx 2.99989a^2 \quad \text{to 6 s.f.} \tag{6.2.15}$$

Therefore the effect of the back-reaction from the thermal and vacuum expectation values of the stress-energy tensor on a background de Sitter space-time is to simply renormalise

the cosmological constant (and therefore the characteristic length scale). The corrections to the cosmological constant are such that the magnitude of the cosmological constant is reduced by a very small factor.

## § 6.3 Vacuum anti-de Sitter space-time

The next background space-time with which the QCEE are constructed considered in this chapter is anti-de Sitter space-time. Since we have already covered anti-de Sitter space in depth in this thesis (see chapter 4), we will not elaborate on any details, nor will its inclusion be justified. The thermal and vacuum expectation values have already been computed in chapter 5, in particular sections 5.1 and 5.2. We only consider the vacuum expectation value in four dimensions in this section, since the back-reaction is somewhat simple in this case, whereas the back-reaction from the thermal expectation value in four-dimensions is much more complex - this forms the basis of chapter 9. In addition, since the vacuum expectation value in three dimensions is zero, the back-reaction problem is trivial and we thus do not consider it further, and back-reaction from the thermal expectation value in three dimensions is considered in chapter 7. Furthermore, we only consider expectation values corresponding to static (i.e. nonrotating) scalar fields, since the expectation values corresponding to rigidly-rotating scalar fields break the underlying maximal symmetry of anti-de Sitter space and thus the back-reaction problem is more complicated.

Recall the vacuum expectation value (5.1.25) of the stress-energy tensor in four dimensions. With this as the source term, the QCEE (3.6.15) read

$$G_\mu{}^\nu + \Lambda\delta_\mu{}^\nu = -\frac{a^2}{960\pi^2}\delta_\mu{}^\nu. \tag{6.3.1}$$

It is immediately obvious that this will follow the same derivation as in the de Sitter case in section 6.2, since the source term is directly proportional to the metric. As such, by moving this term over to the left-hand-side, we can renormalise the cosmological constant

as

$$\widetilde{\Lambda} = \Lambda + \frac{a^2}{960\pi^2} = -\frac{a^2}{960\pi^2}\left(2880\pi^2 - 1\right) \approx -2.99989a^2 \quad \text{to 6 s.f.,} \tag{6.3.2}$$

where the QCEE now read

$$G_\mu{}^\nu + \widetilde{\Lambda}\delta_\mu{}^\nu = 0. \tag{6.3.3}$$

In analogy with the de Sitter case, the effect of the back-reaction from the vacuum expectation value of the stress-energy tensor is to renormalise the cosmological constant (thereby reducing its magnitude by a very small factor) and hence the characteristic length scale.

## § 6.4 The Einstein static universe

The Einstein static universe is *not* a maximally symmetric solution of the classical Einstein equations. However, we argue its inclusion in this chapter by virtue of the fact that Minkowski, de Sitter and anti-de Sitter space-time, which *are* maximally symmetric, are conformal to part of the ESU. For more detail on the conformal relation between the ESU and adS, see section 4.2.

In global coordinates, the line element of the ESU is given as [128]

$$\mathrm{d}s^2 = a^{-2}\left[-\mathrm{d}\tau^2 + \mathrm{d}\rho^2 + \sin^2(\rho)\,\mathrm{d}\theta^2 + \sin^2(\rho)\sin^2(\theta)\,\mathrm{d}\phi^2\right]. \tag{6.4.1}$$

Classically, the ESU is a solution to the Einstein field equations with a positive cosmological constant $\Lambda = a^2$ and a nonzero stress-energy tensor

$${}^{\mathrm{dust}}T_\mu{}^\nu = -2a^2\mathrm{Diag}\{1,0,0,0\}, \tag{6.4.2}$$

which corresponds to pressureless dust. Following [326], for this section only, we reinstate the Newton constant. In this section, we therefore consider the modified QCEE:

$$G_\mu{}^\nu + \Lambda\delta_\mu{}^\nu = 8\pi G_N\left[{}^{\mathrm{dust}}T_\mu{}^\nu + \langle T_\mu{}^\nu\rangle^{\mathrm{ESU}}\right], \tag{6.4.3}$$

where $\langle T_\mu{}^\nu\rangle^{\mathrm{ESU}}$ is the expectation value of the stress-energy tensor in some quantum state. We have raised an index for later convenience, and have set the constants $\vartheta_1$ and $\vartheta_2$

appearing in the full semi-classical Einstein equations (3.2.38) equal to zero. This will be justified *a posteriori*. In the next section, we detail the process of finding the expectation value(s) of the stress-energy tensor.

### 6.4.1 RSET on the ESU

Finding the expectation values of the stress-energy tensor in the ESU is made easier by the fact that anti-de Sitter space is conformal to half of the ESU. Therefore, the vacuum Green function on the ESU is related to the corresponding vacuum Green function on adS when transparent boundary conditions are applied to the massless and conformally-coupled scalar field [31]. Since the vacuum Green functions are used to construct the thermal Green functions, the thermal Green functions will also be related. Indeed, the expectation value of the stress-energy tensor in a thermal state on the ESU is conformally related to the expectation value of the stress-energy tensor on adS in the corresponding thermal state [45, 71]:

$$\langle T_\mu{}^\nu \rangle^{\mathrm{adS}} = \langle \widehat{T}_\mu{}^\nu \rangle^{\mathrm{ESU}} \frac{\sqrt{-g^{\mathrm{ESU}}}}{\sqrt{-g^{\mathrm{adS}}}} - \frac{1}{2880\pi^2} \mathcal{H}^{(3)\nu}_\mu, \tag{6.4.4}$$

where $g^{\mathrm{ESU}}$ and $g^{\mathrm{adS}}$ are the determinants of the ESU (6.4.1) and adS (4.1.8) metrics, respectively, and

$$\mathcal{H}^{(3)}_{\mu\nu} = \frac{1}{3}\nabla_\mu\nabla_\nu R - \frac{1}{3}g_{\mu\nu}\nabla_\sigma\nabla^\sigma R - \frac{1}{6}g_{\mu\nu}R^2 + \frac{1}{3}RR_{\mu\nu} + R^{\rho\sigma}R_{\rho\mu\sigma\nu}, \tag{6.4.5}$$

is a purely geometric, state-independent and conserved tensor, that arises due to ambiguities in the renormalisation procedure - see section 3.2. The determinant of the adS metric is

$$g^{\mathrm{adS}} = -a^{-8}\sec^8(\rho)\sin^4(\rho)\sin^2(\theta), \tag{6.4.6}$$

whilst for the ESU metric, we have

$$g^{\mathrm{ESU}} = -a^{-8}\sin^4(\rho)\sin^2(\theta). \tag{6.4.7}$$

Equation (6.4.4) therefore reduces to

$$\langle T_\mu{}^\nu\rangle^{\mathrm{adS}} = \cos^4(\rho)\langle \widehat{T}_\mu{}^\nu\rangle^{\mathrm{ESU}} - \frac{1}{2880\pi^2}\mathcal{H}_\mu^{(3)\nu}. \tag{6.4.8}$$

Since the tensor $\mathcal{H}^{(3)}$ is state-independent, the difference between the thermal and vacuum expectation values of the stress-energy tensor on adS is conformally related to the corresponding difference on the ESU, yielding

$${}^{\mathrm{adS}}\widetilde{T}_\mu{}^\nu = {}^{\mathrm{ESU}}\widetilde{T}_\mu{}^\nu \cos^4(\rho), \tag{6.4.9}$$

where ${}^{\mathrm{adS}}\widetilde{T}_\mu{}^\nu$ is the difference between thermal and vacuum expectation values of the stress-energy tensor (5.3.42) when transparent boundary conditions are applied to the field on adS, and

$${}^{\mathrm{ESU}}\widetilde{T}_\mu{}^\nu = \langle\beta|\widehat{T}_\mu{}^\nu|\beta\rangle^{\mathrm{ESU}} - \langle 0|\widehat{T}_\mu{}^\nu|0\rangle^{\mathrm{ESU}} \tag{6.4.10}$$

is the corresponding difference on the ESU. We have the difference ${}^{\mathrm{ESU}}\widetilde{T}_\mu{}^\nu$ by using the adS RSET (5.3.42) along with equation (6.4.9), and the expectation value of the stress-energy tensor in the vacuum state is given by [59, 66, 71]

$$\langle 0|\widehat{T}_\mu{}^\nu|0\rangle^{\mathrm{ESU}} = \frac{a^2}{480\pi^2}\mathrm{Diag}\{-3,1,1,1\}. \tag{6.4.11}$$

We can therefore write the expectation value of the stress-energy tensor as

$$\langle \widehat{T}_\mu{}^\nu\rangle_{\mathcal{P}}^{\mathrm{ESU}} = a^2\mathcal{P}\,\mathrm{Diag}\{-3,1,1,1\}, \tag{6.4.12}$$

where $\mathcal{P}$ is a state-dependent constant, given by

$$\mathcal{P} = \begin{cases} \dfrac{1}{480\pi^2}, & \text{vacuum state,} \\ \dfrac{1}{6\pi^2}f_3(a\beta), & \text{difference in thermal and vacuum states,} \\ \dfrac{1+80f_3(a\beta)}{480\pi^2}, & \text{thermal state,} \end{cases} \tag{6.4.13}$$

where $f_3$ is defined in equation (5.1.18).

### 6.4.2 Quantum-corrected Einstein equations

The modified QCEE (6.4.3), after substituting in the expectation value of the stress-energy tensor, read

$$G_\mu{}^\nu + \Lambda\delta_\mu{}^\nu = 8\pi G_N \left[-2a^2\mathrm{Diag}\{1,0,0,0\} + a^2\mathcal{P}\mathrm{Diag}\{-3,1,1,1\}\right]. \tag{6.4.14}$$

A contribution proportional to the metric can be isolated on the right-hand-side:

$$G_\mu{}^\nu + \Lambda\delta_\mu{}^\nu = 8\pi G_N \left[-2a^2\mathrm{Diag}\{1,0,0,0\} + a^2\mathcal{P}\mathrm{Diag}\{-4,0,0,0\} + a^2\mathcal{P}\delta_\mu{}^\nu\right], \tag{6.4.15}$$

and by moving this over to the left-hand-side,

$$G_\mu{}^\nu + \left(\Lambda - 8\pi G_N a^2\mathcal{P}\right)\delta_\mu{}^\nu = 8\pi G_N \left[-2a^2\mathrm{Diag}\{1,0,0,0\} + a^2\mathcal{P}\mathrm{Diag}\{-4,0,0,0\}\right], \tag{6.4.16}$$

we can define a renormalised cosmological constant (and therefore length scale) as:

$$\widetilde{\Lambda} = \widetilde{a}^2 = \Lambda - 8\pi G_N a^2\mathcal{P} = a^2\left(1 - 8\pi G_N\mathcal{P}\right). \tag{6.4.17}$$

By then combining the two terms on the right-hand-side, the modified QCEE read

$$G_\mu{}^\nu + \widetilde{\Lambda}\delta_\mu{}^\nu = -16\pi G_N a^2\mathrm{Diag}\{1+2\mathcal{P},0,0,0\}, \tag{6.4.18}$$

where the stress-energy tensor term on the right-hand-side takes the pressureless dust form. We can go a step further. As in [326], we can define a renormalised Newton constant

$$\widetilde{G}_N = G_N\frac{a^2}{\widetilde{a}^2}(1+2\mathcal{P}) = G_N\frac{1+2\mathcal{P}}{1-8\pi G_N\mathcal{P}}, \tag{6.4.19}$$

such that

$$\widetilde{a}^2\widetilde{G}_N = a^2 G_N(1+2\mathcal{P}). \tag{6.4.20}$$

This is done so that the modified QCEE now read

$$G_\mu{}^\nu + \widetilde{\Lambda}\delta_\mu{}^\nu = -16\pi\widetilde{G}_N\widetilde{a}^2\mathrm{Diag}\{1,0,0,0\}, \tag{6.4.21}$$

which are exactly the classical Einstein equations for the ESU with a renormalised length scale *and* Newton constant. Therefore, provided we renormalise both the Newton constant and length scale, the back-reaction from the expectation value(s) of the stress-energy tensor on the ESU does not change the structure or asymptotic behaviour of the background, and so, the quantum-corrected metric is still of ESU type (6.4.1). By the same reasoning, we are also justified in setting the constants $\vartheta_1$ and $\vartheta_2$ equal to zero in the modified QCEE (6.4.3).

ESU type solutions to the full semi-classical Einstein equations have been studied in depth, in particular in [326], where the author considers massive scalar fields with general coupling. In this section, we have taken a rather less ambitious approach; not only have we considered a massless and conformally-coupled scalar field, but we were only interested in the quantum-corrected metric, and not in solving the full semi-classical Einstein equations.

## § 6.5 The BTZ black hole

In this section, we provide a brief summary of the quantum-corrected Bañados-Teitelboim-Zanelli (BTZ) [32, 33] black hole as laid out in [78] (and also considered in [76, 77]). This section is not intended to be a detailed reproduction; instead, we describe the key and salient features. The reader is referred to the original paper [78] for a more detailed treatment. The reason for its inclusion in this thesis is that the (uncharged) BTZ black hole is locally isometric to the universal covering space of three-dimensional anti-de Sitter space. In addition, the BTZ metric is a later inspiration when we consider quantum-corrected solitons in chapters 7-9, and especially when we consider the 'mass' and 'angular momentum' of the solitons. As well as providing inspiration for our later solitonic approach, due to BTZ's local isometry to three-dimensional anti-de Sitter space, the quantum-corrected geometry provides a useful comparison when we consider (linear) quantum corrections to three-dimensional anti-de Sitter space in chapter 7.

The BTZ space-time is constructed by identifying points in (three-dimensional) anti-de Sitter space using a discrete group of isometries under a process called *orbifolding* [32, 33]. The metric for the classical (uncharged) BTZ geometry is [32, 33]

$$\mathrm{d}s^2 = \left(M - a^2 r^2\right) \mathrm{d}\tau^2 - J\,\mathrm{d}\tau\,\mathrm{d}\phi + \left(a^2 r^2 - M + \frac{J^2}{4r^2}\right)^{-1} \mathrm{d}r^2 + r^2\,\mathrm{d}\phi^2, \tag{6.5.1}$$

where the coordinate ranges are $\tau \in (-\infty, \infty)$, $r \in (0, \infty)$ and $\phi \in [0, 2\pi)$. The BTZ metric represents an uncharged black hole in $(2+1)$-dimensions which is a solution to the vacuum, classical Einstein equations (2.2.33) with a cosmological constant $\Lambda = -a^2$ and Ricci scalar $R = -6a^2$ [32, 33]. The constant $a$ is the characteristic length scale of the space-time, $M$ is the mass of the space-time and $J$ is the angular momentum of the space-time. Provided the bound

$$M \geq |J| > 0 \tag{6.5.2}$$

holds, the metric (6.5.1) describes a spinning black hole, which has an event horizon at

$$r_+ = \frac{1}{2a}\left(\sqrt{M + aJ} + \sqrt{M - aJ}\right). \tag{6.5.3}$$

When the black hole is static, there is no angular momentum $J$ and thus the metric becomes

$$\mathrm{d}s^2 = \left(M - a^2 r^2\right) \mathrm{d}\tau^2 + \left(a^2 r^2 - M\right)^{-1} \mathrm{d}r^2 + r^2\,\mathrm{d}\phi^2, \tag{6.5.4}$$

with the event horizon now at

$$r_+ = \frac{\sqrt{M}}{a}. \tag{6.5.5}$$

We can easily add a classical scalar field as a source term when the black hole is static (i.e. nonrotating). If we construct the action

$$\mathcal{S}_{\mathrm{BTZ}}[\Phi, g] = \int \mathrm{d}^3x \sqrt{-g}\left[\frac{1}{2\kappa}\left(R - 2\Lambda\right) - \frac{1}{2} g^{\mu\nu} \nabla_\mu \Phi \nabla_\nu \Phi - \frac{1}{16} R \Phi^2\right], \tag{6.5.6}$$

we can vary this with respect to the metric tensor $g_{\mu\nu}$ and the field $\Phi$ to obtain the classical Einstein field equations (from the Einstein-Hilbert Lagrangian term (2.2.11)) and the Klein-Gordon equation

$$\left(-\Box_g + \frac{1}{8} R\right) \Phi = 0. \tag{6.5.7}$$

The metric in the case is given by [32, 33, 78, 249]

$$\mathrm{d}s^2 = -f(r)\,\mathrm{d}\tau^2 + \frac{1}{f(r)}\,\mathrm{d}r^2 + r^2\,\mathrm{d}\phi^2, \tag{6.5.8}$$

where the lapse function $f(r)$ is

$$f(r) = \frac{a^2}{r}\,(r+C)^2\,(r-2C)\,, \tag{6.5.9}$$

where $C$ is an arbitrary integration constant, related to the exact form of the scalar field by

$$\Phi(r) = \sqrt{\frac{8C}{\kappa(r+C)}}. \tag{6.5.10}$$

Using the standard form of the classical stress-energy tensor (2.2.43) for conformally-coupled scalar fields, the BTZ space-time with a classical scalar field has stress-energy tensor [32, 33, 78]

$$T_\mu{}^\nu = \frac{a^2C^3}{\kappa r^3}\mathrm{Diag}\{1,1,-2\}. \tag{6.5.11}$$

Whilst we are primarily interested in the rotating solutions (so that we can compare our results in chapter 7), we include the static stress-energy tensor (6.5.11) since the renormalised stress-energy tensor for a quantum scalar field on static BTZ geometries takes a remarkably similar form. We detail the construction of the renormalised stress-energy tensor next.

### 6.5.1 RSET on BTZ

To construct the renormalised stress-energy tensor on the BTZ space-time, an elegant approach exploiting the method of images is used [78, 243, 248, 249, 334, 340]. In particular, since the BTZ space-time is locally isometric to the universal covering space of anti-de Sitter space, the Hadamard Green function can first be constructed on anti-de Sitter space before mapping back across to the BTZ space-time. The Hadamard Green function of anti-de Sitter space-time was constructed by using the conformal mapping between the

ESU and anti-de Sitter space, owing to the lack of global hyperbolicity of anti-de Sitter space (see section 4.6). A similar issue plagues the BTZ space-time. Indeed, since the BTZ space-time is also nonglobally hyperbolic [32, 33, 78], appropriate boundary conditions must be applied to the field. These boundary conditions correspond to the boundary conditions that are placed on the field in anti-de Sitter space (and thus the ESU), i.e. we consider Dirichlet, Neumann and transparent boundary conditions. See section 4.5 for a more detailed treatment of the boundary conditions on anti-de Sitter space. The upshot is that the Hadamard Green function of the BTZ space-time can be written in terms of the Hadamard Green function of anti-de Sitter space as [78, 340]

$$G^{(1)}_{\mathrm{BTZ}}(x,x') = \sum_{n\in\mathcal{I}} G^{(1)}_{\mathrm{adS}}(x, H^n x'). \tag{6.5.12}$$

The summation range $n \in \mathcal{I}$ is over all distinct images, and is dependent on the geometry one chooses (it will be different for say, a static black hole solution compared to a rotating black hole solution); meanwhile, $H^n$ is the *identification matrix* in $\mathbb{R}^{2,2}$ (the space which three-dimensional anti-de Sitter space is embedded in; see section 4.1), which maps every point in $\mathbb{R}^{2,2}$ to its image under the identification between the BTZ and anti-de Sitter space-times [78]. This matrix also depends on the geometry one chooses, with different matrices for, say, static and rotating black hole solutions.

With a suitably chosen identification matrix and summation range, it is straightforward to construct the renormalised stress-energy tensors for a variety of solutions in the BTZ space-times; one would follow the standard procedure [45, 103, 340] as laid out in section 2.7. For example, for a static black hole solution, the renormalised stress-energy tensor (for a quantum scalar field obeying transparent boundary conditions) in some generic Hadamard state $|\psi\rangle$ takes the remarkably simple form [78, 340]

$$\kappa\langle\widehat{T}_\mu{}^\nu\rangle = \frac{\ell_{\mathrm{P}}}{r^3}\mathcal{F}(M)\mathrm{Diag}\{1,1,-2\}, \tag{6.5.13a}$$

where $\ell_{\mathrm{P}}$ is the Planck length, and

$$\mathcal{F}(M) = \frac{M^{3/2}}{2\sqrt{2}} \sum_{n=1}^{\infty} \frac{\cosh\left(2n\pi\sqrt{M}\right) + 3}{\left[\cosh\left(2n\pi\sqrt{M}\right) - 1\right]^{3/2}}. \tag{6.5.13b}$$

What is particularly striking about the renormalised stress-energy tensor (6.5.13) is how similar it is to its classical counterpart (6.5.11); it has the same structure and coordinate dependence ($r^{-3}$). In contrast, the renormalised stress-energy tensor for a rotating black hole solution has the structure

$$\langle \widehat{T}_{\mu}{}^{\nu} \rangle \sim \begin{pmatrix} \langle \widehat{T}_{\tau}{}^{\tau} \rangle & 0 & \langle \widehat{T}_{\phi}{}^{\tau} \rangle \\ 0 & \langle \widehat{T}_{r}{}^{r} \rangle & 0 \\ \langle \widehat{T}_{\tau}{}^{\phi} \rangle & 0 & \langle \widehat{T}_{\phi}{}^{\phi} \rangle \end{pmatrix}, \tag{6.5.14}$$

the components of which can be found in [78, 340].

There has been a plethora of other works constructing renormalised stress-energy tensors on BTZ space-times, for example considering massive quantum scalar fields obeying Robin boundary conditions [69].

### 6.5.2 Quantum-corrected Einstein equations

Now that suitable renormalised stress-energy tensors have been constructed, we move onto solving the QCEE (3.6.15). Since the renormalised stress-energy tensors do not have the maximally-symmetric form (directly proportional to the metric tensor), solving the QCEE will not be such a simple task as renormalising the cosmological constant, as was the case for (vacuum) anti-de Sitter space; see section 6.3. Instead, we proceed by making a suitable ansatz for the quantum-corrected metric, depending on which solution one wishes to consider. In this section, we will briefly outline the two cases of a static and a rotating black hole.

We begin with the static black hole solution. If we make the ansatz

$$\mathrm{d}s^2_{\mathrm{QC}} = -A(r)\,\mathrm{d}\tau^2 + \frac{\mathrm{d}r^2}{B(r)} + r^2\,\mathrm{d}\phi^2, \tag{6.5.15}$$

then the QCEE become

$$\frac{B'}{2r} - a^2 = \kappa\langle\widehat{T}_\tau{}^\tau\rangle, \tag{6.5.16a}$$

$$\frac{BA'}{2rA} - a^2 = \kappa\langle\widehat{T}_r{}^r\rangle, \tag{6.5.16b}$$

$$\frac{AA'B' - B(A'^2 - 2AA'')}{4A^2} - a^2 = \kappa\langle\widehat{T}_\phi{}^\phi\rangle, \tag{6.5.16c}$$

where a prime denotes differentiation with respect to the function's argument. By using the QCEE (6.5.16a) and (6.5.16b), the QCEE (6.5.16c) becomes

$$\langle\widehat{T}_r{}^r\rangle' + \frac{A'}{2A}\left(\langle\widehat{T}_r{}^r\rangle - \langle\widehat{T}_\tau{}^\tau\rangle\right) + \frac{1}{r}\left(\langle\widehat{T}_r{}^r\rangle - \langle\widehat{T}_\phi{}^\phi\rangle\right) = 0. \tag{6.5.16d}$$

By taking the covariant derivative of the renormalised stress-energy tensor (6.5.13), we find the only nonzero component to be

$$\nabla^\mu\langle\widehat{T}_\mu{}^r\rangle = \langle\widehat{T}_r{}^r\rangle' + \frac{A'}{2A}\left(\langle\widehat{T}_r{}^r\rangle - \langle\widehat{T}_\tau{}^\tau\rangle\right) + \frac{1}{r}\left(\langle\widehat{T}_r{}^r\rangle - \langle\widehat{T}_\phi{}^\phi\rangle\right), \tag{6.5.17}$$

the right-hand-side of which is identical to the modified QCEE (6.5.16d). Therefore, provided the QCEE (6.5.16) hold, conservation of the renormalised stress-energy tensor (on the quantum-corrected metric) follows. When we find solutions to the QCEE in part III of this thesis, we find remarkably similar equations to the QCEE (6.5.16) and (6.5.17), in particular when considering nonlinear quantum corrections in four dimensions in chapter 9. In fact, some of the methodology and general techniques of chapter 9 were directly inspired by the corresponding methodology in [78], for example the decision to used the mixed indices version of the QCEE to simplify the algebra, and to rewrite the QCEE in a form that directly matches the conservation equation (see equations (9.2.4) and (9.2.5)).

Thus far, the equations above involving the renormalised stress-energy tensor are valid for a renormalised stress-energy tensor constructed for a conformally-coupled scalar field

satisfying either reflective or transparent boundary conditions. If we first consider reflective (i.e. Dirichlet and Neumann) boundary conditions, by taking the covariant derivative of the renormalised stress-energy tensor on the *background* space-time, one finds the following relation [243]

$$\langle \widehat{T}_r{}^r \rangle' + \frac{r}{r^2 - r_+^2} \left( \langle \widehat{T}_r{}^r \rangle - \langle \widehat{T}_\tau{}^\tau \rangle \right) + \frac{1}{r} \left( \langle \widehat{T}_r{}^r \rangle - \langle \widehat{T}_\phi{}^\phi \rangle \right) = 0, \tag{6.5.18}$$

where $r_+$ (6.5.5) was given earlier. By comparing with the relation (6.5.17), we see that, for fields satisfying reflective boundary conditions, in order for conservation of the RSET to hold (on the background), it must be that

$$\frac{A'}{2A} = \frac{r}{r^2 - r_+^2}. \tag{6.5.19}$$

One can solve the equation (6.5.19) above directly. Doing so gives the solution

$$A(r) = a^2 r^2 - M^2, \tag{6.5.20}$$

and by plugging this into the QCEE (6.5.16), one finds that $B = A$. Therefore, the QCEE (6.5.16) for quantum scalar fields satisfying reflective boundary conditions give the quantum-corrected metric to be the classical, static BTZ black hole (6.5.4), provided conservation of the RSET on the background space-time holds. If this relation does not hold, however, then the solution is incompatible with the quantum-corrected Einstein equations (6.5.16). On the other hand, if $A$ is such that

$$A \propto r^2 - r_+^2 + \mathcal{O}(\ell_{\mathrm{P}}), \tag{6.5.21}$$

then conservation of the RSET holds to linear order (in the Planck length $\ell_{\mathrm{P}}$) and thus the quantum-corrected Einstein equations would only be compatible to linear order. One would then have to consider the linearised, quantum-corrected Einstein equations in order to proceed.

Returning now to the case of transparent boundary conditions, it is clear from the form of the RSET (6.5.13) that the following relations hold [78]:

$$\langle \widehat{T}_\mu{}^\mu \rangle = 0, \quad \text{and} \quad \langle \widehat{T}_\tau{}^\tau \rangle = \langle \widehat{T}_r{}^r \rangle, \tag{6.5.22}$$

using which, the conservation equation (6.5.17) reduces to

$$\nabla^{\mu}\langle\widehat{T}_{\mu}{}^{r}\rangle = \langle\widehat{T}_{r}{}^{r}\rangle' + \frac{3}{r}\langle\widehat{T}_{r}{}^{r}\rangle. \tag{6.5.23}$$

Since $\langle\widehat{T}_{r}{}^{r}\rangle \propto r^{-3}$ (see equation (6.5.13a)), the conservation equation (6.5.23) is automatically satisfied. Next, equating the QCEE (6.5.16a) and (6.5.16b), after a little manipulation, we find the following equation

$$\frac{A'}{A} = \frac{B'}{B}, \tag{6.5.24}$$

and by substituting this back into the QCEE (6.5.16b) and integrating, we find

$$A = B = a^2r^2 - \mathfrak{b}_0 + 2\kappa\int r\langle\widehat{T}_{\tau}{}^{\tau}\rangle'\,\mathrm{d}r, \tag{6.5.25}$$

where $\mathfrak{b}_0$ is an arbitrary constant of integration, which we set equal to the mass, $\mathfrak{b}_0 = M$ (the reason for which becomes clear later). Inserting the explicit form of the renormalised stress-energy tensor (6.5.13a) into the solution (6.5.25), the integral can be computed exactly as

$$2\kappa\int r\langle\widehat{T}_{\tau}{}^{\tau}\rangle'\,\mathrm{d}r = -\frac{2\ell_{\mathrm{P}}F(M)}{r}, \tag{6.5.26}$$

and thus the quantum-corrected metric takes the form

$$\mathrm{d}s^2 = -\left(a^2r^2 - M - \frac{2\ell_{\mathrm{P}}F(M)}{r}\right)\mathrm{d}\tau^2 + \frac{\mathrm{d}r^2}{\left(a^2r^2 - M - \dfrac{2\ell_{\mathrm{P}}F(M)}{r}\right)} + r^2\,\mathrm{d}\phi^2. \tag{6.5.27}$$

Quantum corrections to the static black hole geometry do not modify the mass, but it is found that the horizon (6.5.5) is pushed outwards [76, 78, 243, 248, 249].

If we now consider nonstatic geometries, i.e. when the background space-time is rotating, we make an alternative ansatz

$$\mathrm{d}s^2_{\mathrm{QC}} = -N(r)f(r)\,\mathrm{d}\tau^2 + \frac{\mathrm{d}r^2}{N(r)} + r^2\left(\mathrm{d}\phi + N^{\phi}(r)\,\mathrm{d}\tau\right)^2. \tag{6.5.28}$$

In [78], for the rotating ansatz the quantum-corrected Einstein equations are linearised, by performing the perturbations

$$N(r) = N_0(r) + \ell_{\mathrm{P}}\delta N(r) + \mathcal{O}(\ell_{\mathrm{P}}^2), \tag{6.5.29a}$$

$$f(r) = f_0(r) + \ell_{\mathrm{P}}\delta f(r) + \mathcal{O}(\ell_{\mathrm{P}}^2), \tag{6.5.29b}$$

$$N^\phi(r) = N_0^\phi(r) + \ell_{\mathrm{P}}\delta N^\phi(r) + \mathcal{O}(\ell_{\mathrm{P}}^2). \tag{6.5.29c}$$

It is worth mentioning that, in chapter 7, we take a rather similar approach when considering the LQCEE (3.6.14) for rotating, three-dimensional anti-de Sitter space-time, by making a metric ansatz similar to the ansatz (6.5.28) and performing similar perturbations to the perturbations (6.5.29).

Taking the metric functions (6.5.29) and substituting into the LQCEE (3.6.14), the zeroeth-order equations read

$$f_0' = 0, \quad (N_0^\phi)'' + \frac{3}{r}(N_0^\phi)' = 0, \quad N_0'' + \frac{3}{r}N_0' = 8a^2, \quad N_0' + \frac{r^3(N_0^\phi)'^2}{2f_0^2} = 2a^2 r, \tag{6.5.30}$$

which have solutions

$$f_0 = 1, \quad N_0^\phi = -\frac{J}{2r^2}, \quad N_0 = a^2r^2 - M + \frac{J^2}{4r^2}. \tag{6.5.31}$$

With the zero-order solutions above, one recovers the metric (6.5.1).

The first-order QCEE are far too lengthy to reproduce here, and can be found in [78]. The upshot is that the first order perturbations of the metric functions have solutions [78]

$$\delta f(r) = \frac{\kappa}{\ell_{\mathrm{P}}}\int \mathrm{d}r \left(2r\langle\widehat{T}_{rr}\rangle + \frac{\langle\widehat{T}_{\phi\phi}\rangle}{rN_0(r)}\right) + \mathfrak{b}_1, \tag{6.5.32a}$$

$$\begin{aligned}\delta N(r) = &\int \mathrm{d}r \left[-2N_0(r)\delta f' - \delta f\left(\frac{2M}{r} - \frac{J^2}{r^3}\right)\right.\\ &\left.+\frac{2}{r^3}\int \mathrm{d}r\left(2Mr\delta f + \frac{\kappa}{\ell_{\mathrm{P}}}r^3N_0(r)\langle\widehat{T}_{rr}\rangle\right)\right] + \frac{\mathfrak{b}_2}{r^2} + \mathfrak{b}_3,\end{aligned} \tag{6.5.32b}$$

$$J\,\delta N^\phi(r) = -\delta N - 2N_0(r)\delta f + 2\int \mathrm{d}r\, r\left(2a^2\delta f + \frac{\kappa}{\ell_{\mathrm{P}}}N_0(r)\langle\widehat{T}_{rr}\rangle\right) + \mathfrak{b}_4, \tag{6.5.32c}$$

where the $\mathfrak{b}_i$ are arbitrary constants of integration. The solutions (6.5.32) have asymptotic behaviour at the space-time boundary

$$\delta f \sim r^{-3}, \quad \delta N \sim r^{-1}, \quad \delta N^\phi \sim r^{-3}, \quad r \to \infty. \tag{6.5.33}$$

The zero-order solutions (6.5.31) have asymptotic behaviour at the space-time boundary given by

$$f_0 = 1, \quad N_0 \sim r^2, \quad N_0^\phi \sim r^{-2}, \quad r \to \infty. \tag{6.5.34}$$

By comparing the asymptotic behaviour of the zero- and first-order perturbations of the metric functions, it is clear that the quantum corrections (which induce the higher-order perturbations) do not meaningfully modify the asymptotic structure (at the boundary) of the background space-time. In a similar fashion to the static, quantum-corrected black hole, the quantum corrections to the rotating black hole do not change the mass or angular momentum, but push the horizon (6.5.3) outwards [76, 78, 243, 248, 249].

## § 6.6 Summary

In this chapter, we have presented some simple solutions of the quantum-corrected Einstein equations (3.6.15). We started, in section 6.1, by considering flat space-time, where the thermal expectation value of the stress-energy tensor took the perfect-fluid form and was purely diagonal. We found that quantum corrections lead to an induced cosmological constant that was directly proportional to the pressure of the quantum scalar field under consideration. The quantum-corrected Einstein equations were then modified in such a way that the QCEE described a geometry corresponding to pressureless dust. However, we also found that the induced cosmological constant changed the asymptotic behaviour of the background space-time.

We next, in section 6.2, considered de Sitter space-time as the background. We first constructed the renormalised stress-energy tensor by comparing the Hadamard Green function on de Sitter space with the Hadamard Green function on anti-de Sitter space (constructed in section 4.6), and performing a suitable transformation. Since there is a preferred temperature on de Sitter space, we only considered the 'vacuum' expectation value of the stress-energy tensor. This vacuum expectation value of the stress-energy tensor is pro-

portional to the metric tensor and thus respects the underlying maximal symmetry of (background) de Sitter space. It followed that the quantum corrections amounted to a simple renormalisation of the cosmological constant (and thus the characteristic length scale).

We found a similar scenario in section 6.3, where we considered anti-de Sitter space-time, taking the quantum scalar field to be in the global vacuum state (i.e. the one that preserves anti-de Sitter invariance). The vacuum expectation value of the stress-energy tensor was found to be directly proportional to the metric tensor (thereby preserving anti-de Sitter invariance) and thus the effect of the quantum corrections was to renormalise the cosmological constant.

In section 6.4, we took the background space-time to be the Einstein static universe. Whilst the ESU is not maximally symmetric, its inclusion in this chapter was argued by virtue of its conformal relation with anti-de Sitter space. Using this conformal relation we were able to construct the renormalised stress-energy tensor in a rather elegant manner, exploiting state subtraction methods (see section 2.7.1). In order to fully consider the QCEE, we reinstated Newton's constant. We found that the quantum corrections amounted to a renormalisation of *both* the cosmological constant and Newton's constant, where the quantum-corrected geometry was then sourced by a pressureless-dust stress-energy tensor.

Finally, in section 6.5, we considered the case when the background space-time was the BTZ black hole, presenting work found in [78]. We started by constructing the Hadamard Green function on the BTZ space-time by identifying points on BTZ with points on anti-de Sitter space. Unlike the other background space-times considered in this chapter, the quantum-corrected Einstein equations could not be manipulated into a form where the quantum corrections simply induced a renormalisation of the cosmological constant (and Newton's constant). Instead, we were forced to make an ansatz for the quantum-corrected metric, in the cases where the background was either a static or rotating BTZ black hole.

In the static case, the QCEE were solved exactly, and it was found that the quantum corrections did not change the mass of the black hole, but did push its horizon outwards. In contrast, for the rotating BTZ black hole, it was not possible to find exact solutions, and instead a perturbative approach was utilised; we thus considered the linearised, quantum-corrected Einstein equations (3.6.14). With a suitable quantum-corrected metric ansatz, it was possible to find closed-form solutions to first order in the Planck length in terms of integrals of the renormalised stress-energy tensor components. It was found that the quantum corrections did not modify the global asymptotic structure of the background space-time, nor did it alter the mass of the black hole; instead, as for the static case, the quantum corrections pushed the horizon outwards.

The methodology of the quantum-corrected BTZ black hole, as laid out in [78] and section 6.5, directly inspire certain methods in part III of this thesis. For example, by analogy with the QC-rotating BTZ black hole, linearised quantum corrections in three-dimensional anti-de Sitter space are considered in chapter 7, by making the same metric ansatz as for the QC-rotating BTZ black hole. Additionally, in chapter 9, we consider (nonlinear) quantum corrections to four-dimensional anti-de Sitter space. The exact forms of the QCEE (with a suitably similar quantum-corrected metric ansatz) take remarkably similar forms to the QCEE for the static BTZ black hole. In particular, the choice to use the mixed-indices variant of the QCEE was directly inspired by the QC-static BTZ black hole in [78].

# Chapter 7

# Linear corrections in three dimensions

"Once, men turned their thinking over to machines in the hope that this would set them free. But that only permitted other men with machines to enslave them."

*Frank Herbert*

## § 7.1 Prelude

In this chapter, we consider linear quantum corrections in three-dimensional anti-de Sitter space-time, by solving, to first-order, the LQCEE (3.6.14). As mentioned in chapter 6, this is, in part, motivated by its relation to the (QC-) BTZ black hole, since a classical, uncharged BTZ black hole is locally isometric to three-dimensional anti-de Sitter space. Accordingly, we can compare the (first-order) quantum corrections to anti-de Sitter space with the corresponding corrections to the BTZ black hole, as laid out in [78] and section 6.5. For the BTZ black hole, it was found that the mass of the black hole was unaffected whilst the horizon of the black hole was pushed outwards. By considering quantum corrections to anti-de Sitter space (which does not have a black hole and thus horizon present), we can therefore ascertain the effect of the quantum corrections in the absence of a horizon, and in particular the effect on the mass and angular momentum of the space-time.

In order to facilitate the direct comparison with the BTZ black hole, and to make the proceeding analysis more tractable, we first make a change of radial coordinate. The coordinate transformation, and domain of the new radial variable, are as follows

$$r = \tan\left(\frac{\rho}{2}\right), \quad 0 \leq \rho < \pi/2 \implies 0 \leq r < 1. \tag{7.1.1}$$

The measure $\mathrm{d}\rho$ will transform to the measure $\mathrm{d}r$ in the following way:

$$\frac{\mathrm{d}\rho}{\mathrm{d}r} = \frac{2}{(1+r^2)} \implies \mathrm{d}\rho = \frac{2}{(1+r^2)}\,\mathrm{d}r. \tag{7.1.2}$$

Therefore, under the transformation (7.1.1), the rotating anti-de Sitter space metric (4.4.2) becomes

$$\begin{aligned}\mathrm{d}s_0^2 = a^{-2}\frac{(1+r^2)^2}{(1-r^2)^2}\Bigg\{&-\left[1-\frac{4r^2\Omega^2}{(1+r^2)^2}\right]\mathrm{d}\tau^2 + \frac{4}{(1+r^2)^2}\,\mathrm{d}r^2 \\ &+\frac{8\Omega r^2}{(1+r^2)^2}\,\mathrm{d}\tau\,\mathrm{d}\phi + \frac{4r^2}{(1+r^2)^2}\,\mathrm{d}\phi^2\Bigg\},\end{aligned} \tag{7.1.3}$$

where the zero subscript on the measure $\mathrm{d}s_0^2$ is inserted to distinguish between the zeroth (background) and higher-order perturbations of the metric when linearising later. For later convenience, we can rewrite the zeroth order metric as

$$\mathrm{d}s_0^2 = \frac{a^{-2}}{(1-r^2)^2}\left\{-\widetilde{\Gamma}_{(3)}^{-2}\,\mathrm{d}\tau^2 + 4\,\mathrm{d}r^2 + 8\Omega r^2\,\mathrm{d}\tau\,\mathrm{d}\phi + 4r^2\,\mathrm{d}\phi^2\right\}, \tag{7.1.4}$$

where we have defined the modified Lorentz factor

$$\widetilde{\Gamma}_{(3)} \coloneqq \left[(1+r^2)^2 - 4\Omega^2 r^2\right]^{-1/2}, \tag{7.1.5a}$$

related to the original Lorentz factor (4.4.4a) (after changing coordinates) by

$$\widetilde{\Gamma}_{(3)} = \left(1+r^2\right)^{-1}\Gamma_{(3)}. \tag{7.1.5b}$$

In the following section, we transform the stress-energy tensors constructed in chapter 5 into the new radial coordinate.

The layout of the remainder of this chapter is as follows. In section 7.2 we first take the renormalised stress-energy tensors (5.2.15) and (5.2.35), and the relativistic kinetic theory stress-energy tensor (5.3.23) and transform these under the transformation (7.1.1). In section 7.3, we construct the LQCEE, to zeroth- and first-order, by using an isotropic ansatz for the quantum-corrected metric. We then, in section 7.4, find first-order, analytical solutions to the LQCEE in the form of integrals of the stress-energy tensor components. In sections 7.5 and 7.6 we explicitly find the first-order solutions to the LQCEE when the stress-energy tensor components are given by the RKT-SET and the renormalised stress-energy tensor, respectively. Next, in section 7.7, we make a second metric ansatz that takes the (rotating) BTZ form, in order to interpret the quantum-corrected metric functions as solitons, and directly compare with the quantum-corrected, rotating BTZ black hole; in sections 7.7.1 and 7.7.2 we use the stress-energy tensor constructed using either RKT or QFT, respectively. Finally, in section 7.7.3, we analyse the solitons and compare our results with the QC-rotating BTZ black hole [78].

## § 7.2 Coordinate transformed (renormalised) stress-energy tensors

As we are using a different radial coordinate (in the metric) to find the first order perturbation of the LQCEE, we need to also transform the stress-energy tensor components so that they are expressed in terms of the new radial coordinate. This is the purpose of this section. We first deal with the nonrotating and rotating renormalised stress-energy tensors found in sections 5.2.1 and 5.2.2 respectively, before also transforming the relativistic kinetic theory stress-energy tensor constructed in section 5.3.2. For most components, it suffices to transform explicit instances of the old radial coordinate to the new radial coordinate. However, to transform the $\rho\rho$-components of the stress-energy tensors to $rr$-components, we must include the extra derivative factor as below:

$$\widetilde{T}_{rr} = \left(\frac{\mathrm{d}\rho}{\mathrm{d}r}\right)^2 \widetilde{T}_{\rho\rho}, \tag{7.2.1}$$

where the derivative prefactor is given in equation (7.1.2). We must also transform the $\rho\tau$- and $\rho\phi$-components, however for the stress-energy tensors of interest, these are zero.

### 7.2.1 RSET for static fields

The overall form of the renormalised stress-energy-tensor does not change when transforming coordinates. Indeed, equation (5.2.15b) still holds:

$${}_{(3,\not{Q};\,r)}\langle\widehat{T}_{\mu\nu}\rangle_\beta = -\frac{a}{32\sqrt{2}\pi}\sum_{j\neq 0}\left\{{}_{(3,\not{Q};\,r)}\varpi^j_{\mu\nu}[\mathcal{A}_{(-,3,\not{Q};\,r)}] - \lambda\,{}_{(3,\not{Q};\,r)}\varpi^j_{\mu\nu}[\mathcal{A}_{(+,3,\not{Q};\,r)}]\right\}. \tag{7.2.2a}$$

The functions $\mathcal{A}_{(\pm,3,\not{Q})}$ change, and are now given as

$$\mathcal{A}_{(\pm,3,\not{Q};\,r)} \coloneqq \left(1-r^2\right)^{-2}\left\{\pm\left(1-r^2\right)^2 + \left(1+r^2\right)^2\cosh(j\beta) - 4r^2\right\}. \tag{7.2.2b}$$

The tensor ${}_{(3,\not{Q})}\varpi^j_{\mu\nu}$ and its coefficients change under the coordinate transformation. The $\tau\tau$-component is now written as

$$
{}_{(3,\not{Q};\,r)}\varpi^{j}_{\tau\tau}[\mathcal{A}_{(\pm,3,\not{Q};\,r)}] := -\frac{1}{\mathcal{A}^{5/2}_{(\pm,3,\not{Q};\,r)}}\frac{\left(1+r^2\right)^2}{\left(1-r^2\right)^6}
\times\left\{\mathcal{B}_{(3,\not{Q};\,\tau\tau,2;\,r)}\mathcal{A}^2_{(\pm,3,\not{Q};\,r)}-\mathcal{B}_{(3,\not{Q};\,\tau\tau,1;\,r)}\mathcal{A}_{(\pm,3,\not{Q};\,r)}+\mathcal{B}_{(3,\not{Q};\,\tau\tau,0;\,r)}\right\}, \quad (7.2.2c)
$$

where its coefficients are now given by

$$
\mathcal{B}_{(3,\not{Q};\,\tau\tau,2;\,r)} := 2\left(1-r^2\right)^4, \quad (7.2.2d)
$$

$$
\mathcal{B}_{(3,\not{Q};\,\tau\tau,1;\,r)} := \left(1-r^2\right)^2\left\{\cosh(j\beta)\left[\left(1-r^2\right)^2+5\left(1+r^2\right)^2\right]+3\left(1-r^2\right)^2-5\left(1+r^2\right)^2\right\}, \quad (7.2.2e)
$$

$$
\mathcal{B}_{(3,\not{Q};\,\tau\tau,0;\,r)} := 12r^2\left(1+r^2\right)^2\left[\cosh(j\beta)-1\right]^2+6\left(1-r^2\right)^4\sinh^2(j\beta). \quad (7.2.2f)
$$

The $rr$-component, including the derivative (7.1.2) from the coordinate transformation, can be displayed as

$$
{}_{(3,\not{Q};\,r)}\varpi^{j}_{rr}[\mathcal{A}_{(\pm,3,\not{Q};\,r)}] := \frac{4}{\mathcal{A}^{3/2}_{(\pm,3,\not{Q};\,r)}\left(1-r^2\right)^2}\left\{2\mathcal{A}_{(\pm,3,\not{Q};\,r)}-\mathcal{B}_{(3,\not{Q};\,rr,0;\,r)}\right\}, \quad (7.2.2g)
$$

where the coefficient is defined as

$$
\mathcal{B}_{(3,\not{Q};\,rr,0;\,r)} := \frac{1}{\left(1-r^2\right)^2}\left\{\cosh(j\beta)\left[\left(1-r^2\right)^2+2\left(1+r^2\right)^2\right]+3\left(1-r^2\right)^2-2\left(1+r^2\right)^2\right\}. \quad (7.2.2h)
$$

The last component, $\phi\phi$, is given by

$$
{}_{(3,\not{Q};\,r)}\varpi^{j}_{\phi\phi}[\mathcal{A}_{(\pm,3,\not{Q};\,r)}] := \frac{4r^2}{\mathcal{A}^{5/2}_{(\pm,3,\not{Q};\,r)}\left(1-r^2\right)^2}
\times\left\{2\mathcal{A}^2_{(\pm,3,\not{Q};\,r)}+\mathcal{B}_{(3,\not{Q};\,\phi\phi,1;\,r)}\mathcal{A}_{(\pm,3,\not{Q};\,r)}+12r^2\,\mathcal{B}_{(3,\not{Q};\,\phi\phi,0;\,r)}\right\}, \quad (7.2.2i)
$$

where the coefficients are

$$
\mathcal{B}_{(3,\not{Q};\,\phi\phi,1;\,r)} := \frac{1}{\left(1-r^2\right)^2}\left\{\cosh(j\beta)\left[2\left(1-r^2\right)^2-5\left(1+r^2\right)^2\right]-6\left(1-r^2\right)^2+5\left(1+r^2\right)^2\right\}, \quad (7.2.2j)
$$

$$
\mathcal{B}_{(3,\not{Q};\,\phi\phi,0;\,r)} := \frac{\left(1+r^2\right)^2}{\left(1-r^2\right)^4}\left[\cosh(j\beta)-1\right]^2. \quad (7.2.2k)
$$

### 7.2.2 RSET for rigidly-rotating fields

As for the renormalised stress-energy tensor for static fields in the previous section, the overall form of the renormalised stress-energy tensor for rigidly-rotating fields is invariant under the change of radial coordinate, i.e. equation (5.2.35a) still holds:

$$ {}_{(3,\Omega;\,r)}\langle\widehat{T}_{\mu\nu}\rangle_\beta(\rho) = -\frac{a}{32\sqrt{2}\pi}\sum_{j\neq 0}\left\{{}_{(3,\Omega;\,r)}\varpi^j_{\mu\nu}[\mathcal{A}_{(-,3,\Omega;\,r)}] - \lambda\,{}_{(3,\Omega;\,r)}\varpi^j_{\mu\nu}[\mathcal{A}_{(+,3,\Omega;\,r)}]\right\}, \tag{7.2.3a} $$

where the quantities $\mathcal{A}_{(\pm,3,\Omega;\,r)}$ are given in terms of the new radial coordinate $r$ as

$$ \mathcal{A}_{(\pm,3,\Omega;\,r)} = \left(1-r^2\right)^{-2}\left\{\pm\left(1-r^2\right)^2 + \left(1+r^2\right)^2\cosh(j\beta) - 4r^2\cosh(j\beta\Omega)\right\}. \tag{7.2.3b} $$

The tensor ${}_{(3,\Omega)}\varpi^j_{\mu\nu}$ changes under the radial coordinate mapping, and its components are given below, starting with the $\tau\tau$-component:

$$ \begin{aligned} {}_{(3,\Omega;\,r)}\varpi^j_{\tau\tau}[\mathcal{A}_{(\pm,3,\Omega;\,r)}] :=& -\frac{1}{\mathcal{A}^{5/2}_{(\pm,3,\Omega;\,r)}}\frac{1}{(1-r^2)^2} \\ &\times\left\{\mathcal{B}_{(3,\Omega;\,\tau\tau,2;\,r)}\mathcal{A}^2_{(\pm,3,\Omega;\,r)} + \mathcal{B}_{(3,\Omega;\,\tau\tau,1;\,r)}\mathcal{A}_{(\pm,3,\Omega;\,r)} + \mathcal{B}_{(3,\Omega;\,\tau\tau,0;\,r)}\right\}, \end{aligned} \tag{7.2.3c} $$

where the coefficients $\mathcal{B}_{(3,\Omega;\,\tau\tau,\bullet;\,r)}$ are given by

$$ \mathcal{B}_{(3,\Omega;\,\tau\tau,2;\,r)} := 2\Gamma^{-2}_{(3)}\left(1+r^2\right)^2 = 2\widetilde{\Gamma}^{-2}_{(3)}, \tag{7.2.3d} $$

$$ \begin{aligned} \mathcal{B}_{(3,\Omega;\,\tau\tau,1;\,r)} :=& \mathcal{C}_{(3)}\left(1-r^2\right)^{-2}\left[2\Omega^2(1-r^2)^4 - (1+7\Omega^2)(1-r^4)^2 - 5(1-\Omega^2)(1+r^2)^4\right] \\ &- 4\widetilde{\Gamma}^{-2}_{(3)}\cosh(j\beta\Omega), \end{aligned} \tag{7.2.3e} $$

$$ \mathcal{B}_{(3,\Omega;\,\tau\tau,0;\,r)} := 12\widetilde{\Gamma}^{-2}_{(3)}\mathcal{C}^2_{(3)}\frac{r^2(1+r^2)^2}{(1-r^2)^4} + 6\frac{(1+r^2)^4}{(1-r^2)^2}\mathcal{S}^2_{(3)}, \tag{7.2.3f} $$

where $\mathcal{C}_{(3)}$ is given by equation (5.2.26), and $\mathcal{S}_{(3)}$ (defined in equation (5.2.28)) is given in terms of the new radial coordinate $r$ as

$$ \mathcal{S}_{(3)} = \left(1+r^2\right)^{-2}\left\{\left(1+r^2\right)^2\sinh(j\beta) - 4r^2\Omega\sinh(j\beta\Omega)\right\}. \tag{7.2.3g} $$

The $\tau\theta$-component is given in terms of the $\phi\phi$-component, given below, and is

$$ {}_{(3,\Omega;\,r)}\varpi^{j}_{\tau\phi}[\mathcal{A}_{(\pm,3,\Omega;\,r)}] = \Omega\,{}_{(3,\Omega;\,r)}\varpi^{j}_{\phi\phi}[\mathcal{A}_{(\pm,3,\Omega;\,r)}] - \frac{24}{\mathcal{A}^{5/2}_{(\pm,3,\Omega;\,r)}}\frac{r^2\left(1+r^2\right)^2}{\left(1-r^2\right)^4}\sinh(j\beta)\sinh(j\beta\Omega). \tag{7.2.3h} $$

The $rr$-component is given by

$$ {}_{(3,\Omega;\,r)}\varpi^{j}_{rr}[\mathcal{A}_{(\pm,3,\Omega;\,r)}] := \frac{1}{\mathcal{A}^{3/2}_{(\pm,3,\Omega;r)}}\frac{4}{\left(1-r^2\right)^2}\left\{2\mathcal{A}_{(\pm,3,\Omega;\,r)} - \mathcal{B}_{(3,\Omega;\,rr,0;\,r)}\right\}, \tag{7.2.3i} $$

where

$$ \mathcal{B}_{(3,\Omega;\,rr,0;\,r)} := \mathcal{C}_{(3)}\left(1-r^2\right)^{-2}\left(3+2r^2+3r^4\right) - 4\cosh(j\beta\Omega). \tag{7.2.3j} $$

Finally, the $\phi\phi$-component is as follows:

$$ \begin{aligned} {}_{(3,\Omega;\,r)}\varpi^{j}_{\phi\phi}[\mathcal{A}_{(\pm,3,\Omega;\,r)}] := {} & \frac{1}{\mathcal{A}^{5/2}_{(\pm,3,\Omega;\,r)}}\frac{4r^2}{\left(1-r^2\right)^2} \\ & \times\left\{2\mathcal{A}^2_{(\pm,3,\Omega;\,r)} - \mathcal{B}_{(3,\Omega;\,\phi\phi,1;\,r)}\mathcal{A}_{(\pm,3,\Omega;\,r)} + \frac{12r^2}{(1-r^2)^4}\mathcal{B}_{(3,\Omega;\,\phi\phi,0;\,r)}\right\}, \end{aligned} \tag{7.2.3k} $$

where the coefficients $\mathcal{B}_{(3,\Omega;\,\phi\phi,\bullet;\,r)}$ are given by

$$ \mathcal{B}_{(3,\Omega;\,\phi\phi,1;\,r)} := \mathcal{C}_{(3)}\left(3+14r^2+3r^4\right) + 4\left(1-r^2\right)^2\cosh(j\beta\Omega), \tag{7.2.3l} $$

$$ \mathcal{B}_{(3,\Omega;\,\phi\phi,0;\,r)} := \mathcal{C}^2_{(3)}\left(1+r^2\right)^2 - 2\left(1-r^2\right)^2\sinh^2(j\beta\Omega). \tag{7.2.3m} $$

### 7.2.3 RKT-SET

In order to transform the RKT-SET (5.3.23) into the new space-time coordinates (with line element (7.1.4)), we need to transform the dreibein basis (4.4.29) constructed in chapter 4 into the new coordinates. The dreibein basis (taking care to transform the vector $\partial_\rho$ to the vector $\partial_r$ using the derivative (7.1.2)) in $r$-coordinates is

$$ e^{\mu}_{(\tau)}\partial_\mu = a\Gamma_{(3)}\frac{1-r^2}{1+r^2}\partial_\tau = a\widetilde{\Gamma}_{(3)}\left(1-r^2\right)\partial_\tau, \tag{7.2.4} $$

$$ e^{\mu}_{(r)}\partial_\mu = \frac{1}{2}a\left(1-r^2\right)\partial_r, \tag{7.2.5} $$

$$e^{\mu}_{(\phi)} = \frac{2ar\widetilde{\Gamma}_{(3)}\left(1-r^2\right)}{(1+r^2)}\left[\Omega\partial_\tau + \frac{1}{4r^2}\widetilde{\Gamma}^{-2}_{(3)}\partial_\phi\right], \tag{7.2.6}$$

where the modified Lorentz factor $\widetilde{\Gamma}_{(3)}$ is defined in equation (7.1.5). The RKT-SET (5.3.23) in the frame is given by

$$\overset{\text{RKT}}{(3,\bullet)}\widehat{T}^{(a)(b)} = \frac{\zeta(3)}{2\pi\widetilde{\beta}^3}\text{Diag}\{2,1,1\}, \tag{7.2.7}$$

where the local temperature [357, 359], given in terms of the new coordinate system (7.1.4) is

$$\widetilde{\beta} = \beta\sqrt{-g_{\tau\tau}} = \frac{\beta}{a\widetilde{\Gamma}_{(3)}\left(1-r^2\right)}. \tag{7.2.8}$$

For later convenience, we define the prefactor of equation (7.2.7) as

$$\mathcal{K} := \frac{\zeta(3)}{2\pi}. \tag{7.2.9}$$

By contracting the stress-energy tensor (7.2.7) with the dreibein basis (7.2.4) and then lowering the indices using the space-time metric (7.1.4), we find the following nonzero space-time components of the RKT-SET:

$$\widetilde{T}_{\tau\tau} = \frac{2\mathcal{K}\widetilde{\Gamma}_{(3)}}{a^2\beta^3}\left(1-r^2\right), \tag{7.2.10a}$$

$$\widetilde{T}_{\tau\theta} = -\frac{8\mathcal{K}\widetilde{\Gamma}^3_{(3)}\Omega r^2}{a^2\beta^3}\left(1-r^2\right), \tag{7.2.10b}$$

$$\widetilde{T}_{rr} = \frac{4\mathcal{K}\widetilde{\Gamma}^3_{(3)}}{a^2\beta^3}\left(1-r^2\right), \tag{7.2.10c}$$

$$\widetilde{T}_{\theta\theta} = \frac{4\mathcal{K}\widetilde{\Gamma}^5_{(3)}r^2}{a^2\beta^3}\left(1-r^2\right)\left(\left[1+r^2\right]^2 + 8\Omega^2r^2\right). \tag{7.2.10d}$$

To find the RKT-SET in nonrotating coordinates, one can simply take the RKT-SET (7.2.10) and take the limit $\Omega \to 0$.

## § 7.3 Linearised quantum-corrected Einstein equations

In this section, we will derive the explicit form of the linearised, quantum-corrected Einstein equations (3.6.14), which governs the perturbations, to first order, of the quantum-corrected

metric. We start by making a suitable choice of ansatz, for which we demand it has the same signature, the functions have the same functional dependence, and the metric has the same overall structure as the background anti-de Sitter space metric (7.1.4). The ansatz is inspired, in part, by [78], where the authors find solutions to the quantum-corrected Einstein equations for the BTZ black-hole space-time; see section 6.5 for more details.

The metric is characterised by four unknown functions, $A$, $B$, $C$ and $D$, and is given explicitly as

$$\mathrm{d}s^2 = a^{-2}\left\{-\left[A(r) - \frac{C(r)D(r)^2}{A(r)}\right]\mathrm{d}\tau^2 + \frac{B(r)}{A(r)}\,\mathrm{d}r^2 + 2\frac{C(r)D(r)}{A(r)}\,\mathrm{d}\tau\,\mathrm{d}\phi + \frac{C(r)}{A(r)}\,\mathrm{d}\phi^2\right\}, \tag{7.3.1a}$$

where

$$A(r) = \frac{\left(1+r^2\right)^2}{\left(1-r^2\right)^2} + a\ell_{\mathrm{P}}\,\delta A(r) + \mathcal{O}(a^2\ell_{\mathrm{P}}^2), \tag{7.3.1b}$$

$$B(r) = \frac{4\left(1+r^2\right)^2}{\left(1-r^2\right)^4} + a\ell_{\mathrm{P}}\,\delta B(r) + \mathcal{O}(a^2\ell_{\mathrm{P}}^2), \tag{7.3.1c}$$

$$C(r) = \frac{4r^2\left(1+r^2\right)^2}{\left(1-r^2\right)^4} + a\ell_{\mathrm{P}}\,\delta C(r) + \mathcal{O}(a^2\ell_{\mathrm{P}}^2), \tag{7.3.1d}$$

$$D(r) = \Omega + a\ell_{\mathrm{P}}\,\delta D(r) + \mathcal{O}(a^2\ell_{\mathrm{P}}^2), \tag{7.3.1e}$$

are expansions of the unknown functions $A$, $B$, $C$ and $D$ in the dimensionless parameter $a\ell_{\mathrm{P}}$, where $\ell_{\mathrm{P}}$ is the Planck length. By setting the perturbation parameter $a\ell_{\mathrm{P}}$ to zero, one can verify that the metric ansatz (7.3.1) reduces to the background metric (7.1.4).

With this ansatz, there is some residual gauge freedom that can be exploited, via suitable coordinate transformations. If we make the general coordinate transformation $x^\mu \to x^\mu + a\ell_{\mathrm{P}}\,\xi^\mu$, then the metric tensor is transformed to

$$g_{\mu\nu} \to g_{\mu\nu} + a\ell_{\mathrm{P}}\,\mathcal{L}_\xi g_{\mu\nu}, \tag{7.3.2}$$

where $\mathcal{L}_\xi$ is the Lie derivative along the vector $\xi$, given by

$$\mathcal{L}_\xi g_{\mu\nu} = \xi^\sigma\partial_\sigma g_{\mu\nu} + g_{\mu\sigma}\partial_\nu\xi^\sigma + g_{\nu\sigma}\partial_\mu\xi^\sigma. \tag{7.3.3}$$

There are an infinite number of coordinate transformations we could choose to exploit this gauge freedom, however there are two that are of interest to us: a rescaling of the time coordinate $\tau$, and a perturbation of the radial coordinate $r$.

We start by examining the effect of rescaling the time coordinate. We make the transformation

$$\tau \to \tau + a\ell_{\mathrm{P}}\,\delta\tau, \tag{7.3.4}$$

so that

$$\xi^{\bullet} = (\delta\tau, 0, 0). \tag{7.3.5}$$

The Lie derivative of the metric tensor along $\xi^{\bullet}$ is given by

$$\mathcal{L}_{\xi} g_{\mu\nu} = g_{\mu\tau}\partial_{\nu}\xi^{\tau} + g_{\nu\tau}\partial_{\mu}\xi^{\tau} = g_{\mu\tau}\partial_{\nu}(\delta\tau) + g_{\nu\tau}\partial_{\mu}(\delta\tau), \tag{7.3.6}$$

since the metric tensor is independent of the time coordinate $\tau$. By further assuming that the transformation (7.3.4) is in fact a rescaling, i.e. $\delta\tau = \varkappa\tau$ with $\varkappa \in \mathbb{R}$, then the Lie derivative along $\xi^{\bullet}$ simplifies to

$$\mathcal{L}_{\xi} g_{\mu\nu} = g_{\mu\tau}\partial_{\nu}(\varkappa\tau) + g_{\nu\tau}\partial_{\mu}(\varkappa\tau) = \varkappa g_{\mu\tau}\delta^{\tau}_{\nu} + \varkappa g_{\nu\tau}\delta^{\tau}_{\mu}, \tag{7.3.7}$$

with nonzero components

$$\mathcal{L}_{\xi} g_{\tau\tau} = 2\varkappa g_{\tau\tau}, \qquad \mathcal{L}_{\xi} g_{\tau\phi} = \mathcal{L}_{\xi} g_{\phi\tau} = \varkappa g_{\tau\phi}. \tag{7.3.8}$$

This means that, under a rescaling of the time coordinate $\tau$, the metric tensor is rescaled in the conponents $\mathrm{d}\tau^2$ and $\mathrm{d}\tau\,\mathrm{d}\phi$. We later use this rescaling to fix arbitrary constants of integration, see sections 7.5 and 7.6[1].

The other gauge freedom comes from perturbing the radial coordinate:

$$r \to r + a\ell_{\mathrm{P}}\,\delta r, \quad \text{so that} \quad \xi^{\bullet} = (0, \delta r, 0). \tag{7.3.9}$$

[1] We also use this gauge freedom from the rescaling of the time coordinate in chapters 8 and 9; sections 8.3 and 9.3.2 respectively.

The Lie derivative of the metric tensor along $\xi^\bullet$ is given by

$$\mathcal{L}_\xi g_{\mu\nu} = \xi^r \partial_r g_{\mu\nu} + g_{\mu r}\partial_\nu \xi^r + g_{\nu r}\partial_\mu \xi^r = \delta r \partial_r(g_{\mu\nu}) + g_{\mu r}\partial_\nu(\delta r) + g_{\nu r}\partial_\mu(\delta r), \tag{7.3.10}$$

which has nonzero components

$$\mathcal{L}_\xi g_{rr} = \delta r \partial_r(g_{rr}) + 2g_{rr}\partial_r(\delta r) = \frac{1}{\delta r}\partial_r\left[g_{rr}(\delta r)^2\right], \tag{7.3.11a}$$

$$\mathcal{L}_\xi g_{\tau\tau} = \delta r \partial_r(g_{\tau\tau}), \tag{7.3.11b}$$

$$\mathcal{L}_\xi g_{\tau\phi} = \mathcal{L}_\xi g_{\phi\tau} = \delta r \partial_r(g_{\tau\phi}), \tag{7.3.11c}$$

$$\mathcal{L}_\xi g_{\phi\phi} = \delta r \partial_r(g_{\phi\phi}). \tag{7.3.11d}$$

Since we can use the gauge freedom arising from the Lie derivative once (per transformation), we need to make a (totally arbitrary) choice on which metric component to perturb. Since we are transforming the radial coordinate, it makes sense to consider the transformation of the metric component $g_{rr}$. Combining (7.3.2) and (7.3.11a), and substituting in the metric functions $A(r)$ (7.3.1b) and $B(r)$ (7.3.1c), the metric component $g_{rr}$ transforms as

$$\begin{aligned} g_{rr} &\to \frac{B_0(r)}{A_0(r)} + \frac{B_0(r)}{A_0(r)}\left[\frac{\delta B(r)}{B_0(r)} - \frac{\delta A(r)}{A_0(r)}\right] a\ell_{\mathrm{P}} + \left[\delta r \partial_r(g_{rr}) + 2g_{rr}(\delta r)'\right] a\ell_{\mathrm{P}} + \mathcal{O}(a^2\ell_{\mathrm{P}}^2), \\ &= \frac{B_0(r)}{A_0(r)} + \frac{B_0(r)}{A_0(r)}\left[\frac{\delta B(r)}{B_0(r)} - \frac{\delta A(r)}{A_0(r)} + \delta r\left\{\frac{B_0'(r)}{B_0(r)} - \frac{A_0'(r)}{A_0(r)}\right\} + 2(\delta r)'\right] a\ell_{\mathrm{P}} + \mathcal{O}(a^2\ell_{\mathrm{P}}^2), \end{aligned} \tag{7.3.12}$$

where we are using $A_0(r)$ and $B_0(r)$ to denote the background metric functions (i.e. set $a\ell_{\mathrm{P}} = 0$) for $A(r)$ and $B(r)$ respectively. To exploit the gauge freedom, we take the $a\ell_{\mathrm{P}}$ coefficient of the expansion (7.3.12) and set it to be equal to some function, say $2\mathcal{J}$:

$$\frac{B_0(r)}{A_0(r)}\left[\frac{\delta B(r)}{B_0(r)} - \frac{\delta A(r)}{A_0(r)} + \delta r\left\{\frac{B_0'(r)}{B_0(r)} - \frac{A_0'(r)}{A_0(r)}\right\} + 2(\delta r)'\right] = 2\mathcal{J}(r), \tag{7.3.13}$$

and then solve for the perturbation $\delta r$. Rearranging (7.3.13), we have

$$(\delta r)' + \delta r\left\{\frac{B_0'(r)}{B_0(r)} - \frac{A_0'(r)}{A_0(r)}\right\} = \widetilde{\mathcal{J}}(r), \tag{7.3.14}$$

where

$$\widetilde{\mathcal{J}}(r) = \frac{\mathcal{J}(r)A_0(r)}{B_0(r)} + \frac{\delta B(r)}{B_0(r)} - \frac{\delta A(r)}{A_0(r)}. \tag{7.3.15}$$

Making use of the integrating factor $\sqrt{B_0(r)/A_0(r)} = 2/(1-r^2)$, the differential equation (7.3.14) is readily integrated to give

$$\delta r(r) = \mathcal{J}_0\left(1-r^2\right) + \frac{1-r^2}{2}\int \widetilde{\mathcal{J}}(r)\,\mathrm{d}r, \tag{7.3.16}$$

with $\mathcal{J}_0$ an arbitrary constant of integration and $\widetilde{\mathcal{J}}$ is given by (7.3.15). The idea is then that the gauge freedom is contained within the choice of the function $\mathcal{J}(r)$; by choosing an explicit form for $\mathcal{J}$ we can find the explicit coordinate transform in the radial coordinate required. The specific choice of gauge will be set in section 7.4; in particular, see the discussion around equation (7.4.25).

To find the linearised, quantum-corrected Einstein equations for the metric ansatz (7.3.1), we make the assumption that the stress-energy tensor on the right-hand-side of the LQCEE is of order $a\ell_{\mathrm{P}}$, and substitute the ansatz (7.3.1) into the full LQCEE (3.6.14). The zeroth-order term of the left-hand-side of the LQCEE evaluates to zero, since pure anti-de Sitter space has a zero classical stress-energy tensor, so the lowest, nonzero order of the LQCEE is that of order $a\ell_{\mathrm{P}}$, which is given by:

$$\begin{aligned}
\widetilde{T}_{\tau\tau} = {} & \frac{\left(1-r^2\right)^2\left(1+2\left[1+2\Omega^2\right]r^2+r^4\right)}{8\left(1+r^2\right)^2}\delta A'' \\
& + \frac{\left(1-r^2\right)\left(1-14r^2-8\left[4+3\Omega^2\right]r^4-2\left[9+4\Omega^2\right]r^6-r^8\right)}{8r\left(1+r^2\right)^3}\delta A' \\
& - \frac{3\left(1-r^2\right)^2}{\left(1+r^2\right)^2}\delta A + \frac{\left(1-r^2\right)^3\left(1+4r^2+2\left[3-8\Omega^2\right]r^4+4r^6+r^8\right)}{32r\left(1+r^2\right)^3}\delta B' \\
& - \frac{\left(1-r^2\right)^2\left(1+\left[5+8\Omega^2\right]r^2+2\left[5-16\Omega^2\right]r^4+2\left[5-4\Omega^2\right]r^6+5r^8+r^{10}\right)}{8\left(1+r^2\right)^4}\delta B \\
& - \frac{\left(1-r^2\right)^4}{32r^2}\delta C'' + \frac{\left(1-r^2\right)^3\left(1+11r^2+2r^4\right)}{16r^3\left(1+r^2\right)}\delta C'
\end{aligned}$$

$$- \frac{\left(1-r^2\right)^2\left(1+4r^2+54r^4+4r^6+r^8\right)}{16r^4\left(1+r^2\right)^2}\delta C - r^2\Omega\,\delta D'' - \frac{\Omega r\left(3+r^4\right)}{1-r^4}\delta D', \tag{7.3.17a}$$

$$\begin{aligned}\widetilde{T}_{\tau\phi} = {} & \frac{\Omega r^2\left(1-r^2\right)^2}{2\left(1+r^2\right)^2}\delta A'' - \frac{\Omega r^3\left(1-r^2\right)\left(3+r^2\right)}{\left(1+r^2\right)^3}\delta A' - \frac{\Omega r^3\left(1-r^2\right)^3}{2\left(1+r^2\right)^3}\delta B' \\ & - \frac{\Omega r^2\left(1-r^2\right)^2\left(1-4r^2-r^4\right)}{\left(1+r^2\right)^4}\delta B - \frac{1}{2}r^2\delta D'' - \frac{r\left(3+r^4\right)}{2\left(1-r^4\right)}\delta D',\end{aligned} \tag{7.3.17b}$$

$$\begin{aligned}\widetilde{T}_{rr} = {} & \frac{\left(1-r^2\right)^3}{2r\left(1+r^2\right)^3}\left[\delta A' + \delta C'\right] + \frac{16r^2}{\left(1+r^2\right)^4}\delta A \\ & - \frac{\left(1-r^2\right)^2}{\left(1+r^2\right)^2}\delta B - \frac{\left(1-r^2\right)^2\left(1+6r^2+r^4\right)}{r^2\left(1+r^2\right)^4}\delta C,\end{aligned} \tag{7.3.17c}$$

$$\begin{aligned}\widetilde{T}_{\phi\phi} = {} & \frac{r^2\left(1-r^2\right)^2}{2\left(1+r^2\right)^2}\delta A'' - \frac{r^3\left(1-r^2\right)\left(3+r^2\right)}{\left(1+r^2\right)^3}\delta A' \\ & - \frac{r^3\left(1-r^2\right)^3}{2\left(1+r^2\right)^3}\delta B' - \frac{r^2\left(1-r^2\right)^2\left(1-4r^2-r^4\right)}{\left(1+r^2\right)^4}\delta B.\end{aligned} \tag{7.3.17d}$$

By construction, the stress-energy tensors (7.2.3) and (7.2.10) are traceless. Using this fact, and from the LQCEE (7.3.17), we can obtain a further constraint on the metric perturbations:

$$\begin{aligned}0 = {} & 32r^5\left(1-r^4\right)\delta A' + 32r^4\left(3-2r^2+3r^4\right)\delta A - r^3\left(1-r^2\right)^2\left(1-r^4\right)\left(1+6r^2+r^4\right)\delta B' \\ & - 4r^4\left(1-r^2\right)^2\left(3-7r^2-3r^4-r^6\right)\delta B + r^2\left(1-r^2\right)^2\left(1-r^4\right)^2\delta C'' \\ & - 2r\left(1-r^2\right)^2\left(1-r^4\right)\left(1+9r^2+2r^4\right)\delta C' + 2\left(1-r^2\right)^2\left(1+30r^4+r^8\right)\delta C.\end{aligned} \tag{7.3.18}$$

In addition to the equation resulting from tracelessness, we may obtain further constraints on the metric perturbations by considering conservation of the LQCEE. Indeed, since the right-hand-side of the LQCEE is conserved (by construction), the left-hand-side of the LQCEE must also be conserved. When we compute the covariant derivative of the left-hand-side of the LQCEE, we find the lowest order to be $a^2\ell_{\mathrm{P}}^2$. Therefore, conservation of the LQCEE holds at linear order, and we do not consider further constraints arising from conservation.

In the next section we will detail the procedure to solve the LQCEE (7.3.17).

## § 7.4 Solving the LQCEE

To solve the LQCEE (7.3.17), we first use equations (7.3.17b) and (7.3.17d) to find a decoupled, second-order, inhomogeneous ODE for the perturbation $\delta D$:

$$\delta D'' + \frac{\left(3+r^4\right)}{r\left(1-r^4\right)}\delta D' = -\frac{2}{r^2}\left[\widetilde{T}_{\tau\phi} - \Omega\widetilde{T}_{\phi\phi}\right], \tag{7.4.1}$$

which will be solved using the method of variation of parameters. We will first provide a brief review of the method of variation of parameters, following [54].

We start by considering the general inhomogeneous differential equation

$$y''(t) + p(t)y'(t) + q(t)y(t) = g(t), \tag{7.4.2}$$

and we assume that

$$y_c(t) = \mathfrak{y}_1 y_1(t) + \mathfrak{y}_2 y_2(t), \tag{7.4.3}$$

is a solution to the homogeneous equation

$$y''(t) + p(t)y'(t) + q(t)y(t) = 0. \tag{7.4.4}$$

The key idea is to upgrade the constants $\mathfrak{y}_i$ to functions $u_i(t)$ so that the solution (7.4.3) is now

$$y_c(t) = u_1(t)y_1(t) + u_2(t)y_2(t), \tag{7.4.5}$$

and to determine the functions $u_i(t)$ such that the solution (7.4.5) is a solution to the *in*homogeneous equation (7.4.2). We next differentiate the solution (7.4.5) (dropping the functional dependence):

$$y_c' = u_1'y_1 + u_1y_1' + u_2'y_2 + u_2y_2', \tag{7.4.6}$$

and we further make the assumption that the terms involving derivatives of $u_i$ are zero:

$$u_1'y_1 + u_2'y_2 = 0, \tag{7.4.7}$$

such that the derivative (7.4.6) now reads

$$y_c' = u_1 y_1' + u_2 y_2'. \tag{7.4.8}$$

If we differentiate (7.4.8) once more, we find

$$y_c'' = u_1' y_1' + u_1 y_1'' + u_2' y_2' + u_2 y_2''. \tag{7.4.9}$$

Next, we substitute the solution (7.4.5) and its derivatives (7.4.8,7.4.9) into the inhomogeneous equation (7.4.2), which then reads (grouping terms together)

$$u_1 \underbrace{\left(y_1'' + p y_1' + q y_1\right)}_{=0} + u_2 \underbrace{\left(y_2'' + p y_2' + q y_2\right)}_{=0} + u_1' y_1' + u_2' y_2' = g, \tag{7.4.10}$$

where the terms inside the brackets are zero since $y_1$, $y_2$ are solutions to the homogeneous equation (7.4.4). We therefore have the system of linear (algebraic) equations for $u_1'$ and $u_2'$:

$$u_1' y_1 + u_2' y_2 = 0, \tag{7.4.11}$$

$$u_1' y_1' + u_2' y_2' = g, \tag{7.4.12}$$

which has solutions [54]

$$u_1' = -\frac{y_2 g}{\mathcal{W}[y_1, y_2]}, \qquad u_2' = \frac{y_1 g}{\mathcal{W}[y_1, y_2]}, \tag{7.4.13}$$

where $\mathcal{W}[y_1, y_2]$ is the *Wronskian* of the two functions $y_1$ and $y_2$, given by [197]

$$\mathcal{W}[y_1, y_2] = y_1 y_2' - y_1' y_2. \tag{7.4.14}$$

We can directly integrate the derivatives (7.4.13) to yield the solutions

$$u_1(t) = -\int \frac{y_2(t) g(t)}{\mathcal{W}[y_1, y_2]}\, \mathrm{d}t + \mathfrak{y}_1', \qquad u_2(t) = \int \frac{y_1(t) g(t)}{\mathcal{W}[y_1, y_2]}\, \mathrm{d}t + \mathfrak{y}_2', \tag{7.4.15}$$

where $\mathfrak{y}_1'$ and $\mathfrak{y}_2'$ are arbitrary constants of integration, which we assume vanish [54]. Finally, we can write the general solution of the inhomogeneous differential equation (7.4.2) as

$$y(t) = \mathfrak{y}_1 y_1(t) + \mathfrak{y}_2 y_2(t) - y_1(t) \int \frac{y_1(t) g(t)}{\mathcal{W}[y_1, y_2]}\, \mathrm{d}t + y_2(t) \int \frac{y_2(t) g(t)}{\mathcal{W}[y_1, y_2]}\, \mathrm{d}t, \tag{7.4.16}$$

where $y_1$ and $y_2$ are solutions to the homogeneous equation (7.4.4), the $\mathfrak{y}_i$ are arbitrary constants and $\mathcal{W}[y_1, y_2]$ is the Wronskian (7.4.14) of the solutions $y_1$ and $y_2$.

Now that we have introduced the general technique of using variation of parameters, we can return our attention to the second order, inhomogeneous differential equation (7.4.1). We start by considering the corresponding homogeneous equation

$$\delta D'' + \frac{3 + r^4}{r(1 - r^4)} \delta D' = 0. \tag{7.4.17}$$

Rearranging, we have

$$\frac{\delta D''}{\delta D'} = -\frac{3 + r^4}{r(1 - r^4)}, \tag{7.4.18}$$

which integrates to give

$$\ln\big(\delta D'\big) = \mathfrak{d}_0 + \ln\left(\frac{1 - r^4}{r^3}\right), \tag{7.4.19}$$

or equivalently,

$$\delta D' = \mathfrak{d}_1 \frac{1 - r^4}{r^3}. \tag{7.4.20}$$

Integrating further, we have

$$\delta D = \mathfrak{d}_2 - \mathfrak{d}_1 \frac{1 + r^4}{2r^2}, \tag{7.4.21}$$

where the $\mathfrak{d}_i$ are general constants of integration, and $\mathfrak{d}_1 = e^{\mathfrak{d}_0}$. For the method of variation of parameters, we require two linearly independent solutions of the homogeneous equation, which we can take to be

$$\delta D_1(r) = 1, \qquad \delta D_2(r) = \frac{1 + r^4}{r^2}. \tag{7.4.22}$$

The Wronskian (7.4.14) of the two solutions (7.4.22) is found to be

$$\mathcal{W}[\delta D_1, \delta D_2] = -\frac{2}{r^3}\left(1 - r^4\right), \tag{7.4.23}$$

and thus the general solution to the inhomogeneous equation (7.4.1) is

$$\delta D(r) = \mathcal{D}_1 + \mathcal{D}_2 \frac{1 + r^4}{2r^2} - \int \frac{1 + r^4}{r(1 - r^4)} \left[\widetilde{T}_{\tau\phi} - \Omega \widetilde{T}_{\phi\phi}\right] \mathrm{d}r + \frac{1 + r^4}{r^2} \int \frac{r}{1 - r^4} \left[\widetilde{T}_{\tau\phi} - \Omega \widetilde{T}_{\phi\phi}\right] \mathrm{d}r, \tag{7.4.24}$$

where $\mathcal{D}_1$ and $\mathcal{D}_2$ are arbitrary constants of integration. When a state with vanishing rotation is considered, i.e. $\Omega = 0$, we require that the perturbation $\delta D(r)$ vanishes identically, and therefore set $\mathcal{D}_1 = \mathcal{D}_2 = 0$. In a rotating state, the constants are fixed by considering the behaviour of the solution (7.4.24) at both the origin $r = 0$ and the boundary $r = 1$. These will depend on the stress-energy tensor used, i.e. the RKT-SET (section 7.5) or the QFT-RSET (section 7.6).

The next step in solving the LQCEE (7.3.17) is to exploit the residual gauge freedom from perturbing the radial coordinate (see the discussion between equations (7.3.9) and (7.3.16)). Since the LQCEE (7.3.17c) has factors of $\delta A' + \delta C'$, $\delta A$, $\delta B$ and $\delta C$, we make a choice to express $\delta B$ in terms of $\delta A$ so that the LQCEE (7.3.17c) depends only on factors of $\delta A + \delta C$ and derivatives thereof. A suitable choice is given by

$$\delta B = \frac{\left(1+r^2\right)^2}{r^2\left(1-r^2\right)^2}\delta A, \tag{7.4.25}$$

so that the LQCEE (7.3.17c) reads

$$\begin{aligned}\widetilde{T}_{rr} &= \frac{\left(1-r^2\right)^3}{2r\left(1+r^2\right)^3}\left[\delta A' + \delta C'\right] + \frac{16r^2}{\left(1+r^2\right)^4}\delta A \\ &\quad - \frac{\left(1-r^2\right)^2}{\left(1+r^2\right)^2}\frac{\left(1+r^2\right)^2}{r^2\left(1-r^2\right)^2}\delta A - \frac{\left(1-r^2\right)^2\left(1+6r^2+r^4\right)}{r^2\left(1+r^2\right)^4}\delta C \\ &= \frac{\left(1-r^2\right)^3}{2r\left(1+r^2\right)^3}\left[\delta A' + \delta C'\right] - \frac{\left(1-r^2\right)^2\left(1+6r^2+r^4\right)}{r^2\left(1+r^2\right)^4}\left[\delta A + \delta C\right],\end{aligned} \tag{7.4.26}$$

which, after rearranging, gives

$$\left[\delta A' + \delta C'\right] - \frac{2\left(1+6r^2+r^4\right)}{r\left(1-r^4\right)}\left[\delta A + \delta C\right] = \frac{2r\left(1+r^2\right)^3}{a^2\left(1-r^2\right)^3}\widetilde{T}_{rr}. \tag{7.4.27}$$

We can make use of the integrating factor $r^{-2}\left(1-r^2\right)^4\left(1+r^2\right)^{-2}$ to rearrange this to give

$$\frac{\mathrm{d}}{\mathrm{d}r}\left\{\frac{\left(1-r^2\right)^4}{r^2\left(1+r^2\right)^2}\left[\delta A + \delta C\right]\right\} = \frac{2}{r}\left(1-r^4\right)\widetilde{T}_{rr}. \tag{7.4.28}$$

Directly integrating gives

$$\delta A + \delta C = \frac{r^2\left(1+r^2\right)^2}{\left(1-r^2\right)^4}\left[\mathcal{C}_1 + \int \frac{2}{r}\left(1-r^4\right)\widetilde{T}_{rr}\,\mathrm{d}r\right], \tag{7.4.29}$$

where $\mathcal{C}_1$ is an arbitrary constant of integration which, like the constants $\mathcal{D}_i$ in equation (7.4.24), will be fixed by considering the behaviour of the solutions at the origin or boundary.

In order to isolate one of the perturbations of $\delta A$ or $\delta C$, we must find a separate solution for one of them. By substituting the gauge choice (7.4.25) into the LQCEE (7.3.17d), we find a second-order ODE for the perturbation $\delta A$:

$$\begin{aligned}\widetilde{T}_{\phi\phi} &= \frac{r^2\left(1-r^2\right)^2}{2\left(1+r^2\right)^2}\delta A'' - \frac{r^3\left(1-r^2\right)\left(3+r^2\right)}{\left(1+r^2\right)^3}\delta A' \\ &\quad - \frac{r^3\left(1-r^2\right)^3}{2\left(1+r^2\right)^3}\left[\frac{\left(1+r^2\right)}{r^3\left(1-r^2\right)^3}\left\{r\left(1-r^4\right)\delta A' - 2\left(1-4r^2-r^4\right)\delta A\right\}\right] \\ &\quad - \frac{r^2\left(1-r^2\right)^2\left(1-4r^2-r^4\right)}{\left(1+r^2\right)^4}\frac{\left(1+r^2\right)^2}{r^2\left(1-r^2\right)^2}\delta A \\ &= \frac{r^2\left(1-r^2\right)^2}{2\left(1+r^2\right)^2}\delta A'' - \frac{\left(1-r^2\right)\left(r+8r^3+3r^5\right)}{2\left(1+r^2\right)^3}\delta A', \end{aligned} \tag{7.4.30}$$

which, after some rearrangment, reads

$$\delta A'' - \frac{1+8r^2+3r^4}{r\left(1-r^4\right)}\delta A' = \frac{2\left(1+r^2\right)^2}{r^2\left(1-r^2\right)^2}\widetilde{T}_{\phi\phi}. \tag{7.4.31}$$

This is a second-order inhomogeneous ODE, so we again use the method of variation of parameters. The homogeneous equation

$$\delta A'' - \frac{1+8r^2+3r^4}{r\left(1-r^4\right)}\delta A' = 0 \tag{7.4.32}$$

can be rearranged to give

$$\frac{\delta A''}{\delta A'} = \frac{1+8r^2+3r^4}{r\left(1-r^4\right)}, \tag{7.4.33}$$

which in turn integrates to give

$$\ln\left(\delta A'\right) = \mathfrak{a}_0 + \ln\left(\frac{r\left(1+r^2\right)}{\left(1-r^2\right)^3}\right), \tag{7.4.34}$$

or

$$\delta A' = \mathfrak{a}_1\frac{r\left(1+r^2\right)}{\left(1-r^2\right)^3}. \tag{7.4.35}$$

Integrating once more leaves us with the solution

$$\delta A = \mathfrak{a}_2 + \mathfrak{a}_1 \frac{r^2}{2\left(1-r^2\right)^2}, \tag{7.4.36}$$

where the $\mathfrak{a}_i$ are arbitrary constants of integration. Variation of parameters requires two linearly independent solutions to the homogeneous equation, so we choose

$$\delta A_1(r) = 1, \qquad \text{and} \qquad \delta A_2(r) = \frac{r^2}{\left(1-r^2\right)^2}, \tag{7.4.37}$$

the Wronskian of which is

$$\mathcal{W}[\delta A_1, \delta A_2] = \frac{2r\left(1+r^2\right)}{\left(1-r^2\right)^3}. \tag{7.4.38}$$

Therefore, by the method of variation of parameters, the general solution to the inhomogeneous ODE (7.4.31) is given by

$$\delta A = \mathcal{A}_1 + \frac{r^2}{\left(1-r^2\right)^2}\mathcal{A}_2 - \int \frac{1+r^2}{r\left(1-r^2\right)}\widetilde{T}_{\phi\phi}\,\mathrm{d}r + \frac{r^2}{\left(1-r^2\right)^2}\int \frac{1}{r^3}\left(1-r^4\right)\widetilde{T}_{\phi\phi}\,\mathrm{d}r, \tag{7.4.39}$$

where the $\mathcal{A}_i$ are arbitrary constants of integration.

Therefore, we have the general solutions (7.4.24), (7.4.29) and (7.4.39) to the LQCEE in terms of integrals involving the stress-energy tensor components (RKT and QFT), and five arbitrary constants $\mathcal{A}_1, \mathcal{A}_2, \mathcal{C}_1, \mathcal{D}_1$ and $\mathcal{D}_2$. One point worthy of note is that the solutions (7.4.24), (7.4.29) and (7.4.39) depend only on the stress-energy tensor components $\widetilde{T}_{\tau\phi}$, $\widetilde{T}_{rr}$ and $\widetilde{T}_{\phi\phi}$ and not explicitly on $\widetilde{T}_{\tau\tau}$. However, $\widetilde{T}_{\mu\nu}$ is a difference in expectation values between two quantum states, and is therefore traceless in the QFT case; it is traceless by construction in the RKT case. Thus, $\widetilde{T}_{\tau\tau}$ can be expressed in terms of the other components. Moreover, it can be verified that the solutions (7.4.24), (7.4.29) and (7.4.39) satisfy the unused equation (7.3.18) which, it transpires, is equivalent to equation (7.3.17a) when using the fact that the stress-energy tensor is conserved, i.e. $\nabla_\mu \widetilde{T}^{\mu\nu} = 0$.

In the next two sections, 7.5 and 7.6, we will evaluate the integrals in the solutions (7.4.24), (7.4.29) and (7.4.39) when the stress-energy tensor is constructed using RKT and QFT, respectively.

## § 7.5 RKT-corrected metric perturbations

In this section, we will use the RKT-SET (7.2.10) as a source term in the LQCEE, by substituting into the solutions (7.4.24), (7.4.29) and (7.4.39). Performing the integrations, we find the metric perturbations are

$$\begin{aligned}\delta A(r) = \mathcal{A}_1 + \frac{r^2}{(1-r^2)^2}\mathcal{A}_2 + \frac{\mathcal{K}}{a^2\beta^3(1-r^2)^2}\Bigg\{&4r^2 \operatorname{arctanh}\left(r^2 - \widetilde{\Gamma}_{(3)}^{-1}\right)\\ &-2r^2\log\left(2\Omega^2 - 1 - r^2 + \widetilde{\Gamma}_{(3)}^{-1}\right)\\ &+\frac{\widetilde{\Gamma}_{(3)}\left(1-r^2\right)}{\left(1-\Omega^2\right)^2}\left[\left(1+r^2\right)^2 + \Omega^2\left(1 - 10r^2 + r^4 + 4\Omega^2 r^2\right)\right]\Bigg\},\end{aligned} \tag{7.5.1a}$$

$$\delta B(r) = \frac{\left(1+r^2\right)^2}{r^2\left(1-r^2\right)^2}\delta A(r), \tag{7.5.1b}$$

$$\begin{aligned}\delta A(r) + \delta C(r) = \frac{8\mathcal{K}r^2\left(1+r^2\right)^2}{a^2\beta^3\left(1-r^2\right)^4}\Bigg[&\frac{a^2\beta^3}{8\mathcal{K}}\mathcal{C}_1 + \widetilde{\Gamma}_{(3)}\left(1-r^2\right) + \operatorname{arctanh}\left(r^2 - \widetilde{\Gamma}_{(3)}^{-1}\right)\\ &-\frac{1}{2}\log\left(2\Omega^2 - 1 - r^2 + \widetilde{\Gamma}_{(3)}^{-1}\right)\Bigg],\end{aligned} \tag{7.5.1c}$$

$$\delta D(r) = \mathcal{D}_1 + \frac{1+r^4}{r^2}\mathcal{D}_2 + \frac{\mathcal{K}\Omega\widetilde{\Gamma}_{(3)}\left(1-r^2\right)^3}{2a^2\beta^3\left(1-\Omega^2\right)^2 r^2}. \tag{7.5.1d}$$

In order that the solutions (7.5.1) be real, the arguments of arctanh and log need to have ranges of $(-1,1)$ and $(0,\infty)$ respectively. This can easily be verified; at $\Omega = 0$, the argument of the arctanh is $-1$, and monotonically increases as $\Omega$ increases to $+1$ at $\Omega = 1$, for all $r \in [0,1]$. Similarly, the argument of the logarithm is positive for all $\{r,\Omega\} \in [0,1]$.

To find the corresponding nonrotating solution, we first need to treat the logarithm and hyperbolic arctangent terms. We do this by rewriting the hyperbolic arctangent in terms of logarithms as

$$\operatorname{arctanh}(x) = \frac{1}{2}\log\left|\frac{1+x}{1-x}\right|. \tag{7.5.2}$$

In the solutions for $\delta A$ (7.5.1a) and $\delta A + \delta C$ (7.5.1c), we can thus combine the hyperbolic

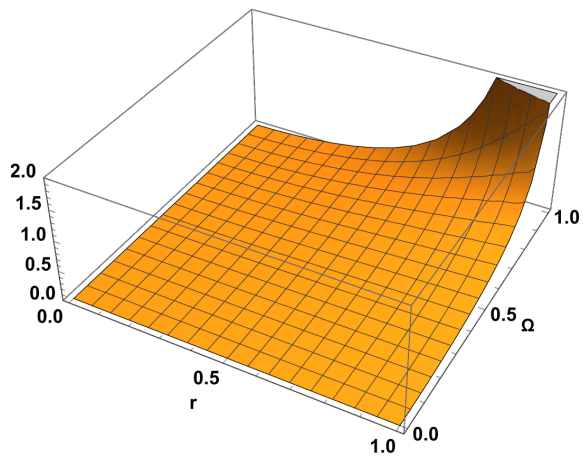


Figure 7.1: The ratio $(1 + r^2 - \widetilde{\Gamma}^{-1}_{(3)})/(1 - r^2 + \widetilde{\Gamma}^{-1}_{(3)})$, for $r, \Omega \in [0, 1)$. This ratio is always nonnegative.

arctangent and logarithms as

$$\begin{aligned}
&\operatorname{arctanh}\left(r^2 - \widetilde{\Gamma}^{-1}_{(3)}\right) - \frac{1}{2}\log\left(2\Omega^2 - 1 - r^2 + \widetilde{\Gamma}^{-1}_{(3)}\right) \\
&\qquad = \frac{1}{2}\log\left|\frac{1 + r^2 - \widetilde{\Gamma}^{-1}_{(3)}}{1 - r^2 + \widetilde{\Gamma}^{-1}_{(3)}}\right| - \frac{1}{2}\log\left(2\Omega^2 - 1 - r^2 + \widetilde{\Gamma}^{-1}_{(3)}\right) \\
&\qquad = \frac{1}{2}\log\left(\frac{1 + r^2 - \widetilde{\Gamma}^{-1}_{(3)}}{\left[1 - r^2 + \widetilde{\Gamma}^{-1}_{(3)}\right]^2 + 2\left(\Omega^2 - 1\right)\left[1 - r^2 + \widetilde{\Gamma}^{-1}_{(3)}\right]}\right), \qquad (7.5.3)
\end{aligned}$$

where in the second line, we have dropped the absolute value, since the argument within it is always nonnegative - this can be seen in figure 7.1.

Having combined the logarithm and hyperbolic arctangent terms, provided we make a suitable branch cut for the logarithm functions, we can safely take the limit $\Omega \to 0$ in the solutions (7.5.1), the result of which is

$$\delta A(r) = \mathcal{A}_1 + \frac{r^2}{\left(1 - r^2\right)^2}\mathcal{A}_2 + \frac{\mathcal{K}}{a^2\beta^3\left(1 - r^2\right)^2}\left[1 - r^4 + 2r^2\log\left(\tfrac{1}{2}r^2\right)\right], \qquad (7.5.4a)$$

$$\delta C(r) = -\delta A(r) + \frac{r^2\left(1+r^2\right)^2}{\left(1-r^2\right)^4}\mathcal{C}_1 + \frac{4\mathcal{K}r^2\left(1+r^2\right)}{a^2\beta^3\left(1-r^2\right)^4}\left[2\left(1-r^2\right)+\left(1+r^2\right)\log\left(\tfrac{1}{2}r^2\right)\right], \tag{7.5.4b}$$

with the perturbation in $B$ still given by equation (7.5.1b), and $\delta D(r) \equiv 0$.

To fix the arbitrary constants in the solutions (7.5.1), we will apply suitable boundary conditions to the perturbations; this will be done in section 7.7. For that purpose, we need the expansions of the metric perturbations (7.5.1) around the origin $r = 0$ and the space-time boundary $r = 1$. Near the origin, to leading order, we have

$$\delta A(r) = \mathcal{A}_1 + \frac{\mathcal{K}\left(1+\Omega^2\right)}{a^2\beta^3\left(1-\Omega^2\right)^2} + \mathcal{O}(r^2), \tag{7.5.5a}$$

$$\delta B(r) = \frac{1}{r^2}\left[\mathcal{A}_1 + \frac{\mathcal{K}\left(1+\Omega^2\right)}{a^2\beta^3\left(1-\Omega^2\right)^2}\right] + \mathcal{O}(r^0), \tag{7.5.5b}$$

$$\delta C(r) = -\left[\mathcal{A}_1 + \frac{\mathcal{K}\left(1+\Omega^2\right)}{a^2\beta^3\left(1-\Omega^2\right)^2}\right] + \mathcal{O}(r^2), \tag{7.5.5c}$$

$$\delta D(r) = \frac{1}{2r^2}\left[2\mathcal{D}_2 + \frac{\mathcal{K}\Omega}{a^2\beta^3\left(1-\Omega^2\right)^2}\right] + \mathcal{O}(r^0), \tag{7.5.5d}$$

whilst close to the space-time boundary $r \to 1$, the leading-order behaviour is

$$\delta A(r) = \frac{1}{4}\left[\frac{1}{(1-r)^2} - \frac{1}{1-r}\right]\left\{\mathcal{A}_2 - \frac{2\mathcal{K}}{a^2\beta^3}\log\left[2\left(1-\Omega^2\right)\right]\right\} + \mathcal{O}(1), \tag{7.5.6a}$$

$$\delta B(r) = \frac{1}{4(1-r)^4}\left\{\mathcal{A}_2 - \frac{2\mathcal{K}}{a^2\beta^3}\log\left[2\left(1-\Omega^2\right)\right]\right\} + \mathcal{O}([1-r]^{-2}), \tag{7.5.6b}$$

$$\delta C(r) = \frac{1}{4(1-r)^4}\left\{\mathcal{C}_1 - \frac{4\mathcal{K}}{a^2\beta^3}\log\left[2\left(1-\Omega^2\right)\right]\right\} + \mathcal{O}([1-r]^{-3}), \tag{7.5.6c}$$

$$\delta D(r) = \mathcal{D}_1 + 2\mathcal{D}_2 + \mathcal{O}(1-r). \tag{7.5.6d}$$

To ensure regularity at the origin, we must fix certain constants. For example, the metric perturbation $\delta B$ is of order $\mathcal{O}(r^{-2})$ at the origin, and in order for it to be regular, we require

$$\mathcal{A}_1 = -\frac{\mathcal{K}\left(1+\Omega^2\right)}{a^2\beta^3\left(1-\Omega^2\right)^2}, \tag{7.5.7}$$

under which, the perturbations $\delta A$ and $\delta C$ are then of order $\mathcal{O}(r^2)$, and hence regular as $r \to 0$. In a similar fashion, $\delta D$ is not divergent at the origin provided we fix

$$\mathcal{D}_2 = -\frac{\mathcal{K}\Omega}{2a^2\beta^3\left(1-\Omega^2\right)^2}. \tag{7.5.8}$$

At the space-time boundary, the situation is not as simple. Nevertheless, we can fix the constants $\mathcal{A}_2$ and $\mathcal{C}_1$ to ensure that the leading order divergences in $\delta A$, $\delta B$ and $\delta C$ vanish, by setting them to be

$$\mathcal{A}_2 = \frac{2\mathcal{K}}{a^2\beta^3}\log\left[2\left(1-\Omega^2\right)\right], \tag{7.5.9a}$$

$$\mathcal{C}_1 = \frac{4\mathcal{K}}{a^2\beta^3}\log\left[2\left(1-\Omega^2\right)\right]. \tag{7.5.9b}$$

In contrast, the perturbation $\delta D$ will be regular at the boundary provided

$$\mathcal{D}_1 = -2\mathcal{D}_2. \tag{7.5.10}$$

We will return to these boundary conditions and discuss them in further detail in section 7.7.

## § 7.6 Quantum-corrected metric perturbations

We next consider the solutions (7.4.24), (7.4.29) and (7.4.39) when the stress-energy tensor is given by the QFT-RSET (7.2.3). Due to the underlying complexity in the stress-energy tensor components, the integrals in the solutions (7.4.24), (7.4.29) and (7.4.39) prove much more challenging to compute. Nevertheless, they are still possible and can be computed using `Mathematica`. The metric perturbations take the form:

$$\begin{aligned}\delta A(r) = \mathcal{A}_1 &+ \frac{r^2}{\left(1-r^2\right)^2}\mathcal{A}_2 + \frac{r^2}{32\pi\left(1-r^2\right)^2} \\ &\times \sum_{j=1}^{\infty}\left[\mathcal{E}_+ \operatorname{cosech}^3\left(\tfrac{1}{2}j\beta\right)\log\left(\mathcal{F}_-\right) - \lambda\mathcal{E}_- \operatorname{sech}^3\left(\tfrac{1}{2}j\beta\right)\log\left(\mathcal{F}_+\right)\right]\end{aligned}$$

$$+\frac{1}{16\sqrt{2}\pi}\left(1-r^2\right)\sum_{j=1}^{\infty}\frac{1}{\mathcal{C}_{(3)}^2}\left[\frac{\mathcal{E}_+\mathcal{G}_-}{\mathcal{A}_{(-,3,\Omega;\,r)}^{3/2}}-\frac{\lambda\mathcal{E}_-\mathcal{G}_+}{\mathcal{A}_{(+,3,\Omega;\,r)}^{3/2}}\right]$$
$$-\frac{r^2}{2\sqrt{2}\pi\left(1-r^2\right)}\sum_{j=1}^{\infty}\frac{1}{\mathcal{C}_{(3)}}\left[\frac{\mathcal{E}_+}{\mathcal{A}_{(-,3,\Omega;\,r)}^{3/2}}\left(2\mathcal{G}_--3\mathcal{H}_-\right)\operatorname{cosech}^2\left(\tfrac{1}{2}j\beta\right)\right.$$
$$\left.-\frac{\lambda\mathcal{E}_-}{\mathcal{A}_{(+,3,\Omega;\,r)}^{3/2}}\left(2\mathcal{G}_+-3\mathcal{H}_+\right)\operatorname{sech}^2\left(\tfrac{1}{2}j\beta\right)\right], \tag{7.6.1a}$$

$$\delta B(r)=\frac{\left(1+r^2\right)^2}{r^2\left(1-r^2\right)^2}\delta A, \tag{7.6.1b}$$

$$\delta A(r)+\delta C(r)=\frac{r^2\left(1+r^2\right)^2}{\left(1-r^2\right)^4}\mathcal{C}_1+\frac{r^2\left(1+r^2\right)^2}{16\sqrt{2}\pi\left(1-r^2\right)^4}$$
$$\times\sum_{j=1}^{\infty}\left[\frac{\mathcal{E}_+}{\mathcal{A}_{(-,3,\Omega;\,r)}^{1/2}}\operatorname{cosech}\left(\tfrac{1}{2}j\beta\right)^2\right.$$
$$\times\left\{4\left(1-r^2\right)+\sqrt{2}\mathcal{A}_{(-,3,\Omega;\,r)}^{1/2}\operatorname{cosech}\left(\tfrac{1}{2}j\beta\right)\log\left(\mathcal{F}_-\right)\right\}$$
$$-\frac{\lambda\mathcal{E}_-}{\mathcal{A}_{(+,3,\Omega;\,r)}^{1/2}}\operatorname{sech}\left(\tfrac{1}{2}j\beta\right)^2$$
$$\left.\times\left\{4\left(1-r^2\right)+\sqrt{2}\mathcal{A}_{(+,3,\Omega;\,r)}^{1/2}\operatorname{sech}\left(\tfrac{1}{2}j\beta\right)\log\left(\mathcal{F}_+\right)\right\}\right], \tag{7.6.1c}$$

$$\delta D(r)=\mathcal{D}_1+\frac{1+r^4}{r^2}\mathcal{D}_2$$
$$+\frac{\left(1-r^2\right)^3}{16\sqrt{2}\pi r^2}\sum_{j=1}^{\infty}\frac{1}{\mathcal{C}_{(3)}^2}\sinh\left(j\beta\right)\sinh\left(j\beta\Omega\right)\left[\mathcal{A}_{(-,3,\Omega;\,r)}^{-1/2}-\lambda\mathcal{A}_{(+,3,\Omega;\,r)}^{-1/2}\right], \tag{7.6.1d}$$

where expressions for $\mathcal{A}_{(\pm,3,\Omega;\,r)}$ (7.2.3b) and $\mathcal{C}_{(3)}$ (5.2.26) were given earlier and we have defined the new quantities

$$\mathcal{E}_\pm=\pm2+\cosh\left(j\beta\right)+\cosh\left(j\beta\Omega\right), \tag{7.6.1e}$$

$$\mathcal{F}_\pm = \mp r^2 \frac{\sqrt{2}\mathcal{A}^{1/2}_{(\pm,3,\Omega;\,r)} \cosh\left(\frac{1}{2}j\beta\right) \mp \left(1-r^2\right) + \left(1+r^2\right)\cosh\left(j\beta\right) - 2\cosh\left(j\beta\Omega\right)}{\sqrt{2}\mathcal{A}^{1/2}_{(\pm,3,\Omega;\,r)} \cosh\left(\frac{1}{2}j\beta\right) \pm \left(1-r^2\right) + \left(1+r^2\right)\cosh\left(j\beta\right) - 2r^2\cosh\left(j\beta\Omega\right)}, \tag{7.6.1f}$$

$$\begin{aligned}\mathcal{G}_\pm = {} & \left(1+r^2\right)^2 \cosh\left(j\beta\right)\left\{\cosh\left(j\beta\right) + \cosh\left(j\beta\Omega\right) \pm 3\right\} - 8r^2\cosh\left(j\beta\Omega\right)^2 \\ & \pm \left(1 - 14r^2 + r^4\right)\cosh\left(j\beta\Omega\right) + 2\left(1-r^2\right)^2,\end{aligned} \tag{7.6.1g}$$

$$\begin{aligned}\mathcal{H}_\pm = {} & \left[\pm\left(1-r^2\right)^2 + \left(1+r^2\right)\cosh\left(j\beta\right) - 2r\cosh\left(j\beta\Omega\right)\right] \\ & \times \left[\pm\left(1+r^2\right)^2 + \left(1+r^2\right)\cosh\left(j\beta\right) + 2r\cosh\left(j\beta\Omega\right)\right].\end{aligned} \tag{7.6.1h}$$

In the nonrotating limit, $\Omega = 0$, the expressions above simplify somewhat, but are still unwieldy; there is no particular insight to be gained from their explicit display.

As in the RKT case in section 7.5, to find the arbitrary constants of integration, suitable boundary conditions will be applied in section 7.7. We therefore need to expand the solutions (7.6.1) around the origin $r = 0$ and boundary $r = 1$. To leading order, the expansions as $r \to 0$ are

$$\delta A(r) = \mathcal{A}_1 + \frac{1}{32\pi}\sum_{j=1}^{\infty}\frac{\mathcal{E}_+\mathcal{E}_-}{\mathcal{C}^2_{(3)}}\left[\operatorname{cosech}\left(\tfrac{1}{2}j\beta\right) - \lambda\operatorname{sech}\left(\tfrac{1}{2}j\beta\right)\right] + \mathcal{O}(r^2), \tag{7.6.2a}$$

$$\delta B(r) = \frac{1}{r^2}\left\{\mathcal{A}_1 + \frac{1}{32\pi}\sum_{j=1}^{\infty}\frac{\mathcal{E}_+\mathcal{E}_-}{\mathcal{C}^2_{(3)}}\left[\operatorname{cosech}\left(\tfrac{1}{2}j\beta\right) - \lambda\operatorname{sech}\left(\tfrac{1}{2}j\beta\right)\right]\right\} + \mathcal{O}(r^0), \tag{7.6.2b}$$

$$\delta C(r) = -\left\{\mathcal{A}_1 + \frac{1}{32\pi}\sum_{j=1}^{\infty}\frac{\mathcal{E}_+\mathcal{E}_-}{\mathcal{C}^2_{(3)}}\left[\operatorname{cosech}\left(\tfrac{1}{2}j\beta\right) - \lambda\operatorname{sech}\left(\tfrac{1}{2}j\beta\right)\right]\right\} + \mathcal{O}(r^2), \tag{7.6.2c}$$

$$\delta D(r) = \frac{1}{r^2}\left\{\mathcal{D}_2 + \frac{1}{32\pi}\sum_{j=1}^{\infty}\frac{1}{\mathcal{C}^2_{(3)}}\sinh\left(j\beta\Omega\right)\left[\cosh\left(\tfrac{1}{2}j\beta\right) - \lambda\sinh\left(\tfrac{1}{2}j\beta\right)\right]\right\} + \mathcal{O}(r^0). \tag{7.6.2d}$$

Recall the corresponding expansions in the RKT case, given by equation (7.5.5). Comparing the two, we see that the behaviour near the origin is very similar in both cases. In particular, the perturbations $\delta A$ and $\delta C$ are both manifestly regular at the origin, and the

perturbation $\delta B$ is divergent at the origin unless we fix

$$\mathcal{A}_1 = -\frac{1}{32\pi}\sum_{j=1}^{\infty}\frac{\mathcal{E}_+\mathcal{E}_-}{\mathcal{C}_{(3)}^2}\left[\operatorname{cosech}\left(\tfrac{1}{2}j\beta\right) - \lambda\operatorname{sech}\left(\tfrac{1}{2}j\beta\right)\right], \tag{7.6.3}$$

and similarly, the perturbation $\delta D$ is only regular at the origin provided we set

$$\mathcal{D}_2 = -\frac{1}{32\pi}\sum_{j=1}^{\infty}\frac{1}{\mathcal{C}_{(3)}^2}\sinh\left(j\beta\Omega\right)\left[\cosh\left(\tfrac{1}{2}j\beta\right) - \lambda\sinh\left(\tfrac{1}{2}j\beta\right)\right]. \tag{7.6.4}$$

Under the assumption that the arbitrary constant $\mathcal{A}_1$ is fixed as in equation (7.6.3), the metric perturbations $\delta A$ and $\delta C$ are both of order $\mathcal{O}(r^2)$ at the origin.

In a similar fashion, the expansions of the solutions (7.6.1) around the boundary $r \to 1$ are given by

$$\delta A(r) = \frac{\mathcal{A}_2}{4\left(1-r\right)^2} - \frac{\mathcal{A}_2}{4\left(1-r\right)} + \frac{1}{16}\left(16\mathcal{A}_1 - \mathcal{A}_2\right) + \mathcal{O}(1-r), \tag{7.6.5a}$$

$$\delta B(r) = \frac{\mathcal{A}_2}{4\left(1-r\right)^4} + \frac{\mathcal{A}_2}{4\left(1-r\right)^3} + \frac{1}{16}\left(16\mathcal{A}_1 - \mathcal{A}_2\right) + \mathcal{O}\left[(1-r)^{-2}\right], \tag{7.6.5b}$$

$$\delta C(r) = \frac{\mathcal{C}_1}{4\left(1-r\right)^4} - \frac{\mathcal{C}_1}{2\left(1-r\right)^3} + \frac{3\mathcal{C}_1 - 2\mathcal{A}_2}{4\left(1-r\right)^2} + \mathcal{O}\left[(1-r)^{-1}\right], \tag{7.6.5c}$$

$$\delta D(r) = \mathcal{D}_1 + 2\mathcal{D}_2 + \mathcal{O}(1-r). \tag{7.6.5d}$$

It is in these expansions that we see markedly different behaviour between the QFT (7.6.5) and RKT (7.5.6) cases. In the RKT case (7.5.6), the leading-order behaviour is dependent on the RKT-SET, whereas in the QFT case (7.6.5), the QFT-RSET makes only a sub-leading contribution to the metric perturbations; the leading-order behaviour is dependent entirely on the arbitrary constants of integration. In order to guarantee that the perturbation $\delta A$ is regular at the boundary, we can set $\mathcal{A}_2 = 0$, and if we also set $\mathcal{C}_1 = 0$, then the perturbations $\delta B$ and $\delta C$ lose their leading-order divergences. In the next section we will return to the imposition of suitable boundary conditions in order to set the arbitrary constants of integration.

## § 7.7 Solitons

In order to aid in the interpretation of the rotating, quantum-corrected metrics (7.5.1,7.6.1), we make a change of coordinates such that we make a new metric ansatz

$$\mathrm{d}s^2 = a^{-2}\left\{ -N(R)f(R)\,\mathrm{d}\tau^2 + N(R)^{-1}\,\mathrm{d}R^2 + R^2\left[N^{\phi}(R)\,\mathrm{d}\tau + \mathrm{d}\phi\right]^2\right\}, \tag{7.7.1}$$

which takes the BTZ-like form [78] - see section 6.5. To find the explicit coordinate transformation, we compare the two metric ansätze (7.3.1) and, (7.7.1), and by focusing on the $\mathrm{d}\phi^2$ component, we have that

$$R^2 = \frac{C(r)}{A(r)} = R_0^2 + a\ell_{\mathrm{P}}\,\delta R^2 + \mathcal{O}\left(a^2\ell_{\mathrm{P}}^2\right), \tag{7.7.2}$$

where we have retained the explicit dependence on the Planck length $\ell_{\mathrm{P}}$. We can find both the background quantity $R_0^2$ and the perturbation $\delta R^2$ by expanding the metric functions $A(r)$ and $C(r)$ in the Planck length, using equations (7.3.1b) and (7.3.1d) respectively. To first order, this yields

$$R^2 = \frac{4r^2}{(1-r^2)^2} + \frac{1}{(1+r^2)^2}\left[\left(1-r^2\right)^2\delta C - 4r^2\delta A\right]a\ell_{\mathrm{P}} + \mathcal{O}(a^2\ell_{\mathrm{P}}^2), \tag{7.7.3}$$

from which we can identify

$$R_0^2 = \frac{4r^2}{(1-r^2)^2}, \qquad \text{and} \qquad \delta R^2 = \frac{1}{(1+r^2)^2}\left[\left(1-r^2\right)^2\delta C - 4r^2\delta A\right]. \tag{7.7.4}$$

If we assume that, at the origin, the perturbation $\delta C(r)$ vanishes and the perturbation $\delta A(r)$ is regular, then the new radial coordinate $R \to 0$ as $r \to 0$. Under this assumption, in both the RKT and QFT cases, this fixes the constant $\mathcal{A}_1$ ((7.5.7) for RKT; (7.6.3) for QFT), ensures the perturbation $\delta A(r)$ ((7.5.1a) for RKT; (7.6.1a) for QFT) is zero at the origin and fixes $\delta B(r)$ ((7.5.1b); (7.6.1b)) to be regular there. See the discussion in sections 7.5 and 7.6. At the space-time boundary, $r \to 1$, the zero-order contribution $R_0^2$ (7.7.4) tends to infinity. Meanwhile, for the perturbed term $\delta R^2$, we recall the expansions of the

perturbations at the space-time boundary for both the RKT (7.5.6) and QFT (7.6.5) cases. By substituting in the leading order terms of $\delta A$ and $\delta C$ into the perturbation $\delta R^2$ (7.7.4), we have

$$\delta R^2 = \frac{1}{(1+r^2)^2}\Big[\left(1-r^2\right)^{-2}\mathscr{C}_{\mathrm{RKT/QFT}} - \left(1-r^2\right)^{-2}\mathscr{A}_{\mathrm{RKT/QFT}}\Big] \sim \left(1-r^2\right)^{-2}, \qquad r\to 1, \tag{7.7.5a}$$

where

$$\mathscr{A}_{\mathrm{RKT}} = \mathcal{A}_2 - \frac{2\mathcal{K}}{a^2\beta^3}\log[2\left(1-\Omega^2\right)], \tag{7.7.5b}$$

$$\mathscr{C}_{\mathrm{RKT}} = \frac{\mathcal{C}_1}{4} - \frac{\mathcal{K}}{a^2\beta^3}\log[2\left(1-\Omega^2\right)], \tag{7.7.5c}$$

$$\mathscr{A}_{\mathrm{QFT}} = \mathcal{A}_2, \tag{7.7.5d}$$

$$\mathscr{C}_{\mathrm{QFT}} = \frac{\mathcal{C}_1}{4}. \tag{7.7.5e}$$

From the expansion (7.7.5a), it is clear that as $r\to 1$, in general the perturbation $\delta R^2$ tends towards infinity, and so the coordinate range is therefore $R\in[0,\infty)$. However, by considering equations (7.7.5b)-(7.7.5e) we see that there exist choices of the integration constants $\mathcal{A}_2$ and $\mathcal{C}_1$ such that the leading-order divergences in $\delta R^2$ (7.7.5) cancel; since these are different depending on whether we are considering an RKT-SET or a QFT-RSET we, in general, keep $\mathcal{A}_2$ and $\mathcal{C}_1$ arbitrary for now and detail specific choices later.

To find the other functions in the metric (7.7.1), we compare with our earlier ansatz (7.3.1), taking care to transform the infinitesimals between the old and new radial coordinate. The functions appearing in the metric (7.7.1) are given in terms of the metric perturbations found in section 7.4 as

$$N(R) = \frac{A(r)}{B(r)}\left(\frac{\mathrm{d}R}{\mathrm{d}r}\right)^2 = \frac{\left(1+r^2\right)^2}{\left(1-r^2\right)^2} + a\ell_{\mathrm{P}}\,\delta N + \mathcal{O}(a^2\ell_{\mathrm{P}}^2), \tag{7.7.6a}$$

$$f(R) = B(r)\left(\frac{\mathrm{d}r}{\mathrm{d}R}\right)^2 = 1 + a\ell_{\mathrm{P}}\,\delta f + \mathcal{O}(a^2\ell_{\mathrm{P}}^2), \tag{7.7.6b}$$

$$N^{\phi}(R) = D(r) = \Omega + a\ell_{\mathrm{P}}\,\delta D(r) + \mathcal{O}(a^2\ell_{\mathrm{P}}^2), \tag{7.7.6c}$$

where we have used the residual gauge freedom to set the perturbation $\delta B$ according to equation (7.4.25), and the leading-order perturbations $\delta N$ and $\delta f$ are given as

$$\begin{aligned}\delta N = &-\frac{1}{4r^2\left(1+r^2\right)^2}\Big[-4r^2\left(1+r^2\right)^2\delta A + r\left(1-r^2\right)\left(1+r^2\right)^3\delta A' \\ &+\left(1-r^2\right)^2\left(1+10r^2+r^4\right)\{\delta A+\delta C\} - r\left(1-r^2\right)^3\left(1+r^2\right)\left\{\delta A'+\delta C'\right\}\Big],\end{aligned} \tag{7.7.6d}$$

$$\begin{aligned}\delta f = \frac{\left(1-r^2\right)^3}{4r^2\left(1+r^2\right)^4}\Big[&-r\left(1+r^2\right)^3\delta A' + r\left(1+r^2\right)\left(1-r^2\right)^2\left\{\delta A'+\delta C'\right\} \\ &-\left(1-r^2\right)\left(1+10r^2+r^4\right)\{\delta A+\delta C\}\Big].\end{aligned} \tag{7.7.6e}$$

In analogy with the BTZ black hole [32, 33, 78], we define new physical quantities which represent the mass and angular momentum of the soliton. In the original BTZ metric, the mass $M$ and angular momentum $J$ (both constant) are defined in terms of the functions $N$ and $N^{\phi}$ as [32, 33]

$$N(R) = R^2 + 1 - M + \frac{J^2}{4R^2}, \qquad N^{\phi}(R) = \frac{J}{2R^2}. \tag{7.7.7}$$

Hence, in an analogous sense, we define a perturbed mass function $\delta m$ and perturbed angular momentum function $\delta j$, defined in terms of the functions $N$ and $N^{\phi}$ as

$$N(R) = R^2 + 1 - a\ell_{\mathrm{P}}\,\delta m + \mathcal{O}(a^2\ell_{\mathrm{P}}^2), \tag{7.7.8a}$$

$$N^{\phi}(R) = \Omega - a\ell_{\mathrm{P}}\frac{\delta j}{2R^2} + \mathcal{O}(a^2\ell_{\mathrm{P}}^2), \tag{7.7.8b}$$

where, unlike in the original BTZ case (6.5.1), the mass and angular momentum functions are no longer constant and instead depend on the radial coordinate. The constant (perturbed) mass and angular momentum of the quantum-corrected space-time are then defined as the boundary limit of the mass and angular momentum functions respectively,

i.e.

$$\delta M = \lim_{R\to\infty} \delta m, \qquad \delta J = \lim_{R\to\infty} \delta j, \tag{7.7.9}$$

provided that these limits exist. In pure (rotating) anti-de Sitter space, the mass is $M \equiv -1$, and the angular momentum (of the space-time) is identically zero, since the co-rotating coordinates just describe the coordinate change of the metric. We are therefore interested in the situation where the perturbed mass (7.7.9) gives additional contributions to the space-time mass that arise from the metric perturbations. Comparing the BTZ functions (7.7.7) with the functions (7.7.8), we see there are two more points of note. Firstly, in the BTZ definition of $N(R)$ (7.7.7) there is an additional factor of $J^2/4R^2$ that is absent in our function $N(R)$ (7.7.8a); by definition, the perturbation $\delta j$ is order $\mathcal{O}(a\ell_{\mathrm{P}})$ and thus the perturbed term analogous to $J^2/4R^2$ would be of order $\mathcal{O}(a^2\ell_{\mathrm{P}}^2)$ - this is absorbed into the higher order terms. The other point of interest arises when considering the angular function $N^\phi(R)$ in the BTZ (7.7.7) and perturbed (7.7.8b) cases, namely the factor of $\Omega$ in the perturbed function. This is inserted to cover the coordinate transform to co-rotating coordinates; without this, by setting the Planck length to zero, the metric (7.7.1) would reduce to the metric in nonrotating coordinates. Physically, this does not pose a problem, since, the $\Omega$ term will not contribute to the physical angular momentum $\delta J$ by virtue of the fact that it is merely a coordinate peculiarity inserted to ensure the metric reduces to the metric in co-rotating coordinates in the zero Planck length limit.

To find expressions for the perturbed mass and angular momentum, we can rearrange the definitions (7.7.8). For the perturbed mass, we have

$$\begin{aligned} a\ell_{\mathrm{P}}\delta m &= R^2 + 1 - N(R) + \mathcal{O}(a^2\ell_{\mathrm{P}}^2) \\ &= \frac{4r^2}{(1-r^2)^2} + 1 - \frac{\left(1+r^2\right)^2}{(1-r^2)^2} + a\ell_{\mathrm{P}}\left[\delta R^2 + \delta N\right] + \mathcal{O}(a^2\ell_{\mathrm{P}}^2) \\ &= a\ell_{\mathrm{P}}\left[\delta R^2 + \delta N\right] + \mathcal{O}(a^2\ell_{\mathrm{P}}^2), \\ \iff \delta m &= \delta R^2 + \delta N + \mathcal{O}(a\ell_{\mathrm{P}}) \end{aligned} \tag{7.7.10}$$

where in the second line we have substituted in the expansions for $R^2$ (7.7.4) and $N(R)$ (7.7.6a). By substituting the subleading-order behaviour of $\delta R^2$ and $\delta N$ into the equation for $\delta m$ (7.7.10), we then have the following expression for the perturbed mass function:

$$\delta m = \frac{1}{4r^2\left(1+r^2\right)^2}\Big[r\left(1-r^2\right)\left(1+r^2\right)^3\delta A' - 8r^2\left(1+r^2\right)^2\delta A \\ - r\left(1+r^2\right)\left(1-r^2\right)^3\left\{\delta A' + \delta C'\right\} + \left(1-r^2\right)^2\left(1+14r^2+r^4\right)\left\{\delta A + \delta C\right\}\Big]. \tag{7.7.11}$$

We can follow the same procedure to find the perturbed angular momentum function. We first rearrange equation (7.7.8b), before substituting in the expansions for $R^2$ (7.7.4) and $N^\phi$ (7.7.6c). This yields

$$\begin{aligned} a\ell_{\mathrm{P}}\,\delta j &= 2R^2\left[\Omega - N^\phi(R)\right] + \mathcal{O}(a^2\ell_{\mathrm{P}}^2) \\ &= 2\left[\frac{4r^2}{\left(1-r^2\right)^2} + a\ell_{\mathrm{P}}\,\delta R^2 + \mathcal{O}(a^2\ell_{\mathrm{P}}^2)\right]\left[-a\ell_{\mathrm{P}}\,\delta D + \mathcal{O}(a^2\ell_{\mathrm{P}}^2)\right] \\ &= -\frac{8r^2\,a\ell_{\mathrm{P}}\delta D}{\left(1-r^2\right)^2} + \mathcal{O}(a^2\ell_{\mathrm{P}}^2), \\ \iff \delta j &= -\frac{8r^2\,\delta D}{\left(1-r^2\right)^2}. \end{aligned} \tag{7.7.12}$$

In order to obtain a finite mass and angular momentum, the limits (7.7.9) must exist. For this to be the case, we require the perturbations (7.7.11) and (7.7.12) to be regular as $r \to 1$; this in particular requires that $\delta D(r) \sim \mathcal{O}(1-r)^2$. Another requirement is that, to avoid a conical singularity, it must be the case that $\delta m$ vanishes at the origin $R \to 0$; in addition, so that the metric functions are all regular, $\delta m$ and $\delta f$ need to be finite at the origin and $\delta j \sim \mathcal{O}(R^2)$ as $R \to 0$. These conditions will help to fix the arbitrary constants of integration $\mathcal{A}_1$, $\mathcal{A}_2$ and $\mathcal{C}_1$ in the next two subsections.

### 7.7.1 RKT sourced solitons

In this subsection, we consider the case when the LQCEE are sourced by the RKT-SET, and thus when we have the metric perturbations (7.5.1). Our primary aim is to find the

perturbed mass and angular momentum of the space-time, however for completeness we will also explicitly calculate the solitonic metric perturbations (7.7.6).

We start by evaluating the perturbation in the transformed radial coordinate, $\delta R^2$. If we rewrite the perturbation (7.7.4) so that it is in the form

$$\delta R^2 = \frac{1}{\left(1+r^2\right)^2}\left[\left(1-r^2\right)^2\left\{\delta A(r)+\delta C(r)\right\}-\left(1+r^2\right)^2\delta A(r)\right], \tag{7.7.13}$$

then we can readily substitute in the perturbations (7.5.1a) and (7.5.1c), and hence, after some simplification, the perturbation $\delta R^2$ reads

$$\begin{aligned}\delta R^2 = -\mathcal{A}_1 + \frac{r^2}{\left(1-r^2\right)^2}\left(\mathcal{C}_1-\mathcal{A}_2\right) - \frac{\mathcal{K}}{a^2\beta^3\left(1-r^2\right)^2}\Bigg\{&\frac{\left(1-r^2\right)\widetilde{\Gamma}_{(3)}\mathscr{N}_R}{\left(1-\Omega^2\right)^2}\\ &+4r^2\operatorname{arctanh}\left(r^2-\widetilde{\Gamma}_{(3)}^{-1}\right)-2r^2\log\left(2\Omega^2-1-r^2+\widetilde{\Gamma}_{(3)}^{-1}\right)\Bigg\},\end{aligned} \tag{7.7.14a}$$

where, for ease of transcription, we have defined

$$\mathscr{N}_R = 1-6r^2+r^4+\Omega^2\left(1+6r^2+r^4\right)-4r^2\Omega^4, \tag{7.7.14b}$$

and both $\mathcal{K}$ (7.2.9) and $\widetilde{\Gamma}_{(3)}$ (7.1.5a) were defined previously. The asymptotic behaviour as $r\to 0$ and $r\to 1$ will be discussed later.

We next consider the perturbation $\delta N$ (7.7.6d). In a similar fashion to the perturbation in the radial coordinate $R^2$, the perturbation $\delta N$ depends only on the metric perturbations $\delta A$ (7.5.1a) and $\delta A+\delta C$ (7.5.1c). Substituting these in, we have

$$\begin{aligned}\delta N = \mathcal{A}_1 - \frac{\left(1+r^4\right)}{2\left(1-r^2\right)^2}\mathcal{A}_2 + \frac{\left(1+r^2\right)^2}{4\left(1-r^2\right)^2}\mathcal{C}_1 + \frac{\mathcal{K}}{a^2\beta^3\left(1-r^2\right)^2}\Bigg\{&\frac{\left(1-r^2\right)\widetilde{\Gamma}_{(3)}^{3}\mathscr{N}_N}{\left(1-\Omega^2\right)^2}\\ &-2r^2\log\left(2\Omega^2-1-r^2+\widetilde{\Gamma}_{(3)}^{-1}\right)+4r^2\operatorname{arctanh}\left(r^2-\widetilde{\Gamma}_{(3)}^{-1}\right)\Bigg\},\end{aligned} \tag{7.7.15a}$$

where, for ease of transcription, we have defined

$$\mathscr{N}_N = \left(1+r^2\right)^2\left[3-2r^2+3r^4-\Omega^2\left(1+10r^2+r^4\right)\right]+16r^4\Omega^4\left(3-\Omega^2\right). \tag{7.7.15b}$$

We can find a similar, but more concise expression for perturbation $\delta f$:

$$\delta f = f_0 + \frac{2\mathcal{K}\widetilde{\Gamma}^3_{(3)}\left(1-r^2\right)^3}{a^2\beta^3\left(1-\Omega^2\right)}, \tag{7.7.16a}$$

where we have defined the constant

$$f_0 = -\frac{1}{2}\mathcal{A}_2 + \frac{1}{4}\mathcal{C}_1. \tag{7.7.16b}$$

To obtain the perturbed mass function for RKT, we substitute the metric perturbations $\delta A$ (7.5.1a) and $\delta A + \delta C$ (7.5.1c) into the perturbed mass (7.7.11), which results in

$$\delta m = m_0 - \frac{4\mathcal{K}\mathcal{M}\widetilde{\Gamma}^3_{(3)}\left(1-r^2\right)}{a^2\beta^3\left(1-\Omega^2\right)^2}, \tag{7.7.17a}$$

where the constant $m_0$ is given in terms of the constants of integration (that appear in the LQCEE solutions (7.4.24), (7.4.29) and (7.4.39)) as

$$m_0 = -2\mathcal{A}_1 + \frac{1}{2}\mathcal{A}_2 - \frac{1}{4}\mathcal{C}_1. \tag{7.7.17b}$$

In addition, for brevity we have defined the quantity

$$\mathcal{M} = \left(1+r^2\right)^2 - 2r^2\Omega^2\left(1+\Omega^2\right). \tag{7.7.17c}$$

Finally, we can find the explicit form of the angular momentum function $\delta j$, which instead depends on the metric perturbation $\delta D$ (7.5.1d) and not the perturbations $\delta A$ and $\delta A + \delta C$. The angular momentum perturbation is therefore

$$\delta j = -\frac{8r^2}{\left(1-r^2\right)^2}\mathcal{D}_1 - \frac{8\left(1+r^4\right)}{\left(1-r^2\right)^2}\mathcal{D}_2 - \frac{4\mathcal{K}\Omega\widetilde{\Gamma}_{(3)}\left(1-r^2\right)}{a^2\beta^3\left(1-\Omega^2\right)^2}. \tag{7.7.18}$$

We can now consider the asymptotic behaviour of the perturbations (7.7.14), (7.7.15), (7.7.16), (7.7.17) and (7.7.18). Starting with the new radial coordinate perturbation $\delta R^2$, the expansion at the origin $r \to 0$ is

$$\delta R^2 = -\mathcal{A}_1 - \frac{\mathcal{K}\left(1+\Omega^2\right)}{a^2\beta^3\left(1-\Omega^2\right)^2} + \mathcal{O}(r^2). \tag{7.7.19}$$

In order for it to be the case that $\delta R^2 = 0$ at the origin, we set

$$\mathcal{A}_1 = -\frac{\mathcal{K}\left(1+\Omega^2\right)}{a^2\beta^3\left(1-\Omega^2\right)^2}, \tag{7.7.20}$$

which is the same condition as equation (7.5.7), which forces the metric perturbation $\delta B$ to be regular at the origin and the metric perturbation $\delta C$ to vanish there. Turning our attention now to the behaviour at the space-time boundary $r \to 1$, we have

$$\delta R^2 = -\frac{1}{4}\left\{\mathcal{A}_2 - \mathcal{C}_1 + \frac{2\mathcal{K}}{a^2\beta^3}\log\left[2\left(1-\Omega^2\right)\right]\right\}\left\{\frac{1}{(1-r)^2} - \frac{1}{1-r}\right\} + \mathcal{O}(1). \tag{7.7.21}$$

If we were to make the choice

$$\mathcal{A}_2 - \mathcal{C}_1 = -\frac{2\mathcal{K}}{a^2\beta^3}\log\left[2\left(1-\Omega^2\right)\right], \tag{7.7.22}$$

then as the boundary is approached, $r \to 1$, the perturbation $\delta R^2$ is finite. However, in analogy with the BTZ metric [32, 33], this is not a requirement, since, to zeroth order, the coordinate $R^2$ (7.7.4) diverges at the boundary. In addition, if we allow the constants $\mathcal{A}_2$ and $\mathcal{C}_1$ to take the values (7.5.9) required to cancel the leading order divergences of the metric perturbations $\delta A$, $\delta B$ and $\delta C$, then the condition (7.7.22) is manifestly satisfied.

We can now consider the asymptotic behaviour of the remaining perturbations. At the origin $r \to 0$ (which corresponds to $R \to 0$), we have

$$\delta N = -m_0 - \mathcal{A}_1 + \frac{\mathcal{K}\left(3-\Omega^2\right)}{a^2\beta^3\left(1-\Omega^2\right)^2} + \mathcal{O}(r^2), \tag{7.7.23a}$$

$$\delta f = f_0 + \frac{2\mathcal{K}}{a^2\beta^3\left(1-\Omega^2\right)} + \mathcal{O}(r^2), \tag{7.7.23b}$$

$$\delta m = m_0 - \frac{4\mathcal{K}}{a^2\beta^3\left(1-\Omega^2\right)^2} + \mathcal{O}(r^2), \tag{7.7.23c}$$

$$\delta j = -4\left[2\mathcal{D}_2 + \frac{\mathcal{K}\Omega}{a^2\beta^3\left(1-\Omega^2\right)^2}\right] + \mathcal{O}(r^2). \tag{7.7.23d}$$

There are a number of conditions we can impose on the expansions (7.7.23) to fix the constants of integration. Firstly, as discussed below equation (7.7.12), we require the

angular momentum perturbation function be $\mathcal{O}(R^2)$ as $R \to 0 \iff r \to 0$, and in order for this to hold, we fix

$$\mathcal{D}_2 = -\frac{\mathcal{K}\Omega}{2a^2\beta^3\left(1-\Omega^2\right)^2}. \tag{7.7.24}$$

Conveniently, this is the same as the condition (7.5.8) required for the perturbation $\delta D$ to be regular at the origin. Another condition we can impose is the requirement that the perturbed mass function $\delta m$ is zero at the origin, which is only the case when

$$m_0 = \frac{4\mathcal{K}}{a^2\beta^3\left(1-\Omega^2\right)^2}. \tag{7.7.25}$$

The remaining condition we wish to impose is finiteness of the remaining perturbations, $\delta f$ and $\delta N$, at the origin. It transpires that this holds irrespective of the choices of the constants $\mathcal{A}_1$, $\mathcal{A}_2$ and $\mathcal{C}_1$. If we were to fix $\mathcal{A}_1$ using the conditions (7.5.7), (7.7.20), then the perturbation $\delta N$ would be vanishing at the origin. In addition, the constant $f_0$ simply corresponds to a rescaling of the time coordinate, which we are free to do without loss of generality (see discussion around equation (7.3.8)). Using the relations (7.7.16b) and (7.7.17b), we can rewrite $f_0$ as

$$f_0 = -m_0 - 2\mathcal{A}_1 = -\frac{2\mathcal{K}}{a^2\beta^3\left(1-\Omega^2\right)}, \tag{7.7.26}$$

where in the last step we have used the relations (7.7.20) and (7.7.25). This fixes the asymptotic behaviour of the perturbations at the origin, so we now turn our attention to the behaviour at the boundary $r \to 1 \iff R \to \infty$.

The metric perturbations expand as follows:

$$\delta m = m_0 + \mathcal{O}(1-r), \tag{7.7.27}$$

$$\delta j = -2\left(\mathcal{D}_1 + 2\mathcal{D}_2\right)\left[\frac{1}{(1-r)^2} + \frac{1}{1-r}\right] + \frac{1}{2}\mathcal{D}_1 - 7\mathcal{D}_2 + \mathcal{O}(1-r), \tag{7.7.28}$$

$$\delta f = f_0 + \mathcal{O}(1-r), \tag{7.7.29}$$

$$\delta N = -\frac{1}{4(1-r)^2}\left\{\mathcal{A}_2 - \mathcal{C}_1 + \frac{2\mathcal{K}}{a^2\beta^3}\log\left[2\left(1-\Omega^2\right)\right]\right\}$$

$$+\frac{1}{4\left(1-r\right)}\left\{\mathcal{A}_2-\mathcal{C}_1+\frac{2\mathcal{K}}{a^2\beta^3}\log\left[2\left(1-\Omega^2\right)\right]-\frac{4\mathcal{K}\Omega^2}{a^2\beta^3\sqrt{1-\Omega^2}}\right\}+\mathcal{O}(1). \quad (7.7.30)$$

It is clear from the expansions (7.7.27) that both $\delta m$ and $\delta f$ are finite on the adS boundary; meanwhile, the angular momentum perturbation diverges on the boundary unless

$$\mathcal{D}_1=-2\mathcal{D}_2=\frac{\mathcal{K}\Omega}{a^2\beta^3\left(1-\Omega^2\right)^2}, \quad (7.7.31)$$

where we have used equation (7.7.24) in the second equality. The conditions (7.7.24) and (7.7.31) match the conditions (7.5.8) and (7.5.10) that ensure the metric perturbation $\delta D$ is both regular at the origin and vanishing on the adS boundary. Finally, the remaining metric perturbation, $\delta N$, diverges as the boundary is approached $r\to 1 \iff R\to\infty$, regardless of the integration constants $\mathcal{A}_2$ and $\mathcal{C}_1$; however, we can at least cancel the leading-order divergence provided we set

$$\mathcal{A}_2-\mathcal{C}_1=-\frac{2\mathcal{K}}{a^2\beta^3}\log\left[2\left(1-\Omega^2\right)\right], \quad (7.7.32)$$

which is equivalent to the condition (7.7.22), that ensures the perturbation $\delta R^2$ is finite as the adS boundary is approached.

Therefore, by imposing regularity of the metric perturbations $\delta m$, $\delta j$, $\delta f$ and $\delta N$ at the origin $r=0$ and adS boundary $r=1$, as well as requiring that $\delta R^2$ vanishes at $r=0$, we fix the constants $\mathcal{D}_1$, $\mathcal{D}_2$, $m_0$, $\mathcal{A}_1$ and the combination $\mathcal{A}_2-\mathcal{C}_1$. Since the relation (7.7.17b) can be rearranged to give

$$4m_0+8\mathcal{A}_1=2\mathcal{A}_2-\mathcal{C}_1, \quad (7.7.33)$$

by fixing $m_0$ and $\mathcal{A}_1$, we also fix the combination $2\mathcal{A}_2-\mathcal{C}_1$, and therefore, all of the constants in the metric perturbations have been fixed. To find the explicit expressions for $\mathcal{A}_2$ and $\mathcal{C}_1$, we simultaneously solve

$$\begin{aligned}\mathcal{A}_2-\mathcal{C}_1 &= -\frac{2\mathcal{K}}{a^2\beta^3}\log\left[2\left(1-\Omega^2\right)\right],\\ 2\mathcal{A}_2-\mathcal{C}_1 &= \frac{8\mathcal{K}}{a^2\beta^3\left(1-\Omega^2\right)},\end{aligned} \quad (7.7.34)$$

which yields

$$\mathcal{A}_2 = \frac{8\mathcal{K}}{a^2\beta^3\left(1-\Omega^2\right)} + \frac{2\mathcal{K}}{a^2\beta^3}\log\left[2\left(1-\Omega^2\right)\right], \tag{7.7.35a}$$

$$\mathcal{C}_1 = \frac{8\mathcal{K}}{a^2\beta^3\left(1-\Omega^2\right)} + \frac{4\mathcal{K}}{a^2\beta^3}\log\left[2\left(1-\Omega^2\right)\right]. \tag{7.7.35b}$$

Somewhat interestingly, these do not match the relations (7.5.9) which are required to cancel the leading-order divergences in the perturbations $\delta A(r)$ and $\delta C(r)$ as the adS boundary is approached, $r \to 1$. We can therefore either cancel the leading-order divergences at the adS boundary in the perturbation $\delta N$ *or* the metric perturbations $\delta A$ and $\delta C$. Since we are primarily interested in the perturbed mass and angular momentum functions, we focus on the solitonic metric ansatz (7.7.1) and thus choose to use the constants (7.7.35).

The conditions (7.7.16b), (7.7.17b), (7.7.24), (7.7.31) and (7.7.35) are enough to uniquely fix the metric perturbations $\delta N$ (7.7.15), $\delta f$ (7.7.16), $\delta m$ (7.7.17) and $\delta j$ (7.7.18), in which case we have

$$\delta m = \frac{4\mathcal{K}\widetilde{\Gamma}^3_{(3)}}{a^2\beta^3\left(1-\Omega^2\right)^2}\left[\widetilde{\Gamma}^{-3}_{(3)} - \left(1-r^2\right)\mathcal{M}\right], \tag{7.7.36a}$$

$$\delta j = \frac{4\mathcal{K}\Omega\widetilde{\Gamma}_{(3)}}{a^2\beta^3\left(1-\Omega^2\right)^2}\left[\widetilde{\Gamma}^{-1}_{(3)} - \left(1-r^2\right)\right], \tag{7.7.36b}$$

$$\delta f = \frac{2\mathcal{K}\widetilde{\Gamma}^3_{(3)}}{a^2\beta^3\left(1-\Omega^2\right)}\left[\left(1-r^2\right)^3 - \widetilde{\Gamma}^{-3}_{(3)}\right], \tag{7.7.36c}$$

$$\begin{aligned}\delta N = \frac{\mathcal{K}}{a^2\beta^3\left(1-r^2\right)^2}\Bigg[&\frac{\left(1-r^2\right)\widetilde{\Gamma}^3_{(3)}\mathscr{N}_N}{\left(1-\Omega^2\right)} + \frac{\left(1+r^4\right)\left(5-7\Omega^2\right)+2r^2\left(3-\Omega^2\right)}{\left(1-\Omega^2\right)^2} \\ &+ \left(3+2r^2+3r^4\right)\log\left[2\left(1-\Omega^2\right)\right] - 2r^2\log\left[2\Omega^2-1-r^2+\widetilde{\Gamma}^{-1}_{(3)}\right] \\ &+ 4r^2\,\mathrm{arctanh}\left(r^2-\widetilde{\Gamma}^{-1}_{(3)}\right)\Bigg].\end{aligned} \tag{7.7.36d}$$

The quantities $\widetilde{\Gamma}_{(3)}$ (7.1.5a), $\mathcal{K}$ (7.2.9), $\mathscr{N}_N$ (7.7.15b), $\mathcal{M}$ (7.7.17c) were defined previously.

In the nonrotating limit $\Omega \to 0$, the perturbations (7.7.36) simplify considerably to

$$\delta m = \frac{8\mathcal{K}r^2\left(1+r^2\right)}{a^2\beta^3}, \tag{7.7.37}$$

$$\delta j = 0, \tag{7.7.38}$$

$$\delta f = -\frac{4\mathcal{K}r^2\left(3+r^4\right)}{a^2\beta^3\left(1+r^2\right)^3}, \tag{7.7.39}$$

$$\delta N = \frac{\mathcal{K}}{a^2\beta^3\left(1-r^2\right)^2\left(1+r^2\right)}\Big[8+3\log(2)+\{6+\log(2)\}\,r^2+\{16+\log(2)\}\,r^4 + \{2+3\log(2)\}\,r^6+2r^2\left(1+r^2\right)\log\left(2r^2\right)\Big]. \tag{7.7.40}$$

We are now in a position to find the perturbed mass $\delta M$ and angular momentum $\delta J$ of the space-time by taking the boundary value limit, $r \to 1$, of the perturbations (7.7.36), in which case we have

$$\delta M = \frac{4\mathcal{K}}{a^2\beta^3\left(1-\Omega^2\right)^2}, \tag{7.7.41}$$

$$\delta J = \frac{4\mathcal{K}\Omega}{a^2\beta^3\left(1-\Omega^2\right)^2}. \tag{7.7.42}$$

It is clear that, for $0 \leq \Omega < 1$, we have $0 \leq \delta J < \delta M$, which is the same bound as for the rotating BTZ black holes [32, 33], required for either a horizon to form or there to be no naked singularity. However, this does not necessarily indicate that a horizon will form in our setup or preclude the case that there will be no naked singularity. In figure 7.2, $\delta M$ and $\delta J$ are shown as functions of $\beta$, for two values of the angular speed $\Omega$. In both cases, the perturbed mass is larger than the perturbed angular momentum, however for angular speeds approaching the speed required to form a speed-of-light surface ($\Omega = 1$), the perturbed angular momentum and mass become very similar. Beyond the speed-of-light surface ($\Omega > 1$), the BTZ bound (6.5.2) will be violated, though we do not consider angular speeds higher than $\Omega = 1$. In addition, increasing the angular speed has a great effect on the size of the perturbed mass and angular momentum, with both being approximately

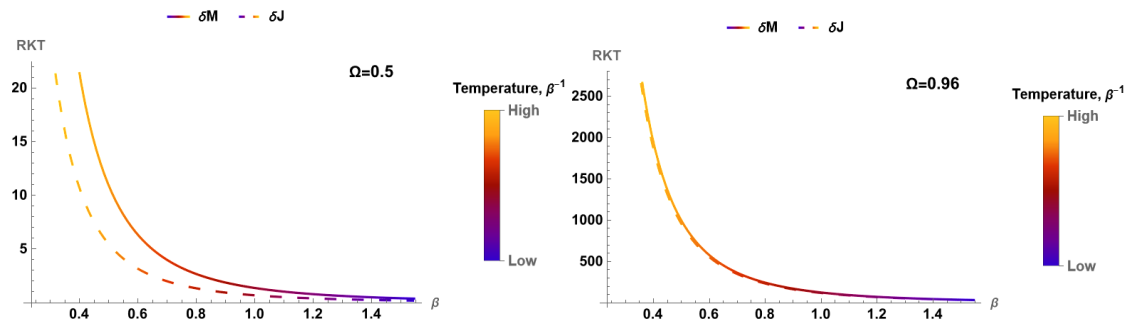


Figure 7.2: The perturbed mass $\delta M$ and angular momentum $\delta J$ against inverse temperature $\beta$. For the BTZ bound (6.5.2) to hold, the perturbed mass must always be greater than the perturbed angular momentum. As the angular speed is increased, the difference between the perturbed mass and angular momentum decreases, and verification of the BTZ bound is less obvious. The inverse adS length scale is fixed $a = 1$, and the inverse temperature is varied in the range $\beta \in [\pi/12, 59\pi/120]$.

one hundred times larger in the $\Omega = 0.96$ case than the $\Omega = 0.5$ case when considering a fixed inverse temperature.

In the nonrotating limit $\Omega = 0$, the angular momentum perturbation vanishes, and the mass perturbation reduces to

$$\delta M|_{\Omega=0} = \frac{4\mathcal{K}}{a^2\beta^3}. \tag{7.7.43}$$

In contrast, when $\Omega \to 1$, both the angular momentum and mass perturbations diverge. For a fixed angular speed $0 < \Omega < 1$, the angular momentum and mass perturbations are both proportional to the temperature cubed, $\beta^{-3}$. Both increase as the angular speed is increased, and increase without bound with increasing temperature. It is expected that, for sufficiently large angular speed ($\Omega \to 1$) or temperature, the linear approximation employed in this chapter will break down. A full nonlinear treatment is required to ascertain where the linear approximation will break down; this is similar to the link between chapters 8 and 9, where we have a linear and nonlinear treatment of the nonrotating problem in

$(3+1)$-dimensions. A more detailed discussion is found in section 9.6.

### 7.7.2 QFT sourced solitons

In this subsection, we consider the case when the LQCEE are sourced by the QFT-RSET, under which, the solutions are given by the perturbations (7.6.1). As for the RKT sourced solitons in section 7.7.1, our primary aim is finding the perturbed angular momentum and mass of the space-time; however, for completeness, we will also calculate the other solitonic metric perturbations (7.7.6). We begin by finding the perturbation $\delta R^2$, following the method in section 7.7.1. We rewrite the perturbation $\delta R^2$ so that it takes the form given in equation (7.7.13), and substitute in the metric perturbations (7.6.1a) and (7.6.1c), which yields, after much algebraic manipulation and simplification, the unwieldy expression

$$\begin{aligned}
\delta R^2 = & -\mathcal{A}_1 + \frac{r^2}{\left(1-r^2\right)^2}\left(\mathcal{C}_1 - \mathcal{A}_2\right) \\
& + \frac{r^2}{4\sqrt{2}\pi\left(1-r^2\right)} \sum_{j=1}^{\infty} \left[ \frac{\mathcal{E}_+}{\mathcal{A}^{1/2}_{(-,3,\Omega;\,r)}} \operatorname{cosech}^2(j\beta/2) - \frac{\lambda \mathcal{E}_-}{\mathcal{A}^{1/2}_{(+,3,\Omega;\,r)}} \operatorname{sech}^2(j\beta/2) \right] \\
& - \frac{\left(1-r^2\right)}{16\sqrt{2}\pi} \sum_{j=1}^{\infty} \frac{1}{\mathcal{C}^2_{(3)}} \left[ \frac{\mathcal{E}_+ \mathcal{G}_-}{\mathcal{A}^{3/2}_{(-,3,\Omega;\,r)}} - \frac{\lambda \mathcal{E}_- \mathcal{G}_+}{\mathcal{A}^{3/2}_{(+,3,\Omega;\,r)}} \right] \\
& + \frac{r^2}{32\pi\left(1-r^2\right)^2} \sum_{j=1}^{\infty} \left[ \mathcal{E}_+ \operatorname{cosech}^3(j\beta/2) \log(\mathcal{F}_-) - \lambda \mathcal{E}_- \operatorname{sech}^3(j\beta/2) \log(\mathcal{F}_+) \right] \\
& + \frac{r^2}{2\sqrt{2}\pi\left(1-r^2\right)} \sum_{j=1}^{\infty} \frac{1}{\mathcal{C}_{(3)}} \left[ \frac{\mathcal{E}_+}{\mathcal{A}^{3/2}_{(-,3,\Omega;\,r)}} \left\{2\mathcal{G}_- - 3\mathcal{H}_-\right\} \operatorname{cosech}^2(j\beta/2) \right. \\
& \qquad \left. - \frac{\lambda \mathcal{E}_-}{\mathcal{A}^{3/2}_{(+,3,\Omega;\,r)}} \left\{2\mathcal{G}_+ - 3\mathcal{H}_+\right\} \operatorname{sech}^2(j\beta/2) \right], \qquad (7.7.44)
\end{aligned}$$

where the quantities $\mathcal{C}_{(3)}$ (5.2.26), $\mathcal{A}_{(\pm,3,\Omega;\,r)}$ (7.2.3b), $\mathcal{E}_\pm$ (7.6.1e), $\mathcal{F}_\pm$ (7.6.1f), $\mathcal{G}_\pm$ (7.6.1g) and $\mathcal{H}_\pm$ (7.6.1h) were defined previously. We need to ensure that the perturbation $\delta R^2$ is zero at the origin, $r = 0 \iff R = 0$, as was the situation in the RKT case. Expanding

about $r = 0$, we have

$$\delta R^2 = -\mathcal{A}_1 - \frac{1}{32\pi}\sum_{j=1}^{\infty}\frac{\mathcal{E}_+\mathcal{E}_-}{\mathcal{C}_{(3)}^2}\left[\operatorname{cosech}(j\beta/2) - \lambda\operatorname{sech}(j\beta/2)\right] + \mathcal{O}(r^2), \tag{7.7.45}$$

from which it is clear that, in order to ensure that the perturbation $\delta R^2$ is zero at the origin, we require

$$\mathcal{A}_1 = -\frac{1}{32\pi}\sum_{j=1}^{\infty}\frac{\mathcal{E}_+\mathcal{E}_-}{\mathcal{C}_{(3)}^2}\left[\operatorname{cosech}(j\beta/2) - \lambda\operatorname{sech}(j\beta/2)\right]. \tag{7.7.46}$$

This is the same condition as the condition (7.6.3) required for the perturbation $\delta B$ to be regular at the origin.

We can similarly expand about the adS boundary, $r = 1$, and either impose regularity of $\delta R^2$ there or allow it to diverge, mimicking the behaviour of the BTZ metric [32, 33]. The expansion is

$$\delta R^2 = -\frac{1}{(1-r)}\left\{\frac{\mathcal{A}_2 - \mathcal{C}_1}{2} + \frac{1}{64\pi}\sum_{j=1}^{\infty}\left[\mathcal{E}_+\operatorname{cosech}^3(j\beta/2) - \lambda\mathcal{E}_-\operatorname{sech}^3(j\beta/2)\right]\right\} + \mathcal{O}([1-r]^0). \tag{7.7.47}$$

If we were to impose regularity at the boundary, then this would fix the combination

$$\mathcal{A}_2 - \mathcal{C}_1 = -\frac{1}{32\pi}\sum_{j=1}^{\infty}\left[\mathcal{E}_+\operatorname{cosech}^3(j\beta/2) - \lambda\mathcal{E}_-\operatorname{sech}^3(j\beta/2)\right], \tag{7.7.48}$$

though, in analogy with the BTZ metric, we need not impose this. If we were to choose this combination of $\mathcal{A}_2$ and $\mathcal{C}_1$, then (at least one of) the metric functions $\delta A$ (7.6.1a), $\delta B$ (7.6.1b) and $\delta C$ (7.6.1c) would be divergent at the boundary - see the expansions (7.6.5).

We can find the other solitonic metric perturbations by substituting the original metric perturbations (7.6.1) into the functions (7.7.6), (7.7.11) and (7.7.12). The perturbation $\delta N$ does not have a particularly nice form and is difficult to transcribe; the general form is given by the expansion (7.7.6d) in conjunction with the solutions (7.6.1a) and (7.6.1c).

In any case, the explicit functional form of $\delta N$ is not required to to fix the other solitonic metric perturbations and in particular the perturbed mass and angular momentum; all that is required is the expansion of $\delta N$ at the origin $r = 0$ and boundary $r = 1$ to help fix the constants of integration $\mathcal{A}_2$ and $\mathcal{C}_1$. They will be shown explicitly later, see equations (7.7.50) and (7.7.54). The remaining solitonic metric perturbations are given as follows:

$$\delta m = m_0 - \frac{\left(1-r^2\right)}{4\sqrt{2}\pi}\sum_{j=1}^{\infty}\frac{1}{\mathcal{C}_{(3)}^2}\left[\frac{\mathcal{E}_+\mathcal{M}_-}{\mathcal{A}_{(-,3,\Omega;\,r)}^{3/2}} - \frac{\lambda\mathcal{E}_-\mathcal{M}_+}{\mathcal{A}_{(-,3,\Omega;\,r)}^{3/2}}\right], \tag{7.7.49a}$$

$$\begin{aligned}\delta j = &-\frac{8r^2}{\left(1-r^2\right)^2}\mathcal{D}_1 - \frac{8\left(1+r^4\right)}{\left(1-r^2\right)^2}\mathcal{D}_2 \\ &- \frac{\left(1-r^2\right)}{2\sqrt{2}\pi}\sum_{j=1}^{\infty}\frac{1}{\mathcal{C}_{(3)}^2}\left[\frac{1}{\mathcal{A}_{(-,3,\Omega;\,r)}^{1/2}} - \frac{\lambda}{\mathcal{A}_{(+,3,\Omega;\,r)}^{1/2}}\right]\sinh\left(j\beta\right)\sinh\left(j\beta\Omega\right),\end{aligned} \tag{7.7.49b}$$

$$\delta f = f_0 + \frac{\left(1-r^2\right)^3}{4\sqrt{2}\pi}\sum_{j=1}^{\infty}\frac{1}{\mathcal{C}_{(3)}}\left[\frac{\mathcal{E}_+}{\mathcal{A}_{(-,3,\Omega;\,r)}^{3/2}}\sinh^2\left(j\beta/2\right) - \frac{\lambda\mathcal{E}_-}{\mathcal{A}_{(+,3,\Omega;\,r)}^{3/2}}\cosh^2\left(j\beta/2\right)\right], \tag{7.7.49c}$$

where, for ease of transcription, we have defined the new algebraic quantities

$$\begin{aligned}\mathcal{M}_\pm = &\left(1-r^2\right)^2 - 2r^2\cosh(j\beta\Omega)\left[\cosh\left(j\beta\Omega\right) + \cosh\left(j\beta\right) \pm 3\right] \\ &+ \left(1+r^2\right)^2\cosh^2(j\beta) \pm 2\left(1+r^2+r^4\right)\cosh(j\beta),\end{aligned} \tag{7.7.49d}$$

and, as for the RKT case, the constant $m_0$ is related to the constants of integration $\mathcal{A}_1$, $\mathcal{A}_2$ and $\mathcal{C}_1$ by

$$m_0 = -2\mathcal{A}_1 + \frac{1}{2}\mathcal{A}_2 - \frac{1}{4}\mathcal{C}_1, \tag{7.7.49e}$$

whilst $f_0$ is given by

$$f_0 = \frac{1}{2}\mathcal{A}_2 + \frac{1}{4}\mathcal{C}_1. \tag{7.7.49f}$$

It is straightforward to explore the behaviour of the perturbations (7.7.49) (as well as $\delta N$)

near the origin; the expansions read

$$\delta m = m_0 - \frac{1}{4\pi}\sum_{j=1}^{\infty}\frac{1}{\mathcal{C}_{(3)}^2}\left[\mathcal{E}_+\sinh\left(j\beta/2\right) - \lambda\mathcal{E}_-\cosh\left(j\beta/2\right)\right] + \mathcal{O}(r), \tag{7.7.50a}$$

$$\delta j = -8\mathcal{D}_2 - \frac{1}{4\pi}\sum_{j=1}^{\infty}\frac{1}{\mathcal{C}_{(3)}^2}\left[\cosh\left(j\beta/2\right) - \lambda\sinh\left(j\beta/2\right)\right]\sinh\left(j\beta\Omega\right) + \mathcal{O}(r^2), \tag{7.7.50b}$$

$$\delta N = -4\left(\mathcal{A}_1 + \frac{1}{32\pi}\sum_{j=1}^{\infty}\frac{\mathcal{E}_+\mathcal{E}_-}{\mathcal{C}_{(3)}^2}\left[\operatorname{cosech}\left(j\beta/2\right) - \lambda\operatorname{sech}\left(j\beta/2\right)\right]\right) + \mathcal{O}(r), \tag{7.7.50c}$$

$$\delta f = f_0 + \frac{1}{16\pi}\sum_{j=1}^{\infty}\frac{1}{\mathcal{C}_{(3)}}\left[\mathcal{E}_+\operatorname{cosech}\left(j\beta/2\right) - \lambda\mathcal{E}_-\operatorname{sech}\left(j\beta/2\right)\right] + \mathcal{O}(r). \tag{7.7.50d}$$

As was the case for the RKT-sourced solitons, we require that the mass perturbation be zero at the origin and the angular momentum perturbation be of order $\mathcal{O}(R^2)$ as $R \to 0$. It is clear from the asymptotic behaviour of the perturbations (7.7.50) that in order for $\delta j$ to be $\mathcal{O}(R^2)$, it must be the case that

$$\mathcal{D}_2 = -\frac{1}{32\pi}\sum_{j=1}^{\infty}\frac{1}{\mathcal{C}_{(3)}^2}\left[\cosh(j\beta/2) - \lambda\sinh(j\beta/2)\right]\sinh(j\beta\Omega), \tag{7.7.51}$$

which matches the condition (7.6.4) required in order for the perturbation $\delta D$ to be regular at the origin. For a vanishing mass perturbation $\delta m$ at the origin, it must be the case that

$$m_0 = \frac{1}{4\pi}\sum_{j=1}^{\infty}\frac{1}{\mathcal{C}_{(3)}^2}\left[\mathcal{E}_+\sinh(j\beta/2) - \lambda\mathcal{E}_-\cosh(j\beta/2)\right]. \tag{7.7.52}$$

Of the remaining perturbations, $\delta f$ is finite and nonzero at the origin, whilst $\delta N$ is zero at the origin, since $\mathcal{A}_1$ is fixed by (7.7.46).

By using the relations (7.7.49e) and (7.7.49f), in conjunction with the explicit forms of the constants $\mathcal{A}_1$ (7.7.46) and $m_0$ (7.7.52), we find that the constant $f_0$ is uniquely determined by fixing $\mathcal{A}_1$ and $m_0$, and is given by

$$f_0 = -m_0 - 2\mathcal{A}_1 = -\frac{1}{16\pi}\sum_{j=1}^{\infty}\frac{1}{\mathcal{C}_{(3)}^2}\left[\mathcal{E}_+\operatorname{cosech}(j\beta/2) - \lambda\mathcal{E}_-\operatorname{sech}(j\beta/2)\right]. \tag{7.7.53}$$

As the space-time boundary $r \to 1$ is approached, the asymptotic behaviour of the perturbations (7.7.49) is exactly the same as the RKT-sourced soliton perturbations (7.7.27), i.e. we have that

$$\delta m = m_0 + \mathcal{O}(1-r), \tag{7.7.54a}$$

$$\delta j = -2\left(\mathcal{D}_1 + 2\mathcal{D}_2\right)\left[\frac{1}{(1-r)^2} - \frac{1}{1-r}\right] + \frac{1}{2}\mathcal{D}_1 - 7\mathcal{D}_2 + \mathcal{O}(1-r), \tag{7.7.54b}$$

$$\delta N = \frac{1}{1-r}\left\{\frac{\mathcal{A}_2 - \mathcal{C}_1}{2} + \frac{1}{64\pi}\sum_{j=1}^{\infty}\left[\mathcal{E}_+ \operatorname{cosech}^3(j\beta/2) - \lambda\mathcal{E}_- \operatorname{sech}^3(j\beta/2)\right]\right\} + \mathcal{O}([1-r]^0), \tag{7.7.54c}$$

$$\delta f = f_0 + \mathcal{O}(1-r). \tag{7.7.54d}$$

For the perturbed mass $\delta M$ and angular momentum $\delta J$ (7.7.9) to exist, it is a requirement that the boundary limit $r \to 1$ is finite for both $\delta m$ and $\delta j$. For the mass perturbation function, this is manifestly satisfied, whereas for the angular perturbation function, finiteness is guaranteed at the adS boundary provided we fix

$$\mathcal{D}_1 = -2\mathcal{D}_2 = \frac{1}{8\pi}\sum_{j=1}^{\infty}\frac{1}{\mathcal{C}_{(3)}^2}\left[\cosh(j\beta/2) - \lambda\sinh(j\beta/2)\right]\sinh(j\beta\Omega). \tag{7.7.55}$$

Considering the behaviour of the perturbation $\delta D$ at the boundary (7.6.5d), we see that the choice (7.7.55) ensures that the perturbation $\delta D$ is zero at the boundary. Meanwhile, the perturbation $\delta f$ is manifestly finite at the boundary and the perturbation $\delta N$ is divergent at the boundary unless we fix

$$\mathcal{A}_2 - \mathcal{C}_1 = -\frac{1}{32\pi}\sum_{j=1}^{\infty}\left[\mathcal{E}_+ \operatorname{cosech}^3(j\beta/2) - \lambda\mathcal{E}_- \operatorname{sech}^3(j\beta/2)\right], \tag{7.7.56}$$

which is the same as the condition (7.7.48) for the perturbation $\delta R^2$ to be regular at the boundary. In order to find the constants $\mathcal{A}_2$ and $\mathcal{C}_1$, we simultaneously solve the equations

$$2\mathcal{A}_2 + \mathcal{C}_1 = -\frac{1}{4\pi}\sum_{j=1}^{\infty}\frac{1}{\mathcal{C}_{(3)}^2}\left[\mathcal{E}_+ \operatorname{cosech}(j\beta/2) - \lambda\mathcal{E}_- \operatorname{sech}(j\beta/2)\right], \tag{7.7.57}$$

$$\mathcal{A}_2 - \mathcal{C}_1 = -\frac{1}{32\pi}\sum_{j=1}^{\infty}\left[\mathcal{E}_+ \operatorname{cosech}^3(j\beta/2) - \lambda\mathcal{E}_- \operatorname{sech}^3(j\beta/2)\right], \tag{7.7.58}$$

which gives rise to the solutions

$$\begin{aligned}\mathcal{A}_2 = -\frac{1}{96\pi}\sum_{j=1}^{\infty}\frac{1}{\mathcal{C}_{(3)}^2}\Big[&\mathcal{E}_+\left\{8+\mathcal{C}_{(3)}^2\operatorname{cosech}^2(j\beta/2)\right\}\operatorname{cosech}(j\beta/2)\\ &-\lambda\mathcal{E}_-\left\{8+\mathcal{C}_{(3)}^2\operatorname{sech}^2(j\beta/2)\right\}\operatorname{sech}(j\beta/2)\Big],\end{aligned} \tag{7.7.59}$$

$$\begin{aligned}\mathcal{C}_1 = -\frac{1}{48\pi}\sum_{j=1}^{\infty}\frac{1}{\mathcal{C}_{(3)}^2}\Big[&\mathcal{E}_+\left\{4-\mathcal{C}_{(3)}^2\operatorname{cosech}^2(j\beta/2)\right\}\operatorname{cosech}(j\beta/2)\\ &-\lambda\mathcal{E}_-\left\{4-\mathcal{C}_{(3)}^2\operatorname{sech}^2(j\beta/2)\right\}\operatorname{sech}(j\beta/2)\Big].\end{aligned} \tag{7.7.60}$$

With these integration constants now fixed, along with $\mathcal{D}_2$ (7.7.51), $m_0$ (7.7.52), $f_0$ (7.7.53) and $\mathcal{D}_1$ (7.7.55), we can uniquely specify the metric perturbations $\delta A$, $\delta B$, $\delta C$, $\delta D$, $\delta R^2$, $\delta m$, $\delta j$, $\delta N$ and $\delta f$. Whilst we could display these explicitly, there is no extra information to be gained from doing so; we find a similar issue when considering the perturbations (7.7.49) in the nonrotating limit $\Omega \to 0$.

Now that the perturbations $\delta m$ and $\delta j$ have been found, and all of the constants of integration are uniquely fixed, we can find the perturbed mass and angular momentum by taking the limit $r \to 1 \iff R \to \infty$. The perturbed mass is therefore given by

$$\delta M = \frac{1}{4\pi}\sum_{j=1}^{\infty}\frac{1}{\mathcal{C}_{(3)}^2}\left[\mathcal{E}_+ \sinh(j\beta/2) - \lambda\mathcal{E}_- \cosh(j\beta/2)\right], \tag{7.7.61}$$

and the perturbed angular momentum is given by

$$\delta J = \frac{1}{2\pi}\sum_{j=1}^{\infty}\frac{1}{\mathcal{C}_{(3)}^2}\left[\cosh(j\beta/2) - \lambda\sinh(j\beta/2)\right]\sinh(j\beta\Omega). \tag{7.7.62}$$

Although not as immediately obvious as in the RKT case (7.7.41,7.7.42), it can be verified that the BTZ bound $0 \leq \delta J < \delta M$ [32, 33] is satisfied. Indeed, taking the difference between $\delta M$ and $\delta J$ yields

$$\delta M - \delta J = \frac{1}{4\pi}\sum_{j=1}^{\infty}\left\{\frac{1}{\mathcal{C}_{(3)}^2}\sinh(j\beta[1-\Omega]/2)\right.$$
$$\left.\times\left[3\left\{\cosh(j\beta\Omega/2)+\lambda\sinh(j\beta\Omega/2)\right\}+\left\{\cosh(j\beta[2+\Omega]/2)-\lambda\sinh(j\beta[2+\Omega]/2)\right\}\right]\right\}, \tag{7.7.63}$$

from which we can consider each factor separately. Firstly, since $0 \leq \Omega < 1$, using the definition of $\mathcal{C}_{(3)}$ (5.2.26), and in particular noting that it is real, it is immediately obvious that $\mathcal{C}_{(3)}^2 > 0$. Secondly, since $0 \leq \Omega < 1$, it also follows that $\sinh\left(\frac{1}{2}j\beta[1-\Omega]\right) > 0$. Thirdly, for $\mathcal{X} \geq 0$, it is true that

$$\cosh(\mathcal{X}) \pm \sinh(\mathcal{X}) \geq 0 \tag{7.7.64}$$

and thus it follows that

$$\cosh(j\beta\Omega/2) + \lambda\sinh(j\beta\Omega/2) \geq 0, \tag{7.7.65}$$

given $\lambda = -1, 0, 1$ as defined in equation (4.6.20). In a similar fashion, if we restrict the domain of $\mathcal{X}$ in the relation (7.7.64) such that it is strictly greater than zero, then the condition (7.7.64) restricts in the same way. It therefore follows that

$$\cosh(j\beta[2+\Omega]/2) - \lambda\sinh(j\beta[2+\Omega]/2) > 0, \tag{7.7.66}$$

since $j \geq 1$, $\beta > 0$ and $0 \leq \Omega < 1 \iff 2 \leq 2+\Omega < 3$. Therefore,

$$3\left\{\cosh(j\beta\Omega/2)+\lambda\sinh(j\beta\Omega/2)\right\}+\left\{\cosh(j\beta[2+\Omega]/2)-\lambda\sinh(j\beta[2+\Omega]/2)\right\} > 0, \tag{7.7.67}$$

and since

$$\sinh(j\beta[1-\Omega]/2) > 0, \qquad \text{and} \qquad \mathcal{C}_{(3)}^{-2} > 0, \tag{7.7.68}$$

it consequently follows that

$$\delta M - \delta J > 0 \iff \delta J < \delta M. \tag{7.7.69}$$

Finally, for the same reasons as outlined above, $\delta J \geq 0$ and thus the BTZ bound is satisfied. In figure 7.3, plots of the perturbed mass and angular momentum are shown for two different angular speeds $\Omega = 0.5$ and $\Omega = 0.96$, and for the cases where the quantum scalar field satisfies Dirichlet, Neumann or transparent boundary conditions. In a similar fashion to the RKT case (see figure 7.2), the BTZ bound is obviously satisfied at lower angular speeds, but as the angular speed increases, the verification of the BTZ bound becomes less obvious, with the difference between the perturbed mass and angular momentum decreasing.

In the nonrotating limit, the perturbed angular momentum vanishes as expected, whilst the perturbed mass reduces to

$$\delta M|_{\Omega=0} = \frac{1}{16\pi} \sum_{j=1}^{\infty} \operatorname{cosech}^3(j\beta/2) \left[3 + \cosh(j\beta/2) - \lambda \sinh(j\beta/2)\right]. \tag{7.7.70}$$

### 7.7.3 Comparison of the RKT and QFT sourced solitons

In this section, we will briefly compare the RKT and QFT sourced solitons. In particular, we will compare the perturbed masses and angular momenta.

In figure 7.4, the perturbed RKT (7.7.41) and QFT (7.7.61) masses are shown, for three different angular speeds of $\Omega = 0$, $\Omega = 0.5$ and $\Omega = 0.96$. The solid lines correspond to Dirichlet boundary conditions (applied to the quantum scalar field), the long dashed line to Neumann boundary conditions, the dotted lines to transparent boundary conditions and the short dashed line to the RKT case. Regardless of the angular speed, the profiles of the perturbed masses remain the same. In all cases of angular speed considered, the masses corresponding to Neumann boundary conditions are largest, with the masses corresponding to Dirichlet boundary conditions being the smallest, with the case corresponding to transparent boundary conditions and the RKT being between the two. What is particularly remarkable is how nearly indistinguishable the transparent and RKT cases are, regardless of the angular speed. This is not entirely unexpected; in chapter 5, in particular section

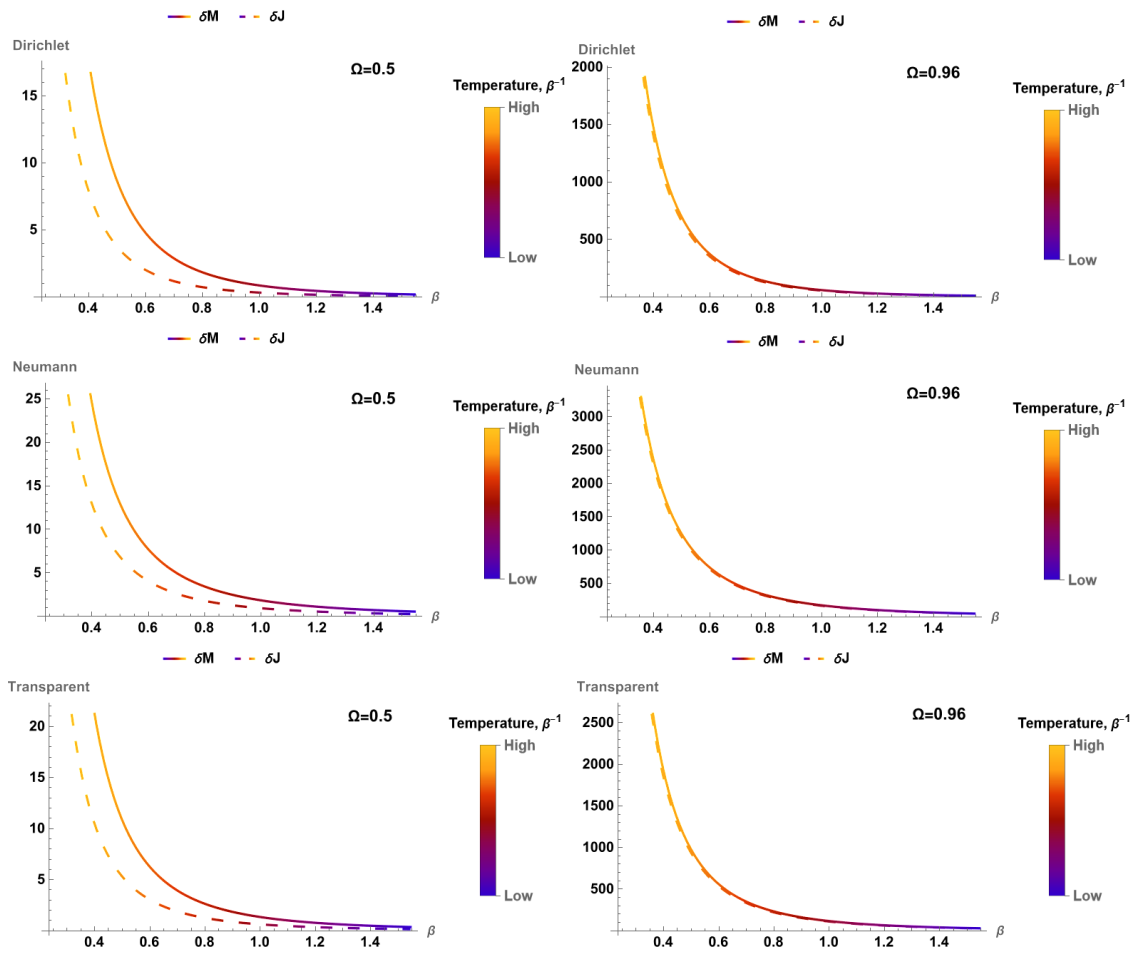


Figure 7.3: Plots of the perturbed mass $\delta M$ (solid line) and angular momentum $\delta J$ (dashed line) against inverse temperature $\beta$. The BTZ bound (6.5.2) requires the perturbed mass to always be greater than the perturbed angular momentum. As the angular speed is increased, the difference between the perturbed mass and angular momentum decreases, and, whilst the BTZ bound is still satisfied, this is less obvious. The left column of plots is for an angular speed of $\Omega = 0.5$ and the right column is for an angular speed of $\Omega = 0.96$. The different rows correspond to different boundary conditions applied to the quantum scalar field, with Dirichlet (top), Neumann (middle) and transparent (bottom) boundary conditions considered. The inverse temperature is varied in the range $\beta \in [\pi/12, 59\pi/120]$, and the inverse adS length scale is fixed $a = 1$.

5.3.4, we find the best agreement between the QFT- and RKT-SETs when transparent boundary conditions are applied to the quantum scalar field. In a similar fashion to the stress-energy tensor comparison in section 5.3.4, as the temperature is increased (right to left on the horizontal axis of the graph), the mass increases rapidly without bound, attaining its largest values at higher angular speeds.

In figure 7.5, we show the perturbed RKT (7.7.42) and QFT (7.7.62) angular momenta for the two angular speeds $\Omega = 0.5$ and $\Omega = 0.96$; we do not show the case of $\Omega = 0$ since the angular momenta vanish there. The figure follows the same format as the perturbed mass plot in figure 7.4, with solid lines corresponding to Dirichlet boundary conditions, long dashed lines to Neumann boundary conditions, dotted lines to transparent boundary conditions and short dashed lines to the RKT case. The profiles of the perturbed angular momenta are very similar to the profiles of the perturbed masses, in particular, the perturbed angular momenta increase without bound as the temperature is increased. This is not unexpected, since we saw similar profiles of the perturbed mass and angular momentum when plotting both on the same figure (see figure 7.2 for the RKT case, and figure 7.3 for the QFT case). Mirroring the perturbed mass plots, the RKT and QFT perturbed angular momenta are most similar when transparent boundary conditions are applied to the field.

In figure 7.6, we show ratios of the perturbed masses, corresponding to the three boundary conditions applied to the quantum scalar field as a ratio with the RKT case. For ease of transcription and in order to avoid potential ambiguity, we shall refer to these as $\delta M^{(\mathfrak{B}/\mathrm{RKT})}$, where $\mathfrak{B} = \{\mathrm{D}, \mathrm{N}, \mathrm{T}\}$, corresponding to, respectively, Dirichlet, Neumann and transparent boundary conditions.

In all cases of angular speed considered, we find that the ratio $\delta M^{(\mathrm{D}/\mathrm{RKT})}$ is the smallest (and always below unity), whilst the ratio $\delta M^{(\mathrm{N}/\mathrm{RKT})}$ is the largest and always above unity. This is not unexpected; this feature was observed in figure 7.4 and additionally in

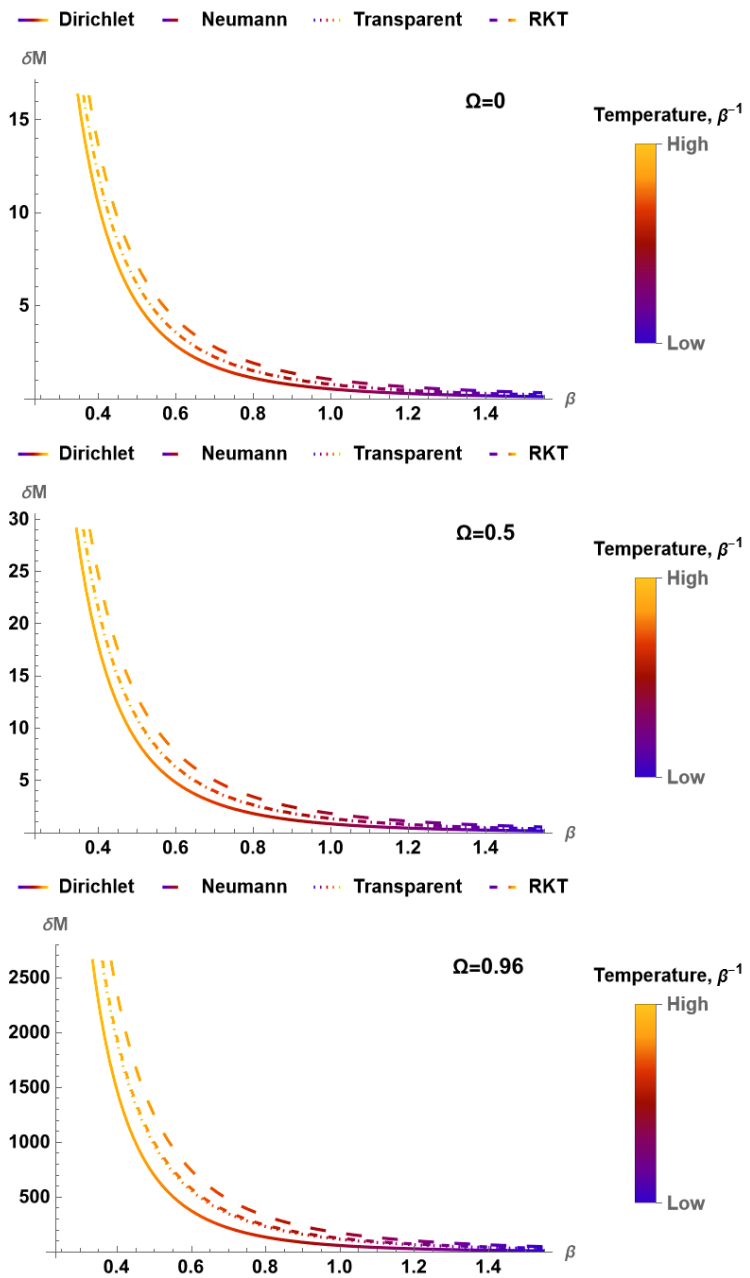


Figure 7.4: The perturbed mass $\delta M$ plotted against inverse temperature $\beta$. The solid line denotes the QFT mass with Dirichlet boundary conditions applied to the field; the long dashed line is for Neumann boundary conditions; the dotted line corresponds to transparent boundary conditions; and the short dashed line denotes the RKT mass. The inverse adS length scale is set to unity, $a = 1$, whilst the inverse temperature is varied in the range $\beta \in [\pi/12, 59\pi/120]$. The angular speed $\Omega$ is $\Omega = 0$ (top row), $\Omega = 0.5$ (middle row) or $\Omega = 0.96$ (top row).

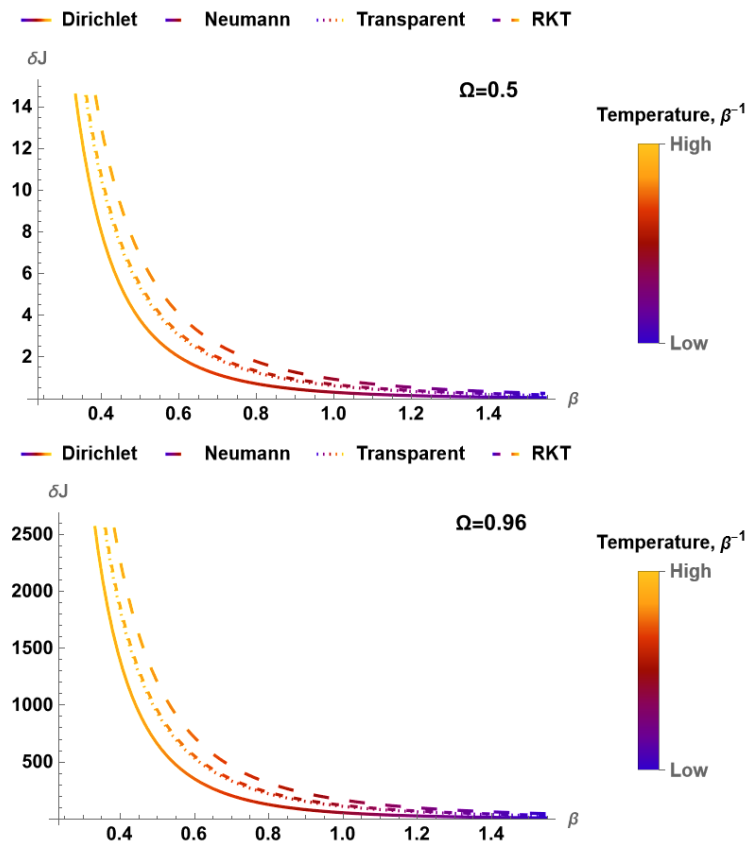


Figure 7.5: The perturbed angular momentum $\delta J$ plotted against inverse temperature $\beta$. The solid line denotes the QFT angular momentum with Dirichlet boundary conditions applied to the field; the long dashed line is for Neumann boundary conditions; the dotted line corresponds to transparent boundary conditions; and the short dashed line denotes the RKT angular momentum. The inverse adS length scale is set to unity, $a = 1$, whilst the inverse temperature is varied in the range $\beta \in [\pi/12, 59\pi/120]$. The angular speed $\Omega$ is $\Omega = 0.5$ or $\Omega = 0.96$ (top row); the angular momentum is identically zero when the angular speed is zero.

section 5.3.4 when comparing the QFT-SETs with the RKT-SETs. For both $\delta M^{(\mathrm{D/RKT})}$ and $\delta M^{(\mathrm{N/RKT})}$, the ratios tend towards unity for higher temperatures. This is an effect that was observed in section 5.3.4, where we found the best agreement between the QFT- and RKT-SETs at higher temperatures. Interestingly, the magnitude of the ratios $\delta M^{(\mathrm{D/RKT})}$ and $\delta M^{(\mathrm{N/RKT})}$ does not seem to change when the angular speed is varied, but only significantly changes when the temperature is varied, indicating that the temperature has a greater effect on the (ratio of the) perturbed masses than the angular speed. Again, this mirrors the observations in section 5.3.4.

The most interesting behaviour is from the ratio $\delta M^{(\mathrm{T/RKT})}$. Looking at the left-hand plots of figure 7.6, the ratio $\delta M^{(\mathrm{T/RKT})}$ is very close to unity regardless of angular speed or temperature, with the most significant deviation away from unity occurring at lower temperatures. It is not until we reduce the vertical scale of the plots (and thereby consider the right-hand plots of figure 7.6) that we see significant differences between the ratio $\delta M^{(\mathrm{T/RKT})}$ and unity. A rather interesting feature is that, whilst the ratios $\delta M^{(\mathrm{D/RKT})}$ and $\delta M^{(\mathrm{N/RKT})}$ did not significantly change when the angular speed was varied, the ratio $\delta M^{(\mathrm{T/RKT})}$ *does* change depending on the angular speed. Indeed, for sufficiently low angular speeds (and in particular zero angular speed), the ratio $\delta M^{(\mathrm{T/RKT})}$ is greater than unity, except for sufficiently high temperatures. This indicates that the perturbed mass corresponding to transparent boundary conditions is larger than the corresponding perturbed mass arising from the RKT-SET. In contrast, as the angular speed is increased (we consider $\Omega \geq 0.5$), the ratio is *always* less than unity regardless of the temperature.

Finally, in figure 7.7, we show the same ratios for the perturbed angular momenta, i.e. $\delta J^{(\mathfrak{B}/\mathrm{RKT})}$, where $\mathfrak{B} = \{\mathrm{D}, \mathrm{N}, \mathrm{T}\}$, corresponding to, respectively, Dirichlet, Neumann and transparent boundary conditions. Many of the features exhibited by the (ratios of the) perturbed masses are also observed for the perturbed angular momenta, such as the fact that the ratio $\delta J^{(\mathrm{D/RKT})}$ is always less than unity regardless of temperature or angular speed, and the fact that the ratio $\delta J^{(\mathrm{N/RKT})}$ is always greater than unity. The greatest dif-

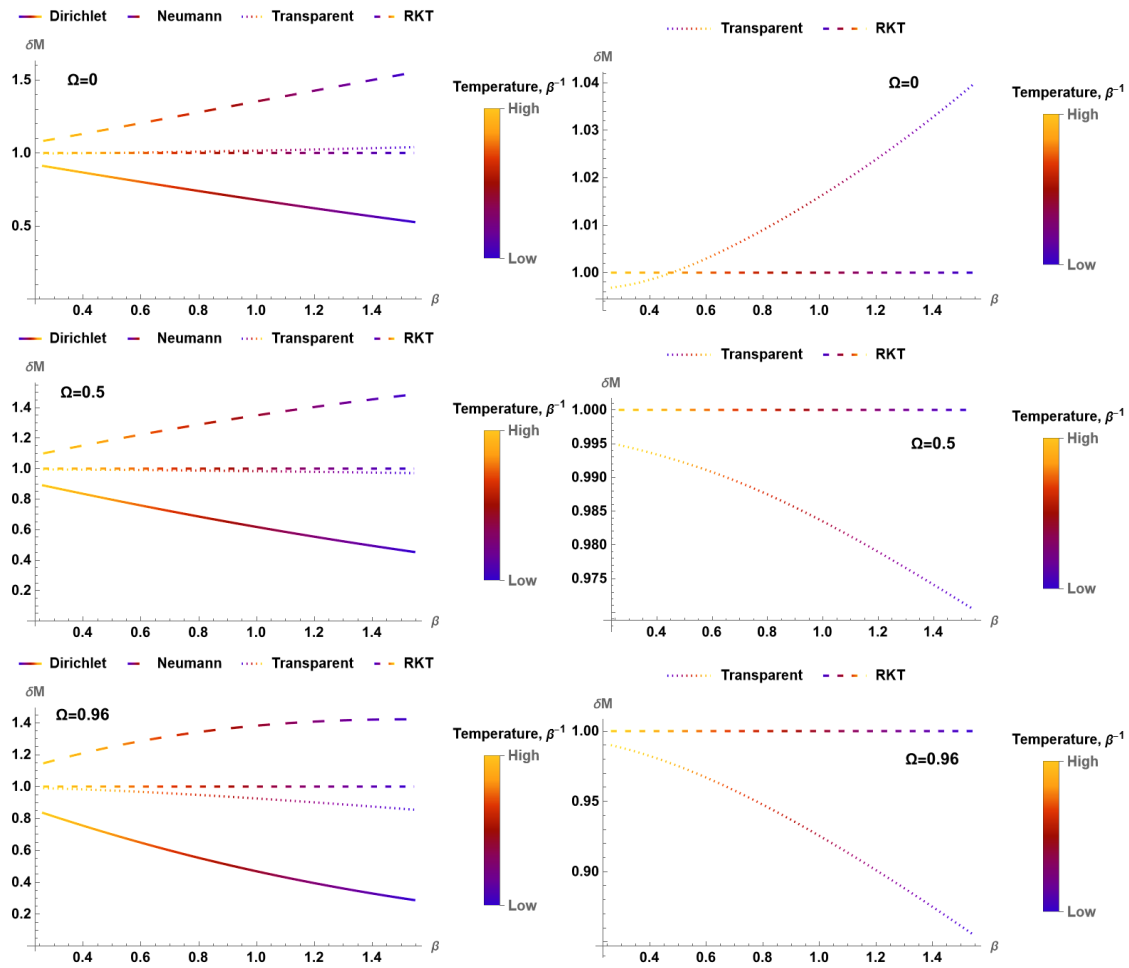


Figure 7.6: Ratios of the perturbed mass $\delta M$, between the three boundary conditions and the RKT case for an angular speed of $\Omega = 0$ (top plots), $\Omega = 0.5$ (middle plots) and $\Omega = 0.96$ (bottom plots). The solid lines correspond to the ratio of (the perturbed mass in the case of) Dirichlet boundary conditions and the RKT; the long dashed lines correspond to the ratio of Neumann boundary conditions and the RKT; the dotted lines correspond to the ratio of transparent boundary conditions with the RKT case; the short dashed lines correspond to the ratio of the RKT case with itself and is thus identically unity. On the left plots, all four ratios are shown, whilst the right plots only show the ratio of transparent boundary conditions with the RKT. The inverse adS length scale is fixed $a = 1$, and the inverse temperature is considered in the range $\beta \in [\pi/12, 59\pi/120]$.

ference compared with the ratios of the perturbed masses arises when considering the ratio $\delta J^{(\mathrm{T/RKT})}$. Whilst in figure 7.6 (for the perturbed masses) the ratio between transparent boundary conditions and the RKT case was extremely close to unity, for the perturbed angular momentum in figure 7.7, the ratio $\delta J^{(\mathrm{T/RKT})}$ is visibly less than unity. Furthermore, whilst the ratio $\delta M^{(\mathrm{T/RKT})}$ was either less than or greater than unity depending on the angular speed, it is interesting to note that, for the angular speeds we consider, the ratio $\delta J^{(\mathrm{T/RKT})}$ is always less than unity.

As well as the salient features discussed above, it is interesting to consider ratios of the perturbed masses and angular momenta for another reason. Namely, the perturbed mass (7.7.41) and angular momentum (7.7.42) in the RKT case have particularly simple analytic expressions and thus the qualitative behaviour is somewhat easy to understand. However, the perturbed mass (7.7.61) and perturbed angular momentum (7.7.62) in the QFT case do *not* have particularly simple analytical expressions and the qualitative behaviour is thus difficult to prognosticate. What is remarkable is that, in spite of their differences in analytical expressions, the perturbed mass and angular momenta in the RKT and QFT cases have rather similar qualitative behaviour as we have demonstrated.

## § 7.8 Summary

In this chapter, we have constructed solutions to the linearised, quantum-corrected Einstein equations (3.6.14) when the background space-time is three-dimensional anti-de Sitter space. We have taken the source term in the LQCEE to be either a relativistic kinetic theory stress-energy tensor or the renormalised stress-energy tensor in a thermal Hadamard state at inverse temperature $\beta$, both of which we assumed were first-order perturbations. In order to solve the LQCEE to first-order, we made two ansätze: an isotropic metric ansatz in section 7.3 and a solitonic (BTZ-like) metric ansatz in section 7.7.

Using the isotropic ansatz, we were able to construct analytic (first-order) solutions to

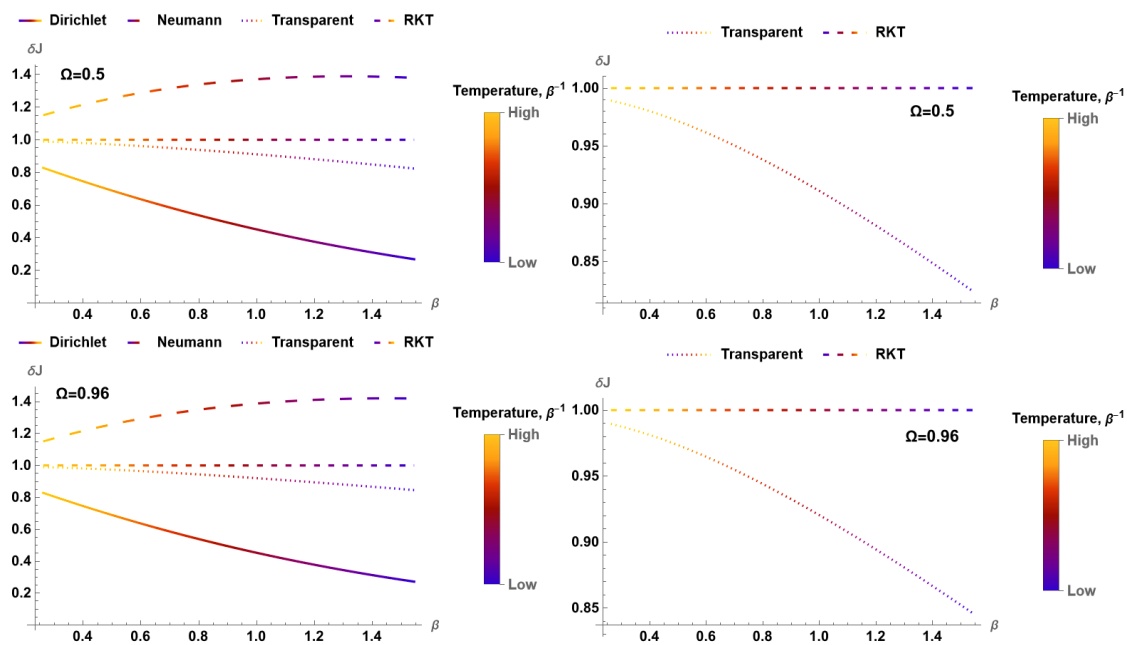


Figure 7.7: Ratios of the perturbed angular momentum $\delta J$, between the three boundary conditions and the RKT case for an angular speed of $\Omega = 0.5$ (top plots) and $\Omega = 0.96$ (bottom plots). The solid lines correspond to the ratio of (the perturbed angular momentum in the case of) Dirichlet boundary conditions and the RKT; the long dashed lines correspond to the ratio of Neumann boundary conditions and the RKT; the dotted lines correspond to the ratio of transparent boundary conditions with the RKT case; the short dashed lines correspond to the ratio of the RKT case with itself and is thus identically unity. On the left plots, all four ratios are shown, whilst the right plots only show the ratio of transparent boundary conditions with the RKT. The inverse adS length scale is fixed $a = 1$, and the inverse temperature is varied in the range $\beta \in [\pi/12, 59\pi/120]$.

the LQCEE in terms of integrals of stress-energy tensor components and five arbitrary constants of integration. By considering the asymptotic behaviour of these metric perturbations around the origin $r = 0$ and space-time boundary $r = 1$, we found conditions on the constants of integration to ensure regularity of the metric perturbations at both the origin and space-time boundary.

We introduced the solitonic, BTZ-like metric ansatz in section 7.7 in order to aid our interpretation of the quantum-corrected geometries as solitons sourced by the stress-energy tensor(s). Moving to the solitonic ansatz also had the added advantage of allowing us to compare our results with the quantum-corrected BTZ black hole [78]. In particular, we found that the perturbed mass $\delta M$ and angular momentum $\delta J$ in both the QFT and RKT cases were such that the effect of the quantum corrections was to increase the mass and angular momentum away from the unperturbed background mass $M_0 = -1$ and angular momentum $J_0 = 0$. This is in contrast to the findings for the quantum-corrected BTZ black hole, where it was observed that the mass (and angular momentum) were unaffected by the quantum corrections, and instead the effect of the quantum corrections was to move the location of the horizon outwards away from the background horizon location [78] (see section 6.5). This is perhaps a consequence of our background metric containing no singularities nor horizons and that, in their absence, the mass and angular momentum are the only remaining quantities that can be modified by the quantum corrections. Indeed, if we were to artificially insert a (naked) singularity and/or a horizon, perhaps the mass and angular momentum of the background space-time would be unaffected by the quantum corrections, suggesting that there may be some hierarchy of quantities that are affected by the quantum corrections.

Finally, it would be interesting to consider a full, nonlinear treatment of the QCEE for three-dimensional anti-de Sitter space. In [78], a full nonlinear treatment was possible only for static (nonrotating) geometries, and more recently, the back-reaction problem was considered for a selection of renormalised stress-energy tensors for nonrotating, three-

dimensional anti-de Sitter space [273, 276]. In [273, 276], it was found that the quantum corrections (from a massless, conformally-coupled scalar field) modified the mass function in such a way that it was increased compared to its background value, beginning at the background value $m(0) = -1$ and increasing away from this. Furthermore, it was found that the mass function converged to a finite value at the boundary, thus allowing the notion of a (solitonic) mass to be defined. The dependence of this mass on the temperature was not discussed in detail. However, if it exhibits a similar profile to the one found for nonlinear quantum corrections in four-dimensional anti-de Sitter space (see chapter 9), it would be rather interesting to investigate the differences and similarities between the full nonlinear and linear treatments.

# Chapter 8

# Linear corrections in four dimensions

"Science doesn't promise absolute certainty — it promises continuous refinement."

*Carlo Rovelli*

## § 8.1 Prelude and a word of warning

In this chapter, we (attempt) to solve the linearised, four-dimensional quantum-corrected Einstein equations. A word of warning regarding this chapter, however: hard harts must be worn at all times - the content in this chapter is still under construction, and the hope is to continue this work in the future. Nevertheless, we present the approach we intend to take and the results we have at this time.

The intention in this chapter is to solve the four-dimensional LQCEE (3.6.14) using rotating anti-de Sitter space as the background space-time. The rotating anti-de Sitter space metric (4.4.3) is written in terms of anti-de Sitter global coordinates (4.1.3). Following the methodology of chapter 7, we instead transform to a different coordinate system that is (still rigidly rotating and) given by the transformation and coordinate range

$$r = \tan(\rho/2), \quad 0 \leq \rho < \pi/2 \implies 0 \leq r < 1. \tag{8.1.1}$$

The other coordinates remain unchanged. The measure $\mathrm{d}\rho$ will transform to the measure $\mathrm{d}r$ as

$$\frac{\mathrm{d}\rho}{\mathrm{d}r} = \frac{2}{(1+r^2)} \implies \mathrm{d}\rho = \frac{2}{(1+r^2)}\,\mathrm{d}r. \tag{8.1.2}$$

The rotating anti-de Sitter space metric (4.4.3), in terms of the new radial coordinate $r$, is therefore

$$\begin{aligned}\mathrm{d}s_0^2 = a^{-2}\frac{\left(1+r^2\right)^2}{\left(1-r^2\right)^2}\Bigg\{-\left[1-\frac{4r^2\Omega^2\sin^2(\theta)}{\left(1+r^2\right)^2}\right]\mathrm{d}\tau^2 + \frac{4}{\left(1+r^2\right)^2}\,\mathrm{d}r^2 + \frac{4r^2}{\left(1+r^2\right)^2}\,\mathrm{d}\theta^2 \\ + \frac{8r^2\Omega\sin^2(\theta)}{\left(1+r^2\right)^2}\,\mathrm{d}\tau\,\mathrm{d}\phi + \frac{4r^2\sin^2(\theta)}{\left(1+r^2\right)^2}\,\mathrm{d}\phi^2\Bigg\}.\end{aligned} \tag{8.1.3}$$

The zero subscript is inserted on the measure $\mathrm{d}s_0^2$ to distinguish between the zeroth (background) and higher order perturbations of the metric when linearising later. We can rewrite the metric (8.1.3) for later convenience using a modified Lorentz(-type) factor

$$\widetilde{\Gamma}_{(4)} \coloneqq \left[\left(1+r^2\right)^2 - 4r^2\Omega^2\sin^2(\theta)\right]^{-1/2}, \tag{8.1.4a}$$

which is related to the original Lorentz factor $\Gamma_{(4)}$ (4.4.4b) by

$$\widetilde{\Gamma}_{(4)} = \left(1 + r^2\right)^{-1} \Gamma_{(4)}. \tag{8.1.4b}$$

Using the modified Lorentz factor, the line element (8.1.3) is therefore

$$\mathrm{d}s_0^2 = \frac{a^{-2}}{\left(1 - r^2\right)^2} \left\{ -\widetilde{\Gamma}_{(4)}^{-2} \,\mathrm{d}\tau^2 + 4\,\mathrm{d}r^2 + 4r^2\,\mathrm{d}\theta^2 + 8r^2\Omega \sin^2(\theta)\,\mathrm{d}\tau\,\mathrm{d}\phi + 4r^2 \sin^2(\theta)\,\mathrm{d}\phi^2 \right\}. \tag{8.1.5}$$

In order to solve the four-dimensional LQCEE, we need to also transform the stress-energy tensors that we use as the source term in the LQCEE (3.6.14). This is detailed in the next section.

## § 8.2 Coordinate transformed stress-energy tensors

In this section, we take both the relativistic kinetic theory stress-energy tensor (5.3.21) and renormalised stress-energy tensor (5.1.42) and transform these into the new radial coordinate $r$ (8.1.1). For most components this is as simple as changing between the radial coordinates $\rho$ and $r$, however for the $rr$- and $r\theta$-components we have to modify the transformation to include an additional factor as

$$\widetilde{T}_{rr} = \left(\frac{\mathrm{d}\rho}{\mathrm{d}r}\right)^2 \widetilde{T}_{\rho\rho}, \quad \widetilde{T}_{r\theta} = \left(\frac{\mathrm{d}\rho}{\mathrm{d}r}\right) \widetilde{T}_{\rho\theta}. \tag{8.2.1}$$

### 8.2.1 RSET for static fields

We start by transforming the renormalised stress-energy tensor (5.1.23) for static fields in order to write it in terms of the new radial coordinate $r$. It is first useful to transform the quantity (5.1.34a) into this new radial coordinate, since this will frequently occur in the renormalised stress-energy tensor components. In terms of the new radial coordinate $r$, it is given by

$$\mathcal{A}_{(\pm,4,\not{\varnothing};\,r)} = \left(1 - r^2\right)^{-2} \left[ \pm \left(1 - r^2\right)^2 + \left(1 + r^2\right)^2 \cosh(j\beta) - 4r^2 \right]. \tag{8.2.2a}$$

We are now in a position to write the renormalised stress-energy tensor components in terms of the new radial coordinate $r$. We can write each component, in general, as an infinite sum over $j$ as

$$ {}_{(4,\not{\Omega};\,r)}\langle \widehat{T}_{\mu\nu}\rangle_\beta = \frac{a^2}{48\pi^2}\sum_{j\neq 0} {}_{(4,\not{\Omega};\,r)}\langle \widehat{T}^j_{\mu\nu}\rangle_\beta, \tag{8.2.3a} $$

where each component ${}_{(4,\not{\Omega};\,r)}\langle \widehat{T}^j_{\mu\nu}\rangle_\beta$ will be specified in turn. The energy density component, ${}_{(4,\not{\Omega};\,r)}\langle \widehat{T}^j_{\tau\tau}\rangle_\beta$, is given by

$$ {}_{(4,\not{\Omega};\,r)}\langle \widehat{T}^j_{\tau\tau}\rangle_\beta = \frac{1}{\left(1+r^2\right)^2\left(1-r^2\right)^4\mathcal{A}^3_{(+,4,\not{\Omega};\,r)}}\left[\mathcal{A}^3_{(+,4,\not{\Omega};\,r)}\mathcal{B}_{(4,\not{\Omega};\,\tau\tau,+;\,r)} - \lambda\mathcal{B}_{(4,\Omega;\,\tau\tau,-;\,r)}\right], \tag{8.2.3b} $$

where we have defined

$$ \mathcal{B}_{(4,\not{\Omega};\,\tau\tau,+;\,r)} = \frac{3}{2}\left(1-r^2\right)^6\left(2+\cosh(j\beta)\right)\operatorname{cosech}^4(j\beta/2), \tag{8.2.3c} $$

$$ \mathcal{B}_{(4,\not{\Omega};\,\tau\tau,-,1;\,r)} = 4\left(1+r^2\right)^4\left[3+14r^2+3r^4+3\left(1+r^2\right)^2\cosh(j\beta)\right]\sinh^2(j\beta/2). \tag{8.2.3d} $$

The next component we consider is the $rr$-component (taking care to include the extra factor corresponding to the derivative (8.2.1)), which is given by

$$ {}_{(4,\not{\Omega};\,r)}\langle \widehat{T}^j_{rr}\rangle_\beta = \frac{2r^2}{\left(1-r^4\right)^2\left(1-r^2\right)^4\mathcal{A}^2_{(+,4,\not{\Omega};\,r)}}\left[\mathcal{A}^2_{(+,4,\not{\Omega};\,r)}\mathcal{B}_{(4,\not{\Omega};\,rr,+;\,r)} - \lambda\mathcal{B}_{(4,\not{\Omega};\,rr,-;\,r)}\right], \tag{8.2.3e} $$

where we have defined

$$ \mathcal{B}_{(4,\not{\Omega};\,rr,+;\,r)} = \left(1-r^2\right)^6\left[2+\cosh(j\beta)\right]\operatorname{cosech}^4(j\beta/2), \tag{8.2.3f} $$

$$ \mathcal{B}_{(4,\not{\Omega};\,rr,-;\,r)} = 8\left(1-r^2\right)^2\left(1+r^2\right)^4\sinh^2(j\beta/2). \tag{8.2.3g} $$

The $\theta\theta$-component is given as

$$ {}_{(4,\not{\Omega};\,r)}\langle \widehat{T}^j_{\theta\theta}\rangle_\beta = \frac{2r^2}{\left(1-r^2\right)\left(1+r^2\right)^4\mathcal{A}^3_{(-,4,\not{\Omega};\,r)}}\left[\mathcal{A}_{(+,4,\not{\Omega};\,r)}\mathcal{B}_{(4,\not{\Omega};\,\theta\theta,+;\,r)} - \lambda\mathcal{B}_{(4,\Omega;\,\theta\theta,-;\,r)}\right], \tag{8.2.3h} $$

where

$$\mathcal{B}_{(4,\not{\Omega};\,\theta\theta,+;\,r)} = \left(1-r^2\right)^3 \left[2+\cosh(j\beta)\right] \operatorname{cosech}^4(j\beta/2), \tag{8.2.3i}$$

$$\mathcal{B}_{(4,\not{\Omega};\,\theta\theta,-;\,r)} = 8\left(1+r^2\right)^4 \left[\left(1-r^2\right)^2 \mathcal{A}_{(+,4,\not{\Omega};\,r)} + 16r^2\right] \sinh^2(j\beta/2). \tag{8.2.3j}$$

Finally, for the $\phi\phi$-component, we can give this in terms of the $\theta\theta$-component simply as

$${}_{(4,\not{\Omega};\,r)}\langle \widehat{T}^j_{\phi\phi}\rangle_\beta = \sin^2(\theta)\, {}_{(4,\not{\Omega};\,r)}\langle \widehat{T}^j_{\theta\theta}\rangle_\beta. \tag{8.2.3k}$$

### 8.2.2 RSET for rigidly-rotating fields

The renormalised stress-energy tensor constructed on rotating, four-dimensional anti-de Sitter space (for rigidly-rotating fields) is not as simple. In order to aid in the transcription of its components, we transform the quantities $\mathcal{A}_{(\pm,4,\Omega)}$, $\widetilde{\mathcal{A}}_{(4)}$ and $\mathcal{S}_{(4)}$ (5.1.34) so that they are written in terms of the new radial coordinate $r$; they are given by

$$\begin{aligned}
\mathcal{A}_{(\pm,4,\Omega;\,r)} = {} & \left(1-r^2\right)^{-2} \Big[\pm\left(1-r^2\right)^2 + \left(1+r^2\right)^2 \cosh(j\beta) \\
& \qquad - 4r^2\cos^2(\theta) - 4r^2\cosh(j\beta\Omega)\sin^2(\theta)\Big], \qquad (8.2.4a)\\
\widetilde{\mathcal{A}}_{(4)} = {} & \left(1-r^2\right)^{-2} \Big[\left(1-r^2\right)^2 - \left(1+r^2\right)^2 \cosh^2(j\beta) \\
& \qquad + 4r^2\cos^2(\theta) + 4r^2\cosh^2(j\beta\Omega)\sin^2(\theta)\Big], \qquad (8.2.4b)\\
\mathcal{S}_{(4)} = {} & \left(1+r^2\right)^{-2} \Big[\left(1+r^2\right)^2 \sinh(j\beta) - 4r^2\sinh(j\beta\Omega)\sin^2(\theta)\Big]. \qquad (8.2.4c)
\end{aligned}$$

We can therefore write the RSET (5.1.42) in terms of the new radial coordinate $r$ as an infinite sum over $j$ as

$${}_{(4,\Omega;\,r)}\langle \widehat{T}_{\mu\nu}\rangle_\beta = \frac{a^2}{24\pi^2} \sum_{j\neq 0} {}_{(4,\Omega;\,r)}\langle \widehat{T}^j_{\mu\nu}\rangle_\beta, \tag{8.2.5a}$$

where each component will be given in turn. Starting with the $\tau\tau$-component, we have

$${}_{(4,\Omega;\,r)}\langle \widehat{T}^j_{\tau\tau}\rangle_\beta = -\frac{\left(1+r^2\right)^2}{\left(1-r^2\right)^2 \mathcal{A}^3_{(-,4,\Omega;\,r)}} \Big[\mathcal{A}^2_{(-,4,\Omega;\,r)} \mathcal{B}_{(4,\Omega;\,\tau\tau,-,2;\,r)}$$

$$+ \mathcal{A}_{(-,4,\Omega;\,r)}\mathcal{B}_{(4,\Omega;\,\tau\tau,-,1;\,r)} - 2\mathcal{B}_{(4,\Omega;\,\tau\tau,-,0;\,r)}\Big]$$
$$+ \frac{\lambda\left(1+r^2\right)^2}{\left(1-r^2\right)^2\mathcal{A}^3_{(+,4,\Omega;\,r)}}\Big[\mathcal{A}^2_{(+,4,\Omega;\,r)}\mathcal{B}_{(4,\Omega;\,\tau\tau,+,2;\,r)}$$
$$+ \mathcal{A}_{(+,4,\Omega;\,r)}\mathcal{B}_{(4,\Omega;\,\tau\tau,+,1;\,r)} - 2\mathcal{B}_{(4,\Omega;\,\tau\tau,+,0;\,r)}\Big]\,, \tag{8.2.5b}$$

where we have defined (recalling that $\Gamma_{(4)}$ was defined previously in terms of $\widetilde{\Gamma}_{(4)}$ (8.1.4)) the quantities

$$\mathcal{B}_{(4,\Omega;\,\tau\tau,-,2;\,r)} = 3\Gamma^{-2}_{(4)} - 1 - \frac{4r^2}{\left(1+r^2\right)^2}\left[2 - 3\Omega^2\sin^2(\theta)\right], \tag{8.2.5c}$$

$$\mathcal{B}_{(4,\Omega;\,\tau\tau,-,1;\,r)} = 3\Gamma^{-2}_{(4)} - \left[2 + \cosh(j\beta) + \cosh(j\beta\Omega)\right] - \frac{4r^2\sin^2(\theta)}{\left(1+r^2\right)^2}\left[2 - 2\cosh(j\beta\Omega) - \Omega^2\left\{4 + \cosh(j\beta) - \cosh(j\beta\Omega)\right\}\right], \tag{8.2.5d}$$

$$\mathcal{B}_{(4,\Omega;\,\tau\tau,-,0;\,r)} = \widetilde{\mathcal{A}}_{(4)}\Gamma^{-2}_{(4)} + 3\mathcal{S}^2_{(4)}\frac{\left(1+r^2\right)^2}{\left(1-r^2\right)^2} + \frac{32r^4\Omega^2\sin^2(\theta)}{\left(1-r^4\right)^2}\left[1 - 2\sinh^2(j\beta\Omega)\sin^2(\theta)\right], \tag{8.2.5e}$$

$$\mathcal{B}_{(4,\Omega;\,\tau\tau,+,2;\,r)} = -\,\mathcal{B}_{(4,\Omega;\,\tau\tau,-,2;\,r)}, \tag{8.2.5f}$$

$$\mathcal{B}_{(4,\Omega;\,\tau\tau,+,1;\,r)} = -\,\mathcal{B}_{(4,\Omega;\,\tau\tau,-,1;\,r)} + 6\Gamma^{-2}_{(4)} - 3 - \frac{4r^2}{\left(1+r^2\right)^2}\left[4 - 7\Omega^2\sin^2(\theta)\right], \tag{8.2.5g}$$

$$\mathcal{B}_{(4,\Omega;\,\tau\tau,+,0;\,r)} = -\,\mathcal{B}_{(4,\Omega;\,\tau\tau,-,0;\,r)}. \tag{8.2.5h}$$

The next component we consider is the $\tau\phi$-component. This can be written down in terms of the $\phi\phi$-component (8.2.5w), which will be given later. We have

$${}_{(4,\Omega;\,r)}\langle\widehat{T}^j_{\tau\phi}\rangle_\beta = -\frac{96r^4\sinh(j\beta)\sinh(j\beta\Omega)}{\left(1-r^4\right)^2\mathcal{A}^3_{(-,4,\Omega;\,r)}\mathcal{A}^3_{(+,4,\Omega;\,r)}}\left[\mathcal{A}^3_{(+,4,\Omega;\,r)} - \lambda\mathcal{A}^3_{(-,4,\Omega;\,r)}\right] - \Omega\,{}_{(4,\Omega;\,r)}\langle\widehat{T}^j_{\phi\phi}\rangle_\beta. \tag{8.2.5i}$$

Next is the $rr$-component, which, making sure to include the extra factor (8.2.1), is given by

$$
\begin{aligned}
{}_{(4,\Omega;\,r)}\langle \widehat{T}^{j}_{rr}\rangle_{\beta} =& \frac{4}{\left(1-r^4\right)^2 \mathcal{A}^3_{(-,4,\Omega;\,r)}} \Big[24r^2\mathcal{A}^2_{(-,4,\Omega;\,r)} - \mathcal{B}_{(4,\Omega;\,rr,-,1;\,r)} \\
& \qquad\qquad + \left(1+r^2\right)^2 \mathcal{B}_{(4,\Omega;\,rr,-,0;\,r)}\Big] \\
& - \frac{4\lambda}{\left(1-r^4\right)^2 \mathcal{A}^3_{(+,4,\Omega;\,r)}} \Big[24r^2\mathcal{A}^2_{(+,4,\Omega;\,r)} - \mathcal{B}_{(4,\Omega;\,rr,+,1;\,r)} \\
& \qquad\qquad + \left(1+r^2\right)^2 \mathcal{B}_{(4,\Omega;\,rr,+,0;\,r)}\Big], \qquad (8.2.5\text{j})
\end{aligned}
$$

where we have defined the quantities

$$
\begin{aligned}
\mathcal{B}_{(4,\Omega;\,rr,-,1;\,r)} =& \cosh(j\beta)\frac{\left(1+r^2\right)^2}{\left(1-r^2\right)^2}\left\{\left(1-r^2\right)^2 + 12\left(1+r^2\right)^2\right\} \\
& - \left[1-\cosh(j\beta\Omega)\right]\left\{\left(1+r^2\right)^2 - 2\sin^2(\theta)\left[\left(1-r^2\right)^2 - 24r^2\right]\right\}, \qquad (8.2.5\text{k})
\end{aligned}
$$

$$
\begin{aligned}
\mathcal{B}_{(4,\Omega;\,rr,-,0;\,r)} =& 6\left\{1-\cosh(j\beta)\frac{\left(1+r^2\right)^2}{\left(1-r^2\right)^2}\right\}^2 - 8\left\{1-\cosh^2(j\beta)\frac{\left(1+r^2\right)^2}{\left(1-r^2\right)^2}\right\} \\
& + \frac{8r^2\sin^2(\theta)}{\left(1+r^2\right)^2}\left\{1-\cosh(j\beta\Omega)\right\}^2\left\{4\sin^2(\theta) + 3\cos^2(\theta)\frac{\left(1+r^2\right)^4}{\left(1-r^2\right)^4}\right\} \\
& - \frac{8r^2}{\left(1-r^2\right)^4}\left\{\cos^2(\theta) + \cosh^2(j\beta\Omega)\sin^2(\theta)\right\}\left[\left(1-r^2\right)^2 + 3\left(1+r^2\right)^2\right], \\
& \qquad (8.2.5\text{l})
\end{aligned}
$$

$$
\begin{aligned}
\mathcal{B}_{(4,\Omega;\,rr,+,1;\,r)} =& \mathcal{B}_{(4,\Omega;\,rr,-,1)} + \frac{4\cos^2(\theta)}{\left(1-r^2\right)^2}\left\{4\left(1-r^2\right)^4 - 3\left(1+r^2\right)^4\right\} \\
& \qquad - 3\left\{4\left(1-r^2\right)^2 - 9\left(1+r^2\right)^2\right\}, \qquad (8.2.5\text{m})
\end{aligned}
$$

$$
\begin{aligned}
\mathcal{B}_{(4,\Omega;\,rr,+,0;\,r)} =& \mathcal{B}_{(4,\Omega;\,rr,-,0)} + \frac{16r^2\sin^2(\theta)}{\left(1+r^2\right)^2}\cosh(j\beta\Omega)\left\{4\sin^2(\theta) + 3\cos^2(\theta)\frac{\left(1+r^2\right)^4}{\left(1-r^2\right)^4}\right\} \\
& + \frac{4\cosh(j\beta)}{\left(1-r^2\right)^4}\Big\{4\left(1-r^2\right)^4 + 6\left(1-r^4\right)^2 \\
& \qquad + \cos^2(\theta)\left[4\left(1-r^2\right)^4 - 3\left(1+r^2\right)^4\right]\Big\} \\
& + 16\frac{\left(1-r^2\right)^2}{\left(1+r^2\right)^2} + \frac{4\cos^2(\theta)}{\left(1-r^2\right)^2}\left[4\left(1-r^2\right)^2 - 3\left(1+r^2\right)^2\right]
\end{aligned}
$$

$$- \frac{16r^2\cos^4(\theta)}{(1+r^2)^2(1-r^2)^4}\left[4\left(1-r^2\right)^4 - 3\left(1+r^2\right)^4\right]. \tag{8.2.5n}$$

For the $r\theta$-component, again making sure to include the correct extra factor (8.2.1), we have

$$\begin{aligned}{}_{(4,\Omega;\,r)}\langle\widehat{T}^j_{r\theta}\rangle_\beta = &- \frac{8r\cos(\theta)\sin(\theta)}{(1-r^4)\,\mathcal{A}^3_{(-,4,\Omega;\,r)}}\left[1-\cosh(j\beta\Omega)\right]\left[\mathcal{A}_{(-,4,\Omega;\,r)} - \mathcal{B}_{(4,\Omega;\,r\theta,-,0;\,r)}\right] \\ &+ \frac{8r\lambda\cos(\theta)\sin(\theta)}{(1-r^4)\,\mathcal{A}^3_{(+,4,\Omega;\,r)}}\left[1-\cosh(j\beta\Omega)\right]\left[\mathcal{A}_{(+,4,\Omega;\,r)} + \mathcal{B}_{(4,\Omega;\,r\theta,+,0;\,r)}\right], \end{aligned} \tag{8.2.5o}$$

where we have defined

$$\mathcal{B}_{(4,\Omega;\,r\theta,-,0)} = \frac{4r^2\sin^2(\theta)}{(1-r^2)^2}\left\{1-\cosh(j\beta\Omega)\right\}, \tag{8.2.5p}$$

$$\mathcal{B}_{(4,\Omega;\,r\theta,+,0)} = \frac{4r^2}{(1-r^2)^2}\left\{2-\left[1-\cosh(j\beta\Omega)\right]\sin^2(\theta)\right\}. \tag{8.2.5q}$$

The $\theta\theta$-component is given as

$$\begin{aligned}{}_{(4,\Omega;\,r)}\langle\widehat{T}^j_{\theta\theta}\rangle_\beta = &- \frac{4r^2}{(1-r^2)^2\,\mathcal{A}^3_{(-,4,\Omega;\,r)}}\left[\mathcal{A}_{(-,4,\Omega;\,r)}\mathcal{B}_{(4,\Omega;\,\theta\theta,-,1;\,r)} + 2\mathcal{B}_{(4,\Omega;\,\theta\theta,-,0;\,r)}\right] \\ &+ \frac{4r^2\lambda}{(1-r^2)^2\,\mathcal{A}^3_{(+,4,\Omega;\,r)}}\left[\mathcal{A}_{(+,4,\Omega;\,r)}\mathcal{B}_{(4,\Omega;\,\theta\theta,+,1;\,r)} + 2\mathcal{B}_{(4,\Omega;\,\theta\theta,+,0)}\right], \end{aligned} \tag{8.2.5r}$$

where

$$\mathcal{B}_{(4,\Omega;\,\theta\theta,-,1;\,r)} = 2\mathcal{C}_{(4)} - 1 + 3\cosh(j\beta) - \cosh(j\beta\Omega), \tag{8.2.5s}$$

$$\mathcal{B}_{(4,\Omega;\,\theta\theta,-,0;\,r)} = \frac{1}{(1-r^2)^2}\left[\left(1-r^2\right)^2 - \left(1+r^2\right)^2\cosh^2(j\beta\Omega) + 4r^2\left\{\mathcal{C}_{(4)} + \cosh(j\beta)\right\}^2\right], \tag{8.2.5t}$$

$$\mathcal{B}_{(4,\Omega;\,\theta\theta,+,1;\,r)} = \mathcal{B}_{(4,\Omega;\,\theta\theta,-,1;\,r)} - 1, \tag{8.2.5u}$$

$$\mathcal{B}_{(4,\Omega;\,\theta\theta,+,0;\,r)} = \mathcal{B}_{(4,\Omega;\,\theta\theta,-,0;\,r)}. \tag{8.2.5v}$$

Finally, for the $\phi\phi$-component, we have

$${}_{(4,\Omega;\,r)}\langle\widehat{T}^j_{\phi\phi}\rangle_\beta = - \frac{4r^2\sin^2(\theta)}{(1-r^2)^2\,\mathcal{A}^3_{(-,4,\Omega;\,r)}}\left[\mathcal{A}_{(-,4,\Omega;\,r)}\mathcal{B}_{(4,\Omega;\,\phi\phi,-,1;\,r)} + 2\mathcal{B}_{(4,\Omega;\,\phi\phi,-,0;\,r)}\right]$$

$$+\frac{4r^2\lambda\sin^2(\theta)}{(1-r^2)^2\,\mathcal{A}^3_{(+,4,\Omega;\,r)}}\left[\mathcal{A}_{(+,4,\Omega;\,r)}\mathcal{B}_{(4,\Omega;\,\phi\phi,+,1;\,r)}+2\mathcal{B}_{(4,\Omega;\,\phi\phi,+,0;\,r)}\right], \tag{8.2.5w}$$

where we have defined the quantities

$$\mathcal{B}_{(4,\Omega;\,\phi\phi,-,1;\,r)}=1+\cosh(j\beta)-\cosh(j\beta\Omega), \tag{8.2.5x}$$

$$\mathcal{B}_{(4,\Omega;\,\phi\phi,-,0;\,r)}=\widetilde{\mathcal{A}}_{(4)}-12\left(1-r^2\right)^{-2}\sinh^2(j\beta\Omega)\sin^2(\theta), \tag{8.2.5y}$$

$$\mathcal{B}_{(4,\Omega;\,\phi\phi,+,1;\,r)}=\mathcal{B}_{(4,\Omega;\,\phi\phi,-,1;\,r)}-1, \tag{8.2.5z}$$

$$\mathcal{B}_{(4,\Omega;\,\phi\phi,+,0;\,r)}=\mathcal{B}_{(4,\Omega;\,\phi\phi,-,0;\,r)}. \tag{8.2.5aa}$$

### 8.2.3 RKT-SET

We next write the four-dimensional RKT-SET (5.3.1) in terms of space-time coordinates, given by the new metric (8.1.3). We start by recalling the general form (in the frame) of the four-dimensional RKT-SET:

$$\widehat{T}^{(a)(b)}=\frac{\pi^2}{90\widetilde{\beta}^4}\mathrm{Diag}\{3,1,1,1\}, \tag{8.2.6}$$

where $\widetilde{\beta}$ is the local inverse temperature, given by the Tolman relation [357, 359] in terms of space-time coordinates and the global inverse temperature as

$$\widetilde{\beta}=\beta\sqrt{-g_{\tau\tau}}=\beta a^{-1}\widetilde{\Gamma}^{-1}_{(4)}\left(1-r^2\right)^{-1}. \tag{8.2.7}$$

Next, we need to specify a suitable vierbein basis. We can do this by simply transforming the vierbein basis (4.4.27) into the new radial coordinate $r$, taking particular care to transform the basis vector $\partial_\rho$ to the new basis vector $\partial_r$ using the derivative (8.1.2). The vierbein in $r$-coordinates is therefore

$$e^{\mu}_{(\tau)}\partial_\mu=a\widetilde{\Gamma}_{(4)}(1-r^2)\partial_\tau, \tag{8.2.8a}$$

$$e^{\mu}_{(r)}\partial_\mu=\frac{1}{2}a(1-r^2)\partial_r, \tag{8.2.8b}$$

$$e^{\mu}_{(\theta)}\partial_\mu = \frac{1}{2}ar^{-1}(1-r^2)\partial_\theta, \tag{8.2.8c}$$

$$e^{\mu}_{(\phi)}\partial_\mu = \frac{2ar\widetilde{\Gamma}_{(4)}(1-r^2)\sin(\theta)}{(1+r^2)}\left[\Omega\partial_\tau + \frac{1}{4r^2\sin^2(\theta)}\widetilde{\Gamma}^{-2}_{(4)}\partial_\phi\right]. \tag{8.2.8d}$$

To find the RKT-SET (8.2.6) in space-time coordinates (8.1.3), we contract the RKT-SET (8.2.6) with the vierbein basis (8.2.8) before lowering the indices using the background metric (8.1.3). This process yields the following nonzero components of the RKT-SET:

$$\widetilde{T}_{\tau\tau} = \frac{a^2\pi^2}{30\beta^4}\left(1-r^2\right)^2\widetilde{\Gamma}^2_{(4)}, \tag{8.2.9a}$$

$$\widetilde{T}_{\tau\phi} = -\frac{2a^2\pi^2}{15\beta^4}r^2\Omega\sin^2(\theta)\left(1-r^2\right)^2\widetilde{\Gamma}^4_{(4)}, \tag{8.2.9b}$$

$$\widetilde{T}_{rr} = \frac{2a^2\pi^2}{45\beta^4}\left(1-r^2\right)^2\widetilde{\Gamma}^4_{(4)}, \tag{8.2.9c}$$

$$\widetilde{T}_{\theta\theta} = \frac{2a^2\pi^2}{45\beta^4}r^2\left(1-r^2\right)^2\widetilde{\Gamma}^4_{(4)}, \tag{8.2.9d}$$

$$\widetilde{T}_{\phi\phi} = \frac{2a^2\pi^2}{45\beta^4}r^2\sin^2(\theta)\left(1-r^2\right)^2\widetilde{\Gamma}^6_{(4)}\left[\left(1+r^2\right)^2 + 12r^2\Omega^2\sin^2(\theta)\right]. \tag{8.2.9e}$$

## § 8.3 Linearised quantum-corrected Einstein equations

In order to explicitly construct the LQCEE (3.6.14), we require a suitable metric ansatz. We choose an isotropic metric ansatz [228], which has the same signature and overall structure as the background metric (8.1.3), and will reduce to the background metric in a suitable limit. The metric is given as

$$\mathrm{d}s^2 = -A(r,\theta)\,\mathrm{d}\tau^2 + \frac{B(r,\theta)}{A(r,\theta)}\left[\mathrm{d}r^2 + r^2\,\mathrm{d}\theta^2\right] + r^2\sin^2(\theta)\frac{C(r,\theta)}{A(r,\theta)}\left[\mathrm{d}\phi + \frac{D(r,\theta)}{r}\,\mathrm{d}\tau\right]^2, \tag{8.3.1}$$

which is characterised by four unknown functions, $A, B, C$ and $D$. One major difference between the ansatz (8.3.1) and the corresponding ansatz (7.3.1) for the three-dimensional case in chapter 7 is that we have assumed the unknown metric functions depend also on $\theta$. This is because the renormalised stress-energy tensor (5.1.42) has functional dependence on $\theta$.

In order to correctly recover the background metric (8.1.3), the functions $A, B, C$ and $D$ must linearise as

$$A(r,\theta) = \frac{\left(1+r^2\right)^2}{a^2\left(1-r^2\right)^2} + a\ell_{\mathrm{P}}\,\delta A(r,\theta) + \mathcal{O}(a^2\ell_{\mathrm{P}}^2), \tag{8.3.2a}$$

$$B(r,\theta) = \frac{4\left(1+r^2\right)^2}{a^4\left(1-r^2\right)^4} + a\ell_{\mathrm{P}}\,\delta B(r,\theta) + \mathcal{O}(a^2\ell_{\mathrm{P}}^2), \tag{8.3.2b}$$

$$C(r,\theta) = \frac{4\left(1+r^2\right)^2}{a^4\left(1-r^2\right)^4} + a\ell_{\mathrm{P}}\,\delta C(r,\theta) + \mathcal{O}(a^2\ell_{\mathrm{P}}^2), \tag{8.3.2c}$$

$$D(r,\theta) = \Omega r + a\ell_{\mathrm{P}}\,\delta D(r,\theta) + \mathcal{O}(a^2\ell_{\mathrm{P}}^2), \tag{8.3.2d}$$

where $a\ell_{\mathrm{P}}$ is a dimensionless parameter, made up of the inverse adS length scale $a$ and the Planck length $\ell_{\mathrm{P}}$. By setting this perturbation parameter to zero, it is easily verifiable that the background metric (8.1.3) is recovered. With this metric ansatz, exactly as was the case in chapter 7 (for the three-dimensional LQCEE), there is some residual gauge freedom that can be exploited by suitable coordinate transformations. This follows the exact same procedure as in three dimensions (see section 7.3), i.e. we make the general coordinate transformation $x^\mu \to x^\mu + a\ell_{\mathrm{P}}\,\xi^\mu$, under which the metric tensor transforms as

$$g_{\mu\nu} \to g_{\mu\nu} + a\ell_{\mathrm{P}}\,\mathcal{L}_\xi g_{\mu\nu}, \tag{8.3.3}$$

where $\mathcal{L}_\xi$ is the Lie derivative along the vector $\xi$ (7.3.2). Since this procedure is exactly the same as in three dimensions (see below equation (7.3.2)), we will not repeat the analysis in this chapter, and instead refer the reader to the original analysis in section 7.3. The upshot is, as in three dimensions, we are always free to rescale the time coordinate and, by perturbing the radial coordinate, we have some residual gauge freedom that we can use to fix one of the metric perturbations.

In order to find the linearised, quantum-corrected Einstein equations, we substitute the metric ansatz (8.3.1) into the left-hand-side of the LQCEE (3.6.14), and assume that the renormalised stress-energy tensor on the right-hand-side is of order $a\ell_{\mathrm{P}}$. We then linearise in the perturbation parameter $a\ell_{\mathrm{P}}$. Since background anti-de Sitter space has a zero classical

stress-energy tensor, the right-hand-side of the LQCEE at zeroth-order is zero; using the background metric (8.1.3) on the left-hand-side of the LQCEE similarly evaluates to zero. Hence, to zeroth-order, the LQCEE is manifestly satisfied. To first order, the LQCEE take the rather lengthy form

$$
\begin{aligned}
\widetilde{T}_{\tau\tau} = & -\frac{a^4\left(1-r^2\right)^4\left(1+2r^2\Omega^2\cos(2\theta)-2r^2\left(\Omega^2-1\right)+r^4\right)}{32r^2\left(1+r^2\right)^2}\left[r^2\frac{\partial^2(\delta B)}{\partial r^2}+\frac{\partial^2(\delta B)}{\partial\theta^2}\right] \\
& -\frac{a^4\left(1-r^2\right)^3\left(1-24r^2-9r^4\right)\left(1+2r^2\Omega^2\cos(2\theta)-2r^2\left(\Omega^2-1\right)+r^4\right)}{32r\left(1+r^2\right)^3}\frac{\partial(\delta B)}{\partial r} \\
& +\frac{a^4\left(1-r^2\right)^2\left(3-5r^2-3r^4-r^6\right)\left(1+2r^2\Omega^2\cos(2\theta)-2r^2\left(\Omega^2-1\right)+r^4\right)}{2\left(1+r^2\right)^4}\delta B \\
& -\frac{1}{32r^2}a^4\left(1-r^2\right)^4\left[r^2\frac{\partial^2(\delta C)}{\partial r^2}+\frac{\partial^2(\delta C)}{\partial\theta^2}+2\cot(\theta)\frac{\partial(\delta C)}{\partial\theta}\right] \\
& -\frac{a^4\left(1-r^2\right)^3\left(3-20r^2-7r^4\right)}{32r\left(1+r^2\right)}\frac{\partial(\delta C)}{\partial r}+\frac{a^4\left(1-r^2\right)^2\left(6-9r^2-4r^4-r^6\right)}{4\left(1+r^2\right)^2}\delta C \\
& +\frac{a^2\left(1-r^2\right)^2}{4r^2}\left[\frac{\partial^2(\delta A)}{\partial\theta^2}+r^2\frac{\partial^2(\delta A)}{\partial r^2}+\cot(\theta)\frac{\partial(\delta A)}{\partial\theta}\right] \\
& +\frac{a^2\left(1-r^2\right)\left(1-5r^2-4r^4\Omega^2\cos(2\theta)-r^4\left(13-4\Omega^2\right)-7r^6\right)}{2r\left(1+r^2\right)^3}\frac{\partial^2(\delta A)}{\partial r} \\
& -\frac{a^2\left(3-2r^2+3r^4\right)\left(3+2r^2\Omega^2\cos(2\theta)-2r^2\left(\Omega^2-3\right)+3r^4\right)}{\left(1+r^2\right)^4}\delta A \\
& -\frac{2\left(1+r^2+2r^4\right)\Omega\sin^2(\theta)}{r\left(1-r^4\right)}\left[r\frac{\partial(\delta D)}{\partial r}-\delta D\right] \\
& -\frac{\Omega\sin^2(\theta)}{r}\left[r^2\frac{\partial^2(\delta D)}{\partial r^2}+\frac{\partial^2(\delta D)}{\partial\theta^2}+3\cot(\theta)\frac{\partial(\delta D)}{\partial\theta}\right], \qquad (8.3.4a) \\
\widetilde{T}_{\tau\phi} = & \frac{a^4\left(1-r^2\right)^4\Omega\sin^2(\theta)}{8\left(1+r^2\right)^2}\left[\frac{\partial^2(\delta B)}{\partial\theta^2}+r^2\frac{\partial^2(\delta B)}{\partial r^2}\right] \\
& +\frac{a^4r\left(1-r^2\right)^3\left(1-24r^2-9r^4\right)\Omega\sin^2(\theta)}{8\left(1+r^2\right)^3}\frac{\partial(\delta B)}{\partial r} \\
& -\frac{2a^4r^2\left(1-r^2\right)^2\left(3-5r^2-3r^4-r^6\right)\Omega\sin^2(\theta)}{\left(1+r^2\right)^4}\delta B \\
& +\frac{4a^2r^2\Omega\sin^2(\theta)}{\left(1+r^2\right)^4}\left[r\left(1-r^4\right)\frac{\partial(\delta A)}{\partial r}+\left(3-2r^2+3r^4\right)\delta A\right]
\end{aligned}
$$

$$+\frac{\left(1+r^2+2r^4\right)\sin^2(\theta)}{r(r^4-1)}\left[r^2\frac{\partial(\delta D)}{\partial r}-\delta D\right]$$
$$-\frac{\sin^2(\theta)}{2r}\left[r^2\frac{\partial^2(\delta D)}{\partial r^2}+\frac{\partial^2(\delta D)}{\partial\theta^2}+3\cot(\theta)\frac{\partial(\delta D)}{\partial\theta}\right], \tag{8.3.4b}$$

$$\widetilde{T}_{rr}=-\frac{a^4\left(r^2-1\right)^3}{8r^2\left(r^2+1\right)^3}\left[r\left(1+6r^2+r^4\right)\frac{\partial(\delta B)}{\partial r}-\left(1-r^2\right)\cot(\theta)\frac{\partial(\delta B)}{\partial\theta}\right]$$
$$-\frac{a^4\left(r^2-1\right)^2\left(r^6+15r^4+31r^2+9\right)}{2\left(r^2+1\right)^4}\delta B$$
$$+\frac{a^4\left(r^2-1\right)^4}{8r^2\left(1+r^2\right)^2}\left[\frac{\partial^2(\delta C)}{\partial\theta^2}+2\cot(\theta)\frac{\partial(\delta C)}{\partial\theta}\right]$$
$$-\frac{a^4\left(1-r^2\right)^2}{8r\left(1+r^2\right)^4}\left[4r\left(3+19r^2+9r^4+r^6\right)\delta C-\left(1-r^4\right)\left(1+6r^2+r^4\right)\frac{\partial(\delta C)}{\partial r}\right]$$
$$+\frac{4a^2}{\left(1+r^2\right)^4}\left[\left(3+14r^2+3r^4\right)\delta A-r\left(1-r^4\right)\frac{\partial(\delta A)}{\partial r}\right], \tag{8.3.4c}$$

$$\widetilde{T}_{r\theta}=\frac{a^4\left(1-r^2\right)^3}{8r\left(1+r^2\right)^3}\left[r\left(1-r^2\right)\cot(\theta)\frac{\partial(\delta B)}{\partial r}+\left(1+6r^2+r^4\right)\frac{\partial(\delta B)}{\partial\theta}\right.$$
$$\left.-4r^2\left(3+r^2\right)\cot(\theta)\delta B\right]+\frac{4a^2r\left(r^2-1\right)}{\left(r^2+1\right)^3}\frac{\partial(\delta A)}{\partial\theta}$$
$$\frac{a^4\left(1-r^2\right)^3}{8\left(1+r^2\right)^3}\left[4r\left(3+r^2\right)\frac{\partial(\delta C)}{\partial\theta}-\left(1-r^4\right)\frac{\partial^2(\delta C)}{\partial r\partial\theta}\right.$$
$$\left.-\left(r^4-1\right)\cot(\theta)\frac{\partial(\delta C)}{\partial r}+4r\left(3+r^2\right)\cot(\theta)\delta C\right], \tag{8.3.4d}$$

$$\widetilde{T}_{\theta\theta}=\frac{a^4\left(1-r^2\right)^3}{8\left(1+r^2\right)^3}\left[\left(1-r^4\right)\cot(\theta)\frac{\partial(\delta B)}{\partial\theta}-r\left(1+6r^2+r^4\right)\frac{\partial(\delta B)}{\partial r}\right]$$
$$-\frac{a^4r^2\left(1-r^2\right)^2\left(3-7r^2-3r^4-r^6\right)}{2\left(1+r^2\right)^4}\delta B+\frac{a^4r^2\left(1-r^2\right)^4}{8\left(1+r^2\right)^2}\frac{\partial^2(\delta C)}{\partial r^2}$$
$$+\frac{a^4r\left(1-r^2\right)^3\left(1-9r^2-4r^4\right)}{4\left(1+r^2\right)^3}\frac{\partial(\delta C)}{\partial r}-\frac{a^4r^2\left(1-r^2\right)^2\left(9-13r^2-9r^4-3r^6\right)}{2\left(1+r^2\right)^4}\delta C$$
$$+\frac{4a^2r^2}{\left(1+r^2\right)^4}\left[r\left(1-r^4\right)\frac{\partial(\delta A)}{\partial r}+\left(3-2r^2+3r^4\right)\delta A\right], \tag{8.3.4e}$$

$$\widetilde{T}_{\phi\phi}=\frac{a^4\left(1-r^2\right)^4\sin^2(\theta)}{8\left(1+r^2\right)^2}\left[\frac{\partial^2(\delta B)}{\partial\theta^2}+r^2\frac{\partial^2(\delta B)}{\partial r^2}\right]$$

$$- \frac{a^4 r \left(1-r^4\right)^2 \sin^2(\theta)}{8\left(1+r^2\right)^4} \left[\left(1-r^2\right) \frac{\partial(\delta B)}{\partial r} + 16r\left(3-5r^2-3r^4-r^6\right)\delta B\right]$$
$$+ \frac{4a^2 r^2 \sin^2(\theta)}{\left(1+r^2\right)^4} \left[r\left(1-r^4\right)\frac{\partial(\delta A)}{\partial r} + \left(3-2r^2+3r^4\right)\delta A\right]. \tag{8.3.4f}$$

In addition to the LQCEE (8.3.4), we can compute the covariant derivative of the left-hand-side of the LQCEE (3.6.14). Since, by Wald's axioms (see section 2.7), the renormalised stress-energy tensor should satisfy conservation, it must follow that the left-hand-side of the LQCEE (3.6.14) must also satisfy conservation. When we compute the covariant derivative, we find the lowest order term to be of order $a^2\ell_{\mathrm{P}}^2$. Therefore, exactly as in the three-dimensional case, conservation of the LQCEE holds to linear order and we do not consider it further.

In the three-dimensional case, the renormalised stress-energy tensor (and the RKT-SET) were traceless, and a further constraint on the metric perturbations was found using this fact. In four dimensions, the renormalised stress-energy tensor (5.1.42) has a nonzero trace (2.7.50), due to the trace anomaly, and the trace depends on the constants of the theory, such as the mass $m$ and coupling constant $\xi$ (see section 2.7). However, on the right hand side of the LQCEE (3.6.14), we use the thermal expectation value of the stress-energy tensor by writing

$$\langle \widehat{T}_{\mu\nu}\rangle_\beta = \left[\langle \widehat{T}_{\mu\nu}\rangle_\beta - \langle \widehat{T}_{\mu\nu}\rangle_0\right] + \langle \widehat{T}_{\mu\nu}\rangle_0, \tag{8.3.5}$$

where we further write

$$\widetilde{T}_{\mu\nu} = \langle \widehat{T}_{\mu\nu}\rangle_\beta - \langle \widehat{T}_{\mu\nu}\rangle_0. \tag{8.3.6}$$

We then absorb the extra vacuum expectation value of the stress-energy tensor (the term outside the square brackets in equation (8.3.5)) into a redefinition of the cosmological constant, and use the difference (8.3.6) as the source term in the LQCEE (8.3.4). See sections 2.7 and 3.2 for more detail. The upshot is that the difference in expectation values (8.3.6) will be traceless, since the trace anomaly is state-independent. Relating this to the

LQCEE (8.3.4), we therefore find a further constraint on the metric perturbations:

$$
\begin{aligned}
0 = & \frac{a^6\left(1-r^2\right)^6}{16\left(1+r^2\right)^2}\frac{\partial^2(\delta B)}{\partial r^2} + \frac{a^6\left(1-r^2\right)^5\left(1-24r^2-9r^4\right)}{16r\left(1+r^2\right)^3}\frac{\partial(\delta B)}{\partial r} \\
& + \frac{a^6\left(1-r^2\right)^6}{16r^2\left(1+r^2\right)^2}\frac{\partial^2(\delta B)}{\partial \theta^2} - \frac{a^6\left(1-r^2\right)^5\left(9+5r^2+2r^4\right)}{2\left(1+r^2\right)^4}\delta B \\
& + \frac{a^6\left(1-r^2\right)^6}{16\left(1+r^2\right)^2}\frac{\partial^2(\delta C)}{\partial r^2} + \frac{a^6\left(1-r^2\right)^5\left(3-16r^2-7r^4\right)}{16r\left(1+r^2\right)^3}\frac{\partial(\delta C)}{\partial r} \\
& + \frac{a^6\left(1-r^2\right)^6}{16r^2\left(1+r^2\right)^2}\frac{\partial^2(\delta C)}{\partial \theta^2} + \frac{a^6\left(1-r^2\right)^6\cot(\theta)}{8r^2\left(1+r^2\right)^2}\frac{\partial(\delta C)}{\partial \theta} \\
& - \frac{a^6\left(1-r^2\right)^5\left(6+3r^2+r^4\right)}{2\left(1+r^2\right)^4}\delta C - \frac{a^4\left(1-r^2\right)^4}{4\left(1+r^2\right)^2}\frac{\partial^2(\delta A)}{\partial r^2} \\
& - \frac{a^4\left(1-r^2\right)^3\left(1-9r^2\right)}{2r\left(1+r^2\right)^3}\frac{\partial(\delta A)}{\partial r} - \frac{a^4\left(1-r^2\right)^4}{4r^2\left(1+r^2\right)^2}\frac{\partial^2(\delta A)}{\partial \theta^2} \\
& - \frac{a^4\left(1-r^2\right)^4\cot(\theta)}{4r^2\left(1+r^2\right)^2}\frac{\partial(\delta A)}{\partial \theta} + \frac{2a^4\left(1-r^2\right)^2\left(9+2r^2+9r^4\right)}{\left(1+r^2\right)^4}\delta A. \qquad (8.3.7)
\end{aligned}
$$

The biggest difference between the three-dimensional LQCEE (7.3.17) and the LQCEE (8.3.4) in four dimensions, is the fact that they are *partial* differential equations, rather than ordinary differential equations. Due to the functional dependence of the metric functions in the ansatz (8.3.1), the LQCEE now include derivatives (of the metric functions) up to second order in terms of both $r$ *and* $\theta$. This obviously increases the difficulty of finding solutions to the LQCEE by a significant margin. In order to solve the LQCEE (8.3.4), (8.3.7), there are different approaches one could take, such as the method of lines, in which the $\theta$ derivatives would be discretised, thereby reducing the LQCEE (8.3.4, 8.3.7) to coupled ordinary differential equations in $r$.

## § 8.4 Summary

In this chapter, we have presented preliminary work in solving the four-dimensional, linearised, quantum-corrected Einstein equations (8.3.4). We started (in section 8.2) by trans-

forming the QFT-RSET (5.1.42) and the RKT-SET (5.3.21) from the global anti-de Sitter space coordinates (4.1.3) into a new coordinate system by transforming to a new radial coordinate $r$ (8.1.1). By making a suitable metric ansatz (inspired by [228]), we were able to compute the explicit forms of the LQCEE, given in terms of four unknown metric functions.

Unfortunately, the cruel mistress of time did not permit further work on this problem, and it would be interesting to continue this in future. In particular, it would be interesting to compare results from this chapter, where the QCEE are linearised, with results in the next chapter, where the full nonlinear QCEE are considered. More will be said about this in the conclusions of this thesis, chapter 10.

# Chapter 9

# Nonlinear corrections in four dimensions

"Freude am Schauen und Begreifen ist die schönste Gabe der Natur."
"Joy in looking and comprehending is nature's most beautiful gift."

*Albert Einstein*

## § 9.1 Prelude

The purpose of this chapter is to present results for the quantum-corrected nonrotating adS metric in four-dimensions. The difference is that, unlike in chapters 7 and 8, we do *not* linearise the semi-classical Einstein equations, and instead proceed nonlinearly, solving the full QCEE (3.6.15). We use the renormalised stress-energy tensor (5.1.23) as the source term in the QCEE (3.6.15).

The layout of this chapter is as follows. In section 9.2 we first derive the explicit form of the QCEE (3.6.15) by making a suitable ansatz on the form of the quantum-corrected metric. In section 9.3 we then solve the QCEE numerically. Then, in section 9.4 we present the results for the cases of Dirichlet, Neumann and transparent boundary conditions applied to the quantum scalar field. In particular, in section 9.4.2 we present the results when transparent boundary conditions are applied, and how these relate to the solutions of the nonlinear, four-dimensional QCEE for both an RKT-SET and the RSET on the ESU. In section 9.5 we then make an alternative metric ansatz in order to aid in our interpretation of the quantum-corrected geometry as quantum-corrected solitons sourced by the (R)SET, and in particular we discuss the masses of these solitons in section 9.5.3. Finally, in section 9.6, we summarise the chapter and discuss some of the important results and features.

## § 9.2 Quantum-corrected Einstein equations

In this section, the explicit form of the QCEE (3.6.15) governing quantum-corrected, non-rotating four-dimensional anti-de Sitter space-times will be derived, under the simplifying assumption that $\kappa = 1$. We start by making an ansatz on the form of the metric, where we make the assumption that it will have the same metric signature, same functional dependence and same overall structure, i.e. static and spherically symmetric. The metric is

characterised by three unknown functions, $A, B$ and $C$; and is given explicitly as

$$\mathrm{d}s^2_{\mathrm{QC}} = -A(\rho)\,\mathrm{d}\tau^2 + B(\rho)\,\mathrm{d}\rho^2 + C(\rho)\left[\mathrm{d}\theta^2 + \sin^2(\theta)\,\mathrm{d}\phi^2\right]. \tag{9.2.1}$$

The functions $A(\rho), B(\rho)$ and $C(\rho)$ are to be determined by the QCEE (3.6.15), which for nonrotating four-dimensional anti-de Sitter space-time are:

$$\widetilde{G}_\mu{}^\nu + \widetilde{\Lambda}\delta_\mu{}^\nu = {}_{(4,\mathscr{A})}\widehat{T}_\mu{}^\nu. \tag{9.2.2}$$

The cosmological constant $\widetilde{\Lambda}$ is the renormalised version derived from the vacuum QCEE in section 6.3. Additionally, we work with the mixed indices version of the QCEE following the method of [78] (see section 6.5), since this simplifies the resultant components of the QCEE.

For brevity and typographical ease, we drop the pre-subscript on the QFT-RSET for brevity, understanding that here and henceforth in this chapter, $\widetilde{T}_{\mu\nu}$ refers to the nonrotating four-dimensional QFT-RSET (5.3.42) (or the RKT-SET (5.3.12) - see section 9.4.2).

We compute the left-hand-side of the QCEE (3.6.15), yielding four equations relating the functions $A, B, C$ (and derivatives thereof) with components of the QFT-RSET (5.1.23):

$$\widetilde{T}_\tau{}^\tau = \frac{4B^2C(\widetilde{\Lambda}C - 1) - 2B'CC' - B(C'^2 - 4CC'')}{4B^2C^2}, \tag{9.2.3a}$$

$$\widetilde{T}_\rho{}^\rho = \frac{2A'CC' + A(4BC[\widetilde{\Lambda}C - 1] + C'^2)}{4ABC^2}, \tag{9.2.3b}$$

$$\begin{aligned}\widetilde{T}_\theta{}^\theta = &-\frac{1}{4A^2B^2C^2}\left[A'^2BC^2 - AC(A'BC' + C\{2A''B - A'B'\})\right.\\ &\left.- A^2(4\widetilde{\Lambda}B^2C^2 - B'CC' - B\{C'^2 - 2CC''\})\right],\end{aligned} \tag{9.2.3c}$$

where a prime denotes differentiation with respect to $\rho$. Only three equations have been shown since, due to the underlying structure of the QFT-RSET (5.3.42), $\widetilde{T}_\theta{}^\theta = \widetilde{T}_\phi{}^\phi$. Due to the underlying structure of the Einstein and metric tensors, the left-hand-side of the $\phi\phi$-component of the QCEE is identical to the corresponding $\theta\theta$-component. Hence the system is not overdetermined.

*A priori* we have three independent equations for the three unknown metric functions. However, after a little algebraic manipulation of equations (9.2.3a), (9.2.3b) we find that equation (9.2.3c) can be written as

$$\left(\widetilde{T}_\theta{}^\theta - \widetilde{T}_\rho{}^\rho\right) - \frac{C}{C'}\widetilde{T}_\rho{}^{\rho\prime} + \frac{A'C}{2AC'}\left(\widetilde{T}_\tau^\tau - \widetilde{T}_\rho{}^\rho\right) = 0. \tag{9.2.4}$$

Wald's axioms (see section 2.7) tell us that for a renormalised stress-energy tensor to be well-defined and physically reasonable, it must satisfy conservation. Taking the covariant derivative of both sides of the QCEE, the only manifestly nonzero component is given by

$$\nabla_\mu \widetilde{T}_\rho{}^\mu = \frac{1}{2B}\left[\frac{2C'}{C}\left(\widetilde{T}_\rho{}^\rho - \widetilde{T}_\theta{}^\theta\right) + 2\widetilde{T}_\rho{}^{\rho\prime} + \frac{A'}{A}\left(\widetilde{T}_\rho{}^\rho - \widetilde{T}_\tau{}^\tau\right)\right]. \tag{9.2.5}$$

This is precisely (9.2.4) multiplied by $-C'/BC$. Provided the QCEE (9.2.3) hold, conservation of the QFT-RSET then follows. The QCEE and conservation of the QFT-RSET therefore give three independent equations for the three unknown metric functions, $A(\rho), B(\rho), C(\rho)$. To simplify the solving of the QCEE, we will attempt to decouple the equations (9.2.3a), (9.2.3b), (9.2.4) and solve them independently. We start by rearranging the three independent governing equations to give

$$0 = \widetilde{\Lambda} - \widetilde{T}_\tau{}^\tau - \frac{C'^2}{4BC^2} + \frac{2BC'' - 2B^2 - B'C'}{2B^2C}, \tag{9.2.6a}$$

$$0 = \widetilde{\Lambda} - \widetilde{T}_\rho{}^\rho + \frac{C'^2}{4BC^2} + \frac{A'C' - 2AB}{2ABC}, \tag{9.2.6b}$$

$$0 = A'C(\widetilde{T}_\rho{}^\rho - \widetilde{T}_\tau{}^\tau) + 2A(C\widetilde{T}_\rho{}^\rho)' - 2AC'\widetilde{T}_\theta{}^\theta. \tag{9.2.6c}$$

Equation (9.2.6c) can be rearranged so that we can express $A'(\rho)/A(\rho)$ in terms of $C(\rho)$ and the QFT-RSET components (and derivates thereof) as:

$$\frac{A'}{A} = 2\frac{(C\widetilde{T}_\rho{}^\rho)' - C'\widetilde{T}_\theta{}^\theta}{C(\widetilde{T}_\tau{}^\tau - \widetilde{T}_\rho{}^\rho)}. \tag{9.2.7}$$

In equation (9.2.6b), the dependence on $A(\rho)$ and $A'(\rho)$ is always $A'(\rho)/A(\rho)$. We can therefore use equation (9.2.7) to eliminate $A$ and its derivatives from equation (9.2.6b), yielding

$$0 = \widetilde{\Lambda} - \widetilde{T}_\rho{}^\rho - \frac{1}{C} + \frac{C'^2}{4BC^2} - \frac{C'(C\widetilde{T}_\rho{}^{\rho\prime} + C'\widetilde{T}_\rho{}^\rho - C'\widetilde{T}_\theta{}^\theta)}{BC^2(\widetilde{T}_\rho{}^\rho - \widetilde{T}_\tau{}^\tau)}. \tag{9.2.8}$$

There are no derivatives of $B(\rho)$ present in equation (9.2.8), only factors of $1/B(\rho)$. We can therefore rearrange equation (9.2.8) to give an expression for $B(\rho)$ in terms of $C(\rho)$ and the QFT-RSET components, and their derivatives. This is given as

$$B = \frac{C'^2(\widetilde{T}_\rho{}^\rho - \widetilde{T}_\tau{}^\tau) - 4C'(C\widetilde{T}_\rho{}^{\rho\prime} + C'\widetilde{T}_\rho{}^\rho - C'\widetilde{T}_\theta{}^\theta)}{4C(\widetilde{T}_\rho{}^\rho - \widetilde{T}_\tau{}^\tau)(1 - C\widetilde{\Lambda} + C\widetilde{T}_\rho{}^\rho)}. \tag{9.2.9}$$

We can then substitute equation (9.2.9) for $B(\rho)$ and (after differentiating) $B'(\rho)$ into equation (9.2.6a). This yields a single equation for $C(\rho)$, depending only on components of the QFT-RSET (and derivatives thereof):

$$0 = \frac{1}{CC'}\left(2CC'' + C'^2\right)\frac{\left(\widetilde{T}_\rho{}^\rho - \widetilde{T}_\tau{}^\tau\right)\Xi_\rho}{\Upsilon} + 2\frac{\mathrm{d}}{\mathrm{d}\rho}\left(\frac{\left(\widetilde{T}_\rho{}^\rho - \widetilde{T}_\tau{}^\tau\right)\Xi_\rho}{\Upsilon}\right) + \frac{\Xi_\tau}{C}, \tag{9.2.10a}$$

where, for brevity, we have defined

$$\Upsilon = C'\left(\widetilde{T}_\tau{}^\tau + 3\widetilde{T}_\rho{}^\rho - 4\widetilde{T}_\theta{}^\theta\right) + 4C\widetilde{T}_\rho{}^{\rho\prime} \tag{9.2.10b}$$

and

$$\Xi_\bullet = C\left(\widetilde{\Lambda} - \widetilde{T}_\bullet{}^\bullet\right) - 1. \tag{9.2.10c}$$

We have now fully decoupled the governing equations (9.2.6) and reduced the problem to solving a single, second-order nonlinear ODE (9.2.10) for the metric function $C(\rho)$. Once we have the solution for $C(\rho)$, we can use equation (9.2.9) to give the metric function $B(\rho)$ and, to give the remaining metric function $A(\rho)$, solve the first order ODE (9.2.7). To solve these ODEs, boundary conditions on the metric functions (not to be confused with boundary conditions on the quantum scalar field) are required. These will be described next, along with the procedure employed to solve the reduced QCEE (9.2.7), (9.2.9), (9.2.10).

## § 9.3 Solving the QCEE

The reduced QCEE (9.2.7), (9.2.9), (9.2.10) are sufficiently complicated that proceeding algebraically is, at this time, intractable. Instead, we have to proceed numerically to

find the quantum-corrected metric functions $A(\rho), B(\rho)$ and $C(\rho)$. Due to assumptions we make on the form of $C(\rho)$ (see (9.3.7c) below), the reduced QCEE are singular at $\rho = 0$, meaning we cannot start the numerical integration directly at the origin. Instead, we start our numerical integration at some small positive constant $\epsilon \ll 1$, and integrate outwards for increasing $\rho$ towards the space-time boundary at $\rho = \pi/2$. To this end, we require boundary conditions on the quantum-corrected metric functions at $\rho = \epsilon$, as well as boundary conditions on the QFT-RSET components. To achieve this, we expand the metric functions and QFT-RSET components in Taylor series[1] around $\rho = 0$. Note, however, that the equation (9.2.9) for the metric function $B(\rho)$ is purely algebraic and involves no derivates of $B(\rho)$ - this means we do not actually require any boundary conditions for the metric function $B(\rho)$. Nevertheless, for self-completeness, we still expand $B(\rho)$ in a Taylor series around $\rho = 0$. The Taylor series for $B(\rho)$ is also present in the Taylor series expansion of the Ricci scalar; something required to ensure there are no curvature singularities.

### 9.3.1 Taylor series expansions of the QFT-RSET components

In order to simplify the process of expanding the QCEE into a Taylor series, we first re-express the QFT-RSET (5.3.42) in the following way:

$$\widetilde{T}_{\mu}{}^{\nu} = \frac{a^2}{8\pi^2}\left\{\mathcal{F}_1(\rho)\delta_{\mu}{}^{\nu} + \mathcal{F}_2(\rho)\mathfrak{t}_{\mu}\mathfrak{t}^{\nu} + \mathcal{F}_3(\rho)\mathfrak{p}_{\mu}\mathfrak{p}^{\nu}\right\}, \tag{9.3.1a}$$

such that

$$\widetilde{T}_{\tau}{}^{\tau} = \frac{a^2}{8\pi^2}\left\{\mathcal{F}_1(\rho) - \mathcal{F}_2(\rho)\right\}, \quad \widetilde{T}_{\rho}{}^{\rho} = \frac{a^2}{8\pi^2}\left\{\mathcal{F}_1(\rho) + \mathcal{F}_3(\rho)\right\}, \quad \widetilde{T}_{\theta}{}^{\theta} = \widetilde{T}_{\phi}{}^{\phi} = \frac{a^2}{8\pi^2}\mathcal{F}_1(\rho). \tag{9.3.1b}$$

The time-like $\mathfrak{t}_{\bullet}$ and space-like $\mathfrak{p}_{\bullet}$ vector fields were defined previously in equation (5.1.21). The functions $\mathcal{F}_i$ are defined as [4] (see section 5.1.1)

$$\mathcal{F}_1(\rho) = \frac{4}{3}\cos^4\rho\, f_3(a\beta)$$

[1] This is somewhat of an arbitrary choice. We could have chosen different series expansions, but chose a Taylor series for its simplicity - for which we assume that the functions are all regular at the origin.

$$
\begin{aligned}
&+\lambda\cot\rho\left[-\frac{1}{6}\csc^2\rho\cos(2\rho)S_0(a\beta,\rho)+\frac{1}{3}\cot\rho\,C_1(a\beta,\rho)+\frac{2}{3}\cos^2\rho\,S_2(a\beta,\rho)\right],\\
\mathcal{F}_2(\rho)=&\frac{16}{3}\cos^4\rho\,f_3(a\beta)+\lambda\cot\rho\\
&\times\left[\frac{1}{6}\left(3-\cot^2\rho\right)S_0(a\beta,\rho)+\cot\rho\left(1-\frac{2}{3}\cos^2\rho\right)C_1(a\beta,\rho)+2\cos^2\rho\,S_2(a\beta,\rho)\right],\\
\mathcal{F}_3(\rho)=&\lambda\cot\rho\left[\frac{1}{6}\left(3\csc^2\rho-4\right)S_0(a\beta,\rho)+\cot\rho\left(\frac{2}{3}\sin^2\rho-1\right)C_1(a\beta,\rho)\right.\\
&\left.-\frac{2}{3}\cos^2\rho\,S_2(a\beta,\rho)\right],
\end{aligned}
\tag{9.3.1c}
$$

where $f_3$ (5.1.18), $S_m$ (5.1.19) and $C_m$ (5.1.20) were defined previously.

We can then more easily perform a Taylor series expansion of the QFT-RSET components (9.3.1b) by first performing a Taylor series expansion around $\rho=0$ of the three functions $\mathcal{F}_i$. First, the Taylor series expansions of $S_0, S_2$ and $C_1$ around $\rho=0$ are given as

$$
S_m(x,\rho)=\sum_{n=1}^{\infty}\left[(-1)^n\left(e^{nx}-1\right)^{-1}\left(2n^{m+1}\rho-\frac{4}{3}n^{m+3}\rho^3+\mathcal{O}(\rho^5)\right)\right],
\tag{9.3.2}
$$

$$
C_m(x,\rho)=\sum_{n=1}^{\infty}\left[(-1)^n\left(e^{nx}-1\right)^{-1}\left(n^m-2n^{m+2}\rho^2+\frac{2}{3}n^{m+4}\rho^4+\mathcal{O}(\rho^6)\right)\right].
\tag{9.3.3}
$$

Using the above expansions, as well as the standard trigonometric Taylor expansions about $\rho=0$, we can write the Taylor series expansions of the functions $\mathcal{F}_i$ as

$$
\begin{aligned}
\mathcal{F}_1(\rho)=&\frac{4}{9}\left[\lambda\widetilde{f}_1(a\beta)+3f_3(a\beta)+2\lambda\widetilde{f}_3(a\beta)\right]\\
&-\frac{8}{45}\left[\lambda\widetilde{f}_1(a\beta)+15f_3(a\beta)+10\lambda\widetilde{f}_3(a\beta)+4\lambda\widetilde{f}_5(a\beta)\right]\rho^2+\mathcal{O}(\rho^4),\\
\mathcal{F}_2(\rho)=&\frac{16}{9}\left[\lambda\widetilde{f}_1(a\beta)+3f_3(a\beta)+2\lambda\widetilde{f}_3(a\beta)\right]\\
&-\frac{16}{45}\left[3\lambda\widetilde{f}_1(a\beta)+30f_3(a\beta)+20\lambda\widetilde{f}_3(a\beta)+7\lambda\widetilde{f}_5(a\beta)\right]\rho^2+\mathcal{O}(\rho^4),\\
\mathcal{F}_3(\rho)=&-\frac{16\lambda}{45}\left[\widetilde{f}_1(a\beta)-\widetilde{f}_5(a\beta)\right]\rho^2+\mathcal{O}(\rho^4),
\end{aligned}
\tag{9.3.4}
$$

where $f_m(a\beta)$ is given by (5.1.18) and

$$
\widetilde{f}_m(x)=\sum_{n=1}^{\infty}n^m(-1)^n(e^{nx}-1)^{-1}.
\tag{9.3.5}
$$

Note that the small $\rho$ expansions (9.3.4) only involve even powers of $\rho$, due to the functional form of (9.3.1c). For example, any square of a trigonometric function will produce an even expansion[2] and, since $S_0$ has an odd expansion, $\cot(\rho)S_0$ will have an even expansion. The sum $C_1$ also has an even expansion, so each individual term in the functions $\mathcal{F}_i$ has an even expansion. The upshot is that we can write the Taylor expansions of the QFT-RSET components involving only even powers of $\rho$, as

$$\begin{aligned}
\widetilde{T}_\tau{}^\tau(\rho) &= T_{\tau|0} + T_{\tau|2}\rho^2 + \mathcal{O}(\rho^4), \\
\widetilde{T}_\rho{}^\rho(\rho) &= T_{\rho|0} + T_{\rho|2}\rho^2 + \mathcal{O}(\rho^4), \\
\widetilde{T}_\theta{}^\theta(\rho) &= T_{\theta|0} + T_{\theta|2}\rho^2 + \mathcal{O}(\rho^4),
\end{aligned} \tag{9.3.6a}$$

where each coefficient $T_{\mu|i}$ is found by substituting equation (9.3.4) into equation (9.3.1), and are given in terms of the functions $f_m(a\beta)$ and $\widetilde{f}_m(a\beta)$ as

$$\begin{aligned}
T_{\tau|0} &= -\frac{a^4}{6\pi^2}\left[\lambda\widetilde{f}_1(a\beta) + 3f_3(a\beta) + 2\lambda\widetilde{f}_3(a\beta)\right], \\
T_{\tau|2} &= \frac{a^4}{9\pi^2}\left[\lambda\widetilde{f}_1(a\beta) + 9f_3(a\beta) + 6\lambda\widetilde{f}_3(a\beta) + 2\lambda\widetilde{f}_5(a\beta)\right], \\
T_{\rho|0} &= \frac{a^4}{18\pi^2}\left[\lambda\widetilde{f}_1(a\beta) + 3f_3(a\beta) + 2\lambda\widetilde{f}_3(a\beta)\right], \\
T_{\rho|2} &= -\frac{a^4}{45\pi^2}\left[3\lambda\widetilde{f}_1(a\beta) + 15f_3(a\beta) + 10\lambda\widetilde{f}_3(a\beta) + 2\lambda\widetilde{f}_5(a\beta)\right], \\
T_{\theta|0} &= T_{\rho 0} = \frac{a^4}{18\pi^2}\left[\lambda\widetilde{f}_1(a\beta) + 3f_3(a\beta) + 2\lambda\widetilde{f}_3(a\beta)\right], \\
T_{\theta|2} &= -\frac{a^4}{45\pi^2}\left[\lambda\widetilde{f}_1(a\beta) + 15f_3(a\beta) + 10\lambda\widetilde{f}_3(a\beta) + 4\lambda\widetilde{f}_5(a\beta)\right].
\end{aligned} \tag{9.3.6b}$$

To ensure a high enough numerical accuracy, we actually found the QFT-RSET component Taylor series expansions up to, but not including, $\mathcal{O}(\rho^8)$. However these expressions are too lengthy to reproduce here and so, for brevity, can instead be found in appendix B.1.

[2]By even or odd expansions, we are referring the powers of $\rho$ in the expansions; a series with only even powers of $\rho$ are even expansions and respectively for odd powers.

### 9.3.2 Taylor series expansions of the quantum-corrected metric functions

We now have a suitable set of boundary conditions at $\rho = \epsilon$ for the QFT-RSET components. However, we still need boundary conditions at $\rho = \epsilon$ for the metric functions $A(\rho)$ and $C(\rho)$. Since we are using the QFT-RSET components as a source term in the QCEE, it is not unreasonable to suggest that the metric functions $A(\rho), B(\rho)$ and $C(\rho)$ will share some properties with the QFT-RSET. One such property, which we assume to be true of the metric functions, is that the Taylor expansions near the origin also only contain even powers of $\rho$. That is, we write the Taylor series expansions (around $\rho = 0$) of the metric functions $A(\rho), B(\rho)$ and $C(\rho)$ as

$$A(\rho) = A_0 + A_2\rho^2 + \mathcal{O}(\rho^4), \tag{9.3.7a}$$

$$B(\rho) = B_0 + B_2\rho^2 + \mathcal{O}(\rho^4), \tag{9.3.7b}$$

$$C(\rho) = C_2\rho^2 + C_4\rho^4 + \mathcal{O}(\rho^6). \tag{9.3.7c}$$

We have also assumed that the coefficients $A_i, B_i, C_i$ are constant, but as of yet unknown. Additionally, in equation (9.3.7c) we have assumed that $C(\rho) \in \mathcal{O}(\rho^2)$ as $\rho \to 0$ to match the behaviour of the original anti-de Sitter metric (4.1.8) at the origin - since, if we have no back-reaction, $C(\rho) = \tan^2(\rho)$.

In order to determine the constants $A_i, B_i, C_i$, we substitute the Taylor series expansions (9.3.6) and (9.3.7) into the governing equations of the QCEE (9.2.7,9.2.8,9.2.10), as well as considering scalar curvature invariants of the quantum-corrected space-time. This process will be detailed below.

To begin, we note that since the quantum-corrected metric (9.2.1) is static, we have the freedom to rescale the time coordinate $\tau$. This means that, without loss of generality, we can set the coefficient $A_0$ to be some nonzero constant. For simplicity, we consider $A_0 = 1$.

We next consider the first- and second-order scalar curvature invariants of the quantum-corrected space-time. The first-order scalar curvature invariant is the Ricci scalar, whilst

the three second-order scalar curvature invariants of the quantum-corrected space-time are: the Kretschmann scalar $K_1$ (2.1.15), the Chern-Pontryagin scalar $K_2$ (2.1.16) and the Euler scalar $K_3$ (2.1.17). These are defined in section 2.1. To avoid a curvature singularity, we require that all four first- and second-order scalar curvature invariants be regular at the origin. We start by expanding the Ricci scalar in a Taylor series about the origin $\rho = 0$:

$$R = 2\left(\frac{1}{C_2} - \frac{1}{B_0}\right)\rho^{-2} + \mathcal{O}(1). \tag{9.3.8}$$

We next consider the second-order invariants. Expanding the Kretschmann scalar in a Taylor series about the origin $\rho = 0$, we have

$$K_1 = 4\frac{(B_0 - C_2)^2}{B_0^2 C_2^2}\rho^{-4} - 8\frac{(B_0 - C_2)\left[C_4 B_0(B_0 + 2C_2) - B_2 C_2^2\right]}{B_0^3 C_2^3}\rho^{-2} + \mathcal{O}(1). \tag{9.3.9}$$

For the quantum-corrected metric (9.2.1), we have that $K_2 \equiv 0$, due to the underlying symmetries of the Riemann tensor. In a similar fashion to the Kretschmann scalar, we expand the Euler scalar in a Taylor series about the origin, yielding

$$K_3 = 8\frac{A_2(B_0 - C_2)}{B_0^2 C_2^2}\rho^{-2} + \mathcal{O}(1). \tag{9.3.10}$$

To ensure regularity at the origin of the Ricci, Kretschmann and Euler scalars, we set

$$B_0 = C_2. \tag{9.3.11}$$

Thus, equation (9.3.11) is a necessary and sufficient condition for there to be no curvature singularities at the origin of the quantum-corrected space-time (9.2.1).

To fix the values of the remaining constant coefficients $A_i$ and $C_i$, we expand equations (9.2.7) and (9.2.10) into Taylor series around the origin, and set each coefficient of $\rho$ equal to zero systematically. We start with equation (9.2.7). We can write the Taylor series expansion as

$$0 = \mathfrak{A}_1\rho + \mathfrak{A}_3\rho^3 + \mathfrak{A}_5\rho^5 + \mathcal{O}(\rho^7), \tag{9.3.12}$$

where $\mathfrak{A}_i$ are expressions involving $A_i$, $C_i$ and coefficients $T_{\mu|i}$ of the Taylor series expansions of the QFT-RSET components. For example, $\mathfrak{A}_1$ is given by

$$\mathfrak{A}_1 = 2A_2 + \frac{4T_{\theta|2} - 8T_{\rho|2}}{T_{\tau|0} - T_{\theta|0}}, \tag{9.3.13}$$

from which, by considering $\mathfrak{A}_1 = 0$, we can fix

$$A_2 = \frac{2\left(2T_{\rho|2} - T_{\theta|2}\right)}{T_{\tau|0} - T_{\theta|0}}, \tag{9.3.14}$$

which is finite, since we have that $T_{\tau|0} \neq T_{\theta|0}$ from equation (9.3.6). The expressions for $\mathfrak{A}_3$ and $\mathfrak{A}_5$ are sufficiently complex that they will be omitted from this section, and instead can be found in appendix B.2. The idea is to then continue the current strategy, i.e. set both $\mathfrak{A}_3$ and $\mathfrak{A}_5$ equal to zero, to find constraints on the remaining coefficients $A_4$ and $A_6$. Note that, due to the form of the QCEE (9.2.7), these will involve contributions from the Taylor series coefficients $C_i$. Once we have the coefficients $A_i$, we proceed to finding the coefficients $C_i$, by expanding the QCEE (9.2.10) into a Taylor series around the origin. This can be written as

$$0 = \mathfrak{C}_0 + \mathfrak{C}_2\rho^2 + \mathfrak{C}_4\rho^4 + \mathcal{O}(\rho^6), \tag{9.3.15}$$

where the terms $\mathfrak{C}_i$ depend on Taylor series coefficients of the QFT-RSET components and the metric function $C(\rho)$. As in the case for the metric function $A(\rho)$, the terms $\mathfrak{C}_i$ are sufficiently complex that they are included only in appendix B.3. The technique to find the coefficients $C_i$ is the same as for the $A_i$, i.e. we systematically set $\mathfrak{C}_i = 0$ to find constraints on the coefficients $C_i$. The term $\mathfrak{C}_0$ is sufficiently succinct that we can demonstrate the method as follows. First, $\mathfrak{C}_0$ is defined as

$$\mathfrak{C}_0 = -T_{\tau|0} + 3T_{\theta|0} - 2\Lambda + \frac{12(T_{\theta|2} - 2T_{\rho|2})}{C_2(T_{\tau|0} - T_{\theta|0})}, \tag{9.3.16}$$

so that, by setting $\mathfrak{C}_0$ equal to zero, we find the following expression for the coefficient $C_2$:

$$C_2 = \frac{12(T_{\theta|2} - 2T_{\rho|2})}{(T_{\tau|0} - T_{\theta|0})(T_{\tau|0} - 3T_{\theta|0} + 2\Lambda)}, \tag{9.3.17}$$

where both terms in the denominator are nonvanishing. We then continue this approach to find expressions for $C_4$ and $C_6$. See appendix B for more details.

### 9.3.3 Numerical method for finding the QC metric functions

We now have a suitable set of boundary conditions for the QCEE (9.2.7) and (9.2.10). Since the QCEE (9.2.7) and (9.2.9) both involve the metric function $C(\rho)$ and derivatives thereof, we begin by solving the QCEE (9.2.10). To do so, we use `Mathematica`'s inbuilt `NDSolveValue` command to integrate the nonlinear ODE for $C(\rho)$. Since we have assumed a singular origin, the QCEE (9.2.10) is thus singular at the origin, and so we begin the numerical integration at $\rho = \epsilon = 10^{-3}$. The boundary conditions used at $\rho = \epsilon$ were $C(\epsilon)$ and $C'(\epsilon)$, both given by equation (9.3.7c) - the latter by simply differentiating the power series at $\rho = \epsilon$. As in the case for the original anti-de Sitter metric (4.1.8), the metric functions $A(\rho), B(\rho)$ and $C(\rho)$ all diverge near the space-time boundary as $\rho \to \pi/2$. To that end, we terminate the numerical integration at $\rho = \pi/2 - \epsilon$. The `NDSolveValue` command gives $C(\rho)$ as an interpolating function. Using this, the metric function $B(\rho)$ can be obtained directly from the QCEE (9.2.9) without further integration. For the remaining metric function $A(\rho)$, we numerically integrate the QCEE (9.2.7), again using the `NDSolveValue` command, with the power series (9.3.7a) at $\rho = \epsilon$ giving the initial conditions, stopping at $\rho = \pi/2 - \epsilon$. For all numerical computations here and henceforth, we set the original anti-de Sitter length scale $a$ to be equal to unity. Therefore, the renormalised adS length scale is given as

$$\widetilde{a} = \sqrt{-\frac{\widetilde{\Lambda}}{3}} = 0.9999824 \quad \text{to 7 significant figures.} \tag{9.3.18}$$

The renormalised cosmological constant $\widetilde{\Lambda}$ is given by equation (6.3.2). For a more detailed treatment of the numerics involved in solving the QCEE, including checks and error estimates, see appendix A.

## § 9.4 Quantum-corrected adS metric

In this section, the results of solving the QCEE (9.2.7), (9.2.9) and (9.2.10) will be presented. These take the form of three quantum-corrected metric functions: $A(\rho), B(\rho)$ and $C(\rho)$. In the following discussion, unless specified otherwise, we will consider the ratio between the QC metric functions and their corresponding pure adS forms. This has the advantage that we can assess the deviation of the QC metric from pure adS by considering the behaviour of the ratios. We primarily consider the effect on the QC metric deviations of changing the boundary conditions (applied to the scalar field), as well as investigate the properties of changing the (inverse) temperature. We split the following section into two parts: firstly, we discuss the QC metric solutions when both Dirichlet and Neumann boundary conditions are applied to the field; and secondly we discuss the QC metric functions when transparent boundary conditions are applied to the field, and their relation to the Einstein Static Universe and RKT.

### 9.4.1 Dirichlet and Neumann boundary conditions

Figure 9.1 shows typical QC metric solutions, for Dirichlet (top) and Neumann (bottom) boundary conditions. The local inverse temperature is fixed at $\beta = \pi/4$ (left) and $\beta = \pi$ (right) in both cases, whilst the original inverse adS length scale is set to unity. When shown on this scale, the metric functions $A^{(\mathrm{D})}(\rho)$ and $A^{(\mathrm{N})}(\rho)$ are virtually indistinguishable from their pure adS counterparts. Conversely, the QC metric functions $B^{(\mathrm{D/N})}(\rho)$ and $C^{(\mathrm{D/N})}(\rho)$ deviate considerably from pure adS, especially for the higher temperature $\beta^{-1} = 4/\pi$. For the lower temperature considered, $\beta^{-1} = 1/\pi$, the vertical scale indicates that all three QC metric functions deviate very little from pure adS. By construction, at the origin we have that $A^{(\mathrm{D/N})}(0) = 1$ and, as seen in figure 9.1, $B^{(\mathrm{D/N})}(\rho)/\sec^2(\rho)$ and $C^{(\mathrm{D/N})}(\rho)/\tan^2(\rho)$ take the same value at the origin. This is a consequence of the power series expansions (9.3.7) - see section 9.3.2 for more details. As the boundary is approached,

the functions $A^{(\mathrm{D/N})}(\rho)/\sec^2(\rho)$ begin to deviate more from pure adS, by either decreasing (Dirichlet boundary conditions) or increasing (Neumann boundary conditions) away from unity, although only by a marginal amount.

The functions $B^{(\mathrm{D/N})}(\rho)/\sec^2(\rho)$ monotonically increase away from the origin, and are always less than unity in the region of monotonic increase. The ratios then attain a local maximum close to the boundary, exceeding unity. Sufficiently close to the boundary, the ratios $B^{(\mathrm{D/N})}(\rho)/\sec^2(\rho)$ then decrease back towards unity at the boundary, taking a value very similar in magnitude to the functions $A^{(\mathrm{D/N})}(\rho)/\sec^2(\rho)$. This does not apply to the top right plot of figure 9.1, where the ratio $B^{(\mathrm{D})}(\rho)/\sec^2(\rho)$ sharply increases away from unity at the boundary; however we think that this is likely a consequence of numerical error. At higher inverse temperatures $\beta$, the numerical errors (particularly at the boundary) accumulate rapidly.

Whilst the functions $B^{(\mathrm{D/N})}(\rho)/\sec^2(\rho)$ are less than unity only in the interval of monotonic increase, and are greater than unity elsewhere, we observe a different situation for the ratios $C^{(\mathrm{D/N})}(\rho)/\tan^2(\rho)$. Indeed, the functions $C^{(\mathrm{D/N})}(\rho)/\tan^2(\rho)$ are less than unity across the whole space-time, suggesting that the back-reaction from the quantum matter has the most significant effect on the angular part of the metric - since the functions $C^{(\mathrm{D/N})}(\rho)$ represent the square of the radius of the corresponding two-sphere metric. The behaviour away from both the origin and space-time boundary of the functions $C^{(\mathrm{D/N})}(\rho)/\tan^2(\rho)$ is markedly different from the behaviour of the functions $B^{(\mathrm{D/N})}(\rho)/\sec^2(\rho)$. The functions $C^{(\mathrm{D/N})}(\rho)/\tan^2(\rho)$ decrease close to the origin before attaining a local minimum close to $\rho = \pi/4$, before increasing towards the boundary. The rates of increase and decrease are slow, owing to the fact that the magnitude of the local minimum is very similar in size to the magnitude of the functions at both the origin and boundary. The difference between the magnitude of the local minimum and values at both the origin and boundary is less for lower temperatures.

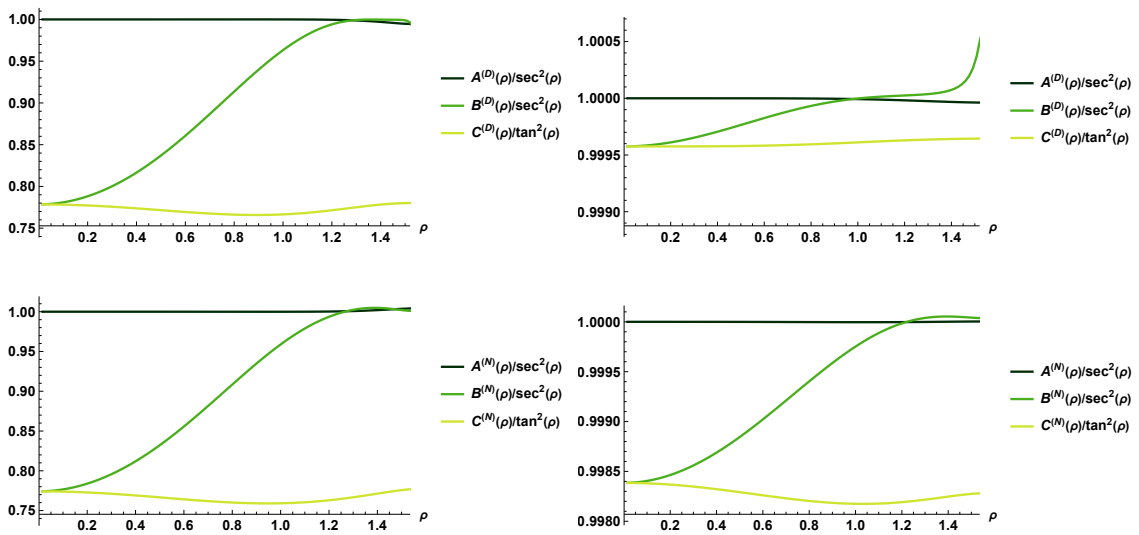


Figure 9.1: The three QC metric functions as ratios with their pure adS counterparts. In the top row, Dirichlet boundary conditions are applied to the field; in the bottom row, Neumann boundary conditions are applied. The left column shows the functions when the local inverse temperature is fixed at $\beta = \pi/4$, whilst in the right column, the local inverse temperature is fixed at $\beta = \pi$. The original inverse adS length scale is fixed at $a = 1$.

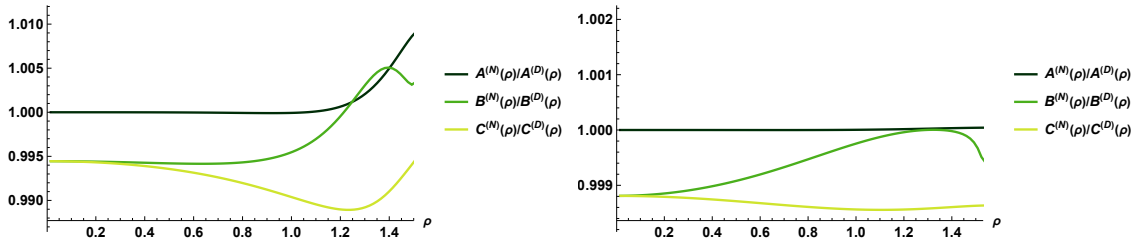


Figure 9.2: Ratios of the three QC metric functions when Neumann and Dirichlet boundary conditions are applied to the field. The left column shows the functions when the local inverse temperature is fixed at $\beta = \pi/4$, whilst in the right column, the local inverse temperature is fixed at $\beta = \pi$. The original inverse adS length scale is fixed at $a = 1$.

Figure 9.2 shows the same QC metric functions as in figure 9.1, but now as a ratio between the corresponding solutions for Neumann and Dirichlet boundary conditions. As expected, the smallest deviation between the two boundary conditions occurs for the QC metric functions $A^{(\mathrm{D/N})}(\rho)$, with the ratio $A^{(\mathrm{N})}(\rho)/A^{(\mathrm{D})}(\rho)$ (at the higher temperature considered) remaining close to unity except close to the boundary, where it rapidly increases to a fixed value greater than unity. For the lower temperature considered (right plot of figure 9.2), the ratio $A^{(\mathrm{N})}(\rho)/A^{(\mathrm{D})}(\rho)$ remains very close to unity throughout the whole space-time. This suggests that, at lower temperatures, the quantum corrections to the metric function $A(\rho)$ have very little dependence on the boundary conditions applied to the field. In contrast, at higher temperatures, the quantum corrections arising from applying Neumann boundary conditions to the quantum scalar field are larger than the corresponding quantum corrections for Dirichlet boundary conditions close to the space-time boundary, but are indistinguishable near the origin.

For both high and low temperatures considered, the ratio $B^{(\mathrm{N})}(\rho)/B^{(\mathrm{D})}(\rho)$ begins at a fixed value lower than unity at the origin, monotonically increases to a maximum at around $\rho \approx 1.35$ before decreasing to a particular value at the space-time boundary. For the higher temperature considered (left plot of figure 9.2), this value is greater than unity; for the lower temperature considered (right plot), this value is less than unity. The quantum corrections to the metric function $B(\rho)$ are therefore greater when Dirichlet boundary conditions are applied to the quantum scalar field compared with applying Neumann boundary conditions.

The final ratio of metric functions shown in figure 9.2 to consider is $C^{(\mathrm{N})}(\rho)/C^{(\mathrm{D})}(\rho)$. The ratios take the same value at the origin as $B^{(\mathrm{N})}(\rho)/B^{(\mathrm{D})}(\rho)$ by construction. In contrast to the behaviour of $B^{(\mathrm{N})}(\rho)/B^{(\mathrm{D})}(\rho)$, the ratio $C^{(\mathrm{N})}(\rho)/C^{(\mathrm{D})}(\rho)$ monotonically decreases away from the origin to a global minimum at around $\rho \approx 1.25$, before increasing to a value less than unity at the space-time boundary. For the higher temperature considered (left plot of figure 9.2), the rate of increase away from the global minimum is higher than for the lower temperature (right plot). For both temperatures considered, the ratio $C^{(\mathrm{N})}(\rho)/C^{(\mathrm{D})}(\rho)$ is

less than unity across the entire space-time. As was the case for the metric function $B(\rho)$, this indicates that the quantum corrections to the metric function $C(\rho)$ are greater for Dirichlet boundary conditions than for Neumann boundary conditions.

We will now consider the effect of changing the (inverse) temperature on the metric functions $A(\rho), B(\rho)$ and $C(\rho)$ when either Dirichlet or Neumann boundary conditions are applied to the field. Figures 9.3 and 9.4 show the quantum-corrected metric functions as ratios with their pure adS counterparts for Dirichlet and Neumann boundary conditions respectively. Figure 9.5 shows the ratio of the three quantum-corrected metric functions between the two boundary conditions, and figure 9.6 shows the ratio $A^{(\mathrm{D/N})}(\rho)/B^{(\mathrm{D/N})}(\rho)$ since, in pure anti-de Sitter space-time, this is exactly unity. In all four figures, the left column shows the high temperature range $\beta \in [\pi/12, 11\pi/24]$ and the right column shows the low temperature range $\beta \in [5\pi/8, \pi]$. Thus, in the proceeding analysis, the highest temperature we consider corresponds to $\beta = \pi/12$ and the lowest corresponds to $\beta = \pi$. Recall that in the zero-temperature limit $\beta \to \infty$, the (thermal) QFT-RSET (5.1.23) reduces to the vacuum case; when the quantum corrections to adS are simply a renormalisation of the cosmological constant as detailed in section 6.3. We therefore expect that all quantities considered will approach unity as the zero-temperature limit is approached.

We start by considering the effect of changing the temperature on the quantum-corrected metric functions when Dirichlet boundary conditions are applied to the quantum scalar field. The top row in figure 9.3 shows the ratio $A^{(\mathrm{D})}(\rho)/\sec^2(\rho)$. For all values of the inverse temperature studied, the ratio is approximately unity for $\rho \in [0, \pi/4]$, and only begins to deviate from unity at values of $\rho$ close to the boundary. Furthermore, by looking at the vertical scale of both the high temperature (left) and low temperature (right) plots, the deviation from pure adS is very small throughout the whole space-time, corresponding to a deviation of around 1% at most. The magnitude of the deviation increases with increasing temperature $\beta^{-1}$.

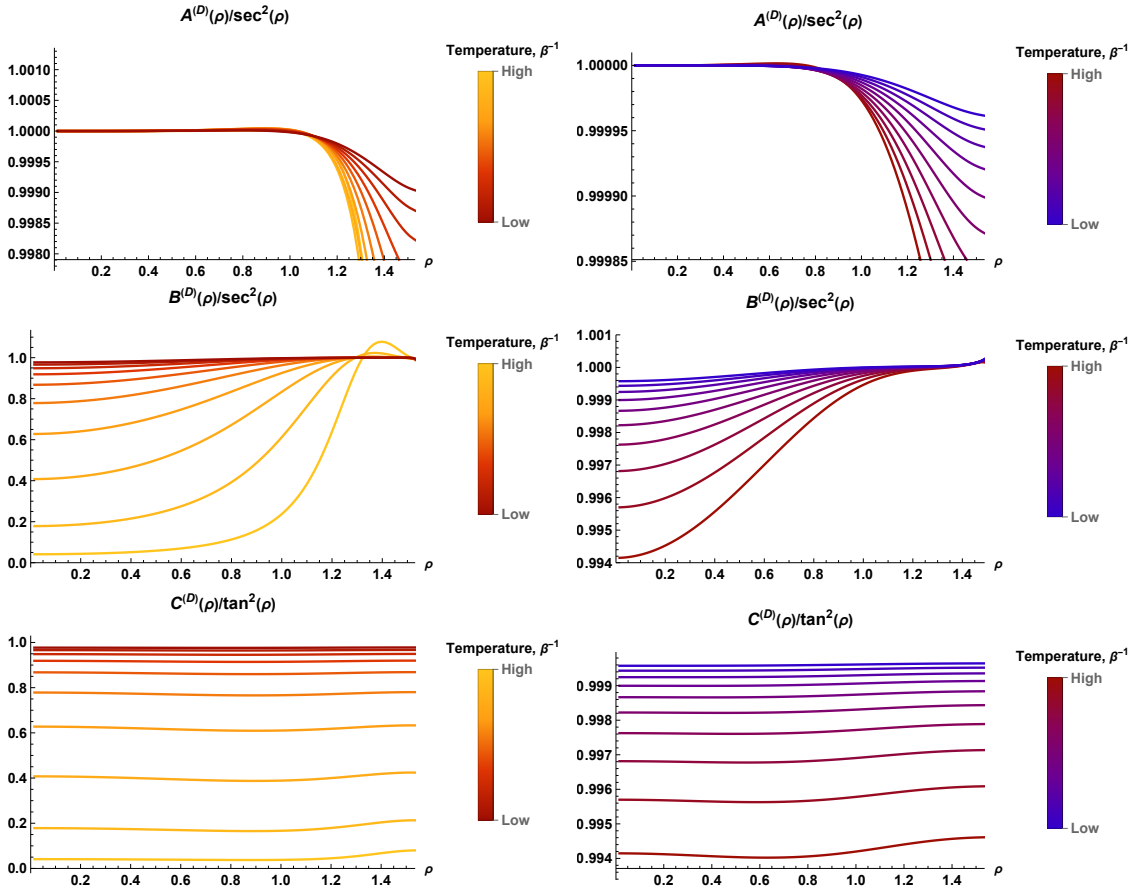


Figure 9.3: The three quantum-corrected metric functions as ratios with their pure adS counterparts. The local inverse temperature is varied in the range $\beta \in [\pi/12, 11\pi/24] \cup [5\pi/8, \pi]$ for the left and right plots respectively. The unrenormalised inverse adS length scale is fixed $a = 1$, whilst Dirichlet boundary conditions are applied to the quantum scalar field.

Turning our attention to the ratio $B^{(\mathrm{D})}(\rho)/\sec^2(\rho)$ (the middle plots of figure 9.3), we observe markedly different behaviour from the metric function $A^{(\mathrm{D})}(\rho)$. Namely, the most significant deviation from pure adS occurs at the origin, with the value of the ratio $B^{(\mathrm{D})}(\rho)/\sec^2(\rho)$ decreasing rapidly for increasing temperature. In contrast, as the boundary is approached, it appears to be the case that (to within the accuracy of our numerical integration) $B^{(\mathrm{D})}(\rho)/\sec^2(\rho)$ approaches unity. The behaviour of the ratio in between the origin and space-time boundary is as follows. The value of the ratio increases away from its global minimum at the origin towards the boundary, and at sufficiently high temperatures, the value of the ratio becomes greater than unity for a short interval, before decreasing to unity at the boundary. For the lowest temperature studied, $\beta^{-1} = 1/\pi$, the value of the ratio is very close to unity throughout the space-time. Contrastingly, for the highest temperature studied, $\beta^{-1} = 12/\pi$, the value of the ratio is very close to zero at the origin, and only approaches unity close to the boundary.

We finally discuss the behaviour of the ratio $C^{(\mathrm{D})}(\rho)/\tan^2(\rho)$, shown in the bottom row of figure 9.3. By construction, the ratio $C^{(\mathrm{D})}(\rho)/\tan^2(\rho)$ takes the same value at the origin as the ratio $B^{(\mathrm{D})}(\rho)/\sec^2(\rho)$. For all values of the inverse temperature studied, the value of the ratio then decreases away from the origin to a minimum close to $\rho = \pi/4$, before increasing to a global maximum at the space-time boundary. Unlike the ratios $A^{(\mathrm{D})}(\rho)/\sec^2(\rho)$ and $B^{(\mathrm{D})}(\rho)/\sec^2(\rho)$, the deviations in $C^{(\mathrm{D})}(\rho)$ are more consistent across the space-time, with the global minima and maxima of the ratio taking a similar magnitude. As expected, the effect of increasing the temperature is to decrease the value of the ratio $C^{(\mathrm{D})}(\rho)/\tan^2(\rho)$, with it being closest to unity for the smallest temperature considered ($\beta^{-1} = 1/\pi$) and close to zero for the highest temperature considered ($\beta^{-1} = 12/\pi$).

We now turn our attention to the results for Neumann boundary conditions, shown in figure 9.4. In the top row of figure 9.4, the ratio $A^{(\mathrm{N})}(\rho)/\sec^2(\rho)$ is shown. As for Dirichlet boundary conditions (top row of figure 9.3), the value of the ratio is very close to unity close to the origin $\rho = 0$, and the magnitude of the deviation away from unity increases for

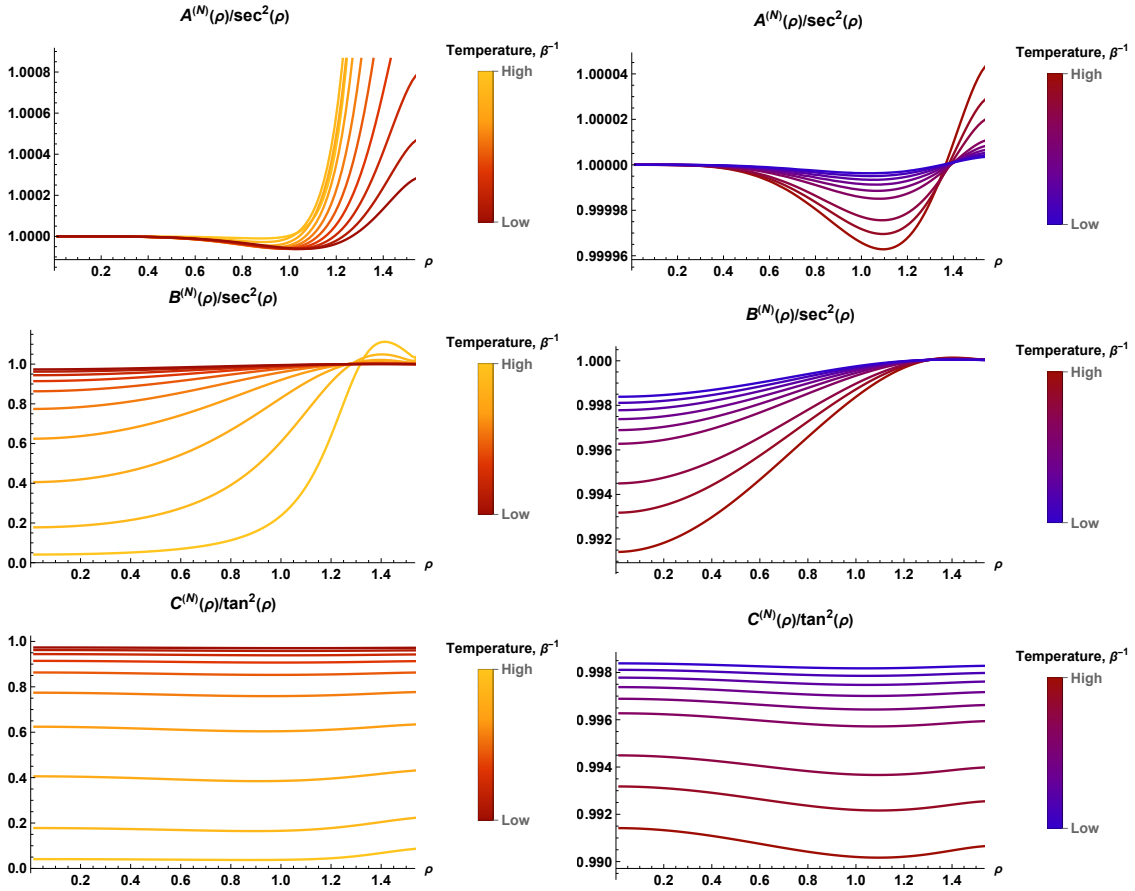


Figure 9.4: The three quantum-corrected metric functions as ratios with their pure adS counterparts. The local inverse temperature is varied in the range $\beta \in [\pi/12, 11\pi/24] \cup [5\pi/8, \pi]$ for the left and right plots respectively. The unrenormalised inverse adS length scale is fixed $a = 1$, whilst Neumann boundary conditions are applied to the quantum scalar field.

increasing temperature. However, unlike the situation for Dirichlet boundary conditions, where the value of the ratio $A^{(\mathrm{D})}(\rho)/\sec^2(\rho)$ decreases away from unity close to the boundary, we have the opposite effect here. As the radial coordinate $\rho$ increases away from the origin, the value of the ratio $A^{(\mathrm{N})}(\rho)/\sec^2(\rho)$ begins to decrease, attaining its minimum value close to $\rho \approx 1.1$, before rapidly increasing away from unity and toward its global maximum at the boundary. For the lowest temperature studied, corresponding to $\beta = \pi$, the value of the ratio $A^{(\mathrm{N})}(\rho)/\sec^2(\rho)$ is within $10^{-5}$ of unity, indicating that the quantum corrections are minimal, as expected. Conversely, the ratios $B^{(\mathrm{N})}(\rho)/\sec^2(\rho)$ (middle row) and $C^{(\mathrm{N})}(\rho)/\tan^2(\rho)$ (bottom row) are very similar by eye to the corresponding solutions for Dirichlet boundary conditions in figure 9.3, and they share many features. The only difference is that for the lower temperature range considered (right plot), the global maximum of the ratio $C^{(\mathrm{N})}(\rho)/\tan^2(\rho)$ is now located at the origin, unlike for the ratio $C^{(\mathrm{D})}(\rho)/\tan^2(\rho)$, where the global maximum is at the space-time boundary.

To understand the difference in quantum corrections between the boundary conditions, figure 9.5 shows each quantum-corrected metric component as a ratio between the solutions for Neumann and Dirichlet boundary conditions. Looking at the vertical scale of each plot, we see that the differences between the quantum-corrected metric functions for the different boundary conditions are rather small, and typically no greater than 1%. We will first consider the ratio $A^{(\mathrm{N})}(\rho)/A^{(\mathrm{D})}(\rho)$, shown in the top row. Except for a small dip at around $\rho \approx 0.85$, the value of the ratio is always greater than unity. The magnitude of the dip below unity is of the order $10^{-5}$ indicating that, on average, the quantum corrections to $A(\rho)$ arising from applying Neumann boundary conditions to the quantum scalar field are larger than for Dirichlet boundary conditions. As the temperature is increased, the value of the global maximum (at the boundary) increases.

For the ratio $B^{(\mathrm{N})}(\rho)/B^{(\mathrm{D})}(\rho)$ (shown in the middle row of figure 9.5), we see somewhat different behaviour. Towards the higher end of the temperatures studied, close to the origin, the ratio $B^{(\mathrm{N})}(\rho)/B^{(\mathrm{D})}(\rho)$ is closer to unity for higher temperatures. In contrast, for

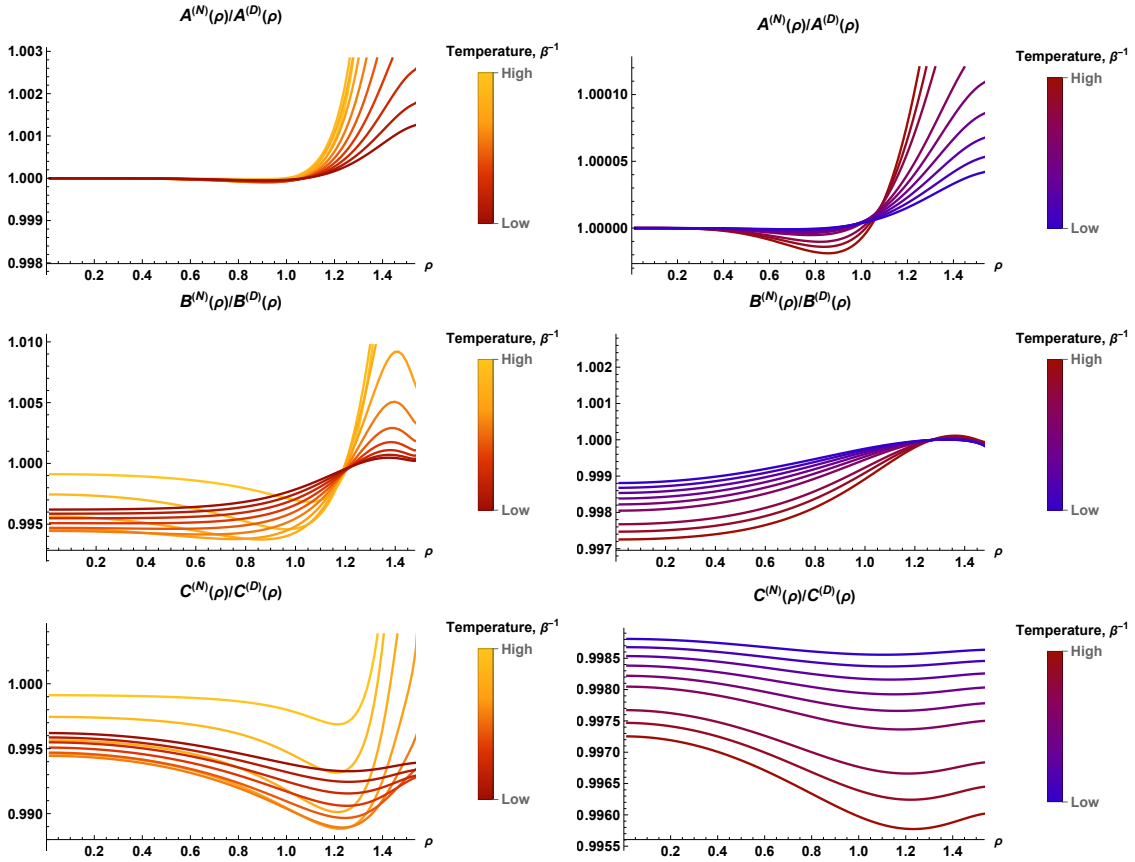


Figure 9.5: Ratios of the three quantum-corrected metric functions between the cases when Neumann and Dirichlet boundary conditions are applied to the field. The local inverse temperature is varied in the range $\beta \in [\pi/12, 11\pi/24] \cup [5\pi/8, \pi]$ for the left and right plots respectively, and the unrenormalised inverse adS length scale is fixed $a = 1$.

the lower temperatures studied, we observe the exact opposite; the lower the temperature, the closer to unity the ratio $B^{(\mathrm{N})}(\rho)/B^{(\mathrm{D})}(\rho)$ is. We also observe the same behaviour in the ratio $C^{(\mathrm{N})}(\rho)/C^{(\mathrm{D})}(\rho)$, shown in the bottom row of figure 9.5. This suggests that at both sufficiently high *and* low temperatures, the effect of the boundary conditions on the quantum-corrected metric is less significant. This is somewhat to be expected. At sufficiently low temperatures, the quantum-corrected metric functions $B^{(\mathrm{D/N})}(\rho)$ and $C^{(\mathrm{D/N})}(\rho)$ deviate very little from pure adS since, as the zero-temperature limit is approached, the quantum-corrections to adS purely amount to a renormalisation of the cosmological constant (see section 6.3), and have no effect on the metric functions themselves. Conversely, at sufficiently high temperatures, the components of the QFT-RSET (9.3.1) show very little dependence on the boundary conditions applied to the quantum scalar field [266]. This fact is inherited by the quantum-corrected metric functions. At values of the inverse temperature between the higher and lower end, the quantum-corrected metric functions depend in a complex way on the temperature and boundary conditions. At the boundary, except for sufficiently high temperatures, the values of the ratios $B^{(\mathrm{D/N})}(\rho)$ and $C^{(\mathrm{D/N})}(\rho)$ are below unity.

Finally, in figure 9.6 the ratio between the quantum-corrected metric functions $A^{(\mathrm{D/N})}(\rho)$ and $B^{(\mathrm{D/N})}(\rho)$, for both cases of Dirichlet and Neumann boundary conditions is shown. The reason this quantity is of interest is that, in pure adS, it is identically unity. This therefore provides a further chance to examine quantum-correction induced deviations from pure adS. As expected, as the temperature is increased, the value of the ratio increases away from unity, taking its greatest value at the origin. Close to the boundary, the value of the ratios $A^{(\mathrm{D/N})}(\rho)/B^{(\mathrm{D/N})}(\rho)$ are close to unity. What is particularly striking is the overall profile of the ratios, especially at higher temperatures, which exactly mimic the profile of the QFT-RSET components (5.3.42). In particular, see figures 5.1, 5.2 and 5.3. This provides an additional motivation for the solitonic approach taken in section 9.5.

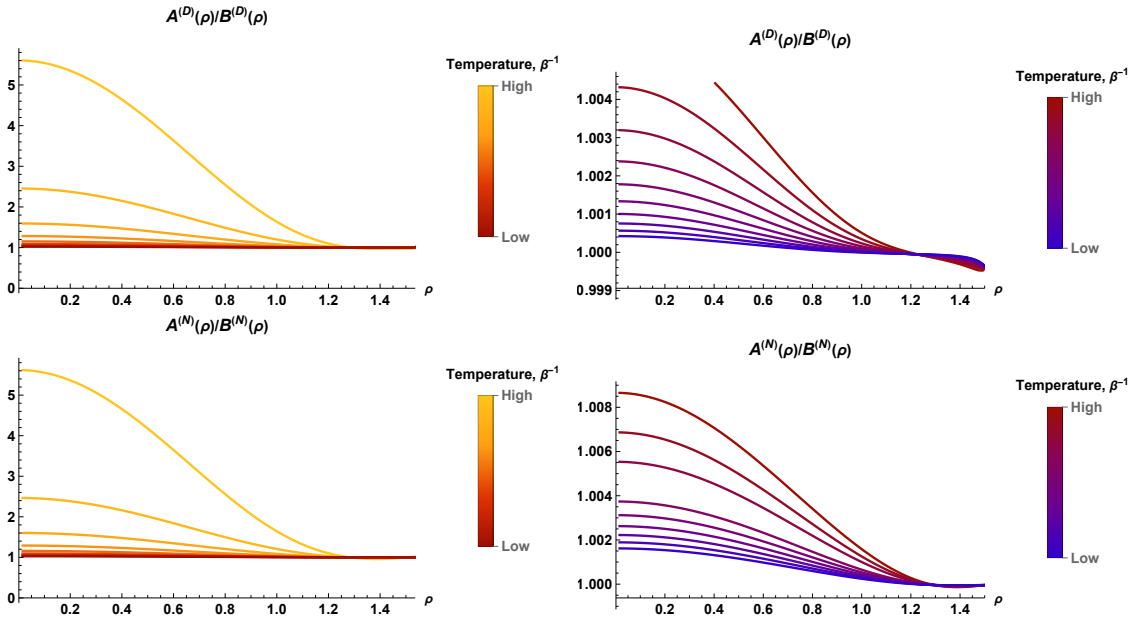


Figure 9.6: The ratio of the metric functions $A(\rho)$ and $B(\rho)$ for both Dirichlet (top row) and Neumann (bottom row) boundary conditions. The local inverse temperature is varied in the range $\beta \in [\pi/12, 11\pi/24] \cup [5\pi/8, \pi]$ for the left and right plots respectively, and the unrenormalised inverse adS length scale is fixed to be $a = 1$.

### 9.4.2 Transparent boundary conditions, the ESU and RKT

Before commencing with the discussion of the QC metric solutions for the case of transparent boundary conditions, it proves pertinent to take a step back and reassess both the form of the QFT-RSET (9.3.1) and the QCEE when transparent boundary conditions are applied to the quantum scalar field, and how these relate to RKT. When setting $\lambda = 0$ in the QFT-RSET (9.3.1), we find that the QFT-RSET simplifies considerably, taking the form (after raising one index):

$$\widetilde{T}_{\mu}{}^{\nu} = \frac{a^2}{6\pi^2}\cos^4(\rho)\, f_3(a\beta)\mathrm{Diag}\{-3,1,1,1\}, \tag{9.4.1}$$

where $f_3(a\beta)$ is defined in equation (5.1.18). Now recall the form of the RKT-SET, given by equation (5.3.12). If we raise one index, it can be written as

$$\widetilde{T}_{\mu}{}^{\nu} = \frac{a^2\pi^2}{90\beta^4}\cos^4(\rho)\,\mathrm{Diag}\{-3,1,1,1\}. \tag{9.4.2}$$

It is clear that, for nonrotating four-dimensional anti-de Sitter space-time, the RKT-SET (5.3.12) and the QFT-RSET (9.4.1) when transparent boundary conditions are applied are the same up to an overall constant. Indeed, if we define the prefactors of the SETs as

$$\mathcal{P}_{\mathrm{QFT}} = \frac{a^2}{6\pi^2}\cos^4(\rho)\, f_3(a\beta), \quad \text{and} \quad \mathcal{P}_{\mathrm{RKT}} = \frac{a^2\pi^2}{90\beta^4}\cos^4(\rho), \tag{9.4.3}$$

the ratio of the two does not depend on space-time coordinates; only the local inverse temperature:

$$\mathcal{P}_{\mathrm{QFT}}/\mathcal{P}_{\mathrm{RKT}} = \frac{15\beta^4}{\pi^4} f_3(a\beta). \tag{9.4.4}$$

This ratio is shown in figure 9.7. The best agreement between the two prefactors is at $\beta = 0$, where the ratio is unity; this suggests that the two are more closely related when the temperature of the system is higher. This is in agreement with the findings in section 5.3.4. Conversely, at higher $\beta$ (corresponding to a lower temperature), the prefactor ratio tends towards zero, implying that the prefactor in the RKT-SET increases more rapidly with the inverse temperature. The temperature range considered in section 9.4.1 was

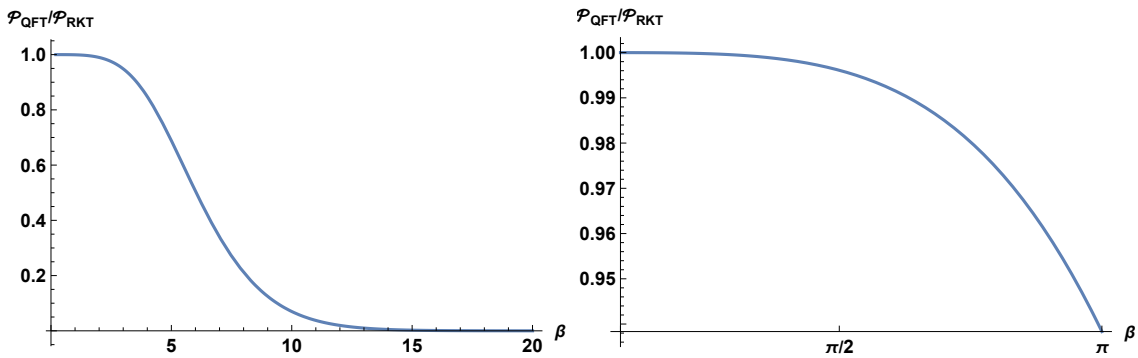


Figure 9.7: Ratio of the prefactors of the mixed indices RKT-SET and QFT-RSET when transparent boundary conditions are applied to the field. The left shows the inverse temperature over a domain of $\beta \in (0, 20]$ and the right over the reduced domain $\beta \in [\pi/12, \pi]$. The unrenormalised inverse adS length scale is set to unity.

$\beta \in [\pi/12, \pi]$. For consistency, we will only consider the same region of values for $\beta$ in the following analysis. As can be seen from the right plot of figure 9.7, within this region, the prefactor ratio is very close to unity, approximately within 6%. To this end, in the following analyses, we do not consider RKT since it is well approximated by the QFT-RSET (9.4.1) when transparent boundary conditions are applied (this corroborates the results of section 5.3.4). This means that the resulting RKT-corrected metric functions will be very similar to the quantum-corrected metric functions when transparent boundary conditions are applied, and in particular will be qualitatively the same.

Now that neglecting an RKT based analysis has been justified, we can commence with the solutions to the QCEE when the QFT-RSET (9.4.1) with transparent boundary conditions acts as the source term. Since the form of the QFT-RSET can be simplified considerably to the form in equation (9.4.1), we can also make certain simplifications to the QCEE. Recall the governing equation of the QCEE for $A(\rho)$, given by equation (9.2.7). If we let

$$\widetilde{T}_{\mu}{}^{\nu} = \mathcal{P}_{\text{QFT}} \text{ Diag}\{-3, 1, 1, 1\}, \tag{9.4.5}$$

where the prefactor is defined in equation (9.4.3), we can simplify the QCEE (9.2.7) to (dropping the QFT subscript for brevity):

$$\frac{A'}{A} = -\frac{1}{2}\frac{(C\,\mathcal{P})' - C'\,\mathcal{P}}{C\,\mathcal{P}} = -\frac{1}{2}\frac{\mathcal{P}'}{\mathcal{P}}. \tag{9.4.6}$$

This can be directly integrated to give

$$A = \tilde{A}_0\,\mathcal{P}^{-1/2} = \tilde{A}_0\frac{\pi\sqrt{6}}{a}\sec^2(\rho)\,[f_3(a\beta)]^{-1/2}\,, \tag{9.4.7}$$

where $\widetilde{A}_0$ is an arbitrary constant of integration. To set the constant of integration, we mirror the behaviour at the origin of the power series (9.3.7a), whereby we have $A(0) = 1$. This fixes

$$\tilde{A}_0 = \frac{a}{\pi\sqrt{6}}\sqrt{f_3(a\beta)}, \tag{9.4.8}$$

and so, the quantum-corrected metric function $A(\rho)$ when transparent boundary conditions are applied is given by

$$A^{(\mathrm{T})}(\rho) = \sec^2(\rho), \tag{9.4.9}$$

which is identical to pure adS with the unrenormalised adS length scale set to unity. This means that, when transparent boundary conditions are applied to the quantum scalar field, there are no quantum corrections to the temporal component of the adS metric.

However, the quantum-corrected metric functions $B^{(\mathrm{T})}(\rho)$ and $C^{(\mathrm{T})}(\rho)$ are not the same as in pure adS. In spite of this, the governing QCEE (9.2.9) and (9.2.10) simplify somewhat. For the metric function $B^{(\mathrm{T})}(\rho)$, the QCEE reduces to

$$B^{(\mathrm{T})}(\rho) = -\frac{C'}{4C\Xi_\rho}\left(C' + 4C\tan\rho\right), \tag{9.4.10}$$

and the QCEE for $C^{(\mathrm{T})}(\rho)$ reduces to

$$0 = \frac{\Xi_\tau}{C} + \frac{4}{CC'}\left(2CC'' + C'^2\right)\frac{\Xi_\rho\widetilde{T}_\rho{}^\rho}{\Upsilon} + 8\frac{\mathrm{d}}{\mathrm{d}\rho}\left(\frac{\Xi_\rho\widetilde{T}_\rho{}^\rho}{\Upsilon}\right), \tag{9.4.11a}$$

where $\Upsilon$ (9.2.10b) is now

$$\Upsilon = 4\left(C\widetilde{T}_\rho{}^{\rho\prime} - C'\widetilde{T}_\rho{}^\rho\right), \tag{9.4.11b}$$

and $\Xi_\bullet$ (9.2.10c) is unchanged. To solve the reduced (transparent) QCEE (9.4.10) and (9.4.11), we follow the same method as in section 9.3; i.e. we find a suitable set of initial conditions on the function $C^{(\mathrm{T})}(\rho)$ from which we numerically integrate the nonlinear ODE (9.4.11) using `Mathematica`'s inbuilt `NDSolveValue` command, following the methodology of section 9.3.3. This process will be outlined below.

Following section 9.3.2, to determine the initial conditions we expand both the QFT-RSET (9.4.1) components and metric function $C^{(\mathrm{T})}(\rho)$ into Taylor series about the origin. The series for the QFT-RSET components take the form

$$\widetilde{T}_\mu{}^\nu = \frac{a^2}{18\pi^2} f_3(a\beta)\left[3 - 6\rho^2 + 5\rho^4 + \mathcal{O}(\rho^6)\right] \mathrm{Diag}\{-3,1,1,1\}, \tag{9.4.12}$$

whilst the metric function $C^{(\mathrm{T})}(\rho)$ takes the form

$$C^{(\mathrm{T})}(\rho) = C_2^T\rho^2 + C_4^T\rho^4 + C_6^T\rho^6 + \mathcal{O}(\rho^8) \quad \text{as} \quad \rho \to 0, \tag{9.4.13}$$

where the coefficients $C_i^T$ are constants to be determined. Note that we make the same assumptions on this power series as we did for the corresponding series (9.3.7c) in the cases of Dirichlet and Neumann boundary conditions, i.e. we assume the leading order term is $\mathcal{O}(\rho^2)$ to match the behaviour of the original adS metric at the origin, and that the series contains only even powers of $\rho$ to match the power series expansion (9.4.12) of the QFT-RSET. We then substitute these power series into equation (9.4.11), also expanding this into a power series about the origin. This takes the general form

$$0 = \mathfrak{C}_0^T + \mathfrak{C}_2^T\rho^2 + \mathfrak{C}_4^T\rho^4 + \mathcal{O}(\rho^6), \tag{9.4.14a}$$

where

$$\mathfrak{C}_0^T = -\frac{2}{C_2^T}\left[3 - C_2^T\left\{4f_3(a\beta) - \Lambda\right\}\right], \tag{9.4.14b}$$

$$\mathfrak{C}_2^T = \frac{2}{3(C_2^T)^2}\left[30C_4^T + 25C_2^T - (C_2^T)^2\left\{52f_3(a\beta) - 15\Lambda\right\}\right], \tag{9.4.14c}$$

$$\mathfrak{C}_4^T = -\frac{1}{5(C_2^T)^3}\left[480(C_4^T)^2 + 5C_2^T\left\{122C_4^T - 63C_6^T\right\}\right.$$

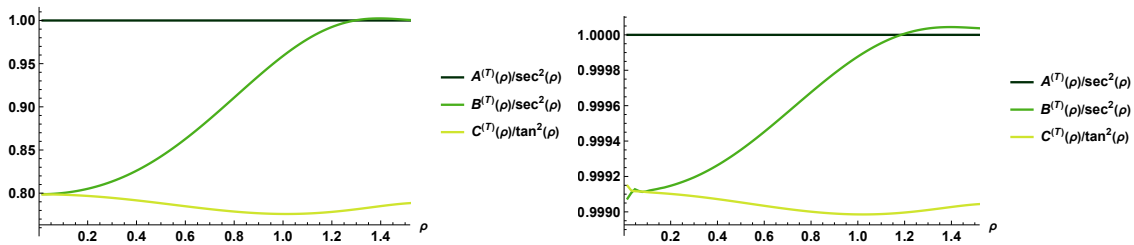


Figure 9.8: The three QC metric functions as ratios with their pure adS counterparts (although $A^{(\mathrm{T})}(\rho)/\sec^2(\rho)$ is exactly unity). Transparent boundary conditions are applied to the field. In the left plot, the local inverse temperature is fixed at $\beta = \pi/4$, while in the right it is fixed at $\beta = \pi$. The unrenormalised inverse adS length scale is fixed at $a = 1$.

$$+ (C_2^T)^2 \left\{294 - 5C_4^T \left(44 f_3(a\beta) - 27\Lambda\right)\right\} - 5(C_2^T)^3 \left\{136 f_3(a\beta) - 35\Lambda\right\}\Big] . \tag{9.4.14d}$$

To find constraints on the coefficients $C_i^T$ of the power series (9.4.13), we systematically set each term $\mathfrak{C}_i^T$ in equation (9.4.14) to zero. For the first four nonzero terms of the series (9.4.13), this yields the following expressions:

$$C_2^T = \frac{3}{4f_3(a\beta) - \Lambda}, \tag{9.4.15}$$

$$C_4^T = \frac{2\left\{14 f_3(a\beta) - 5\Lambda\right\}}{5\left\{4 f_3(a\beta) - \Lambda\right\}^2}, \tag{9.4.16}$$

$$C_6^T = \frac{7696[f_3(a\beta)]^2 - 4880 f_3(a\beta)\Lambda + 595\Lambda^2}{525\left\{4 f_3(a\beta) - \Lambda\right\}^3}. \tag{9.4.17}$$

Now that we have a suitable set of initial conditions in the form of the power series (9.4.13) at $\rho = \epsilon = 10^{-3}$ (the reasoning for such a choice is the same as in section 9.3.3), we can directly apply `Mathematica`'s inbuilt `NDSolveValue` command to the QCEE (9.4.11) to find the quantum-corrected metric functions when transparent boundary conditions are applied.

Figure 9.8 shows typical QC metric solutions for two different inverse temperatures. Comparing this with figure 9.1, we see that the overall profiles of the QC metric functions when

transparent boundary conditions are applied are similar to the corresponding solutions when both Dirichlet and Neumann boundary conditions are applied. The main difference is that, in the cases of Dirichlet and Neumann boundary conditions, near the boundary the ratios $A^{(\mathrm{D/N})}(\rho)/\sec^2(\rho)$ began to deviate slightly away from unity, whereas for the case of transparent boundary conditions, $A^{(\mathrm{T})}(\rho)$ takes the pure adS form and thus the ratio $A^{(\mathrm{T})}(\rho)/\sec^2(\rho)$ is unity throughout the space-time. Additionally, the values the ratios $B^{(\mathrm{T})}(\rho)/\sec^2(\rho)$ and $C^{(\mathrm{T})}(\rho)/\tan^2(\rho)$ take at the origin are slightly greater than the corresponding values for both Dirichlet and Neumann boundary conditions. In the right plot of figure 9.8, very close to the origin the ratios $B^{(\mathrm{T})}(\rho)/\sec^2(\rho)$ and $C^{(\mathrm{T})}(\rho)/\tan^2(\rho)$ exhibit some strange behaviour and no longer appear smooth. We think that this is simply down to numerical error since, by construction, the ratios should take the same value at the origin.

In figure 9.9, the ratios $B^{(\mathrm{T})}(\rho)/\sec^2(\rho)$ and $C^{(\mathrm{T})}(\rho)/\tan^2(\rho)$ are shown for varied inverse temperature. By eye, these look almost indistinguishable from the corresponding figures for Dirichlet (figure 9.3) and Neumann (figure 9.4) boundary conditions. As expected, the least deviation from pure adS (for both QC metric functions) occurs at lower temperatures, with the greatest deviation occurring at the highest temperature studied. Regardless of temperature, the greatest deviation in the QC metric function $B^{(\mathrm{T})}(\rho)$ occurs at the origin (with the extent of this deviation increasing with increasing temperature), and at the boundary the ratio $B^{(\mathrm{T})}(\rho)/\sec^2(\rho)$ tends towards unity. For sufficiently high temperatures, the ratio $B^{(\mathrm{T})}(\rho)/\sec^2(\rho)$ increases above unity very close to the boundary before decreasing to unity at the boundary. Conversely, the ratio $C^{(\mathrm{T})}(\rho)/\tan^2(\rho)$ remains more consistent in its deviations from pure adS across the whole space-time. It is still the case that the QC metric function $C^{(\mathrm{T})}(\rho)$ attains a greater deviation from pure adS at higher temperatures, and a lower deviation at lower temperatures.

Figure 9.10 shows the ratios of the QC metric function $B(\rho)$ when transparent boundary conditions are applied to those when both Dirichlet (top row) and Neumann (bottom row)

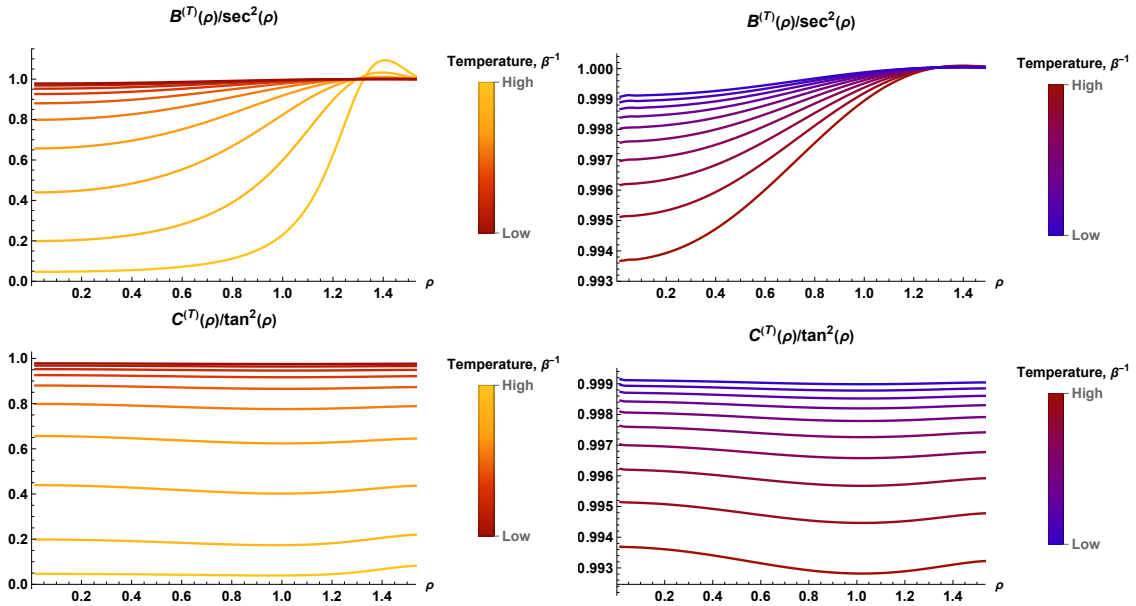


Figure 9.9: The QC metric functions $B^{(\mathrm{T})}(\rho)$ and $C^{(\mathrm{T})}(\rho)$ as ratios with their pure adS counterparts. The inverse temperature is varied in the range $\beta \in [\pi/12, 11\pi/24] \cup [5\pi/8, \pi]$ for the left and right plots respectively. Transparent boundary conditions are applied to the field, and the original inverse adS length scale is fixed at $a = 1$.

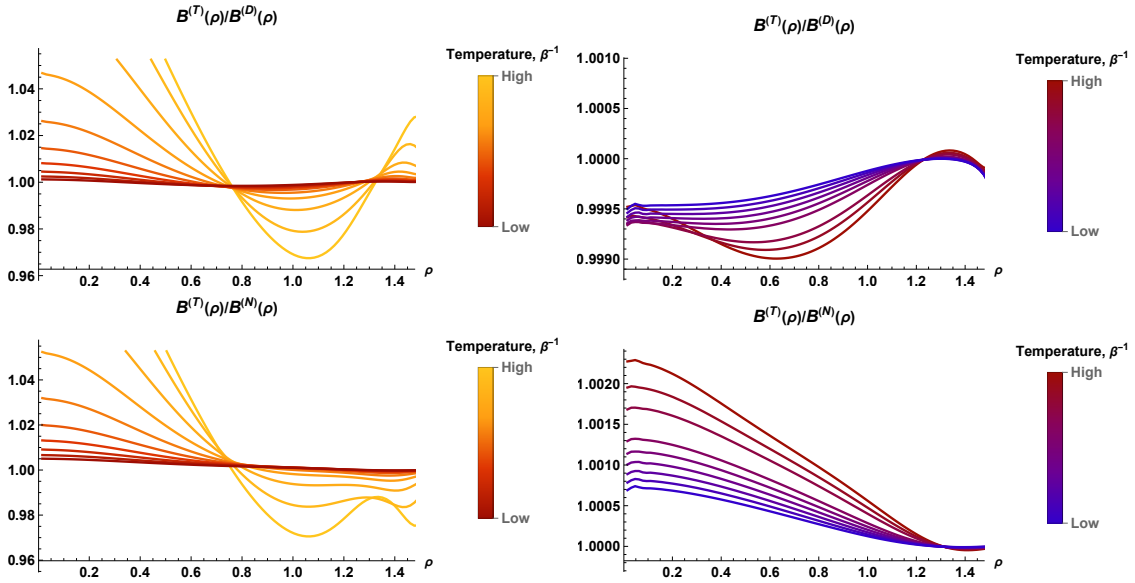


Figure 9.10: Ratios of the QC metric function $B(\rho)$ when transparent and Dirichlet boundary conditions (top row) are applied, and when transparent and Neumann boundary conditions are applied (bottom row). The local inverse temperature is varied in the range $\beta \in [\pi/12, 11\pi/24] \cup [5\pi/8, \pi]$ for the left and right columns respectively, and the original inverse adS length scale is fixed at $a = 1$.

boundary conditions are applied. In both cases, the ratios tend towards unity as the temperature is decreased, and increase away from unity as the temperature is increased. At sufficiently high temperatures (left column of figure 9.10), the ratios $B^{(\mathrm{T})}(\rho)/B^{(\mathrm{D})}(\rho)$ and $B^{(\mathrm{T})}(\rho)/B^{(\mathrm{N})}(\rho)$ are similar in profile, from the origin up to around $\rho \approx 1.3$, where they begin at a value greater than unity, decrease to a minimum less than unity at around $\rho \approx 1.05$, and begin to increase towards $\rho \approx 1.3$. At $\rho \approx 1.3$, the ratio $B^{(\mathrm{T})}(\rho)/B^{(\mathrm{D})}(\rho)$ continues to increase towards a value greater than unity at the boundary. In contrast, at $\rho \approx 1.3$, the ratio $B^{(\mathrm{T})}(\rho)/B^{(\mathrm{N})}(\rho)$ begins to increase before attaining a local maximum, decreasing to a specific value less than unity at the boundary. At lower temperatures (right column of figure 9.10), the ratios $B^{(\mathrm{T})}(\rho)/B^{(\mathrm{D})}(\rho)$ and $B^{(\mathrm{T})}(\rho)/B^{(\mathrm{N})}(\rho)$ do not share a similar profile. Indeed, at the origin, the ratio $B^{(\mathrm{T})}(\rho)/B^{(\mathrm{D})}(\rho)$ takes a value less than unity, whilst for the ratio $B^{(\mathrm{T})}(\rho)/B^{(\mathrm{N})}(\rho)$, this value is greater than unity. For sufficiently low temperatures, the ratio $B^{(\mathrm{T})}(\rho)/B^{(\mathrm{N})}(\rho)$ begins at a value greater than unity, and monotonically decreases until $\rho \approx 1.3$, where it attains a local minimum, before marginally increasing towards its value at the boundary, which at this scale appears to be close to unity. Conversely, the ratio $B^{(\mathrm{T})}(\rho)/B^{(\mathrm{D})}(\rho)$ begins at a value less than unity at the origin, before decreasing towards its global minimum close to $\rho \approx 0.65$, before increasing and attaining a global maximum at $\rho \approx 1.3$, followed by a short period of decrease towards its value at the boundary, which is less than unity.

In figure 9.11, we show the ratios $C^{(\mathrm{T})}(\rho)/C^{(\mathrm{D})}(\rho)$ (top row) and $C^{(\mathrm{T})}(\rho)/C^{(\mathrm{N})}(\rho)$ (bottom row), for varied inverse temperature. As expected, in all four plots shown, the deviations away from unity increase as temperature is increased. In a similar fashion to the plots (figure 9.10) for the QC metric function $B(\rho)$, at sufficiently high temperatures (left column of figure 9.11) both ratios $C^{(\mathrm{T})}(\rho)/C^{(\mathrm{D})}(\rho)$ and $C^{(\mathrm{T})}(\rho)/C^{(\mathrm{N})}(\rho)$ take their maximum value, which is greater than unity, at the origin. They then decrease until $\rho \approx 1.3$, where they either attain a local minium and increase as the boundary is approached ($C^{(\mathrm{T})}(\rho)/C^{(\mathrm{D})}(\rho)$) or continue to decrease towards the boundary ($C^{(\mathrm{T})}(\rho)/C^{(\mathrm{N})}(\rho)$). Except for the highest

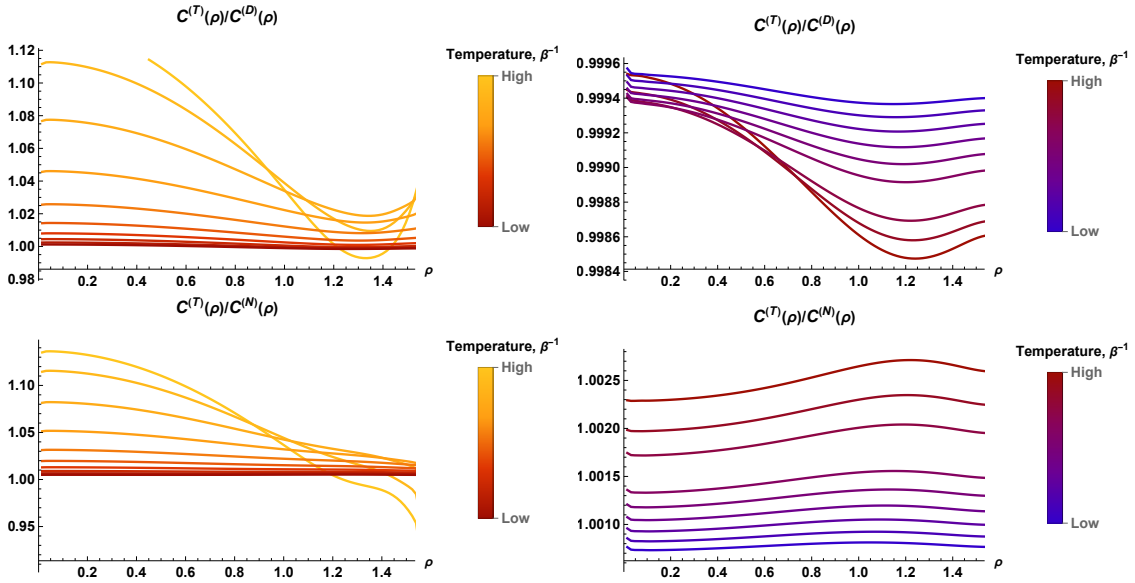


Figure 9.11: Ratios of the QC metric function $C(\rho)$ when transparent and Dirichlet boundary conditions (top row) are applied, and when transparent and Neumann boundary conditions are applied (bottom row). The local inverse temperature is varied in the range $\beta \in [\pi/12, 11\pi/24] \cup [5\pi/8, \pi]$ for the left and right columns respectively, and the original inverse adS length scale is fixed at $a = 1$.

temperatures studied, both ratios are everywhere greater than unity for the plots in the left column. In the lower temperature plot (right column), we see different behaviour. Whilst the ratio $C^{(\mathrm{T})}(\rho)/C^{(\mathrm{N})}(\rho)$ is always greater than unity, the ratio $C^{(\mathrm{T})}(\rho)/C^{(\mathrm{D})}(\rho)$ is always less than unity. In contrast, the profile of the ratio $C^{(\mathrm{T})}(\rho)/C^{(\mathrm{D})}(\rho)$ at the lower temperature matches that of its higher temperature counterparts, whereas the ratio $C^{(\mathrm{T})}(\rho)/C^{(\mathrm{N})}(\rho)$ exhibits the opposite behaviour to its higher temperature counterparts; it begins at its global minimum at the origin, before monotonically increasing to its global maximum at $\rho \approx 1.3$, before decreasing to its value on the boundary.

In section 6.4, we computed the quantum corrections to the background ESU space-time, when using the QFT-RSET (6.4.12) in a thermal state as a source term. We found that the effect of the back-reaction was a non-trivial renormalisation of both the inverse length scale and Newton's constant, but that it had no effect on the functional forms of the metric functions. We also found that the QFT-RSET (6.4.12) arising in the ESU is conformally related to the QFT-RSET (5.3.42) arising in anti-de Sitter space-time when transparent boundary conditions are applied to the quantum scalar field. One might expect, therefore, that the solutions to the QCEE in the case of a quantum scalar field conformally coupled to gravity in anti-de Sitter space-time, subject to transparent boundary conditions at the space-time boundary, might be conformally related to the solutions to the QCEE for a conformal quantum scalar in the ESU. However, as evidenced by the content of this section, the solution to the QCEE on anti-de Sitter space-time (where the field is subject to transparent boundary conditions) is not of adS form, whilst the solution to the QCEE on the ESU has ESU form. This is due to the nonlinearity of the QCEE.

## § 9.5 Quantum-corrected adS solitons

In the previous section, we found solutions to the QCEE (3.6.15) in the form of quantum-corrected adS metrics. In the low-temperature limit, the quantum-corrected adS metrics approach pure adS space-time. When we increase the temperature of the thermal quantum state, the deviations away from pure adS increase. Aside from this, however, there is no obvious way to interpret the solutions $A(\rho)$, $B(\rho)$ and $C(\rho)$ in a physical sense. In this section, we make an alternative metric ansatz for the quantum-corrected adS metric, which will aid their interpretations as solitons sourced by the quantum scalar field. This is motivated by the form of the energy density of the QFT-RSET (5.3.42), which has a solitonic profile - see, for example, sections 5.1.1 and 5.3.4. This alternative ansatz is inspired, in part, by the work of [40], where the authors consider solutions to the full semi-classical Einstein equations for conformally-coupled quantum scalars, using the vacuum polarisation as the source, on a static and spherically-symmetric four-dimensional space-time. It is additionally motivated by the quantum-corrected BTZ geometries [78] - see section 6.5.

### 9.5.1 Spherically symmetric quantum-corrected Einstein equations

We make the following ansatz for the form of the solitonic quantum-corrected metric:

$$\mathrm{d}s^2 = -f(r)e^{\psi(r)}\,\mathrm{d}\tau^2 + f(r)^{-1}\,\mathrm{d}r^2 + r^2\,\mathrm{d}\theta^2 + r^2\sin^2(\theta)\,\mathrm{d}\phi^2, \tag{9.5.1a}$$

where $f(r)$ and $\psi(r)$ are functions to be determined by the QCEE (3.6.15). This is just the general form of the metric for any static and spherically symmetric space-time, where the distinction between different space-times is encoded in the unknown functions $f(r)$ and $\psi(r)$. The function $f(r)$ can be written in a more familiar form,

$$f(r) = 1 - \frac{2m(r)}{r} - \frac{\widetilde{\Lambda}}{3}r^2, \tag{9.5.1b}$$

where $\widetilde{\Lambda}$ is the renormalised cosmological constant (6.3.2), and $m(r)$ is another unknown function to be determined by the QCEE. In pure adS, both functions $m(r)$ and $\psi(r)$ are identically zero. These functions, therefore, can be used to express deviations away from pure adS.

Recall the initial metric ansatz (9.2.1). By comparing the coefficient of the two-sphere metric with the corresponding term in the second ansatz (9.5.1), we find the following relation:

$$r^2 = C(\rho), \tag{9.5.2}$$

which will be our coordinate transformation between the two ansätze. The behaviour at the origin of the new radial coordinate $r$ can be discerned by comparing with the behaviour at the origin of the metric function $C(\rho)$ from the power series expansion (9.3.7c), from which we see that as $\rho \to 0$, $C(\rho) \to 0$ and thus $r \to 0$. Similarly, at the boundary, since $C(\rho)/\tan^2(\rho)$ tends to some finite, nonzero limit (see, for example, figures 9.1 and 9.8), it must be the case that $C(\rho) \to \infty$ as $\rho \to \pi/2$. Therefore, as $\rho \to \pi/2$, we have that $r \to \infty$ and hence the domain of the new radial coordinate is $r \in [0, \infty)$, as is usually the case in spherical polar coordinates.

To find relations between the new QC metric functions $f(r)$ (and thus $m(r)$) and $\psi(r)$, we must compare the two forms of the QC adS metric (9.2.1) and (9.5.1), and equate term by term. Since the radial coordinate is different in the two metric ansätze, we need to express one differential in terms of the other. We differentiate the coordinate transformation (9.5.2), yielding

$$2r\,\frac{\mathrm{d}r}{\mathrm{d}\rho} = C'(\rho) \qquad \Longrightarrow \qquad \mathrm{d}\rho^2 = \frac{4C(\rho)}{C'(\rho)^2}\,\mathrm{d}r^2, \tag{9.5.3}$$

meaning the original metric ansatz (9.2.1) can be written in terms of spherical polars as

$$\mathrm{d}s^2 = -A(\rho)\,\mathrm{d}\tau^2 + \frac{4B(\rho)C(\rho)}{C'(\rho)^2}\,\mathrm{d}r^2 + C(\rho)\,\mathrm{d}\theta^2 + C(\rho)\sin^2(\theta)\,\mathrm{d}\phi^2. \tag{9.5.4}$$

By comparing with the new ansatz (9.5.1), we find the following relations between the new

and old QC metric functions:

$$f(r) = \frac{C'(\rho)^2}{4B(\rho)C(\rho)}, \tag{9.5.5a}$$

$$m(r) = \frac{\sqrt{C(\rho)}}{2}\left(1 - \frac{\widetilde{\Lambda}}{3}C(\rho) - \frac{C'(\rho)^2}{4B(\rho)C(\rho)}\right), \tag{9.5.5b}$$

$$e^{\psi(r)} = \frac{4A(\rho)B(\rho)C(\rho)}{C'(\rho)^2}, \tag{9.5.5c}$$

where the relation for $m(r)$ (9.5.5b) was found by also using equation (9.5.1b). By attempting to use the expressions (9.5.5) along with the results found in section 9.4 for the QC metric functions $A(\rho)$, $B(\rho)$ and $C(\rho)$, we find that numerical errors accumulate rapidly. Hence, to find numerically satisfactory results for the QC metric functions $f(r), m(r)$ and $\psi(r)$, we instead recompute the QCEE (9.2.2) using the new radial coordinate and integrate directly.

The QCEE (9.2.2), given in terms of the metric ansatz (9.5.1), are as follows:

$$\widetilde{T}_\tau{}^\tau = \frac{1}{r^2}\left[-1 + r^2\widetilde{\Lambda} + f(r) + rf'(r)\right], \tag{9.5.6a}$$

$$\widetilde{T}_\rho{}^\rho = \frac{1}{r^2}\left[-1 + r^2\widetilde{\Lambda} + f(r) + rf'(r) + rf(r)\psi'(r)\right], \tag{9.5.6b}$$

$$\widetilde{T}_\theta{}^\theta = \frac{1}{4r}\left[f'(r)\left\{4 + 3r\,\psi'(r)\right\} + f(r)\left\{2\psi'(r) + r\,\psi'(r)^2 + 2r\,\psi''(r)\right\} + 2r\left\{2\widetilde{\Lambda} + f''(r)\right\}\right]. \tag{9.5.6c}$$

In much the same way as in section 9.2, by taking a derivative of equation (9.5.6b) and combining certain multiples of all three equations (9.5.6), we can show that one equation is a consequence of the other two. In this case, we have that

$$\frac{r\left\{f'(r) + f(r)\psi'(r)\right\}}{4f(r)}\left[\widetilde{T}_\tau{}^\tau - \widetilde{T}_\rho{}^\rho\right] + \widetilde{T}_\theta{}^\theta - \widetilde{T}_\rho{}^\rho - \frac{1}{2}r(\widetilde{T}_\rho{}^\rho)' = 0. \tag{9.5.7}$$

By construction, conservation of the QFT-RSET will hold independent of coordinate choice, due to the contracted Bianchi identity. Taking the covariant derivative, we find the only nonzero component of the divergence of the QFT-RSET is given by

$$\nabla_\mu\widetilde{T}_\rho{}^\mu = \frac{f'(r) + f(r)\psi'(r)}{2}\left[\widetilde{T}_\rho{}^\rho - \widetilde{T}_\tau{}^\tau\right] - \frac{2f(r)}{r}\left[\widetilde{T}_\theta{}^\theta - \widetilde{T}_\rho{}^\rho - \frac{1}{2}r(\widetilde{T}_\rho{}^\rho)'\right], \tag{9.5.8}$$

from which it is clear to see that this is simply equation (9.5.7) multiplied by an overall factor of $-2f(r)/r$.

The solitonic QCEE (9.5.6) can be simplified. By substituting equation (9.5.6a) into equation (9.5.6b), we find the following relation

$$\widetilde{T}_{\rho}{}^{\rho} - \widetilde{T}_{\tau}{}^{\tau} = \frac{f(r)\psi'(r)}{r}, \tag{9.5.9}$$

from which we have the following ODE for $\psi(r)$:

$$\frac{\mathrm{d}\psi}{\mathrm{d}r} = \frac{r}{f(r)}\left[\widetilde{T}_{\rho}{}^{\rho} - \widetilde{T}_{\tau}{}^{\tau}\right]. \tag{9.5.10}$$

Recall the explicit form for the function $f(r)$ (9.5.1b). By invoking this, equation (9.5.6a) simplifies to following ODE for $m(r)$:

$$\frac{\mathrm{d}m}{\mathrm{d}r} = -\frac{r^2}{2}\widetilde{T}_{\tau}{}^{\tau}, \tag{9.5.11}$$

which depends on the (new) radial coordinate $r$ (9.5.2) and the energy density $-\widetilde{T}_{\tau}{}^{\tau}$ of the quantum field.

Equations (9.5.10) and (9.5.11) are our governing equations that will be used to solve the solitonic QCEE, which is detailed in the next section.

### 9.5.2 Solving the solitonic QCEE

Since we do not have the explicit functional form of the QFT-RSET (9.3.1) components in terms of the new radial coordinate $r$, we transform the unknown metric functions $m(r), f(r)$ and $\psi(r)$ into functions of $\rho$ and integrate the QCEE (9.5.10) and (9.5.11) directly. Since the ODE for $\psi(r)$ includes contributions from $f(r)$ (and hence $m(r)$), we will focus our attention on solving equation (9.5.11) first. Recall the coordinate transformation rule (9.5.2). We can compute the derivative as

$$\frac{\mathrm{d}r}{\mathrm{d}\rho} = \frac{C'(\rho)}{\sqrt{C(\rho)}}, \tag{9.5.12}$$

so that, by using the chain rule, we can express the ODE for $m(r)$ (9.5.11) as

$$\frac{\mathrm{d}m}{\mathrm{d}\rho} = \frac{\mathrm{d}m}{\mathrm{d}r}\frac{\mathrm{d}r}{\mathrm{d}\rho} = -\frac{1}{4}C'(\rho)\sqrt{C(\rho)}\widetilde{T}_{\tau}{}^{\tau}(\rho), \tag{9.5.13}$$

where all the quantities on the right-hand-side are now functions of the original radial coordinate $\rho$. In a similar fashion, we can write the ODE (9.5.10) for $\psi(r)$ in terms of the original radial coordinate:

$$\frac{\mathrm{d}\psi}{\mathrm{d}\rho} = \frac{\mathrm{d}\psi}{\mathrm{d}r}\frac{\mathrm{d}r}{\mathrm{d}\rho} = \frac{2B(\rho)C(\rho)}{C'(\rho)}\left[\widetilde{T}_{\rho}{}^{\rho}(\rho) - \widetilde{T}_{\tau}{}^{\tau}(\rho)\right]. \tag{9.5.14}$$

We take equations (9.5.13) and (9.5.14), and integrate using `Mathematica`'s inbuilt command `NDSolveValue`. This gives the metric functions $m$ and $\psi$ as functions of $\rho$; we then transform these to functions of $r$ using the relationship (9.5.2) and the metric function $C(\rho)$, computed in section 9.4.

Prior to solving the QCEE (9.5.13) and (9.5.14), below we show plots of the derivatives $\frac{\mathrm{d}m}{\mathrm{d}r}$, $\frac{\mathrm{d}m}{\mathrm{d}\rho}$, $\frac{\mathrm{d}\psi}{\mathrm{d}r}$ and $\frac{\mathrm{d}\psi}{\mathrm{d}\rho}$. In particular, figure 9.12 shows the derivative of $m$ with respect to the original radial coordinate $\rho$. For all values of the temperature considered, and for all three boundary conditions, the derivative is zero at the origin. In contrast, the behaviour as the boundary $\rho \to \pi/2$ is approached is strongly dependent on the boundary conditions. For Dirichlet boundary conditions (top row of figure 9.12), the derivative increases away from the origin, attains its maximum at a value of $\rho$ close to the boundary before monotonically decreasing towards the boundary. In addition, the location of the maximum lies closer to the boundary as temperature increases. Conversely, for both Neumann (middle row of figure 9.12) and transparent (bottom row of figure 9.12) boundary conditions, it appears to be the case that the derivative monotonically increases away from the origin to a finite nonzero value on the boundary, which increases with increasing temperature.

In contrast, in figure 9.13, the derivative of $m$ with respect to the new radial coordinate $r$ is shown. Unlike for the derivative with respect to $\rho$, the derivative $\frac{\mathrm{d}m}{\mathrm{d}r}$ does not appear to show any strong dependence on the choice of boundary conditions applied to the field.

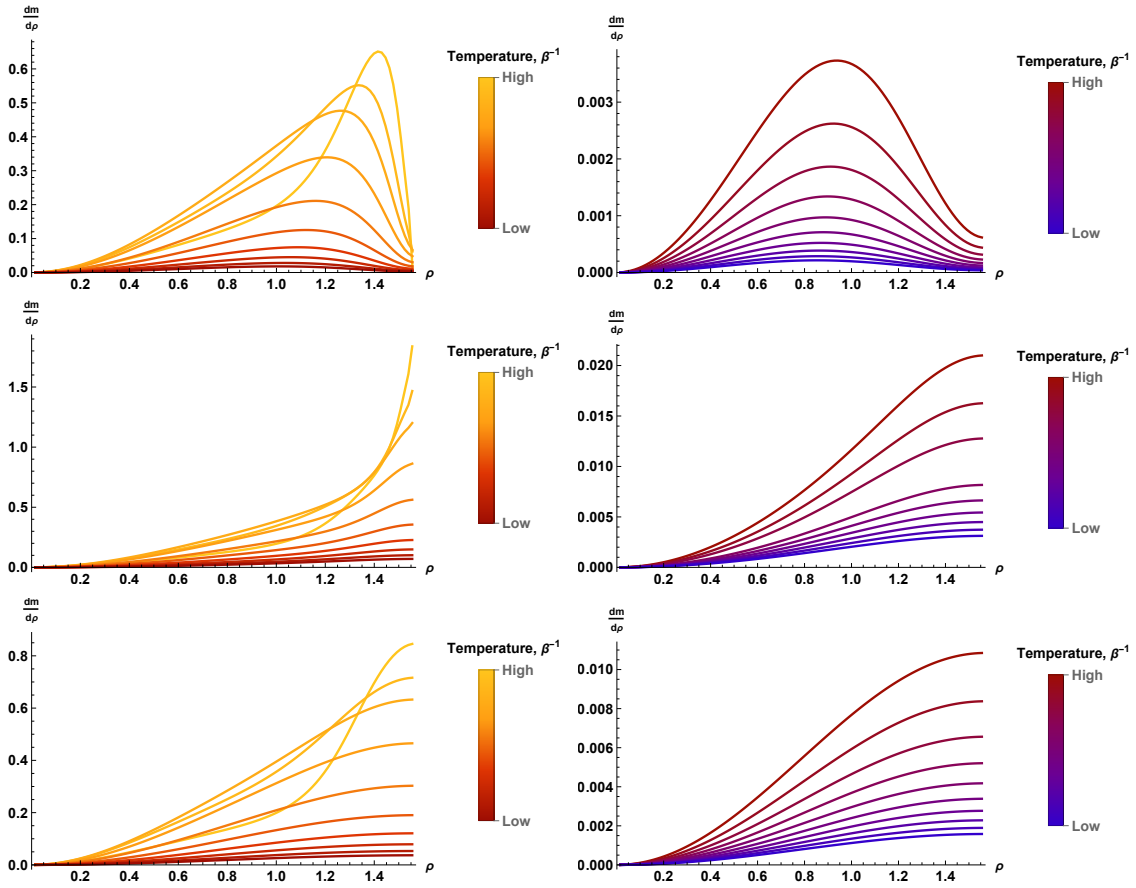


Figure 9.12: The derivative $\frac{\mathrm{d}m}{\mathrm{d}\rho}$ for Dirichlet (top row), Neumann (middle row) or transparent (bottom row) boundary conditions. The inverse temperature lies in the range $\beta \in [\pi/12, 11\pi/24] \cup [5\pi/8, \pi]$ for the left and right columns respectively. The unrenormalised adS length scale is $a = 1$.

Indeed, the overall profiles are indistinguishable by eye; the only notable difference is the scale on the vertical axes, which for high temperature ranges is largest for transparent boundary conditions, and for low temperature ranges it is largest for the case of Neumann boundary conditions. In all cases, the derivative is zero at the origin and tends towards zero at the boundary, attaining its maximum value very close to the origin. For sufficiently high temperatures, the location of the maximum shifts closer to the origin. Otherwise, the temperature dependence is exactly as expected; the higher the temperature, the greater the size of the derivative.

Figure 9.14 shows the derivative of $\psi$ with respect to the original radial coordinate $\rho$. Unlike the derivative of $m$ with respect to $\rho$, the derivative $\frac{\mathrm{d}\psi}{\mathrm{d}\rho}$ does not show any strong dependence on the boundary conditions. By eye, the plots for the differing boundary conditions look almost identical, with the biggest difference occurring in the scale on the vertical axes. For the lower temperature plots (right column), the derivative is largest when Neumann boundary conditions are applied to the field. For all boundary conditions and temperatures considered, the derivative is zero at both the origin and on the boundary at $\rho = \pi/2$, and attains its maximum between these. For sufficiently high temperatures, the location of the maximum begins to shift towards the boundary.

In figure 9.15, the derivative of $\psi$ with respect to the new radial coordinate $r$ is shown. As is expected, the derivative is zero at both the origin and on the boundary $r \to \infty$. In all cases, the derivative rapidly increases away from the origin to its maximum, which occurs close to the origin, before decreasing at a marginally slower rate to zero as the boundary is approached. Aside from sufficiently high temperatures, where the location of the maximum shifts closer to the origin, the derivative shows a simple dependence on the temperature; as the temperature is increased, so does the size of the derivative. The differences between the derivatives when the boundary conditions are altered are negligible at this scale, with the only visible change occurring in the scale of the vertical axes at lower temperatures.

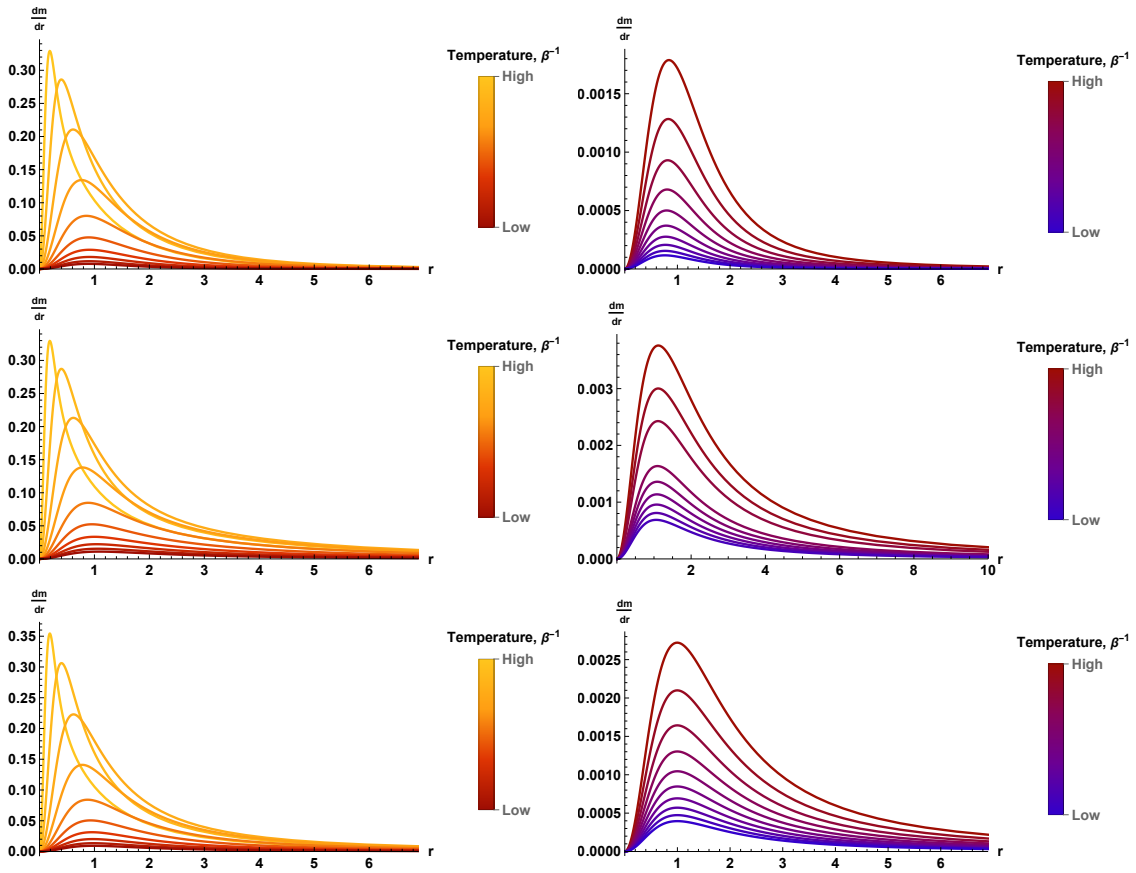


Figure 9.13: The derivative $\frac{\mathrm{d}m}{\mathrm{d}r}$ for Dirichlet (top row), Neumann (middle row) or transparent (bottom row) boundary conditions. The inverse temperature lies in the range $\beta \in [\pi/12, 11\pi/24] \cup [5\pi/8, \pi]$ for the left and right columns respectively. The unrenormalised adS length scale is $a = 1$.

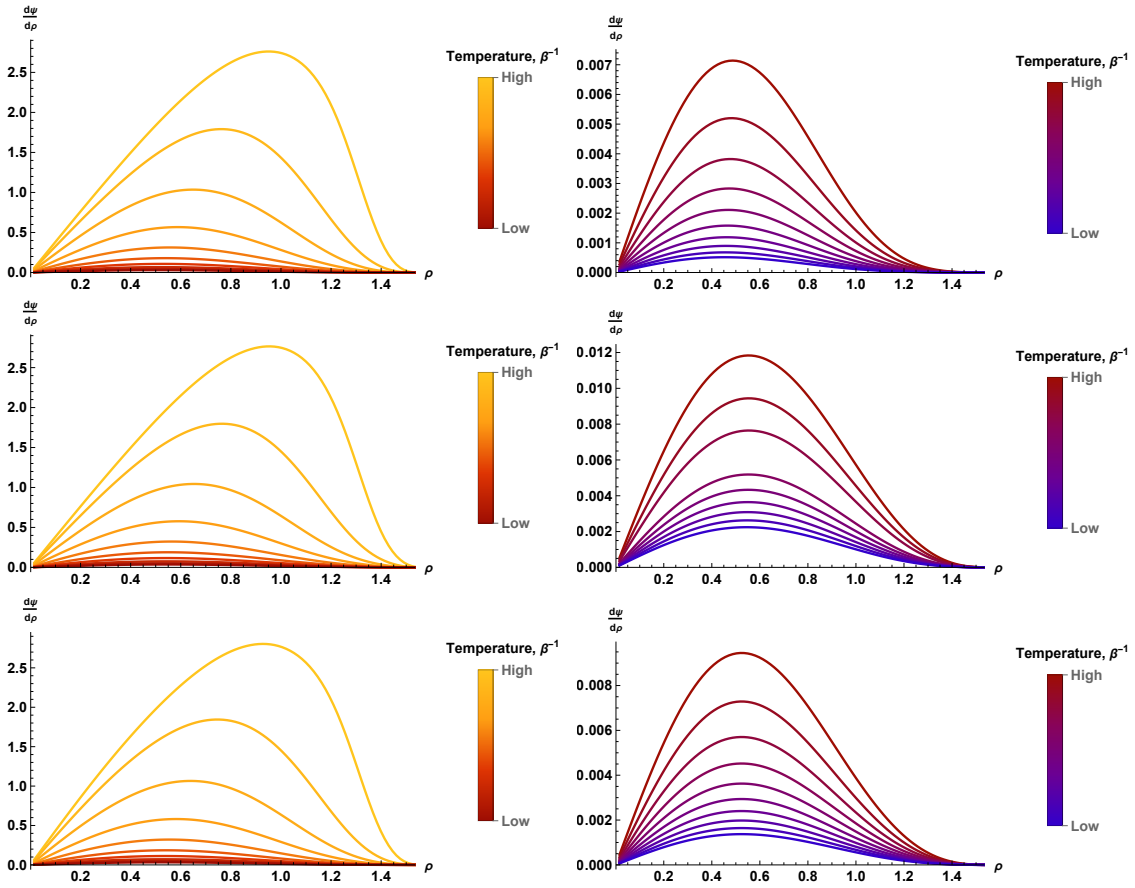


Figure 9.14: The derivative $\frac{\mathrm{d}\psi}{\mathrm{d}\rho}$ for Dirichlet (top row), Neumann (middle row) or transparent (bottom row) boundary conditions. The inverse temperature lies in the range $\beta \in [\pi/12, 11\pi/24] \cup [5\pi/8, \pi]$ for the left and right columns respectively. The unrenormalised adS length scale is $a = 1$.

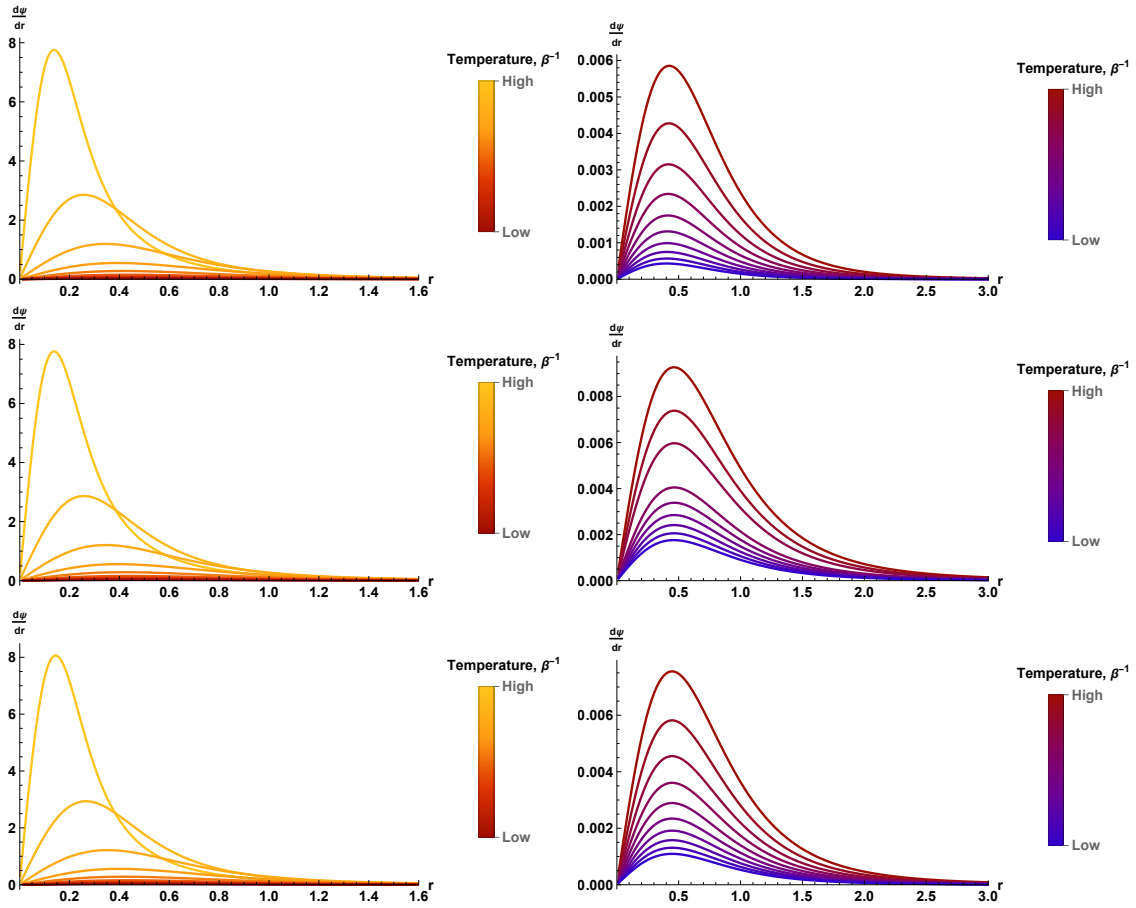


Figure 9.15: The derivative $\frac{\mathrm{d}\psi}{\mathrm{d}r}$ for Dirichlet (top row), Neumann (middle row) or transparent (bottom row) boundary conditions. The inverse temperature lies in the range $\beta \in [\pi/12, 11\pi/24] \cup [5\pi/8, \pi]$ for the left and right columns respectively. The unrenormalised adS length scale is $a = 1$.

Finally, in figure 9.16, all four derivatives are shown for a single fixed inverse temperature $\beta = \pi/4$ whilst the boundary conditions are varied. For the derivatives of $\psi$, the difference in boundary conditions is virtually indistinguishable by eye; $\psi$ clearly does not depend strongly on the choice of boundary conditions. Conversely, we see a significant difference between the boundary conditions for the derivatives of $m$, in particular $\frac{\mathrm{d}m}{\mathrm{d}\rho}$. In the approximate interval $\rho \in [0, 0.8]$, the curves corresponding to the three boundary conditions are almost identical, but as the boundary is approached, they display different behaviours. The curves corresponding to Neumann and transparent boundary conditions continue to increase, with the rate of increase much greater in the case of Neumann boundary conditions. In contrast, the curve representing Dirichlet boundary conditions hits its global maximum around $\rho \approx 1.2$ before decreasing to a value close to zero at the boundary. For the derivative of $m$ with respect to $r$, the three curves share a similar profile, being rather similar close to the origin, before spreading out as $r$ is increased, before marginally coming together as the boundary $r \to \infty$ is approached. For all four derivatives, the value of the derivative is greatest when Neumann boundary conditions are applied; Dirichlet boundary conditions produce the smallest derivative; and transparent boundary conditions lie somewhere between the two. This is more apparent for the derivatives of $m$, but is certainly also the case for the derivatives of $\psi$.

Before we integrate the QCEE (9.5.13) and (9.5.14), it is important to verify that the functions $m$ and $\psi$ will converge to a finite limit at the boundary $r \to \infty$. We start by expanding the QFT-RSET (9.3.1) in a series expansion about $\rho = \pi/2$. The (mixed) $\tau\tau$-component is

$$\widetilde{T}_\tau{}^\tau \sim -\mathcal{T}_\infty^\lambda \left(\frac{\pi}{2} - \rho\right)^4 + \mathcal{O}\left(\frac{\pi}{2} - \rho\right)^6, \tag{9.5.15}$$

as $\rho \to \pi/2$, where

$$\mathcal{T}_\infty^\lambda = \frac{a^2}{2\pi^2} \sum_{n=1}^{\infty} \left[n^3 - \frac{\lambda}{9} n \left(1 + 8n^2\right)\right] \left(e^{na\beta} - 1\right)^{-1}, \tag{9.5.16}$$

and $\lambda$ still controls the boundary conditions (4.6.20). For the mixed indices $\rho\rho$-component

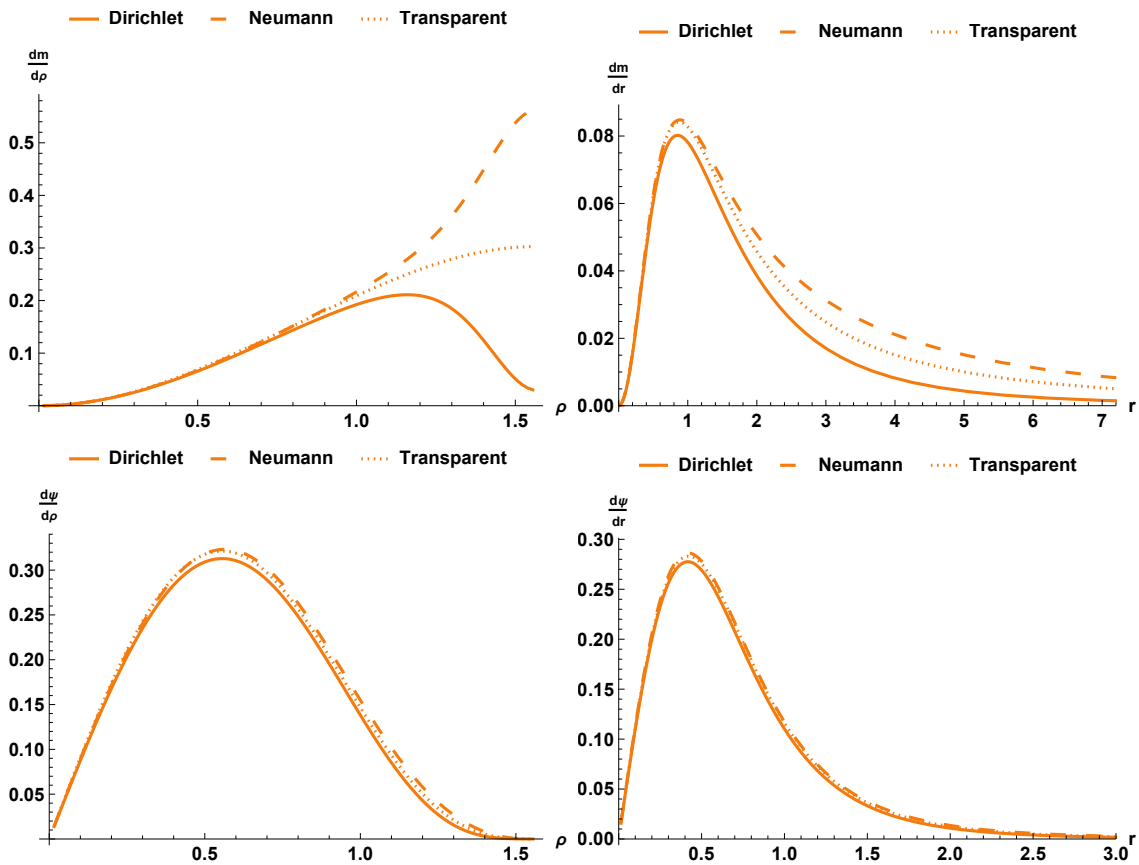


Figure 9.16: All four derivatives $\frac{\mathrm{d}m}{\mathrm{d}\rho}$ (top left), $\frac{\mathrm{d}m}{\mathrm{d}r}$ (top right), $\frac{\mathrm{d}\psi}{\mathrm{d}\rho}$ (bottom left) and $\frac{\mathrm{d}\psi}{\mathrm{d}r}$ (bottom right). Dirichlet boundary conditions are represented by a solid line, Neumann boundary conditions by a dashed line and transparent boundary conditions by a dotted line. The inverse temperature is fixed at $\beta = \pi/4$ and the original inverse adS length scale is $a = 1$.

of the QFT-RSET, expanding into a power series about $\rho = \pi/2$, we have

$$\widetilde{T}_\rho{}^\rho \sim \mathfrak{T}_\infty^\lambda \left(\frac{\pi}{2} - \rho\right)^4 + \mathcal{O}\left(\frac{\pi}{2} - \rho\right)^6, \tag{9.5.17}$$

as $\rho \to \pi/2$, where

$$\mathfrak{T}_\infty^\lambda = \frac{a^2}{6\pi^2} \sum_{n=1}^{\infty} \left[n^3 - \lambda n\right] \left(e^{na\beta} - 1\right)^{-1}. \tag{9.5.18}$$

Finally, for the mixed $\theta\theta$-component, we have

$$\widetilde{T}_\theta{}^\theta \sim \mathfrak{T}_\infty^\lambda \left(\frac{\pi}{2} - \rho\right)^4 + \mathcal{O}\left(\frac{\pi}{2} - \rho\right)^6, \tag{9.5.19}$$

as $\rho \to \pi/2$, where

$$\mathfrak{T}_\infty^\lambda = \frac{a^2}{18\pi^2} \sum_{n=1}^{\infty} \left[3n^3 + \lambda n \left(1 - 4n^2\right)\right] \left(e^{na\beta} - 1\right)^{-1}. \tag{9.5.20}$$

Now that we have the behaviour of the QFT-RSET components at the boundary, we need to ascertain the behaviour of the radial coordinate $r$ at the boundary, by invoking the coordinate transformation rule (9.5.2). We start by recalling the behaviour of the metric function $C(\rho)$ near the boundary from section 9.4. We observe that, in all cases, $C(\rho)/\tan^2(\rho)$ tends to some finite nonzero limit (which we shall denote by $\mathcal{C}_\infty^\lambda(\beta)$) that depends on the boundary conditions and temperature. Since, as $\rho \to \pi/2$, it is the case that $\tan^2(\rho) \sim \mathcal{O}\left(\frac{\pi}{2} - \rho\right)^{-2}$, for $C(\rho)/\tan^2(\rho)$ to attain a finite nonzero limit as $\rho \to \pi/2$ it must be the case that

$$C(\rho) \sim \mathcal{C}_\infty^\lambda(\beta) \left(\frac{\pi}{2} - \rho\right)^{-2} + \mathcal{O}\left(\frac{\pi}{2} - \rho\right)^0. \tag{9.5.21}$$

Due to the coordinate transformation rule (9.5.2), we therefore have that

$$r^2 \sim \mathcal{O}\left(\frac{\pi}{2} - \rho\right)^{-2}, \tag{9.5.22}$$

as $\rho \to \pi/2$. We now substitute the series expansions (9.5.15) and (9.5.21) into the QCEE (9.5.11), yielding

$$\frac{\mathrm{d}m}{\mathrm{d}r} \sim \frac{1}{2}\mathcal{C}_\infty^\lambda(\beta)\mathcal{T}_\infty^\lambda \left(\frac{\pi}{2} - \rho\right)^2 \sim \mathcal{O}(r^{-2}), \tag{9.5.23}$$

as $\rho \to \pi/2$, which is identical to $r \to \infty$. Therefore, the function $m(r)$ will converge to a nonzero finite limit $M = \lim_{r\to\infty} m(r)$ as the boundary is approached. We interpret this limit as the mass of the soliton, which we discuss in section 9.5.3.

We can perform a similar analysis on the derivative $\frac{\mathrm{d}\psi}{\mathrm{d}r}$. From the expansions (9.5.15) and (9.5.17), it is clear that the difference present in the QCEE (9.5.10) is $\widetilde{T}_\tau{}^\tau - \widetilde{T}_\rho{}^\rho \sim \left(\frac{\pi}{2} - \rho\right)^4 \sim \mathcal{O}(r^{-4})$. In a similar fashion, recall the definition of the function $f(r)$ (9.5.1b). It is straightforward to show that, since $\frac{\mathrm{d}m}{\mathrm{d}r} \sim \mathcal{O}(r^{-2})$ then $m(r) \sim M + \mathcal{O}(r^{-1}) \sim \mathcal{O}(1)$ and hence, the function $f(r)$ as $r \to \infty$ behaves as

$$f(r) \sim \mathcal{O}(r^0) - 2\mathcal{O}(1)\mathcal{O}(r^{-1}) + \mathcal{O}(r^2) \sim \mathcal{O}(r^2). \tag{9.5.24}$$

We combine these in the QCEE (9.5.10) to yield

$$\frac{\mathrm{d}\psi}{\mathrm{d}r} \sim \frac{\mathcal{O}(r)}{\mathcal{O}(r^2)}\mathcal{O}(r^{-4}) \sim \mathcal{O}(r^{-5}), \tag{9.5.25}$$

from which it is clear to see that $\psi(r)$ converges to a finite, nonzero limit as the boundary is approached, $r \to \infty$. Additionally, $\psi$ converges at the boundary much more rapidly than $m$.

We now understand the behaviour of the metric functions $m$ and $\psi$ at the boundary, but to apply `Mathematica`'s `NDSolveValue` command, we require initial conditions in the form of values of the metric functions at the origin, such as in section 9.3.2. To find the initial conditions, we expand both equations (9.5.13) and (9.5.14) in a series expansion about the origin, using the corresponding series expansions (9.3.6) and (9.3.7) for the QFT-RSET components and metric functions $B(\rho), C(\rho)$ respectively, before performing a term-by-term integration in $\rho$. For the function $m$, we have

$$m = m_3\rho^3 + m_5\rho^5 + \mathcal{O}(\rho^7), \tag{9.5.26}$$

where the $m_i$ are constants, with the first two nonzero coefficients taking the values

$$m_3 = -\frac{1}{6}C_2^{3/2}T_{\tau|0} \quad \text{and} \quad m_5 = -\frac{1}{20}C_2^{1/2}\left[5C_4T_{\tau|0} + 2C_2T_{\tau|2}\right]. \tag{9.5.27}$$

In a similar fashion, we can construct the series expansion for $\psi$ as

$$\psi = \psi_2\rho^2 + \psi_4\rho^4 + \mathcal{O}(\rho^6), \tag{9.5.28}$$

where the first two nonzero terms are

$$\psi_2 = -\frac{2}{3}C_2T_{\tau|0} \quad \text{and} \quad \psi_4 = \frac{1}{12}\left[4T_{\tau|0}\left\{C_4 - B_2\right\} - 3C_2\left\{T_{\tau|2} - T_{\rho|2}\right\}\right]. \tag{9.5.29}$$

Note that, for both functions, the leading order term in the power series is either $\rho^2$ or $\rho^3$, meaning that, at the origin, both functions will be zero. This can be justified *a posteriori*. For the function $\psi$, since we have a static metric, changing the value at the origin $\psi(0)$ corresponds to a rescaling of the time coordinate $\tau$, and so, without loss of generality we are free to fix $\psi(0) = 0$. In order to have a regular origin, it must be the case that $m(0) = 0$, otherwise there would be a curvature singularity at $r = 0$. These fix the constants of integration arising in the integration of the QCEE (9.5.13) and (9.5.14).

We integrate the QCEE (9.5.13) and (9.5.14) between $\rho = \epsilon$ and $\rho = \pi/2-\epsilon$ for all values of the inverse temperature considered. We take $\epsilon = 10^{-3}$, however we verify that changing the value of $\epsilon$ results in a small relative error in our results. For more details, see appendix A. In terms of the new radial coordinate $r$, the integration limits are $r = \sqrt{C_2}\epsilon$ (corresponding to $\rho = \epsilon$) and for the upper limit, $r = \sqrt{C(\pi/2 - \epsilon)}$. As can be seen from, for example, figures 9.3, 9.4 and 9.9 the value of $C(\rho)/\tan^2(\rho)$ at the boundary $\rho = \pi/2$ decreases with increasing temperature. Therefore, the upper limit in our numerical integration, $r = \sqrt{C(\pi/2 - \epsilon)}$, will also decrease with increasing temperature and hence, the largest value of $r$ in the numerical evaluation of the metric functions $m(r)$ and $\psi(r)$ will decrease with increasing temperature.

### 9.5.3 Quantum-corrected adS soliton masses

In this section, we discuss the solutions of the QCEE (9.5.13) and (9.5.14) as well as the nonzero, finite limit $M = \lim_{r\to\infty} m(r)$, which we interpret as the mass of the solitons

sourced by the QFT-RSET (9.3.1). Whilst our main focus in this section is the soliton masses, we first present results for the metric function $\psi(r)$.

Figure 9.17 shows the quantum-corrected metric function $\psi(r)$. In the top row, Dirichlet boundary conditions are applied to the field; in the middle row we apply Neumann boundary conditions; and in the bottom row, transparent boundary conditions are applied. It is clear that $\psi$ is greatest when transparent boundary conditions are applied to the field, being approximately seven times larger than the corresponding functions when Dirichlet and Neumann boundary conditions are applied at sufficiently high temperatures (left column). However, the profile of $\psi(r)$ shows very little dependence on the boundary conditions. For all values of the temperature studied, $\psi(r)$ is zero at the origin and takes a finite, nonzero limit at the boundary, which increases with increasing temperature. The function very rapidly increases away from the origin, and converges to its limit quickly, which is shown by the 'flattening' effect present in figure 9.17. The rapid convergence of $\psi$ is predicted by the behaviour of the derivative $\frac{\mathrm{d}\psi}{\mathrm{d}r}$ at the boundary, given in equation (9.5.25). Finally, we have that $\psi(r) \geq 0 \; \forall r$. This is a direct consequence of the renormalised stress-energy tensor (9.3.1) satisfying the null energy condition (NEC). To see this, consider the following.

Let us suppose we have a null vector given by $k^\mu = (1, 1, 0, 0)$. Contracting this with the stress-energy tensor (9.3.1) yields

$$\widetilde{T}_\mu{}^\nu k^\mu k_\nu = a^{-2} \sec^2(\rho) \left[ \widetilde{T}_\rho{}^\rho - \widetilde{T}_\tau{}^\tau \right]. \tag{9.5.30}$$

The (NEC) will hold provided the contraction (9.5.30) is positive. Clearly, for $\rho \in [0, \pi/2)$, $\sec^2(\rho) > 0$. Thus the (NEC) will hold provided

$$\widetilde{T}_\rho{}^\rho - \widetilde{T}_\tau{}^\tau = \widetilde{T}_\rho{}^\rho + (-\widetilde{T}_\tau{}^\tau) > 0, \tag{9.5.31}$$

which holds since both $\widetilde{T}_\rho{}^\rho$ and $-\widetilde{T}_\tau{}^\tau$ are positive for $\rho \in [0, \pi/2)$ - see section 5.1.1, in particular see figures 5.1-5.3. Now consider the differential equation (9.5.10) for the derivative of $\psi$ with respect to $r$. The right-hand-side includes a prefactor of $r/f(r)$; the

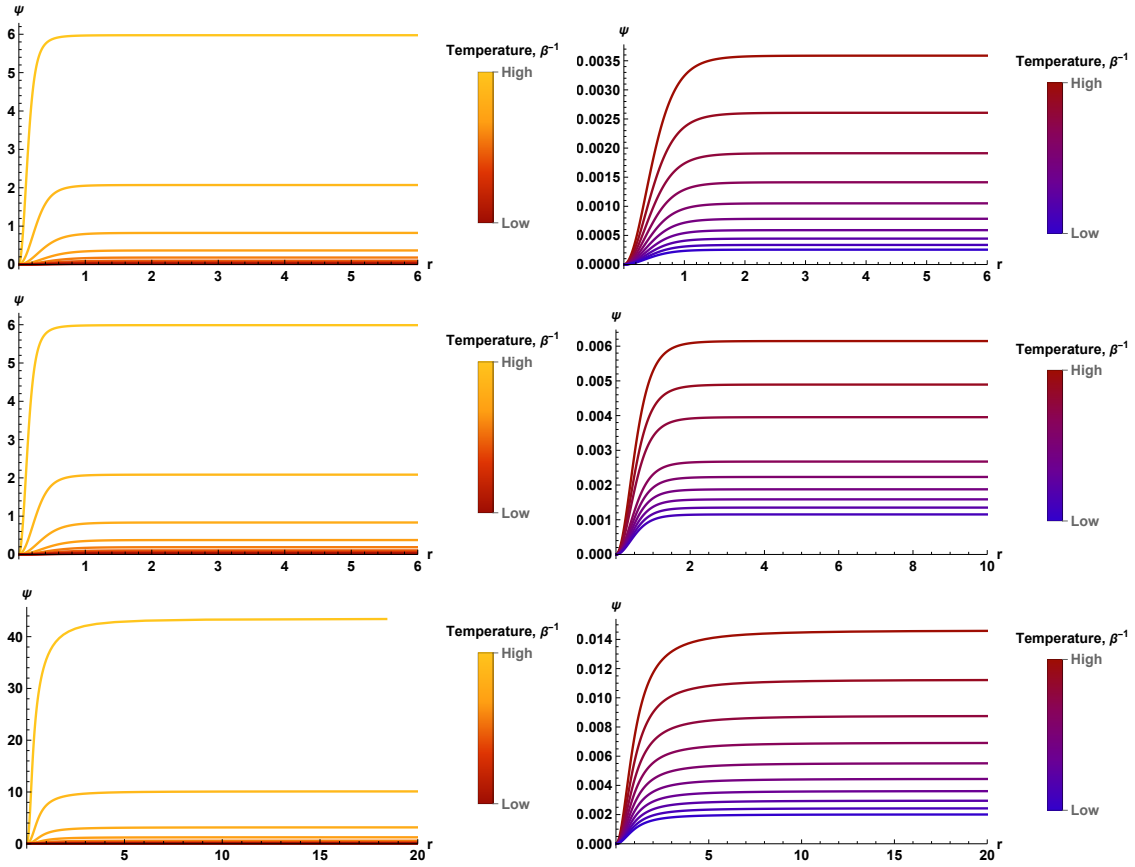


Figure 9.17: The quantum-corrected metric function $\psi(r)$ as a function of the new radial coordinate $r$. The quantum scalar field satisfies either Dirichlet (top row), Neumann (middle row) or transparent (bottom row) boundary conditions. The inverse temperature is in the range $\beta \in [\pi/12, 11\pi/24] \cup [5\pi/8, \pi]$ for the left and right columns respectively. The original inverse adS length scale is fixed $a = 1$.

coordinate $r$ (9.5.2) is always nonnegative for all $\rho \in [0, \pi/2) \iff r \in [0, 1)$, and by virtue of the relation (9.5.5a), the function $f(r)$ is also positive for all $\rho \in [0, \pi/2) \iff r \in [0, 1)$. Therefore, the sign of the derivative (9.5.10) is determined by the sign of the difference (9.5.31), which is always positive on account of the (NEC) holding. Therefore, the derivative of $\psi$ with respect to $r$ is always positive, meaning the function $\psi(r)$ is an increasing function. Since we constructed the function $\psi$ such that it is zero at the origin (see equation (9.5.28)), then it must be positive for all $r \in [0, 1)$.

To fully understand how changing the boundary conditions affects $\psi(r)$, in figure 9.18 we show ratios of the metric function $\psi$ for different boundary conditions. In the top row, the ratio between Neumann and Dirichlet boundary conditions is shown. We see that, for the highest temperatures, the ratio is approximately unity; whereas at the lowest temperatures, the ratio is over four. This indicates that, at high temperatures, the temperature dependence is stronger than the boundary condition dependence, and as the temperature is decreased, the boundary conditions play a greater role in the metric function $\psi(r)$. For all temperatures, the ratio is always greater than unity, meaning Neumann boundary conditions produce larger quantum corrections to $\psi(r)$. We see a different picture when we consider transparent boundary conditions (middle and bottom rows of figure 9.18). Indeed, the best agreement between Neumann and transparent boundary conditions occurs at the lowest temperatures, when the ratio $\psi^{(\mathrm{T})}/\psi^{(\mathrm{N})}$ is closest to unity. For sufficiently small temperatures, the ratio dips below unity at the origin; otherwise the ratio is always greater than unity. When we consider the ratio between Dirichlet and transparent boundary conditions (middle row), we see that, at high temperatures (left column), the ratios $\psi^{(\mathrm{T})}/\psi^{(\mathrm{D})}$ and $\psi^{(\mathrm{T})}/\psi^{(\mathrm{N})}$ are virtually indistinguishable by eye. However, at lower temperatures (right column), we see markedly different behaviour in the ratio $\psi^{(\mathrm{T})}/\psi^{(\mathrm{D})}$ than in $\psi^{(\mathrm{T})}/\psi^{(\mathrm{N})}$. For the lowest temperatures considered, the ratio is higher than that of the highest temperature considered. As the temperature is increased from the lowest value studied, the ratio $\psi^{(\mathrm{T})}/\psi^{(\mathrm{D})}$ begins to decrease toward unity. This occurs until a certain

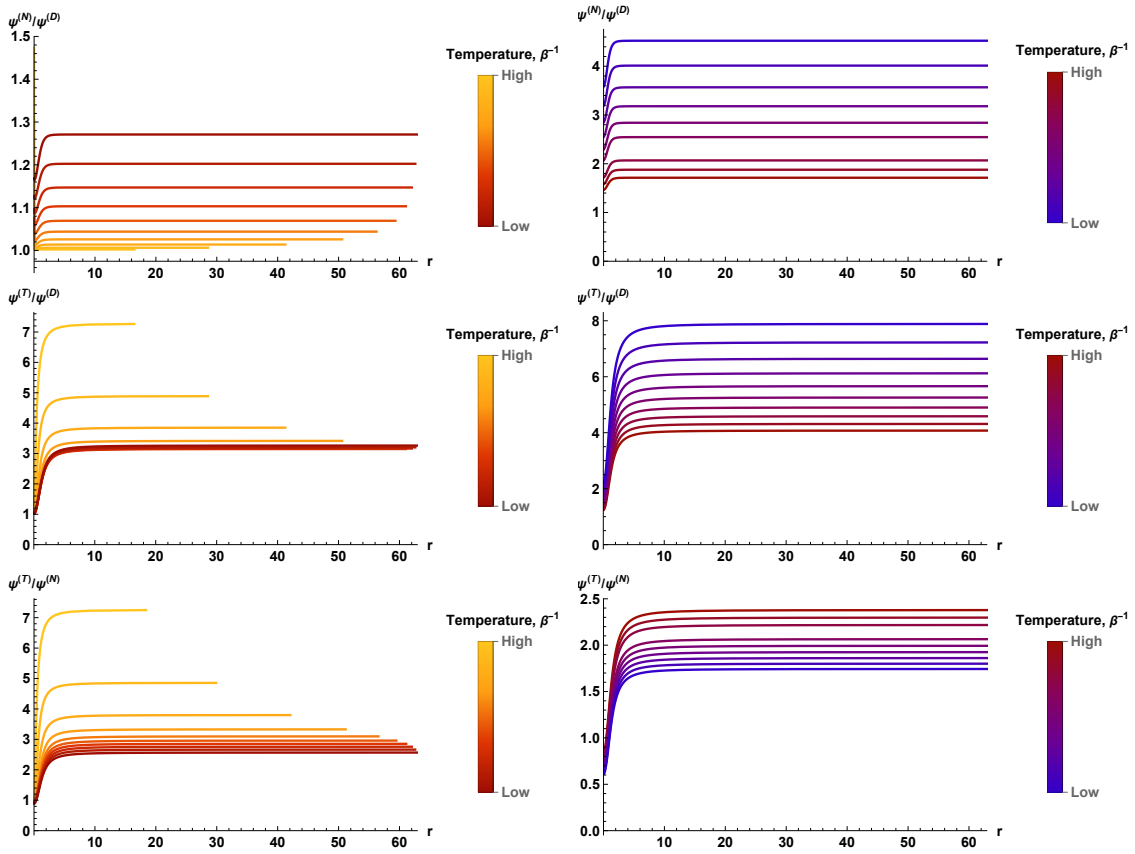


Figure 9.18: Ratios between the QC metric function $\psi(r)$ when the boundary conditions are altered. The original inverse adS length scale $a = 1$ is fixed, whilst the inverse temperature is varied in the range $\beta \in [\pi/12, 11\pi/24] \cup [5\pi/8, \pi]$ for the left and right columns respectively.

critical temperature is attained, at which point the ratio $\psi^{(\mathrm{T})}/\psi^{(\mathrm{D})}$ begins to increase away from unity again. This suggests that at both sufficiently low *and* high temperatures, the relative deviations between Dirichlet and transparent boundary conditions are significant, whereas for a small range of temperatures between the high and low cases, the difference between the boundary conditions is less significant than the temperature dependence of the quantum-corrected metric function $\psi(r)$.

We now consider the quantum-corrected mass function $m(r)$. Figure 9.19 shows the QC mass function for Dirichlet (top row), Neumann (middle row) and transparent (bottom row) boundary conditions. Like $\psi(r)$, for all values of the temperature studied, and for all boundary conditions, the mass function $m(r)$ is a monotonically increasing function. This follows from equation (9.5.11) and the fact that the energy density, $-\widetilde{T}_{\tau}{}^{\tau}$, is always positive. Additionally, the overall profile of all of the curves is similar to that of $\psi(r)$, i.e. they are zero at the origin, have a short period of rapid increase, before converging to a fixed value at the boundary. The rate of convergence for $m(r)$ is lower than the corresponding rate for $\psi(r)$, which is predicted by the behaviour of the derivative $\frac{\mathrm{d}m}{\mathrm{d}r}$ at the boundary (9.5.23). The rate of convergence to this limit is fastest when Dirichlet boundary conditions are applied, and slowest when Neumann boundary conditions are applied. By considering the vertical scales, one can see that the value at the boundary is greatest when considering Neumann boundary conditions, smallest when Dirichlet boundary conditions are applied, with transparent boundary conditions lying somewhere between the two. This is predicted by the behaviour of the energy density at the boundary (9.5.16), where we have that

$$0 < \mathcal{T}_{\infty}^{1} < \mathcal{T}_{\infty}^{0} < \mathcal{T}_{\infty}^{-1}, \tag{9.5.32}$$

from which it follows that the derivative $\frac{\mathrm{d}m}{\mathrm{d}r}$ - and therefore the soliton mass, since $m(r)$ is monotonically increasing - will be largest for Neumann boundary conditions, smallest for Dirichlet boundary conditions and transparent boundary conditions will lie between the two.

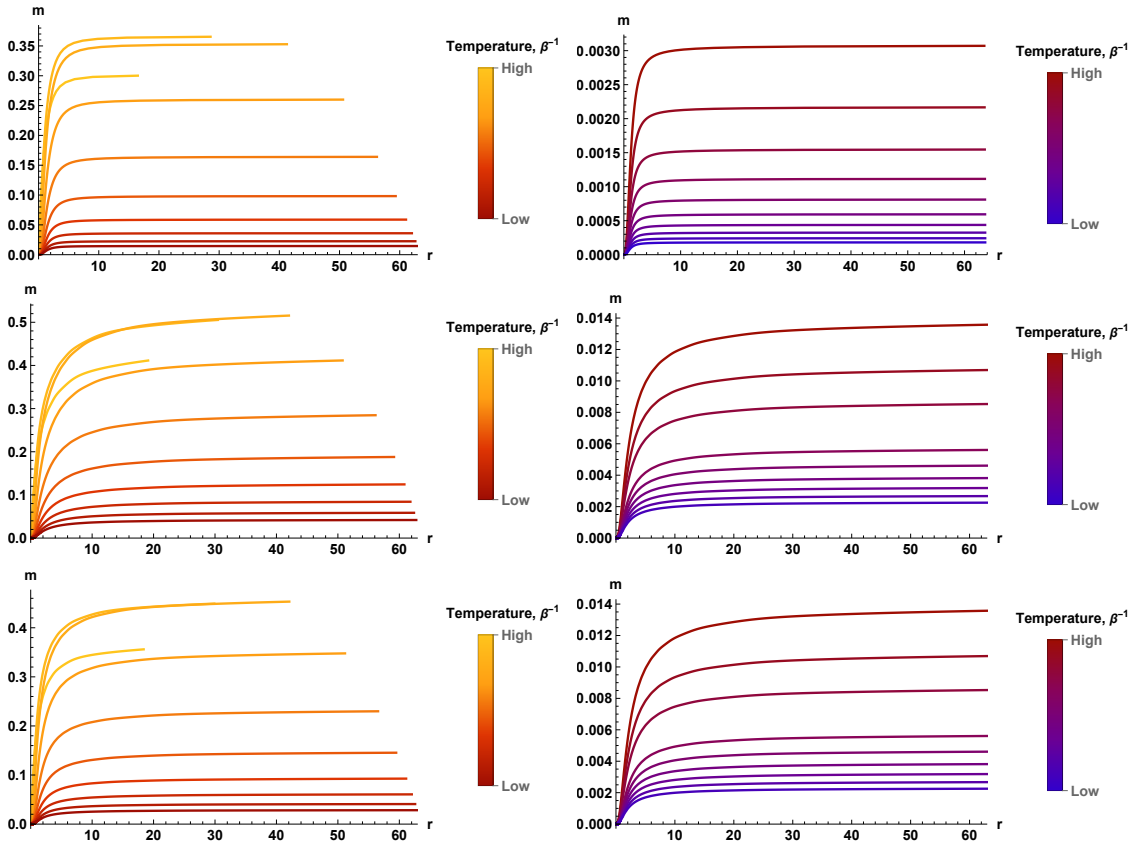


Figure 9.19: The quantum-corrected mass function $m(r)$ as a function of the new radial coordinate $r$. The quantum scalar field satisfies either Dirichlet (top row), Neumann (middle row) or transparent (bottom row) boundary conditions. The inverse temperature is in the range $\beta \in [\pi/12, 11\pi/24] \cup [5\pi/8, \pi]$ for the left and right columns respectively. The original inverse adS length scale is fixed $a = 1$.

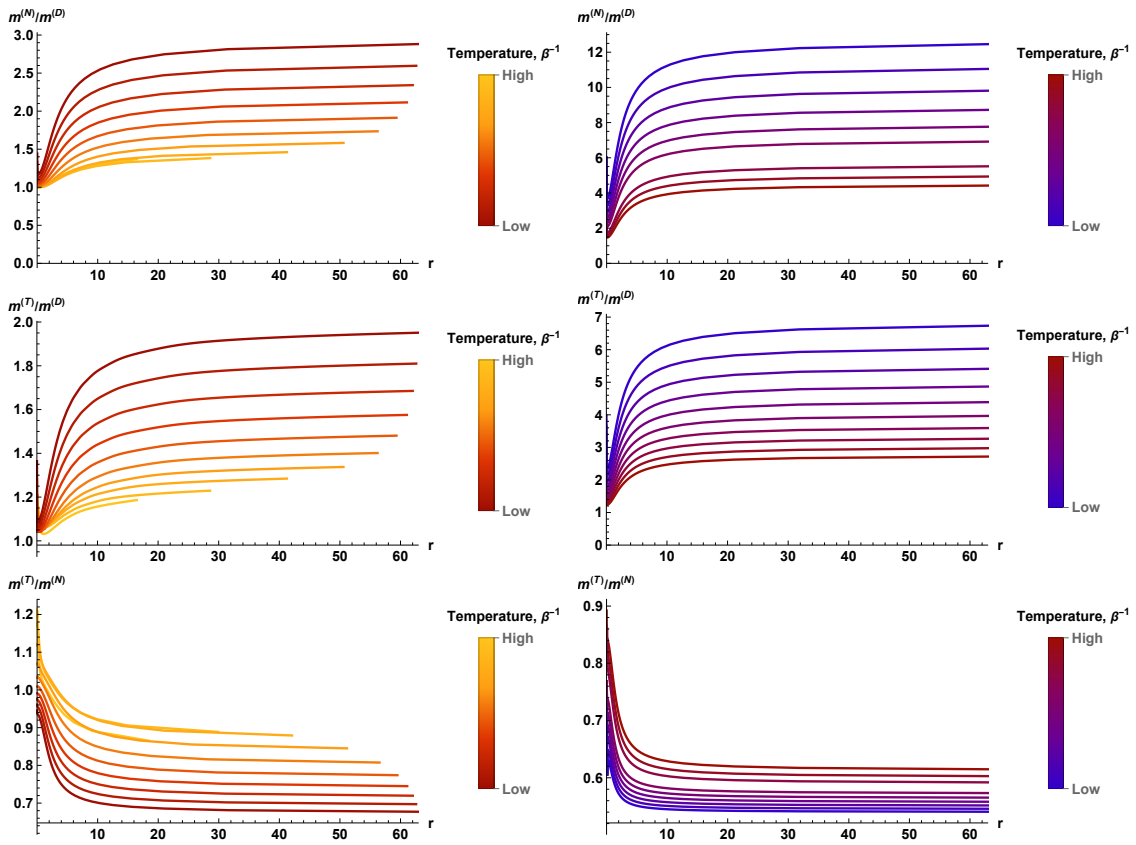


Figure 9.20: Ratios between the QC mass function $m(r)$ when the boundary conditions are altered. The original inverse adS length scale $a = 1$ is fixed, whilst the inverse temperature is varied in the range $\beta \in [\pi/12, 11\pi/24] \cup [5\pi/8, \pi]$ for the left and right columns respectively.

To further investigate the role of the boundary conditions in the mass function $m(r)$, in figure 9.20 we plot ratios of the mass functions when the boundary conditions are changed. This corroborates the fact that the quantum corrections to the mass function are largest when Neumann boundary conditions are applied, since the ratio $m^{(\mathrm{N})}/m^{(\mathrm{D})}$ is everywhere greater than unity, and the ratio $m^{(\mathrm{T})}/m^{(\mathrm{N})}$ is less than unity everywhere except close to the origin at sufficiently high temperatures. For each ratio considered, we find the closest agreement (i.e., when the ratio is closest to unity) occurs at higher temperatures, with the farthest agreement occurring at lower temperatures. This is unlike the case for $\psi(r)$ (see figure 9.18), where there was a complex interplay between the temperature and boundary condition dependence, causing there to be better agreement at both high *and* low temperatures. Rather, for $m(r)$, it appears to be the case that the temperature dependence is much stronger than the dependence on boundary conditions.

We finally turn our attention to the finite limit $M = \lim_{r\to\infty} m(r)$ of the mass function, which we interpret as the mass of the quantum-corrected solitons. In figure 9.21, we show the mass as a function of inverse temperature $\beta$ for Dirichlet (solid line), Neumann (dashed line) and transparent (dotted line) boundary conditions. As previously mentioned, the mass is greatest when Neumann boundary conditions are applied, whilst it is smallest when Dirichlet boundary conditions are applied. The mass for transparent boundary conditions lies between the Dirichlet and Neumann boundary condition masses. Since the horizontal scale is inverse temperature, temperature increasing is interpreted by considering the graph from right to left. As expected, at the lowest temperatures, the mass is very small. Although the axis only goes to $\beta \approx 1.5$, by increasing $\beta \to \infty$, it is verifiable that the mass tends towards zero, at a rapid rate. To see this, recall the definition of the derivative of the mass function (9.5.11), which depends on the energy density of the quantum field and a factor of $r^2$. We have shown (see section 5.1.1) that as we decrease the temperature (and thus increase $\beta$), the energy density of the quantum field tends towards its vacuum value; however, the energy density that appears in the derivative (9.5.11) is actually the difference

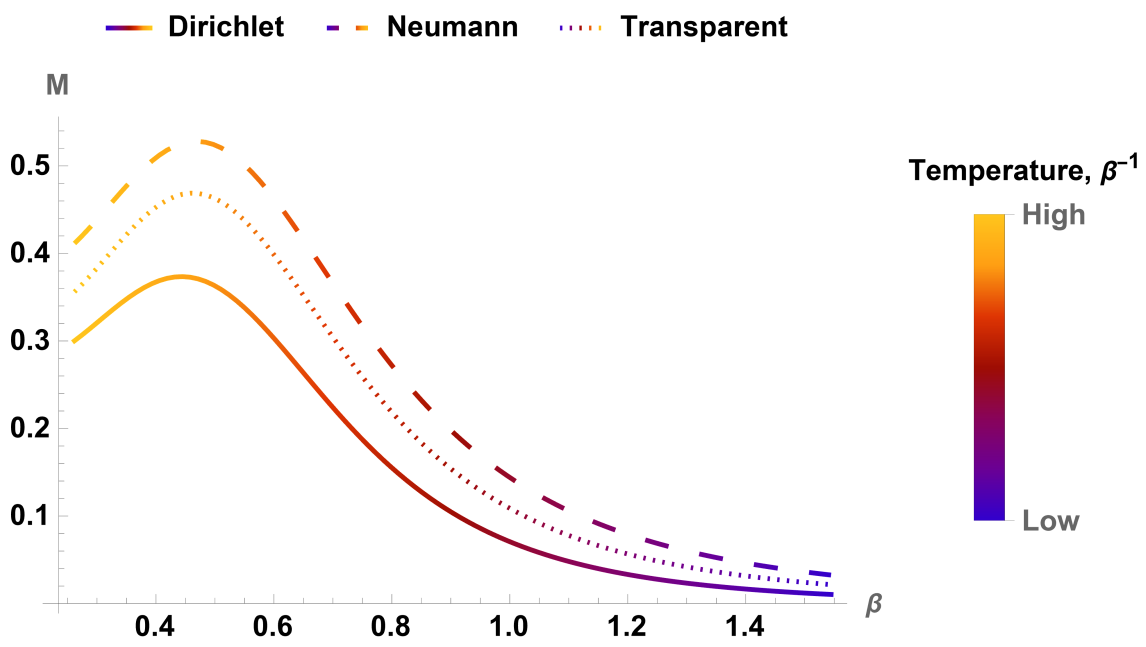


Figure 9.21: The quantum-corrected soliton mass $M = \lim_{r\to\infty} m(r)$ as a function of the inverse temperature $\beta$. The quantum scalar field satisfies either Dirichlet (solid line), Neumann (dashed line) or transparent (dotted line) boundary conditions. The inverse adS length scale is fixed to be $a = 1$.

between the thermal and vacuum energy densities, since we are considering the difference between thermal and vacuum expectation values of the renormalised stress-energy tensor. Therefore, the energy density will tend towards zero and, as the temperature is decreased, the derivative of the mass function will also tend towards zero:

$$\frac{\mathrm{d}m}{\mathrm{d}r} \overset{\beta\to\infty}{\longrightarrow} 0. \tag{9.5.33}$$

If the derivative of the mass function is zero, then the mass function must be constant. By construction, we chose the value of $m(0)$ to be zero to match pure anti-de Sitter space. It therefore follows that, in the limit $\beta \to \infty$, the mass function must be zero everywhere, and hence the mass must also be zero. This behaviour is entirely to be expected; the limit $\beta \to \infty$ corresponds to the zero temperature limit, and as was already shown in section 6.3, the quantum corrections to adS from the vacuum QFT-RSET amount to a simple renormalisation of the cosmological constant, and no changes to the structure of the metric (in any parametrisation). As we increase the temperature, the mass also increases. However, this trend does not continue for all temperatures. For all boundary conditions, at approximately $\beta \approx 0.5$, we find a maximum mass $M$. Once this is attained, increasing temperature further results in a *decrease* of the mass.

This is a somewhat unexpected result. When we consider the energy density in the quantum field, for all boundary conditions, it increases monotonically with increasing temperature. Additionally, by integrating the energy density with respect to the radial coordinate $\rho$, we find the total energy in the quantum field, which is a finite quantity that also monotonically increases with increasing temperature. One would therefore naïvely expect this to be proportional to the quantum-corrected soliton mass, and that the mass of the quantum-corrected soliton would monotonically increase with increasing temperature. However, this is at odds with the findings in figure 9.21. In an effort to understand this, recall the QCEE (9.5.11) for $m(r)$. The mass is the finite limit of the solution to the QCEE at the boundary. By writing the QCEE in terms of the original radial coordinate $\rho$ (given in

equation (9.5.13)), we can express the mass as the integral

$$M = -\frac{1}{4}\int_{\rho=0}^{\pi/2} C'(\rho)\sqrt{C(\rho)}\widetilde{T}_{\tau}{}^{\tau}\,\mathrm{d}\rho. \tag{9.5.34}$$

From this, it is clear that the behaviour of the mass is dictated not just by the behaviour of the energy density, but also the quantum-corrected metric function $C(\rho)$. Whilst the energy density is monotonically increasing with increasing temperature, this is not the case for the QC metric function $C(\rho)$. Indeed, by observing, for example, the bottom row of figure 9.3, we see that, at the boundary $\rho = \pi/2$, the QC metric function $C(\rho)$ decreases as the temperature increases. It follows that the temperature dependence of the mass is a complicated interplay between the behaviours of the energy density in the quantum field and the resulting quantum-corrected adS metric. We will discuss this further in the summary section 9.6 of this chapter and in the conclusions chapter 10 of this thesis.

## § 9.6 Summary

In this chapter, we have solved the full (nonlinear) quantum-corrected Einstein equations (3.6.15), with (nonrotating) four-dimensional anti-de Sitter space as the background space-time. We used the four-dimensional stress-energy tensors (corresponding to a static, massless and conformally-coupled scalar field) constructed in chapter 5 (in particular sections 5.1.1 and 5.3.1) as the source terms in the QCEE.

We began by making an ansatz for the quantum-corrected metric corresponding to a static and spherically symmetric space-time, characterised by three unknown functions: $A(\rho)$, $B(\rho)$ and $C(\rho)$. Substituting this ansatz into the left-hand-side of the QCEE (3.6.15) yielded a set of nonlinear, coupled, second-order ODEs for the three metric functions. After some algebraic manipulation, we were able to decouple this set of ODEs into equations for $A(\rho)$ and $B(\rho)$ in terms of $C(\rho)$, and a second-order ODE for $C(\rho)$ that depended only on components of the (renormalised) stress-energy tensor. Due to the complexity of the

ODEs, an analytic solution was not possible and we were forced to proceed numerically. We expanded the metric functions $A, B$ and $C$ as well as the (renormalised) stress-energy tensor components as Taylor series about the origin $\rho = 0$ in order to determine a suitable set of boundary conditions with which to numerically integrate the ODEs. Upon successful numerical integration of the ODEs, we presented results for the quantum-corrected metric functions $A, B$ and $C$ for the cases when the (renormalised) stress-energy tensor was constructed with respect to a quantum scalar field obeying Dirichlet, Neumann or transparent boundary conditions, or a stress-energy tensor arising from relativistic kinetic theory. In particular, we found that the stress-energy tensor arising from a quantum scalar field obeying transparent boundary conditions had the same structure as the stress-energy tensor arising from RKT (which corroborates the results from section 5.3.4), and they differed only by an overall numerical factor. For the range of inverse temperatures considered, the overall numerical factor was sufficiently close to unity that the quantum-corrected metric arising from an RKT stress-energy tensor would be qualitatively the same as the quantum-corrected metric arising from a renormalised stress-energy tensor constructed with respect to a quantum scalar field obeying transparent boundary conditions.

In addition, we plotted (in sections 9.4.1 and 9.4.2) the quantum-corrected metric functions as functions of the radial coordinate $\rho$ in order to discern their qualitative behaviour. For all three cases of boundary conditions (applied to the quantum scalar field with which the renormalised stress-energy tensor was constructed), we showed typical solutions (as ratios with their pure-adS counterparts) at fixed inverse temperatures $\beta = \{\pi/4, \pi\}$. We found that, in general, the quantum-corrected metric function $A(\rho)$ was the closest to unity, and was identically unity in the case of transparent boundary conditions. In contrast, the metric function $C(\rho)$ deviated away from pure-adS the most, with the metric function $B(\rho)$ being somewhere in the middle. At the origin, by construction, the metric function $A(\rho)$ was always equal to unity, and the metric functions $B(\rho)$ and $C(\rho)$ were equal there. Conversely, as the space-time boundary was approached, the metric function $B(\rho)$ rapidly

tended toward unity.

In addition to typical solutions, we showed plots of ratios of the quantum-corrected metric functions between the differing boundary conditions. In general, we found the quantum-corrections arising from a renormalised stress-energy tensor whose corresponding quantum scalar field obeyed Neumann boundary conditions were greatest. In order to determine the effect of changing the (inverse) temperature, we also showed plots of the quantum-corrected metric functions (as ratios with their pure-adS counterparts) for varying temperature. As expected (in particular when considering the results of section 5.3.4), we found that increasing the temperature increased the quantum-corrections to the metric, visualised as a greater deviation away from unity in the plots.

In order to help interpret the quantum-corrected metrics, in section 9.5 we made a second metric ansatz corresponding to the general form of a static and spherically-symmetric metric in spherical coordinates. Using this ansatz, we were able to construct a 'mass' function, and by reconsidering the profile of the energy density of the (renormalised) stress-energy tensors (shown in chapter 5), we thus interpreted the quantum-corrected metrics as massive solitons sourced by the (renormalised) stress-energy tensors.

To find the quantum-corrected metric functions of the new ansatz, we related the new and old ansätze by considering the coordinate transformation $r^2 = C(\rho)$, where $r$ was the radial coordinate of the solitonic ansatz, and $C(\rho)$ was one of the quantum-corrected metric functions of the first ansatz. Using this coordinate transformation, we were able to express the new, solitonic, quantum-corrected metric functions in terms of the quantum-corrected metric functions $A, B$ and $C$. However, we found that the numerical errors rapidly combined when trying to evaluate the solitonic metric functions, rendering the results uninterpretable. We therefore recomputed the left-hand-side of the QCEE (3.6.15) using the new ansatz, finding somewhat simple first-order ODEs for the solitonic metric functions, given in terms of (renormalised) stress-energy tensor components and functions

of the radial coordinate $r$, which is found by its relation to the quantum-corrected metric function $C(\rho)$. We solved the solitonic QCEE using previous results for $C(\rho)$ numerically using `Mathematica`'s inbuilt `NDSolveValue` command. We then presented various plots of the solitonic metric functions and their derivatives, examining their qualitative behaviour.

The solitonic metric function we were most interested in was the mass function $m(r)$. After some functional analysis at the boundary, where we showed that $m(r)$ must converge to a finite value, we interpreted its boundary limit as the mass of the soliton. We showed plots of the mass function against the new radial coordinate, where it was obvious that the mass function converged to a finite value. The pièce de résistance of the chapter, however, was undoubtedly the final figure presented, where we plotted the mass of the quantum-corrected soliton against (inverse) temperature. Remarkably, as the temperature increased, the mass did *not* increase for ever-increasing temperature, hitting a limiting value at around $\beta \approx 0.5$ where the mass attained its maximum value before *decreasing* with further increasing temperature. This was at odds with the behaviour of the energy density in the quantum field, which increased monotonically with increasing temperature. Nevertheless, this was an interesting result. By rewriting the mass as an integral of a quantity depending on the metric function $C(\rho)$ and the energy density of the quantum field, it became clear that this behaviour was the result of a complicated interplay between the behaviours of the energy density in the quantum field and the resulting quantum-corrected metric.

This limiting value of the mass may allude to limits beyond which the semi-classical regime breaks down. We refer the reader to the conclusions chapter (chapter 10) of this thesis, where this will be discussed further.

# Part IV

# Conclusions, appendices and the bibliography

# Chapter 10

# Conclusions and outlook

"Science is like sex: sometimes something useful comes out, but that is not the reason we are doing it."

*Richard P. Feynman*

In this thesis, we have used the framework of quantum field theory in curved space-time to study the back-reaction of a massless and conformally-coupled scalar field, that is either static or rigidly-rotating, propagating on classical, background three- and four-dimensional anti-de Sitter space-time.

In part I of the thesis, the necessary background theory was introduced for the study of back-reaction in the semi-classical regime. Part I was split into three chapters: chapter 1 introduced the conceptual background material, whilst chapters 2 and 3 introduced the necessary technical background. Chapter 2 focussed on classical and quantum fields propagating on flat and curved space-times and, in particular, the Wightman (Green function) approach to quantising fields and calculating expectation values. Since, in general, expectation values of the stress-energy tensor are divergent, we also detailed methods of remedying this pathological behaviour, i.e. Wick normal ordering for fields on flat space-time and the framework of Hadamard renormalisation for general curved space-times. Also of interest was the relativistic kinetic theory approach, where the scalar field was modelled as a thermal gas of noninteracting particles, distributed according to Bose-Einstein statistics. This facilitated comparisons between the relativistic kinetic theory stress-energy tensor (RKT-SET) and the renormalised stress-energy tensor of QFT (QFT-RSET). Chapter 3 discussed different approaches to a theory of quantum gravity, with a particular focus on the semi-classical regime, and how the divergent expectation values of the stress-energy tensor are handled in this approach, by defining an effective action. Of particular interest in this thesis were maximally-symmetric space-times, and so we discussed how the semi-classical regime simplifies somewhat when considering background, maximally-symmetric space-times.

The focus of part II was to take the background theory introduced in the previous part and apply this to anti-de Sitter space-time. In chapter 4 we introduced, in detail, anti-de Sitter space-time, covering both classical and quantum aspects. In particular, its geometry, conformal structure and maximal symmetry were discussed, with a particular focus

on the fact that anti-de Sitter space possesses a time-like boundary, and how anti-de Sitter space is conformal to half of the Einstein static universe (ESU). Also discussed were rigidly-rotating fields on anti-de Sitter space, and how this rigid rotation transformed the background metric, and we detailed the construction of orthonormal frames (vielbeins) for anti-de Sitter space. Furthermore, the necessity of imposing boundary conditions for a well-defined quantum field theory was discussed, and how these are imposed by conformally mapping to the ESU. Using this, we then constructed a quantum field theory for a massless and conformally-coupled scalar field on anti-de Sitter space by explicitly constructing the Hadamard Green function. Finally, the chapter was ended with a brief discussion of quantum states on anti-de Sitter space, focussing on those states that are rigidly rotating.

The final chapter of part II, chapter 5, was devoted to constructing stress-energy tensors to use in the back-reaction problem. In particular, we constructed four renormalised stress-energy tensors (QFT-RSETs), corresponding to both static and rigidly-rotating scalar fields on three- and four-dimensional anti-de Sitter space-time. Of the four QFT-RSETs, the static field on four-dimensional anti-de Sitter space was a reproduction of results found in [4], whilst the remaining three cases were computed following the framework of state-subtraction via Hadamard renormalisation as laid out in [103], using a thermal Hadamard state $|\beta\rangle$ (at inverse temperature $\beta$) and the global anti-de Sitter space vacuum. In addition, using the framework of relativistic kinetic theory we constructed RKT-SETs for the same four situations (static or rigidly-rotating fields on three- or four-dimensional anti-de Sitter space). Much of chapter 5 was then devoted to comapring the QFT-RSETs with the RKT-SETs, in order to ascertain how good an approximation the RKT-SETs are for the QFT-RSETs. To aid in the comparisons, both QFT-RSETs and RKT-SETs were transformed into the thermometer frame, which allowed us to write the stress-energy tensors in terms of four physical quantities: the energy density, isotropic pressure, anisotropic pressure and heat flux. We investigated the dependence of these quantities on the temperature of the thermal state (and the thermal gas), the boundary conditions applied to the quantum

scalar field and the angular speed of rigid rotation.

It was found that the best agreement between RKT-SETs and QFT-RSETs (for all four physical quantities) came at higher temperatures, irrespective of the boundary conditions applied to the quantum scalar field or angular speed of the field. In contrast, at lower temperatures, the agreement was no longer as strong. These results were not unexpected, since increasing the temperature of the quantum state effectively increases the number of quantum particles in the state, and any large number of quantum particles will be well approximated by a classical, thermal gas of particles. On the other hand, at lower particle numbers, quantum effects became more significant. These results were in accordance with the findings for both static scalars [13] and static fermions [16] in anti-de Sitter space-time. Furthermore, we found that as the angular speed of the rigid-rotation was increased, the agreement between the RKT-SETs and QFT-RSETs worsened. In addition, we found that the rigid rotation seemed to have less of an effect on scalar fields than it does on fermion fields [15]. We speculated that this may be due to the nonzero spin of a fermion field coupling to the rigid rotation. Of the boundary conditions applied to the quantum scalar field (Dirichlet, Neumann or transparent boundary conditions), it was found that the QFT-RSETs and RKT-SETs were in best agreement when transparent boundary conditions were applied to the field. We speculated that this was a result of the choice of distribution function used to model the classical gas. This was argued on the basis that, since transparent boundary conditions essentially allow the quantum scalar field to pass beyond the anti-de Sitter space boundary, we are effectively 'losing' information about the quantum scalar field. With the Bose-Einstein distribution chosen to model the classical gas (and thus the RKT-SET), no boundary conditions were applied to the distribution function itself at the anti-de Sitter space boundary, and thus the classical gas was free to 'pass beyond' the boundary, effectively 'losing' information about the classical gas. In order to improve the approximation for reflective (Dirichlet or Neumann) boundary conditions, we postulated that boundary conditions would need to be imposed on the distribution

function. It is as of yet unclear what boundary conditions would need to be applied to the distribution function in order to better approximate the cases of Dirichlet or Neumann boundary conditions, but this would be an interesting avenue of further work to explore.

The first chapter of part III was chapter 6, where back-reaction from a quantum scalar field was studied on some simple (maximally-symmetric) space-times: Minkowski space, de Sitter space, anti-de Sitter space (for a scalar field in the global anti-de Sitter vacuum), the Einstein static universe (its inclusion argued on the basis that anti-de Sitter space is conformal to half of the ESU) and the BTZ geometry, with (schematic) results presented from [78]. The effect of the back-reaction was ascertained by studying quantum corrections to the classical, background geometry. We found that, on Minkowski space-time, the back-reaction had the effect of inducing a cosmological constant that is proportional to the pressure of the quantum scalar field under consideration, and the quantum-corrected geometry corresponded to a system of pressureless dust. However, we also found that the back-reaction modified the asymptotics of the background space-time and thus it was not studied further. We next considered back-reaction on de Sitter space-time, when the scalar field was in the de Sitter 'vacuum' (the unique de Sitter invariant Hadamard state). We found that the quantum corrections to de Sitter space were somewhat trivial, with the effect being to renormalise the cosmological constant and thus the characteristic length scale. When we next considered a massless and conformally-coupled scalar field in the anti-de Sitter space 'vacuum', we found the back-reaction had the same effect as it did on de Sitter space-time, with a simple renormalisation of the cosmological constant and thus characteristic length scale. Next, we considered quantum corrections to the Einstein static universe; the back-reaction amounted to a renormalisation of *both* the cosmological constant and Newton's constant. Finally, we studied the back-reaction of the quantum scalar field on the BTZ geometry, presenting results from [78]. It was found that for a static BTZ black hole, the quantum corrections pushed the event horizon of the black hole outwards, but the mass of the black hole remained unchanged. Considering a rotating

BTZ black hole, the quantum corrections (to first order in the Planck length) also did not modify the mass of the black hole, but pushed the event horizon outwards. This provided partial motivation for the work in the following chapter.

In chapter 7 we studied quantum corrections, to first order in the quantity $a\ell_{\mathrm{p}}$ (the inverse length scale of anti-de Sitter space multiplied by the Planck length), to three-dimensional anti-de Sitter space. The field sourcing the back-reaction was taken to be a massless and conformally-coupled scalar field, modelled either as a classical gas of bosonic particles via RKT, or using quantum field theory on curved space-times to model the scalar as a quantum field. In particular, the stress-energy tensors constructed in chapter 5 were used. The field was taken to be either static or rigidly rotating, with an angular speed $\Omega$, where the static case corresponds to an angular speed of $\Omega = 0$. We interpreted the quantum-corrected geometry as describing solitons sourced by the quantum field or classical bosonic gas. These solitons had a mass $M$ and (for rigidly-rotating fields) an angular momentum $J$; these were the quantities of primary interest to our analysis. For the background anti-de Sitter space geometry (i.e. one with no quantum corrections), the angular momentum of the space-time is zero, and the mass is given by $M = -1$. We found that the quantum corrections (sourced either by the scalar field corresponding to a classical gas of particles or the quantum field) altered the space-time in such a way as to increase the mass and angular momentum, with the magnitude of the mass and angular momentum increasing rapidly with increasing temperature. In analogy with the analysis in chapter 5, we also studied the differences in quantum corrections when the back-reaction is sourced by the RKT-scalar field or the quantum scalar field. Mirroring the findings of chapter 5, it was found that the perturbed mass and angular momentum of the quantum-corrected solitons had the closest agreement when the quantum scalar field was subject to transparent boundary conditions. We then compared our results to those of [78], which we discussed in chapter 6. This was a natural comparison, since the BTZ geometry is locally-isometric to anti-de Sitter space-time. Whilst quantum corrections to the BTZ geometry resulted in an unchanged mass

(and angular momentum) but outwardly-moving event horizon, our results were rather different: the mass and angular momenta were greatly increased by the back-reaction. We postulated that this may be due to a lack of event horizon and/or (naked) singularity in our background space-time, and that, if we were to perhaps artificially insert one or both, then perhaps the quantum corrections would leave the mass and angular momentum unchanged. If this were the case, we speculated that there might exist some hierarchy of quantities that are affected by the quantum corrections.

In chapter 8 we considered quantum corrections (to first order in $a\ell_{\mathrm{P}}$) to four-dimensional anti-de Sitter space-time, when the field undergoes rigid rotation. We derived, explicitly, the linearised, quantum-corrected Einstein equations. However, unfortunately, time was not on our side, and this work remains unfinished. Irregardless, it was clear to see that there would be additional challenges compared with the three-dimensional, linearised case of chapter 7. For example, a complication due to the rigid-rotation of the field is that in the ansatz for the quantum-corrected metric, we were forced to assume that the metric functions depended on both the radial coordinate *and* the polar angular coordinate. This meant that the resulting first-order quantum-corrected Einstein equations were not ordinary differential equations as in the three-dimensional case, but were in fact partial differential equations. Since the dependence of the first-order quantum-corrected Einstein equations on the polar angular coordinate was somewhat simple, (i.e. they include only sporadic instances of linear or quadratic trigonometric functions), we speculate that a suitable line of attack would be to use the method of lines. This entails discretising the polar angular coordinate (and derivatives thereof), thereby reducing the set of PDEs to a set of coupled ODEs. However, this method has obvious drawbacks. For example, whilst tempting to use a mesh with constant intervals, this might not be the best choice; when analysing the (four-dimensional) stress-energy tensors in chapter 5, it was found that a lot of the interesting behaviour occurred near the equatorial plane and the boundaries. Furthermore, in order to gain sufficient accuracy, one would have to discretise the polar angular coordinate

into smaller and smaller mesh steps, thereby increasing the computational cost. In order to keep the computational costs reasonable, one would be forced to choose a mesh with somewhat large increments, reducing accuracy in the polar angular coordinate. One would additionally be forced to interpolate the behaviour between mesh steps, and it is not a priori clear what the best interpolation scheme would be (linear, quadratic etc). However, this is still a more tractable approach than solving the full set of coupled PDEs.

The final work in this thesis can be found in chapter 9. Like the other chapters in part III, the focus of this chapter was ascertaining the effects of back-reaction from the renormalised stress-energy tensor of a massless and conformally-coupled quantum scalar field. However, unlike chapters 7 and 8, we did not consider quantum corrections at first order in $a\ell_{\mathrm{P}}$, but instead, we undertook a *full nonlinear* treatment of the back-reaction problem, with the background space-time taken to be four-dimensional anti-de Sitter space. We considered two quantum-corrected metric ansätze, with the second, the solitonic ansatz, being the primary focus of the physical analysis. As with the other solitonic analyses in this thesis (in particular in chapter 7), the quantum-corrected geometry was that of massive solitons sourced by the quantum scalar field. The mass of the solitons was found to be dependent on two quantities: the energy density in the quantum field and the square of the area radius of the initial quantum-corrected geometry (i.e. the function in front of the two-sphere metric in the first ansatz). The dependence of this mass on the temperature of the quantum state and the boundary conditions the quantum scalar field satisfied was investigated. The key finding was that, as the temperature increased, the mass of the soliton increased, as one might expect, up to a limiting value beyond which the mass begins to *decrease*. This result was unexpected, and is a consequence of the complicated interplay between the behaviours of the energy density in the quantum field and the 'effective surface area' of the soliton, proportional to the square of the area radius.

However, we postulate that the limiting value of the mass is a manifestation of the breakdown of the semi-classical regime. Indeed, it was shown that at sufficiently high temper-

atures, the semi-classical regime will break down on account of the quantum fluctuations in the thermal stress-energy tensor becoming no longer negligible when compared with the mean value of the stress-energy tensor [104, 151, 232]. This can lead to, for example, back-reaction of the Hawking radiation resulting in an information-loss paradox [374]. It is therefore likely that the semi-classical regime will break down at some temperature below the temperature at which the mass attains its maximum value, rendering the results beyond this temperature effectively meaningless. An interesting direction for further work would be to continue the analysis of chapter 8, in order to acquire a similar mass plot for linear corrections to first order in $a\ell_{\mathrm{P}}$. In analogy with the three-dimensional case (see chapter 7), it is thought that the mass plot for linear corrections in four dimensions will have a similar structure, i.e. the mass increasing without bound as the temperature increases. It would then be interesting to discuss *why* there is this inherent difference between the linear and nonlinear, quantum-corrected mass. In addition to the breakdown of the semi-classical regime at sufficiently high temperatures, one may expect that at temperatures above the Hawking-Page transition [191], a black hole would form. In the preceding work, we were unable to model this scenario as we assumed a regular origin, and it is anticipated that a full, self-consistent semi-classical treatment would be required to model such a scenario (though this may not be fruitful on account of the high temperature breakdown of the semi-classical regime).

In future, it would be interesting to extend (and finish) the work carried out in this thesis. Whilst finishing the work of chapter 8 is the obvious next step, it would be rather intriguing to carry out a linear treatment of the back-reaction problem for static quantum fields in four-dimensional anti-de Sitter space-time. This would facilitate a direct comparison with the nonlinear treatment of chapter 9. In particular, it would potentially shed some light on the limiting value of the mass found for the nonlinearly-quantum-corrected solitons, and whether, as speculated, this is a nonlinear effect. Another interesting avenue of further study would be to extend the work of chapter 7, by artificially including a horizon and

singularity, facilitating a more direct comparison with the quantum-corrected BTZ black hole [78]. This would potentially provide credence to the speculation that there exists some global hierarchy of quantities that are affected by the quantum corrections. There is currently work being undertaken [273, 276] to find nonlinear quantum corrections to three-dimensional anti-de Sitter space-time, and it would be interesting to compare the linear and nonlinear approaches. Finally, it would be interesting to ascertain whether the relativistic kinetic theory approximation employed in this thesis could be improved, in particular for reflective boundary conditions.

Whilst the semi-classical approximation to quantum gravity is exactly that, an *approximation*, it is nevertheless an important subject to study, since it is expected that in certain limits a full theory of quantum gravity should reduce to the semi-classical approximation. Whilst the work of this thesis is rather modest compared to the depth and breadth of research in the subject of semi-classical approximations to quantum gravity, it is nevertheless important to study toy models of back-reaction such as we have in this thesis. It is expected back-reaction will play an important role in full semi-classical theories, and whilst the mechanism of back-reaction is widely understood in the literature, explicit calculations have not received as much attention as they perhaps deserve. Analysing simple models such as anti-de Sitter space in the absence of a black hole or more exotic geometry can thus provide an important staging ground for more complicated calculations and perhaps provide some insight into future work.

Whilst it may be argued that finding a full theory of quantum gravity is one of the greatest challenges of modern theoretical physics, it is the author's sincere belief that, sometimes, it is interesting enough to do science for the sake of doing science. As Einstein once remarked,

> *"The important thing is not to stop questioning. Curiosity has its own reason for existence."*

□

# Appendices

"A cup of tea would restore my normality."

*Douglas Adams*

# Appendix A

# Checks and balances on the numerics

Throughout this thesis, we have made extensive use of `Mathematica`, and in particular the `GeneralRelativityTensor` package from the `BlackHolePerturbationToolkit` repository [198] to perform numerical and algebraic calculations. Throughout the calculations, it was necessary to perform certain numerical checks to ensure the numerics were well behaved. Most of these checks followed the same method. In the interest of brevity, therefore, in this appendix we present just two of the numerical checks performed, both for calculations in chapter 9, under the understanding that all other numerical checks were the same or very similar.

There are two instances when solving the QCEE (9.2.7), (9.2.9) and (9.2.10), where using `Mathematica`'s inbuilt `NDSolveValue` command we must perform some checks on the numerics. The first involves the coefficients of the power series expansions (9.3.6) and (9.3.7); the second is regarding the choice on the value of $\epsilon$ that we begin our numerical integration from.

The coefficients of the power series expansions (9.3.6) (and by extension, (9.3.7)) involve rapidly converging infinite sums. Since it is computationally intractable to include all terms up to infinity, we must cut the sums off at some arbitrary number, $N$. To ensure a reasonable numerical accuracy, whilst simultaneously not incurring a high computational cost, we had to find the most efficient number of terms. To illustrate the method, we focus on the sum $f_m(a\beta)$ (5.1.18) below. To find the most efficient number of `NSumTerms` to include, the following `While` loop was employed:

```
fError[x_]:= Module[{err=1, sum=0, n=1},
  While[err>10^(-8),
   term = N[n^m (Exp[n x] - 1)^(-1)];
   sum = sum + term;
   err = term/sum;
   n++
   ];
  n
 ]
```

This terminated at a number of terms $N$ in the sum such that the relative error

$$\frac{N^m}{e^{Nx}-1}\left\{\sum_{n=1}^{N}\frac{n^m}{e^{nx}-1}\right\}^{-1}, \tag{A.0.1}$$

was less than $10^{-8}$. Below, figure A.1 shows a plot of inverse temperature $\beta$ against number of terms required. As can be seen, for the highest temperatures considered (corresponding to the lowest $\beta$; here, that is $\beta = \pi/12$), the number of terms required is always lower than 100. In the numerical integration employed by `NDSolveValue` we therefore terminate every infinite sum after 100 terms. This goes not only for the power series expression at $\rho = \epsilon$, but also for the general forms of the QFT-RSET components in the QCEE (9.2.7), (9.2.9) and (9.2.10) to maintain consistency.

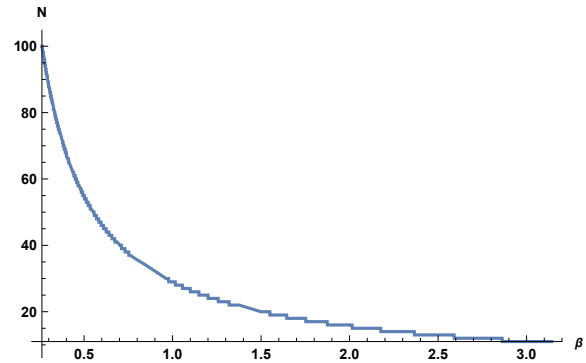


Figure A.1: `NSumTerms` required against inverse temperature $\beta$ such that the relative error in the infinite sums (5.1.18) is less than $10^{-8}$. The inverse adS length scale is fixed at $a = 1$.

The value of $\epsilon$ chosen when employing the `NDSolveValue` command on the QCEE (9.2.7) and (9.2.10) was $\epsilon = 10^{-3}$. For consistency, we checked the relative error in the solutions to the QCEE for changing the value of $\epsilon$ in the range $10^{-2} - 10^{-4}$. Figure A.2 shows the relative error in the metric functions $A(\rho), B(\rho)$ and $C(\rho)$ when changing $\epsilon$. The highest relative error occurs at the highest temperature, as was the case in figure A.1, where the highest number of `NSumTerms` was required at the highest temperature. As such, figure A.2 is for the highest temperature in the range we consider; that is, $\beta = \pi/12$. The blue curves show the relative error between $\epsilon = 10^{-3}$ and $\epsilon = 10^{-2}$, whilst the orange curves show the relative error between $\epsilon = 10^{-3}$ and $\epsilon = 10^{-4}$. For the metric functions $A(\rho)$ and $C(\rho)$, the relative error is approximately $10^{-8}$, whilst for the metric function $B(\rho)$, the relative error is approximated at $10^{-7}$.

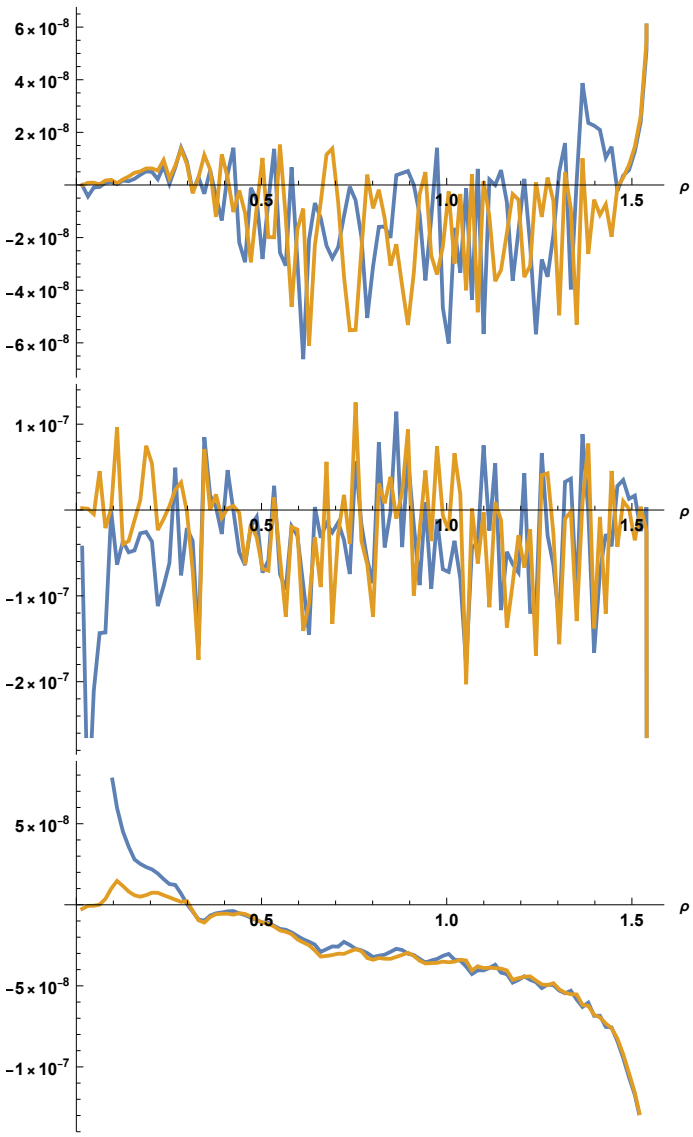


Figure A.2: The relative error in the metric functions $A(\rho)$ (top), $B(\rho)$ (middle) and $C(\rho)$ (bottom). The blue curves represent the relative error between $\epsilon = 10^{-3}$ and $\epsilon = 10^{-2}$, whilst the orange curves represent the relative error between $\epsilon = 10^{-3}$ and $\epsilon = 10^{-4}$. Dirichlet boundary conditions are applied to the field, and the adS length scale is fixed $a = 1$. The temperature is chosen to be the highest in the range we consider, that is $\beta = \pi/12$, since this is where the highest relative error occurs.

# Appendix B

# Taylor series coefficients for the nonlinear, four-dimensional QCEE

This appendix contains the remainder of the Taylor series coefficients calculated in section 9.3. These are included in this thesis merely for self-completeness. In isolation, they are not particularly illuminating; instead, see section 9.3 for all of the details.

Before proceeding, it is important to identify some nomenclature used in this appendix. If we have some power series

$$\mathcal{S}(x) = \sum_{n=0}^{\infty} \mathfrak{a}_n x^n, \tag{B.0.1}$$

then the $k$-th coefficient is denoted by

$$\left[x^k\right] \mathcal{S}(x) = \mathfrak{a}_k. \tag{B.0.2}$$

## § B.1 QFT-RSET components

In equation (9.3.4), we present results up to and including $\mathcal{O}(\rho^2)$. We also have the fourth- and sixth-order coefficients. For the function $\mathcal{F}_1(\rho)$, these are:

$$\left[\rho^4\right]\mathcal{F}_1(\rho) = \frac{4}{945}\left[-\lambda\widetilde{f}_1(a\beta) + 525 f_3(a\beta) + 224\lambda\widetilde{f}_3(a\beta) + 266\lambda\widetilde{f}_5(a\beta) + 35\lambda\widetilde{f}_7(a\beta)\right], \tag{B.1.1a}$$

$$\left[\rho^6\right]\mathcal{F}_1(\rho) = \frac{8}{42525}\Big[3\lambda\widetilde{f}_1(a\beta) - 5355 f_3(a\beta) - 970\lambda\widetilde{f}_3(a\beta) - 3108\lambda\widetilde{f}_5(a\beta) - 1155\lambda\widetilde{f}_7(a\beta)\Big], \tag{B.1.1b}$$

whilst for the function $\mathcal{F}_2(\rho)$, we have

$$\left[\rho^4\right]\mathcal{F}_2(\rho) = \frac{4}{945}\left[48\lambda\widetilde{f}_1(a\beta) + 2100 f_3(a\beta) + 980\lambda\widetilde{f}_3(a\beta) + 952\lambda\widetilde{f}_5(a\beta) + 119\lambda\widetilde{f}_7(a\beta)\right], \tag{B.1.1c}$$

$$\left[\rho^6\right]\mathcal{F}_2(\rho) = \frac{16}{42525}\Big[-81\lambda\widetilde{f}_1(a\beta) - 10710 f_3(a\beta) - 2600\lambda\widetilde{f}_3(a\beta) - 5859\lambda\widetilde{f}_5(a\beta) - 1995\lambda\widetilde{f}_7(a\beta)\Big], \tag{B.1.1d}$$

and finally, the fourth- and sixth-order coefficients of the function $\mathcal{F}_3(\rho)$ are given by

$$\left[\rho^4\right]\mathcal{F}_3(\rho) = \frac{4}{945}\left[52\lambda\widetilde{f}_1(a\beta) + 84\lambda\widetilde{f}_3(a\beta) - 112\lambda\widetilde{f}_5(a\beta) - 21\lambda\widetilde{f}_7(a\beta)\right], \tag{B.1.1e}$$

$$\left[\rho^6\right]\mathcal{F}_3(\rho) = \frac{16}{14175}\left[-29\lambda\widetilde{f}_1(a\beta) - 220\lambda\widetilde{f}_3(a\beta) + 119\lambda\widetilde{f}_5(a\beta) + 105\lambda\widetilde{f}_7(a\beta)\right]. \tag{B.1.1f}$$

The fourth- and sixth-order coefficients of the QFT-RSET components can be found using the above coefficients (B.1.1) along with equation (9.3.1). Proceeding term by term, we can write down the fourth-order coefficients of the QFT-RSET components as

$$\begin{aligned}\widetilde{T}_{\tau|4} &= \frac{a^2}{8\pi^2}\left\{\left[\rho^4\right]\mathcal{F}_1(\rho) - \left[\rho^4\right]\mathcal{F}_2(\rho)\right\} \\ &= -\frac{a^4}{270\pi^2}\left[7\lambda\widetilde{f}_1(a\beta) + 225 f_3(a\beta) + 108\lambda\widetilde{f}_3(a\beta) + 98\lambda\widetilde{f}_5(a\beta) + 12\lambda\widetilde{f}_7(a\beta)\right],\end{aligned} \tag{B.1.2}$$

$$\widetilde{T}_{\rho|4} = \frac{a^2}{8\pi^2}\left\{\left[\rho^4\right]\mathcal{F}_1(\rho) - \left[\rho^4\right]\mathcal{F}_3(\rho)\right\}$$
$$= \frac{a^4}{1890\pi^2}\left[51\lambda\widetilde{f}_1(a\beta) + 525 f_3(a\beta) + 308\lambda\widetilde{f}_3(a\beta) + 154\lambda\widetilde{f}_5(a\beta) + 14\lambda\widetilde{f}_7(a\beta)\right], \tag{B.1.3}$$

$$\widetilde{T}_{\theta|4} = \frac{a^2}{8\pi^2}\left[\rho^4\right]\mathcal{F}_1(\rho)$$
$$= -\frac{a^4}{1890\pi^2}\left[\lambda\widetilde{f}_1(a\beta) - 525 f_3(a\beta) - 224\lambda\widetilde{f}_3(a\beta) - 266\lambda\widetilde{f}_5(a\beta) - 35\lambda\widetilde{f}_7(a\beta)\right]. \tag{B.1.4}$$

In a similar fashion, the sixth-order coefficients are given by

$$\widetilde{T}_{\tau|6} = \frac{a^2}{8\pi^2}\left\{\left[\rho^6\right]\mathcal{F}_1(\rho) - \left[\rho^6\right]\mathcal{F}_2(\rho)\right\}$$
$$= \frac{a^4}{2835\pi^2}\left[11\lambda\widetilde{f}_1(a\beta) + 1071 f_3(a\beta) + 282\lambda\widetilde{f}_3(a\beta) + 574\lambda\widetilde{f}_5(a\beta) + 189\lambda\widetilde{f}_7(a\beta)\right], \tag{B.1.5}$$

$$\widetilde{T}_{\rho|6} = \frac{a^2}{8\pi^2}\left\{\left[\rho^6\right]\mathcal{F}_1(\rho) - \left[\rho^6\right]\mathcal{F}_3(\rho)\right\}$$
$$= -\frac{a^4}{42525\pi^2}\Big[171\lambda\widetilde{f}_1(a\beta) + 5355 f_3(a\beta) + 2290\lambda\widetilde{f}_3(a\beta) + 2394\lambda\widetilde{f}_5(a\beta) + 525\lambda\widetilde{f}_7(a\beta)\Big], \tag{B.1.6}$$

$$\widetilde{T}_{\theta|6} = \frac{a^2}{8\pi^2}\left[\rho^6\right]\mathcal{F}_1(\rho)$$
$$= -\frac{a^4}{42525\pi^2}\Big[-3\lambda\widetilde{f}_1(a\beta) + 5355 f_3(a\beta) + 970\lambda\widetilde{f}_3(a\beta) + 3108\lambda\widetilde{f}_5(a\beta) + 1155\lambda\widetilde{f}_7(a\beta)\Big]. \tag{B.1.7}$$

## § B.2 Metric function $A(\rho)$

This subsection contains the full Taylor series calculations to ascertain the coefficients $A_i$ from equation (9.3.7a). Recall that by expanding the QCEE (9.2.7) into a Taylor series about the origin, we can write it as

$$0 = \mathfrak{A}_1\rho + \mathfrak{A}_3\rho^3 + \mathfrak{A}_5\rho^5 + \mathcal{O}(\rho^7) \tag{B.2.1a}$$

where

$$\mathfrak{A}_1 = 2A_2 + \frac{4T_{\theta|2} - 8T_{\rho|2}}{T_{\tau|0} - T_{\theta|0}} \tag{B.2.1b}$$

$$\begin{aligned}\mathfrak{A}_3 = & -2A_2^2 + 4A_4 - \frac{4}{C_2(T_{\tau|0} - T_{\theta|0})^2}\left\{C_2\left[(T_{\tau|0} - T_{\theta|0})(3T_{\rho|4} - T_{\theta|4}) + T_{\tau|2}(T_{\theta|2} - 2T_{\rho|2})\right.\right. \\ & \left.\left. + 2T_{\rho|2}^2 - T_{\rho|2}T_{\theta|2}\right] + C_4(T_{\tau|0} - T_{\theta|0})(T_{\rho|2} - T_{\theta|2})\right\}\end{aligned} \tag{B.2.1c}$$

$$\begin{aligned}\mathfrak{A}_5 = & 2A_2^3 - 6A_2A_4 + 6A_6 \\ & - 2\frac{(4T_{\rho|2} - 2T_{\theta|2})}{C_2^2(T_{\tau|0} - T_{\theta|0})^3}\left\{\left(C_2^2\left[(T_{\tau|0} - T_{\theta|0})(T_{\rho|4} - T_{\tau|4}) + (T_{\tau|2} - T_{\rho|2})^2\right]\right.\right. \\ & \left.\left. + (T_{\tau|0} - T_{\theta|0})^2\left(C_4^2 - C_2C_6\right) + C_2C_4(T_{\tau|0} - T_{\theta|0})(T_{\tau|2} - T_{\rho|2})\right)\right\} \\ & + \frac{4}{C_2^2(T_{\tau|0} - T_{\theta|0})^2}\left\{\left[C_2(T_{\tau|2} - T_{\rho|2}) + C_4(T_{\tau|0} - T_{\theta|0})\right]\right. \\ & \left. \times \left[C_2(3T_{\rho|4} - T_{\theta|4}) + C_4(3T_{\rho|2} - 2T_{\theta|2})\right]\right\} \\ & - \frac{4}{C_2(T_{\tau|0} - T_{\theta|0})}\left\{C_2(4T_{\rho|6} - T_{\theta|6}) + 2C_4(2T_{\rho|4} - T_{\theta|4}) + C_6(4T_{\rho|2} - 3T_{\theta|2})\right\}\end{aligned} \tag{B.2.1d}$$

To find the coefficients $A_i$, by equate each term $\mathfrak{A}_i$ to zero, order-by-order in $\rho$. Starting with the lowest order, we have

$$\begin{aligned} 0 = \mathfrak{A}_1 &= 2A_2 + \frac{4T_{\theta|2} - 8T_{\rho|2}}{T_{\tau|0} - T_{\theta|0}} \\ \implies A_2 &= 2\frac{2T_{\rho|2} - T_{\theta|2}}{T_{\tau|0} - T_{\theta|0}}, \end{aligned} \tag{B.2.2}$$

which gives the coefficient $A_2$ purely in terms of the QFT-RSET component Taylor series coefficients. By setting the third order $\rho$ coefficient to zero, i.e. $\mathfrak{A}_3 = 0$, and substituting in equation (B.2.2) for $A_2$, we find that the coefficient $A_4$ is given by

$$\begin{aligned} A_4 = & \frac{1}{C_2(T_{\tau|0} - T_{\theta|0})^2}\left\{C_4(T_{\tau|0} - T_{\theta|0})(T_{\rho|2} - T_{\theta|2})\right. \\ & \left. + C_2\left[(T_{\tau|0} - T_{\theta|0})(3T_{\rho|4} - T_{\theta|4}) - (T_{\tau|2} - 5T_{\rho|2} + 2T_{\theta|2})(2T_{\rho|2} - T_{\theta|2})\right]\right\}, \end{aligned} \tag{B.2.3}$$

which not only depends on the QFT-RSET component Taylor series coefficients, but also the coefficients $C_i$ of the Taylor series for the metric function $C(\rho)$ (9.3.7c). We finally consider the fifth order in $\rho$, equivalent to setting $\mathfrak{A}_5 = 0$, which yields, after substituting the known expressions for $A_2$ (B.2.2) and $A_4$ (B.2.3), the following expression for the coefficient $A_6$:

$$\begin{aligned} A_6 = & -\frac{2}{3C_2^2(T_{\tau|0}-T_{\theta|0})^3}\left\{C_4^2(T_{\tau|0}-T_{\theta|0})^2(T_{\rho|2}-T_{\theta|2}) - 2C_2C_6(T_{\tau|0}-T_{\theta|0})^2(T_{\rho|2}-T_{\theta|2})\right. \\ & - C_2C_4(T_{\tau|0}-T_{\theta|0})\left[(T_{\tau|0}-T_{\theta|0})(T_{\rho|4}-T_{\theta|4}) - (T_{\rho|2}-T_{\theta|2})(T_{\tau|2}-7T_{\rho|2}+3T_{\theta|2})\right] \\ & + C_2^2\left[(T_{\tau|0}-T_{\theta|0})(3T_{\rho|4}-T_{\theta|4})(T_{\tau|2}-7T_{\rho|2}+3T_{\theta|2}) - (T_{\tau|0}-T_{\theta|0})^2(4T_{\rho|6}-T_{\theta|6})\right. \\ & \quad - (2T_{\rho|2}-T_{\theta|2})(T_{\tau|2}-3T_{\rho|2}+T_{\theta|2})(T_{\tau|2}-5T_{\rho|2}+2T_{\theta|2}) \\ & \quad\quad \left.\left. + (T_{\tau|0}-T_{\theta|0})(T_{\tau|4}-T_{\rho|4})(2T_{\rho|2}-T_{\theta|2})\right]\right\}. \end{aligned} \tag{B.2.4}$$

This also depends on the QFT-RSET component Taylor series coefficients and the coefficients $C_i$ of the series expansion for $C(\rho)$.

## § B.3 Metric function $C(\rho)$

In this subsection, we compute the explicit expressions for the Taylor series coefficients $C_i$ for the metric function $C(\rho)$, with Taylor series expansion (9.3.7c). We first recall the series expansion of the QCEE (9.2.10). This is:

$$0 = \mathfrak{C}_0 + \mathfrak{C}_2\rho^2 + \mathfrak{C}_4\rho^4 + \mathcal{O}(\rho^6), \tag{B.3.1}$$

where

$$\mathfrak{C}_0 = -T_{\tau|0} + 3T_{\theta|0} - 2\Lambda + \frac{12(T_{\theta|2}-2T_{\rho|2})}{C_2(T_{\tau|0}-T_{\theta|0})}, \tag{B.3.2}$$

$$\begin{aligned} \mathfrak{C}_2 = & \frac{1}{C_2^2(T_{\tau|0}-T_{\theta|0})^2}\left\{20C_4(T_{\tau|0}-T_{\theta|0})(3T_{\rho|2}-T_{\theta|2})\right. \\ & - C_2^2(T_{\tau|0}-T_{\theta|0})[(T_{\tau|0}-T_{\theta|0})(T_{\tau|2}-5T_{\rho|2}) + 20(2T_{\rho|2}-T_{\theta|2})(T_{\theta|0}-\Lambda)] \end{aligned}$$

$$+ 20C_2[(2T_{\rho|2} - T_{\theta|2})(T_{\tau|2} + 7T_{\rho|2} - 4T_{\theta|2}) - (T_{\tau|0} - T_{\theta|0})(3T_{\rho|4} - T_{\theta|4})]\big\}\,, \quad \text{(B.3.3)}$$

$$\begin{aligned}
\mathfrak{C}_4 = &- \frac{1}{C_2^3(T_{\tau|0} - T_{\theta|0})^3}\big\{4C_4^2(T_{\tau|0} - T_{\theta|0})^2(41T_{\rho|2} - 9T_{\theta|2}) \\
&+ C_2^3(T_{\tau|0} - T_{\theta|0})\big[(T_{\tau|0} - T_{\theta|0})^2(T_{\tau|4} - 7T_{\rho|4}) \\
&\quad - 28(2T_{\rho|2} - T_{\theta|2})(T_{\theta|0} - \Lambda)(T_{\tau|2} + 7T_{\rho|2} - 4T_{\theta|2}) \\
&\quad + 28(T_{\tau|0} - T_{\theta|0})\{T_{\rho|2}(2T_{\rho|2} - T_{\theta|2}) + (3T_{\rho|4} - T_{\theta|4})(T_{\theta|0} - \Lambda)\}\big] \\
&+ 2C_2^2\big[C_4(T_{\tau|0} - T_{\theta|0})^2\{T_{\rho|2}(T_{\tau|0} - T_{\theta|0}) - 2(11T_{\rho|2} - 2T_{\theta|2})(T_{\theta|0} - \Lambda)\} \\
&\quad + 14\big\{(T_{\tau|0} - T_{\theta|0})[(T_{\tau|2} - T_{\rho|2})(T_{\theta|4} - 3T_{\rho|4}) \\
&\qquad + (T_{\theta|2} - 2T_{\rho|2})(T_{\tau|4} + 23T_{\rho|4} - 8T_{\theta|4})] \\
&\quad + (T_{\tau|0} - T_{\theta|0})^2(4T_{\rho|6} - T_{\theta|6}) + (2T_{\rho|2} - T_{\theta|2})(T_{\tau|2} + 7T_{\rho|2} - 4T_{\theta|2})^2\big\}\big] \\
&- 4C_2(T_{\tau|0} - T_{\theta|0})\big[C_4\{(T_{\tau|0} - T_{\theta|0})(41T_{\rho|4} - 9T_{\theta|4}) \\
&\qquad - (25T_{\rho|2} - 9T_{\theta|2})(T_{\tau|2} + T_{\rho|2} - T_{\theta|2}) - (103T_{\rho|2} - 27T_{\theta|2})(2T_{\rho|2} - T_{\theta|2})\} \\
&\qquad + 7C_6(T_{\tau|0} - T_{\theta|0})(4T_{\rho|2} - T_{\theta|2})\big]\big\}\,. \qquad \text{(B.3.4)}
\end{aligned}$$

By equating each order of $\rho$ to zero, we can find expressions for three coefficients $C_2$, $C_4$ and $C_6$. By equating $\mathfrak{C}_0$ to zero, we find the following expression for $C_2$:

$$C_2 = \frac{12(T_{\theta|2} - 2T_{\rho|2})}{(T_{\tau|0} - T_{\theta|0})(T_{\tau|0} - 3T_{\theta|0} + 2\Lambda)}, \qquad \text{(B.3.5)}$$

which depends on only Taylor series coefficients of the QFT-RSET component expansions. Similarly, by setting $\mathfrak{C}_4 = 0$, we find an expression for $C_4$ in terms of the QFT-RSET component Taylor series coefficients, after also substituting equation (B.3.5). This is given as

$$\begin{aligned}
C_4 = &\frac{12(2T_{\rho|2} - T_{\theta|2})}{5(T_{\tau|0} - T_{\theta|0})^2(T_{\tau|0} - 3T_{\theta|0} + 2\Lambda)^2(3T_{\rho|2} - T_{\theta|2})}\big\{5(T_{\tau|0} - T_{\theta|0})^2(T_{\theta|4} - 3T_{\rho|4}) \\
&- 10(T_{\tau|0} - T_{\theta|0})(T_{\theta|4} - 3T_{\rho|4})(T_{\theta|0} - \Lambda) + 2(2T_{\rho|2} - T_{\theta|2})[9T_{\tau|2}(T_{\tau|0} - T_{\theta|0}) \\
&- 5(T_{\tau|0} - \Lambda)(T_{\tau|2} - 2T_{\rho|2} + 2T_{\theta|2}) + 15T_{\rho|2}(T_{\theta|0} - \Lambda)]\big\}\,. \qquad \text{(B.3.6)}
\end{aligned}$$

Finally, by setting $\mathfrak{C}_6$ equal to zero and substituting in the known expressions for both $C_2$ (B.3.5) and $C_4$ (B.3.6), we yield the following lengthy expression for the final Taylor series coefficient for the metric function $C(\rho)$:

$$\begin{aligned} C_6 = \frac{4(T_{\theta|2} - 2T_{\rho|2})}{14175(T_{\tau|0} - T_{\theta|0})^3(4T_{\rho|2} - T_{\theta|2})(3T_{\rho|2} - T_{\theta|2})^2(T_{\tau|0} - 3T_{\theta|0} + 2\Lambda)^3} \\ \times \left\{170100\mathfrak{c}_0 + 30\mathfrak{c}_1(T_{\tau|0} - T_{\theta|0}) + \mathfrak{c}_2(T_{\tau|0} - T_{\theta|0})^2 \right. \\ \left. + 90\mathfrak{c}_3(T_{\tau|0} - T_{\theta|0})^3 + 14175\mathfrak{c}_4(T_{\tau|0} - T_{\theta|0})^4\right\} \end{aligned} \tag{B.3.7a}$$

where the $\mathfrak{c}_i$ are defined as

$$\begin{aligned} \mathfrak{c}_4 &= 2T_{\theta|2}(3T_{\rho|4} - T_{\theta|4})^2 - 2T_{\theta|4}(3T_{\rho|4} - T_{\theta|4})(3T_{\rho|2} - T_{\theta|2}) + 3(4T_{\rho|6} - T_{\theta|6})(3T_{\rho|2} - T_{\theta|2})^2 \\ \mathfrak{c}_3 &= 10(T_{\theta|2} - 3T_{\rho|2})^3(45T_{\tau|4} + 336T_{\rho|4} - 182T_{\theta|4}) \\ &\quad - 3(T_{\theta|2} - 3T_{\rho|2})^2[T_{\tau|2}(894T_{\rho|4} - 410T_{\theta|4}) - 75T_{\tau|4}T_{\theta|2} \\ &\qquad + 910T_{\theta|2}(T_{\theta|4} - 2T_{\rho|4}) + 630(T_{\theta|0} - \Lambda)(4T_{\rho|6} - T_{\theta|6})] \\ &\quad + 3(T_{\theta|2} - 3T_{\rho|2})[T_{\theta|2}(T_{\tau|2}(225T_{\rho|4} - 19T_{\theta|4}) + 70T_{\theta|2}(T_{\theta|4} - 7T_{\rho|4})) \\ &\qquad + 420T_{\theta|4}(T_{\theta|0} - \Lambda)(T_{\theta|4} - 3T_{\rho|4})] \\ &\quad + 28T_{\theta|2}(3T_{\rho|4} - T_{\theta|4})[4T_{\theta|2}(3T_{\tau|2} - 5T_{\theta|2}) + 45(T_{\theta|0} - \Lambda)(T_{\theta|4} - 3T_{\rho|4})] \\ \mathfrak{c}_2 &= 27T_{\tau|2}^2(T_{\theta|2} - 2T_{\rho|2})\left[896T_{\theta|2}^2 - 592T_{\theta|2}(T_{\theta|2} - 3T_{\rho|2}) - 3823(T_{\theta|2} - 3T_{\rho|2})^2\right] \\ &\quad - 90T_{\tau|2}(T_{\theta|2} - 2T_{\rho|2})\left\{9T_{\theta|2}\left[364(T_{\theta|0} - \Lambda)(3T_{\rho|4} - T_{\theta|4}) - 475(T_{\theta|2} - 3T_{\rho|2})^2\right]\right. \\ &\quad - 12771T_{\rho|4}(T_{\theta|0} - \Lambda)(T_{\theta|2} - 3T_{\rho|2}) + 896T_{\theta|2}^3 - 408T_{\theta|2}^2(T_{\theta|2} - 3T_{\rho|2}) \\ &\quad \left. + 5895T_{\theta|4}(T_{\theta|0} - \Lambda)(T_{\theta|2} - 3T_{\rho|2}) - 1451(T_{\theta|2} - 3T_{\rho|2})^3\right\} \\ &\quad + 25\left\{-(T_{\theta|2} - 3T_{\rho|2})^2\left[54T_{\theta|2}(T_{\theta|0} - \Lambda)(51T_{\tau|4} + 574T_{\rho|4} - 287T_{\theta|4})\right.\right. \\ &\quad \left. - 6804(T_{\theta|0} - \Lambda)^2(4T_{\rho|6} - T_{\theta|6}) + 5971T_{\theta|2}^3\right] \\ &\quad + 4(T_{\theta|2} - 3T_{\rho|2})^3\left[9(T_{\theta|0} - \Lambda)(-153T_{\tau|4} + 168T_{\rho|4} + 35T_{\theta|4}) - 3752T_{\theta|2}^2\right] \\ &\quad + 14(T_{\theta|2} - 3T_{\rho|2})\left[27T_{\theta|2}^2(T_{\theta|0} - \Lambda)(11T_{\rho|4} + T_{\theta|4}) + 324T_{\theta|4}(T_{\theta|0} - \Lambda)^2(3T_{\rho|4} - T_{\theta|4})\right. \\ &\quad \left. + 112T_{\theta|2}^4\right] + 56T_{\theta|2}\left[63T_{\theta|2}^2(T_{\theta|0} - \Lambda)(3T_{\rho|4} - T_{\theta|4}) + 81(T_{\theta|0} - \Lambda)^2(T_{\theta|4} - 3T_{\rho|4})^2\right. \end{aligned}$$

$$
\begin{aligned}
&+\ 16T_{\theta|2}^{4}\Big] - 8183T_{\theta|2}(T_{\theta|2}-3T_{\rho|2})^{4} - 518(T_{\theta|2}-3T_{\rho|2})^{5}\Big\} \\
\mathfrak{c}_1 = {} & (T_{\theta|0}-\Lambda)(T_{\theta|2}-2T_{\rho|2})\Big\{3(T_{\theta|2}-3T_{\rho|2})^{2}\Big[2901T_{\tau|2}^{2} - 2268T_{\tau|2}T_{\theta|2} \\
&+\ 210(T_{\theta|0}-\Lambda)(9T_{\tau|4}-120T_{\rho|4}+47T_{\theta|4}) - 3955T_{\theta|2}^{2}\Big] \\
&+ 2\,(T_{\theta|2}-3T_{\rho|2})\Big[T_{\theta|2}\Big(585T_{\tau|2}^{2} - 1611T_{\tau|2}T_{\theta|2} + 1750T_{\theta|2}^{2}\Big) \\
&+\ 315(T_{\theta|0}-\Lambda)(-45T_{\tau|2}T_{\rho|4} + 21T_{\tau|2}T_{\theta|4} + 27T_{\rho|4}T_{\theta|2} - 7T_{\theta|2}T_{\theta|4})\Big] \\
&+\ 56T_{\theta|2}(3T_{\tau|2}+T_{\theta|2})[4T_{\theta|2}(5T_{\theta|2}-3T_{\tau|2}) + 45(T_{\theta|0}-\Lambda)(3T_{\rho|4}-T_{\theta|4})] \\
&+\ 2(T_{\theta|2}-3T_{\rho|2})^{3}(5289T_{\tau|2}-14525T_{\theta|2}) - 9065(T_{\theta|2}-3T_{\rho|2})^{4}\Big\} \\
\mathfrak{c}_0 = {} & (T_{\theta|0}-\Lambda)^{2}(T_{\theta|2}-2T_{\rho|2})^{2}(T_{\tau|2}-5T_{\rho|2}+2T_{\theta|2}) \\
&\times\Big\{(5T_{\rho|2}-T_{\theta|2})(T_{\tau|2}-4T_{\rho|2}+T_{\theta|2}) - (T_{\rho|2}-T_{\theta|2})^{2} + 2T_{\rho|2}(T_{\rho|2}+T_{\theta|2})\Big\}\,.
\end{aligned}
\tag{B.3.7b}
$$

As for the lower-order coefficients, this only depends on known QFT-RSET component Taylor series coefficients as well as the cosmological constant, $\Lambda$.

# Bibliography


[1] A. A. Abrikosov, L. P. Gorkov, and I. E. Dzyaloshinski. *Methods of Quantum Field Theory in Statistical Physics*. Dover Books on Physics Series. Dover Publications, 1975.

[2] O. Aharony, S. S. Gubser, J. M. Maldacena, H. Ooguri, and Y. Oz. Large $N$ field theories, string theory and gravity. *Phys. Rept.*, 323:183, 2000.

[3] B. Allen. Vacuum states in de Sitter space. *Phys. Rev. D*, 32:3136, 1985.

[4] B. Allen, A. Folacci, and G.W. Gibbons. Anti-de Sitter space at finite temperature. *Phys. Lett. B*, 189:304, 1987.

[5] B. Allen and T. Jacobson. Vector two point functions in maximally symmetric spaces. *Commun. Math. Phys.*, 103:669, 1986.

[6] J. Ambjørn and R. Loll. Causal dynamical triangulations: gateway to nonperturbative quantum gravity. In R. Szabo and M. Bojowald, editors, *Encyclopedia of Mathematical Physics, Second Edition*, page V1:555. Elsevier, Netherlands, 2024.

[7] J. Ambjørn, J. Jurkiewicz, and R. Loll. Emergence of a 4D world from causal quantum gravity. *Phys. Rev. Lett.*, 93, 2004.

[8] J. Ambjørn, J. Jurkiewicz, and R. Loll. Causal dynamical triangulations and the quest for quantum gravity. In J. Murugan, A. Weltman, and G. F. R. Ellis, edi-

tors, *Foundations of Space and Time: Reflections on Quantum Gravity*, page 321. Cambridge University Press, 2012.

[9] V. E. Ambruş and R. Blaga. Relativistic Rotating Boltzmann Gas Using the Tetrad Formalism. *Ann. West Univ. Timisoara - Phys.*, 58:89–108, 2015.

[10] V. E. Ambruş and M. N. Chernodub. Rigidly rotating scalar fields: Between real divergence and imaginary fractalization. *Phys. Rev. D*, 108:085016, 2023.

[11] V. E. Ambruş and M. N. Chernodub. Vortical effects in Dirac fluids with vector, chiral and helical charges. *Eur. Phys. J. C*, 83:111, 2023.

[12] V. E. Ambruş and I. I. Cotăescu. Maxwell-Jüttner distribution for rigidly rotating flows in spherically symmetric spacetimes using the tetrad formalism. *Phys. Rev. D*, 94:085022, 2016.

[13] V. E. Ambruş, C. Kent, and E. Winstanley. Analysis of scalar and fermion quantum field theory on anti-de Sitter spacetime. *Int. J. Mod. Phys. D*, 27:1843014, 2018.

[14] V. E. Ambruş, E. Molnár, and D. H. Rischke. Relativistic second-order dissipative and anisotropic fluid dynamics in the relaxation-time approximation for an ideal gas of massive particles. *Phys. Rev. D*, 109:076001, 2024.

[15] V. E. Ambruş and E. Winstanley. Dirac fermions on an anti-de Sitter background. *AIP Conf. Proc.*, 1634:40, 2015.

[16] V. E. Ambruş and E. Winstanley. Quantum corrections in thermal states of fermions on anti-de Sitter space-time. *AIP Conf. Proc.*, 1916:020005, 2017.

[17] V. E. Ambruş and E. Winstanley. Thermal expectation values of fermions on anti-de Sitter space-time. *Class. Quant. Grav.*, 34:145010, 2017.

[18] V. E. Ambruş and E. Winstanley. Exact solutions in quantum field theory under rotation. In F. Becattini, J. Liao, and M. Lisa, editors, *Strongly Interacting Matter under Rotation*. Springer International Publishing, Cham, 2021.

[19] V. E. Ambruş and E. Winstanley. Vortical effects for free fermions on anti-de Sitter space-time. *Symmetry*, 13:2019, 2021.

[20] P. R. Anderson, W. A. Hiscock, and D. A. Samuel. Stress-energy tensor of a quantized scalar field in static spherically symmetric spacetimes. *Phys. Rev. D*, 51:4337, 1995.

[21] R. Apéry. Irrationalité de $\zeta(2)$ et $\zeta(3)$ [Irrationality of $\zeta(2)$ and $\zeta(3)$]. In *Journées arithmétiques de Luminy*, pages 11–13. Astérisque, 1979.

[22] H. Araki and U. Carow-Watamura. *Mathematical Theory of Quantum Fields*. International Series of Monographs on Physics. OUP Oxford, 1999.

[23] J. Arrechea. *Hydrostatic equilibrium in the semiclassical approximation*. PhD thesis, Universidad de Granada, 2023.

[24] J. Arrechea, C. Barceló, R. Carballo-Rubio, and L. J. Garay. Schwarzschild geometry counterpart in semiclassical gravity. *Phys. Rev. D*, 101:064059, 2020.

[25] J. Arrechea, C. Barceló, R. Carballo-Rubio, and L. J. Garay. Reissner–Nordström geometry counterpart in semiclassical gravity. *Class. Quant. Grav.*, 38:115014, 2021.

[26] J. Arrechea, C. Barceló, R. Carballo-Rubio, and L. J. Garay. Semiclassical relativistic stars. *Sci. Rep.*, 12:15958, 2022.

[27] J. Arrechea, C. Barceló, R. Carballo-Rubio, and L. J. Garay. Ultracompact horizonless objects in order-reduced semiclassical gravity. *Phys. Rev. D*, 109:104056, 2024.

[28] J. Arrechea, C. Breen, A. Ottewill, and P. Taylor. Renormalized stress-energy tensor for scalar fields in Hartle-Hawking, Boulware, and Unruh states in the Reissner-Nordström spacetime. *Phys. Rev. D*, 108:125004, 2023.

[29] J. Arrechea, G. Neri, and S. Liberati. Inner horizon instability via the trace anomaly effective action. *Phys. Rev. D*, 111:084036, 2025.

[30] A. Ashtekar. New variables for classical and quantum gravity. *Phys. Rev. Lett.*, 57:2244–2247, 1986.

[31] S. J. Avis, C. J. Isham, and D. Storey. Quantum field theory in anti-de Sitter space-time. *Phys. Rev. D*, 18:3565, 1978.

[32] M. Banados, M. Henneaux, C. Teitelboim, and J. Zanelli. Geometry of the (2+1) black hole. *Phys. Rev. D*, 48:1506, 1993.

[33] M. Banados, C. Teitelboim, and J. Zanelli. The black hole in three-dimensional space-time. *Phys. Rev. Lett.*, 69:1849, 1992.

[34] V. S. Barroso and J. P. M. Pitelli. Boundary conditions and vacuum fluctuations in $AdS_4$. *Gen. Rel. Grav.*, 52:29, 2020.

[35] G. Barton. *Elements of Green's Functions and Propagation: Potentials, Diffusion, and Waves*. Oxford Science Publications. Clarendon Press, 1989.

[36] F. Becattini, L. Bucciantini, E. Grossi, and L. Tinti. Local thermodynamical equilibrium and the beta frame for a quantum relativistic fluid. *Eur. Phys. J. C*, 75:191, 2015.

[37] K. Becker, M. Becker, and J. H. Schwarz. *String Theory and M-Theory: A Modern Introduction*. Cambridge University Press, 2006.

[38] J. D. Bekenstein. Black holes and entropy. *Phys. Rev. D*, 7:2333, 1973.

[39] A. Belokogne and A. Folacci. Renormalized stress tensor for massive fields in Kerr-Newman spacetime. *Phys. Rev. D*, 90:044045, 2014.

[40] P. Beltrán-Palau, A. del Río, and J. Navarro-Salas. Quantum corrections to the Schwarzschild metric from vacuum polarization. *Phys. Rev. D*, 107(8):085023, 2023.

[41] I. Bengtsson. Anti-de Sitter space. https://3dhouse.se/ingemar/relteori/Kurs.pdf, 1998. Lecture notes.

[42] M. Benini, C. Dappiaggi, and A. Schenkel. Algebraic quantum field theory on spacetimes with timelike boundary. *Annales Henri Poincaré*, 19:2401, 2018.

[43] D. Bernard and A. Folacci. Hadamard function, stress tensor, and de Sitter space. *Phys. Rev. D*, 34:2286, 1986.

[44] L. Bianchi. Sui simboli a quattro indici e sulla curvatura di Riemann [On the four-index symbols and the Riemann curvature]. *Rendiconti della Reale Accademia dei Lincei*, 11:3, 1902.

[45] N. D. Birrell and P. C. W. Davies. *Quantum Fields in Curved Space*. Cambridge Monographs on Mathematical Physics. Cambridge University Press, 1982.

[46] R. Blumenhagen, D. Lüst, and S. Theisen. *Basic Concepts of String Theory*. Theoretical and Mathematical Physics. Springer, 2012.

[47] C. G. Bollini and J. J. Giambiagi. Dimensional renormalization: The number of dimensions as a regularizing parameter. *Nuovo Cim. B*, 12:20, 1972.

[48] L. Bombelli, J. Lee, D. Meyer, and R. D. Sorkin. Space-time as a causal set. *Phys. Rev. Lett.*, 59:521, 1987.

[49] M. Born, W. Heisenberg, and P. Jordan. Zur Quantenmechanik II [On quantum mechanics II]. *Z. Phys.*, 35:557, 1926.

[50] M. Born, W. Heisenberg, and P. Jordan. On quantum mechanics II. In B. L. van der Waerden, editor, *Sources of Quantum Mechanics*, page 321. North-Holland Publishing Company, 1967. [English translation].

[51] M. Born and P. Jordan. Zur Quantenmechanik [On quantum mechanics]. *Z. Phys.*, 34:858, 1925.

[52] M. Born and P. Jordan. On quantum mechanics. In B. L. van der Waerden, editor, *Sources of Quantum Mechanics*, page 277. North-Holland Publishing Company, 1967. [English translation].

[53] S. N. Bose. Plancks Gesetz und Lichtquantenhypothese [Planck's law and the hypothesis of light quanta]. *Zeitschrift für Physik*, 26:178, 1924. Translated by A. Einstein.

[54] W. E. Boyce and R. C. DiPrima. *Elementary differential equations and boundary value problems.* Wiley, Hoboken, N.J, tenth edition, 2013.

[55] C. Breen, G. Montagnon, P. Taylor, and E. Winstanley. Mode-sum prescription for renormalized expectation values for a charged quantum scalar field on a charged black hole. *Phys. Rev. D*, 111:045010, 2025.

[56] M. Bronstein. Quantum theory of weak gravitational fields. *Gen. Rel. Grav.*, 44:267, 2012.

[57] J. Bros, H. Epstein, and U. Moschella. Towards a general theory of quantized fields on the anti-de Sitter space-time. *Commun. Math. Phys.*, 231:481, 2002.

[58] J. Bros and U. Moschella. Two-point functions and quantum fields in de Sitter universe. *Rev. Math. Phys.*, 08:327, 1996.

[59] L. S. Brown and J. P. Cassidy. Stress tensors and their trace anomalies in conformally flat space-time. *Phys. Rev. D*, 16:1712, 1977.

[60] M. R. Brown and A. C. Ottewill. Effective actions and conformal transformations. *Phys. Rev. D*, 31:2514, 1985.

[61] M. R. Brown and A. C. Ottewill. Photon propagators and the definition and approximation of renormalized stress tensors in curved space-time. *Phys. Rev. D*, 34:1776, 1986.

[62] P. J. Brown, C. J. Fewster, and E.-A. Kontou. Classical and quantum strong energy inequalities and the Hawking singularity theorem. In *15th Marcel Grossmann Meeting on Recent Developments in Theoretical and Experimental General Relativity, Astrophysics, and Relativistic Field Theories*, 2019.

[63] R. Brunetti, C. Dappiaggi, K. Fredenhagen, and J. Yngvason. *Advances in Algebraic Quantum Field Theory*. Mathematical Physics Studies. Springer International Publishing, 2015.

[64] R. Brunetti, K. Fredenhagen, and K. Rejzner. Perturbative algebraic quantum field theory and beyond, 2025. [Published as preprint arXiv:2512.14227].

[65] R. Brunetti, K. Fredenhagen, and R. Verch. The generally covariant locality principle: A new paradigm for local quantum field theory. *Commun. Math. Phys.*, 237:31, 2003.

[66] T. S. Bunch and P. C. W. Davies. Covariant point-splitting regularization for a scalar quantum field in a Robertson-Walker universe with spatial curvature. *Proc. Roy. Soc. Lond. A*, 357:381, 1977.

[67] T. S. Bunch and P. C. W. Davies. Quantum field theory in de Sitter space: renormalization by point splitting. *Proc. Roy. Soc. Lond. A*, 360:117, 1978.

[68] C. Burgess and G. Moore. *The Standard Model: A Primer*. Cambridge University Press, 2006.

[69] F. Bussola, C. Dappiaggi, H. R. C. Ferreira, and I. Khavkine. Ground state for a massive scalar field in the BTZ spacetime with Robin boundary conditions. *Phys. Rev. D*, 96:105016, 2017.

[70] C. G. Callan, S. R. Coleman, and R. Jackiw. A new improved energy-momentum tensor. *Ann. Phys.*, 59:42, 1970.

[71] P. Candelas and J. S. Dowker. Field theories on conformally related space-times: Some global considerations. *Phys. Rev. D*, 19:2902, 1979.

[72] R. Carballo-Rubio. Stellar equilibrium in semiclassical gravity. *Phys. Rev. Lett.*, 120:061102, 2018.

[73] R. Carballo-Rubio, F. Di Filippo, S. Mukohyama, and K. Okabayashi. Macroscopic backreaction of the trace anomaly on classical vacuum backgrounds, 2025. [Published as preprint arXiv:2512.10710].

[74] C. Y. Cardall, E. Endeve, and A. Mezzacappa. Conservative 3+1 general relativistic Boltzmann equation. *Phys. Rev. D*, 88:023011, 2013.

[75] S. M. Carroll. *Spacetime and Geometry: An Introduction to General Relativity.* Cambridge University Press, Cambridge, 2019.

[76] M. Casals, A. Fabbri, C. Martínez, and J. Zanelli. Quantum backreaction on three-dimensional black holes and naked singularities. *Phys. Rev. Lett.*, 118:131102, 2017.

[77] M. Casals, A. Fabbri, C. Martínez, and J. Zanelli. Quantum fields as cosmic censors in $(2+1)$-dimensions. *Int. J. Mod. Phys. D*, 27:1843011, 2018.

[78] M. Casals, A. Fabbri, C. Martínez, and J. Zanelli. Quantum-corrected rotating black holes and naked singularities in $(2+1)$ dimensions. *Phys. Rev. D*, 99:104023, 2019.

[79] C. Cercignani. *The Boltzmann Equation and Its Applications.* Springer-Verlag, New York, 1988.

[80] S. Chakraborty, S. Singh, and T. Padmanabhan. A quantum peek inside the black hole event horizon. *JHEP*, 2015:157, 2015.

[81] S. Chandrasekhar. *The Mathematical Theory of Black Holes.* Oxford Classic Texts in the Physical Sciences. Oxford Univ. Press, Oxford, 2002.

[82] S.-S. Chern. A simple intrinsic proof of the Gauss-Bonnet formula for closed Riemannian manifolds. *Ann. Math.*, 45:747, 1944.

[83] N. A. Chernikov and E. A. Tagirov. Quantum theory of scalar field in de Sitter space-time. *Ann. Inst. H. Poincare Phys. Theor. A*, 9:109, 1968.

[84] S. M. Christensen. Vacuum expectation value of the stress tensor in an arbitrary curved background: The covariant point-separation method. *Phys. Rev. D*, 14:2490, 1976.

[85] E. G. D. Cohen and W. Thirring, editors. *The Boltzmann Equation: Theory and Applications*, volume 10 of *Few-Body Systems.* Springer Vienna, 1973.

[86] S. R. Coleman. There are no Goldstone bosons in two-dimensions. *Commun. Math. Phys.*, 31:259, 1973.

[87] S. R. Coleman. *Lectures of Sidney Coleman on quantum field theory.* World Scientific, Singapore, 2018.

[88] Wikimedia Commons. Standard model of elementary particles, 2025. By Cush - Own work using:PBS NOVA [1], Fermilab, Office of Science, United States Department of Energy, Particle Data Group, Public Domain, https://commons.wikimedia.org/w/index.php?curid=4286964.

[89] I. I. Cotăescu. Dirac fermions in de Sitter and anti-de Sitter backgrounds. *Rom. J. Phys.*, 52:895, 2007.

[90] E. Curiel. A Primer on Energy Conditions. In *Towards a Theory of Spacetime Theories*, page 43. Springer New York, 2017.

[91] C. Dappiaggi and H. R. C. Ferreira. Hadamard states for a scalar field in anti–de Sitter spacetime with arbitrary boundary conditions. *Phys. Rev. D*, 94:125016, 2016.

[92] C. Dappiaggi and H. R. C. Ferreira. On the algebraic quantization of a massive scalar field in anti-de-Sitter spacetime. *Rev. Math. Phys.*, 30:1850004, 2017.

[93] C. Dappiaggi, H. R. C. Ferreira, and B. A. Juárez-Aubry. Mode solutions for a Klein-Gordon field in anti–de Sitter spacetime with dynamical boundary conditions of Wentzell type. *Phys. Rev. D*, 97:085022, 2018.

[94] C. Dappiaggi, K. Fredenhagen, and N. Pinamonti. Stable cosmological models driven by a free quantum scalar field. *Phys. Rev. D*, 77:104015, 2008.

[95] C. Dappiaggi, B. A. Juárez-Aubry, and A. Marta. Ground state for the Klein-Gordon field in anti–de Sitter spacetime with dynamical Wentzell boundary conditions. *Phys. Rev. D*, 105:105017, 2022.

[96] C. Dappiaggi and A. Marta. Fundamental solutions and Hadamard states for a scalar field with arbitrary boundary conditions on an asymptotically AdS spacetimes. *Math. Phys. Anal. Geom.*, 24:28, 2021.

[97] P. C. W. Davies, T. Dray, and C. A. Manogue. Detecting the rotating quantum vacuum. *Phys. Rev. D*, 53:4382, 1996.

[98] L. de Broglie. Waves and quanta. *Nature*, 112:540, 1923.

[99] J.-L. de La Grange. Essai d'une nouvelle méthode pour déterminer les maxima et les minima des formules intégrales indéfinies [Essay on a new method to determine the maxima and minima of indefinite integral formulas]. *Miscellanea Taurinensia*, 2:173, 1762.

[100] W. de Sitter. On the curvature of space. *Proc. Kon. Ned. Acad. Wet.*, 20:229, 1917.

[101] W. de Sitter. On the relativity of inertia. Remarks concerning Einstein's latest hypothesis. *Proc. K. Ned. Akad. Wet., Ser. B.*, 19:1217, 1917.

[102] L. De Souza Campos, C. Dappiaggi, and L. Sinibaldi. Hidden freedom in the mode expansion on static spacetimes. *Gen. Rel. Grav.*, 55:50, 2023.

[103] Y. Décanini and A. Folacci. Hadamard renormalization of the stress-energy tensor for a quantized scalar field in a general spacetime of arbitrary dimension. *Phys. Rev. D*, 78:044025, 2008.

[104] A. del Rio. The backreaction problem for black holes in semiclassical gravity. *Gen. Rel. Grav.*, 57:30, 2025.

[105] B. S. DeWitt. Dynamical theory of groups and fields. In C. DeWitt and B. S. DeWitt, editors, *Relativité, Groupes et Topologie*, page 585, 1964.

[106] B. S. DeWitt. *Dynamical Theory of Groups and Fields.* Documents on Modern Physics. Gordon and Breach, New York, 1965.

[107] B. S. DeWitt. Quantum theory of gravity. I. The canonical theory. *Phys. Rev.*, 160:1113, 1967.

[108] B. S. DeWitt. Quantum field theory in curved space-time. *Phys. Rept.*, 19:295, 1975.

[109] B. S. DeWitt and R. W. Brehme. Radiation damping in a gravitational field. *Ann. Phys.*, 9:220, 1960.

[110] P. A. M. Dirac. The quantum theory of the emission and absorption of radiation. *Proc. Roy. Soc. Lond. A*, 114:243, 1927.

[111] P. A. M. Dirac. The quantum theory of the electron. *Proc. Roy. Soc. Lond. A*, 117:610, 1928.

[112] P. A. M. Dirac. A theory of electrons and protons. *Proc. Roy. Soc. Lond. A*, 126:360, 1930.

[113] P. A. M. Dirac. *The Principles of Quantum Mechanics*. The International Series of Monographs on Physics. Clarendon Press, Oxford, 1930.

[114] P. A. M. Dirac. Generalized Hamiltonian dynamics. *Proc. Roy. Soc. Lond. A*, 246:326, 1958.

[115] J. S. Dowker and G. Kennedy. Finite temperature and boundary effects in static space-times. *J. Phys. A*, 11:895, 1978.

[116] G. Duffy and A. C. Ottewill. The rotating quantum thermal distribution. *Phys. Rev. D*, 67:044002, 2003.

[117] M. Dütsch. *From Classical Field Theory to Perturbative Quantum Field Theory*. Springer, 2019.

[118] E. Dyer and K. Hinterbichler. Boundary Terms, Variational Principles and Higher Derivative Modified Gravity. *Phys. Rev. D*, 79:024028, 2009.

[119] F. Dyson. Is a graviton detectable? In *Poincare Prize Lecture, International Congress of Mathematical Physics*. Aalborg, Denmark, 2012. Published in: Proceedings of the Conference in Honour of the 90th Birthday of Freeman Dyson, World Scientific, 2014.

[120] T. Eguchi, P. B. Gilkey, and A. J. Hanson. Gravitation, gauge theories and differential geometry. *Phys. Rept.*, 66:213, 1980.

[121] A. Eichhorn. An asymptotically safe guide to quantum gravity and matter. *Front. Astron. Space Sci.*, 5:47, 2019.

[122] A. Einstein. Über einen die Erzeugung und Verwandlung des Lichtes betreffenden heuristischen Gesichtspunkt [On a heuristic point of view concerning the generation and transformation of light]. *Ann. Phys. (Berlin)*, 322:132, 1905.

[123] A. Einstein. Zur Elektrodynamik bewegter Körper [On the electrodynamics of moving bodies]. *Ann. Phys. (Berlin)*, 322:891, 1905.

[124] A. Einstein. Die Feldgleichungen der Gravitation [The field equations of gravitation]. *Sitzungsber. Preuß. Akad. Wiss. Berlin (Math. Phys.)*, 1915:844, 1915.

[125] A. Einstein. Zur Allgemeinen Relativitätstheorie [On the general theory of relativity]. *Sitzungsber. Preuß. Akad. Wiss. Berlin (Math. Phys.)*, 1915:778, 1915. [Addendum: *Sitzungsber. Preuß. Akad. Wiss. Berlin (Math. Phys.)* (1915)].

[126] A. Einstein. Die Grundlage der allgemeinen Relativitätstheorie [The foundation of the general theory of relativity]. *Ann. Phys. (Berlin)*, 49:769, 1916.

[127] A. Einstein. Näherungsweise Integration der Feldgleichungen der Gravitation [Approximative integration of the field equations of gravitation]. *Sitzungsber. Preuß. Akad. Wiss. Berlin (Math. Phys.)*, 1916:688, 1916.

[128] A. Einstein. Kosmologische Betrachtungen zur allgemeinen Relativitätstheorie [Cosmological considerations in the general theory of relativity]. *Sitzungsber. Königlich Preuß. Akad. Wiss. Berlin*, 1917:142, 1917.

[129] A. Einstein. Quantentheorie des einatomigen idealen Gases [Quantum theory of a monoatomic ideal gas]. *Sitzungsber. Preuß. Akad. Wiss. Berlin (Math. Phys.)*, 1924:261, 1924.

[130] E. Elizalde, S. D. Odintsov, A. Romeo, A. A. Bytsenko, and S. Zerbini. *Zeta regularization techniques with applications.* World Scientific Publishing, Singapore, 1994.

[131] H. Epstein, V. Glaser, and A. Jaffe. Nonpositivity of energy density in quantized field theories. *Nuovo Cim.*, 36:1016, 1965.

[132] L. Euler. *Methodus inveniendi lineas curvas maximi minimive proprietate gaudentes, sive solutio problematis isoperimetrici latissimo sensu accepti [A method for finding*

*curved lines enjoying properties of maximum or minimum, or solution of isoperimetric problems in the broadest accepted sense].* Marcum-Michaelem Bousquet, Lausanne and Geneva, 1744.

[133] L. C. Evans. *Partial Differential Equations*, volume 19 of *Graduate Studies in Mathematics*. American Mathematical Society, Providence, R.I., 2010.

[134] S. P. Eveson, C. J. Fewster, and R. Verch. Quantum inequalities in quantum mechanics. *Ann. Henri Poincaré*, 6:1, 2005.

[135] A. Fabbri and J. Navarro-Salas. *Modeling Black Hole Evaporation*. Imperial College Press, 2005.

[136] A. L. Fetter and J. D. Walecka. *Quantum Theory of Many-particle Systems*. International series in pure and applied physics. McGraw-Hill, 1971.

[137] C. J. Fewster. A general worldline quantum inequality. *Classical and Quantum Gravity*, 17:1897, 2000.

[138] C. J. Fewster. Lectures on quantum field theory in curved spacetime, 2008. Lectures given at the Max Planck Institute for Mathematics in the Sciences, Leipzig. [Available at https://www.mis.mpg.de/preprints/ln/lecturenote-3908.pdf].

[139] C. J. Fewster. Lectures on quantum energy inequalities, 2012. Lectures given at the Albert Einstein Institute, Golm. [Available as preprint arXiv:1208.5399].

[140] C. J. Fewster. Quantum energy inequalities. In F. S. N. Lobo, editor, *Wormholes, Warp Drives and Energy Conditions*, page 215. Springer International Publishing, Cham, Switzerland, 2017.

[141] C. J. Fewster and S. P. Eveson. Bounds on negative energy densities in flat spacetime. *Phys. Rev. D*, 58:084010, 1998.

[142] C. J. Fewster and E.-A. Kontou. Quantum strong energy inequalities. *Phys. Rev. D*, 99:045001, 2019.

[143] C. J. Fewster and K. Rejzner. Algebraic Quantum Field Theory. In F. Finster, D. Giulini, J. Kleiner, and J. Tolksdorf, editors, *Progress and Visions in Quantum Theory in View of Gravity*, Cham, Switzerland, 2020. Springer International Publishing.

[144] C. J. Fewster and J. C. Thompson. Quantum energy inequalities along stationary worldlines. *Class. Quant. Grav.*, 40:175008, 2023.

[145] C. J. Fewster and R. Verch. The necessity of the Hadamard condition. *Class. Quant. Grav.*, 30:235027, 2013.

[146] C. J. Fewster and R. Verch. Algebraic quantum field theory in curved spacetimes. In *Advances in Algebraic Quantum Field Theory*, page 125. Springer International Publishing, Cham, Switzerland, 2015.

[147] M. V. Fischetti, J. B. Hartle, and B.-L. Hu. Quantum effects in the early universe. I. Influence of trace anomalies on homogeneous, isotropic, classical geometries. *Phys. Rev. D*, 20:1757, 1979.

[148] É. É. Flanagan and R. M. Wald. Does back reaction enforce the averaged null energy condition in semiclassical gravity? *Phys. Rev. D*, 54:6233, 1996.

[149] É. É. Flanagan. Quantum inequalities in two-dimensional Minkowski spacetime. *Phys. Rev. D*, 56:4922, 1997.

[150] L. H. Ford. Quantum coherence effects and the second law of thermodynamics. *Proc. Roy. Soc. Lond. A*, 364:227, 1978.

[151] L. H. Ford. Quantum field theory in curved space-time. In J. C. A. Barata, A. P. C. Malbouisson, and S. F. Novaes, editors, *Particles and Fields. Proceedings, 9th Jorge Andre Swieca Summer School, Campos do Jordao, Brazil*, page 345, 1997.

[152] K. Fredenhagen and K. Rejzner. Perturbative algebraic quantum field theory. In D. Calaque and T. Strobl, editors, *Winter School in Mathematical Physics: Mathematical Aspects of Quantum Field Theory*, page 17. Springer, 2012.

[153] A. Friedmann. Über die Krümmung des Raumes [On the curvature of space]. *Z. Phys.*, 10:377, 1922.

[154] A. Friedmann. Über die Möglichkeit einer Welt mit konstanter negativer Krümmung des Raumes [On the possibility of a world with constant negative curvature of space]. *Z. Phys.*, 21:326, 1924.

[155] V. P. Frolov and A. I. Zelnikov. Vacuum polarization of massive fields in algebraically special spaces. *Phys. Rev. D*, 35:3031, 1987.

[156] S. A. Fulling. Nonuniqueness of canonical field quantization in Riemannian space-time. *Phys. Rev. D*, 7:2850, 1973.

[157] S. A. Fulling. *Aspects of quantum field theory in curved space-time.* London Mathematical Society student texts. Cambridge University Press, 1989.

[158] S. A. Fulling, F. J. Narcowich, and R. M. Wald. Singularity structure of the two-point function in quantum field theory in curved spacetime, II. *Ann. Phys.*, 136:243, 1981.

[159] S. A. Fulling, M. Sweeny, and R. M. Wald. Singularity structure of the two point function in quantum field theory in curved space-time. *Commun. Math. Phys.*, 63:257, 1978.

[160] R. Gambini and J. Pullin. *A First Course in Loop Quantum Gravity.* Oxford University Press, 2011.

[161] G. Gamow. The evolutionary universe. *Sci. Am.*, 195:136, 1956.

[162] G. Gamow. *My World Line: An Informal Autobiography.* Viking Press, New York, 1970.

[163] O. Gannot and M. Wrochna. Propagation of singularities on AdS spacetimes for general boundary conditions and the holographic Hadamard condition. *J. Inst. Math. Jussieu*, 21:67, 2022.

[164] S. Gasiorowicz. *Quantum Physics.* John Wiley & Sons, 2003.

[165] E. Gath. Lehmann representation of the spinor two-point function in anti-de Sitter space. *Class. Quant. Grav.*, 6:745, 1989.

[166] J. Géhéniau and C. Schomblond. Green's functions in a de Sitter universe. *Bull. Acad. Roy. Sci. Belgique*, 64:555, 1968.

[167] G. W. Gibbons. Anti-de-Sitter spacetime and its uses. In S. Cotsakis and G. W. Gibbons, editors, *2nd Samos Meeting on Cosmology, Geometry and Relativity: Mathematical and Quantum Aspects of Relativity and Cosmology*, page 102, 2011.

[168] G. W. Gibbons and S. W. Hawking. Action Integrals and Partition Functions in Quantum Gravity. *Phys. Rev. D*, 15:2752, 1977.

[169] G. W. Gibbons and S. W. Hawking. Cosmological event horizons, thermodynamics, and particle creation. *Phys. Rev. D*, 15:2738, 1977.

[170] K. Gödel. An example of a new type of cosmological solutions of Einstein's field equations of gravitation. *Rev. Mod. Phys.*, 21:447, 1949.

[171] H. Gottschalk, N. R. Rothe, and D. Siemssen. Cosmological de Sitter solutions of the semiclassical Einstein equation. *Ann. Henri Poincare*, 24:2949, 2023.

[172] G. Green. *An Essay on the Application of Mathematical Analysis to the Theories of Electricity and Magnetism.* T. Wheelhouse, Nottingham, 1828.

[173] G. Green. *An Essay on the Application of Mathematical Analysis to the Theories of Electricity and Magnetism*, page 1–82. Cambridge Library Collection - Mathematics. Cambridge University Press, 2014. [Remastered version].

[174] M. B. Green, J. H. Schwarz, and E. Witten. *Superstring Theory: Volume 1, Introduction.* Cambridge Monographs on Mathematical Physics. Cambridge University Press, 1987.

[175] M. B. Green, J. H. Schwarz, and E. Witten. *Superstring Theory: Volume 2, Loop Amplitudes, Anomalies and Phenomenology.* Cambridge Monographs on Mathematical Physics. Cambridge University Press, 1987.

[176] R. D. Gregory. *Classical Mechanics.* Cambridge University Press, 2006.

[177] J. B. Griffiths and J. Podolský. *Exact Space-Times in Einstein's General Relativity.* Cambridge Monographs on Mathematical Physics. Cambridge University Press, 2009.

[178] S. R. Groot, W. A. Leeuwen, and C. G. van Weert. *Relativistic Kinetic Theory: Principles and Applications.* North-Holland Publishing Company, 1980.

[179] A. H. Guth. Inflationary universe: A possible solution to the horizon and flatness problems. *Phys. Rev. D*, 23(2):347–356, 1981.

[180] R. Haag. *Local Quantum Physics: Fields, Particles, Algebras.* Theoretical and Mathematical Physics. Springer-Verlag, 1992.

[181] R. Haag and D. Kastler. An algebraic approach to quantum field theory. *J. Math. Phys.*, 5:848, 1964.

[182] J. Hadamard. *Lectures on Cauchy's problem in linear partial differential equations.* Yale University. Yale University Press, New York, 1923.

[183] R. J. Hakim. *Introduction to Relativistic Statistical Mechanics: Classical and Quantum.* World Scientific Publishing Co., Singapore, 2011.

[184] W. R. Hamilton. On a general method in dynamics; by which the study of the motions of all free systems of attracting or repelling points is reduced to the search and differentiation of one central relation, or characteristic function. *Phil. Trans. Roy. Soc. Lond.*, 124:247, 1834.

[185] J. B. Hartle and B.-L. Hu. Quantum effects in the early universe. II. Effective action for scalar fields in homogeneous cosmologies with small anisotropy. *Phys. Rev. D*, 20:1772, 1979.

[186] J. B. Hartle and B.-L. Hu. Quantum effects in the early universe. III. Dissipation of anisotropy by scalar particle production. *Phys. Rev. D*, 21:2756, 1980.

[187] S. W. Hawking. Black hole explosions? *Nature*, 248:30, 1974.

[188] S. W. Hawking. Particle creation by black holes. *Comm. Math. Phys.*, 43:199, 1975.

[189] S. W. Hawking. Zeta function regularization of path integrals in curved space-time. *Commun. Math. Phys.*, 55:133, 1977.

[190] S. W. Hawking and G. F. R. Ellis. *The Large Scale Structure of Space-Time.* Cambridge Monographs on Mathematical Physics. Cambridge University Press, 1973.

[191] S. W. Hawking and D. N. Page. Thermodynamics of black holes in anti-de Sitter space. *Commun. Math. Phys.*, 87:577, 1983.

[192] W. Heisenberg. Über quantentheoretische Umdeutung kinematischer und mechanischer Beziehungen [Quantum theoretical re-interpretation of kinematic and mechanical relations]. *Z. Phys.*, 33:879, 1925.

[193] W. Heisenberg. Bemerkungen zur Diracschen Theorie des Positrons [Remarks on the Dirac theory of the positron]. *Z. Phys.*, 90:209, 1934. [Erratum: Z.Phys. 92, 692 (1934)].

[194] W. Heisenberg. Quantum-Theoretical Re-interpretation of Kinematic and Mechanical Relations. In B. L. van der Waerden, editor, *Sources of Quantum Mechanics*, page 261. North-Holland Publishing Company, 1967. [English translation].

[195] J. Henson. The causal set approach to quantum gravity. In D. Oriti, editor, *Approaches to Quantum Gravity: Toward a New Understanding of Space, Time and Matter*, page 393. Cambridge University Press, 2009.

[196] D. Hochberg, A. Popov, and S. V. Sushkov. Self-consistent wormhole solutions of semiclassical gravity. *Phys. Rev. Lett.*, 78:2050, 1997.

[197] J. M. Hoene-Wroński. *Réfutation de la théorie des fonctions analytiques de Lagrange [Refutation of the theory of analytic functions of Lagrange]*. Chez Blankenstein, Paris, 1812. Dediée à l'Institut Impérial de France.

[198] S. Hopper and B. Wardell. Black Hole Perturbation Toolkit: GeneralRelativityTensors. (bhptoolkit.org).

[199] B.-L. Hu and A. Matacz. Back reaction in semiclassical cosmology: The Einstein-Langevin equation. *Phys. Rev. D*, 51:1577, 1995.

[200] B.-L. Hu and L. Parker. Anisotropy damping through quantum effects in the early universe. *Phys. Rev. D*, 17:933, 1978.

[201] B.-L. Hu and E. Verdaguer. *Semiclassical and Stochastic Gravity: Quantum Field Effects on Curved Spacetime*. Cambridge University Press, 2020.

[202] E. Hubble. A relation between distance and radial velocity among extra-galactic nebulae. *Proc. Natl. Acad. Sci. USA*, 15:168, 1929.

[203] C. J. Isham. Canonical quantum gravity and the problem of time. *NATO Sci. Ser. C*, 409:157, 1993.

[204] C. J. Isham. Prima facie questions in quantum gravity. In J. Ehlers and H. Friedrich, editors, *Canonical Gravity: From Classical to Quantum*, page 1. Springer, Berlin, Heidelberg, 1994.

[205] A. Ishibashi and R. M. Wald. Dynamics in non-globally-hyperbolic static spacetimes: II. General analysis of prescriptions for dynamics. *Class. Quant. Grav.*, 20:3815, 2003.

[206] A. Ishibashi and R. M. Wald. Dynamics in non-globally-hyperbolic static spacetimes: III. Anti-de Sitter spacetime. *Class. Quant. Grav.*, 21:2981, 2004.

[207] C. Itzykson and J. B. Zuber. *Quantum Field Theory*. International Series in Pure and Applied Physics. McGraw-Hill, New York, 1980.

[208] B. A. Juárez-Aubry. Semi-classical gravity in de Sitter spacetime and the cosmological constant. *Phys. Lett. B*, 797:134912, 2019.

[209] B. A. Juárez-Aubry. Semiclassical gravity in static spacetimes as a constrained initial value problem. *Ann. Henri Poincaré*, 23:1451, 2022.

[210] B. A. Juárez-Aubry. Recent developments in semiclassical gravity. In *24th International Conference on General Relativity and Gravitation (GR24) and 16th Edoardo Amaldi Conference on Gravitational (Amaldi16) Waves*, 2025.

[211] B. A. Juárez-Aubry, B. S. Kay, T. Miramontes, and D. Sudarsky. On the initial value problem for semiclassical gravity without and with quantum state collapses. *J. Cosmol. Astropart. Phys.*, 01:040, 2023.

[212] B. A. Juárez-Aubry and M. C. Mamani-Leqque. Renormalisation in maximally symmetric spaces and semiclassical gravity in Anti-de Sitter spacetime. *Class. Quant. Grav.*, 42:085009, 2025.

[213] B. A. Juárez-Aubry and S. K. Modak. Semiclassical gravity with a conformally covariant field in globally hyperbolic spacetimes. *J. Math. Phys.*, 63:092303, 2022.

[214] B. A. Juárez-Aubry. A new class of semiclassical gravity solutions, gravitational quantum stealths and regular cauchy horizons. *Phys. Lett. B*, 875:140349, 2026.

[215] L. P. Kadanoff and G. Baym. *Quantum Statistical Mechanics.* W.A. Benjamin Inc., New York, 1962.

[216] J. I. Kapusta and C. Gale. *Finite-Temperature Field Theory: Principles and Applications*, volume 2. Cambridge University Press, Cambridge, 2006.

[217] B. S. Kay. Linear spin-zero quantum fields in external gravitational and scalar fields. *Commun. Math. Phys.*, 71:29–46, 1978.

[218] B. S. Kay. The double wedge algebra for quantum fields on Schwarzschild and Minkowski space-times. *Commun. Math. Phys.*, 100:57, 1985.

[219] B. S. Kay and R. M. Wald. Theorems on the uniqueness and thermal properties of stationary, nonsingular, quasifree states on spacetimes with a bifurcate Killing horizon. *Phys. Rept.*, 207:49, 1991.

[220] C. Kent. *Quantum scalar field theory on anti-de Sitter space.* PhD thesis, University of Sheffield, 2013.

[221] C. Kent and E. Winstanley. Hadamard renormalized scalar field theory on anti–de Sitter spacetime. *Phys. Rev. D*, 91:044044, 2015.

[222] C. Kent and E. Winstanley. The global rotating scalar field vacuum on anti-de Sitter space–time. *Phys. Lett. B*, 740:188, 2015.

[223] R. P. Kerr. Gravitational field of a spinning mass as an example of algebraically special metrics. *Phys. Rev. Lett.*, 11:237, 1963.

[224] I. Khavkine and V. Moretti. Algebraic QFT in curved spacetime and quasifree Hadamard states: An introduction. In R. Brunetti, C. Dappiaggi, K. Fredenhagen, and J. Yngvason, editors, *Advances in Algebraic Quantum Field Theory*, page 191. Springer International Publishing, 2015.

[225] T. W. B. Kibble and F. H. Berkshire. *Classical Mechanics*. Imperial College Press, 2004.

[226] E. Kiritsis. *String Theory in a Nutshell*. Princeton University Press, 2007.

[227] C. Kittel and H. Kroemer. *Thermal Physics*. W. H. Freeman and Company, San Francisco, 1980.

[228] B. Kleihaus and J. Kunz. Static black hole solutions with axial symmetry. *Phys. Rev. Lett.*, 79:1595, 1997.

[229] S. Konewko and E. Winstanley. Charge superradiance on charged BTZ black holes. *Eur. Phys. J. C*, 84:594, 2024.

[230] E.-A. Kontou. Wormhole restrictions from quantum energy inequalities. *Universe*, 10:291, 2024.

[231] E.-A. Kontou and K. Sanders. Energy conditions in general relativity and quantum field theory. *Class. Quant. Grav.*, 37:193001, 2020.

[232] C.-I. Kuo and L. H. Ford. Semiclassical gravity theory and quantum fluctuations. *Phys. Rev. D*, 47:4510, 1993.

[233] C. Lanczos. A remarkable property of the Riemann-Christoffel tensor in four dimensions. *Ann. Math.*, 39:842, 1938.

[234] L. D. Landau and E. M. Lifshitz. *The Classical Theory of Fields*, volume 2 of *Course of Theoretical Physics*. Butterworth-Heinemann, 4th edition, 1975.

[235] L. D. Landau and E. M. Lifshitz. *Statistical Physics, Part 1*, volume 5 of *Course of Theoretical Physics*. Butterworth-Heinemann, Oxford, 1980.

[236] S. Lang. *Complex Analysis*. Graduate Texts in Mathematics. Springer-Verlag, New York, 1999.

[237] U. Le Verrier. Lettre de M. Le Verrier à M. Faye sur la théorie de Mercure et sur le mouvement du périhélie de cette planète [Letter from Mr Le Verrier to Mr Faye on the theory of Mercury and on the perihelion movement of this planet]. *Compt. Rend. Hebd. Seances Acad. Sci.*, 49:379, 1859.

[238] G. Lemaître. Un Univers homogène de masse constante et de rayon croissant rendant compte de la vitesse radiale des nébuleuses extra-galactiques [Expansion of the universe, a homogeneous universe of constant mass and increasing radius accounting for the radial velocity of extra-galactic nebulae]. *Ann. Soc. Sci. Brux.*, 47:49, 1927.

[239] G. Lemaître. L'Univers en expansion [The expanding Universe]. *Ann. Soc. Sci. Brux.*, 53:51, 1933.

[240] J. R. Letaw and J. D. Pfautsch. The quantized scalar field in the stationary coordinate systems of flat space-time. *Phys. Rev. D*, 24:1491, 1981.

[241] A. Levi, E. Eilon, A. Ori, and M. van de Meent. Renormalized stress-energy tensor of an evaporating spinning black hole. *Phys. Rev. Lett.*, 118:141102, 2017.

[242] A. Levi and A. Ori. Versatile method for renormalized stress-energy computation in black-hole spacetimes. *Phys. Rev. Lett.*, 117:231101, 2016.

[243] G. Lifschytz and M. Ortiz. Scalar field quantization on the (2+1)-dimensional black hole background. *Phys. Rev. D*, 49:1929, 1994.

[244] M. Livio. *Brilliant Blunders: From Darwin to Einstein - Colossal Mistakes by Great Scientists That Changed Our Understanding of Life and the Universe.* Simon and Schuster, New York, 2013.

[245] D. Lovelock. The Einstein tensor and its generalizations. *J. Math. Phys.*, 12:498, 1971.

[246] M. Ludvigsen. *General Relativity: A Geometric Approach.* Cambridge University Press, Cambridge, 1999.

[247] J. M. Maldacena. The Large $N$ limit of superconformal field theories and supergravity. *Adv. Theor. Math. Phys.*, 2:231, 1998.

[248] C. Martínez and J. Zanelli. Conformally dressed black hole in 2 + 1 dimensions. *Phys. Rev. D*, 54:3830, 1996.

[249] C. Martínez and J. Zanelli. Back reaction of a conformal field on a three-dimensional black hole. *Phys. Rev. D*, 55:3642, 1997.

[250] T. Matsubara. A new approach to quantum statistical mechanics. *Prog. Theor. Phys.*, 14:351, 1955.

[251] R. D. Mattuck. *A Guide to Feynman Diagrams in the Many-Body Problem.* Dover Books on Physics. Dover Publications, 2012.

[252] J. Matyjasek. Stress-energy tensor of neutral massive fields in the Reissner-Nordström spacetime. *Phys. Rev. D*, 61:124019, 2000.

[253] J. Matyjasek. Vacuum polarization of massive scalar fields in the spacetime of the electrically charged nonlinear black hole. *Phys. Rev. D*, 63:084004, 2001.

[254] J. Matyjasek. Quantized massive scalar fields in the spacetime of a charged dilatonic black hole. *Acta Phys. Pol. B*, 34:3921, 2003.

[255] J. Matyjasek and P. Sadurski. Stress-energy tensor of the quantized massive fields in Schwarzschild-Tangherlini spacetimes: The back reaction. *Phys. Rev. D*, 91:044027, 2015.

[256] J. Matyjasek and D. Tryniecki. Next-to-leading term of the renormalized stress-energy tensor of the quantized massive scalar field in Schwarzschild spacetime: The back reaction. *Phys. Rev. D*, 79:084017, 2009.

[257] J. Matyjasek, D. Tryniecki, and K. Zwierzchowska. Vacuum polarization of the quantized massive scalar field in Reissner-Nordström spacetime. *Phys. Rev. D*, 81:124047, 2010.

[258] J. Matyjasek and K. Zwierzchowska. Next-to-leading terms of the renormalized stress-energy tensor of the quantized massive fields in the Reissner-Nordström spacetime. *Phys. Rev. D*, 85:024009, 2012.

[259] P. Meda, N. Pinamonti, and D. Siemssen. Existence and uniqueness of solutions of the semiclassical Einstein equation in cosmological models. *Ann. Henri Poincaré*, 22:3965, 2021.

[260] M. R. Mehdizadeh, A. H. Ziaie, and F. S. N. Lobo. Trace anomaly contributions to semiclassical wormhole geometries. *Phys. Rev. D*, 113:064008, 2026.

[261] A. A. Michelson and E. W. Morley. On the relative motion of the Earth and the luminiferous ether. *Am. J. Sci.*, s3-34:333, 1887.

[262] C. W. Misner, K. S. Thorne, and J. A. Wheeler. *Gravitation*. W. H. Freeman, San Francisco, 1973.

[263] S. Morales-Tejera, V. E. Ambruş, and M. N. Chernodub. Vortical waves in a quantum fluid with vector, axial, and helical charges. I. Non-dissipative transport. *Eur. Phys. J. C*, 84:1320, 2024.

[264] S. Morales-Tejera, V. E. Ambruş, and M. N. Chernodub. Vortical waves in a quantum fluid with vector, axial and helical charges. II. Dissipative effects. *Eur. Phys. J. C*, 85:89, 2025.

[265] V. Moretti. On the global Hadamard parametrix in QFT and the signed squared geodesic distance defined in domains larger than convex normal neighbourhoods. *Lett. Math. Phys.*, 111:130, 2021.

[266] T. Morley, S. Namasivayam, and E. Winstanley. Renormalized stress-energy tensor on global anti-de Sitter space-time with Robin boundary conditions. *Gen. Rel. Grav.*, 56:38, 2024.

[267] T. Morley, P. Taylor, and E. Winstanley. Quantum field theory on global anti-de Sitter space-time with Robin boundary conditions. *Class. Quant. Grav.*, 38:035009, 2021.

[268] T. Morley, P. Taylor, and E. Winstanley. Vacuum polarization on topological black holes with Robin boundary conditions. *Phys. Rev. D*, 103:045007, 2021.

[269] U. Moschella. The de Sitter and anti-de Sitter sightseeing tour. In *Einstein's Greatest Secret: Séminaire Poincaré*, page 1. Birkhäuser, Basel, 2005.

[270] E. Mottola. Particle creation in de Sitter space. *Phys. Rev. D*, 31:754, 1985.

[271] V. Mukhanov and S. Winitzki. *Introduction to Quantum Effects in Gravity*. Cambridge University Press, 2007.

[272] V. F. Mukhanov and G. V. Chibisov. Quantum fluctuations and a nonsingular universe. *JETP Lett.*, 33(10):532–535, 1981.

[273] S. Namasivayam. *Quantum scalar field theory on anti-de Sitter space-time with Robin boundary conditions*. PhD thesis, The University of Sheffield, 2024.

[274] S. Namasivayam and E. Winstanley. Vacuum polarization on three-dimensional anti-de Sitter space-time with Robin boundary conditions. *Gen. Rel. Grav.*, 55:13, 2023.

[275] S. Namasivayam and E. Winstanley. Nonminimal coupling, quantum scalar field stress-energy tensor and energy conditions on global anti-de Sitter space-time. *Gen. Rel. Grav.*, 57:81, 2025.

[276] S. Namasivayam and E. Winstanley. Quantum-corrected adS3. In preparation, 2026.

[277] S. Navas et al. Review of particle physics. *Phys. Rev. D*, 110:030001, 2024.

[278] Isaac Newton. *Philosophiæ Naturalis Principia Mathematica [Mathematical Principles of Natural Philosophy]*. Roy. Soc. Lond., England, 1687.

[279] K. Numajiri, K. Okabayashi, and S. Mukohyama. Boulware vacuum vs regularity: Thoughts on anomaly-induced effective action. *Phys. Rev. D*, 111:085024, 2025.

[280] F. Olver, D. Lozier, R. Boisvert, and C. Clark. *The NIST Handbook of Mathematical Functions*. Cambridge University Press, New York, NY, 2010.

[281] J. R. Oppenheimer and G. M. Volkoff. On massive neutron cores. *Phys. Rev.*, 55:374, 1939.

[282] C. O'Raifeartaigh and S. Mitton. Interrogating the legend of Einstein's "Biggest Blunder". *Phys. Perspect.*, 20:318, 2018.

[283] D. N. Page. Thermal stress tensors in static Einstein spaces. *Phys. Rev. D*, 25:1499, 1982.

[284] A. Palatini. Deduzione invariantiva delle equazioni gravitazionali dal principio di Hamilton. *Rend. Circ. Mat. Palermo*, 43:203, 1919.

[285] A. Palatini. Invariant deduction of the gravitational equations from the principle of Hamilton. In P. G. Bergmann and V. De Sabbata, editors, *Cosmology and Gravita-*

*tion: Spin, Torsion, Rotation, and Supergravity*, page 477. Plenum Press, New York, 1980. [English translation].

[286] R. Parentani and T. Piran. The internal geometry of an evaporating black hole. *Phys. Rev. Lett.*, 73:2805, 1994.

[287] L. Parker. Quantized fields and particle creation in expanding universes. I. *Phys. Rev.*, 183:1057, 1969.

[288] L. Parker. Quantized fields and particle creation in expanding universes. II. *Phys. Rev. D*, 3:346, 1971.

[289] L. E. Parker. *The Creation of particles in an expanding universe.* PhD thesis, Harvard University, 1966. [Remastered version by A. Ferreiro, J. Navarro-Salas, and S. Pla, available as preprint arXiv:2507.05372].

[290] L. E. Parker and S. A. Fulling. Adiabatic regularization of the energy-momentum tensor of a quantized field in homogeneous spaces. *Phys. Rev. D*, 9:341, 1974.

[291] L. E. Parker and J. Navarro-Salas. Fifty years of cosmological particle creation, 2017. [Interview with L. Parker at the ERE 2014 conference in Valencia, Spain. Published as preprint arXiv:1702.07132].

[292] L. E. Parker and J. Z. Simon. Einstein equation with quantum corrections reduced to second order. *Phys. Rev. D*, 47:1339, 1993.

[293] L. E. Parker and D. Toms. *Quantum Field Theory in Curved Spacetime: Quantized Fields and Gravity.* Cambridge Monographs on Mathematical Physics. Cambridge University Press, 2009.

[294] R. K. Pathria and P. D. Beale. *Statistical Mechanics.* Elsevier, Amsterdam; Boston, 2011.

[295] T. Pătuleanu, A. D. Fodor, V. E. Ambruş, and C. Crucean. Dirac fermions under imaginary rotation. *Phys. Rev. D*, 111:116004, 2025.

[296] W. Pauli and F. Villars. On the invariant regularization in relativistic quantum theory. *Rev. Mod. Phys.*, 21:434, 1949.

[297] R. Penrose and R. M. Floyd. Extraction of rotational energy from a black hole. *Nature*, 229:177, 1971.

[298] S. Perlmutter, G. Aldering, G. Goldhaber, R. A. Knop, P. Nugent, P. G. Castro, S. Deustua, S. Fabbro, A. Goobar, D. E. Groom, I. M. Hook, A. G. Kim, M. Y. Kim, J. C. Lee, N. J. Nunes, R. Pain, C. R. Pennypacker, R. Quimby, C. Lidman, R. S. Ellis, M. Irwin, R. G. McMahon, P. Ruiz-Lapuente, N. Walton, B. Schaefer, B. J. Boyle, A. V. Filippenko, T. Matheson, A. S. Fruchter, N. Panagia, H. J. M. Newberg, W. J. Couch, and The Supernova Cosmology Project. Measurements of $\Omega$ and $\Lambda$ from 42 high-redshift supernovae. *Astrophys. J.*, 517:565, 1999.

[299] M. E. Peskin and D. V. Schroeder. *An Introduction to Quantum Field Theory.* Addison-Wesley, Reading, USA, 1995.

[300] N. Pinamonti. On the initial conditions and solutions of the semiclassical Einstein equations in a cosmological scenario. *Commun. Math. Phys.*, 305:563, 2011.

[301] N. Pinamonti and D. Siemssen. Global existence of solutions of the semiclassical Einstein equation for cosmological spacetimes. *Commun. Math. Phys.*, 334:171, 2015.

[302] J. P. M. Pitelli, B. S. Felipe, C. Dappiaggi, and E. Winstanley. Quantum superposition of boundary conditions in PAdS2. *Phys. Rev. D*, 111:125011, 2025.

[303] J. P. M. Pitelli, B. S. Felipe, and R. A. Mosna. Unruh-DeWitt detector in AdS2. *Phys. Rev. D*, 104:045008, 2021.

[304] Max Planck. Über das Gesetz der Energieverteilung im Normalspectrum [On the law of distribution of energy in the normal spectrum]. *Ann. Phys. (Berlin)*, 309:553, 1901.

[305] E. Poisson, A. Pound, and I. Vega. The motion of point particles in curved spacetime. *Living Reviews in Relativity*, 14:7, 2011.

[306] J. Polchinski. *String Theory: Volume 1, An Introduction to the Bosonic String*. Cambridge Monographs on Mathematical Physics. Cambridge University Press, 1998.

[307] J. Polchinski. *String Theory: Volume 2, Superstring Theory and Beyond*. Cambridge Monographs on Mathematical Physics. Cambridge University Press, 1998.

[308] M. J. Radzikowski. Micro-local approach to the Hadamard condition in quantum field theory on curved space-time. *Commun. Math. Phys.*, 179:529, 1996.

[309] K.-H. Rehren. A proof of the AdS / CFT correspondence. In H.-D. Doebner, editor, *1st International Symposium on Quantum Theory and Symmetries*, page 278. World Scientific, 1999.

[310] K.-H. Rehren. Algebraic holography. *Ann. Henri Poincaré*, 1:607–623, 2000.

[311] K. Rejzner. *Perturbative Algebraic Quantum Field Theory: An Introduction for Mathematicians*. Mathematical Physics Studies. Springer, New York, 2016.

[312] M. Reuter. Nonperturbative evolution equation for quantum gravity. *Phys. Rev. D*, 57:971, 1998.

[313] A. G. Riess, A. V. Filippenko, P. Challis, A. Clocchiatti, A. Diercks, P. M. Garnavich, R. L. Gilliland, C. J. Hogan, S. Jha, R. P. Kirshner, B. Leibundgut, M. M. Phillips, D. Reiss, B. P. Schmidt, R. A. Schommer, R. C. Smith, J. Spyromilio, C. Stubbs, N. B. Suntzeff, and J. Tonry. Observational evidence from supernovae for an accelerating universe and a cosmological constant. *Astron. J.*, 116:1009, 1998.

[314] W. Rindler. *Essential Relativity: Special, General, and Cosmological.* Springer, New York, 1977.

[315] G. Rizzi and M. L. Ruggiero. Space geometry of rotating platforms: An operational approach. *Foundations of Physics*, 32:1525, 2002.

[316] H. P. Robertson. Kinematics and world-structure. *Astrophys. J.*, 82:284, 1935.

[317] H. P. Robertson. Kinematics and world-structure II. *Astrophys. J.*, 83:187, 1936.

[318] H. P. Robertson. Kinematics and world-structure III. *Astrophys. J.*, 83:257, 1936.

[319] P. Romatschke. Relativistic (lattice) Boltzmann equation with nonideal equation of state. *Phys. Rev. D*, 85:065012, 2012.

[320] T. Rothman and S. Boughn. Can gravitons be detected? *Found. Phys.*, 36:1801, 2006.

[321] C. Rovelli. Notes for a brief history of quantum gravity. In V. G. Gurzadyan, R. T. Jantzen, and R. Ruffini, editors, *9th Marcel Grossmann Meeting on Recent Developments in Theoretical and Experimental General Relativity, Gravitation and Relativistic Field Theories (MG 9)*, page 742. World Scientific, 2000.

[322] C. Rovelli. *Quantum Gravity.* Cambridge Monographs on Mathematical Physics. Cambridge University Press, 2004.

[323] C. Rovelli and L. Smolin. Knot theory and quantum gravity. *Phys. Rev. Lett.*, 61:1155, 1988.

[324] C. Rovelli and L. Smolin. Loop space representation of quantum general relativity. *Nucl. Phys. B*, 331:80, 1990.

[325] C. Rovelli and F. Vidotto. *Covariant Loop Quantum Gravity: An Elementary Introduction to Quantum Gravity and Spinfoam Theory.* Cambridge University Press, 2014.

[326] K. Sanders. Static symmetric solutions of the semi-classical Einstein–Klein–Gordon system. *Ann. Henri Poincaré*, 23:1321, 2022.

[327] L. I. Schiff. *Quantum Mechanics.* McGraw-Hill, 1968.

[328] C. Schomblond and P. Spindel. Unicity conditions of the scalar field propagator $\Delta^{(1)}(x, y)$ in de Sitter universe. *Ann. Inst. H. Poincaré Phys. Theor.*, 25:67, 1976.

[329] E. Schrödinger. Quantisierung als Eigenwertproblem [Quantisation as an eigenvalue problem]. *Ann. Phys.*, 384:361, 1926.

[330] M. D. Schwartz. *Quantum Field Theory and the Standard Model.* Cambridge University Press, Cambridge, 2014.

[331] J. Schwinger. On gauge invariance and vacuum polarization. *Phys. Rev.*, 82:664, 1951.

[332] R. U. Sexl and H. K. Urbantke. Production of particles by gravitational fields. *Phys. Rev.*, 179:1247, 1969.

[333] R. Shankar. *Principles of Quantum Mechanics.* Springer, 2012.

[334] K. Shiraishi and T. Maki. Quantum fluctuation of stress tensor and black holes in three dimensions. *Phys. Rev. D*, 49:5286, 1994.

[335] J. Z. Simon. Higher derivative Lagrangians, nonlocality, problems and solutions. *Phys. Rev. D*, 41:3720, 1990.

[336] L. Smolin. *The Trouble with Physics: The Rise of String Theory, the Fall of a Science, and What Comes Next.* Houghton Mifflin Harcourt, 2006.

[337] R. D. Sorkin. Forks in the road, on the way to quantum gravity. *Int. J. Theor. Phys.*, 36:2759, 1997.

[338] M. Srednicki. *Quantum Field Theory.* Cambridge University Press, Cambridge, 2007.

[339] A. A. Starobinskii. Amplification of waves during reflection from a rotating "black hole". *Sov. Phys. JETP*, 37:28, 1973.

[340] A. R. Steif. Quantum stress tensor in the three-dimensional black hole. *Phys. Rev. D*, 49:R585, 1994.

[341] H. Stephani. *Relativity: An Introduction to Special and General Relativity.* Cambridge University Press, 2004.

[342] W. A. Strauss. *Partial Differential Equations: An Introduction.* John Wiley & Sons, 2007.

[343] R.F. Streater and A.S. Wightman. *PCT, spin and statistics, and all that.* The mathematical physics monograph series. W.A. Benjamin, New York, 1964.

[344] W.-M. Suen. The stability of the semiclassical Einstein equation. *Phys. Rev. D*, 40:315, 1989.

[345] S. Surya. The causal set approach to quantum gravity. *Living Rev. Relativ.*, 22, 2019.

[346] L. Susskind. Structure of hadrons implied by duality. *Phys. Rev. D*, 1:1182, 1970.

[347] J. L. Synge. *Relativity: The General Theory.* Series in Physics. North-Holland Pub. Co.; Interscience Publishers, Amsterdam; New York, 1960.

[348] G. 't Hooft and M. J. G. Veltman. Regularization and renormalization of gauge fields. *Nucl. Phys. B*, 44:189, 1972.

[349] S. Tadaki. Stress tensor in de Sitter space. *Prog. Theor. Phys.*, 80:654, 1988.

[350] P. Taylor and C. Breen. Semiclassical backreaction on asymptotically anti–de Sitter black holes. *Phys. Rev. D*, 103:025006, 2021.

[351] P. Taylor, C. Breen, and A. Ottewill. Mode-sum prescription for the renormalized stress energy tensor on black hole spacetimes. *Phys. Rev. D*, 106:065023, 2022.

[352] T. Thiemann. *Modern Canonical Quantum General Relativity.* Cambridge University Press, 2007.

[353] J. C. Thompson and E. Winstanley. Quantum-corrected anti–de Sitter spacetime. *Phys. Rev. D*, 110:125003, 2024.

[354] J. C. Thompson and E. Winstanley. Quantum-corrected three-dimensional AdS space-time. In *24th International Conference on General Relativity and Gravitation (GR24) and 16th Edoardo Amaldi Conference on Gravitational (Amaldi16) Waves*, 2025.

[355] J. C. Thompson and E. Winstanley. Quantum effects in rotating thermal states on anti-de Sitter space-time. *Phys. Lett. B*, 868:139780, 2025.

[356] M. Thomson. *Modern particle physics.* Cambridge University Press, New York, 2013.

[357] R. C. Tolman. On the weight of heat and thermal equilibrium in general relativity. *Phys. Rev.*, 35:904, 1930.

[358] R. C. Tolman. Static solutions of Einstein's field equations for spheres of fluid. *Phys. Rev.*, 55:364, 1939.

[359] R. C. Tolman and P. Ehrenfest. Temperature equilibrium in a static gravitational field. *Phys. Rev.*, 36:1791, 1930.

[360] W. G. Unruh. Second quantization in the Kerr metric. *Phys. Rev. D*, 10:3194, 1974.

[361] W. G. Unruh. Notes on black-hole evaporation. *Phys. Rev. D*, 14:870, 1976.

[362] H. K. Urbantke. Remark on noninvariance groups and field quantization in curved space. *Nuovo Cim. B*, 63:203, 1969.

[363] P. Ván and T. S. Biró. Dissipation flow-frames: particle, energy, thermometer. In M. Pilotelli and G. P. Beretta, editors, *12th Joint European Thermodynamics Conference*. Cartolibreria Snoopy, 2013.

[364] B. L. van der Waerden, editor. *Sources of Quantum Mechanics*. North-Holland Publishing Company, Amsterdam, 1967. Contains English translations of the 1925–1926 papers by Heisenberg, Born, and Jordan.

[365] J. H. Van Vleck. The correspondence principle in the statistical interpretation of quantum mechanics. *Proc. Nat. Acad. Sci.*, 14:178, 1928.

[366] G. Veneziano. Construction of a crossing-symmetric, Regge-behaved amplitude for linearly rising trajectories. *Nuovo Cim. A*, 57:190, 1968.

[367] M. Visser. van Vleck determinants: Geodesic focusing in Lorentzian spacetimes. *Phys. Rev. D*, 47:2395, 1993.

[368] A. Voss. Zur Theorie der Transformation quadratischer Differentialausdrücke und der Krümmung höherer Mannigfaltigketien [On the theory of the transformation of quadratic differential expressions and the curvature of higher manifolds]. *Math. Ann.*, 16:129, 1880.

[369] R. M. Wald. The back reaction effect in particle creation in curved space-time. *Commun. Math. Phys.*, 54:1, 1977.

[370] R. M. Wald. Axiomatic renormalization of the stress tensor of a conformally invariant field in conformally flat spacetimes. *Ann. Phys.*, 110:472, 1978.

[371] R. M. Wald. Trace anomaly of a conformally invariant quantum field in curved space-time. *Phys. Rev. D*, 17:1477, 1978.

[372] R. M. Wald. Dynamics in nonglobally hyberbolic, static space-times. *J. Math. Phys.*, 21:2802, 1980.

[373] R. M. Wald. *General Relativity.* Chicago Univ. Pr., Chicago, USA, 1984.

[374] R. M. Wald. *Quantum field theory in curved spacetime and black hole thermodynamics.* Chicago lectures in physics. University of Chicago Press, Chicago, 1994.

[375] A. G. Walker. On Milne's theory of world-structure. *Proc. Lond. Math. Soc.*, s2-42:90, 1937.

[376] S. Weinberg. Critical Phenomena for Field Theorists. In A. Zichichi, editor, *Understanding the Fundamental Constitutents of Matter*, page 1. Springer US, 1976.

[377] S. Weinberg. *The Quantum Theory of Fields, Volume 1: Foundations.* Cambridge University Press, Cambridge, UK, 2005.

[378] S. Weinberg. *Cosmology.* Oxford University Press, Oxford, UK, 2008.

[379] U. Weiss. *Quantum Dissipative Systems.* World Scientific, 2021.

[380] J. A. Wheeler and K. Ford. *Geons, Black Holes, and Quantum Foam: A Life in Physics.* W. W. Norton, 2010.

[381] E. T. Whittaker and G. N. Watson. *A Course of Modern Analysis.* Cambridge Mathematical Library. Cambridge University Press, 1996.

[382] E. H. Wichmann and J. H. Crichton. Cluster decomposition properties of the $S$ matrix. *Phys. Rev.*, 132:2788, 1963.

[383] G. C. Wick. The evaluation of the collision matrix. *Phys. Rev.*, 80:268, 1950.

[384] A. S. Wightman. Quantum field theory in terms of vacuum expectation values. *Phys. Rev.*, 101:860, 1956.

[385] A. S. Wightman and L. Gårding. Fields as operator-valued distributions in relativistic quantum theory. *Arkiv för Fysik*, 28:129, 1964.

[386] E. Witten. Anti de Sitter space and holography. *Adv. Theor. Math. Phys.*, 2:253, 1998.

[387] P. Woit. *Not Even Wrong: The Failure of String Theory and the Search for Unity in Physical Law.* Basic Books, 2006.

[388] M. C. M. Wright. Green function or Green's function? *Nature Physics*, 2:646, 2006.

[389] J. W. York, Jr. Role of conformal three geometry in the dynamics of gravitation. *Phys. Rev. Lett.*, 28:1082, 1972.

[390] A. Zee. *Quantum Field Theory in a Nutshell.* Princeton University Press, Princeton, NJ, 2010.

[391] Y. B. Zel'Dovich. Particle production in cosmology. *Pisma Zh. Eksp. Teor. Fiz.*, 12:307, 1970.

[392] Y. B. Zel'Dovich. Generation of waves by a rotating body. *Sov. J. Exp. Theor. Phys. Lett.*, 14:180, 1971.

[393] Y. B. Zel'Dovich and A. A. Starobinsky. Particle production and vacuum polarization in an anisotropic gravitational field. *Sov. Phys. JETP*, 34:1159, 1972.

[394] B. Zwiebach. *A First Course in String Theory.* Cambridge University Press, 2009.